Roles of TRIM24 in macrophage activation and experimental visceral leishmaniasis

Edward William Muscutt

Doctor of Philosophy (PhD)

The University of Hull and The University of York
Hull York Medical School

February 2024

Abstract

Visceral leishmaniasis (VL) causes immune and haematological dysfunction and is fatal in >95% of cases if left untreated. While macrophages are vital for efficient *Leishmania* parasite clearance, parasite-macrophage interactions are critical for VL progression. The transcription factor tripartite motif protein 24 (TRIM24) was recently predicted to be downregulated in an experimental VL mouse model. However, roles of TRIM24 in macrophage activation remain poorly understood, and have not been explored in VL. Here, we use TRIM24 knockout (KO) C57BL/6 mice to investigate roles of TRIM24 in bone marrow-derived macrophage (BMDM) activation *in vitro*, and the effects of TRIM24 deletion in an experimental model of VL *in vivo* using a combination of microscopy, flow cytometry, and single cell RNA sequencing (scRNA-seq).

Firstly, we show that TNF and IL-6 production in KO BMDMs is unaffected after TLR4 stimulation. However, more nitric oxide was released by KO BMDMs, attributed to higher iNOS expression. Accompanying increases in IFNβ release and interferon response-related transcriptional signatures indicated an increased propensity for KO BMDMs to produce and respond to interferons. Uptake of *L. donovani* amastigotes was unaffected in KO BMDMs. ScRNA-seq of *L. donovani*-infected BMDMs revealed a metabolic shift in KO BMDMs towards parasite-permissive oxidative phosphorylation, while also potentiating interferon responses.

Flow cytometric analysis of total KO lymphoid organs revealed the dispensability of TRIM24 during homeostatic leukocyte development. However, assessment of relative fitness during 50:50 mixed bone marrow (BM) chimeric reconstitution revealed an advantage of KO leukocytes in lymphoid organs, with 80% of BM $CD45^+$ cells deficient in TRIM24 at 10 weeks post-reconstitution. *L. donovani* infection reduced this skew in spleen and liver but not in BM, identifying a potential role for TRIM24 in BM retention that persists during infection independently of the CXCR4-CXCL12 axis. Immune responses characteristic of VL were unaffected by TRIM24 deletion (IFNγ, TNF, IL-10, IL-6 production, granuloma size and number, Kupffer cell iNOS expression), and hepatic parasite burden was slightly increased. Elevated mRNA abundance of interferon-stimulated genes was observed in KO spleen 24 hours post-infection.

Finally, we used scRNA-seq to report a transcriptional landscape of *L. donovani*-infected WT murine BM, providing evidence for an emergency myelopoiesis-promoting environment. Haematopoietic stem and progenitor cells were directly responding to $CD4^+$ T cell-derived IFNγ, and we identify $CD4^+$ T cells as a major source of *Csf1* during infection. *Ccl5* was expressed by several cell types, and parasite-permissive metabolic shifts were also observed, all contributing factors to myelopoiesis. These metabolic shifts were exacerbated by TRIM24 deletion, probably through modulation of mTOR signalling. This data therefore provides an interesting avenue for future investigation of TRIM24 in immunometabolism.

Table of Contents

List of Figures

List of Tables

Acknowledgements

Firstly, I would like to extend my gratitude to my supervisors, Prof. Paul M. Kaye and Dr Elmarie Myburgh, for their support throughout my PhD. They have given me the opportunity to work in an interesting field and have allowed me to grow as a scientist through exposure to many advanced lab techniques. I am also grateful to them for their guidance working through the challenges presented to my project during the COVID-19 pandemic. Elmarie was also instrumental in training me in many lab techniques including cell culture and IVIS imaging, which were core parts of my project. I would also like to express my gratitude to my thesis advisory panel members, Prof. Ian Hitchcock, Prof. Simon Hart, and Dr Francisco Rivero for their advice during my TAP meetings.

I would like to thank Hull York Medical School for their financial support, and in particular Elaine Brookes, who was always available for assistance.

My lab members were invaluable to the generation of data presented in this thesis, and it would not have been possible without their support. In particular, I would like to thank Dr Najmeeyah Brown for always being available to assist with experiments and for answering my endless questions about the lab when I started. I could not have progressed without her constant collaboration, technical support, and for taking over the time consuming job of mouse genotyping!
Dr Helen Ashwin was instrumental in her training and assistance with large *in vivo* experiments, and for her knowledge of histological techniques, microscopy, and image analysis. Dr Marcela Montes de Oca guided me through the ropes of multi-parameter flow cytometry, and was always happy to discuss data results or just to chat. As bioinformatics unexpectedly became a large portion of this thesis, I am extremely indebted to Dr Shoumit Dey for all his assistance teaching me the basics of transcriptomic data analysis using R.
I would like to acknowledge all other current and past members of the lab, Dr. Katrien Van Bocxlaer, Dr. Mohamed Osman, Dr. Nidhi Dey, Dr Gulab Rani, Damian Perez Mazliah, for being a great team to work with and providing valuable contributions and ideas when I presented data to them. I also would like to acknowledge Sergios Antoniou for being a great friend throughout my PhD and being my sounding board during the stressful times.

I would like to thank the staff in the York Technology Facility for their help training me in many techniques used in this thesis. In particular, Karen Hogg and Graeme Park were an endless pool of flow cytometry knowledge which I was able to tap into many times. Their

assistance with designing flow cytometry panels was extremely valuable. Dr Sally James and Dr Lesley Gilbert were extremely helpful and flexible when planning our large transcriptomics experiments, and were essential in sample preparation. I would also like to thank the bioinformatics team for assisting with transcriptomic data analysis.

Similarly, I would like to thank the members of Biological Services Facility for all their support for *in vivo* experiments and maintenance of our knockout mouse colony. In particular, Chris Turnbull was extremely helpful when I started *in vivo* work, training me in core *in vivo* techniques and in mouse colony management.

I would like to thank my family for their support and encouragement, and for putting up with me during the gruelling write up period. Lastly, I would like to thank my fiancée, Anjuli, who has been my rock throughout the whole process. You believe in me when I don't believe in myself.

Author's Declaration

I confirm that this work is original and that if any passage(s) or diagram(s) have been copied from academic papers, books, the internet, or any other sources these are clearly identified by the use of quotation marks and the reference(s) is fully cited. I certify that, other than where indicated, this is my own work and does not breach the regulations of HYMS, the University of Hull or the University of York regarding plagiarism or academic conduct in examinations. I have read the HYMS Code of Practice on Academic Misconduct, and state that this piece of work is my own and does not contain any unacknowledged work from any other sources.

COVID-19 Statement

A major part of my research project is based on *in vivo* work, working with TRIM24 knockout mice to investigate visceral leishmaniasis. The restrictions brought about by the COVID-19 pandemic were a major delay and obstruction to my work, as both the lab and the Biological Services Facility (BSF) were shut down for ~6 months during lockdown. This heavily impacted and delayed wet lab work, *in vivo* work and delayed the arrival of the TRIM24 knockout mice to York. Important pilot studies were delayed, therefore important data acquisition influential to my project was delayed. The continued restrictions after lab re-opening further impacted lab work. Social distancing and inability to work in pairs/groups severely slowed training of new techniques (particularly *in vivo* techniques) important for my project. Plans to mitigate the effects of the COVID-19 restriction resulted in heavier use of transcriptomic and bioinformatic analysis which forms a significant part of this thesis.

Chapter 1. General Introduction

1.1. Macrophages

1.1.1. Macrophages and the Mononuclear Phagocyte System

Macrophages were first described in 1882 by Elie Metchnikoff, who identified phagocytic cells that were recruited to sites of inflammation and infection, where they actively take up and destroy bacteria such as *Cholera vibrio*, *Bacillus pyocyaneum*, and *Mycobacterium*, as well as host cells (e.g. erythrocytes) (Gordon 2008). Perhaps the most successful description of macrophages is the mononuclear phagocyte system (MPS), a term originally used to encompass monocytes, macrophages, and their precursors derived in the bone marrow, based on thymidine-^{3}H incorporation assays (van Furth & Cohn 1968; van Furth et al. 1972). The definitions of MPS cells have since been updated to include DCs (Guilliams et al. 2014). The MPS has a diverse range of roles that are vital in protecting the body from infection and maintaining tissue homeostasis, and as such is implicated in a vast number of diseases, ranging from infection (e.g. leishmaniasis and tuberculosis), autoimmune disease (e.g. rheumatoid arthritis), and cancer (Guirado et al. 2013; Bogdan 2020; Edilova et al. 2021; Duan & Luo 2021). High phagocytic activity, response to cytokine and chemokine signals to quickly migrate towards sites of inflammation or infection, release of chemokines and cytokines, and presentation of antigens on the surface of their membrane are all characteristics of MPS cells. DCs are more specialised for antigen presentation to activate naive T cells, whereas macrophages possess higher phagocytic and pathogen killing capability, thus are classed as “professional phagocytes” (Cabeza-Cabrerizo et al. 2021; Sreejit et al. 2020). Despite this nomenclature defining macrophages based on their phagocytic capacity, macrophages possess a spectrum of functions, ranging from wound healing and tissue repair to removal of foreign bodies. Macrophage phenotypes can also vastly differ depending on tissue environment, with tissue-specific macrophages playing vital roles in tissue homeostasis (Wynn et al. 2013).

1.1.2. Macrophage Origins

It has long been known that macrophages can differentiate from circulating blood monocytes, which originate from bone marrow myeloid precursor cells as described by van Furth et al. (van Furth et al. 1972). Mature monocytes are released from the bone marrow

into the circulation where they detect and respond to cytokine/chemokine signals and other environmental cues to differentiate into macrophages (Wynn et al. 2013). However, it is now understood that the embryonic yolk sac and foetal liver are sources of macrophages during embryonic development, and haematopoiesis during development occurs in "waves". These are highlighted in **Figure 1.1**. The first wave is referred to as "primitive hematopoiesis", and occurs in the embryonic yolk sac.

Palis et al. used a combination of colony formation assays and mRNA abundance determination to show the presence of erythroid and macrophage progenitors (EMPs) in the yolk sac at embryonic day 7 (E7) and E7.5, respectively, prior to foetal liver development in Swiss Webster mice (Palis et al. 1999; Naito et al. 1989). These EMPs developed independently of c-Myb expression (a key transcription factor in HSC maintenance), and express the myeloid-specific colony stimulating factor 1 receptor (CSF1R) and CD41 markers (Palis et al. 1999; Gomez Perdiguero et al. 2015). Takahashi et al. also observed that primitive macrophages matured without detecting any peroxidase activity (used as an indication of the presence of monocyte intermediates), therefore indicating that primitive macrophages were not differentiating via monocytes (Takahashi et al. 1989).

As the embryonic circulatory system develops (~E8.5) (McGrath et al. 2003), these haematopoietic precursor cells are no longer trapped in yolk sac blood islands, and therefore are mobilised and colonise the foetal liver, which becomes the next primary site of haematopoiesis, so-called "transient definitive" haematopoiesis (Palis et al. 1999; Palis et al. 2001). Here, c-Myb$^+$ CSFR1$^+$ myeloid progenitor cells are generated, which give rise to foetal monocytes and eventually migrate and differentiate into tissue resident macrophages (Hoeffel et al. 2015). For example, primitive macrophages have been shown to colonise the foetal brain, where they retain their high self-renewal potential and maintain the pool of microglia throughout adult life (Alliot et al. 1999). This has been confirmed more recently using fate-mapping experiments reconstituting newborn CD45.2$^+$ B6 mice with haematopoietic cells derived from CD45.1$^+$ donor mice, and revealing that 95% of microglia were of host origin 3 months post-reconstitution (Ginhoux et al. 2010). Furthermore, similar results have been observed in the skin (Langerhans cells) (Hoeffel et al. 2012), liver (Kupffer cells; KCs) (Scott et al. 2016), and lungs (alveolar macrophages) (Gomez Perdiguero et al. 2015). Thus, tissue resident macrophages appear to be of embryonic origin, and possess the ability to self-renew thereby maintaining the tissue resident macrophage pool. Monocyte-derived macrophages are still important for some tissues, however, as evidenced by the contribution of circulating monocytes in maintaining the pool of intestinal macrophages (Bain et al. 2014).

Haematopoietic stem cells (HSCs) begin to emerge and rapidly engraft in the foetal liver from E10.5, leading to the development of foetal monocytes with capacity to differentiate into

macrophages, marking the start of “definitive haematopoiesis” (Bertrand et al. 2005; Hoeffel et al. 2015). Shortly before birth (~E16.5), myeloid progenitors differentiating from HSCs in the foetal liver, umbilical and placental regions, are taken over by the bone marrow and give rise to monocytes through several intermediate steps, marking the haematopoietic system that persists through adulthood (Mikkola et al. 2005; Kieusseian et al. 2012; Coskun et al. 2014).

Although there is also heterogeneity observed in monocyte populations, highlighted by recent bioinformatics focused studies on the monocyte transcriptomes (Trzebanski et al. 2023; Mildner et al. 2017), monocytes are most commonly split into two major subsets that are defined by their expression of Ly6C, CCR2 and CX3CR1 (Geissmann et al. 2003; Mildner et al. 2017). CX3CR1^{-} Ly6C^{hi} CCR2^{+} monocytes are classed as “classical” and are inflammatory in nature, and CX3CR1^{+} Ly6C^{lo} CCR2^{-} monocytes are classed as “non-classical” (Geissmann et al. 2003). Monocytes exit the bone marrow into the peripheral circulation via CCR2 signalling. CCR2 was shown to be vital for this process by Serbina and Pamer, who showed *Ccr2*$^{-/-}$ mice to have significantly fewer circulating Ly6C^{hi} monocytes after infection with *Listeria monocytogenes*, and instead found Ly6C^{hi} monocytes to accumulate in the bone marrow (Serbina & Pamer 2006). Monocytes are short-lived in the circulation (~20 hours (Yona et al. 2013)), and migrate into tissue where they differentiate into macrophages to either maintain pools of tissue resident macrophage populations, or extravasate in response to damage-associated molecular patterns (DAMPs) or pathogen-associated molecular patterns (PAMPs) to assist in host immune response or tissue remodelling and repair.

1.1.3. Macrophage Development

Macrophages exhibit heterogeneous phenotypes as they are shaped by specific tissue environments, epigenetic programming and transcription factor (TF) expression. Despite this broad spectrum of heterogeneity among differing tissue resident macrophages, there is a core transcriptional landscape common to all macrophages, indicating the importance for lineage-specific TFs in shaping macrophage precursor development (**Figure 1.2**).

PU.1 is a key TF in the macrophage lineage commitment, regulated by RUNX1/AML1 (Huang et al. 2008). PU.1 is a TF belonging to the ETS family which plays an important role in the development of many haematopoietic cells, including macrophages, B cells, dendritic cells, and neutrophils (Zhang et al. 1994; Celada et al. 1996; Wang et al. 2019; Carotta et al. 2010; Watt et al. 2021). Genetic deficiency of PU.1 is embryonic lethal at ~E18.5, so PU.1 is seen as an essential TF (Polli et al. 2005). PU.1 was found to interact with and activate the

promoter of the M-CSF receptor gene in monocytes and myeloid progenitor cells. Abrogation of PU.1 signalling via mutation severely inhibited the activity of the M-CSF receptor promoter and led to an inhibition in macrophage development (Zhang et al. 1994). PU.1 expression is also important for B cell development as well as macrophages, and a later study showed abundance of PU.1 is important in the balance between macrophage and B cell development. A low level of PU.1 expression favoured B cell development, whereas higher abundances of PU.1 favoured macrophage development and simultaneously inhibited B cell development (DeKoter & Singh 2000). Furthermore, PU.1 is also involved in chromatin remodeling and enhancer activity (van Riel & Rosenbauer 2014; Minderjahn et al. 2020), and can interact with other TFs such as c-Jun to enhance its promoter activating function (Behre et al. 1999).

GATA-1 is another TF that is important in lineage commitment of HSCs to the myeloerythroid lineage, as it together with PU.1 drives differentiation of HSCs to common myeloid progenitors (CMPs) (Arinobu et al. 2007). However, expression of GATA-1 beyond this causes a bias towards the erythroid lineage and megakaryocyte development (Zhu & Emerson 2002). Several other TFs play important roles in macrophage differentiation, such as C/EBPα (Yeamans et al. 2007), C/EBPβ (Mildner et al. 2017; Tamura et al. 2017), EGR1 (Krishnaraju et al. 2001), interferon regulatory factor 5 (IRF5) (Barnes et al. 2020), IRF8 (Tamura et al. 2015), and KLF4 (Kurotaki et al. 2013).

Macrophage phenotypes are further shaped by tissue-specific expression of TFs, leading to highly specialised tissue-resident macrophage populations (**Table 1.1**). For example, splenic red pulp macrophages express high levels of SPIC which plays important roles in shaping the red pulp macrophage functions of senescent erythrocyte recycling. Kohyama et al. explored this, showing a significant enrichment of SPIC expression in red pulp macrophages ($F4/80^{hi}$ $CD68^{+}$ $CD11b^{-}$) compared to other leukocytes, and deletion of SPIC led to a specific loss of red pulp macrophages (Kohyama et al. 2009). Furthermore, while the accumulation of trapped erythrocytes was unaffected by *Spic* deletion in 129/SvEv mice, $Spic^{-/-}$ red pulp macrophages failed to efficiently phagocytose these erythrocytes, leading to a build up of iron stores as shown by splenic Perl's Prussian Blue staining (Kohyama et al. 2009).

In Kupffer cells, ID3 (a TGFβ-regulated TF (Strong et al. 2013)) has been shown to play a role in development, with Mass et al. demonstrating a significant reduction of Kupffer cell precursors during embryogenesis in *Id3*-deficient B6 mice, which persisted into adulthood leading to impairment of Kupffer cell development (Mass et al. 2016).

Macrophage development is also reliant on growth factor signals in the surrounding tissue environment (**Figure 1.2**). Colony stimulating factor 1 (also known as macrophage colony

stimulating factor, M-CSF) is perhaps the most important growth factor for macrophage development. M-CSF is indispensable for macrophage maturation. Mice that possess the *osteopetrosis* mutation have a naturally-occurring frameshift mutation in both *Csf1* alleles that renders the gene inactive (Yoshida et al. 1990; Wiktor-Jedrzejczak et al. 1990). These $CSF^{op/op}$ mice are deficient in tissue macrophage populations, and have defects in bone remodelling leading to decreased body weight (Wiktor-Jedrzejczak et al. 1982). Implantation of diffusion chambers containing L929 fibroblast cells that constitutively produce M-CSF led to partial recovery of the severe macrophage deficiency (Wiktor-Jedrzejczak et al. 1990), and injections of M-CSF in osteopetrotic mice effectively cured them of histological abnormalities (Kodama et al. 1991). Interestingly, mice deficient in *Csf1r* had even more severe defects than osteopetrotic mice (Dai et al. 2002), indicating that the other known CSF1R ligand, IL-34 (Ma et al. 2012), also plays an important role in macrophage development.

Small molecule inhibition of CSF1R reduced numbers of $CX3CR1^+$ bone marrow-derived macrophages (BMDMs), $CCR2^+$ monocyte progenitor cells, $CD34^+$ cells, and $CD117^+$ cells (Lei et al. 2020). Furthermore, CSF1R inhibition led to reduced IL-1β expression from BMDMs exposed to LPS, as well as impaired phagocytosis (Lei et al. 2020), indicating a role for M-CSF in the activated phenotypes of macrophages.

1.1.4. Macrophage Activation

Due to their importance in developing and resolving the immune response, the activation of macrophages has been extensively studied. From early studies, two main activated macrophage subtypes emerged: M1 (or classically activated; CAM) and M2 (or alternatively activated; AAM) (Mosser & Zhang 2008; Mosser & Edwards 2008). These polarisation phenotypes are critically dependent on several TFs that play non-redundant roles in respective CAM/AAM polarisation. However, analysing almost 300 human macrophage transcriptomes representative of different types of stimulation, Xue et al. demonstrated that phenotypes of activated macrophages are much more accurately described as a spectrum, with the CAM and AAM subtypes representing the inflammatory and immunoregulatory extremes at either end (Xue et al. 2014).

1.1.4.1 Classically activated macrophages (CAMs)

Classically activated (inflammatory) macrophages are core inflammatory cells in the innate immune response, and are a first line of defence before the involvement of the adaptive response. Inflammatory macrophages are typically polarised *in vitro* by priming with IFNγ,

which activates the JAK/STAT1 signalling cascade. Following this, a second signal is required in the form of stimulation of pattern recognition receptors (PRRs) during detection and phagocytosis of foreign material (Plüddemann et al. 2011) & **Figure 1.3**). The most well known PRRs are Toll-like receptors, of which there are 12 in mice and ten in humans. Lipopolysaccharide (LPS, endotoxin), which is a component of the outer membrane of Gram-negative bacteria, and a ligand for TLR4 on macrophages (Park & Lee 2013) induces inflammatory macrophage polarisation. Binding of LPS to TLR4 initiates a signalling cascade resulting in activation of the TF NF-kB and subsequent expression of many inflammatory cytokines (**Figure 1.4**).

The TLR4 pathway is divided into the MyD88-dependent and the MyD88 independent (also called the TRIF-dependent) pathways. The MyD88-independent signalling pathway is activated by TLR3 or TLR4 stimulation, and mediates the induction of type I interferons and IFN-inducible genes. This pathway involves the recruitment of TNF receptor associated factor 3 (TRAF3) to TIR domain-containing adapter molecule 1 (TICAM1/TRIF). Studies using TRIF-deficient mice showed significantly impaired expression of IFNβ, CCL5, CXCL10 and CCL2 after injection with the dsRNA TLR3 ligand poly(I:C). Furthermore, TRIF-deficient peritoneal macrophages failed to produce TNF, IL-6, IL-12 after LPS stimulation (Yamamoto et al. 2003). Activation of TRIF causes ubiquitination and activation of TANK-binding kinase 1 (TBK1) and IKKε (Fitzgerald et al. 2003). Activated TBK1 and IKKε phosphorylate the TF IRF3 (Fitzgerald et al. 2003), inducing IRF3 dimerisation (Z. Wang et al. 2016), translocation to the nucleus, and induction of type I interferon (IFNα/β) expression. TLR3 is the only TLR to lack the MyD88 adapter molecule (Zheng et al. 2019), and as such only utilises TRIF and therefore is a stronger inducer of the MyD88-independent pathway compared to TLR4. IRF7 is an even stronger inducer of a type I IFN response than IRF3, the activity of which occurs downstream of IRF3 signalling. Initial TLR stimulation leads to IRF3 activation and induction of an initial wave of IFNβ production, which signals in an autocrine manner to strongly induce expression of IRF7, which mediates a much more robust second wave of IFN-I production to further induce IFN-I ISG expression (Honda et al. 2005; Honda & Taniguchi 2006).

The MyD88-dependent pathway is largely responsible for the activation of NF-kB. A series of phosphorylation and ubiquitination steps results in the proteasomal degradation of the inhibitory NF-kB protein IkBα, allowing NF-kB to translocate to the nucleus and initiate inflammatory cytokine gene expression. At the steady state, NF-kB is sequestered in the cytoplasm in complex with Inhibitor of kB (IkB) (Beg et al. 1992). After TLR stimulation, MyD88 forms a complex with TIRAP, IRAK1, and IRAK4 (Lin et al. 2010). IRAK1 is

phosphorylated, leading to its release from MyD88 and association with TRAF6, an E3 ubiquitin ligase (Cao et al. 1996). This allows TRAF6 to undergo self-ubiquitination and to conjugate ubiquitin chains onto other signalling molecules that are involved in the activation of a ubiquitin-dependent kinase, TAK1. The activated TAK1 complex (consisting of TAK1, TAB1, TAB2, and TAB3) then phosphorylates IkB kinase (IKK). Activated IKK phosphorylates IkBα, which releases it from complex with NF-kB and subsequently undergoes proteasomal degradation. NF-kB is no longer inhibited by IkBα, and can translocate to the nucleus to induce gene expression of key inflammatory cytokines (IL-6, IL-1β, IL-12, TNF), chemokines (CXCL10, CXCL5, CXCL9, CCL2), and metabolic enzymes important for reactive oxygen and nitrogen species (ROS/RNS) production (iNOS, NAPDH oxidases, cyclooxygenase-2) (Liu et al. 2017).

Production of nitric oxide (NO) and other ROS is a hallmark for CAMs, and is vital for the effective removal of tumour cells and invading pathogens (Stuehr & Nathan 1989; Hibbs et al. 1988). iNOS-deficient mice are susceptible to many bacterial infections, for example *Mycobacterium tuberculosis*, *Listeria monocytogenes* (MacMicking et al. 1997; MacMicking et al. 1995), and *Salmonella enterica* (Alam et al. 2002). NO is also important in controlling infections with SARS-CoV-2 (Akaberi et al. 2020), *Escherichia coli*, *Staphylococcus aureus*, and *Candida albicans* (Ghaffari et al. 2006), and in controlling granulomatous infections such as *Tuberculosis* and visceralising *Leishmania* infections (Scanga et al. 2001; Salguero et al. 2018). This will be discussed in more detail in **Section 1.2.4**.

The activation of the NF-kB pathway is essential for the polarisation of macrophages to an inflammatory phenotype. This is evidenced by peritoneal macrophages from cRel-/- p50-/- double knockout B6 mice showing severe impairment of phagocytosis and bacterial killing, and reduced expression of inflammatory cytokines 3 days post-injection of LPS (Courtine et al. 2012).

Other TFs are also indispensable for the polarisation of CAMs, notably STAT1, which is phosphorylated following stimulation of IFNGR, and translocates to the nucleus where it induces interferon stimulated gene (ISG) expression.

IRF5 is also vital to CAM polarisation, and is involved in the expression of *Il12b* and *Il23a* as well as the repression of *Il10* (Krausgruber et al. 2011; Weiss et al. 2013). GM-CSF differentiated BMDMs have a higher basal expression of IRF5 compared to M-CSF differentiated BMDMs, and mice injected with methylated bovine serum albumin to induce arthritis had macrophages with higher levels of MHCII, iNOS and IRF5, and lower mRNA abundance of regulatory macrophage markers (Weiss et al. 2013). Other work used

chromatin immunoprecipitation to show that IRF5 directly binds to promoters of several inflammatory cytokine genes (*Il12a, Il12b, Il23a*) to promote their expression, and also to *Il10* promoter where it exerts a transcriptional repressor effect. Furthermore, BMDMs from *Irf5*$^{-/-}$ mice produced less IL-12, IL-23, TNF, IL-6, IL-1β, and more IL-10 (Krausgruber et al. 2011).

Although CAMs are important for the innate response to infection, the abundance of inflammatory cytokines they release can lead to tissue damage which could be harmful to the host during, for example, chronic inflammation (Cucak et al. 2014). On the other hand, alternatively activated macrophages possess immunoregulatory phenotypes and act to resolve inflammation to limit excessive tissue damage (Stein et al. 1992).

1.1.4.2 Alternatively activated macrophages (AAMs)

Stein et al. in 1992 demonstrated that Th2 cell-derived IL-4 was a strong activator of CD206 expression and activity on murine peritoneal macrophages, and also reduced production of inflammatory cytokines, in contrast to IFNγ (Stein et al. 1992). In the same year, Geng and Hansson showed that exposure of human monocyte-derived macrophages to IFNγ reduced the expression of scavenger receptors (Geng & Hansson 1992). These IL-4-polarised macrophages were coined alternatively activated macrophages, and lie at the other end of the macrophage polarisation spectrum. AAMs are polarised by IL-4 or IL-13, which share a receptor and lead to similar macrophage phenotypes (Doyle et al. 1994). Because IL-4 and IL-13 share a receptor, there is also some functional redundancy between them. This was shown in 1999 by McKenzie et al., who demonstrated that infection of *Il4*$^{-/-}$ and *Il13*$^{-/-}$ single knockout mice with *Schistosoma mansoni* eggs led to a reduction in the recruitment of eosinophils, IL-10 abundance, and serum IgE and IgG1 levels. However, when using double knockout *Il4*$^{-/-}$ *Il13*$^{-/-}$ mice, these effects were exacerbated, showing almost no serum IgG1 or IgE, more significant reduction in IL-10 abundance, and a significant increase in IFNγ abundance (McKenzie et al. 1999). IL-4 and IL-13 exert their effects through phosphorylation and activation of STAT6, which is critical to the transcriptional induction of AAM marker genes discussed below.

AAMs are characterised by several markers (**Figure 1.4**). They possess high expression levels of scavenger receptors (for example the mannose receptor, CD206), indicating elevated homeostatic endocytic and phagocytic activity of circulating mannose glycoproteins (Lee et al. 2002). CD209 (DC-SIGN) is upregulated by IL-4 stimulation in monocytes (Relloso et al. 2002), and is expressed by several tissue resident macrophage subsets including alveolar and adipose tissue macrophages (Tailleux et al. 2005; Fujisaka et al. 2011).

Arginase-1 is another marker of AAMs, and is involved in the metabolism of arginine to ornithine, which contributes to processes such as cell division and tissue repair (Rőszer 2015). The *Arg1* gene contains response elements for STAT6 (induced by IL-4 and IL-13 stimulation) upstream of the promoter region, thus its expression is induced by these two cytokines (Gray et al. 2005). Analysis of an ischemic stroke model in STAT6 knockout B6 mice showed decreased *Arg1* expression in microglia and macrophages, which contributed to impaired efferocytosis of neurons and exacerbation of post-stroke inflammation (Cai et al. 2019). Additionally, TGF-β and IL-10 have been shown to increase *Arg1* expression (Kupani et al. 2020). Arginase-1 and iNOS share a substrate (L-arginine) to produce either ornithine and urea or NO and citrulline, respectively (Rath et al. 2014). Therefore, substrate competition occurs between Arginase-1 and iNOS, and the resulting dominating enzyme is an important indicator of CAM vs AAM polarisation.

Other markers for AAMs include Ym1 (in mice but not in humans (Raes et al. 2005)) and FIZZ-1 (also known as RELMα/*Retnla*). Expression of these are induced by IL-4 and IL-13 signalling and their genes contain a response element for STAT6, much like *Arg1* (Welch et al. 2002; Raes et al. 2002).

The indispensability of STAT6 in AAM polarisation was shown via STAT6 knockout mice, which had almost no protein expression of Ym1, Arg1, Fizz1 in a mouse model of neurocysticerosis (a tape worm infection caused by *Mesocestoides corti*). Simultaneous elevation of iNOS was also seen, and STAT6 knockout mice were significantly more susceptible to infection (Mishra et al. 2011). Recent work has also shown that STAT6 binding to chromatin is required for transcriptional repression in macrophages, and promotes the recruitment and activity of histone modification proteins (e.g. HDAC3) (Czimmerer et al. 2018). This mechanism led to inhibition of NLRP3 inflammasome activation, IL-1β production, and pyroptosis (Czimmerer et al. 2018).

Another important TF for AAM polarisation is IRF4, which is induced by IL-4 stimulation in macrophages 4 hours post-stimulation (El Chartouni et al. 2010). A more recent study demonstrated that human PBMCs and B6 BMDMs stimulated with human serum amyloid A (SAA) induced expression of many AAM-related genes, including *Il10, Retnla, Ym1, Mrc1, Arg1,* and *Irf4* (Sun et al. 2015). THP-1 cells transfected with a human IRF4 promoter-driven luciferase reporter showed luciferase activity upon SAA treatment, confirming SAA-induced IRF4 expression. Knockdown of IRF4 via siRNA transfection led to a reduction in the SAA-induced expression of AAM-related genes in RAW 264.7 cells and human $CD14^+$ monocytes, confirming the requirement of IRF4 for AAM polarisation (Sun et al. 2015).

1.1.4.3 AAM subsets

Additional subtypes of AAMs have been described in mice and humans, each polarised by varying stimuli and possessing distinct functions (**Figure 1.4**). In 2002, Anderson et al. provided evidence for a macrophage phenotype that arises after exposure to IgG immune complexes in combination with LPS (Anderson et al. 2002). They found these macrophages to possess anti-inflammatory roles, producing high amounts of IL-10 and almost no IL-12, while also producing TNF, IL-1α, IL-6 and MIF in amounts comparable to CAMs (Anderson et al. 2002). Therefore, these macrophages were termed type 2 activated macrophages, or M2b macrophages (Anderson et al. 2002). Further work has identified several markers associated with M2b macrophages, such as LIGHT, a secreted protein which can act as a co-stimulatory molecule for T cell activation (Wan et al. 2002). M2b macrophages are also the only subtype to produce CCL1, which induces recruitment of other immunoregulatory leukocytes such as eosinophils and regulatory T cells (Asai et al. 2012; Sironi et al. 2006).

M2c macrophages are polarised by IL-10, TGF-β and/or glucocorticoids, and are involved in tissue remodelling through the release of high amounts of IL-10 and TGFβ (Mantovani et al. 2004). M2c macrophages also express high levels of MerTK, which binds phosphatidylserine on apoptotic cells and thus are more efficient in their clearance (Zizzo et al. 2012). Tumour-associated macrophages (also called M2d) are characterised by their expression of high levels of immunoregulatory and pro-fibrotic factors, such as vascular endothelial growth factor (VEGF), IL-10, and TGFβ, allowing for a permissive phenotype for tumour progression (Duluc et al. 2007; Wang et al. 2010; Ferrante et al. 2013).

1.1.5. Macrophage heterogeneity and plasticity

Heterogeneity of macrophages exists at the steady state. *In vitro* differentiation of bone marrow-derived monocytes into BMDMs can be performed using recombinant M-CSF, or using L929 fibroblast cell conditioned media. It is generally assumed that *in vitro* differentiation of BMDMs results in a homogeneous population of cells that will respond in the same way to stimuli exposure (e.g. LPS stimulation). However, a recent single cell transcriptomic study has highlighted the heterogeneity that exists between BMDMs differentiated with recombinant M-CSF (McCarty et al. 2023). Furthermore, proteomics analysis of L929 cell-conditioned media has shown that other macrophage-modulating factors are present as well as M-CSF, ultimately resulting in a macrophage phenotype that is closer to CAMs (Heap et al. 2021). This will be discussed in more detail in **Chapter 4**.

Macrophages also possess a high degree of plasticity (**Figure 1.4**), and their functional phenotypes can change depending on the surrounding environment. This was demonstrated by Stout et al. in 2005, who investigated the effects of sequential treatment of B6 peritoneal macrophages with different cytokines (IFNγ, IL-4, IL-10, IL-12, LPS), and observed sequential differences in cytokine release detected by ELISA depending on the cytokine stimulus sequence (Stout et al. 2005). This plasticity has also been shown using transcriptome analysis. After *in vitro*-polarisation of macrophages into AAMs/CAMs, removal of stimulants causes a phenotypic shift towards an unpolarised state (M0) after ~96 hours as determined by bulk RNA sequencing of B6 BMDMs (Liu et al. 2020). Furthermore, macrophages that were previously polarised and then exposed to a different cytokine stimulus (e.g. stimulated with IFNγ + LPS, then with IL-4) showed a transcriptional profile that corresponded with the newest cytokine stimulus. B6 BMDMs treated with IFNγ + LPS rapidly displayed a CAM-associated transcriptional profile, but treatment of these macrophages with IL-4 shifted the transcriptional profile to that of AAMs within 72 hours (Liu et al. 2020). These shifts in transcriptional profile are accompanied by changes in chromatin accessibility associated with each polarisation state. Therefore, the functional phenotype of macrophages is reflective of their surrounding tissue environment.

Recent transcriptomic studies have also highlighted the heterogeneity within macrophage populations. In 2019, Orecchioni et al. performed a transcriptomic analysis comparing datasets of *in vitro*-polarised M1 (LPS+IFNγ-stimulated) and M2 (IL-4-stimulated) macrophages (Jablonski et al. 2015), and *in vivo* isolated classically/alternatively activated macrophages from B6 mice (Buscher et al. 2017; Orecchioni et al. 2019). They revealed a surprising heterogeneity between *in vivo* and *in vitro*-polarised macrophages. *In vitro*-polarised M1 macrophages expressed genes significantly enriched for cell migration and chemotaxis (*Cxcl1, Cxcl2, Ccl3, Ccr7*), whereas *in vivo* classically activated macrophages exhibited a transcriptional phenotype more in line with anti-bacterial response (*MyD88, Nfkb1, Rela, Ifnb1, Irf1, Csf2, Ccl2, Il12a/b, Nos2*) (Orecchioni et al. 2019). Alternatively activated macrophages isolated from B6 mice appeared to be more metabolically active than *in vitro*-IL-4-polarised macrophages, possessing a signature of fatty acid oxidation, with genes such as *Acadm* (encoding medium chain Acyl-CoA Dehydrogenase (Tucci et al. 2017)) and *Cpt1a* (encoding Carnitine Palmitoyltransferase 1A (Nomura et al. 2016)) (Orecchioni et al. 2019). In contrast, *in vitro*- IL-4-stimulated macrophages upregulated well-defined M2-related genes such as *Mrc1* (Mannose receptor; CD206), *Arg1* (Arginase-1), *Cd9* (a tetraspanin that is known to play roles in anti-inflammatory macrophage phenotypes (Suzuki et al. 2009; Ha et al. 2005), and is decreased after IFNγ stimulation in murine

peritoneal macrophages (Wang et al. 2002)) (Orecchioni et al. 2019). Therefore, macrophage activation states are finely tuned by their exposure to environmental stimuli.

1.2. Leishmaniasis

The leishmaniases are a collection of diseases that are caused by infection with protozoan parasites of the genus *Leishmania* (with two subgenera *L. Leishmania* and *L. Viannia*). The leishmaniases are vector-borne diseases spread through the bite of female sand flies (either of the genus *Phlebotomus* or *Lutzomyia*) during taking of a blood meal (Claborn 2010). There are around 31 different species of *Leishmania* that are known to infect mammals, 21 of which are known to infect humans (Akhoundi et al. 2016). In total, there are 99 countries endemic for some form of leishmaniasis (WHO 2019). *Leishmania* infections are geographically separated into two groups; new world infections are generally restricted to countries in South America and typically caused by the species complex *L. (L.) mexicana* and the two species complexes *L. (V.) braziliensis* and *L. (V.) guyanensis* (Llanes et al. 2018)). Old world infections are restricted to tropical regions in Asia, Africa, and the Middle East and typically involve *L. tropica, L. major, L. aethiopica, L. donovani,* and *L. infantum* in the subgenus *Leishmania* (Torres-Guerrero et al. 2017).

1.2.1. Clinical forms of leishmaniasis and global disease burden

The clinical form of leishmaniasis commonly depends on the species of *Leishmania* parasite, as outlined in **Table 1.2**. The most common clinical form of leishmaniasis is cutaneous leishmaniasis (CL) (caused by infection with *L. mexicana, L. braziliensis, L. major, L. aethiopica*), in which *Leishmania* parasites are restricted to the skin (Gurel et al. 2020). CL presents with skin lesions that may ulcerate as the infection progresses. While CL lesions can self-heal, more complex forms of CL can also occur with varying degrees of severity, leading to significant scarring, disfigurement and social stigma (Gurel et al. 2020). Mucocutaneous CL (MCL) is another clinical form of CL typically associated with *L. braziliensis* in the New World and *L aethiopica* in the Old World, in which parasites disseminate to mucosal barriers (usually the nose and mouth), causing mucosal membrane damage and significant disfigurement, and is sometimes fatal (Abadías-Granado et al. 2021).

Visceral leishmaniasis (VL; also known as kala-azar) is the most severe clinical form of leishmaniasis, caused mainly by infection with either *L. donovani* (in India and Eastern

Africa) or *L. infantum* (in Europe, North Africa and Latin America, where it is also known as *L. chagasi*) (Mann et al. 2021). *L. tropica* and *L. amazonensis* are also known to cause VL in rare circumstances (Mann et al. 2021). VL differs from CL as parasites are not restricted to the skin, and instead the infection is systemic (Chappuis et al. 2007; Mann et al. 2021). Dissemination of parasites to immune organs (importantly liver, spleen, and bone marrow) results in hepatosplenomegaly, anaemia, weight loss, and fever (Mann et al. 2021). VL is fatal in >95% of cases if it is left untreated. Furthermore, following seemingly successful treatment of VL, dormant parasite reservoirs can remain leading to post kala-azar dermal leishmaniasis (PKDL), another clinical form which is characterised by skin lesions. Though PKDL is not fatal, it can lead to significant social stigma (Pal et al. 2017). PKDL patients also act as parasite reservoirs, which adds additional difficulties to the successful control of VL (Zijlstra et al. 2003).

The global disease burden of leishmaniases sees an estimated 700,000 to 1 million new cases per year, between 26-65,000 deaths per year, and there are a further estimated 1 billion people at risk worldwide (WHO 2019). 89% of global cases of VL reported in November 2022 came from eight countries: Brazil, Eritrea, Ethiopia, India, Kenya, Somalia, South Sudan, and Sudan (WHO 2019). As leishmaniasis is most prevalent in developing countries, there are problems with the lack of appropriate case recording measures, thus the reported numbers are likely a significant underestimate.

1.2.2. Life cycle of *Leishmania* parasites

The life cycle of *Leishmania* is multi-stage and spans across two hosts (**Figure 1.5**). In an infected sand fly, *Leishmania* are found in the sand fly midgut where they proliferate as procyclic promastigotes, prior to migration to the fore-gut where they differentiate into metacyclic promastigotes (which are infective to the mammalian host (Bates 2007)). When the sand fly takes a blood meal, metacyclic promastigotes are regurgitated into the mammalian host, where they are internalised by various cell types with phagocytic capacity, including neutrophils, dermal resident macrophages and dendritic cells and monocytes (with macrophages as the final host cells) (Kaye & Scott 2011). Within the macrophage phagolysosomal niche, metacyclic promastigotes further differentiate into amastigotes, surviving and proliferating in this form within the macrophage until the macrophages burst, releasing amastigotes to infect more cells and leading to disease progression (Kaye & Scott 2011).

Several mechanisms have been identified for parasite entry into macrophages. Early studies identified direct uptake of free promastigotes and amastigotes occurring through receptor-

mediated phagocytosis, via complement receptors 1 and 3 (CR1/CR3) (Mosser & Edelson 1984; Wilson & Pearson 1988), mannose receptor (which binds to exposed mannose residues on parasite lipophosphoglycan (Pimenta et al. 1994)) (Blackwell et al. 1985), and fibronectin receptors (Brittingham et al. 1999) for promastigotes. Amastigote phagocytosis also occurs through CR3, fibronectin receptors and via FcγRs. Kima et al. showed that BALB/c mice lacking the γ chain common to the FcγRs FcγRI, FcγRIII, and FcεRI developed significantly fewer lesions compared to WT over 13 weeks after infection with *L. mexicana* amastigotes (Kima et al. 2000). Furthermore, FcγR-mediated phagocytosis of IgG-opsonised sheep erythrocytes by BALB/c BMDMs led to induction of IL-10 expression (Gallo et al. 2010), a cytokine that facilitates *Leishmania* survival. A recent study has also implicated a role for caveolin-mediated endocytosis in the uptake of *L. donovani* parasites into J774A.1 murine macrophages. Inhibition of caveolin-mediated endocytosis via genistein treatment reduced the entry of *L. donovani* promastigotes in a dose dependent manner (Kumar et al. 2019).

Another route of entry into macrophages by *Leishmania* parasites is through phagocytosis of apoptotic neutrophils, in the “Trojan horse hypothesis”. This was postulated by Laskay et al., who suggested that neutrophil apoptosis induced by *L. major* infection leads to phagocytosis of apoptotic neutrophils by macrophages without triggering macrophage leishmanicidal mechanisms (Laskay et al. 2003). This was confirmed by van Zandbergen et al., who showed murine macrophages readily phagocytosing *L. major*-induced apoptotic neutrophils (van Zandbergen et al. 2004). Furthermore, it has been shown that both *L. major* and *L. braziliensis* induce neutrophil apoptosis in C57BL/6 and BALB/c mice, respectively (Ribeiro-Gomes et al. 2012; Falcão et al. 2015).

Uninfected sand flies can take blood meals from infected mammalian hosts, acquiring amastigote-infected cells in the process. Establishment of infection in the sand fly follows transformation of amastigotes into procyclic promastigotes, and completion of the *Leishmania* life cycle (Kaye & Scott 2011).

1.2.3. Visceral leishmaniasis (VL)

VL is the most severe clinical form of leishmaniasis, causing hepatosplenomegaly, fever, weight loss, and haematological alterations (e.g. anaemia, thrombocytopenia) (Mann et al. 2021; Varma & Naseem 2010), and is fatal in >95% of cases if left untreated.

Current treatments for VL vary by region and include pentavalent antimonials (effective in Africa despite high cardiotoxicity), amphotericin B (an extremely effective polyene antibiotic in the Indian subcontinent, though high nephro- and cardio-toxicity is an issue), miltefosine (an oral drug that initially showed high efficacy in the Indian subcontinent, but efficacy

eventually waned), and paromomycin (high cure rate in Africa, but is administered as painful injections) (Chakravarty & Sundar 2019). A lipid formulation of amphotericin B, AmBisome®, has also been developed, which shows high efficacy in the Indian subcontinent (97% in Bangladesh (Mondal et al. 2014)) while avoiding toxic side effects of amphotericin B treatment (Chakravarty & Sundar 2019). However, there are also problems with AmBisome®, such as low efficacy in some regions (40% and 58% in East Africa (Khalil et al. 2014)), and cold chain issues for storage of the drug (Maintz et al. 2014). There are currently no approved vaccines for VL.

1.2.4. VL immune response

Studying immune responses during VL in humans has provided valuable insights to assist the development of novel therapeutics. However, intrusive tissue biopsy procedures are required to analyse human tissue-specific responses to VL, and manipulation of immunity is not easily performed in humans. Therefore, animal models of experimental VL (particularly in mice) have been extremely successful in elucidating immune responses to infection and allowing manipulation of immunity (Kaye et al. 2004).

However, using mouse models to study VL immunity is not without limitations. The majority of literature describe mouse models that involve infection with a high dose of *Leishmania* amastigotes via intravenous injection of the lateral tail vein. This has the benefit of speeding up parasite dissemination and causing highly reproducible establishment of infection, however it also bypasses the sand fly bite stage and therefore the host response in the skin. The size of the parasite dose and route of infection have also shown differing effects on the immune response to *L. donovani* in BALB/c mice (Kaur et al. 2008). Furthermore, while chronic VL is fatal in humans (and Syrian hamsters (Requena et al. 2000)), murine experimental VL is not fatal and becomes chronic in the spleen and the bone marrow, while the liver is self-healing. Some work has been done to overcome these limitations; a model of vector-initiated experimental *L. donovani* infection in hamsters has been developed, showing five-fold increases in spleen weight compared to intracardiac inoculation. However, infection progressed slower in hamsters bitten by sand flies, showing a survival of ~28 weeks compared to 20~ weeks in inoculated hamsters (Aslan et al. 2013). More recent work has progressed towards the development of a controlled *L. major* infection model in humans infected via sand fly bites (Parkash et al. 2021).

The immune response during murine experimental VL is dominated by an inflammatory Th1 response, beginning with the granuloma-mediated self-healing infection of the liver, and

subsequent establishment of chronic infection in the spleen and bone marrow. The formation of granulomas is critical to the clearance of parasites in the liver. The initiation of the hepatic granulomatous response occurs after Kupffer cell phagocytosis of parasites (via mechanisms discussed previously). Kupffer cell infection induces their release of chemokines (MIP-1α, MCP-1, and CXCL10) to attract other leukocytes such as monocytes, neutrophils, and T cells (Cotterell et al. 1999). Liver dendritic cells are also activated when exposed to parasites, and have been shown to be a major source of IL-12 during the first three days of *L. donovani* infection in BALB/c mice (Gorak et al. 1998). $CD4^+$ T cell activation via IL-12 signalling polarises them to a Th1 phenotype, associated with abundant release of cytokines such as IFNγ, IL-12, GM-CSF, IL-2, and TNF (Stanley & Engwerda 2007). Of these cytokines, IFNγ and TNF are critical for the activation of macrophages towards an inflammatory CAM phenotype, and subsequent release of reactive oxygen intermediates and reactive nitrogen intermediates, of which nitric oxide (NO) produced by iNOS is well characterised (discussed in next paragraph). $CD8^+$ T cell activation also has an important role in the hepatic granulomatous response; depletion of $CD8^+$ T cells led to delayed granuloma formation (Stern et al. 1988; Stäger & Rafati 2012), while enhancing survival of $CD8^+$ T cells through PD-L1 blockade led to greater control of splenic parasite burden in B6 mice (Joshi et al. 2009).

Studies in mice deficient in *Nos2* (the gene encoding the iNOS protein) have shown a complete abrogation in the ability to resolve hepatic *L. donovani* infection (Murray & Nathan 1999). *Nos2-/-* mice were still able to form granulomas after *L. donovani* infection, though this was delayed compared to WT controls, and the maturation of granulomas was also impaired (Murray & Nathan 1999). The functions of iNOS for control of *Leishmania* infections is not restricted to directly leishmanicidal mechanisms. Recent studies revealed that NO released from phagocytes during *L. major* infection inhibits the recruitment of additional inflammatory cells in a concentration-dependent manner to modulate cellular metabolism. Treatment of mice with an iNOS inhibitor led to increased TNF, CCL3, and pro-IL-1β in monocyte derived cells during *L. major* infection *in vivo*, that was confirmed *in vitro* with *Nos2*$^{-/-}$ BMDMs stimulated with LPS+IFNγ. These observations were ultimately linked to NO-mediated dampening of cellular metabolism (Postat et al. 2018). During *L. major* infection, areas with high density of macrophages releasing NO alters surrounding cellular metabolism. This reduces release of inflammatory and chemotactic cytokines, thereby inhibiting further immune cell recruitment (Postat et al. 2018), including the recruitment of monocyte-derived macrophages that could aid in the proliferation of the parasite (Formaglio et al. 2021). The role of this pathway in murine VL has not yet been established.

The immune response to *L. donovani* infection in the spleen and BM is insufficient to clear the infection, resulting in establishment of chronic infection in these tissues. The mechanisms by which this occurs are still poorly understood, though some factors have been implicated. A major hallmark of the splenic response to *L. donovani* infection is the destruction of the splenic microarchitecture (Montes de Oca et al. 2020). In healthy mice, the spleen contains the red pulp (RP) zone, the T and B cell-rich white pulp (WP) zone, and the marginal zone (MZ), which separates the WP and RP (Mebius & Kraal 2005). Notably, the splenic marginal zone is severely disrupted and marginal zone macrophages (MZMs) lost during *L. donovani* infection. These changes are dependent on abundant TNF levels with TNF-deficient mice retaining MZMs during infection (Engwerda et al. 2002). More recently, it was found that type I IFN signalling plays an important role in the suppression of $CD4^+$ T cell-derived IFN-γ production, and also stimulates IL-10 expression in $CD4^+$ T cells. Deficiency of *Ifnar1* in B6 mice led to more rapid destruction of the splenic marginal zone. Almost no marginal zone tissue staining was observed at day 14 days post-infection in mutant mice while the marginal zone was still intact in WT mice at the same time point (Kumar et al. 2020).

The BM is another site of chronic infection during VL, and the response to infection is less well characterised than the liver and the spleen. Haematological complications are known to occur during *L. donovani* infection, with thrombocytopenia and anaemia frequently seen in human, hamster, canine, and murine VL (Varma & Naseem 2010; Lafuse et al. 2013; Leão Dias et al. 2008; Rani et al. 2021). A general view of the bone marrow response indicates that *L. donovani* infection leads to increased haematopoietic activity, notably myelopoiesis in mice (Pinto et al. 2017; Abidin et al. 2017; Romano et al. 2021). Earlier studies show that *L. donovani* infection greatly enhances hematopoietic activity in BALB/c mouse bone marrow, with increases in colony forming units (CFU-GM and BFU-E and CFU-GEMM) seen from 7 days post-infection (Cotterell et al. 2000a). Further study revealed *L. donovani* parasites to be present in BALB/c BM stromal macrophages, leading to the release of GM-CSF and TNF and subsequent enhancement of CFU-GM from spleen and bone marrow cells (Cotterell et al. 2000b), indicating that *L. donovani* infection in bone marrow can selectively increase myelopoiesis.

More recently, Pinto et al. showed that *L. donovani* infection pushed most long-term HSCs (LT-HSCs) into the cell cycle, adding to evidence of increased myelopoiesis during VL (Pinto et al. 2017). Interestingly, HSCs from *L. donovani*-infected RAG2 knockout C57BL/6 mice BM retained their LT-HSC quiescence. Increased presence of IFNγ-producing $CD4^+$ T cells was shown to be essential for the loss of LT-HSC quiescence. This was confirmed by the

introduction of IFNγ-sufficient but not IFNγ-deficient $CD4^+$ T cells inducing loss of LT-HSC quiescence in infected RAG2 knockout C57BL/6 mice. Mixed bone marrow chimera experiments revealed that intrinsic TNF signalling is a requirement for the production of IFNγ by $CD4^+$ and $CD8^+$ T cells. Together, this study demonstrated the essential roles for TNF signalling-induced $CD4^+$ T cell-derived IFNγ on the loss of LT-HSC quiescence during *L. donovani* infection (Pinto et al. 2017).

IL-10 has also been shown to be important in abrogating a successful anti-parasite response in the spleen and the BM. Excessive production of IL-10 by human PBMCs was shown to correlate with progression of human VL (Ghalib et al. 1993). Subsequent studies identified a distinct CD25- Foxp3- T cell population as the major source of IL-10 in the spleen during human VL, the accumulation of which decreased after treatment with amphotericin B (Nylén et al. 2007). Furthermore, deletion of IL-10 in both BALB/c and B6 mice resulted in significant resistance to *L. donovani* infection (Murphy et al. 2001). T cell exhaustion has also been implicated in the insufficiency of the Th1 response in the spleen in BALB/c mice, as identified by increased expression of CTLA-4 (Murphy et al. 1998; Murray et al. 2003). Macrophages exposed to IL-10 take on an AAM-like phenotype, producing cytokines such as IL-10 and TGFβ, causing differentiation of naive T cells into IL-4-producing Th2 cells and induction of Arginase-1 expression in macrophages (Sundar et al. 1997; Kupani et al. 2020). In humans, IL-4 and IL-10 activate immunoregulatory AAM signalling pathways in macrophages, leading to suppression of anti-parasite mechanisms (e.g. iNOS expression) and induction of parasite survival mechanisms (IL-10 and Arginase production) (Kupani et al. 2020). IL-10 and IL-27 contribute both to the suppression of Th17 cell differentiation and the induction of Treg differentiation, which further exacerbates the immunoregulatory response to *L. donovani* infection (Quirino Gustavo F. S. et al. 2016; Ansari et al. 2011). Recent work has also highlighted the importance of LyC^{hi} monocytes in the progression of VL. In 2017, Terrazas et al. showed LyC^{hi} monocytes to be continually recruited to the liver and the spleen, and while hepatic monocytes adopted a phenotype high in iNOS expression, splenic monocytes adopted an arginase-dominant phenotype. Furthermore, inhibition of monocyte recruitment through treatment with a CCR2 antagonist significantly improved parasite burden in the spleen by decreasing IL-10 production while leaving IFN-γ production intact (Terrazas et al. 2017). Together, this allows for parasite survival and progression of VL. Absence of IL-4, however, limits granuloma maturation, implicating this cytokine both in the early regulation of Th1 responses and in subsequent granuloma organisation (Stäger et al. 2003).

1.2.5. Tissue resident macrophages in *L. donovani* infection

Depending on the infection model, the balance between CAMs and AAMs becomes skewed, which can contribute to the pathogenesis of the disease. In *Leishmania donovani* infection there is a skew towards AAMs, accompanied by increased levels of arginase and AAM phenotypic markers such as IL-10, CD163, and CXCL13, and a reduction in NO and oxidative burst (Abebe et al. 2013; Roy et al. 2018; Sarkar et al. 2011). As discussed in **1.1.3.**, tissue resident macrophages are phenotypically shaped by epigenetic and specific TF expression during development, resulting in highly specialised populations. Tissue-specific immune responses are observed during VL, and tissue resident macrophages are vital for these differing responses.

1.2.5.1. Liver

The liver is the primary site of parasite localisation during the first four weeks of experimental infection. Formation of hepatic granulomas serves as an effective infection control mechanism for these early stages of infection, resulting in clearance of parasites from the liver within 6-8 weeks (Bankoti & Stäger 2012). Tissue resident macrophages in the liver (Kupffer cells; KC) are core to this clearance. *L. donovani* parasites disseminate to the liver soon after infection, where KCs lining sinusoids entering the liver are the first cells to phagocytose parasites, and initiate granuloma formation with infected KCs at the core (McElrath et al. 1988). Infection of KCs leads to release of inflammatory cytokines and chemokines (TNF, IL-12, IL-6, IL-1β, CCL2, CCL3) and subsequent recruitment of leukocytes to the KC, surrounding it and forming a granuloma (Sato et al. 1999). The presence of pro-inflammatory cytokines within the granulomas leads to expression of iNOS by KCs, and subsequent release of NO is a vital step in hepatic parasite clearance (as discussed in **1.2.4**). An important role for *L. donovani*-harbouring KCs is their ability for continued antigen presentation, which activates antigen-specific $CD8^+$ T cells (Beattie et al. 2010). This built upon a previous study showing anti-parasitic activity of $CD8^+$ T cells was dependent on cognate antigen (Polley et al. 2006). Beattie et al. found that $CD8^+$ T cells harbouring transgenic ovalbumin-specific T cell receptors localised to granulomas in B6 mice infected with ovalbumin-expressing *L. donovani*, but not in mice infected with WT parasites (Beattie et al. 2010). $CD11c^{int}$ $F4/80^{int}$ KCs were subsequently found to be the sole cell type presenting *L. donovani* cognate antigen to $CD8^+$ T cells within granulomas, and this inter-cell dynamic plays an important role in hepatic clearance of *L. donovani* (Beattie et al. 2010). Furthermore, IRF7 was found to be an important TF in the induction of iNOS expression in KCs during *L. donovani* infection in B6 mice. *Irf7*-deficient B6 mice had lower expression of

iNOS in granulomas at 28 days post-infection, which was attributed to defects in the production of IFNγ from T cells, NK cell, and NKT cells and simultaneous elevation of IL-10 expression in T cells (Beattie et al. 2011). While parasites in the liver begin to clear at ~d28 post-infection in mice, chronic infection continues in the spleen and the bone marrow.

1.2.5.2. Spleen

MZMs and metallophilic macrophages (MMMs) reside within the marginal zone of the spleen and are vital for clearance of pathogens (including *L. donovani*) from the circulation on first pass through the spleen. These macrophages play important homeostatic functions in the clearance of blood borne pathogens such as *Mycobacterium tuberculosis* (Koppel et al. 2004), *Streptococcus pneumoniae* (Lanoue et al. 2004), *Escherichia coli*, and *Salmonella typhimurium* (Nagaoka et al. 2005; Borges da Silva et al. 2015). MZMs and MMMs express distinct surface markers that allow them to perform their specific functions. MZMs express SIGN-R1 and MARCO, allowing them to effectively detect microbial polysaccharides. MMMs do not express SIGN-R1 or MARCO, and instead express CD169, which aids in the detection of viruses such as HIV-1, and binds to sialic acid on apoptotic bodies and sialylated bacteria (Grabowska et al. 2018; Chang et al. 2014).

During *L. donovani* infection, splenic marginal zone macrophage subtypes are responsible for the clearance of the majority of parasites 5-24 hours post-infection (Phillips et al. 2010). Interestingly, this clearance was IRF7-dependent but was uncoupled from NO production. While NO production was important for initial leishmanicidal activity independent of IRF7, a later stage of leishmanicidal activity was dependent on IRF7, but not on NO production (Phillips et al. 2010). Maintenance of the splenic architecture is important for its effective function. During *L. donovani* infection, parasite proliferation in the spleen leads to splenomegaly and destruction of the tissue architecture, aiding in progression of the disease and serving as a major reservoir for parasites during chronic infection (Hermida et al. 2018).

1.2.5.3. Bone marrow (BM)

Little is known about the roles of tissue-resident BM macrophages during *L. donovani* infection. A recent study showed abrogation of the final stages of medullary erythropoiesis occurs during *L. donovani* infection in C57BL/6 mice (Preham et al. 2018). This was linked to reductions in the number of $CD169^+$ stromal macrophages and CXCL12-expressing cells, indicating stromal cell support for medullary erythropoiesis is significantly reduced during infection (Preham et al. 2018). Interestingly, RAG2 knockout C57BL/6 mice did not show the same phenotype, and reconstitution with $CD4^+$ T cells either sufficient or deficient in IFNγ

revealed that loss of medullary erythropoiesis is dependent on the presence of IFNγ-producing $CD4^+$ T cells (Preham et al. 2018).

1.2.6. Intra-macrophage alterations following *L. donovani* infection

Various TFs have been shown to be important in macrophage-mediated immunity to *L. donovani* infection, many of which have been discussed in **Section 1.1.4**. Activity of a diverse range of TFs in *Leishmania*-infected macrophages have been shown to be important in eliciting immune responses by modulating inflammatory cytokine expression and altering metabolism to favour parasite killing macrophage phenotypes (Bichiou et al. 2021). For example, IRF1 expression in macrophages is known to bind to the *Nos2* promoter to promote its transcription, and *Irf1*$^{-/-}$ knockout macrophages failed to produce NO in response to *Mycobacterium bovis* infection (Kamijo et al. 1994; Martin et al. 1994). IRF1 activation and DNA binding activity on the *Nos2* promoter is also induced by *L. donovani*-derived lipophosphoglycan (LPG), independently of MAPK and p38 signalling (Balaraman et al. 2004).

Hypoxia Inducible Factor 1α (HIF1α), a TF that is usually expressed in response to oxidative stress (Taylor & Scholz 2022), contributes to metabolic reprogramming of macrophages towards glycolysis and away from oxidative phosphorylation (Marín-Hernández et al. 2009), favouring CAM-like phenotypes (Cramer et al. 2003).

However, it has now been shown that while HIF1α is induced in *L. donovani*-infected BALB/c peritoneal and splenic macrophages, parasite survival is favoured via prolyl hydroxylase-mediated stabilisation of HIF1α. Overexpression of stabilised HIF1α in *L. donovani*-infected macrophages significantly promoted intracellular parasite growth, whereas inhibition of HIF1α impaired parasite growth (Singh et al. 2012). Furthermore, HIF1α plays a permissive role favouring parasite survival in *L. donovani*-infected B6 mouse spleen by promoting AAM polarisation during extramedullary haematopoiesis (Hammami et al. 2017). Therefore, while CAM polarisation is essential for the protective response to *L. donovani* infection, the modulation of intra-macrophage signalling by intracellular parasites plays an important role in parasite survival and VL progression.

In 2001, Buates and Matlashewski performed a cDNA expression array analysis on BALB/c BMDMs infected or not with *L. donovani* amastigotes for four days to identify alterations in the macrophage transcriptome (Buates & Matlashewski 2001). They found that ~40% of the

588 genes detected were downregulated in infected BMDMs compared to uninfected (including CD40), and only eight genes were upregulated (including MIP-1α and MIP-1β) (Buates & Matlashewski 2001). This indicates that intracellular *L. donovani* has a general dampening effect on macrophage gene expression and acts to prevent CD40-mediated activation of T cells (Buates & Matlashewski 2001). This is consistent with another more recent study that performed dual Illumina RNA-seq on BALB/c peritoneal macrophages infected with either a virulent (vLd) or non-virulent (nvLd) strain of *L. donovani in vitro* for 3, 24, 48, and 72 hours (Shadab et al. 2019). This study also found the majority (363) of differentially expressed genes (DEGs) detected were downregulated in the vLd-infected macrophages compared to controls, whereas 93 genes were upregulated. Gene set enrichment analysis (GSEA) of the down-regulated genes revealed a dampening of important cellular processes such as mRNA processing, gene expression, endocytosis, and PI3K-Akt signalling (Shadab et al. 2019). In contrast, the nvLd strain led to a more even spread of up- and down-regulated genes in host macrophages (247 up, 236 down), and expression of more inflammatory cytokine genes was observed compared to vLd-infected macrophages (Shadab et al. 2019). Therefore, the general suppression of host gene expression is important to establish a parasite-permissive niche within host macrophages.

However the molecular mechanisms by which this occurs remains incompletely understood. Activation of the MAPK and PI3K signalling pathways has been shown to be beneficial to macrophage control of *L. donovani* infection, and inhibition of p38 MAPK favours parasite survival (Junghae & Raynes 2002). Shadab et al. showed that vLd-infected macrophages induced p38 MAPK activity to a much lesser and shorter extent than nvLd-infected macrophages, and was associated with dampened inflammatory gene expression, indicating a potential mechanism for intra-macrophage parasite survival (Shadab et al. 2019). Furthermore, it is known that *L. donovani* amastigotes are more virulent than promastigotes when exposed to macrophages (Zhang & Matlashewski 1997), and recent transcriptomics analysis has shown distinct macrophage transcriptional profiles that depends on life cycle stage of the parasite, with more dampening of inflammatory gene expression (*Ccl5, Cd14,* MHC-II genes, *Irf7*) seen in amastigote-infected macrophages compared with those infected with promastigote (Chaparro et al. 2022).
Additionally, activation of mTOR signalling has been consistently reported following *L. donovani* infection in human and mouse macrophages, and will be discussed in more detail in **Chapter 4** (Cheekatla et al. 2012; Nandan et al. 2012; Zhang et al. 2018; Chaparro et al. 2020). It is important to identify the molecular regulators of these pathways so that they can be targeted to modulate macrophages towards a parasite killing phenotype.

1.3. Tripartite motif (TRIM)-containing protein family

1.3.1. The TRIM family of proteins

The TRIpartite Motif (TRIM) proteins are a highly conserved family of proteins that consist of around 80 different members in humans and 64 in mice (van Gent et al. 2018; Ozato et al. 2008). They are characterised by the presence of a conserved sequence of domains (a "TRIpartite Motif") on the N-terminus that consists of a Really Interesting New Gene (RING) domain, one or two B-Box domains, and a Coiled-Coil domain (collectively named an RBCC domain) (Meroni & Diez-Roux 2005) (**Figure 1.6**).

The RING finger domain exhibits E3 ubiquitin ligase activity in most TRIM proteins, although there are eight known TRIM proteins in humans that do not contain a RING domain (Hatakeyama 2017). The B-Box zinc finger domains are involved in protein-protein interactions, and mutations in B-Box domains have also been shown to affect subcellular localisation of TRIM proteins (Reymond et al. 2001).
The coiled-coil domain mediates oligomerization in TRIM proteins that assists with quaternary protein structure (Sanchez et al. 2014). For example, TRIM5α forms a 2D lattice of homodimers, forming a 'net' that allows for multi-valent detection of retroviral capsids (e.g. HIV) to restrict viral replication (Ganser-Pornillos et al. 2011). The B-Box domain of TRIM5α also contributes to higher order assembly for retroviral capsid restriction (Wagner et al. 2016).

The TRIM members are further subdivided according to their C-terminal domains (labelled C-I to C-XI), which vary in number and function, and are shown in **Figure 1.6** (Lu et al. 2022). Further sub-categorisation has also been reported (Hatakeyama 2017) (**Figure 1.6**). Emerging literature also identifies "TRIM-like" proteins that lack RING domains but still possess similar domains to other TRIM proteins, categorised in the UC TRIM subgroup (**Figure 1.6**) (Marín 2012).
The largest subgroup of the TRIM proteins, the C-IV group, consists of proteins that contain PRY and/or SPRY domains on their C-termini. TRIM members with PRY-SPRY C-terminal domains have been well characterised in relation to innate immunity, particularly in viral infection models. PRY/SPRY domains are usually involved in protein-protein interactions, and in some cases are critical for RNA binding activity (Choudhury et al. 2017).

TRIM5α possesses a single SPRY domain, and in Rhesus monkeys has been shown to restrict HIV-1 by interacting and polyubiquitinating the intracellular viral capsid, causing capsid uncoating and inhibition of its translocation to the nucleus, thereby stopping reverse transcription occurring (Wu et al. 2006; Campbell et al. 2016). While this is not the case with human TRIM5α, a similar mechanism has been shown between human TRIM5α and N-tropic murine leukaemia virus (N-MLV), and the SPRY domain is essential for this action, evidenced by a single mutation in the human TRIM5α SPRY domain causing a similar restriction event on B-tropic murine leukemia virus, while WT human TRIM5α did not (Diaz-Griffero et al. 2008).

TRIM21 is another well-researched TRIM protein with functions in innate immunity against viral infection. TRIM21 possesses a PRY-SPRY domain, which in this context is important for its interaction with the Fc region of antibodies. TRIM21 acts as an intracellular IgG receptor, and rapidly targets antibody-bound viruses for proteasomal degradation upon infection (Mallery et al. 2010; James et al. 2007). As well as being a receptor for IgG Fc regions, TRIM21 is a negative regulator of Interferon Regulatory Factor (IRF) signalling by ubiquitinating IRF3, IRF5, and IRF7, targeting them for degradation and thus inhibiting transcription of their target genes (Higgs et al. 2008; Lazzari et al. 2014; Higgs et al. 2010).

Other TRIMs have been implicated in other diseases, particularly in viral infections, play important roles in modulating immune signalling pathways (e.g. targeting immune TFs like the IRFs for proteasomal degradation, inhibiting SOCS activity, or modulating transcriptional activity via chromatin binding) (**Figure 1.7**). The number of reports of immune functions of other TRIM subgroups is more limited but has been increasing in recent years.

1.3.2. The TIF1 Family

The Transcription Intermediary Factor 1 (TIF1) group a subgroup of the TRIM family (C-VI) and is comprised of TIF1α (TRIM24), TIF1β (TRIM28/KAP1), TIF1γ (TRIM33), and TIF1δ (TRIM66). TRIM66 (a member of the TRIM UC subgroup) is a paralog of the other three TIF1 proteins, due to its lack of RING domain on the N-terminus, and is only found in the testis, whereas TRIM24, TRIM28 and TRIM33 are all ubiquitously expressed (Khetchoumian et al. 2004). TIF1 proteins are primarily involved in the regulation of gene expression, and are the only TRIM proteins to possess a plant homeodomain (PHD) zinc finger and a bromo-domain at the C-terminus of the protein (McAvera & Crawford 2020). PHD and Bromo domains generally function as histone readers and facilitate protein-protein interactions, resulting in regulation of gene transcription (Sanchez & Zhou 2011; Fujisawa &

Filippakopoulos 2017). Little is known about the functions of TRIM66 outside its function as a histone reader contributing to DNA damage responses in embryonic stem cells (Chen et al. 2019).

TRIM28 is perhaps the most well studied of the C-VI TRIM subgroup, and has been implicated in a number of immune pathways. TRIM28 is overexpressed in many cancers, including glioma (Su et al. 2018), hepatocellular carcinoma (Y. Wang et al. 2016), and non-small cell lung cancer (Liu et al. 2013), and as such is generally considered to be an oncogenic protein through several mechanisms. One such mechanism is through E3 ligase activity of the TRIM28 RBCC domain together with MDM2, leading to ubiquitination and degradation of p53 and contributing to cancer progression (Wang et al. 2005). The TRIM28-SETDB1 complex also conveys oncogenic activity through suppression of PD-L1 expression and prevention of effector $CD8^+$ T cell recruitment to tumours (Lin et al. 2021).

Some immune functions of TRIM28 have also been explored. For example, TRIM28 was found to suppress the transcriptional activity of endogenous retroviruses (ERVs) in various cell types, such as embryonic stem cells and neuronal progenitors (Rowe et al. 2010; Fasching et al. 2015). This occurs through TRIM28 association with ERV chromatin where it acts as a scaffold for epigenetic machinery (e.g. SETDB1 (Schultz et al. 2002)), which leads to transcriptional repression through epigenetic modification and chromatin compaction (Rowe et al. 2010). In macrophages, Eames et al. used affinity purification to identify TRIM28 an interacting factor with IRF5 (Eames et al. 2012). TRIM28 was then found to inhibit IRF5 transcriptional activity through recruitment of SETDB1 and addition of H3K9me3 chromatin modification (**Figure 1.7D**) (Eames et al. 2012). TRIM28 was also found to interact with IRF7 (but not IRF3), and act as an E3 SUMO ligase, facilitating the SUMOylation of IRF7 in a RING-domain dependent manner (Liang et al. 2011). Furthermore, knockdown of TRIM28 potentiated IRF7-dependent expression of type I interferons induced by Sendai virus infection, highlighting a role for TRIM28 as a negative regulator of interferon signalling (Liang et al. 2011).

TRIM33 has been studied to a lesser extent than TRIM28, however some immune functions have been uncovered. TRIM33 has been shown to play a role in the differentiation of monocytes and granulocytes ($CD11b^+$ $Ly6G^{hi}$/$Ly6G^{lo}$). Deletion of TRIM33 in mice led to significantly more monocytes and polymorphonuclear cells, and fewer lymphocytes (Chrétien et al. 2016). More TGFβ release and *Stat3* mRNA abundance was also observed in $Ly6G^{hi}$ cells. Increased circulating CCL2 also led to higher myeloid cell recruitment to skin and spleen, and recombinant M-CSF treatment of TRIM33-deficient BM cells *in vitro* delayed differentiation of BMDMs and caused dysmorphia (Chrétien et al. 2016). Subsequent work

confirmed this dependency of TRIM33 in macrophage differentiation, demonstrating an accumulation of myeloid progenitors (GMPs, MDPs, cMoPs), more neutrophils, and fewer Ly6C^{hi} monocytes upon TRIM33 deletion (Gallouet et al. 2017).
A recent study investigated the roles of TRIM33 during dextran sulfate sodium (DSS)-induced colitis by using a myeloid-specific TRIM33 knockout mouse model (Petit et al. 2019). Accumulation of neutrophils and monocytes was observed in the colon, but macrophage numbers were severely reduced in *Trim33*$^{-/-}$ mice. Furthermore, inflammation was more severe in *Trim33*$^{-/-}$ mice, with increased colon width and decreases in AAM markers (*Retnla, Cd206*) (Petit et al. 2019).
Other roles for TRIM33 have also been investigated. For example, TRIM33 modulates late phase transcription of *Ifnb1* after LPS treatment (Ferri et al. 2015), and is involved in the NLRP3 inflammasome activation (Weng et al. 2014). TRIM33 exerts E3 ligase activity via its RBCC domain to target viral integrase in HIV-1 for proteasomal degradation, thereby preventing viral replication (Ali et al. 2019). TRIM33 is also important for Th17 cell function, as *Trim33*$^{-/-}$ Th17 cells produced less IL-17 following TGFβ treatment, and less IL-17, IFNγ and IL-10 following keyhole limpet hemocyanin (KLH) treatment (Tanaka et al. 2018).

Due to the similarities in domain structure, the C-VI TRIM proteins have been shown to exert their roles through similar mechanisms, albeit in different cancer and infection contexts. However, there is also some evidence of these C-VI TRIM proteins forming complexes with each other. For example, complexes consisting of TRIM24, TRIM33, and/or TRIM28 were found by Herquel et al. by immunoprecipitation of epitope-tagged TRIM24 (Herquel et al. 2011). Some epigenetic machinery proteins such as HDAC1, HDAC2, and HP1α were also found associated with TRIM24, evidencing its role as a transcriptional modulator. This TRIM complex has a suppressive effect on hepatocellular carcinoma (HCC) progression, and interestingly, each of the C-VI TRIM proteins appears to have non-redundant functional roles (Herquel et al. 2011). This is further evidenced by deletion of TRIM28 and TRIM33 being embryonic lethal, respectively (Cammas et al. 2000; Kim & Kaartinen 2008). Despite this, investigation of TRIM24 has not been as widely reported.

1.3.3. TRIM24/TIF1α

1.3.3.1. Discovery

In 1991, Miki et al. used a plasmid vector-based cDNA cloning system to isolate the oncogene in tumour T18 in furfural-induced hepatoma in B6C3F1 mice (Miki et al. 1991). The T18 oncogene encoded a chimeric protein containing the murine homolog of the human

proto-oncogene B-RAF at the C-terminus and an unknown protein at the N-terminus (Miki et al. 1991). Subsequently, this unknown protein was identified as (TIF1α/TRIM24) and described as a putative mediator in the activation function 2 (AF-2) of nuclear receptors (Le Douarin et al. 1995). TRIM24 was isolated from yeast as an intermediary transcriptional regulator that enhances retinoid X receptor alpha (RXRα) activity through ligand-dependent interaction with the AF-2 activating domain (Le Douarin et al. 1995). TRIM24 was further shown to interact with other nuclear receptors in mammalian cells via its LXXLL motif (**Figure 1.8**), particularly oestrogen receptor (ER), in the same manner as in yeast cells, but does not interact with transcription factors involved in RXRα- and ER-mediated transcription (TATA-binding protein (TBP) or transcription factor II B (TFIIB)) (Le Douarin et al. 1995).

1.3.3.2. Regulation of TRIM24

Since its discovery, TRIM24 has been studied mostly in the context of cancers, where it is aberrantly expressed. Despite this, little is known about the underpinning mechanisms that regulate the expression of TRIM24 itself. Studies in 2008 and 2009 used systematic qPCR arrays to investigate TRIM gene mRNA abundance in response to type 1 and 2 interferons in mouse and human leukocytes, respectively (Rajsbaum et al. 2008; Carthagena et al. 2009). In both studies, mRNA abundance of TRIM24 was unaffected by type 1 and type 2 interferon signalling, although Rajsbaum et al. identified higher TRIM24 mRNA abundance in plasmacytoid dendritic cells than other cell types tested (macrophages, myeloid dendritic cells) (Rajsbaum et al. 2008).

Recent studies have reported mechanisms that regulate TRIM24 abundance. A study in 2017 showed an inverse correlation between TRIM24 protein abundance and microRNA (miR)-511 abundance in gastric cancer (Fang et al. 2017). TRIM24 is highly expressed in gastric cancer, and was found to be a direct target for miR-511 demonstrated by TRIM24 luciferase reporter constructs resulting in lower luciferase activity following miR-511 mimic transfection. Low levels of miR-511 in gastric cancer tissues therefore led to higher TRIM24 expression, and subsequent activation of PI3K/AKT and Wnt/β-catenin signalling pathways driving tumour progression (Fang et al. 2017).

TRIM28 has been identified as an upstream regulator of TRIM24 stability in prostate cancer (Fong et al. 2018). Mechanistically, TRIM28 forms a complex with TRIM24 and protects TRIM24 from Speckle-type POZ protein (SPOP; an E3 ubiquitin ligase)-mediated ubiquitination and subsequent proteasomal degradation. The TRIM28-TRIM24 complex also stabilises TRIM24 binding to chromatin, and enhances androgen receptor signalling, thereby facilitating tumour progression (Fong et al. 2018).

A more recent study used a genome-wide CRISPR-Cas9 screen to determine gene networks that regulate the expression of TRIM24 in human cancer cell lines (Patel et al. 2023). Patel et al. introduced an in-frame knock-in of *mClover3* to the *TRIM24* gene that caused endogenously expressed TRIM24 to be fluorescent and detectable via flow cytometry. Transduction of these cells with a genome-wide CRISPR-Cas9 knockout library allowed for TRIM24 over-expressors to be detected, sequenced, and analysed for upstream negative regulators using a novel scoring system designated SLIDER. This resulted in the identification of 220 potential negative regulators of *TRIM24* expression, which were subsequently assigned to regulatory gene networks. Patel et al. validated three of these networks, and the KAP1 (TRIM28) corepressor complex was identified as an upstream negative regulator of *TRIM24* expression, an interesting result given the data from Fong et al. discussed previously (Patel et al. 2023; Fong et al. 2018). Interestingly, another identified network that could regulate *TRIM24* expression was a phospholipase and immune receptor signalling network that included JAK2 and SOCS1. Though this network was not validated by the authors (Patel et al. 2023), this could point to unexplored functions of TRIM24 in the immune system.

1.3.3.3. TRIM24 as an oncogene/tumour suppressor

There is some controversy in the literature surrounding TRIM24, as its role as an oncogene or tumour suppressor appears to be context-dependent. For example, in 2008, TRIM24 was identified as a tumour suppressor protein in hepatocellular carcinoma (HCC) (Khetchoumian et al. 2008). Deletion of *Trim24* led to spontaneous hepatic tumour formation and lung metastasis with increases in $Ki67^{+}$ proliferating hepatocytes maintained with increasing age (Khetchoumian et al. 2008). Further study showed that deletion of a single retinoic acid receptor alpha (*Rara*) allele in $Trim24^{-/-}$ mice abrogated HCC formation, however this knockout mouse showed not all TRIM24 isoforms to be deleted (Khetchoumian et al. 2007; Khetchoumian et al. 2008). Subsequently, Jiang et al. generated a B6 mouse model lacking all isoforms of TRIM24, and saw spontaneous development to HCC, similar to the aforementioned study (Jiang et al. 2015). Furthermore, hepatic inflammation was observed in $Trim24^{-/-}$ mice, with upregulation of *Ccr2, Il-1a, Il-1b, Il-16,* and *Il-33* seen compared to WT mice (Jiang et al. 2015). Conversely, a more recent study found a positive correlation between TRIM24 protein abundance and human HCC tumour grade (Zhu et al. 2018). Mechanistically, this was shown to be through TRIM24-mediated regulation of the AMPK signalling pathway, the dampening of which was induced by TRIM24 knockdown, and slowing tumour growth (Zhu et al. 2018).

TRIM24 has been implicated in other cancers as well. TRIM24 was shown to act as an oncogenic protein in human bladder carcinoma by activating NF-kB and AKT pathways, and upregulating cell cycle genes (cyclin D1, cyclin E) (Xue et al. 2015). TRIM24 has also been overexpressed and oncogenic in gastric cancer, as mentioned previously (Fang et al. 2017).

The PHD-Bromo domains present on TRIM24 have been shown to play important roles in the progression of breast cancer. Tsai et al. in 2011 showed that TRIM24 binds to unmethylated H3K4 (H3K4me0) and to acetylated H3K23 (H3K23ac) via its PHD-Bromo domains (Tsai et al. 2010). Subsequently, they found that this chromatin binding stabilises the oestrogen receptor (ER) at ER-response elements, and confers a co-activating function with ER-induced transcriptional activity (Tsai et al. 2010). TRIM24 is highly expressed in breast cancer patients, and high TRIM24 expression correlates with poor survival (Tsai et al. 2010). Aberrant PI3K/mTOR signalling due to TRIM24 overexpression was observed recently in breast cancer patients, and thus could be a potential target for novel therapies (Shah et al. 2021).

TRIM24 also interacts with the tumour suppressor protein, p53, to facilitate its degradation. Mass spectrometry analysis of proteins directly interacting with p53 (via tandem affinity purification (TAP) tagging of p53 followed by TAP-chromatography) revealed TRIM24 as a binding partner with p53 (Allton et al. 2009). Subsequent experiments revealed that TRIM24 directly ubiquitinates p53 via E3 ubiquitin ligase activity of its RING domain. Mutation of the TRIM24 RING domain inhibited the ubiquitination levels of p53, and ectopic expression of TRIM24 increased p53 ubiquitination and decreased overall p53 levels (Allton et al. 2009). A subsequent study by the same group demonstrated the destabilisation of TRIM24 as result of its DNA damage-induced ATM-mediated phosphorylation. TRIM24 phosphorylation activates its ability to self-ubiquitinate, thereby targeting itself for proteasomal degradation (Jain et al. 2014). This study also highlighted a regulatory feedback loop in which DNA damage-induced phosphorylated p53 induces de novo TRIM24 expression. TRIM24 then targets p53 for proteasomal degradation to bring the DNA damage response to an end (Jain et al. 2014).

Therefore, TRIM24 has many roles involving its various functional domains in a context-specific manner in cancer. While the majority of research on TRIM24 has been conducted in the cancer setting, a role for TRIM24 as a regulator of immune cell function is becoming evident.

1.3.3.4. TRIM24 in STAT signalling

In recent years, an immune function of TRIM24 has emerged with a theme of regulating STAT pathways (**Figure 1.9**). In 2011, Tisserand et al. revealed a role for TRIM24 as a negative regulator of IFNγ/STAT signalling. Upon retinoic acid (RA) treatment, TRIM24 is recruited to the STAT1 promoter, where it binds to retinoic acid receptor alpha (Rara). This interaction inhibits Rara-induced STAT1 transcription, thereby preventing ISG expression and suppressing HCC (Tisserand et al. 2011). Differential Gene Expression and Ingenuity Pathway Analysis (IPA) of genes identified as both TRIM24- and Rara-dependent revealed the pathway with the most altered genes as the IFN/STAT pathway (among other IFN-related pathways e.g. pattern recognition and IRF activation) (Tisserand et al. 2011). Recent work has also shown a negative regulation of STAT1 by TRIM24 in head and neck squamous cell carcinoma (HNSCC) in a co-regulatory loop that mediates a balance between proliferation and apoptosis. *Trim24* mRNA abundance was increased in *Stat1* siRNA-treated CAL27 cells (HNSCC cell line), and STAT1 protein abundance was increased in *Trim24* siRNA-treated CAL27 cells (Anderson et al. 2022).

Conversely, a recent study showed that TRIM24 inhibits the IL-4-stimulated STAT6 pathway (Yu et al. 2019). Following IL-4 stimulation, TRIM24 directly binds and ubiquitinates the transcriptional co-activator and acetyltransferase CREB-binding protein (CBP), which in turn acetylates STAT6 at position K383. The acetylation of STAT6 by CBP causes a decrease in DNA binding activity of STAT6, thereby inhibiting the induction of AAM-related genes (Yu et al. 2019). It is known that CBP is able to acetylate not just STAT6 but most other STAT proteins as well (Krämer et al. 2009; Icardi et al. 2012), and so with the STAT proteins being important for phenotypic changes and macrophage activation, it is reasonable to hypothesise that this TRIM24-CBP interaction may be relevant in many STAT signalling pathways.

Finally, Lv et al. observed an upregulation of TRIM24 in human glioblastoma samples, and linked it with endothelial growth factor receptor (EGFR) and STAT3 signalling (Lv et al. 2017), which promotes glioma progression and correlates negatively with survival (Fan et al. 2013). Mechanistically, this study showed an upregulation of the histone modification H3K23ac following EGFR activation in glioblastoma cells. Immunoprecipitation assays revealed direct binding between TRIM24 and STAT3/p-STAT3, downstream of EGFR signalling in glioblastoma cells. TRIM24 binds to this histone modification and recruits STAT3 to the chromatin thereby facilitating its transcriptional activity (Lv et al. 2017).

1.3.3.5. TRIM24 in infectious disease

In the past few years, roles of TRIM24 in infectious diseases have been emerging (**Figure 1.10**), with limited studies focussing on macrophage biology. In 2020, a study investigating ubiquitination modulation during infection with vesicular stomatitis virus (VSV) revealed a role for TRIM24 in the RIG-I signalling cascade (Zhu et al. 2020). ShRNA knockdown of *Trim24* led to a two-fold increase in VSV viral titre in HEK293T cells, while *Trim24* overexpression significantly reduced it after 24 hours infection (Zhu et al. 2020). Further signalling pathway analysis in B6 peritoneal macrophages revealed that following infection TRIM24 relocates to the mitochondria, where it associates with TRAF3 and mediates its ubiquitination and therefore activation. Activation of TRAF3 led to TBK1 activation, which in turn activates IRF3 to induce IRF3-stimulated gene expression, including *Ifnb1*. Knockdown of *Trim24* reduced VSV-induced *Ifnb1*, and IRF3 can also bind to the *Trim24* promoter and inhibit its expression, thus forming a negative feedback loop (Zhu et al. 2020). Since this study, TRIM24 has been implicated in other viral infections such as HIV-1 (Horvath et al. 2023) and Epstein-Barr virus (De La Cruz-Herrera et al. 2023), and in sterile inflammation in macrophages (Hui et al. 2023).

A recent study identified the E3 ubiquitin ligase MARCH1 as a negative regulator of IFN-I signalling during infection with two different strains of the protozoan parasite *Plasmodium yoelii* (N67 and YM) (Wu et al. 2020). Subsequent microarray analysis of *P. yoelii*-infected *March1*$^{-/-}$ B6 mouse splenic mRNA (1 and 4 days post-infection) revealed TRIM24 as an upstream negative regulator of the IFN-I response, and was predicted to be activated 1 day but not 4 days post-infection (as the output of Ingenuity Pathway Analysis (IPA)). Other activated upstream regulators included IL10RA, SOCS1, SOCS3, and USP18, which are all known inhibitors of IFN-I production (Wu et al. 2020). Interestingly however, in WT mice, *P. yoelii* infection led to a reduction of TRIM24 protein at day 4 post-infection, indicating TRIM24 is rapidly downregulated in the early stages of infection, possibly providing evidence of TRIM24's role in the IFN-I response. Furthermore, in *March1*$^{-/-}$ mice, reduction of TRIM24 protein was observed at day 1 and remained low at day 4 post-infection. The authors did not explore a further time point than 4 days, or reconcile the discrepancy between TRIM24 protein reduction and simultaneous TRIM24 activation during *P. yoelii* infection (Wu et al. 2020).

TRIM24 has also been implicated in Th2 response-driven infections and the airway allergy response. In a murine B6 model of airway allergy (by house dust mite exposure), and helminth infection (*Heligmosomoides polygyrus*), TRIM24 was predicted to be active in Th2

cells but not in other T cell subtypes. Although TRIM24 mRNA was not differentially expressed in Th2 cells by microarray data analysis and qPCR mRNA abundance determination, TRIM24 protein was higher in *in vitro*-generated Th2 cells compared with naive ($CD4^+$ $CD44^-$ $CD62L^{hi}$) T cells (Perez-Lloret et al. 2016). A mechanistic role for TRIM24 was subsequently identified, where TRIM24 deletion reduced Th2-mediated inflammation during the allergic response, characterised by reduced IL-10, IL-5, and IL-13 release after 4 days on *in vitro*- house dust mite challenge. In *H. polygyrus* infection, TRIM24 deletion led to reduced mRNA abundance of *Arg1, Il13,* and *Retnla* (RELMα) and impaired parasite clearance in the small intestine after 14 days, indicating a requirement for TRIM24 in developing a Th2 response (Perez-Lloret et al. 2016). Further work revealed a requirement for TRIM24 in the expression of IL1R on Th2 cells, and therefore in the IL-1β-mediated activation of Th2 cells (Perez-Lloret et al. 2016).

1.3.3.6. TRIM24 in *Leishmania* infections

Until recently, the roles of TRIM24 during *Leishmania* infections have remained unexplored. However, considering the roles of TRIM24 in the interferon response during other infections and cancers, it can be hypothesised that TRIM24 may play important roles in *Leishmania* infections where an IFN-driven Th1 response mediates resolution of disease.

In 2018, Ashwin et al. published a transcriptomics analysis study on spleen, liver and peripheral blood taken from BALB/c mice during chronic infection of *Leishmania donovani* in (Ashwin et al. 2018). Differential gene expression (DGE) analysis of the transcriptomics data revealed several differentially expressed genes during *L. donovani* infection at days 15, 17, 21, 36, and 42 post-infection. IPA further revealed the major pathways affected by *L. donovani* infection, most of which are immune signalling pathways such as the IFNγ and STAT pathways. Based on the DGE analysis of 41 genes observed to be upregulated in the spleen during infection, IPA analysis predicted TRIM24 (and IL10RA) to be downregulated in response to *L. donovani* infection (Ashwin et al. 2018).

Since this study, several other studies have also identified TRIM24 as an upstream negative regulator predicted to be downregulated during *Leishmania* infections. For example, Terrazas et al. performed microarray analysis of sorted $Ly6C^{hi}$ $Ly6G^-$ $CD11b^+$ monocytes from naive and 30-day *L. donovani*-infected BALB/c mice, and their IPA on DEGs also predicted that TRIM24 and RICTOR (involved in mTOR signalling) were upstream negative regulators that were downregulated. Upstream positive regulators were STAT1, STAT3, IRF1, and IRF7 (Terrazas et al. 2017).

Venugopal et al. recently used a single cell mRNA sequencing (scRNA-seq) approach to investigate the immune landscape of B6 mouse ears four weeks after infection with *L. major* (Venugopal et al. 2022). IPA of DEGs from macrophages, blood endothelial cells (BECs), and lymphatic endothelial cells (LECs) present in infected ears identified TRIM24 as an inhibited transcriptional regulator in BECs and LECs, but interestingly not in macrophages (Venugopal et al. 2022).

Finally, Chaparro et al. used scRNA-seq to show surprisingly different *in vitro L. donovani*-infected macrophage transcriptional profiles that were dependent on the parasite life stage (promastigotes vs amastigotes) (discussed in further detail in **Chapter 6**) (Chaparro et al. 2022). TRIM24 was predicted by IPA to be inhibited in BMDMs infected with promastigotes, but not with amastigotes. This perhaps makes sense as the transcriptional profile of these BMDMs were more inflammatory than that of amastigote-infected BMDMs, with a strong IFN signalling-related signature and IFN-related TFs such as IRF3 and IRF7 predicted to be activated (Chaparro et al. 2022). The authors did not pursue the study in relation to TRIM24 any further than its identification.

It is important to note that TRIM24 has been consistently identified as an upstream negative regulator based on IPA analysis, and while IPA is extremely powerful, other methods of pathway analysis may not lead to similar results. Nevertheless, despite the identification of TRIM24 in the aforementioned transcriptomics studies, its functions during *L. donovani* infection have not been formally investigated. In this thesis, we endeavour to elucidate some of these roles of TRIM24 and provide further insight into the murine response to experimental *L. donovani* infection that may assist in the development of novel therapies.

1.4. Project Aims

1) To determine the role of TRIM24 in inflammatory CAM activation *in vitro* (**Chapter 3**).

2) To use a transcriptomics approach to determine *L. donovani*-induced alterations to murine bone marrow macrophages *in vitro* at a single cell level, and assess how TRIM24 deletion affects naïve and infected cells (**Chapter 4**).

3) To characterise important lymphoid organs of KO mice, and to investigate the effect of TRIM24 deletion on the progression and outcome of experimental *L. donovani* infection *in vivo* (**Chapter 5**).

4) To use single cell transcriptomics to profile the bone marrow during experimental *L. donovani* infection, and to assess the effects of TRIM24 deletion on cellular phenotype (**Chapter 6**).

1.5. Figures

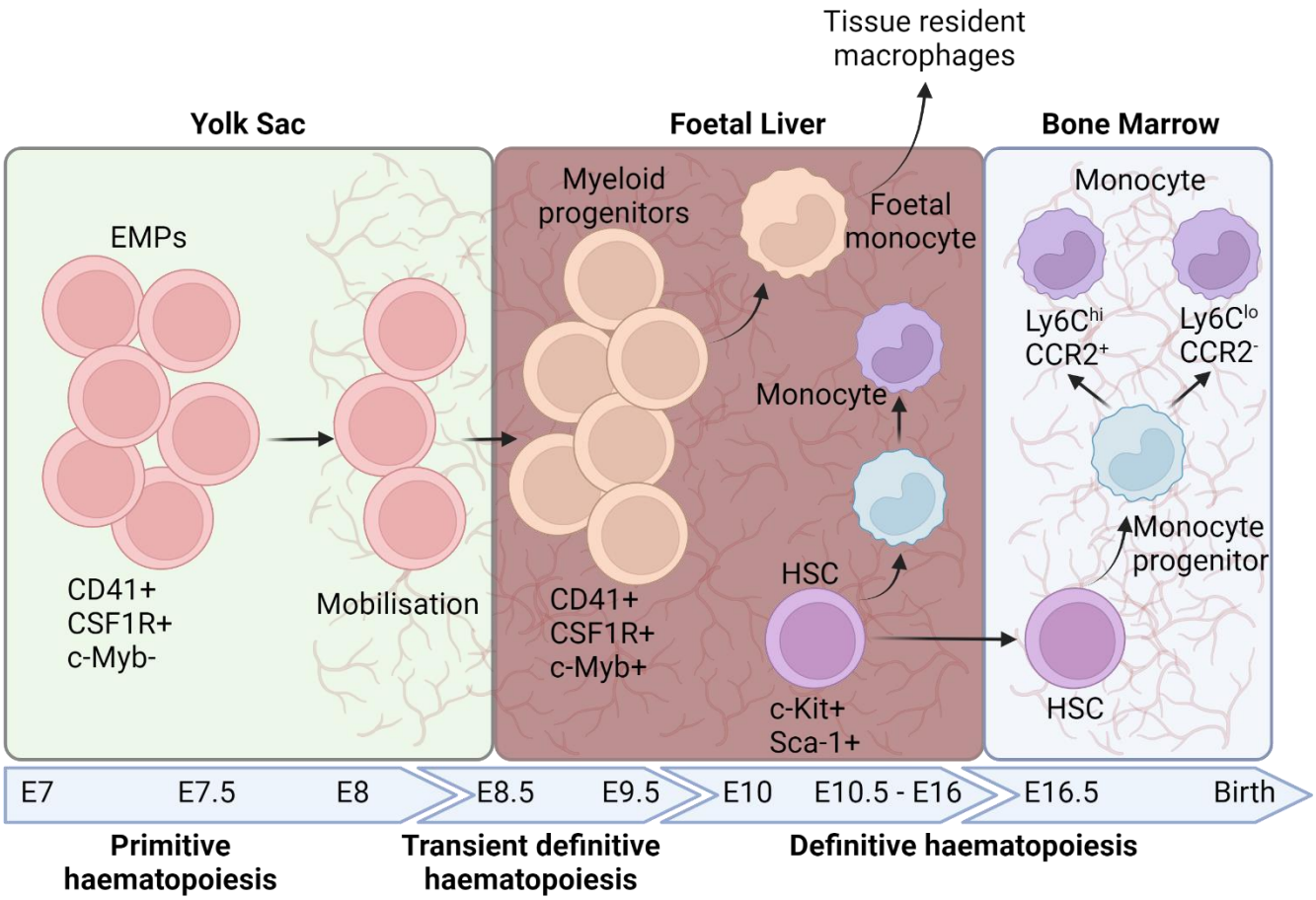

Figure 1.1. Haematopoiesis during foetal development. Primitive haematopoiesis occurs when early erythro-myeloid progenitor cells (EMPs) arise from the foetal yolk sac around E7, characterised by CD41^{+} CSF1R^{+} c-Myb^{-}. When vasculature develops (~E8-8.5), EMPs are mobilised to the foetal liver, and c-Myb^{+} EMPs arise that in turn give rise to foetal monocytes, in transient definitive haematopoiesis. Foetal monocytes migrate and differentiate into tissue resident macrophages. Definitive haematopoiesis begins with the emergence of c-Kit^{+} Sca-1^{+} haematopoietic stem cells (HSCs), which differentiate through monocyte intermediates into mature monocytes. This occurs in the foetal liver between ~E10.5 and ~E16. Bone marrow haematopoiesis occurs from ~E16.5 and persists through birth and adulthood, where HSCs differentiate into Ly6C^{hi} CCR2^{+} and Ly6C^{lo} CCR2^{-} monocytes through sequential monocyte intermediary cells.

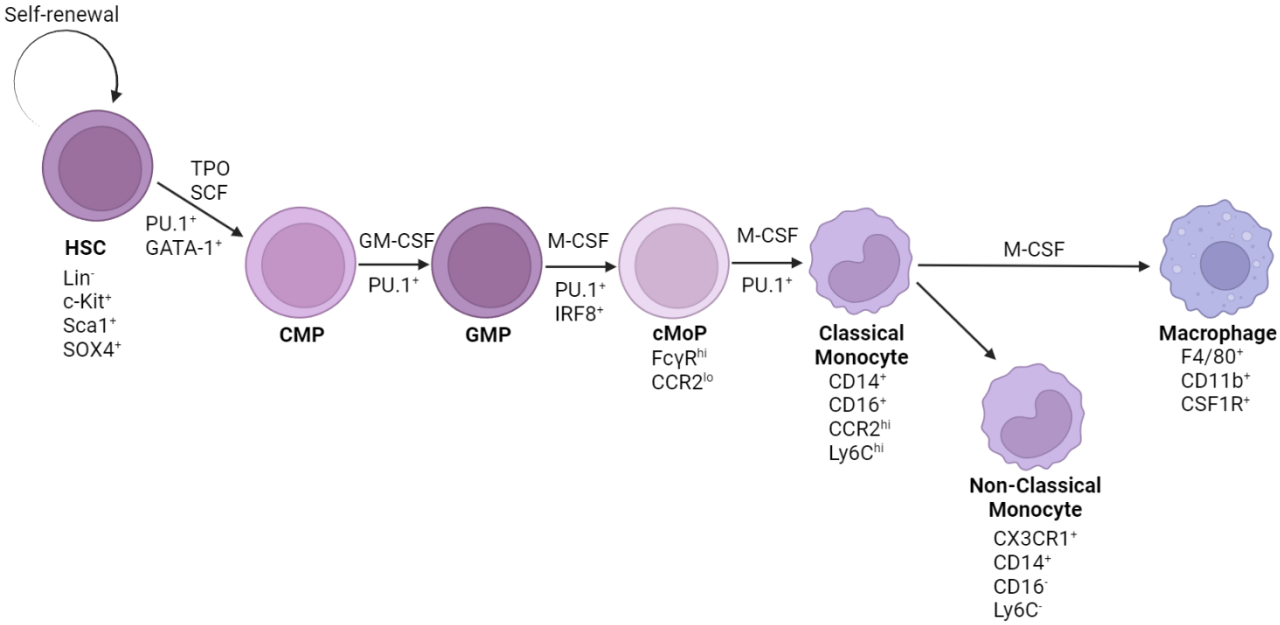

Figure 1.2. Simplified bone marrow-derived macrophage (BMDM) development. Monocyte and macrophage differentiation are shaped by a combination of growth factor signalling and transcription factor expression for lineage commitment. HSC = haematopoietic stem cell, CMP = common myeloid progenitor, GMP = granulocyte-monocyte progenitor, cMoP = common monocyte progenitor, TPO = thrombopoietin, SCF = stem cell factor.

Tissue	Macrophage subset	Markers	Function
Spleen	Marginal Zone Macrophage	$CD11b^{lo}$ $F4/80^{-}$ $SIGNR1^{+}$	Immune surveillance, detection of microbial polysaccharides
	Metallophilic Macrophage	$CD11b^{lo}$ $F4/80^{-}$ $CD169^{+}$	Immune surveillance, detection of sialylated bacteria & apoptotic bodies
	Red Pulp Macrophage	$CD11b^{lo}$ $F4/80^{+}$ $CD68^{+}$ $CD206^{+}$ $SPIC^{+}$	Senescent erythrocyte removal, iron homeostasis
Liver	Kupffer cells	$CD11b^{-}$ $F4/80^{+}$ $CD68^{+}$ $ID3^{+}$ $CD169^{+}$	Immune surveillance, phagocytosis
Lung	Alveolar macrophages	$CD11b^{-}$ $F4/80^{+}$ $CD206^{+}$ $CD11c^{+}$ $MARCO^{+}$	Immune surveillance Scavenging of foreign particles
Skin	Langerhans cells	$CD11b^{+}$ $CD11c^{+}$ $F4/80^{+}$ $Langerin^{+}$	Antigen presentation
Brain	Microglia	$CD11b^{+}$ $F4/80^{+}$ $TMEM199^{+}$	Immune surveillance, synaptic remodelling, removal of dead neurons
Bone marrow	Osteoclasts	Calcitonin R^{+} $RANK^{+}$ Cathepsin K^{+} $CD13^{+}$	Bone remodelling
	$CD169^{+}$ macrophage	$CD11b^{+}$ $F4/80^{+}$ $CD68^{+}$ $CD169^{+}$	HSC retention & promotion of haematopoiesis

Table 1.1. Tissue macrophage identities and functions. HSC = Haematopoietic stem cell.

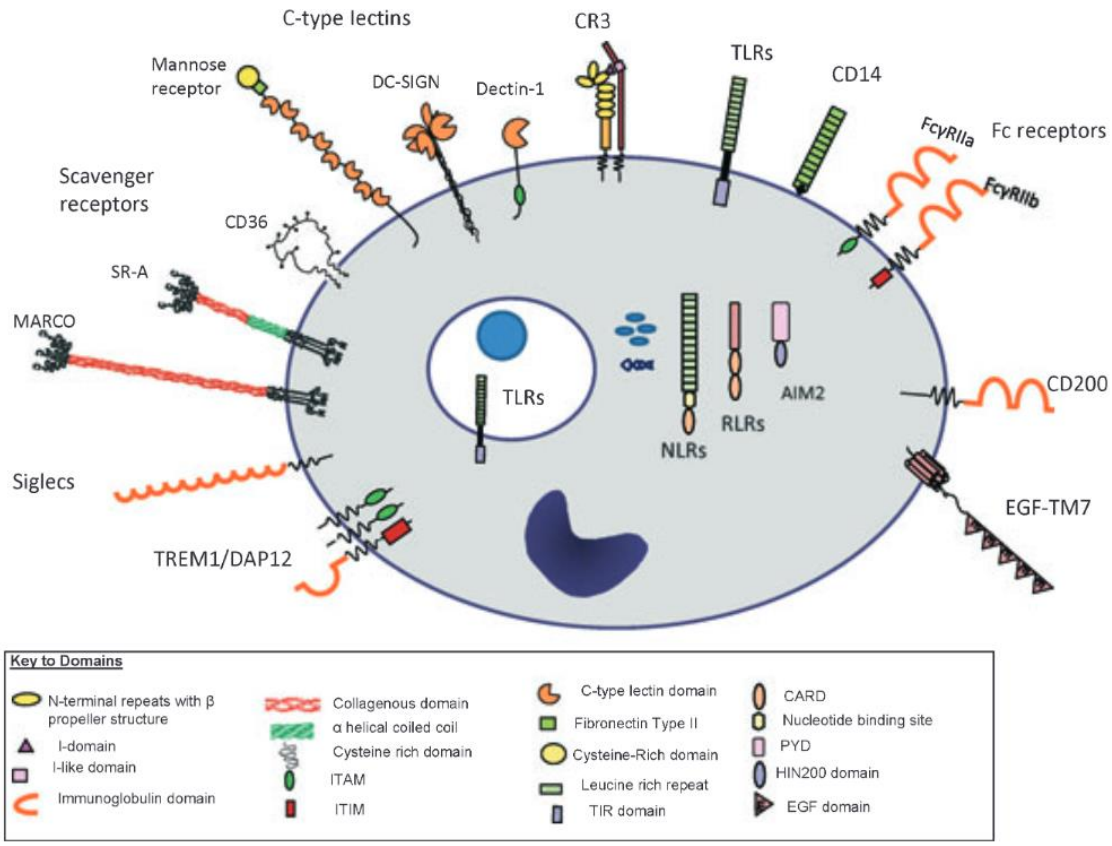

Figure 1.3. Pattern recognition receptors in macrophages. Macrophages express a wide range of PRRs including scavenger receptors, C-type lectins, Fc receptors, and Toll-like receptors, to allow detection of foreign material and initiation of the appropriate response e.g. phagocytosis and destruction of bacteria, or recycling of senescent erythrocytes. Figure taken from Pluddemann et al. (2011).

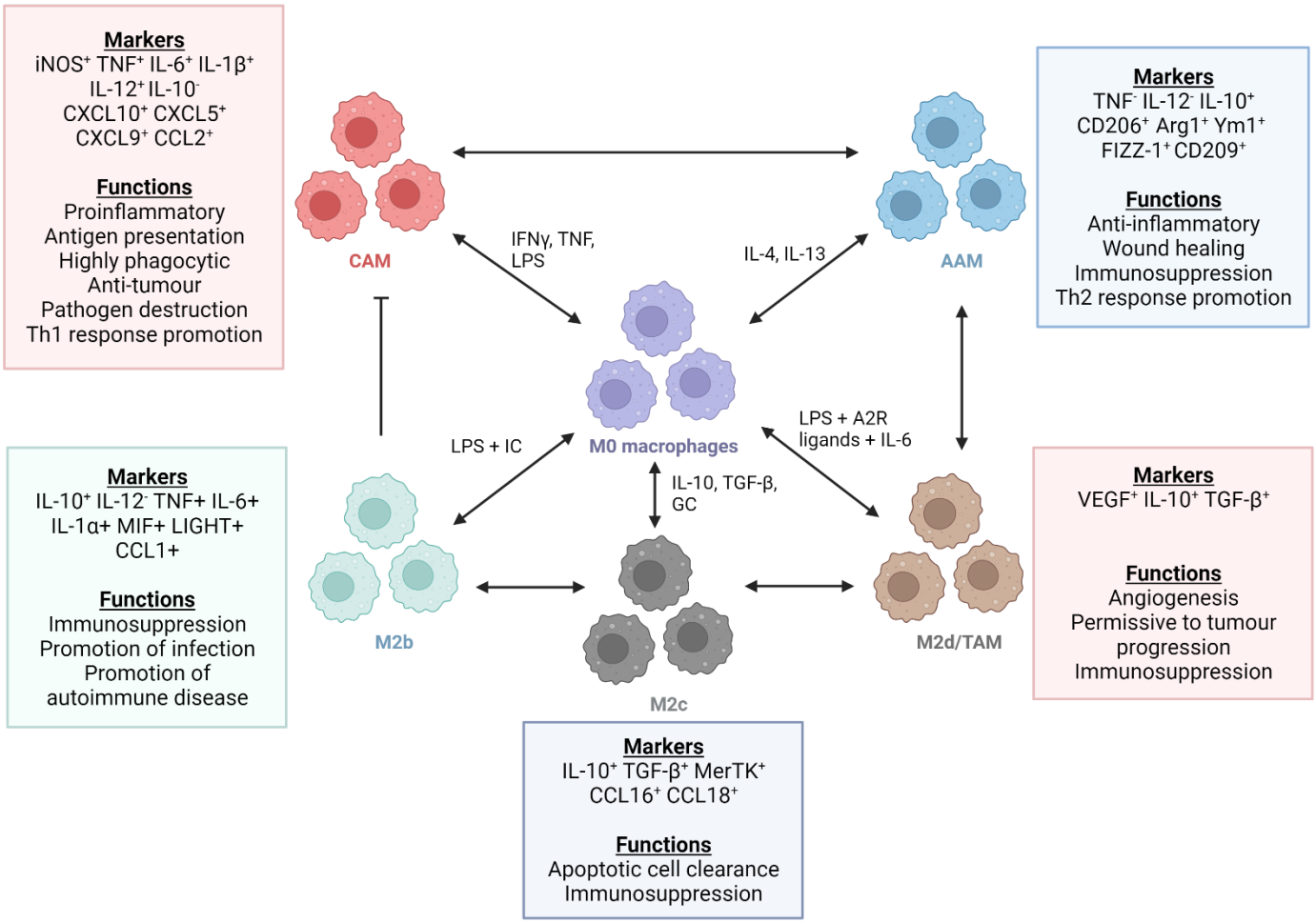

Figure 1.4. Macrophage polarisation, markers and functions. CAM = classically activated macrophage, AAM = alternatively activated macrophage, TAM = tumour-associated macrophage, IC = immune complex, GC = glucocorticoids, A2R = A2 adenosine receptor.

Disease pattern	Old World species	New World species	Symptoms, exam, lab findings
Visceral leishmaniasis	*L. donovoni*, *L. infantum*, *L. tropica*	*L. chagasi* (identical species to *L. infantum* but in New World), *L. amazonensis*	Fever, weight loss, fatigue, hepatosplenomegaly, pancytopenia, hypergammaglobulinemia
Post-kala azar dermal leishmaniasis	*L. donovoni, L. infantum*	*L. chagasi* (identical species to *L. infantum*)	Skin lesions (always starts on face) 6 months following VL
Cutaneous leishmaniasis	*L. tropica*, *L. major*, *L. aethiopica*, *L. infantum*, *L. donovani*	*L. mexicana* species complex, *L. mexicana*, *L. amazonensis*, *L. venezuelensis*, *L. Vianna (V) subgenus*, *L. (V) braziliensis*, *L. (V) panamensis*, *L. (V) guyanesis*, *L. (V) peruviana*, *L. major* like organisms, *L. chagasi*	Skin lesions on extremities and face:Painless papules which progress to nodules then ulcers
Leishmaniasis recidivans	*L. tropica, L. major*	*N/A*	Satellite lesions around prior ulcer site difficult to treat and may relapse
Diffuse cutaneous leishmaniasis	*L. aethiopica*	*L. mexicana*, *L. amazonensis*, *L. panamensis (rarely)*	Diffuse, anergic skin lesions with non-ulcerative nodules and plaques progressing from primary lesion. Rare but more common in immunocompromised individuals
Disseminated leishmaniasis	N/A	*L. Vianna subgenus*, *L. (V) braziliensis* (most common), *L. amazonensis*	Noncontiguous pleomorphic lesions in immunocompetent hosts. Difficult to treat
Mucosal leishmaniasis	*L. tropica*, *L. major*, *L. donovani*, *L. infantum*	*L. Vianna (V)* subgenus, *L. (V) brazilensis*, *L. (V) panamensis*, *L. (V) guyanesis*, *L. (V) peruviana*, *L. amazonensis*	Nasal secretions, nasal obstruction, pain, epistaxis. Destructive lesions in nose, oropharynx. Initially involves nose and mouth, can progress to include pharynx and larynx

Table 1.2. *Leishmania* species and their associated leishmaniasis disease type and clinical manifestation. Table taken from Mann et al. 2021.

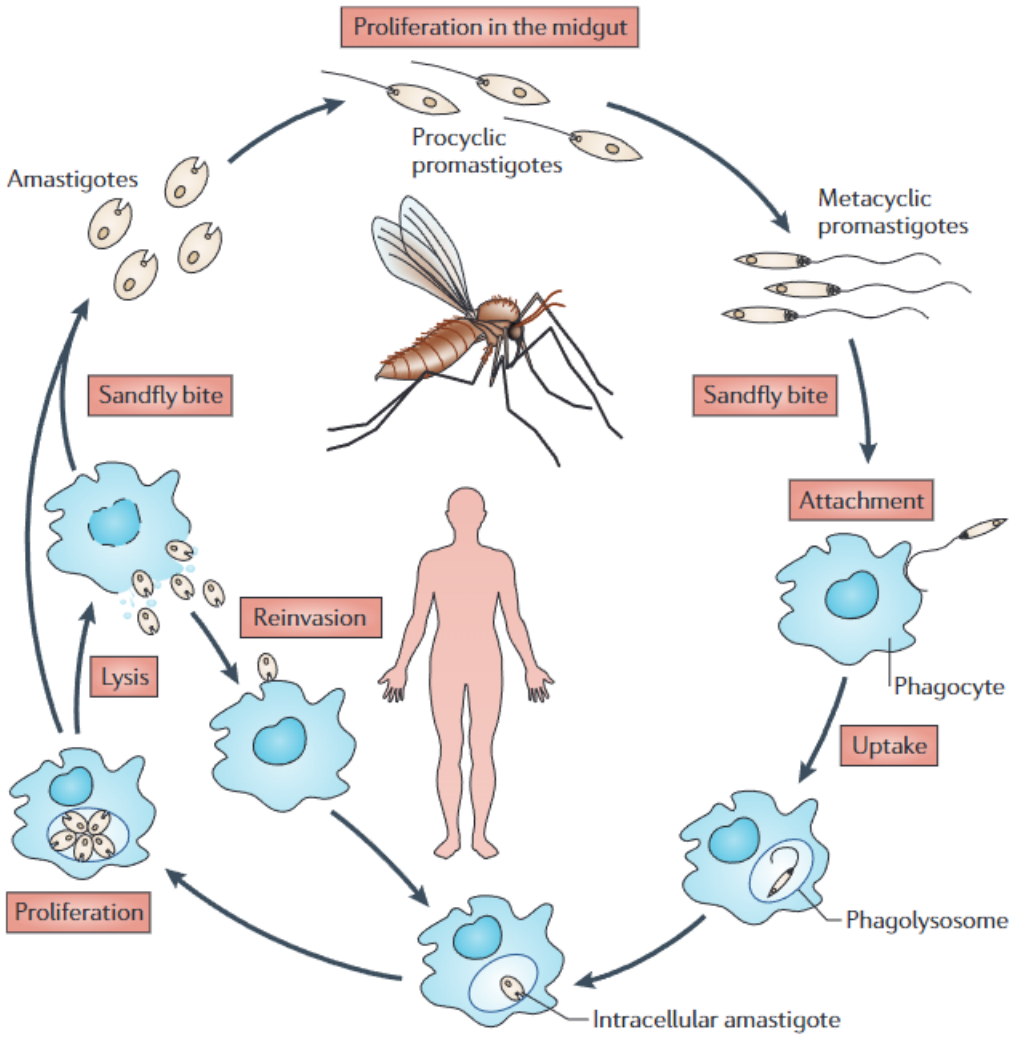

Figure 1.5. Life cycle of *Leishmania* parasites. *Leishmania* parasites proliferate as procyclic promastigotes in the sand fly midgut. Differentiation into mammalian infective metacyclic promastigotes occurs in the sand fly foregut prior to blood meal. Metacyclic promastigotes are transmitted to the mammalian host during blood feeding, and are phagocytosed by phagocytic cells (neutrophils, monocytes, macrophages). Parasites then differentiate into amastigotes within their intracellular niche (predominantly in macrophages), where they are able to survive and proliferate. Excessive intracellular amastigote replication leads to host cell rupture, releasing amastigotes, and allowing continued infection of nearby phagocytes. Uninfected sand flies take up amastigotes when taking a blood meal from an infected mammalian host, and the amastigotes differentiate into procyclic promastigotes in the midgut, completing the life cycle. Adapted from Kaye and Scott 2011.

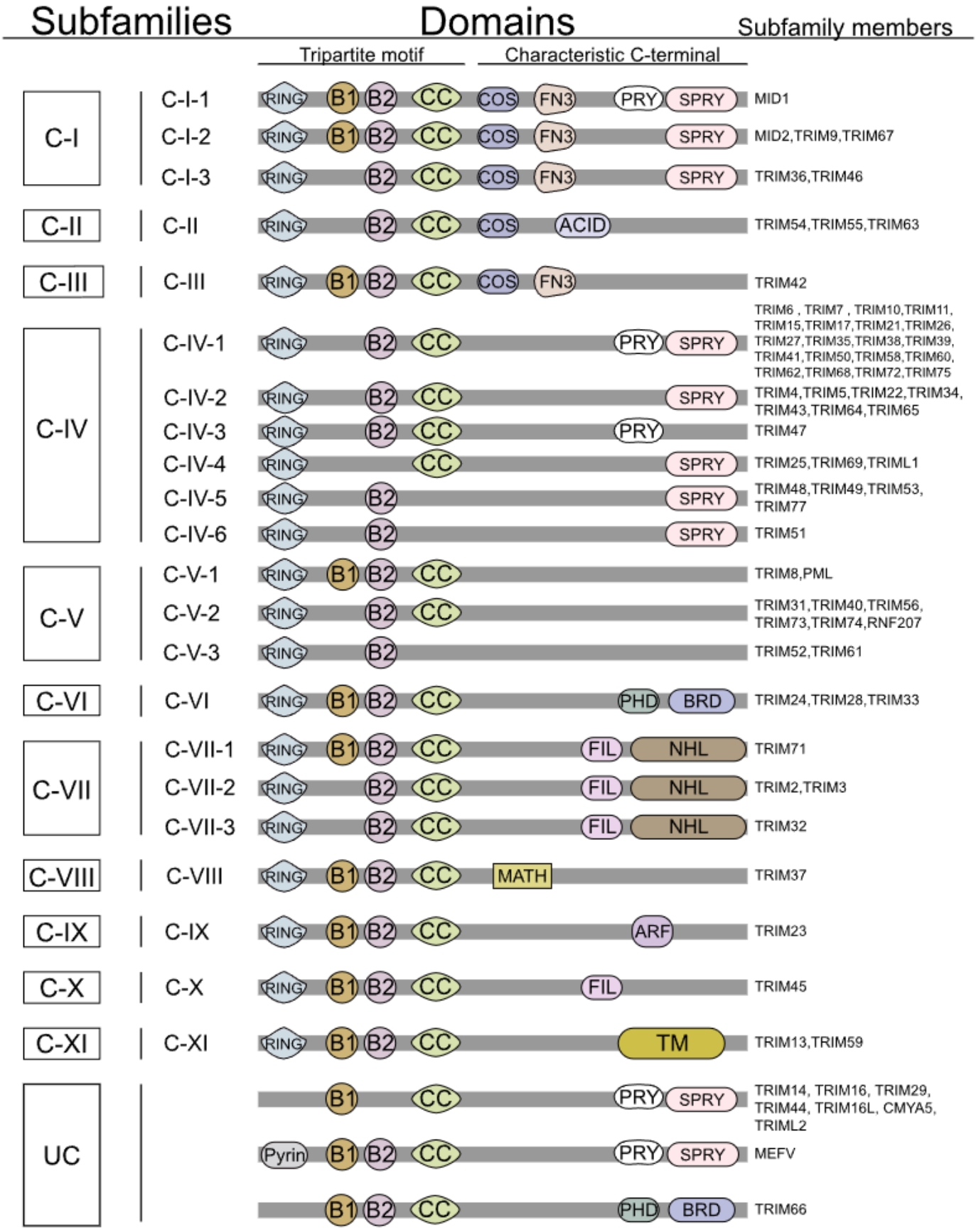

Figure 1.6. TRIM protein family sub-classification and domain structure. RING = Really Interesting New Gene; B1/B2 = B-Box 1/2; CC = coiled coil; COS = C-terminal subgroup one signature domain; FN3 = fibronectin type 3 domain; ACID = acid rich region; PHD = plant homeodomain; BRD = bromodomain; FIL = filamin type I domain; TM = transmembrane region; MATH = Meprin and TRAF-homology domain; ARF = ADP-ribosylation factor family domain. Taken from Lu et al. 2022.

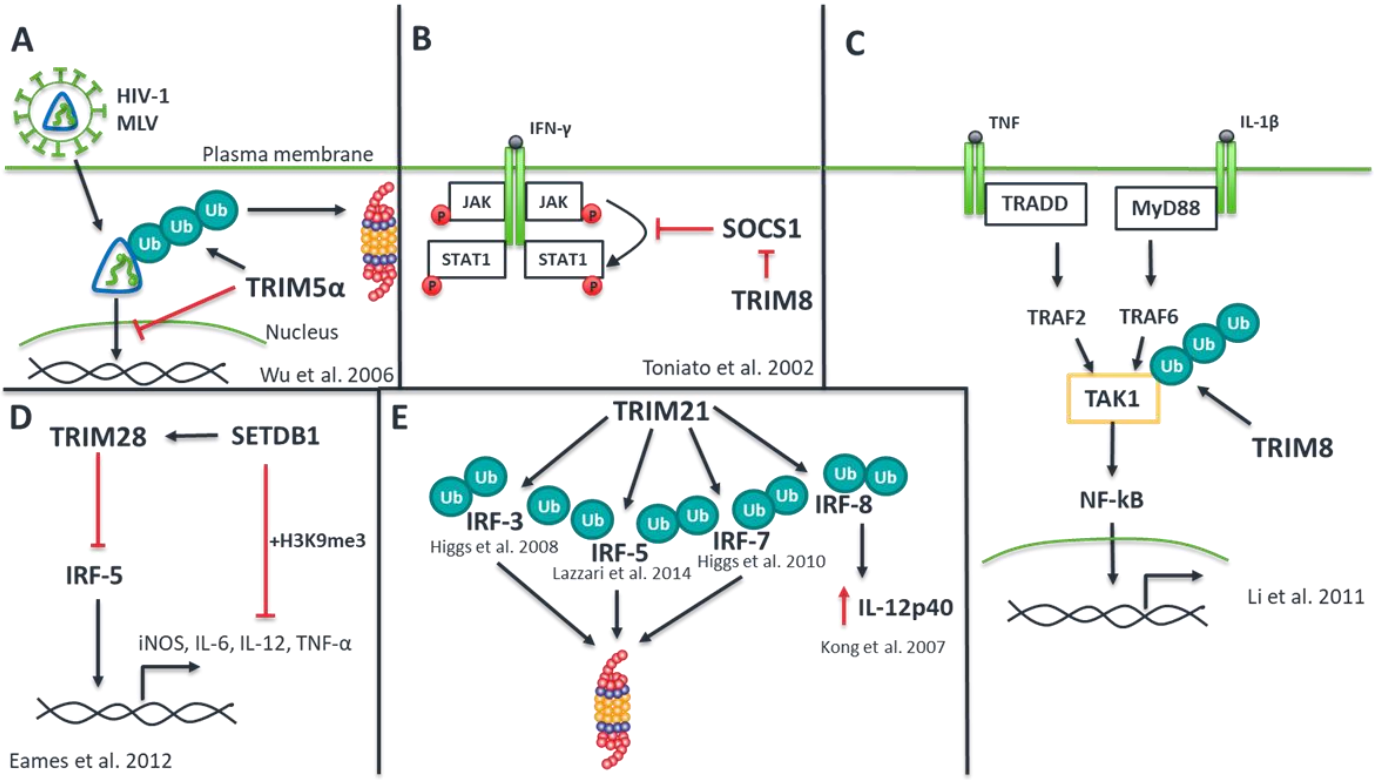

Figure 1.7. Simplified examples of TRIM protein roles in immune pathways. (A) TRIM5α prevents HIV-1 viral capsid trafficking to the nucleus, and targets the viral core for polyubiquitination-mediated proteasomal degradation in rhesus macaques (Wu et al. 2006). **(B)** TRIM8 interacts with SOCS1 to inhibit the repressive activity of SOCS1 in type II interferon signalling (Toniato et al. 2002). **(C)** TRIM8 also ubiquitinates TAK1 after TNF and IL-1β stimulation, thereby activating TAK1 and promoting NF-kB activation (Li et al. 2011). **(D)** TRIM28 indirectly inhibits transcription of pro-inflammatory factors in inflammatory macrophages. IRF5 recruits TRIM28, which recruits SETDB1 to the IRF5 locus. SETDB1 deposits H3K9me3 histone modifications, resulting in conversion to heterochromatin and repression of gene transcription (Eames et al. 2012). **(E)** TRIM21 directly ubiquitinates many of the IRF proteins, resulting either in targeting for proteasomal degradation (Higgs et al. 2008; Lazzari et al. 2014; Higgs et al. 2010), or enhancement of pro-inflammatory IL12p40 expression through a non-proteasomal degradation pathway (Kong et al. 2007).

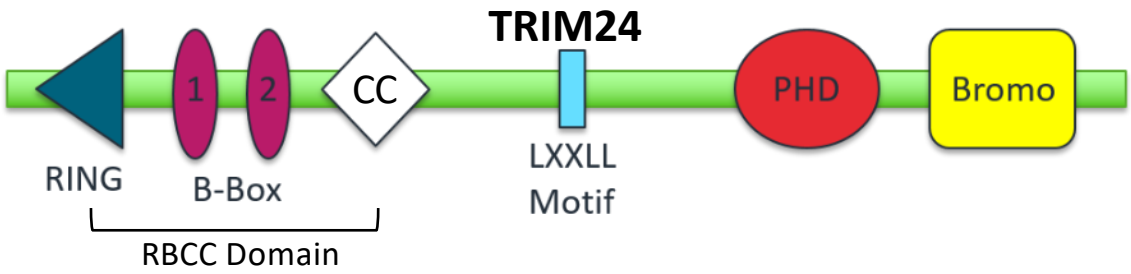

Figure 1.8. Domain structure of TRIM24. TRIM24 protein consists of an N-terminal tripartite motif domain containing a RING domain, two B-Box domains, and a coiled coil (CC) domain. Together, these domains are referred to as an RBCC domain. At the C-terminus, TRIM24 possesses a plant homeodomain (PHD) and a Bromo domain. A conserved LXXLL motif is also found which binds nuclear receptors.

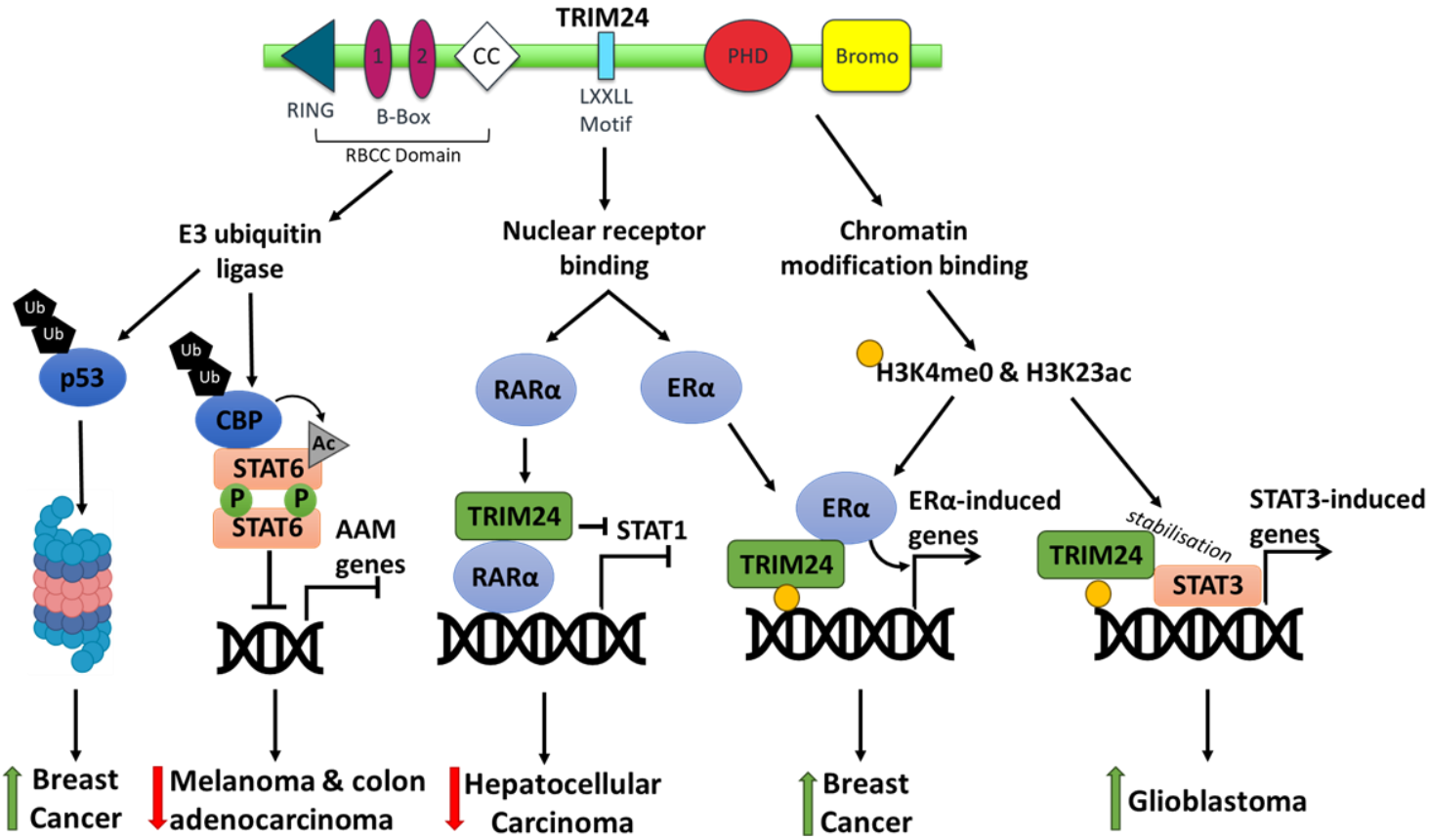

Figure 1.9. Domain-specific functions of TRIM24 in cancer. From left to right: The RBCC domain of TRIM24 conveys E3 ubiquitin ligase activity. TRIM24 ubiquitinates and targets p53 for proteasomal degradation, promoting breast cancer progression (Jain et al. 2014).

TRIM24 directly interacts and ubiquitinates CREB-Binding Protein (CBP). Ubiquitinated CBP acetylates phosphorylated STAT6, which inhibits its DNA binding activity, repressing AAM-related gene expression, and inhibiting progression of melanoma and colon adenocarcinoma in B6 mice (Yu et al. 2019).

The LXXLL motif of TRIM24 conveys nuclear receptor binding activity. In HCC, TRIM24 binds to RARα and prevents retinoic acid-induced STAT1 expression, inhibiting expression of ISGs and preventing HCC progression (Tisserand et al. 2011).

TRIM24 binds to chromatin modifications H3K4me0 and H3K23ac, stabilising Oestrogen receptor α (ERα) and promoting ERα-induced gene expression, promoting breast cancer progression (Tsai et al. 2010).

In a similar vein, TRIM24 binds to H3K4me0 upstream of STAT3-induced genes following endothelial growth factor receptor (EGFR) signalling in glioblastoma cells. This stabilises STAT3 binding to target promoters and enhances STAT3-induced gene expression thereby promoting glioblastoma progression (Lv et al. 2017).

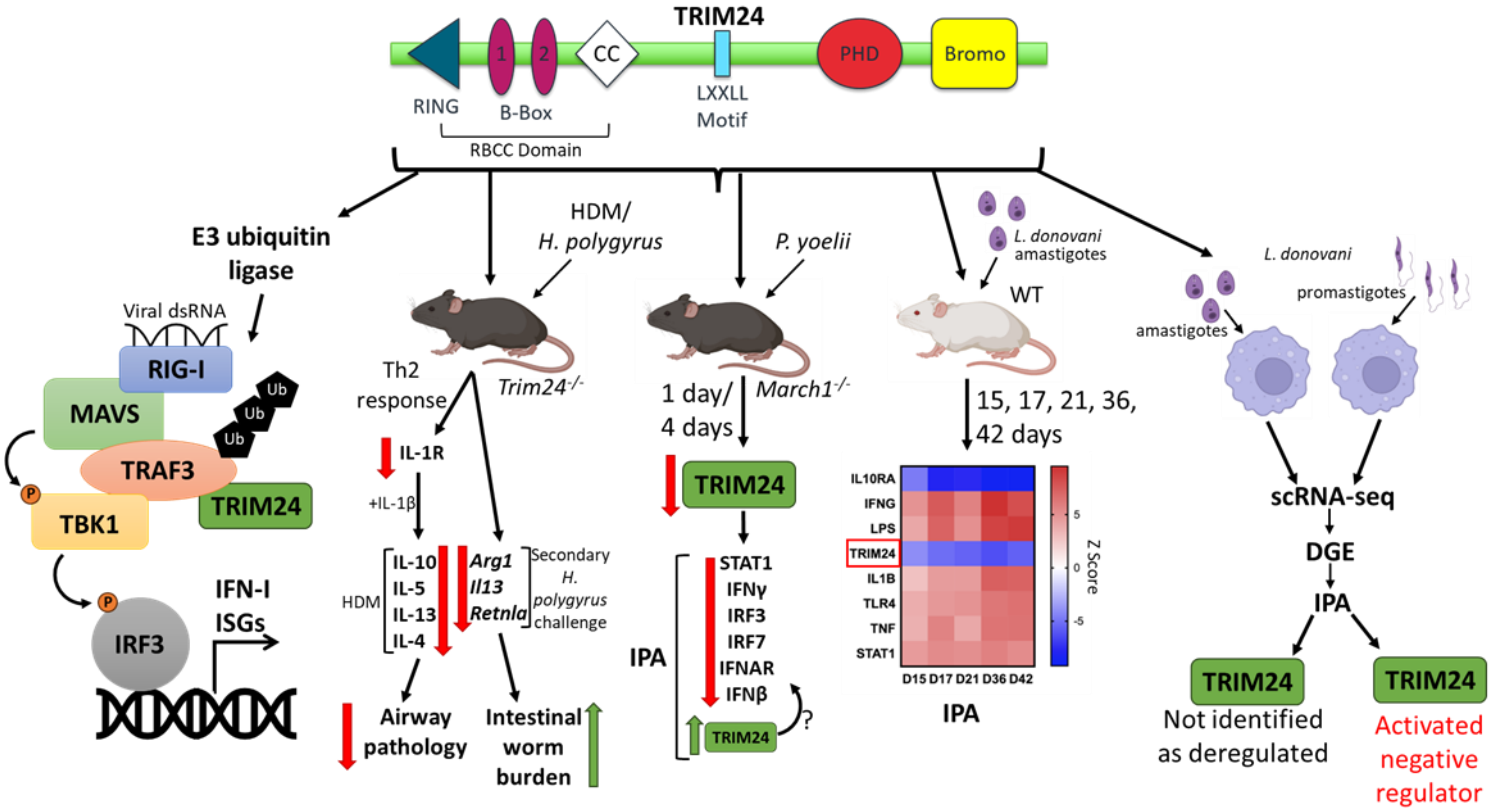

Figure 1.10. Functions of TRIM24 in infectious disease. From left to right: E3 ubiquitin ligase activity of TRIM24 after vesicular stomatitis virus (VSV) infection in macrophages. Following VSV infection, TRIM24 associates with TRAF3 and ubiquitinates it. This activates a phosphorylation cascade resulting in activation of IRF3 and the induction of IFN-I genes and ISG expression (Modified from Zhu et al. 2020).

TRIM24 was identified as a critical regulator of Th2 function and mediated of the type 2 allergic response and in helminth immunity. TRIM24 was required for IL-1R expression in Th2 cells, and TRIM24 deletion led to decreased Th2 cytokine release and reduced IL-1β-induced exacerbation of the airway allergic response. TRIM24 deletion also led to reduced mRNA abundance of *Arg1, Il13,* and *Retnla* in the small intestine, impairing clearance of a secondary challenge infection of *H. polygyrus* (Perez-Lloret et al. 2016).

Plasmodium yoelii infection of *March1*$^{-/-}$ mice led to downregulation of TRIM24 protein one day post-infection. TRIM24 was also predicted by IPA to be activated one day post-infection in *March1*$^{-/-}$ mice based on downregulation of interferon-related genes, however this has not been formally validated (Wu et al. 2020).

A transcriptional study of BALB/c mice infected with *L. donovani* amastigotes for the indicated time points revealed TRIM24 to be predicted to be inhibited based on upregulation of 41 inflammatory and interferon-related genes (Ashwin et al. 2018).

Single cell RNA sequencing of murine macrophages infected with either *L. donovani* amastigotes or promastigotes revealed an IPA-predicted activation of TRIM24 in promastigotes-infected macrophages, but not in amastigote-infected macrophages (Chaparro et al. 2022).

Chapter 2. Materials and Methods

2.1. Mice and cell culture

2.1.1. Mouse strains

All C57BL/6 mouse strains used in this study (B6.CD45.2.*Rag2*$^{-/-}$, B6.CD45.1, B6.*Trim24*$^{dlE1/+}$) were bred and maintained at the University of York Biological Services Facility (BSF). Mice were weaned and re-caged at 3 weeks of age (5 mice per cage) in individually ventilated cages maintained under specific-pathogen free (SPF) conditions according to Home Office guidelines. Cage enrichments were added, and mice had access to food and water *ad libitum*. Individual mice in each cage were identified by ear notching, and ear notches were used for genotyping. A mixture of male and female mice were used for experimental work at 8-12 weeks of age. All experiments were performed under the Home Office Project Licence (Ref # P49487014) and ARRIVE guidelines. Mice were sacrificed at experimental endpoints using schedule-1 killing (S1k) methods.

Germline-deleted *Trim24*$^{-/-}$ mice were originally developed by Dr Michelle Barton (MD Anderson Cancer Centre, University of Texas, Houston, USA) (Jiang et al. 2015). Briefly, homologous recombination was used to generate a vector that targeted the core promoter and exon 1 regions of the *Trim24* gene. This was achieved through the insertion of LoxP sites into the promoter region and into intron 1 of the *Trim24* gene. An FRT-flanked neomycin resistance gene fused to the phosphoglycerokinase promoter was also inserted behind the LoxP site in intron 1. This targeting vector was electroporated into TC-1 mouse embryonic stem cells. Positive clones were selected through neomycin treatment and were used to generate chimeric mice. The progeny of these chimeric mice were then backcrossed with C57BL/6 mice to generate heterozygous *Trim24*$^{LoxPNeo/+}$ mice. The FRT-flanked neomycin resistance cassette was removed by crossing *Trim24*$^{LoxPNeo/+}$ mice with ROSA26-FLPeR mice (mice constitutively expressing flippase recombinase). The resulting *Trim24*^{LoxP} mice were then crossed with *Zp3-Cre* mice (mice with Cre recombinase driven by the *Zp3* promoter) to generate *Trim24*$^{dlE1/+}$ heterozygous mice. These were intercrossed to generate homozygous B6:*Trim24*$^{dlE1/dlE1}$ knockout mice (KO; *Trim24*$^{-/-}$) and wild-type (WT) littermate control mice (Jiang et al. 2015). Sperm from B6*:Trim24*$^{dlE1/+}$ mice were kindly provided by Dr. Michelle Barton. B6*:Trim24*$^{dlE1/+}$ mice were re-derived at MRC Harwell before being sent to the University of York. Re-derived B6*:Trim24*$^{dlE1/+}$ mice were bred in-house to produce 25% KO mice, 25% WT littermate controls, and 50% *Trim24*$^{dlE1/+}$ mice.

B6:CD45.2.*Rag2*$^{-/-}$ mice were used for the maintenance of *L. donovani* parasites by serial passage. Mice were infected for a minimum of three and maximum of 14 months before passage or use for experiments.
We also used B6.CD45.1 mice as recipient mice for mixed BM chimera experiments.

2.1.2. Genotyping of B6:*Trim24*$^{dlE1/+}$ mice

When mice reached 3 weeks of age, mice were ear notched and re-caged as described above. Ear notches were used as a source of DNA for genotype determination by PCR and DNA gel electrophoresis. For DNA extraction, ear notches were incubated in 40 µL 40 mM NaOH at 95°C for 15 mins in 1.5 mL tubes. After 15 mins, tubes were allowed to cool, and 40 µL of 40 mM Tris-HCl was added to each tube to neutralise the NaOH. DNA was then diluted 1:10 for use in PCR reaction.
For PCR, a reaction mixture of the following reagents was used per reaction (25 µL reaction volume):

0.5 µL	DNA template
1 µL	100 µg mL^{-1} 5’ Big11 primer (CAAGTCTTTGGGAATTACAGA)
1 µL	100 µg mL^{-1} 5’ LoxPseq1R primer (AGGTTTACAGAAGGAGACAAT)
1 µL	100 µg mL^{-1} 3’ Arm1R primer (CCTGGTAACATAAGCAAAGGA)
12.5 µL	2x PCRBIO Ultra Mix Red (PCR Biosystems, London, UK)
9 µL	Ultra pure water (Milli-Q water filtration system, Merck)

PCR thermal cycling conditions:

Step	Temperature (°C)	Time	Cycles
Initial denaturation & enzyme activation	95	2 min	1
Denaturation	95	15 seconds	40
Annealing	50	15 seconds	
Extension	72	15 seconds	
End	4	Hold	-

PCR reaction product was loaded onto a 1.8% agarose gel for DNA gel electrophoresis. To make up the 1.8% agarose gel, 1.8g of molecular biology grade agarose (Invitrogen, UK) was dissolved in 100 mL 1x Tris-Borate-EDTA (TBE) Buffer by microwaving for 1-2 minutes. TBE buffer was made up as a 10X stock as follows: 108g Tris base (Invitrogen, UK), 55g boric acid (Thermo Fisher Scientific, UK), 40 mL 0.5M EDTA (pH 8.0) (Fisher Scientific, UK) was dissolved in 900 mL deionized water, and the volume was adjusted to 1 L. A working concentration of 1X TBE was made by adding 100 mL 10X TBE to 900 mL ultrapure water. After agarose had dissolved completely, the mixture was left until cool enough to touch, and 10 µL 10,000X SYBR Safe (Stratech, Ely, UK) was added. Agarose with SYBR safe was poured into a gel cast, a comb was added and the gel was left to set for ~2 hours.
After agarose gel has set, the gel was used for DNA gel electrophoresis. 5 µL PCR reaction product per well was used, and a 1,500 bp DNA ladder (PCRBIO Ladder IV, PCR Biosystems) was used to determine size of DNA bands. A WT control and blank negative control were also loaded. DNA gel electrophoresis was run for ~40 mins at 100V using a Bio Rad PowerPac 300. Gel was imaged using a Bio-Rad ChemiDoc system.

Two bands were observed to determine the genotype of each mouse; a band at ~380 bp for WT, and a band at ~600 bp for KO (**Figure 2.1**).
Samples with only the WT band identified WT mice.
Samples with only the KO band identified KO mice.
Samples with both WT and KO bands identified heterozygous mice.

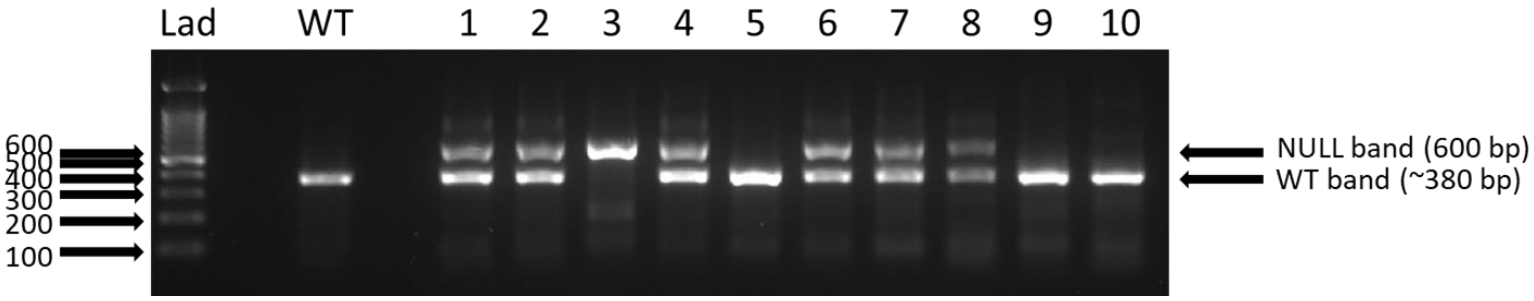

Figure 2.1. Representative DNA gel electrophoresis for KO mouse genotyping. DNA was extracted from mouse ear samples and loaded onto a 1.8% agarose gel with SYBR Safe DNA stain with a 1,500 bp ladder. Electrophoresis was performed, and DNA fragment bands were visualised with a Bio-Rad ChemiDoc system. NULL (KO) band was 600 bp, and WT band was ~380 bp.

2.1.3. Bone marrow (BM) cell isolation

WT and KO mice were euthanized by CO2 inhalation followed by cervical dislocation. Femurs and tibias from both hind legs were removed, and muscle tissue around bones was removed using scissors and tweezers. Bones from each mouse were kept separate. The bones were then placed into tubes containing Dulbecco's Modified Eagle Medium (Gibco, ThermoFisher, Paisley, UK) (one tube per set of mouse bones). The rest of the procedure was conducted in a tissue culture hood to ensure sterility. Bones were washed once with fresh DMEM to remove residual tissue and hair, then submerged in 100% ethanol in a well of a 6-well plate for ~1 minute. Bones were then transferred to fresh DMEM in another well of a 6-well plate. The ends of the bones were cut, and each bone was flushed with 5mL fresh DMEM into a 70 µm cell strainer inserted into a 50 mL Falcon tube (Sarstedt AG & Co, Germany). A single cell strainer was used for each set of four bones per mouse. The BM was then forced through the cell strainer using the rubber end of a 2 mL sterile syringe plunger, and the cell strainer was washed with a further 5 mL DMEM to ensure the highest possible yield of BM cells. The Falcon tube was then centrifuged at 300 xg for 6 mins at 4°C, the supernatant was discarded without disturbing the cell pellet, and the cell pellet was resuspended in 1 mL fresh DMEM. For counting, a 1:20 of BMDMs in 0.4% Trypan blue (Sigma-Aldrich, Dorset, UK) was made. Viable leukocytes were then counted by dye exclusion of the Trypan blue stain on an Improved Neubauer haemocytometer (Weber Scientific International, Middlesex, UK), and adjusted to the desired concentration.

2.1.4. L929 cell culture and supernatant harvest

L929 cells (ATCC, UK) were cultured in complete DMEM (DMEM (Gibco, ThermoFisher, Paisley, UK) supplemented with 100 U mL^{-1} penicillin (Gibco, ThermoFisher, Paisley, UK), 100 µg mL^{-1} streptomycin (Gibco, ThermoFisher, Paisley, UK), 2 mM L-Glutamine (Gibco, ThermoFisher, Paisley, UK), and 10% FCS (Cytiva, HyClone, Fisher Scientific; heat-inactivated by incubation at 56°C for 30 minutes)). Cells were defrosted and initially cultured at 37°C, 5% CO_2 in a sterile 25 cm^3 cell culture flask (Corning) until confluency was reached (2-3 days). Cells were then harvested by incubation with 3-4mL 0.25% Trypsin-EDTA (Gibco, ThermoFisher, Paisley, UK) for 10 minutes to detach cells from the flask, and subcultured into 75 cm^3, then into 175cm^3 flasks. Once cells had been transferred to 175cm^3 flasks ($8.75x10^5$ cells in 50 mL complete DMEM per flask), they were incubated at 37°C, 5% CO_2 for 7 days. After 7 days, supernatant was harvested and filtered through a 0.2 µm filter. 50 mL fresh complete DMEM was added and the cells were incubated for a further 7 days. After 7 days the supernatant was harvested and filtered through a 0.2 µm filter. L929 media was frozen at -80°C until needed.

2.1.5. Bone marrow-derived macrophage (BMDM) differentiation

BM cells were isolated from mice as in section 2.1.3. BM cells were resuspended in macrophage differentiation media (DMEM supplemented with 100 U mL^{-1} penicillin, 100 µg mL^{-1} streptomycin, 2mM L-Glutamine, 20% heat-inactivated FCS, and 30% L929-cell culture supernatant) at a concentration of $5x10^5$ cells mL^{-1}. BM cells were then plated on sterile petri dishes (10 mL per dish; $5x10^6$ cells per dish). Cells were incubated at 37°C, 5% CO_2 for 3 days. On day 3, macrophage differentiation media was replaced with fresh macrophage differentiation media and incubated for a further 3 days. On day 6, macrophage differentiation media was replaced with complete DMEM. Cells were incubated overnight to acclimate to the new cell culture medium. Macrophages were harvested on day 7 for use in experiments.

For BMDM harvest from petri dishes, media was removed and replaced with 5mL ice cold complete DMEM to loosen BMDMs from the dish. BMDMs were detached from the dish using a cell scraper (VWR International), then transferred to a 50 mL Falcon tube. Dishes were scraped twice, each time with 5mL media, then rinsed with a further 5 mL complete DMEM. Falcon tubes were centrifuged at 300 xg for 6 minutes and resuspended in 1mL complete DMEM. Viable cells were counted as described in **2.1.3.** Confirmation of BMDM differentiation was performed by flow cytometry to detect CD11b and F4/80, and BMDMs were adjusted to the desired concentration for experiments.

2.1.6. BMDM stimulants

Lipopolysaccharide (LPS) from *E. coli* O26:B6 (Sigma-Aldrich L2654) was used at final concentrations indicated. Recombinant mouse interferon gamma (IFNγ) (Biolegend; specific activity 1-10x10^7 units mg^{-1}) was used at a final concentration of 10 ng mL^{-1}. Polyinosinic:polycytidylic acid (poly I:C; Sigma-Aldrich P1530) was used at a final concentration of 20 µg mL^{-1}. For cytokine analysis BMDMs were stimulated in sterile flat-bottomed 96-well plates (2x10^5 cells per well in 100 µL). Stimulants were made up at 2X the final concentration, then 100 µL stimulant was added to the 100 µL cells per well, resulting in 1X final concentration.

For flow cytometric analysis, 1x10^6 cells per well were added to a non-tissue culture treated 24-well plate (Eppendorf) in 250 µL. Stimulants were made up at 2X final concentration, then 250 µL stimulant was added per well to the cells, resulting in 1X final concentration.

2.2. Flow cytometry for cell surface markers

Single cell suspensions were prepared as previously described. 1-2x10^6 cells in 250 µL per sample were transferred to individual wells on a U-bottomed 96-well plate (Sarstedt, Germany). The plate was centrifuged at 400 xg for 1 min at 4°C, after which the supernatant was discarded (plate was upturned and supernatant flicked into the sink). Cells were resuspended via brief vortexing. Cells were incubated with 2.5 µg mL^{-1} FcBlock (anti-CD16 (FcγRIII) and anti-CD32 (FcγRII) antibodies) for 15 mins at 4°C (30 µL per well). 150 µL FACS buffer was added per well, and cells were centrifuged at 400 xg for 1 minute at 4°C. Supernatant was discarded by flicking the plate into the sink, and cells were resuspended by briefly vortexing. The cells were then incubated with primary surface antibodies at optimised concentrations (**Table 2.1**) diluted in FACS buffer (1X PBS + 0.01% FCS + 5 mM EDTA) (30 µL per well for 45 mins at 4°C in the dark). For panels that required secondary antibody incubation, cells were washed twice with 150-200 µL FACS buffer, and then incubated with secondary antibodies diluted in FACS buffer (30 µL per well) at 4°C in the dark for 45 mins. Cells were washed twice with 150-200 µL FACS buffer, and then resuspended in 200 µL FACS buffer for acquisition on a CytoFlex LX flow cytometer (Beckman-Coulter). For I-A^b-$PEPCK_{335-351}$ staining, antibody incubation steps were performed at 37°C for 30 mins. Data was analysed in FCS Express 7 Research Edition (DeNovo Software).

Table 2.1 List of monoclonal antibodies used in detection of cell surface markers and intracellular cytokines/transcription factors

Antibodies for surface flow cytometry					
Fluorochrome	**Marker**	**Clone**	**Supplier**	**Product #**	**Dilution**
FITC	CD11c	N418	Biolegend	117311	1:100
FITC	CD45.1	A20	BD Biosciences	553775	1:200
FITC	CD45.2	104	eBioscience	11-0454-81	1:200
PerCP-Cy5.5	Ly6G	1A8	Biolegend	127616	1:100
PE	TCRγ/δ	GL3	eBioscience	12-5711-82	1:100
PE	B220	RA3-6B2	eBioscience	12-0452-81	1:200
PE/dazzle	MHCII	M5/114.15.2	Biolegend	107648	1:200
PE/dazzle	CD45.1	A20	Biolegend	110747	1:200
Pe-Cy5	B220	RA3-6B2	eBioscience	15-0452-82	1:200
-	CD206-bio	MR5D3	Bio-Rad	MCA2235B	1:10
PE-Cy7	Streptavidin	-	eBioscience	25-4317-82	1:50
AF647	Ly6C	HK1.4	Biolegend	128010	1:200
APC	PEPCK	-	Genescript	-	1:40
Alexa 700	F4/80	BM8	Biolegend	123130	1:100
APC-Cy7	CD8a	53-6.7	Biolegend	100714	1:200
eFluor 450	NK1.1	PK136	eBioscience	48-5941-82	1:50
BV510	CD11b	M1/70	Biolegend	101263	1:200
BV510	CD8a	53-6.7	Biolegend	100752	1:200
BV605	CD19	6D5	Biolegend	115539	1:200
BV650	TCRβ	H57-597	Biolegend	109251	1:200
BV785	CD4	GK1.5	Biolegend	563877	1:200
BV785	CD11c	N418	Biolegend	117336	1:100
BV785	CD44	IM7	Biolegend	103059	1:100
BUV395	CD4	GK1.5	BD Biosciences	563790	1:200
IR 876	Live/Dead	-	Invitrogen	L34982	1:200

Intracellular flow cytometry					
APC	iNOS	CXNFT	eBioscience	17-5920-82	1:100
PerCP-Cy5.5	FOXP3	R16-715	BD Biosciences	563902	1:40
PE	IL-10	JES5-16E3	Biolegend	505008	1:40
PE-Cy7	T-bet	4B10	Biolegend	644824	1:40
AF700	TNF	MP6-XT22	Biolegend	506338	1:50
BV421	IFNγ	XMG1.2	Biolegend	505830	1:90
BV605	IL-4	11b11	Biolegend	504126	1:50
Immunofluorescence imaging					
DAPI	Nuclear stain	-	Thermo Fisher	D1306	1:5000
AF488	F4/80	BM8	Biolegend	123120	1:300
AF647	iNOS	EPR16635	Abcam	ab209027	1:100

2.3. Griess Assay for nitric oxide (NO) determination

Griess assay was used to detect nitrite in supernatants of stimulated BMDMs. Nitrite is one of the breakdown products of NO (which has a very short half-life (Thomas et al. 2001)), and as such the detection of nitrite is used as an indirect measurement of NO in cell culture supernatants. Briefly, 100 µL cell culture supernatants were added per well in a flat-bottomed 96-well plate (Fisher Scientific). $NaNO_2$ (Thermo Fisher) solution was also added (two-fold dilutions ranging from 100 µM to 0 µM in DMEM) to generate a standard curve. 50 µL 1% sulfanilamide (Sigma) in 5% phosphoric acid was added to each well and the plate was incubated for 5 minutes at RT in the dark. 50 µL 0.1% N-1-napthylethylenediamine dihydrochloride (NED) (Sigma) in distilled water was then added to each well, and the plate was incubated for 5 minutes at RT in the dark. Absorbance was measured within 30 minutes on a plate reader at 550 nm. Concentration of nitrite in each sample was measured through interpolation of the standard curve.

2.4. Enzyme Linked Immunosorbent Assay (ELISA)

ELISAs were performed using Peprotech ELISA TMB Development Kits, following the manufacturer's protocol with a few changes. Briefly, 96-well flat-bottomed ELISA plates (Costar High Binding 96-well assay plates, Fisher Scientific) were coated in capture antibody (1 µg mL^{-1} diluted in PBS, 100 µL per well). Plates were sealed and incubated overnight at RT. The following day, wells were aspirated and washed with wash buffer (0.05% Tween-20 in PBS) four times. Wells were then blocked with 300 µL blocking buffer (1% BSA in PBS) for 1 hour at RT. Wells were washed with wash buffer four times. 50 µL sample or standards were added to respective wells, and incubated at RT for 2 hours. Wells were washed four times with wash buffer. 50 µL detection antibody diluted in diluent (0.05% Tween-20, 0.1% BSA in PBS) (concentration varied between different cytokine kits, and manufacturer's protocol was followed) was then added to each well and incubated for 2 hours at RT. Wells were washed four times with wash buffer. Avidin-HRP Conjugate (Biolegend) was diluted 1:5,000 in diluent, and 100 µL was added to each well and incubated for 30 minutes at RT. Wells were washed four times with wash buffer. 100 µL TMB substrate (Biolegend) was added per well and incubated for 5-10 minutes. 100 µL 2N H_2SO_4 was added to each well to stop the reaction, and absorbances were recorded with a plate reader at 450 nm with wavelength correction set to 620 nm. Concentrations were calculated through interpolation of a standard curve.

2.5. RNA isolation and mRNA abundance estimation by Quantitative Polymerase Chain Reaction (qPCR)

2.5.1. Sample preparation

BMDMs were stimulated in 6-well plates ($2x10^6$ cells per well). At the end point of the experiment, the media was removed, and the cells were washed once with sterile PBS (carefully to not detach BMDMs from the plate). PBS was removed and 800 µL QIAzol Lysis Reagent (Qiagen, Hilden, Germany) was added to each well. Each well was scraped using the plunger of a 2 mL syringe to encourage cell lysis and left for 5 minutes at RT. QIAzol in each well was pipetted up and down a few times to further encourage lysis, and then transferred to fresh 2 mL RNAse free microcentrifuge tubes. Samples were then frozen at -80°C until ready for RNA extraction.

For preparation of tissue samples, tissue samples (10-20 mg) were harvested and stored in RNAlater™ (Qiagen) at -80°C. Tissue samples were defrosted and added to 2 mL round

bottom microcentrifuge tubes along with 800 µL QIAzol and one 5mm stainless steel bead (Qiagen) per tube. Tissue samples were lysed using a TissueLyser LT (Qiagen) at 50 oscillations for 60 seconds. Samples were then incubated at RT for 5 minutes to allow cell lysis, and the steel beads were removed. Samples were then centrifuged at 16,000 xg for 1 minute and supernatants were transferred to a fresh microcentrifuge tube.

2.5.2. RNA extraction

For RNA extraction, a ZYMO Direct-zol Miniprep kit was used (Zymo Research Corporation, Irvine, USA), following the manufacturer's protocol. Briefly, samples in QIAzol were defrosted, and 800 µL 100% ethanol was added to each tube and mixed thoroughly. The mixture was transferred to a Zymo-Spin™ IICR Column in a collection tube (one per sample), and centrifuged at 16,000 xg for 30 seconds. The flow-through was discarded, and then columns containing RNA were washed twice with 400 µL Direct-zol™ RNA PreWash, centrifuged at 10,000 xg for 30 seconds after each wash. Columns were then washed with 700 µL RNA Wash Buffer, and centrifuged at 16,000 xg for 1 minute. RNA was eluted from columns into 1.5 mL RNAse-free microcentrifuge tubes with 50 µL DNase/RNase-Free water.

To remove contaminating DNA, RNA samples were treated with DNAse using a TURBO DNA-free™ kit (Ambion) and following the manufacturer's protocol. Briefly, 0.1 volume of 10X TURBO DNase Buffer and 1 µL TURBO DNase was added to RNA samples and mixed. Samples were incubated at 37°C for 20-30 minutes. To stop the reaction, 0.1 volume DNase Inactivation Reagent was added to the samples and samples were incubated at 25°C for 5 minutes. Samples were centrifuged at 16,000xg for 1.5 minutes, and transferred to a new microcentrifuge tube. RNA concentrations were quantified using a NanoDrop™ 2000 spectrophotometer (Thermo Fisher Scientific, Loughborough, UK). RNA was considered sufficiently pure when the ratio of 260/280 and 260/230 was close to 2.0 and 2.2, respectively.

2.5.3. cDNA synthesis

To synthesise cDNA for use in qPCR reactions, reverse transcription (RT) was performed using SuperScript™ III or IV (Invitrogen). RT reactions were performed in 0.2 mL DNase/RNase free PCR tubes (Starlab, Milton Keynes, UK). RNA sample concentrations were normalised within individual experiments to 40-100 ng μL^{-1} (depending on the experiment). For initial annealing of $Oligo(dT)_{20}$ primer to the template RNA, a mixture of 1 µL 50 µM $Oligo(dT)_{20}$, 1 µL 10 mM deoxynucleotide triphosphates (dNTPs), 5 µL RNA

template, and 13 µL sterile water per sample was incubated at 65°C for 5 minutes. Samples were then chilled on ice for 1 minute. A master mix for the reverse transcriptase was prepared containing 4 µL 5X First-strand buffer, 1 µL 0.1M Dithiothreitol (DTT), 1 µL RNaseOUT™ Recombinant Ribonuclease Inhibitor (Invitrogen), and 1 µL SuperScript™ III or IV. 7 µL of the master mix was added to each sample tube, and samples were incubated at 50°C for 50 minutes (SuperScript™ III) or 10 minutes (SuperScript™ IV). The reaction was terminated by incubation 70°C for 15 minutes (SuperScript™ III) or 80°C for 10 minutes (SuperScript™ IV), then chilled on ice. Finally, 1 µL RNase H (New England Biolabs, UK) was added to each tube and incubated for 37°C for 20 minutes. cDNA samples were then stored at -20°C until ready for qPCR.

2.5.4. Quantitative polymerase chain reaction (qPCR)

qPCR was performed using Fast SYBR™ Green Master Mix (Applied Biosystems, Warrington, UK). A master mix was prepared per sample for each primer pair (gene of interest), containing 10 µL SYBR™ Green master mix, 6 µL RNase-free water, 1 µL forward primer, and 1 µL reverse primer (**Table 2.2**). 18 µL master mix was added to individual wells in a MicroAmp Optical 96-well plates (Applied Biosystems), and 2 µL cDNA was added to respective wells on the plate. The plate was sealed and centrifuged to remove air bubbles and ensure the mixture was at the bottom of the wells. qPCR reactions were performed using a QuantStudio™ 3 system (Applied Biosystems) using the following cycling conditions: 95°C for 20 seconds, followed by 40 cycles of 95°C for 1 second and 60°C for 20 seconds, followed by a continuous melt curve of 95°C for 1 second, 60°C for 20 seconds and a continuous increase of 0.1°C/second to reach 95°C. Data were analysed using Thermo Fisher Connect™ Design and Analysis Cloud software (Thermo Fisher). mRNA abundance was normalised to the GAPDH housekeeping gene using the ΔΔCt method, and mRNA abundance between control and experimental samples was calculated using the $2^{-\Delta\Delta Ct}$ method.

Table 2.2. Primers used for qPCR determination of mRNA abundance

Gene	Sequence
Ifit1	5’-CAGGATATTCACCTCCGCTATG-3’
	5’-CAGGGTCAGAAAGACCAGAAA-3’
Ifit3	5’-GAAGGATGGACACGCCTAAA-3’
	5’-GTACTCCTGGAGGTTGCAATAG-3’
Usp18	5’-ATGCTGCTCAACTCTACCTTAC-3’
	5’-AGAGGCTTTGCGTCCTTATC-3’
Nos2	5’-GTTCTCAGCCCAACAATACAAGA-3’
	5’-GTGGACGGGTCGATGTCAC-3’
Oas1	5’-CTGACCTGGTGGTGTTCCTT-3’
	5’-ACCTCGCACAGCTGTTTCTT-3’
Isg15	5’-CACAGTGATGCTAGTGGTACAG-3’
	5’-CTGCGTCAGAAAGACCTCATAG-3’
Irf7	5’-CCTTGGCAGAGGAATCTACAC-3’
	5’-CAAGTGTGACCCAGGTATTAGG-3’
Gapdh	5’-TGTGTCCGTCGTGGATCTGA-3’
	5’-CCTGCTTCACCACCTTCTTGA-3’

2.6. Bulk RNA sequencing (RNA-seq) of stimulated BMDMs

Sample preparation for bulk RNA-seq was performed by Dr Elmarie Myburgh. WT and KO BM cells were isolated as described in **2.1.3.** and differentiated into BMDMs as described in **2.1.5..** 1 mL BMDMs were plated in 6-well plates (Eppendorf) at a concentration of $2x10^6$ cells/mL. Two wells per mouse for each stimulant were plated out, and duplicate wells were combined when BMDMs were harvested, resulting in $4x10^6$ BMDMs per mouse being used for RNA extraction. BMDMs were left to rest for 3-4 hours at 37°C, 5% CO_2, and then stimulants were added. Stimulants and final concentrations are shown below:

1) Media control
2) IFNγ 10 ng mL^{-1}
3) LPS 100 ng mL^{-1}
4) IFNγ 10 ng mL^{-1} + LPS 100 ng mL^{-1} co-stimulation

Stimulants were prepared at 2X the final concentration, and 1 mL stimulant was added to the 1 mL cells already in the plate, resulting in a 1:2 dilution of stimulant and correct final concentration. Stimulants were also added in staggered times to account for time taken to harvest, ensuring BMDMs were all stimulated for exactly 12 hours. After 12 hours stimulation, BMDMs were harvested as described in **2.5.2.** with some changes. Cells were washed with 900 µL PBS, and then 900 µL QIAzol was added to each well. Wells were scraped with the plunger of a 2 mL syringe. QIAzol from duplicate wells containing cells from the same mouse was combined and transferred to a QIAshredder column (Qiagen) in a 2 mL microcentrifuge tube. Columns were centrifuged at 16,000 xg for 2 minutes, and flow-throughs were transferred to 2 mL RNase-free microcentrifuge tubes. Samples were stored at -80°C overnight.

RNA extraction of samples was performed as described in **2.5.2.** with some changes. Instead of treatment with TURBO DNA-free™ kit (Ambion), samples were treated on-column with DNase I (Zymo Directzol kit) as described in the manufacturer's protocol (this step was performed before the column wash steps). RNA was eluted from the column in 50 µL DNase/RNase-free water. RNA concentrations were measured with a NanoDrop™ 2000 spectrophotometer. RNA concentrations and integrity were also measured by Dr Lesley Gilbert using an Agilent 2100 Bioanalyzer (Agilent, CA, USA). Samples were stored at -80°C until ready for further sample preparation. Sample concentrations and volumes were adjusted to 25 ng $µL^{-1}$ in 40 µL RNase-free water. 2 µL ERCC spike-in RNA standard (Invitrogen) (diluted 1:100 in deionized water) was then added to each sample. ERCC spike-in RNA standards were to allow for more precise comparison between sample sequencing data and identification of variation between samples (Jiang et al. 2011). RNA-seq library

preparation was performed by Novogene, and samples were sequenced using a NovaSeq 6000 PE150.
Standard bioinformatics analysis was also performed by Novogene, including data quality control, data filtering, mapping to reference genome, gene expression quantification and differential gene expression analysis. Gene Set Enrichment Analysis (GSEA) analysis was performed at the University of York using GSEA Software 4.1.0, and figures were generated using R Studio.

2.7. Tissue cell isolation and single cell suspension preparation

2.7.1. Processing of splenic tissue into single cell suspension

Experimental mice were sacrificed at the experimental endpoint via CO_2 inhalation, and spleens were removed into a 15 mL tube (Sarstedt AG & Co, Germany) containing 10 mL of 1% FCS in 1X PBS. Each spleen was tipped into a 100 µm cell strainer (Scientific Laboratory Supplies (SLS), East Riding of Yorkshire, UK) inside a 90mm petri dish. Each spleen was forced through the cell strainer using the plunger of a sterile 5mL syringe. The resulting single cell suspension was transferred to a new 15 mL tube, and the dish and strainer was rinsed 1-2 times with 2-3 mL 1% FCS in 1X PBS to ensure as many cells were kept as possible. Cells were then centrifuged at 300 xg for 6 minutes at room temperature (RT). The supernatant was discarded, and the pellet was resuspended in 1 mL ACK lysis buffer (Gibco, ThermoFisher, Paisley, UK). Cells were incubated at RT for 5-7 minutes to lyse red blood cells (RBC). To stop lysis, 9 mL 1% FCS in 1X PBS was added to the cells. Cells were centrifuged at 300 xg for 6 minutes at room temperature (RT). The supernatant was discarded and the pellet was resuspended in 5 mL 1% FCS in 1X PBS. Viable leukocytes were counted by Trypan blue dye exclusion as described in **2.1.3**. Cell concentration was adjusted according to experimental requirements.

2.7.2. Processing of liver tissue into single cell suspension

Experimental mice were sacrificed at the experimental endpoint via CO_2 inhalation. Livers were perfused via intravenous injection of 2-3 mL 1X PBS for naive mice (4-6 mL for infected mice) into the hepatic portal vein. Livers were then excised into a 50 mL Falcon tube (Sarstedt AG & Co, Germany) containing 5 mL of 1% FCS in 1X PBS. Livers were gently eased apart with a scalpel, and then incubated with final concentrations of 10 µg/mL Collagenase IV (Fisher Scientific), 50 ng/mL DNase I (Fisher Scientific), and 0.02% BSA (Sigma) in 10 mL HBSS at 37°C for 20 minutes. Digestion was stopped by adding ice cold

2% FCS in 1X PBS. Livers were poured into a 100 µm cell strainer placed in a fresh 50 mL Falcon tube and forced through using the plunger of a sterile 5mL syringe. Cells were then centrifuged at 300 xg for 6 minutes at RT. The supernatant was discarded, and 25 mL 33% Percoll solution (9 mL Percoll (Merck Life Science UK Limited), 1 mL 10X PBS, and 17 mL 1X PBS per liver) was added to each liver sample and mixed well. Livers were then centrifuged at 400 xg for 15 minutes at RT with the centrifuge brake off. Supernatant containing hepatocytes was discarded and the pellet containing leukocytes and erythrocytes was resuspended in 1 mL ACK lysis buffer. Cells were incubated at RT for 5-7 mins to remove erythrocytes. 9 mL 1% FCS was added to stop lysis and, and cells were centrifuged at 400 xg for 6 minutes at RT. The supernatant was discarded and the pellet was resuspended in 1-5 mL 1% FCS in 1X PBS (volume dependent on pellet size). Viable leukocytes were counted by Trypan blue dye exclusion as described in **2.1.3**. Cell concentration was adjusted according to experimental requirements.

2.7.3. Processing of inguinal lymph nodes (iLN) into single cell suspension

Experimental mice were sacrificed at the experimental endpoint via CO_2 inhalation, and both iLNs were removed into a 15 mL tube containing 10 mL of 1% FCS in 1X PBS. Each set of iLNs was tipped into a 100 µm cell strainer inside a 90mm petri dish. iLNs were forced through the cell strainer using the plunger of a sterile 5 mL syringe. The resulting single cell suspension was transferred to a new 15 mL tube, and the dish and strainer was rinsed 1-2 times with 2-3 mL 1% FCS in 1X PBS. Cells were then centrifuged at 400 xg for 6 minutes at RT, and cells were resuspended in 1 mL 1% FCS in 1X PBS. Viable leukocytes were counted by Trypan blue dye exclusion as described in **2.1.3**. Cell concentration was adjusted according to experimental requirements.

2.7.4. Processing of BM into single cell suspension

Experimental mice were sacrificed at the experimental endpoint via CO_2 inhalation. BM cells were isolated as described in **2.1.3.**, however for flow cytometry experiments BM cells were treated with ACK lysis as described in **2.7.1.** to remove RBCs. The supernatant was discarded and the pellet was resuspended in 1 mL 1% FCS in 1X PBS. Viable leukocytes were counted by Trypan blue dye exclusion as described in **2.1.3**. Cell concentration was adjusted according to experimental requirements.

2.8. Leukocyte re-stimulation and intracellular staining for cytokine and transcription factor detection by flow cytometry

Single cell suspensions were prepared as previously described. 1-2x10^6 cells in 100 µL per sample were transferred to individual wells on a U-bottomed 96-well plate (Sarstedt, Germany). T cell stimulation mixture was prepared containing final concentrations of 25 ng mL^{-1} Phorbol-12-myristate-13-acetate (PMA) (Sigma-Aldrich), 2 µg mL^{-1} Ionomycin (Sigma-Aldrich), and 10 µg mL^{-1} Brefeldin A (BFA) (Sigma-Aldrich) in complete DMEM. Myeloid cell stimulation mixture was prepared containing final concentrations of 10 µg mL^{-1} Brefeldin A (BFA) (Sigma-Aldrich) and 100 ng mL^{-1} LPS (Sigma-Aldrich) in complete DMEM. 100 µL cell stimulation mixture was added to respective wells and incubated at 37°C, 5% CO_2 for 3 hours. After stimulation, cells were washed twice with 200 µL FACS buffer. Cells were then incubated with FcBlock and surface marker staining as described in **2.2..** After surface staining, cells were fixed and permeabilised using the Foxp3 / Transcription Factor Staining Kit (eBioscience). Briefly, cells were incubated with 100 µL fixation buffer (eBioscience) for 30 mins at 4°C in the dark. 100 µL permeabilisation buffer (eBioscience) was then added to each well, and the cells were centrifuged at 400 xg for 1 minute at 4°C. Cells were then washed in 200 µL permeabilisation buffer once and intracellular antibodies were added to the cells diluted in permeabilisation buffer (30 µL per well) (**Table 2.1**). Cells were incubated at RT for 45-60 minutes. Cells were washed twice in 200µL permeabilisation buffer, then once in 200 µL FACS buffer. Cells were resuspended in 200 µL FACS buffer and kept at 4°C in the dark until acquisition on a CytoFlex LX flow cytometer (Beckman-Coulter).

2.9. Generation of 50:50 WT:*Trim24*$^{-/-}$ mixed bone marrow chimeric mice

BM cells were isolated from female naive donor mice (B6.CD45.1 WT and B6.CD45.2 KO) as described in **2.1.3.** Donor cells were confirmed to be $CD45.1^+$ or $CD45.2^+$ by flow cytometry as described in **2.5.6.** A 50:50 mixture of WT:KO donor cells was prepared and adjusted to 5x10^7 cells/mL ready for adoptive transfer. The mixture of donor cells was confirmed to be a 50:50 mixture by flow cytometry to detect CD45.1 and CD45.2 as described in **2.1.3.** B6.CD45.1 WT recipient mice were treated with acidified water (pH adjusted to 2.5 with hydrochloric acid) for 5 days before irradiation. Recipient mice were then lethally irradiated (split dose over two consecutive days; 550 rads over 13 minutes for a total of 1100 rads). After first dose, recipient mice were placed on antibiotic water (1 g L^{-1}

Enrobactin) for 2 weeks. On the same day following the second irradiation dose, recipient mice were reconstituted with the mixture of donor cells by intravenous injection into the lateral tail vein ($5x10^6$ cells in 100 µL per mouse). Recipient mice were monitored over the following 4 weeks to allow for engraftment and initial reconstitution of donor BM cells.

2.10. Extraction and processing of mouse peripheral blood

Peripheral blood from the lateral tail vein of experimental mice was collected in EDTA-coated tubes (Microvette CB300 EDTA, Sarstedt, Germany) to prevent clotting. For flow cytometric analysis, ~50 µL blood was pipetted from EDTA-coated tubes into 1.5 mL tubes containing 500 µL ACK lysis buffer. Tubes were incubated at RT for 5-10 minutes and centrifuged at 500 xg for 3 minutes to remove erythrocytes. The supernatant was discarded, and the pellet was resuspended in 200 µL 1% FCS in 1X PBS. Cells were then transferred to a 96-well plate for antibody staining and flow cytometric analysis.

2.11. Infections

2.11.1 *L. donovani* parasite isolation and *in vivo* infections

Leishmania donovani amastigotes were used to infect experimental animals and for in vitro infections. An Ethiopian strain of *L. donovani* parasites (*LV9*) was used for *in vitro* infections, and *LV9*-RE9H parasites that express red-shifted firefly luciferase were used for *in vivo* infections (Branchini et al. 2010). Parasites were maintained in B6.*Rag2*$^{-/-}$ mice infected for at least 3 months before parasite isolation. For parasite isolation, passage B6.*Rag2*$^{-/-}$ mice were euthanized by CO_2 inhalation followed by cervical dislocation, and spleens were collected into Roswell Park Memorial Institute (RPMI) 1640 medium (Gibco, ThermoFisher, Paisley, UK). Under sterile conditions, spleens were homogenised using a glass tissue homogeniser (Fisher Scientific, UK) in RPMI and transferred to a 50 mL Falcon tube. The suspension was centrifuged at 100 xg (Heraeus Multifuge 3S-R (DJB labcare, UK)) for 5 minutes at RT. The supernatant was transferred to a fresh 50 mL Falcon tube, and the tissue pellet discarded. The supernatant was centrifuged at 1100 xg for 10 minutes. The supernatant was discarded, and the pellet was resuspended in 1 mL ACK Lysis buffer and incubated at RT for 5 mins. RPMI was added up to 50 mL and centrifuged at 3100 for 10 mins. Parasites were washed twice more with 50 mL RPMI, then resuspended in 10 mL RPMI. Parasites were passed through a 26-gauge needle (BD Biosciences, San Jose, CA,

USA) in a 10 mL syringe (BD Biosciences, San Jose, CA, USA) to break up parasite clumps. Parasites were then counted using an Improved Neubauer haemocytometer (Weber Scientific International, Middlesex, UK) and resuspended to the desired concentration in RPMI. For infection experiments, mice were infected via lateral tail vein injection with $3x10^7$ parasites in 100 µL.

2.11.2. In Vivo Imaging System (IVIS) imaging

An IVIS Spectrum (PerkinElmer, UK) was used to track parasite burdens over time in mice. Experimental WT and KO C57BL/6 mice were infected with *LV9*-RE9H amastigotes as described in **2.11.1.** These parasites express red-shifted luciferase (Branchini et al. 2010), that produces light after injection of the substrate D-luciferin into mice. Experimental mice were injected with 15 mg kg^{-1} D-luciferin (Syd Labs) in Dulbecco's modified PBS via sub-cutaneous or intra-peritoneal injection. After 5 mins, mice were anaesthetized by inhalation of 3-4% Isoflurane /1.5L O_2/minute in an anaesthesia chamber. After anaesthetic treatment, mice were transferred to the IVIS Spectrum chamber, and mice were imaged 10 minutes post-injection with D-luciferin. Mice were imaged in groups of 1-3, and where the signal differed, mice with lower signal were re-imaged individually. Mice were imaged on the ventral side for 3 minutes followed by the lateral side for 3 minutes. The IVIS system settings were as follows: open emission filter, medium binning, f1/stop, FOV 12.5. After imaging, mice were transferred to a heat pad and monitored until they had recovered. Captured images were analysed using the Living Images Software ver. 4.7.3 (PerkinElmer, UK). Regions of interest (ROIs) of equal size were drawn around each mouse, and the total flux was measured within each ROI to give a readout for parasite burden.

2.11.3. Estimation of parasite burden by counting Leishman Donovan Units

After infected mice had reached the experimental end point, mice were sacrificed, and small pieces of spleen and liver tissue were removed. Excess blood was removed for the tissue segments via dabbing on tissue paper. Tissue segments were then pressed on a Superfrost slide (Thermo Fisher Scientific, UK) to leave impression smears. 100% methanol was then pipetted on the slides with impression smears to fix and allowed to dry. This was repeated one more time. Slides were then stained with Giemsa staining solution for 30-40 minutes at RT. Slides were rinsed in running tap water to remove excess Giemsa stain and the = the number of amastigotes was counted per 1000 host cells using microscopy. This number was

multiplied by the total organ weight in grams to give the Leishman Donovan units (LDUs), a measure of organ parasite burden.

2.12. Histology

2.12.1. Cryopreservation & cryo-sectioning of tissues

At the end point of each experiment mice were sacrificed, and tissues were removed. Tissues were cut into small cross-sectional pieces that fit into cryomolds, and then embedded in cryomolds using Tissue-Tek® OCT™ compound (Labtech, East Sussex, UK), and transferred directly to dry ice to freeze, then to -80°C freezer until ready for cryosectioning.

For cryosectioning, samples in cryomolds were placed in a CM1900 cryostat (Leica, Microsystems, Wetzlar, Germany), and allowed to equilibrate to the temperature of the cryostat (-20°C) for 10-15 mins. OCT-embedded tissues were attached to cryostat mounting knobs with OCT and then attached to the sectioning apparatus. Tissues were cut to 8-10 µm and attached to superfrost glass slides (3 sections per slide). Sections on slides were allowed to air dry, and then were transferred to -20°C until ready for staining.

2.12.2. Immunofluorescence staining

Immunofluorescence staining was performed on liver tissue sections from B6 WT and KO mice. Superfrost slides with tissue sections were removed from -20°C and immediately dipped in ice cold acetone for 10 mins to fix the tissue. Slides were then allowed to air dry, and sections were drawn around using an ImmEDGE™ Hydrophobic Barrier pen (Vector Laboratories Ltd., Peterborough, UK) which was allowed to dry. Sections were then washed with wash buffer (0.05% w/v bovine serum albumin (BSA; Sigma-Aldrich, USA) in sterile 1x PBS) for 5 mins. Sections were then blocked with blocking buffer (wash buffer with 5% serum from same species in which secondary antibody was raised) for 30 mins at RT. Sections were washed with wash buffer three times (3-5 mins each). A primary antibody mix was prepared in blocking buffer using antibodies and dilutions shown in **Table 2.1**. 100 µL of primary antibody mix was added to each section, and sections were stained at RT in the dark (if primary antibodies are directly-conjugated to fluorophores) for 45-60 mins. Slides were then washed with wash buffer three times (3-5 mins each) to remove unbound antibody. Sections were then washed twice with sterile 1x PBS (5 mins each) prior to nuclear counterstaining. Sections were then counterstained with 4',6-diamidino-2-phenylindole (DAPI; 1 µg mL^{-1} in sterile 1x PBS) for 5 mins. Sections were washed with sterile 1x PBS

twice (5 mins each), and then mounted with coverslips using ProLong Gold antifade mounting medium (Thermo Fisher Scientific, UK). Slides were left overnight in the dark at RT to allow the mounting medium to cure, and then slides were transferred to 4°C for storage until imaging.
Images were collected using a Zeiss AxioScan Z1 Slide Scanner (Zeiss, Oberkochen, Germany) at 20x and 5x resolution. Images were analysed using Zeiss Zen Blue software (Zeiss, Oberkochen, Germany).

2.13. Transcriptomics

Bone marrow from d28-infected WT and KO B6 mice was processed into a single cell suspension as described previously. Single cell RNA-seq library preparation was then performed following the Chromium Next GEM Single Cell 3' Kit v3.1 (10X Genomics), with targeted capture of 10,000 cells. Libraries were sequenced on the Illumina NovaSeq 6000 platform, to achieve approximately 20,000 reads sets per cell.

FASTQ files were aligned to the mouse genome (GRCm38 mm10) using 10x Genomics Cell Ranger 6.1.0. Generated .h5 files were loaded as Seurat objects (Butler et al. 2018) and quality controlled by removing cells with more than 10% mitochondrial reads, cells with too low (<500) or high (>6000), high haemoglobin gene read count (>2%), and platelet gene read count >0.5%. Each sample was regressed for ribosomal genes, mitochondrial reads, total RNA count, unique feature count using SCTransform() using Gamma-Poisson generalised linear models (glmGamPoi (Ahlmann-Eltze and Huber 2021)). Anchors for all samples were calculated using SelectIntegrationFeatures() and FindIntegrationAnchors(). Samples were then integrated into one Seurat object.

Dimensionality reduction was then performed by principal component analysis (PCA), and the top 15-20 dims were used for downstream analysis. The number of dims were selected according to elbow plots indicating the number of dims that contain the most variance within the dataset. Louvain cluster was then performed using a resolution of 0.5 to identify distinct cell clusters, which were visualised on a scatter plot showing UMAP projection or principal components 1 and 2.
Sub-clustering was performed by selection of desired clusters, re-integrating the samples together and repeating Louvain clustering at a resolution of 0.6-0.9. Cluster identification was performed using the Seurat functions PrepSCTFindMarkers() and FindAllMarkers(), and clusters were renamed according to top genes expressed per cluster.

Differential gene expression analysis between samples was performed using the FindMarkers() Seurat function (Wilcoxon-Rank sum test) with a log2FC threshold of 0 and FDR threshold of 0.05. Volcano plots were generated using ggplot2. Heatmaps were generated by calculating the average expression of each gene per cluster per sample using the Seurat function AverageExpression(), and the pheatmap R package was used to plot heatmaps. Dot plots and feature plots were generated using the Seurat functions DotPlot() and FeaturePlot(), respectively.

Gene Set Enrichment Analysis (GSEA) and Over Representation Analysis (ORA) were performed using the R package clusterProfiler. For GSEA, gene lists were ranked by log2FC. Either all differentially expressed genes (DEGs) or all detected genes were used (where there were few DEGs). ORA was performed using up- and down-regulated genes separately. GSEA and ORA were performed using HALLMARK gene lists (https://www.gsea-msigdb.org/gsea/index.jsp) or using Gene Ontology 'Biological Process' terms. Calculated FDR or q values are presented as $-\log_{10}$FDR in figures.
For STRING analysis, differentially expressed genes were submitted to StringDB (https://string-db.org/) using default settings, and function and physical protein interaction networks were generated.

Inference of ligand-receptor communication was performed using the CellChat R package, which performs permutation tests on assigned interaction probabilities to calculate statistical significance. CellChat utilises a curated database of ligand-receptor cell communication networks (CellChatDB; http://www.cellchat.org/) and integrates this with gene expression data from scRNA-seq data to infer ligand receptor interactions in a given dataset. CellChat uses models of mass action to assign probability values to interactions, and not only considers expression levels of the ligand and receptor genes, but also takes into account multimeric ligands and receptors that are encoded by different genes (e.g. *Ifngr1+Ifngr2*), along with other cofactors that may influence cell communication (soluble agonists/antagonists, co-stimulatory/co-inhibitory receptors) (Jin et al. 2021).

2.14. Statistical Analysis

All data excluding RNA sequencing data were analysed using GraphPad Prism 9 software (GraphPad Software, San Diego, CA). Appropriate statistical tests were chosen based on the distribution and desired comparison of the data. The statistical test used is detailed in the figure legend of the corresponding figure. The most commonly used statistical tests were Student's T-test, Two-Way ANOVA with Bonferroni post-hoc test. Results were considered

significant when *P* value < 0.05. Levels of significance were shown as not significant (ns; >0.05), *$P < 0.05$, **$P < 0.01$, ***$P < 0.001$, ****$P < 0.0001$.

2.15. Illustrations

BioRender (https://www.biorender.com/) was used to create illustrations presented in this thesis.

Chapter 3. Investigating the functions of TRIM24 in the activation of murine macrophages *in vitro*

3.1. Introduction

Macrophages are an essential part of both immunity to *Leishmania* infection and survival of *Leishmania* parasites within the mammalian host, as discussed in detail in Chapter 1. The activation states of macrophages are best described as a spectrum, with functions ranging from progression of inflammatory response, repression of inflammatory responses, wound healing/repair of tissues and angiogenesis (Mosser & Edwards 2008). Activation of macrophages is fine-tuned to the many activation signals they can respond to. Inflammatory or classically activated macrophages (M1) are a pro-inflammatory type of macrophage that are typically induced through exposure to Th1-derived pro-inflammatory cytokines such as IFNγ and TNF (Mosser & Zhang 2008). M1-like characteristics can also be induced through exposure to other cytokines such as CXCL10 (Liang et al. 2022). Furthermore, Toll-like receptor (TLR) signalling is a potent inducer of inflammatory phenotypes in macrophages, and in most experimental cases in which inflammatory macrophages are investigated, a combination of recombinant IFNγ and lipopolysaccharide (LPS; a TLR4 agonist) is used to induce this phenotype (Mosser & Zhang 2008). After polarisation, M1 macrophages release various pro-inflammatory cytokines and factors such as TNF, IL-6, IL-12, and nitric oxide (NO) (Orecchioni et al. 2019), which contribute further to the inflammatory response.

Immunoregulatory or alternatively activated macrophages (M2) are much more anti-inflammatory in their phenotype compared to M1 macrophages, and play roles in the dampening of inflammation and resolution of the immune response through the expression and release of anti-inflammatory cytokines (IL-10, TGF-β) (Porcheray et al. 2005). They also play roles in wound healing and tissue repair through their expression of scavenger receptors such as CD206 and CD163 (Rőszer 2015; Abraham & Drummond 2006). The nomenclature for activation status for M2 macrophages has been widened over the last decade, with further subdivisions of M2 macrophages emerging (M2a, M2b, M2c) as discussed in Chapter 1. This highlights the complex nature of macrophage heterogeneity as an important factor when studying disease.

Macrophages play vital roles in *Leishmania* infection, as discussed in Chapter 1. Briefly, macrophages are the numerically dominant host cells for *Leishmania* parasites after

mammalian infection. During a blood meal, infected sand flies introduce parasites into the dermis. Neutrophils are the first cells recruited to the site of infection, where they phagocytose the majority of parasites. This initial removal of parasites by neutrophils is insufficient for complete parasite clearance, and *Leishmania* parasites interact with neutrophils to suppress parasite killing mechanisms, while allowing neutrophils to release chemokines to recruit macrophages to the site of infection. Once infected neutrophils become apoptotic, macrophages phagocytose the infected neutrophils, thereby providing a mechanism for *Leishmania* parasites to enter macrophages undetected. Efferocytosis of *L. major*- infected neutrophils suppresses inflammatory cytokine production (IL-1β and TNF) (Fadok et al. 1998), shifting them more towards an M2 phenotype inducing the release of TGF-β and enabling parasite persistence within the macrophage (van Zandbergen et al. 2004). In *L. donovani* infection, parasites in infected neutrophils induce autophagy, which is then used as a method for transfer from neutrophils to macrophages (Pitale et al. 2019). This M2 macrophage shift has been further characterised by increased levels of M2 phenotypic markers such as IL-10, CD163, and CXCL13, and a promotion in arginase activity, which subsequently inhibits NO production and oxidative burst (Abebe et al. 2013; Roy et al. 2018; Sarkar et al. 2011). There are still knowledge gaps concerning the interactions between the parasite and macrophage that allow for effective parasite survival and evasion of the immune response. However, it is generally thought that if inflammatory pathways in macrophages can be switched back on during *L. donovani* infection, effective killing of parasites can be induced.

Little is known about the immune functions of TRIM24, particularly in macrophages. TRIM24 has been shown to regulate various STAT signalling pathways in different disease contexts. TRIM24 was found to positively regulate STAT3 signalling in a murine model of glioblastoma, in which Epidermal Growth Factor Receptor (EGFR) activation upregulated the histone modification H3K23ac. H3K23ac was bound by TRIM24, resulting in recruitment of phosphorylated STAT3 to transcriptional binding sites (Lv et al. 2017). In a murine model of hepatocellular carcinoma, TRIM24 was also found to negatively regulate IFN/STAT signalling through interaction with retinoic acid receptor alpha to inhibit *Stat1* transcription (Tisserand et al. 2011). More recently in a B16 melanoma mouse model, TRIM24 was found to be a negative regulator of macrophage M2 polarisation. Here, TRIM24 indirectly caused acetylation of STAT6 via ubiquitination of CBP, curtailing the ability for STAT6 to bind to its promoter (Yu et al. 2019). Thus, roles of TRIM24 in immune signalling appear to vary, contributing to both pro- and anti-inflammatory signalling pathways.

Here, we sought to investigate the effects of *Trim24* deletion on functions of primary murine bone marrow-derived macrophages (BMDMs) *in vitro* to elucidate alterations that may impact the macrophage-mediated progression of *L. donovani* infection. As our main hypothesis is that TRIM24 is a negative regulator of type 1 immunity during *L. donovani* infection, and given the data already published focussing on roles of TRIM24 responses to IL-4 (albeit in a tumour setting) (Yu et al. 2019), we decided to focus our efforts on inflammatory roles of KO macrophages. We assessed the ability for KO bone marrow cells to differentiate into macrophages and conducted a series of *in vitro* experiments to assess the potential for KO BMDMs to produce important pro-inflammatory cytokines, elucidating mechanisms of TRIM24-mediated regulation of these pathways.

3.2. Chapter Aims

- To investigate the effects of TRIM24 deletion on functional phenotypes of murine BMDMs following TLR3/4 stimulation

- To perform transcriptional analysis of WT and TRIM24 knockout (KO) BMDMs at the steady state and following stimulation with lipopolysaccharide (LPS) and/or IFNγ

3.3. Results

3.3.1. Differentiation of bone marrow cells to BMDMs is not affected by TRIM24 deletion

It has previously been reported that deletion of TRIM33 impairs early events during myeloid cell development but not at later stages (Gallouet et al. 2017). Given that TRIM33 is a member of the same subfamily of TRIM proteins as TRIM24, we first assessed the ability for KO bone marrow cells to differentiate into BMDMs to ensure that TRIM24 is not an essential regulator of macrophage differentiation (**Fig. 3.1A**). We found no significant difference in the total number of BM cells isolated from WT and KO mice (**Fig. 3.1B**). After BM was harvested from the femur and tibia of WT and KO mice, BM cells were differentiated into BMDMs by exposure to serum-rich cell media supplemented with 30% conditioned media from culturing L929 cells. L929 cells are mouse adipose fibroblast cells that are known to release M-CSF into the surrounding medium during their culture and are widely used for the differentiation of BM cells into macrophages (Boltz-Nitulescu et al. 1987; Heap et al. 2021). After the differentiation period (6-7 days), a population of ~95% BMDMs was obtained (as assessed through the detection of CD11b and F4/80 by flow cytometry) (Boltz-Nitulescu et al. 1987) **(Fig. 3.1C**). There was no significant difference in the ability of KO and WT BM cells to differentiate into BMDMs (**Figure 3.1D**). Flow cytometry of WT and KO BMDM populations for the macrophage markers CD11b and F4/80 showed ~90% of both WT and KO populations to be $F4/80^+$ $CD11b^+$ (**Fig. 3.1D&E**). Together, these results demonstrate that TRIM24 is not required for differentiation of BMDMs under the influence of M-CSF.

3.3.2. LPS-induced release of IL-6 and TNF is not affected by the absence of TRIM24

Release of pro-inflammatory factors is a hallmark for inflammatory M1 macrophages. At the pro-inflammatory phenotypic end of the activation spectrum, M1 macrophages can be polarised by IFNγ (mainly released by activated T cells) and LPS, which activate the JAK/STAT1 and TLR4 pathways, respectively (Schroder et al. 2004; Lu et al. 2008). Signalling through these pathways induces the expression of proinflammatory factors (e.g. IL-6, TNF, IL-12) which can be released from the cell to propagate activation signals and aid in the recruitment of further immune cells (Orecchioni et al. 2019).

Previously, it was shown that deletion of TRIM24 in macrophages does not affect expression of IL-6, TNF, or IL-1β in response to LPS or a combination of LPS and IFNγ, or in the phosphorylation states of NF-κB pathway proteins at 15, 30 and 60 minutes post-stimulation with LPS (Yu et al. 2019). We first confirmed this, showing no difference in the release of TNF or IL-6 in response to LPS or LPS+IFNγ 24 hours post-stimulation (**Figure 3.2**). Our data shows that IFNγ alone is not sufficient for TNF or IL-6 release, whereas LPS stimulation alone induces release of both cytokines (**Figure 3.2**). Interestingly, addition of IFNγ in combination with LPS does not lead to a synergistic effect of TNF or IL-6 release (**Figure 3.2**). No difference in TNF or IL-6 release from WT and KO BMDMs was observed (**Figure 3.2**).

To further add to this data, we also performed a stimulation time-course using WT and KO BMDMs, harvesting supernatants at different time points over a 24-hour period. The release of TNF and IL-6 was assessed by sandwich ELISA, as before. TNF was released rapidly, peaking at around 4 hours post-stimulation (**Figure 3.3A**). This was largely sustained over the subsequent 20 hours, with a marginal increase observed between 10- and 16-hours post-stimulation (**Figure 3.3A**). IL-6 kinetics was slightly delayed and rose steadily from 2h post stimulation until the last time point observed (**Figure 3.3B**). No difference was observed in the release of either TNF or IL-6 over the 24-hour period between KO and WT BMDMs (**Figure 3.3**), confirming that TRIM24 does not play a role in the release of these cytokines following TLR4 stimulation.

3.3.3. Enhanced release of NO from TLR-stimulated *Trim24*$^{-/-}$ BMDMs

Macrophage polarisation also induces large changes in metabolism, with M1 macrophages activating aerobic glycolysis as their main source of ATP, and M2 macrophages activating oxidative phosphorylation and the TCA cycle (reviewed in (Qing et al. 2020). L-arginine metabolism is another important and distinct metabolic process in the balance between macrophage M1 and M2 polarisation, occurring through the upregulation of either inducible nitric oxide synthase (iNOS) or arginase (Arg-1) (Rath et al. 2014).

iNOS is a critical factor in *Leishmania* immunity, responsible for the destruction of intracellular parasites, as discussed in detail in **Chapter 1**. To explore this further, BMDMs were generated from WT and KO mice, and nitrite concentration (a readout for NO concentration) in the cell supernatant was quantified 6 and 24 hours post-stimulation with LPS, IFNγ, or a combination of IFNγ and LPS via the Griess reaction assay (Tsikas 2007).

Compared to unstimulated control BMDMs, IFNγ did not induce release of NO at 6 hours or at 24 hours post-stimulation (**Figure 3.4A**). LPS alone induced the release of NO from BMDMs at both 6 hours and 24 hours post-stimulation, with a higher concentration of NO observed at 24 hours post-stimulation (**Figure 3.4A**). Co-stimulation with LPS and IFNγ led to a further increase in NO release compared to LPS alone (**Figure 3.4A**), consistent with previously published literature (Lin et al. 2008; Held et al. 1999; Müller et al. 2017).

Comparing WT and KO BMDMs, we observed a significant increase in the release of NO in LPS-stimulated KO BMDMs compared to WT controls at both 6 and 24 hours post-stimulation (**Figure 3.4A**). We also observed this phenotype with a range of concentrations of LPS (**Figure 3.4B**). To validate the link between TRIM24 and NO release, we transiently overexpressed TRIM24 in a RAW264.7 macrophage cell line. This resulted in suppression of NO release after 24 hours stimulation with either LPS or a combination of IFNγ and LPS (**Figure 3.5**; generated by Nina Krauss). Collectively, these data are consistent with the hypothesis that TRIM24 is a negative regulator of NO production following TLR4 stimulation in macrophages.

3.3.4. Enhanced detection of nitrate after TLR stimulation is due to increased expression of iNOS in BMDMs

The enhanced release of NO from KO BMDMs raises the question of whether the expression of iNOS is increased but the number of iNOS-expressing macrophages remains the same, or whether there is an increase in the number of iNOS-expressing macrophages (or both).

To address whether increased nitrate production was also associated with increased expression of iNOS, flow cytometry was used to detect intracellular iNOS on a single cell level following stimulation with LPS, IFNγ, or a combination of LPS and IFNγ. To provide a quantitative assessment of iNOS expression, gates were placed to capture cells with both low and high iNOS expression (**Figure 3.6A**).

As shown for nitrite production (**Figure 3.3**)**,** no detectable expression of iNOS was observed in unstimulated BMDMs or BMDMs stimulated with IFNγ alone. Upon LPS stimulation, 80% of WT BMDMs became $iNOS^{+}$, half of which were $iNOS^{hi}$ and half of which were $iNOS^{lo}$. In contrast, 90% of KO BMDMs became $iNOS^{+}$, two thirds of which were $iNOS^{hi}$ and one third $iNOS^{lo}$. This was accentuated with LPS + IFNγ co-stimulation, with an increase in the

percentage of WT iNOS^{hi} BMDMs (from 40% in LPS to 50% in the co-stimulation) (**Figure 3.6B&C**).

KO BMDMs showed a significantly higher percentage proportion of iNOS^{hi} cells compared to WT controls, after both LPS stimulation and co-stimulation with LPS and IFNγ (**Figure 3.6A&C**), confirming the hypothesis that the increase in NO release is due to increases in iNOS expression in KO cells. WT BMDMs did express iNOS in response to TLR4 stimulation, however more WT BMDMs were present in the iNOS^{lo} population compared to KO BMDMs, further indicating that TRIM24 acts as a brake to iNOS expression (**Figure 3.6B**).

3.3.5. Enhanced release of IFNβ from TLR-stimulated *Trim24-/-* BMDMs reveals potential upstream mechanism for increased iNOS expression

IFN-I are known to be involved in (and in some cases required for) the expression of iNOS in primary macrophages and macrophage cell lines in response to *Leishmania* infection and *in vitro* TLR stimulation (Vadiveloo et al. 2000; Zhang et al. 1994; Mattner et al. 2000). Given this relationship between IFN-I signalling and iNOS expression, we were also interested in testing whether TRIM24 deficiency is also associated with differential expression of IFN-I. We stimulated WT and KO BMDMs with LPS alone and analysed supernatants for presence of IFNβ by ELISA at several early and late time points over a 24-hour period (**Figure 3.7A**). A two-fold increase in IFNβ release was observed from KO macrophages compared to WT controls after LPS stimulation, confirming our hypothesis. RNA from WT and KO BMDMs was also harvested 24 hours post-stimulation for qPCR analysis (**Figure 3.7B**), and this further confirmed an increase in the expression of iNOS in KO BMDMs at this time point. TLR3 stimulation of WT and KO BMDMs also revealed a significant increase in the release of IFNβ from KO BMDMs compared to WT (**Figure 3.7C**).

3.3.6. Bulk RNA-seq of WT and KO BMDMs

Having demonstrated increased expression of IFN-I by KO BMDMs, we next investigated broader functional differences between KO and WT BMDMs using transcriptional profiling. Bulk RNA-sequencing was used to compare WT and KO BMDMs stimulated or not with LPS alone, IFNγ alone, or a combination of LPS+IFNγ (**Figure 3.8**). RNA was extracted from

stimulated BMDMs and after ensuring RNA was of high quality (this was performed by Elmarie Myburgh), RNA was sequenced by Novogene.

We analyzed four samples per stimulation condition, and we detected ~24,000 genes per sample. Pearson correlation between samples showed a high degree of similarity between cells within each stimulation condition stimulated BMDMs (**Figure 3.9**). Samples stimulated with LPS (alone or in combination with IFNγ) correlated highly with other LPS-stimulated samples, but less highly correlated with control and IFNγ-stimulated samples (**Figure 3.9**). The lowest Pearson correlation score was still high at >0.8 (KO_LI vs WT_Med) (**Figure 3.9**).

Principal Component Analysis (PCA) reflected these correlations (**Figure 3.10**). Close clustering of biological replicate samples within each stimulation condition was observed. IFNγ-stimulated BMDMs clustered away from both the unstimulated BMDMs and LPS and co-stimulated BMDMs. Likewise, LPS- and co-stimulated BMDMs clustered away from control and IFNγ-stimulated BMDMs. Furthermore, Principal Component 1 (PC1) contained the majority (74.4%) of the variation between samples, while PC2 contained 4.51%. Thus, the separation of samples along the PC1 axis indicates that LPS- and co-stimulated samples are more transcriptionally different to the control and IFNγ-stimulated samples. Interestingly, LPS + IFNγ co-stimulated BMDMs clustered with LPS-stimulated BMDMs, indicating that the addition of IFNγ to LPS stimulation did not drastically alter the transcriptional signature of BMDMs. PCA revealed some clustering by genotype, indicating differences in transcriptional signature of KO BMDMs for each stimulation. IFNγ stimulation revealed few differences between WT and KO BMDMs, while LPS stimulation led to greater differences between WT and KO samples (**Figure 3.10**).

Differential gene expression was then performed for each stimulation condition between WT and KO BMDMs, and numbers of differentially expressed genes (DEGs) were determined (q-value <0.05 and log2FC >0.5 or <-0.5) (**Figure 3.11**). In control unstimulated BMDMs, we found 36 downregulated genes and 167 upregulated genes in KO compared to WT (**Figure 3.11**). IFNγ stimulation results in similar numbers of DEGs in WT and KO BMDMs compared to unstimulated controls (521 and 523 downregulated, 740 and 825 upregulated) (**Figure 3.11**). We found 34 down-regulated and 223 up-regulated genes in IFNγ-stimulated KO BMDMs compared to WT (**Figure 3.11**).
LPS stimulation led to many more DEGs in WT and KO BMDMs compared to unstimulated controls, with slightly more DEGs in KO BMDMs (3443 down and 3349 up vs 3674 down and

3720 up) (**Figure 3.11**). We found 502 down-regulated and 1141 up-regulated genes in LPS-stimulated KO BMDMs compared to WT (**Figure 3.11**).
Interestingly, co-stimulation with LPS and IFNγ resulted in a similar number of DEGs than LPS stimulation alone (3570 down and 3465 up vs 3443 down and 3349 up, respectively) (**Figure 3.11**). In WT BMDMs, DEGs between LI-stimulated and IFNγ-stimulated samples were 3228 down- and 3213 up-regulated (**Figure 3.11**), whereas DEGs between LI-stimulated and LPS-stimulated WT BMDMs were only 124 down- and 142 up-regulated (**Figure 3.11**). We saw 584 up-regulated and 1258 down-regulated genes in LI-stimulated KO BMDMs compared to WT, slightly more than LPS stimulation alone (**Figure 3.11**). Thus, while IFNγ stimulation leads to significant transcriptional changes, LPS stimulation induces a much stronger transcriptional change. Further, co-stimulation with LPS and IFNγ leads to minor increases in the number of DEGs compared to LPS stimulation alone.

In unstimulated control BMDMs, *Trim24* was highly downregulated in KO BMDMs, as expected (**Figure 3.12**). We saw a higher number of upregulated genes than downregulated genes, and upregulated genes were also more highly significant, evidencing TRIM24's role as a negative transcriptional regulator (**Figure 3.12**). The top 10 significantly enriched genes in KO BMDMs were *Atp1b3, Hgsnat, Tgfbi, Def8, Fcgr2b, Lgmn, Pomk, Sel1l3, Resf1,* and *Cblb* (**Figure 3.12**). We also detected several significantly upregulated genes which were highly enriched by log2FC (*BC021767, Selenbp2, Tubb3, Capn11, Pde11a,* and *AI606473*) (**Figure 3.12**). Over representation analysis (ORA) of these genes did not reveal any significantly enriched gene sets.

GSEA of all genes ranked by log2FC revealed gene sets relating to both type 1 and 2 interferon responses among the top significantly upregulated gene sets in unstimulated KO BMDMs compared to WT controls, indicating an elevation in the capacity of KO BMDMs to respond to interferon stimulation (**Figure 3.13A**). This adds to our previous data, suggesting that as well as KO BMDMs producing more IFN-I following TLR3/4 stimulation, KO BMDMs also appear to have a basal elevation in their capacity to respond to IFN-I, which contributes to the enhancement of iNOS expression. The genes contributing to the enhancement of the IFN-I response were *Rsad2, Usp18, Isg15, Ifit3, Ifi44, Oasl1, Ifit2, Csf1,* and *Cmpk2* (**Figure 3.13B**). *Irf7* is also significantly enriched in KO BMDMs compared to WT controls (**Figure 3.13B**), and we did not see a significant difference in the expression levels of *Irf3* in unstimulated BMDMs, indicating that TRIM24 may exert its effects during IRF7-dependent IFN-I expression (**Figure 3.13B**).

We next aimed to confirm our previous *in vitro* data of LPS-stimulated KO BMDMs (unaffected IL6 and TNF release, increased iNOS and IFNβ release) at the mRNA level. LPS-stimulated KO BMDMs showed more differentially expressed genes in KO BMDMs compared with WT controls, and two thirds of differentially expressed genes were upregulated (**Figure 3.11**). We observed significant upregulation of *Nos2* and *Ifnb,* and no significant differences in *Il6* or *Tnf* in KO BMDMs compared to WT (**Figure 3.14**). GSEA analysis again revealed type 1 and type 2 IFN responses as enriched gene sets (*Ifit2, Cxcl10, H2-Q10, Gbp10, Oasl1*) (**Figure 3.15 & 3.16A**), however there are gene sets in KO BMDMs that were more significantly enriched than the IFN response gene sets (**Figure 3.15**). Among other top enriched gene sets were gene sets for TNF signalling, inflammatory response, IL-2/STAT5 signalling, and IL-6/JAK/STAT3 signalling (**Figure 3.15**). Upregulated cytokine, chemokine and associated receptor genes within the inflammatory response gene set included *Il4ra, Nlrp3, Cxcl10, Cxcl11, Il7r, Ccl2, Il10, Il1r1, Il15ra, Tlr3, Serpine1, Ccl7, Slc7a2,* and *Csf1* (**Figure 3.16B**). Interestingly, *Irf7* was not upregulated in LPS-stimulated KO BMDMs; the only IRF gene to surpass the padj and log2FC thresholds was *Irf2bpl*, which is associated with neurological disorders (Marcogliese et al. 2018). Interestingly, the Oxidative Phosphorylation gene set was downregulated in KO BMDMs (**Figure 3.15**), with associated downregulated genes such as *Cox7b, Atp5l, Atp5e, Atp5k, Atp5g1, Timm9, Timm10, Retsat, Etfb,* and *Ndufc1* (**Figure 3.16C**).

IFNγ stimulation of WT BMDMs led to increases in the number of DEGs detected (521 downregulated, 740 upregulated; **Figure 3.11**). Type 1 and type 2 interferon signalling gene sets appeared as the top two enriched gene sets in WT BMDMs following IFNγ stimulation compared to unstimulated (**Figure 3.17A**). Within these gene sets, we saw upregulation of genes related directly to IFN signalling (*Isg15, Ifi35, Oasl1, Ifi44, Ifit2, Ifit3, Stat2*), proteasome activation (*Psme1, Psmb8, Psmb9, Psme2, Casp1*), interferon regulatory factors (*Irf1, Irf2, Irf7*), and antigen presentation (*B2m, H2-Q7, Cd74, Tap1*) (**Figure 3.17B**). IFNγ-stimulated KO BMDMs showed upregulation of these same genes, and a similar GSEA output (**Figure 3.18**). Comparison of KO and WT IFNγ-stimulated BMDMs revealed type 1 and type 2 interferon response gene sets as significantly enriched in KO BMDMs (**Figure 3.19A**). Interferon stimulated genes were upregulated in IFNγ-stimulated KO BMDMs (*Isg15, Oas3, Ifit2, Ifit3, Usp18, Isg20, Ifi44*) (**Figure 3.19B**). Additionally, *Irf7* and *Stat2* were also significantly upregulated in IFNγ-stimulated KO BMDMs, genes that are important for transduction of type 1 interferon signalling (**Figure 3.19B**).

Together, these results confirm our findings *in vitro* that TRIM24 acts as a negative regulator of inflammatory macrophage activation in a selective manner that is likely due to an

enhanced production of and response to interferon signalling. We also postulate that TRIM24-mediated regulation of macrophage inflammatory response is multifactorial, and TRIM24 is able to act upon a variety of signalling pathways to affect pro- and anti-inflammatory phenotypes.

3.4. Discussion

Here, we investigated the roles of TRIM24 in M1 macrophage polarisation in more detail. We first confirmed that TRIM24 is dispensable for primary murine BMDM differentiation. TRIM24 falls within a subgroup of the TRIM proteins with TRIM33 and TRIM28 (all containing PHD-Bromo functional domains), both of which have been more extensively studied than TRIM24. Induced deficiency of TRIM33 has been shown to impair haematopoiesis and differentiation of monocytes and macrophages in B6 mice, but notably only when TRIM33 deficiency occurs at earlier stages of haematopoiesis (Gallouet et al. 2017). MxCre/*Trim33*$^{-/-}$ mice treated with polyinosinic:polycytidylic acid (PIPC) to induce *Trim33* deficiency had higher numbers of myeloid progenitor populations one month after injection compared to control mice (Gallouet et al. 2017). These mice also had higher numbers of mature neutrophils and Ly6C^{hi} monocytes in the BM (Gallouet et al. 2017). Lower numbers of BMDMs and DCs were also seen when MxCre/*Trim33*$^{-/-}$ BM cells were treated *in vitro* with M-CSF and GM-CSF, respectively (Gallouet et al. 2017). Abnormal myelopoiesis in *Trim33*$^{-/-}$ mice has also been linked with a decrease in the expression of CSF1 receptor, and *Trim33*$^{-/-}$ BMDMs had significant impairments in the production of TNF, IL-6, IL10, MCP1 and IL1β after LPS stimulation (Chrétien et al. 2016).
Interestingly, this phenotype was not observed when *Trim33* deficiency was restricted to mature myeloid cells (using LyzMCre mice), indicating that *Trim33* is important for early stages of myelopoiesis (Gallouet et al. 2017). Our data indicates that TRIM24 likely does not share these same roles of TRIM33 in BMDM differentiation *in vitro*, as no change in KO BMDM number was observed compared to WT control BMDMs despite *Trim24*$^{-/-}$ deficiency in early haematopoietic cells.

As mentioned previously, *Trim33* deficiency in mouse BMDMs led to impaired release of inflammatory cytokines after LPS simulation (Chrétien et al. 2016). However, a more recent study showed no change in mRNA abundance of *Tnf* or *Il1b*, or in the release of IL-6 from LPS-stimulated *Trim24*$^{-/-}$ BMDMs (Yu et al. 2019). We confirmed this at the protein level, showing that release of TNF and IL-6 was not affected by TRIM24 deletion in a comprehensive time course study assessing both early and late time points post-LPS stimulation. We further confirmed this at the mRNA level through our bulk RNAseq data. While these cytokines (among others) are important for mounting a type 1 immune response and subsequent *Leishmania* parasite immunity, nitric oxide is vital to macrophage-mediated removal of parasites, and is characteristic of M1 polarisation in macrophages (Murray & Nathan 1999). Here we show that while the release of TNF and IL-6 were unchanged in KO BMDMs exposed to LPS, we did observe a significant increase in the release of NO from KO

BMDMs compared to WT controls, an effect that was seen at both low and high concentrations of LPS treatment.
We further confirmed that this was due to an increase in the proportion of iNOS^{hi} BMDMs among KO BMDMs compared to WT controls. We then hypothesised an involvement of TRIM24 in pathways that also regulate the expression of iNOS. Previous data has shown no changes in the activation of the NF-kB pathway in *Trim24*$^{-/-}$ macrophages (Yu et al. 2019), though other pathways have not been investigated.

iNOS expression following TLR stimulation occurs mainly through activation of the NF-kB pathway. As discussed previously, many of the TRIM proteins (including TRIM24) are regulators of STAT signalling pathways, in response to cytokine signalling (Giraldo et al. 2020). While macrophages are known to respond strongly to type 2 interferon (IFNγ) released by Th1 cells during infection, they are not known to be able to produce their own IFNγ. However, it is widely documented that macrophages are able to induce type 1 interferon (IFN-I) (IFNα and IFNβ) following TLR signalling (Kumaran Satyanarayanan et al. 2019). While TLR3 stimulation is the strongest inducer of IFN-I expression in macrophages (activated by double-stranded RNA from e.g. viruses), stimulation of other TLRs also induces expression of IFN-I, albeit at lower levels. The exception to this is TLR7/9, highly expressed on plasmacytoid dendritic cells, which rapidly induces IFN-I after viral infections.

Some early studies indicate that IFN-I signalling is a requirement for iNOS expression following TLR4 stimulation, as shown by the inability for *Ifnar1*$^{-/-}$ BMDMs to produce NO or express iNOS (Vadiveloo et al. 2000). This phenotype was rescued by the addition of exogenous IFNγ, indicating that interferon signalling is required for iNOS expression, but there is some redundancy in the type of interferon required (Vadiveloo et al. 2000). Furthermore, adding increasing concentrations of IFNβ to macrophages exposed to heat-killed *Staphylococcus aureus* led to an increase in NO release in parallel with increasing IFNβ concentrations, while not affecting TNF release (Zhang et al. 1994). This is consistent with our data on *Trim24*$^{-/-}$ macrophages, thus we hypothesised that TRIM24 plays a role in IFN-I signalling during LPS stimulation in macrophages.

We show that KO BMDMs release 2-fold more IFNβ than WT BMDMs in response to TLR4 stimulation; higher *Ifnb1* expression was also confirmed at the mRNA level. This was an interesting result, as a recent study investigating the roles of TRIM24 in vesicular stomatitis virus (VSV) infection showed a significant reduction in IFN-I production during infection when TRIM24 expression was ablated in murine macrophages, thus impairing the antiviral response (Zhu et al. 2020). Mechanistically, Zhu et al. showed that TRIM24 exerts its effect

by ubiquitinating and activating TRAF3, which leads to phosphorylation of IRF3 and induction of IFN-I and ISG expression (Zhu et al. 2020). A negative feedback loop was also identified, where phosphorylated IRF3 binds to the *Trim24* promoter and inhibits *Trim24* expression (Zhu et al. 2020). Treatment of macrophages with the TLR3 ligand polyI:C led to similar results (Zhu et al. 2020). This is not consistent with the data presented here, as we have shown an increase in release of IFNβ from KO BMDMs stimulated with TLR4 (LPS) and TLR3 (polyI:C) ligands, respectively. This could be due to differences in peritoneal macrophages stimulated with polyI:C used in Zhu et al.'s study compared with the BMDMs used in the study presented here. Peritoneal macrophages have been shown to respond differently to BMDMs, with BMDMs exhibiting a more CAM-like phenotype at the steady state and responding more potently to LPS stimulation. BMDMs upregulated Ly6C, CD124, TLR4, TLR2, and CD64 after LPS stimulation compared to peritoneal macrophages, and had a higher phagocytic capacity in response to *E. coli* and Zymosan exposure (Zajd et al. 2020). It must also be noted that differentiation of BMDMs using L929 cell-conditioned media leads to a heterogeneous population of macrophages. While L929-cell conditioned media contains a large amount of M-CSF, other signalling proteins are present in the media (CCL2, CCL9, CCl7, TGFβ) which can prime BMDMs and lead to enhanced responses observed by Zajd et al. (Zajd et al. 2020; Heap et al. 2021). This will be discussed in more detail in **Chapter 4.** A more recent study has reported an increase in the production of IL-10 from TRIM24-deficient B6 BMDMs that was attributed to CBP/p300-dependent expression of IFNβ following LPS stimulation, which is consistent with and builds upon our data presented here (Hui et al. 2023).

Our bulk transcriptomic analysis of stimulated WT and KO BMDMs reflected our other *in vitro* data, with the upregulation of *Nos2* and *Ifnb1* in KO BMDMs and no change in *Tnf* or *Il6* in LPS-stimulated KO BMDMs. Interestingly, we saw upregulation of many IFN-I stimulated genes that contribute to the HALLMARK interferon alpha response gene set in unstimulated KO BMDMs, suggesting a basal elevation in the propensity for KO BMDMs to respond to IFN-I. Importantly, the mild but significant upregulation of *Irf7* at the steady state is indicative of a role of TRIM24 in IRF7-mediated IFNβ expression.

IRF7 (along with IRF3) is a major regulator of IFN-I expression following TLR stimulation (Honda et al. 2005), and in WT cells, IRF7 is expressed at lower levels than IRF3 at the steady state (Izaguirre et al. 2003). Following TLR stimulation, IRF3 becomes activated and induces an initial wave of IFN-I (mainly IFNβ), which is released from the cell. This IFN-I can then bind to IFNAR receptors in autocrine and paracrine manners, which induces a strong expression of IRF7 through activation of the ISGF3 complex (formed of IRF9, STAT1 and STAT2). This IRF7 then mediates a strong induction of more IFN-I in a second, much larger,

wave of IFN-I release from the cell (Honda et al. 2006). Furthermore, it has been shown that IFNγ is able to induce the formation and activity of the ISGF3 complex, which includes STAT2 (Platanitis et al. 2019), indicating that TRIM24 may be regulating this pathway at the level of the ISGF3 complex. However, this requires further investigation.

The exact mechanism by which TRIM24 regulates *Nos2* and iNOS expression still remains unclear. However, deletion of TRIM24 leads to upregulation of both *Nos2* and *Arg1* after LPS stimulation (Yu et al. 2019), indicating that arginine metabolism is increased in KO macrophages. One interesting hypothesis is from the identification of *Slc7a2* upregulation in LPS-stimulated KO BMDMs in our bulk RNA-seq data. *Slc7a2* encodes the Cationic Amino Acid Transporter 2 (CAT2) protein, an inducible amino acid channel that is vital for the transport of extracellular arginine into the cell for metabolism. CAT2 is one of three channels part of the y+ arginine transport system, considered to be the main transport system for arginine (the other two channels being CAT1 and CAT3, encoded by *Slc7a1* and *Slc7a3*, respectively) (MacLeod et al. 1994). CAT2 is an inducible protein channel that is closely associated with expression of iNOS; it has been shown to be upregulated in macrophages after LPS stimulation, simultaneously to iNOS expression (Kakuda et al. 1999). Further, it has been shown that LPS-stimulated macrophages require L-arginine uptake in order to sustain high levels of NO production (Nicholson et al. 2001). Therefore, given the upregulation of *Slc7a2* we observed in *Trim24* KO BMDMs, it is reasonable to hypothesise that the upregulation of iNOS and Arg1 seen in KO BMDMs can be attributed to increased arginine transport into the cell. Inhibition of L-Arg uptake by L-lysine treatment (competitive inhibitor) and monitor rate of nitric oxide decay could therefore be an interesting experiment to perform.

IFN-I has also been implicated in *Leishmania* infections. An interesting study showed that *L. major*-induced release of IFN-I was required for the expression of iNOS in macrophages 1 day after infection (Mattner et al. 2000). Further study indicated that timing and dose of IFN-I exposure is critical in the response to *L. major* (Mattner et al. 2000). Low level of IFN-I and simultaneous exposure of macrophages to *L. major* and IFN-I led to efficient expression of iNOS and subsequent parasite killing, whereas higher concentrations of IFN-I led to little to no induction of iNOS expression (Mattner et al. 2000). Furthermore, macrophages pre-treated with IFN-I before exposure to *L. major* led also failed to produce iNOS. Thus, timing of IFN-I exposure alters macrophage responses to infection (Mattner et al. 2000). Therefore, deletion of TRIM24 leading to increased IFN-I expression and subsequent paracrine signalling could aid in leishmaniasis pathogenesis despite the important role for IFN-I in iNOS expression.

In general, IFN-I is thought to play a detrimental role to the host during *Leishmania* infection. For example, IFN-I promotes phagocytosis of parasites by macrophages via mechanisms such as upregulation of CD163 (Van Bockstal et al. 2020), and acts via TLR2, TLR4, TLR3 and Protein Kinase R (PKR) to facilitate parasite survival (Dias et al. 2022). Neutrophil elastase also plays a role in the induction of IFNβ in *L. donovani* infected macrophages to facilitate parasite survival, evidenced by improved parasite burdens in neutrophil elastase knockout mice infected with *L. donovani* (Dias et al. 2019). Targeting of IFN-I signalling during *L. donovani* infection decreases parasite burden in B6 mice and in whole blood sample derived from VL patients by enhancing $CD4^+$ T cell anti-parasite mechanisms through increased release of IFNγ and TNF, and dampening of DC-mediated suppression of Th1 cell expansion (Kumar et al. 2020).

Together our data has revealed novel roles for TRIM24 in the regulation of iNOS and NO production in murine macrophages and confirmed and built upon its role as a negative regulator of interferon signalling. In the following chapters, we will aim to characterise *Trim24*$^{-/-}$ mice and elucidate the role(s) of TRIM24 during *L. donovani* infection.

3.5. Figures

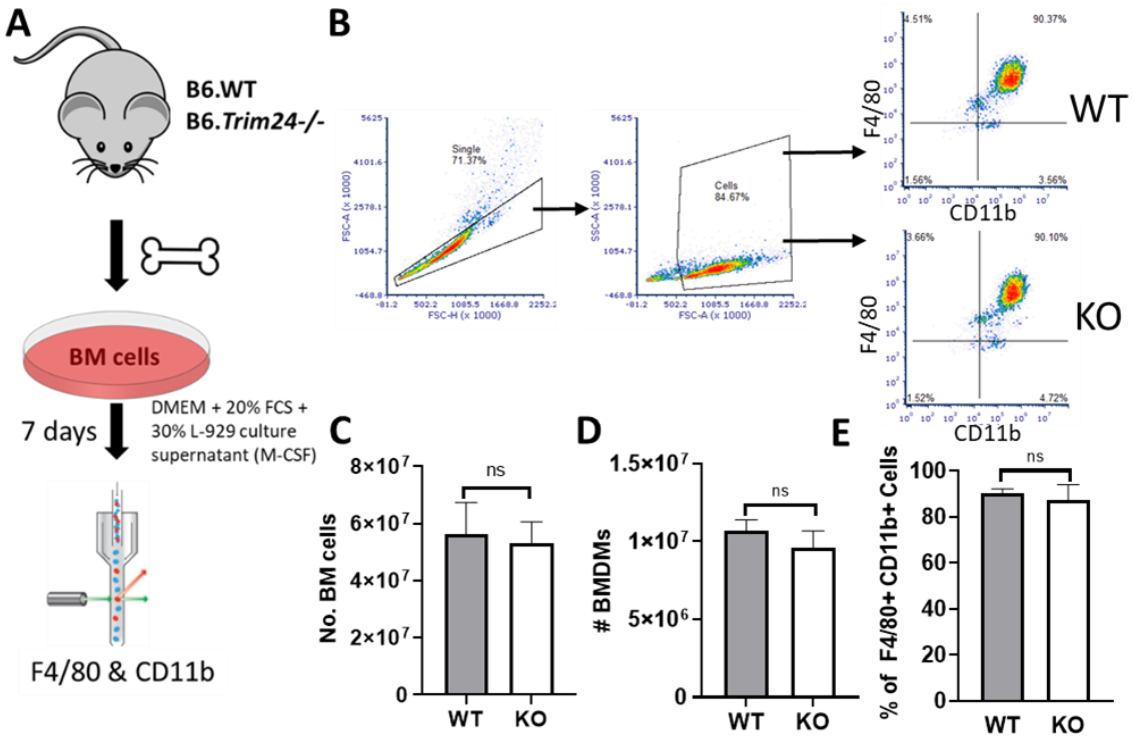

Figure 3.1. Differentiation of bone marrow cells to BMDMs is not affected by TRIM24 deletion. (A) Bone marrow cells were isolated from femurs and tibias of B6.*Trim24-/-* and B6.WT littermate control mice. BM cells were cultured with macrophage differentiation media ($5x10^6$ cells seeded per plate), containing 30% L929 cell supernatant (which contains M-CSF), for 6 days, replaced with fresh macrophage media after 3 days. Macrophage media was then replaced with DMEM + 20% FCS and cells were allowed to recover overnight, before being harvested, counted, and stained for detection of F4/80 and CD11b by flow cytometry. **(B)** Gating strategy for detection of single cells positive for both F4/80 and CD11b expression. **(C-E)** Summary data for number of total bone marrow cells **(C)**, number of BMDMs **(D)**, and percentage of F4/80+ CD11b+ BMDMs. **(E)** Gating strategy for F4/80 and CD11b detection. Data is Mean ± SD; n=3-6 mice per group; ns = not significant, student's t-test.

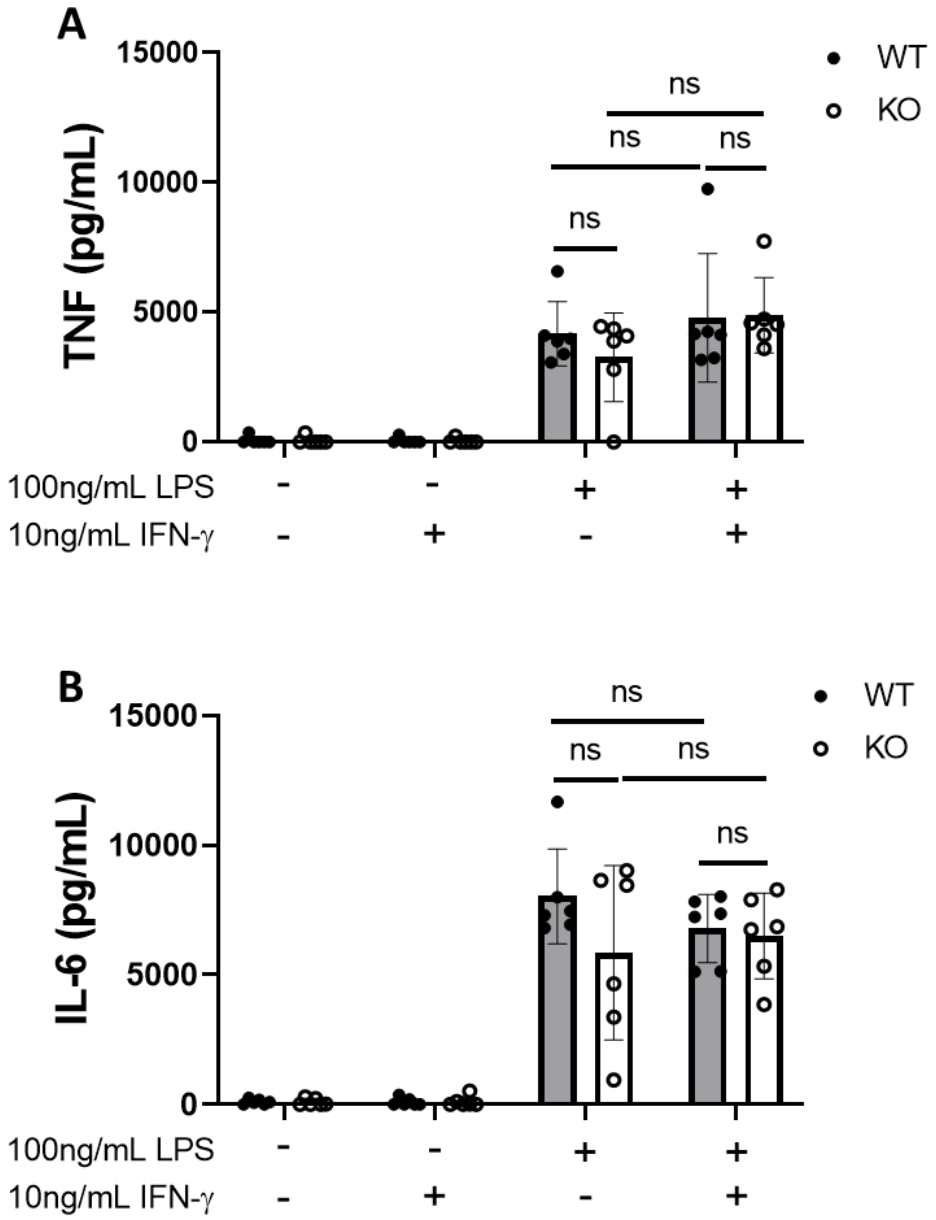

Figure 3.2. TNF (A) and IL-6 (B) release are not affected by TRIM24 deletion in CAMs. Bone marrow-derived macrophages (BMDM) were generated from B6 *Trim24-/-* and *Trim24+/+* littermate control mice. BMDMs were seeded on a 96-well non-tissue culture treated plate ($2x10^5$ cells/well), and allowed to adhere overnight. Indicated concentrations of LPS and/or IFN-γ were added to the respective wells and cells were stimulated for 24 hours. Supernatants were harvested, and concentration of cytokines were measured by sandwich ELISA. Data are mean ± SD; n = 6 mice (2 independent experiments); ns = not significant, Two Way ANOVA with Tukey's correction.

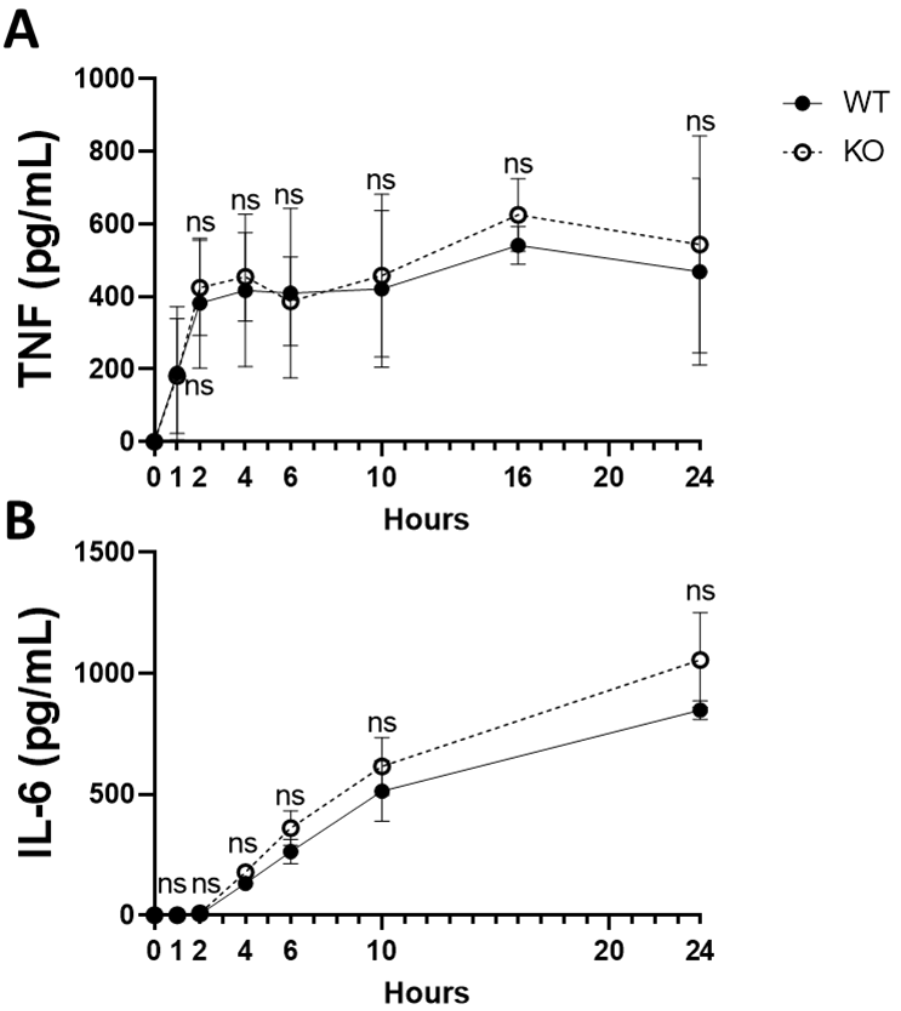

Figure 3.3. TRIM24 deletion does not affect kinetics of TNF (A) or IL-6 (B) release from TLR4-stimulated murine macrophages. Bone marrow-derived macrophages (BMDM) were generated from B6 *Trim24-/-* and *Trim24+/+* littermate control mice. BMDMs were seeded on a 96-well non-tissue culture treated plate ($2x10^5$ cells/well), and allowed to adhere overnight. 50ng/mL LPS was added or not to the respective wells. Cells were stimulated for the indicated times before supernatants were harvested, and concentration of cytokines were measured by sandwich ELISA. Data are mean ± SD; n=3-6 mice (1-2 independent experiments); ns = not significant, mixed effects model ANOVA with Šidák's correction.

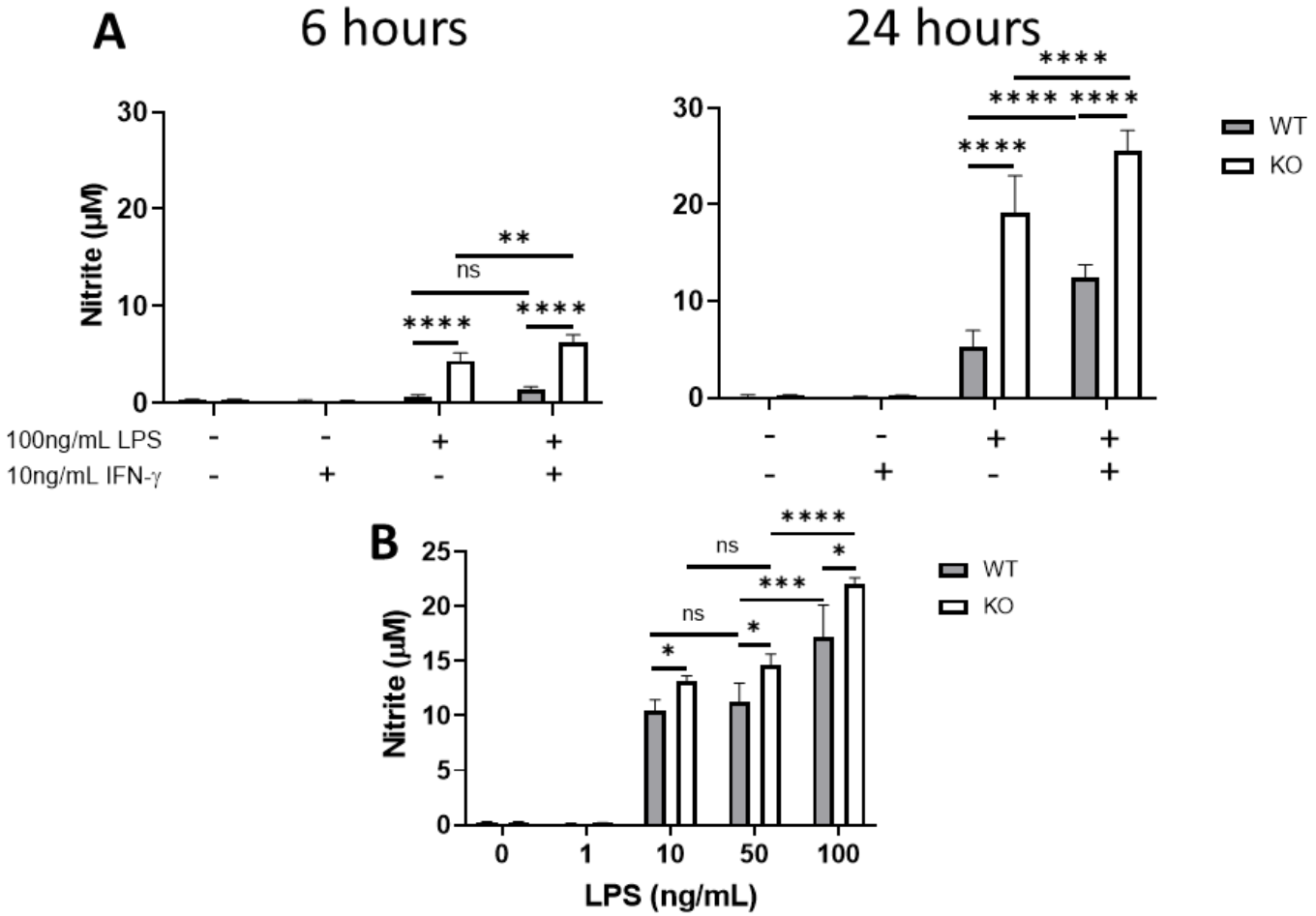

Figure 3.4. Nitric oxide release is increased in activated KO primary murine macrophages. BMDMs were generated from KO and WT littermate control mice, seeded on a 24-well non-tissue culture treated plate ($1x10^6$ cells/well) and allowed to adhere overnight. 100ng/mL LPS, 10ng/mL IFN-γ, or 100ng/mL LPS + 10ng/mL IFN-γ was added to the respective wells for stimulation. **(A)** Cells were stimulated for 6 and 24 hours, cell supernatant was harvested, and nitrate was quantified using a Griess reaction assay in a 96-well flat-bottomed plate. **(B)** Cells were stimulated with LPS alone at the indicated concentrations for 24 hours. Supernatants were harvested and nitrate was quantified using a Griess reaction assay. Optical densities of the wells were measured at 550nm and concentration was determined by comparison to a standard curve. Data are mean ± SD of two combined experiments (Experiment was repeated 5 times with similar results); n=3-5 mice per group; *$P < 0.05$; **$P < 0.01$; ***$P < 0.001$; ****$P < 0.0001$, two-way ANOVA with Tukey's post-hoc test.

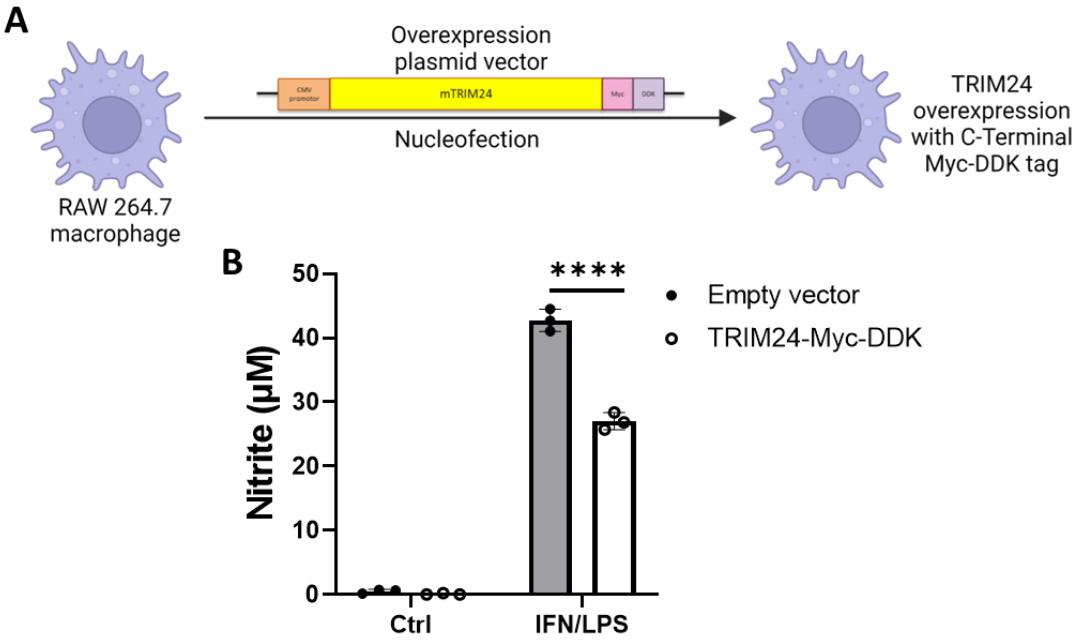

Figure 3.5. Nitric oxide release is decreased in RAW 264.7 macrophages with overexpressed TRIM24. (A) TRIM24 was transiently overexpressed in RAW 264.7 macrophages by nucleofection with an overexpression plasmid vector. **(B)** Cells were stimulated with 100 ng/mL IFN-γ (IFN) + 100 ng/mL LPS for 24 hours. Supernatants were harvested and nitrate was quantified using a Griess reaction assay. Optical densities of the wells were measured at 550nm and concentration was determined by comparison to a standard curve. Data are mean ± SD; n=3; ****$P < 0.0001$, two-way ANOVA with Tukey's post-hoc test. Data generated by Nina Krauss.

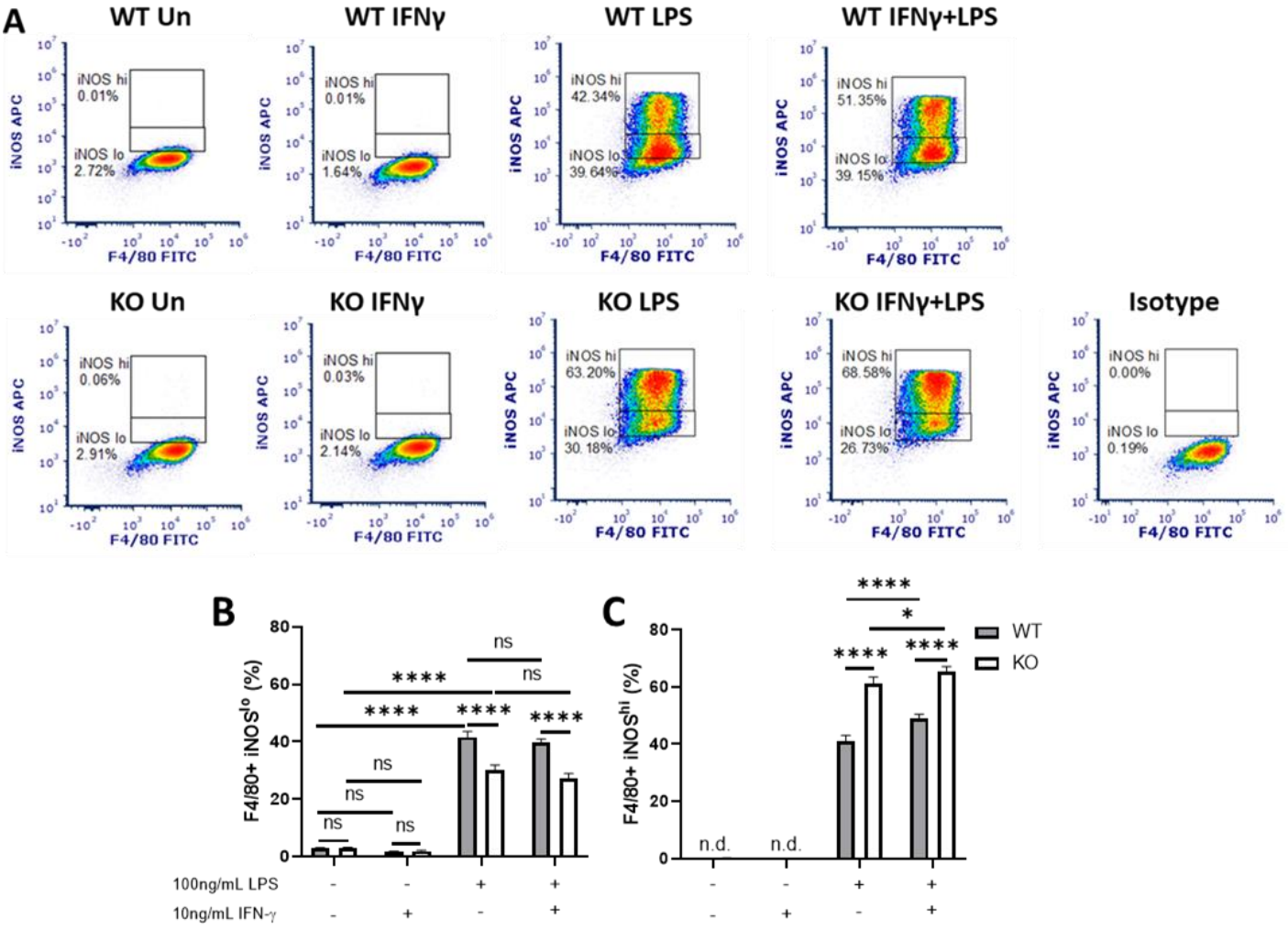

Figure 3.6. Expression of iNOS is increased in KO primary murine macrophages. BMDMs from KO and WT littermate control mice were seeded on a 24-well non-tissue culture treated plate (1x10^6 cells/well) and allowed to adhere overnight. Fresh DMEM, 100ng/mL LPS, 10ng/mL IFN-γ, or 100ng/mL LPS + 10ng/mL IFN-γ was added to the respective wells. At 24 hours post-stimulation, cells were stained for the macrophage marker F4/80 and intracellular iNOS. **(A)** Gating strategy to identify iNOS+ macrophages. Frequencies of F4/80+ iNOS^{lo} **(B)** and F4/80+ iNOS^{hi} **(C)** BMDMs under each condition. Data are mean ± SD from one of two independent experiment showing similar results; n=6 mice (2 independent experiments); *P < 0.05; **P < 0.01; ***P < 0.001; ****P < 0.0001, two-way ANOVA.

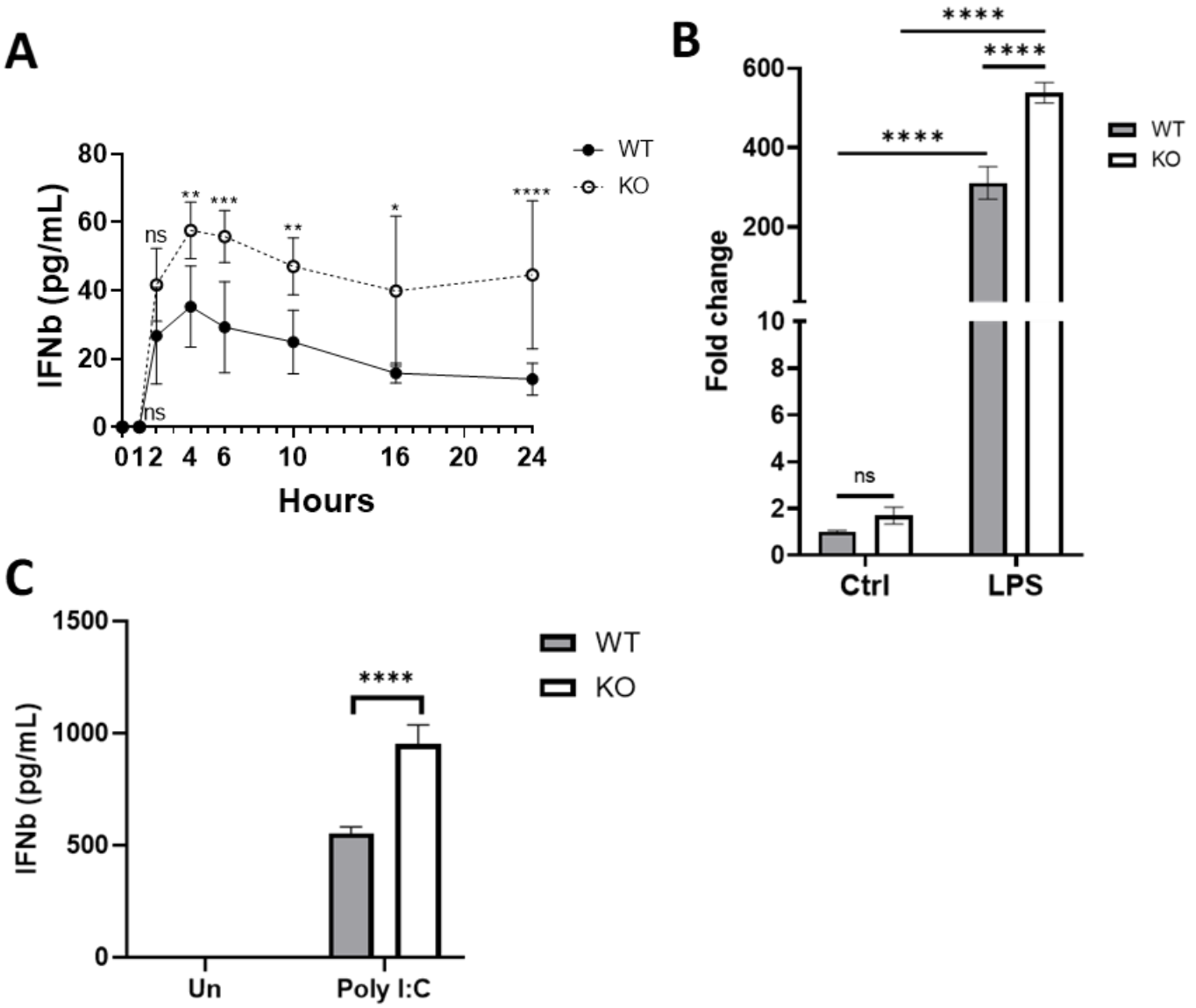

Figure 3.7. Enhanced type 1 interferon release by KO stimulated BMDMs. 50 ng/mL LPS **(A&B)** or 20 ng/mL polyI:C **(C)** was added or not to the respective wells. **(A)** Cells were stimulated for the indicated times before supernatants were harvested, and concentration of IFNβ was measured by sandwich ELISA. Data are mean ± SD; n=6 mice (2 independent experiments); **P* < 0.05; ***P* < 0.01, ****P* < 0.001 two-way ANOVA with Šidák's correction. **(B)** RNA was harvested after 24 hours stimulation and *Ifnb* mRNA abundance was measured by qPCR. Data are mean ± SD; n=BMDMs from 3 mice; **P* < 0.05; ***P* < 0.01, one-way ANOVA. **(C)** Cells were stimulated with 20 ng/mL polyI:C for 24 hours, supernatant was harvested and ELISA was performed to detect IFNβ was performed. Data are mean ± SD; n=BMDMs from 3 WT and 3 KO mice (cells from individual mice kept separate); ns = not significant, *****P* < 0.0001, two way ANOVA with Tukey's post-hoc test.

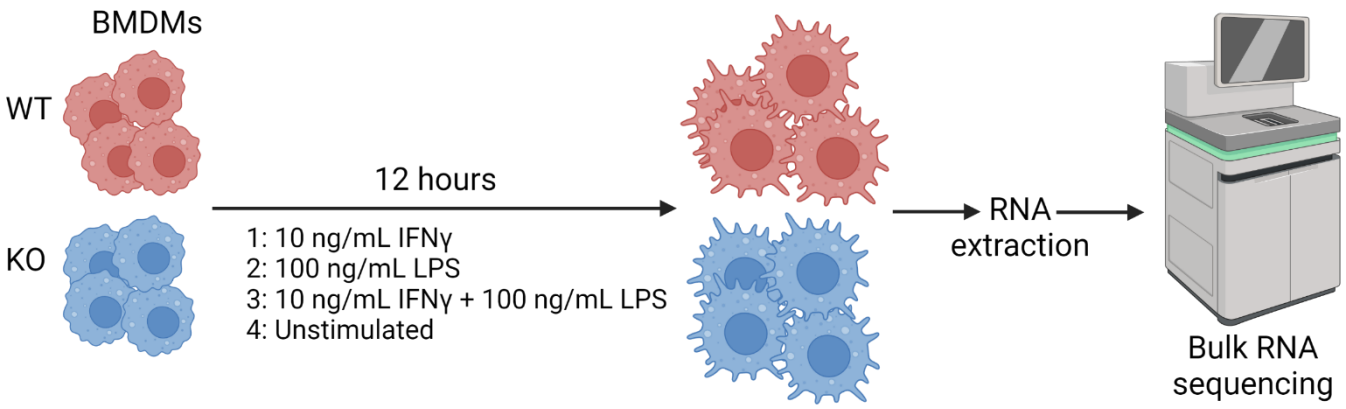

Figure 3.8. Bulk RNA sequencing of WT & KO BMDMs experimental plan. Bone marrow cells were harvested from WT and KO B6 mice, and differentiated into BMDMs. BMDMs were stimulated or not with IFN-γ, LPS, or a combination of IFN-γ + LPS (4 samples per genotype and condition). After 12 hours of stimulation, RNA was extracted and sent for RNA sequencing.

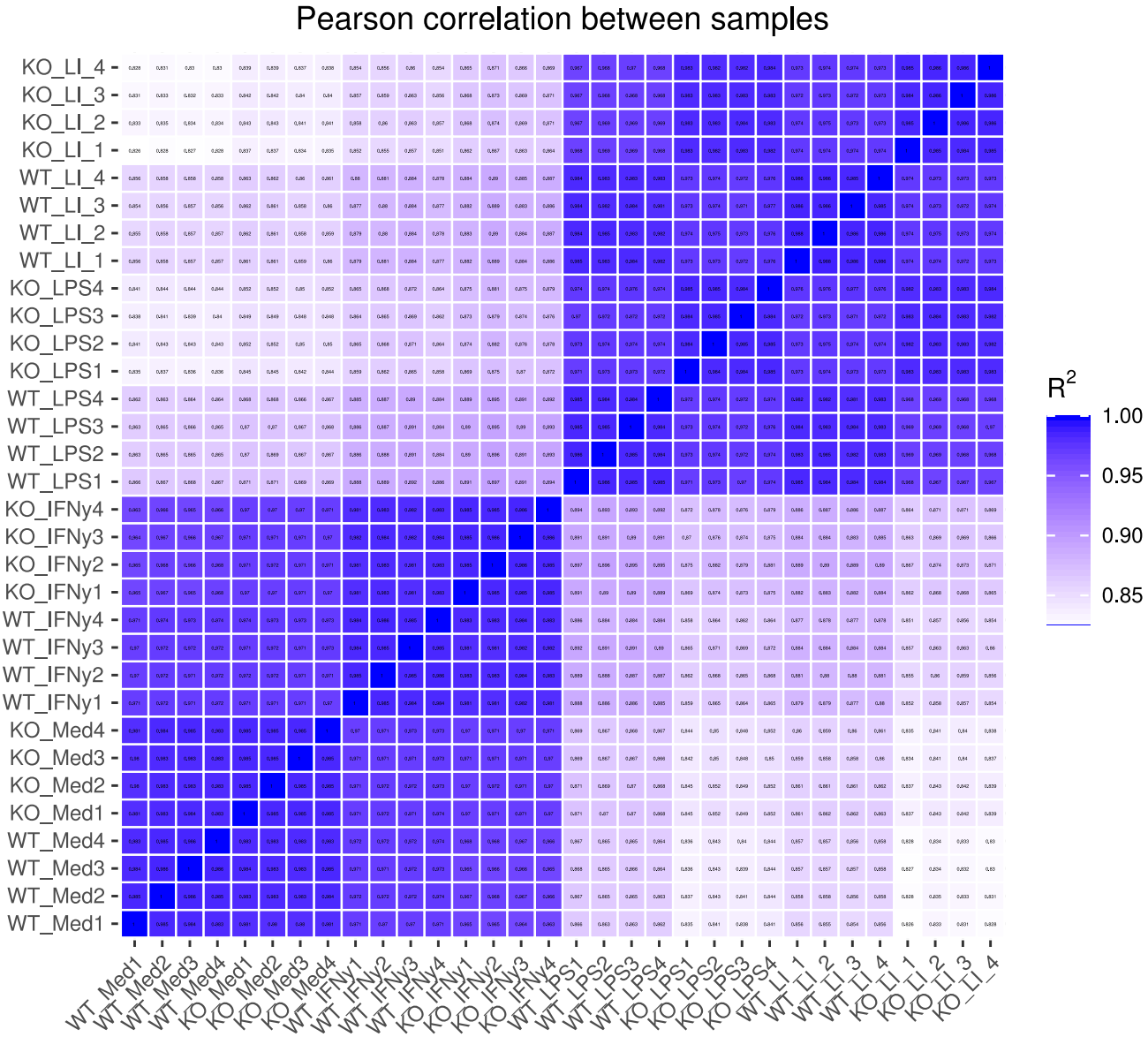

Figure 3.9. Pearson correlation scores between bulk RNA-seq samples. Med = unstimulated, IFNy = IFN-γ stimulated, LPS = LPS-stimulated, LI = LPS+IFN-γ co-stimulated. Figure generated by Novogene.

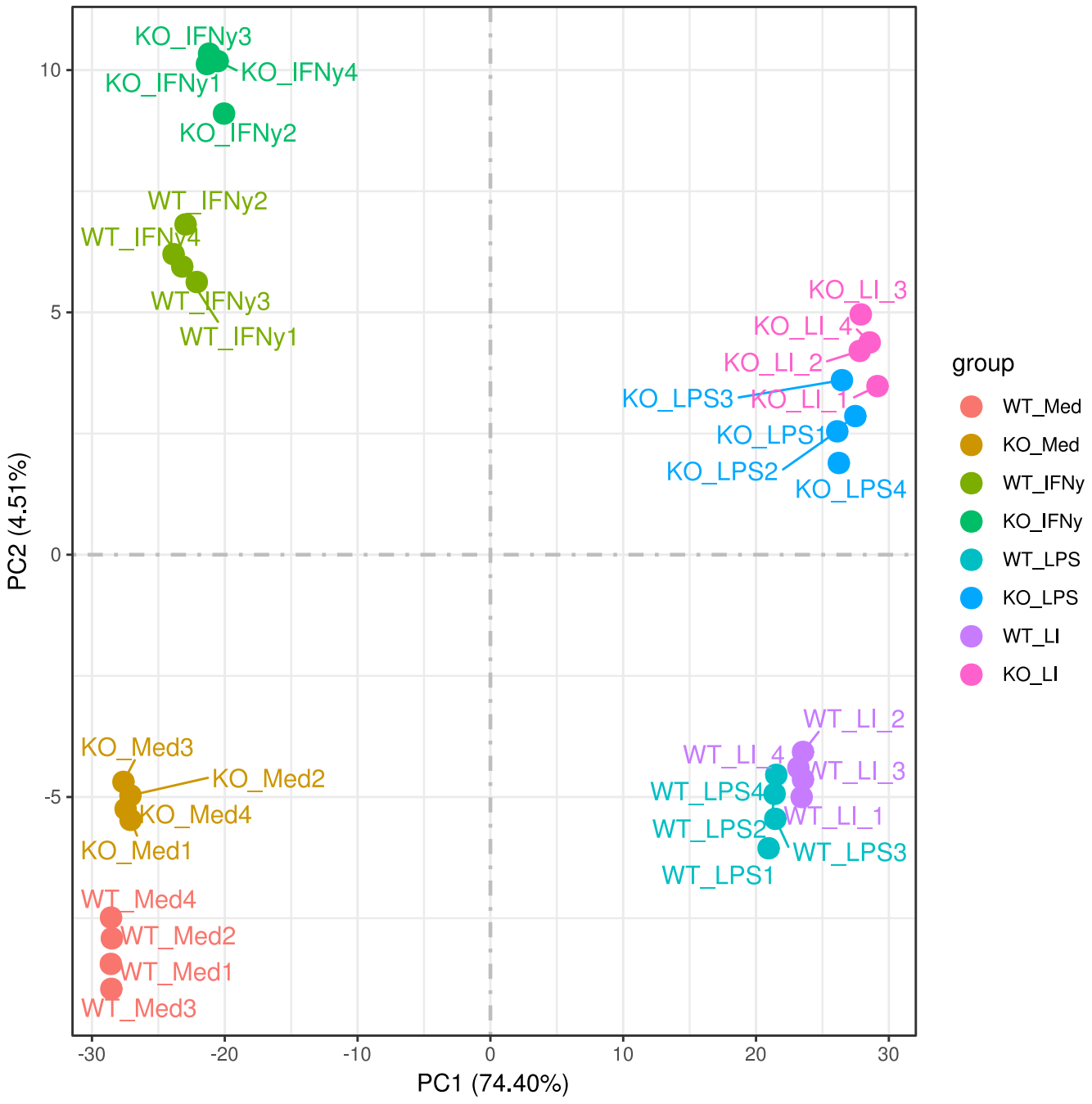

Figure 3.10. Principal Component Analysis of bulk RNA-seq samples. Med = unstimulated, IFNy = IFN-γ stimulated, LPS = LPS-stimulated, LI = LPS+IFN-γ co-stimulated. Figure generated by Novogene.

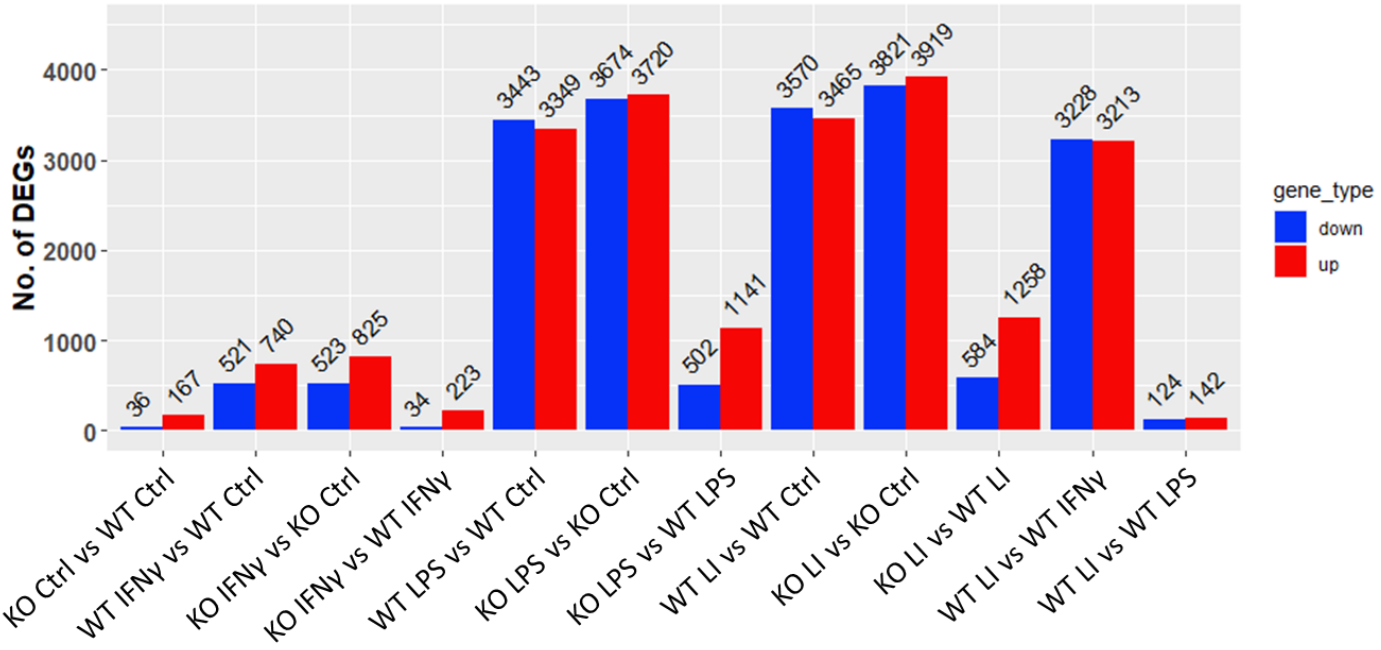

Figure 3.11. Number of DEGs detected between WT & KO BMDMs between stimulation conditions. Differential gene expression was performed, and the numbers of DEGs were identified using the thresholds: q-value <0.05 and log2FC >0.5 or <-0.5. LI = LPS + IFNγ co-stimulation; Ctrl = unstimulated control.

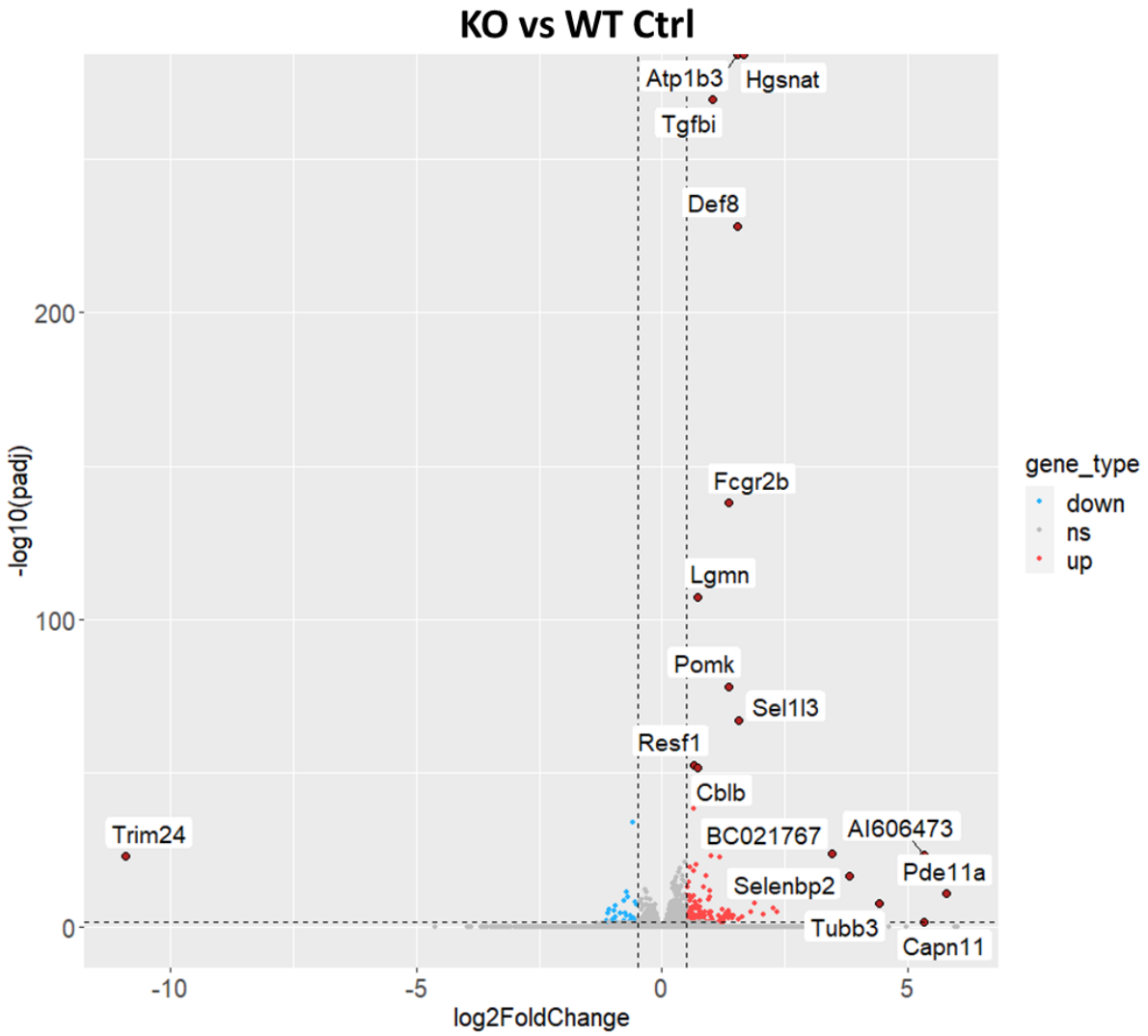

Figure 3.12. Top enriched genes in unstimulated KO BMDMs. Differential gene expression was performed on normalized count data. Significantly differentially expressed genes had thresholds of padj < 0.05 and log2FoldChange (log2FC) ± 0.5. Calculated padj values were converted to -log10(padj) for visualization. ns = not significant (grey); up = upregulated (orange); down = downregulated (blue).

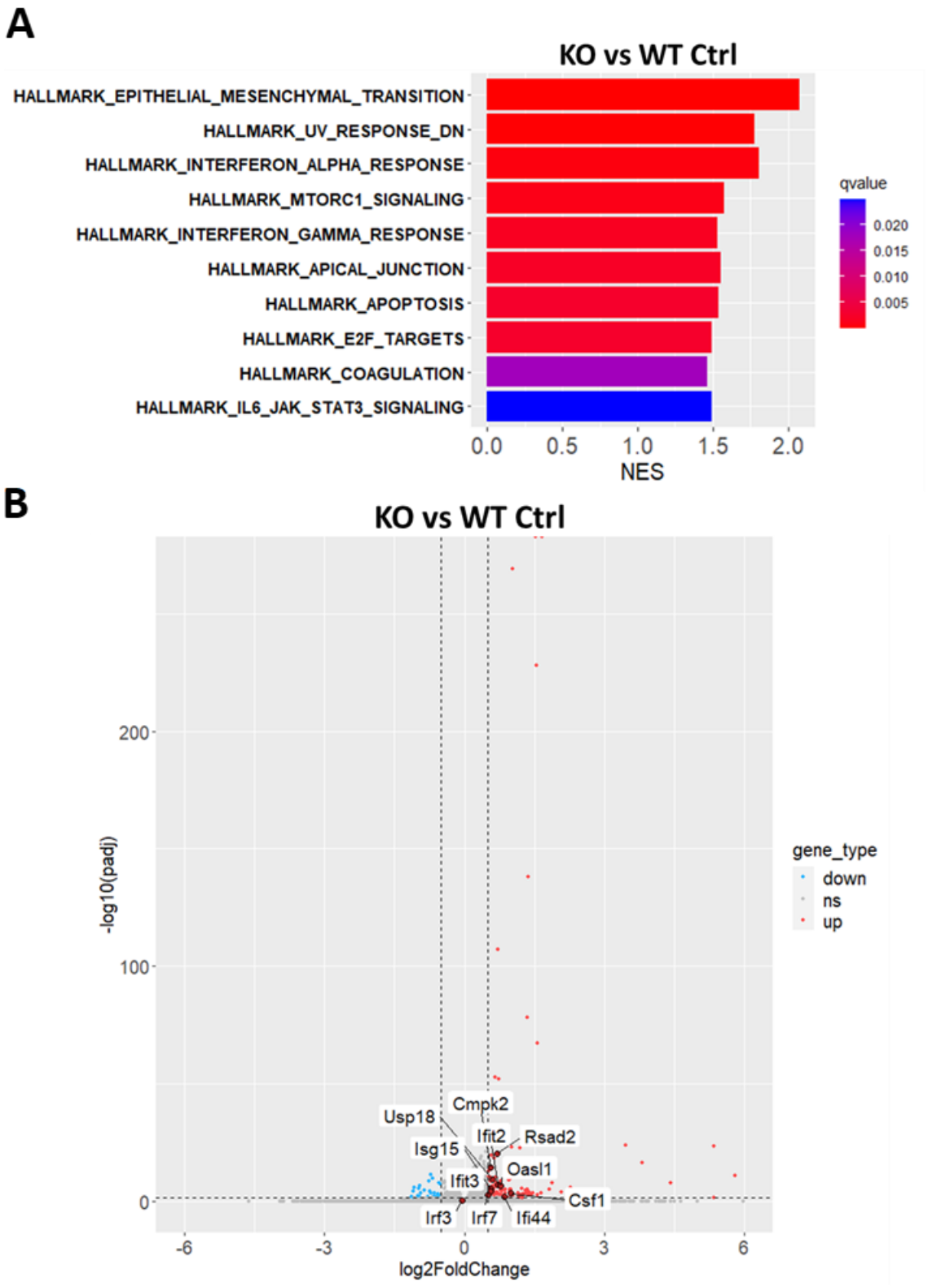

Figure 3.13. Enhanced interferon response transcriptomic profiles of unstimulated KO BMDMs. Differential gene expression was performed on normalized count data between KO and WT unstimulated control samples. Gene Set Enrichment Analysis (GSEA) using HALLMARK gene lists (MSigDB) was performed on all genes ranked by log2 Fold Change (log2FC). Top enriched gene sets are displayed by decreasing q-value **(A).** Genes within the HALLMARK_INTERFERON_ALPHA_RESPONSE gene set upregulated based on thresholds padj <0.05 and log2FC >0.5 **(B)**. NES = Normalized Enrichment Score.

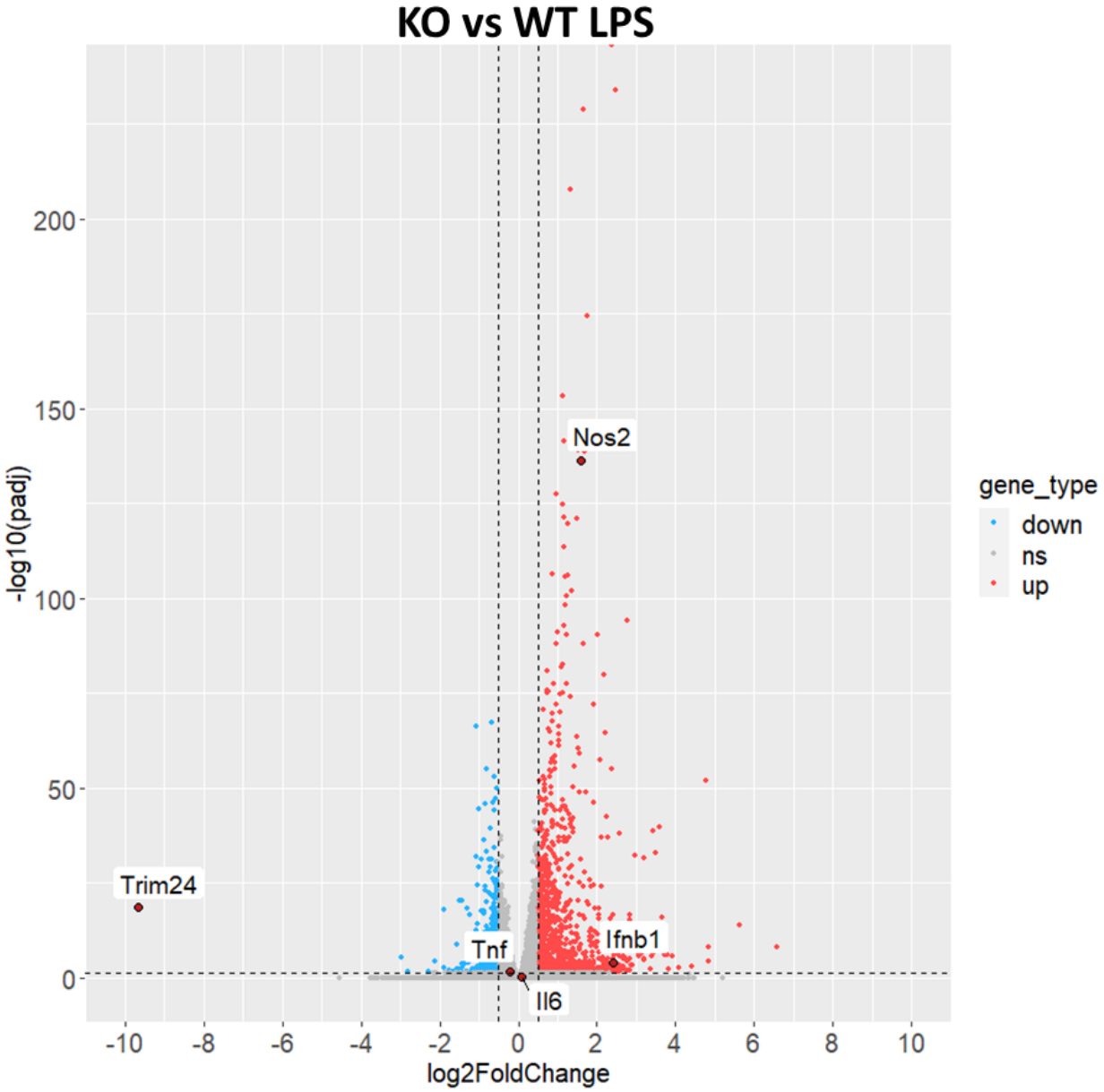

Figure 3.14. Upregulation of *Nos2* and *Ifnb1* but not *Tnf* or *Il6* in LPS-stimulated KO BMDMs. Differential gene expression was performed on normalized count data. Significantly differentially expressed genes had thresholds of padj ± 0.05 and log2FoldChange (log2FC) ± 0.5. Calculated padj values were converted to -log10(padj) for visualization. ns = not significant (grey); up = upregulated (orange); down = downregulated (blue).

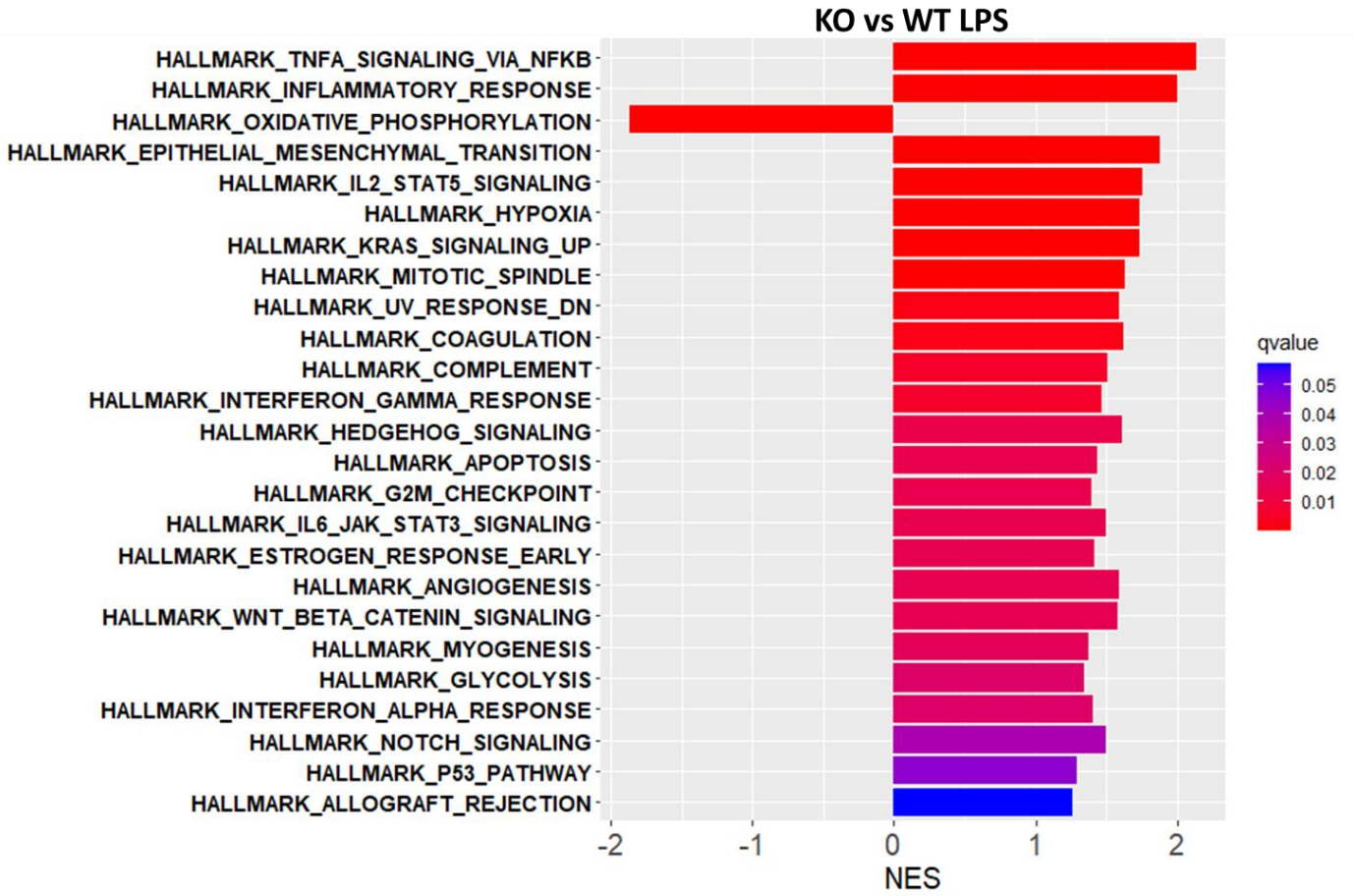

Figure 3.15. Top up- and down-regulated gene sets in LPS-stimulated KO compared to WT BMDMs. Differential gene expression was performed on normalized count data between KO and WT unstimulated control samples. Gene Set Enrichment Analysis (GSEA) using HALLMARK gene lists (MSigDB) was performed on all genes ranked by log2 Fold Change (log2FC). Top enriched gene sets are displayed by decreasing q-value. Positive NES scores indicate gene set enrichment in KO BMDMs. NES = Normalized Enrichment Score.

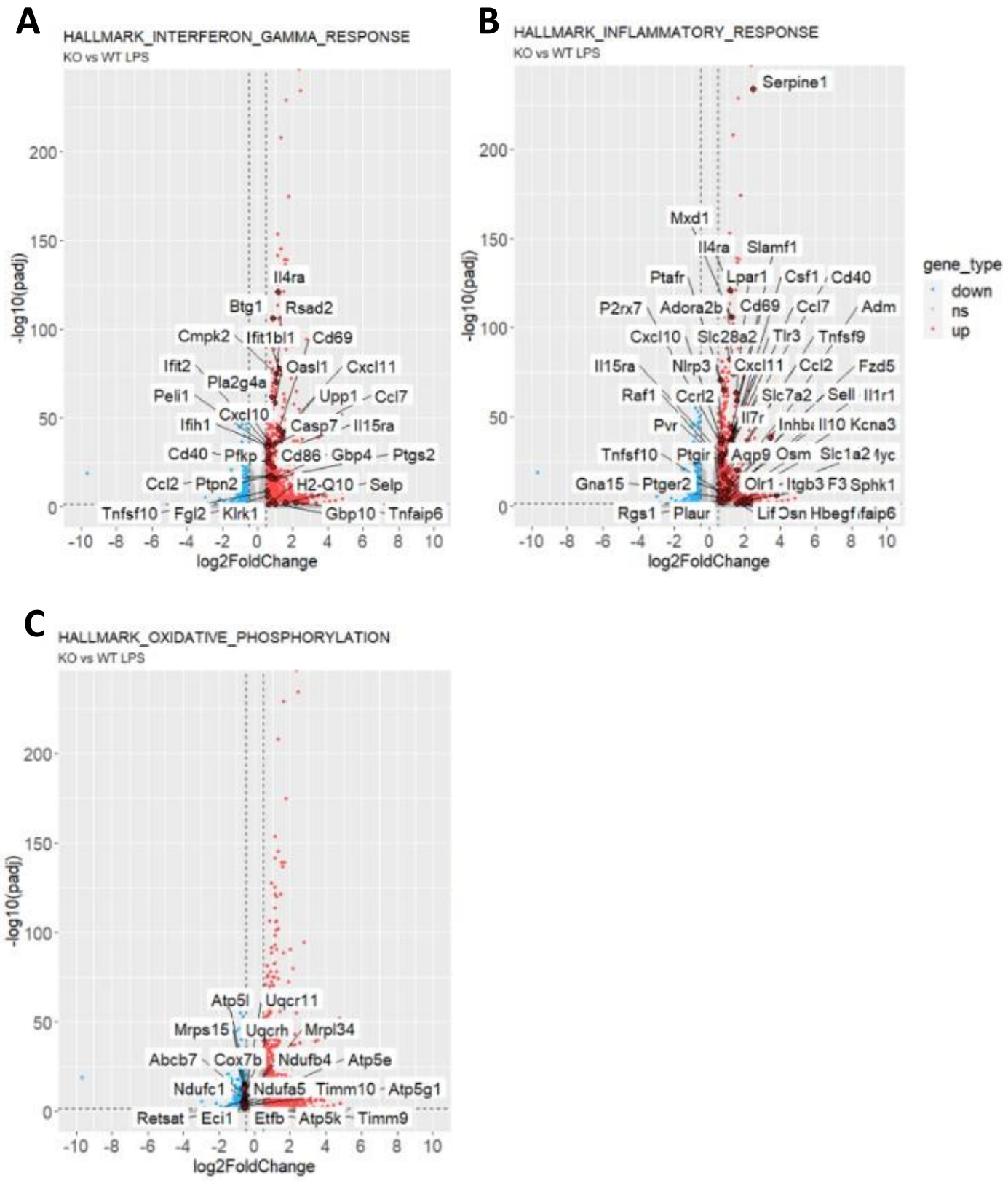

Figure 3.16. Transcriptional changes in LPS-stimulated KO compared to WT BMDMs. Volcano plot were generated to indicate genes within the significant altered gene sets HALLMARK_INTERFERON_GAMMA_RESPONSE **(A),** HALLMARK_INFLAMMATORY_RESPONSE **(B),** and HALLMARK_OXIDATIVE_PHOSPHORYLATION **(C)**. Only genes that met the threshold of padj<0.05 & log2FoldChange <0.5 or >-0.5 are shown.

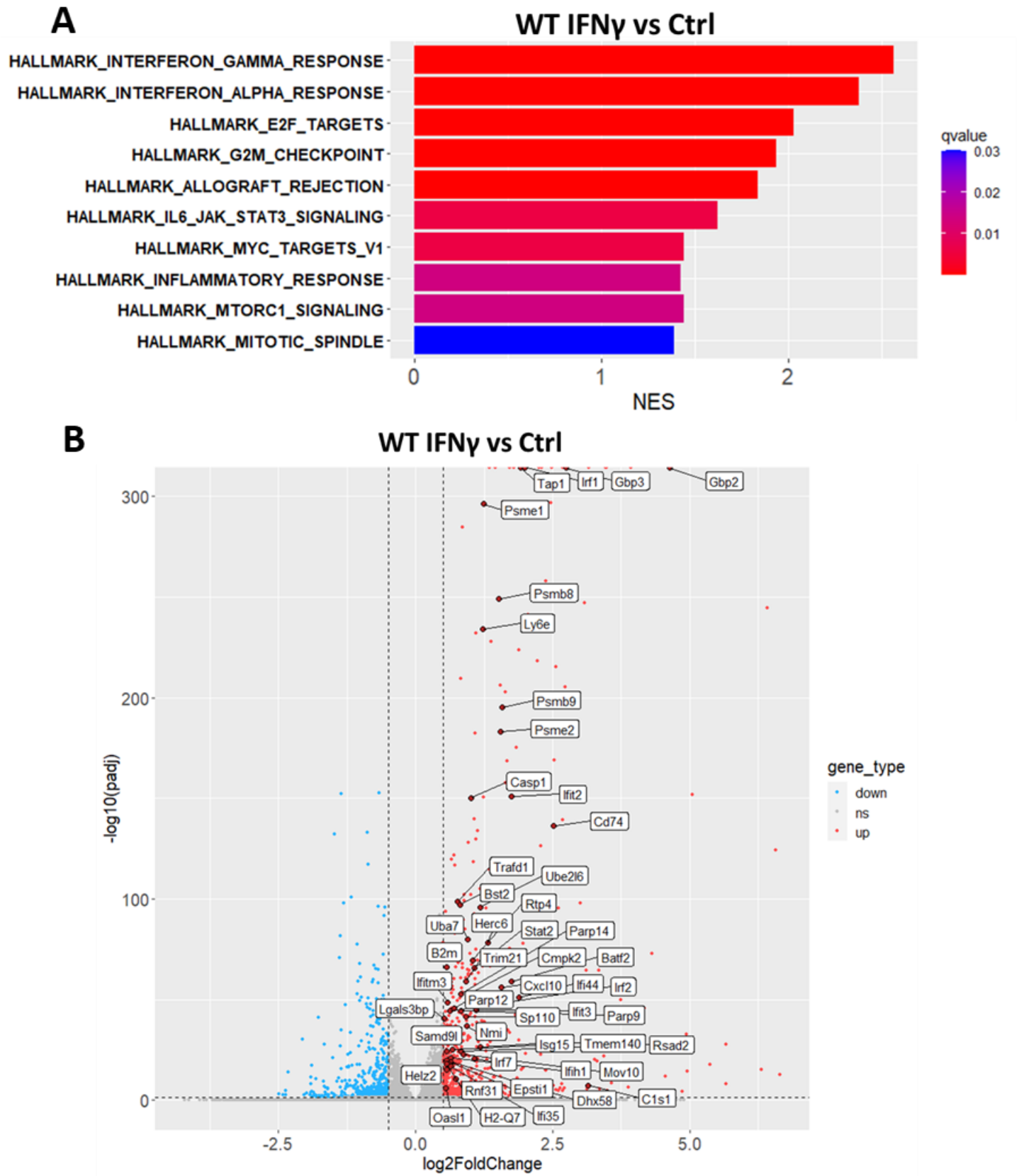

Figure 3.17. IFNγ stimulation causes upregulation of interferon-stimulated genes in WT BMDMs. Differential gene expression was performed on normalized count data between WT IFNγ-stimulated and WT unstimulated control samples. Gene Set Enrichment Analysis (GSEA) using HALLMARK gene lists (MSigDB) was performed on all genes ranked by log2 Fold Change (log2FC). Top 10 enriched gene sets are displayed by decreasing q-value for WT BMDMs **(A)**. Significantly upregulated genes (padj < 0.05, log2FC > 0.5) for interferon response gene sets are plotted in **(B)**. NES = Normalized Enrichment Score.

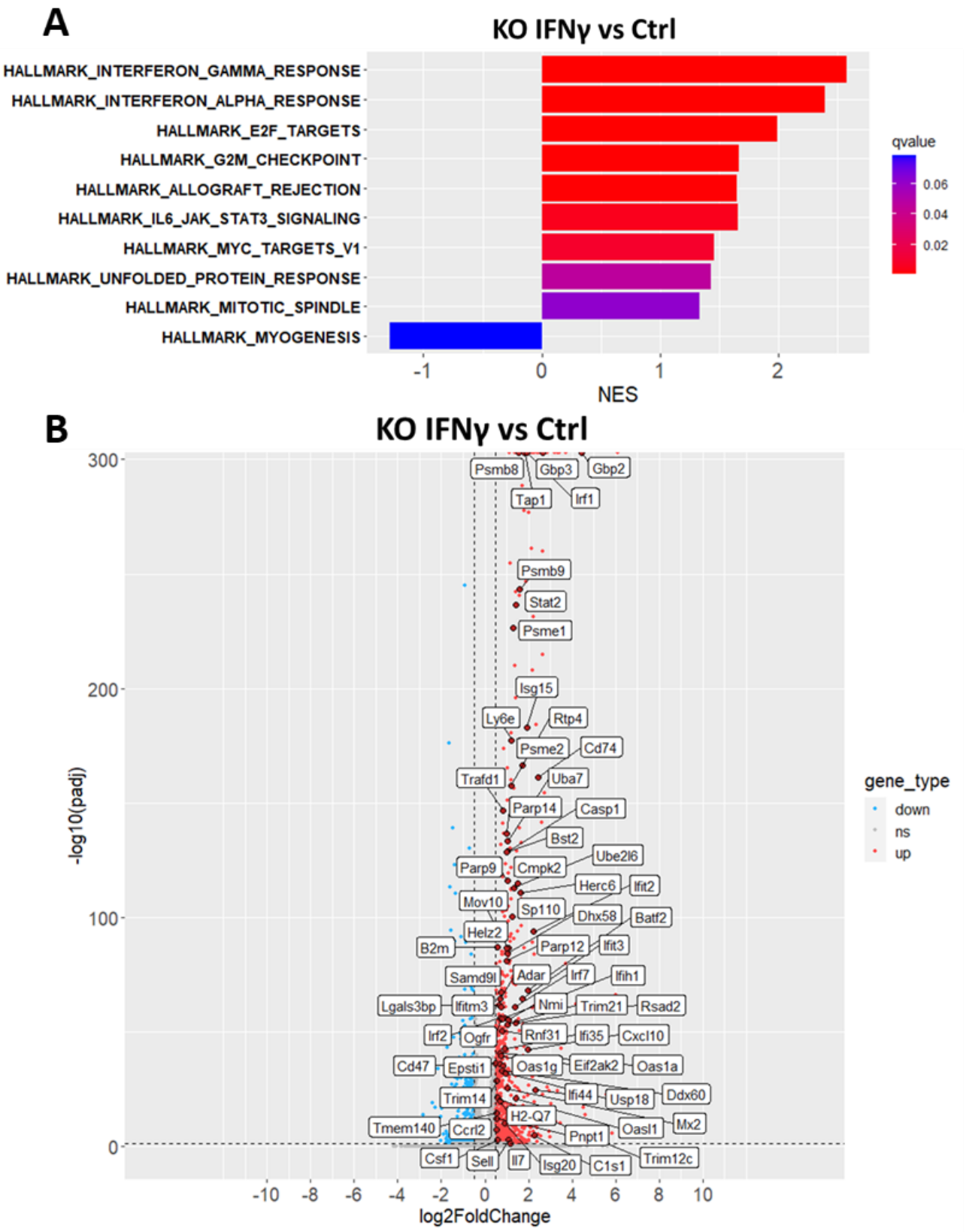

Figure 3.18. IFNγ stimulation causes upregulation of interferon-stimulated genes in KO BMDMs. Differential gene expression was performed on normalized count data between KO IFNγ-stimulated and KO unstimulated control samples. Gene Set Enrichment Analysis (GSEA) using HALLMARK gene lists (MSigDB) was performed on all genes ranked by log2 Fold Change (log2FC). Top 10 enriched gene sets are displayed by decreasing q-value for KO BMDMs **(A)**. Significantly upregulated genes (padj < 0.05, log2FC > 0.5) for interferon response gene sets are plotted in **(B)**. NES = Normalized Enrichment Score.

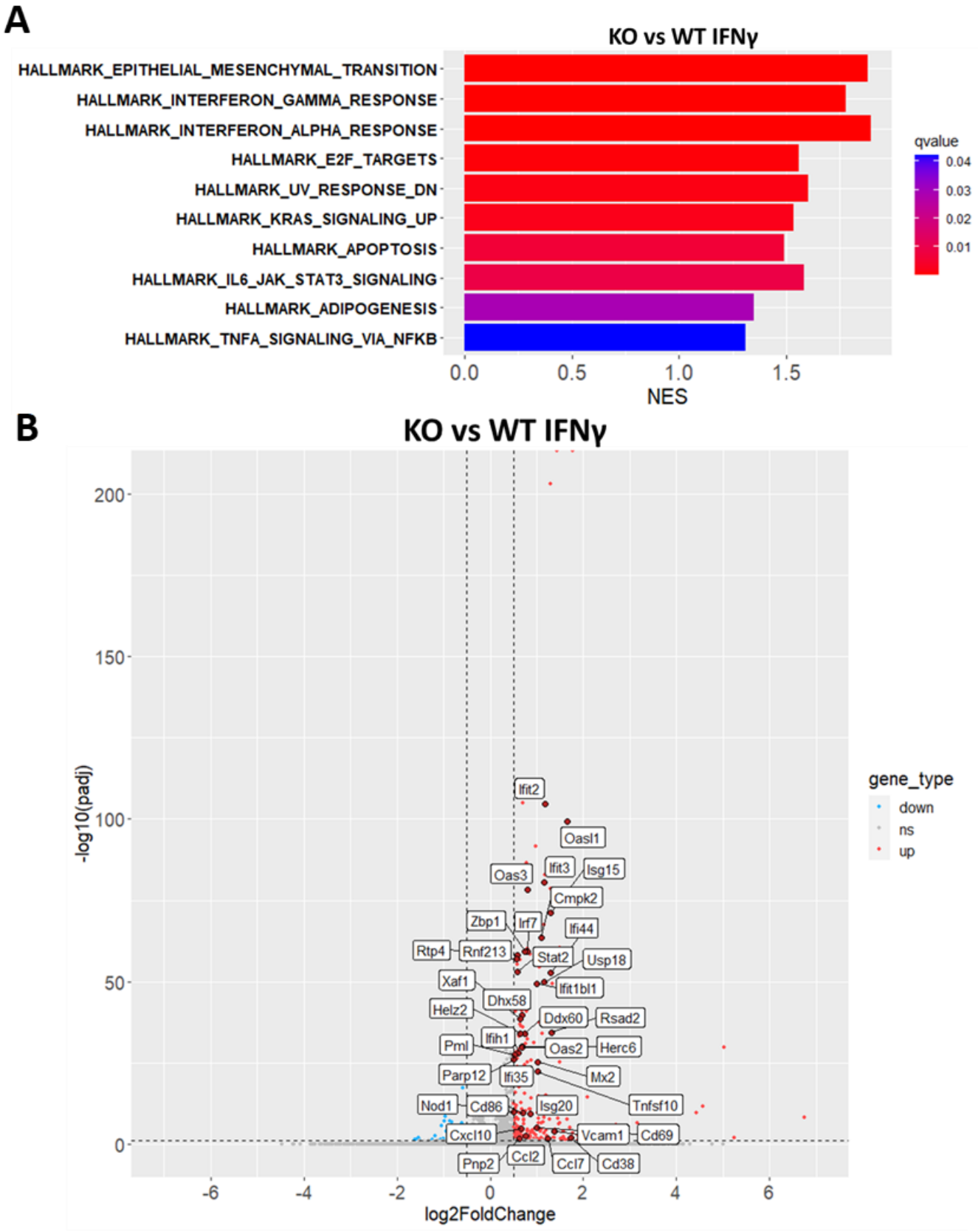

Figure 3.19. KO BMDMs have an enhanced transcriptional response to IFNγ stimulation. Differential gene expression was performed on normalized count data between KO and WT IFNγ-stimulated samples. Gene Set Enrichment Analysis (GSEA) using HALLMARK gene lists (MSigDB) was performed on all genes ranked by log2 Fold Change (log2FC). Top 10 enriched gene sets are displayed by decreasing q-value for KO BMDMs **(A)**. Significantly upregulated genes (padj < 0.05, log2FC > 0.5) for interferon response gene sets are plotted in **(B)**. NES = Normalized Enrichment Score.

Chapter 4. Transcriptional alterations in WT and KO BMDMs infected with *L. donovani* at a single cell level

4.1. Introduction

BMDMs are usually analysed at a bulk population level which obscures any population heterogeneity. Mouse strain-specific differences in BMDMs differentiated with an identical M-CSF differentiation protocol have been studied through bulk RNA sequencing, revealing prominent differences in gene expression across strains (Link et al. 2018). For example, the authors showed BMDMs from SPRET mice had an impaired IFN-I response following TLR4 stimulation compared to C57BL/6 BMDMs (Link et al. 2018). Furthermore, ChIP-seq and ATAC-seq revealed significant effects of mouse strain variation on transcription factor binding to chromatin which were attributable to local strain-specific motif mutations (Link et al. 2018). However, within a BMDM population there is also a striking amount of heterogeneity. BMDM differentiation conditions can influence the phenotype of the BMDM population heavily. Generally, there are two methods for differentiating BMDMs; supplementing cell growth media with recombinant M-CSF (rM-CSF) (Zhang et al. 2008), or L929-fibroblast cell-conditioned media, which contains high concentrations of M-CSF (Heap et al. 2021). Several studies have shown differences between BMDMs differentiated under these two conditions, revealing differences in surface marker expression, cytokine release following TLR stimulation, and metabolic reprogramming (de Brito Monteiro et al. 2020; Heap et al. 2021; Rice et al. 2020). Recently, scRNA-seq was performed on B6 BMDMs differentiated with rM-CSF to explore heterogeneity of this cell population (McCarty et al. 2023). Varying BMDM phenotypes were found within this population, defined by MHC-II genes (*H2-Aa, H2-Ab1*), cell cycle G2m and S phase genes (*Top2a, Mcm6*), complement genes (*C1qa*), monocyte-like BMDM progenitors (*S100a4, S100a6*), and *Fabp4* (McCarty et al. 2023). However, scRNA-seq has not yet been performed on BMDMs differentiated with L929-conditioned media.

Until recently, transcriptomics of *Leishmania*-infected macrophages *in vitro* has only been performed on a bulk population (microarray analysis and bulk RNA-sequencing), where analysed gene expression levels are averaged across a whole population of cells (Chaussabel et al. 2003; Rabhi et al. 2016; Gregory et al. 2008; Chaparro et al. 2022). This therefore removes the ability to identify differences in gene expression between cells with

varying parasite burdens. A recent bulk transcriptomic study revealed distinct early macrophage phenotypic differences following 6 hours *in vitro L. donovani* amastigote and promastigote infection, highlighting transcriptional signatures specific to parasite life cycle stage (Chaparro et al. 2022). Infection with amastigotes resulted in inhibition of immune cell function-related genes and concomitant upregulation of genes related to cell survival (apoptosis inhibition, DNA repair, protein modification) (Chaparro et al. 2022). In contrast, promastigote infection led to more transcriptional changes related to immune signalling (both inflammatory and immunoregulatory), redox homeostasis, and cell survival being upregulated, while inhibition of antigen presentation, chemotaxis, and cell death was detected (Chaparro et al. 2022). Interestingly, *Trim24* was identified as a predicted upstream regulator of differentially expressed genes in this study following infection with *L. donovani* promastigotes but not amastigotes (Chaparro et al. 2022). However, the roles of TRIM24 on macrophage function during *L. donovani* infection were not explored.

In this chapter, we aim to explore transcriptional alterations in KO BMDMs at the steady state and at different levels of *L. donovani* parasite burden *in vitro* at a single cell resolution. We use single cell RNA sequencing to explore the heterogeneity of L929 cell-conditioned BMDMs, identify differentially expressed genes in KO BMDMs compared to WT at the steady state, uncover transcriptional changes in WT BMDMs infected with *L. donovani* amastigotes, and elucidate potential roles for TRIM24 in macrophage function as a consequence of *L. donovani* infection.

4.2. Chapter Aims

- To use scRNA-seq to:
    - Investigate the heterogeneity of WT murine BMDMs differentiated with L929 cell-conditioned media.
    - Assess transcriptional differences between L929-differentiated WT and KO BMDMs at the steady state.
    - Use a highly expressed *L. donovani*-specific gene to detect highly parasitized BMDMs, and assess transcriptional changes associated with parasite burden.
    - To elucidate effects of TRIM24 deletion on the parasitized BMDM transcriptome.

4.3. Results

4.3.1. scRNA-seq Experimental Design

To uncover transcriptional alterations in macrophages during *L. donovani* infection, we performed single-cell RNA-sequencing (scRNAseq) on WT and KO BMDMs infected with *L. donovani* amastigotes (Multiplicity of Infection (MOI) of 5) or not for 12 hours *in vitro* (**Figure 4.1**). After dead cell exclusion, confirmation of infection by Giemsa staining was performed, and numbers of intracellular parasites were counted for WT and KO samples. We detected parasites in >70% of BMDMs in both WT and KO pools (**Figure 4.2**). The majority of BMDMs harboured 1-3 parasites (35%), and the percentage of BMDMs with each progressive infection bin decreased, with only ~1% of BMDMs harbouring 20-30 parasites (**Figure 4.2**). Importantly, no significant difference in the ability of KO BMDMs to phagocytose *L. donovani* amastigotes was seen (**Figure 4.2**). We also checked *L. donovani* uptake in WT and KO BMDMs at 1, 3, 24, and 48 hours (MOI of 10), and saw no difference in the ability of KO BMDMs to phagocytose parasites compared to WT, and no difference in parasite burdens at 24 or 48 hours post-infection (**Figure 4.3**).
Single cell RNA-seq was then performed on naive and infected WT and KO BMDMs from **Figure 4.2**. Sample preparation was performed by Elmarie Myburgh, and scRNAseq library preparation was performed by Sally James.

4.3.2. Genome alignment, quality control (QC) and filtering steps

After sequencing of samples, sequencing data was aligned to the mm10 (mouse) genome (NCBI build GRCm39), with the *L. donovani* gene encoding alpha-tubulin (*LdBPK_130330.1;* TriTrypDB) appended to allow for detection of infected BMDMs. The *L. donovani* alpha-tubulin gene was selected based on previous data indicating it is among the highest expressed and most readily detected genes in *L. donovani*-infected BALB/c mice in liver and spleen samples (Forrester et al. 2022). Of note, alpha-tubulin is a multicopy gene that is present in tandem repeats in the *Leishmania* genome (Curotto de Lafaille & Wirth 1992; Akhoundi et al. 2016).

QC steps are important for accurate representation of biological differences between samples in sequencing data. Low-quality cells, doublets, dead or dying cells are all variables that can confound sequencing data, leading to biologically inaccurate results (Haque et al. 2017). Therefore, the filtering of samples to remove low quality cells is a vital step in the

scRNA-seq data analysis workflow (**Figure 4.1**). We visualised various metrics within each sample to determine the overall quality and set thresholds for filtering steps, as follows.

Firstly, the nFeature_RNA metric is a read of the total number of expressed genes detected per cell (**Figure 4.4A**). We observed that the majority of cells within each sample possessed between ~1000 and ~5000 features (genes), with some cells showing higher nFeature_RNA counts and some cells showing lower nFeature_RNA counts (**Figure 4.4A**). High feature counts are indicative of doublet cells, and low feature counts are indicative of dead or dying cells or empty droplets. Therefore, these were removed by filtering out cells with <1000 or >5000 features (**Figure 4.4A**).

Cells with high mitochondrial transcript percentage are indicative of dead or dying cells (e.g. apoptotic cells). Thus, these are also commonly filtered out during scRNA-seq QC. The majority of our cells showed <10% mitochondrial transcript percentage ("percent.mt"), though presence of cells with higher percent.mt values were also observed (**Figure 4.4B**). Therefore, cells with a percent.mt value of >10% were filtered out (**Figure 4.4B**).

The percentage of ribosomal transcripts ("percent.rb") is also shown in the QC steps, although they are not usually filtered out as ribosomal gene profiles can differ between samples and indicate biological signal. In our data, there is little difference in ribosomal gene profiles between samples (**Figure 4.4C**). However, we still included percent.rb as a variable to regress during the SCTransform step to ensure downstream dimensionality reduction and UMAP clustering was not influenced by ribosomal transcript percentage.

Detection of haemoglobin transcripts was also investigated in each sample as an indicator of erythrocyte contamination. Our data showed <1% haemoglobin gene content in each sample, indicating very little erythrocyte contamination (**Figure 4.4D**).

Finally, we confirmed that reads for *Trim24* were detected in WT but not in KO samples (**Figure 4.5A**), and reads for *LdBPK-130330.1* were detected in infected but not in naive samples (**Figure 4.5B**). Interestingly, we observed a lower proportion of *LdBPK-130330.1*$^{+}$ cells in the KO_Inf sample, though this was not reflected in the parasite burden counts for this experiment (**Figure 4.2**) or in previous *in vitro* infection data (**Figure 4.3**).

4.3.3. Dimensionality reduction and UMAP projection

After sample integration, linear dimensionality reduction by principal component analysis (PCA) (**Figure 4.6**) was performed and plotted using PC1 and PC2. Little difference was observed between samples on the PCA plot (**Figure 4.6**). Next, non-linear dimensionality reduction was performed and a UMAP projection was generated (**Figure 4.7A**). Unbiased cell clustering revealed 13 cell clusters were identified, most of which clustered close together (**Figure 4.7A**). Marker genes for clusters 10 and 12 indicated that these were contaminating cells that resembled neutrophils (*Ly6g, Cxcr2*) and T cells (*Cd3d, Ms4a4b, Ltb*), respectively (**Figure 4.7B**). These were removed, and cells were re-clustered.

4.3.4. UMAP marker interrogation reveals heterogeneity in BMDM transcriptomes

The Final UMAP projection and unbiased clustering of 15,683 cells (WT_Naive 3,601; WT_Inf 4,033; KO_Naive 5,693; KO_Inf 2,356) revealed 13 cell clusters (**Figure 4.8A**). Expression of the pan-leukocyte marker *Ptprc* (CD45) was found in all clusters, and expression of the macrophage markers *Adgre1* (F4/80), *Itgam* (CD11b), and *Lyz2* was also found across all clusters (**Figure 4.8B**).

We then identified the most highly expressed genes in each cluster to further characterise the heterogeneity of the BMDM population. Mac.1 contains macrophages that appear to be skewed towards M2 macrophages, with the top genes (*Gclc, Gclm*) recorded as being upregulated in M2 macrophages (Tsai et al. 2021; He et al. 2021). Interestingly, *Mt2* and *Bnip3* (other highly expressed genes in Mac.1), are reported to be more involved in macrophage M1 polarisation (Kanekiyo et al. 2002; Romano et al. 2018).

Mac.2 highly expresses *Hspa5* and *Hsp90b1*, encoding stress proteins known to exhibit inflammatory effects (Gao et al. 2022; Ratna et al. 2021). Heat shock proteins are also among the top expressed genes in Mac.3 (*Hspa1a, Hspa1b* and *Hsp90aa1*) (**Figure 4.9**). We also saw high expression of genes related to the classical complement pathway (*C1qa, C1qb, C1qc*) in Mac.3 (**Figure 4.9**), shared with Mac.6, Mac.7, and Mac.8.

Mac.4 expresses a high level of *Eif4e*, which plays a regulatory role in macrophage activation through modulation of the NF-kB pathway (Bao et al. 2017) (**Figure 4.9**). *Eif4e* is also a downstream effector of mTOR pathway signalling (Hay & Sonenberg 2004). *Samd8* was also a top expressed gene of Mac.4 (**Figure 4.9**), and has previously been found to be

upregulated in type II-activated (M2b) BALB/c BMDMs (primed with IFN-γ and stimulated with LPS and immune complexes) (Edwards et al. 2006).

Mac.5 is a distinct activated macrophage cluster that shows similarity to Mac.1 but has high expression of many interferon-stimulated genes (*Ifit1, Ifit2, Ifit3, Rsad2, Cmpk2*), known to be induced by type 1 interferons (Fensterl & Sen 2015; Zhou et al. 2021) (**Figure 4.9**). Mac.1 and Mac.5 also expressed the highest levels of *Nos2* (**Figure 4.9**).

Mac.6 was characterised by the expression of *Ywhah* (involved in PI3K-Akt pathway (Zhang et al. 2017)) and *Msr1* (encoding macrophage scavenger receptor/CD204; highly expressed on tumour associated M2-like macrophages (Sun & Xu 2018)).

Mac.7 possessed high expression of *Cxcr4* (also found to a lower degree in Mac.3 and Mac.8) and *Junb* (found in all other clusters but at lower levels) (**Figure 4.9**). *Cebpb* was also expressed at higher levels in this cluster. *Cxcr4* is important protein for HPSC and myeloid cell retention and development in the bone marrow (Singh et al. 2020), and while *Cebpb* is dispensable for steady state myelopoiesis (McPeak et al. 2017), a role for *Cebpb* stress-induced myelopoiesis has previously been described (Hirai et al. 2015). Mac.7 also expresses *Pim1*, a gene involved in driving haematopoiesis as evidenced by the enhanced ability for leukocyte reconstitution following lethal irradiation in FVB/J mice (An et al. 2013). Therefore, this cluster could represent a more immature form of macrophage.

Mac.8 represented proliferating macrophages due to high expression of cell cycle genes including *Stmn1, Mki67, Top2a, Ube2c,* and *Tubb5* (**Figure 4.9**). This is a similar case with cluster Mac.11, however Mac.11 expresses some cytokine and chemokine genes such as *Tnf, Cxcl2* and *Ccl4* (**Figure 4.9**).

Mac.9 was defined by expression of MHC-II genes (*H2-Aa, H2-Ab1, H2-Eb1*) and the MHC-II chaperone gene *Cd74* (Farr et al. 2020) (**Figure 4.9**), and was interestingly the only cluster to express MHC-II-related genes (**Figure 4.9**).
Mac.10 expresses high levels of *Mmp12*, a known pro-inflammatory elastase identified in human synovial fluid macrophages during rheumatoid arthritis (Soler Palacios et al. 2015) and in human alveolar macrophages (Shapiro et al. 1993).

Mac.12 and Mac.13 are the clusters with the fewest number of cells (120 and 56, respectively). While we did not detect genes restricted to the Mac.12 cluster, the cells in Mac.12 express higher levels of *Anxa1* compared to other clusters (Annexin-1; known to

negatively regulate expression of TNF and IL-6 in LPS-stimulated B6 peritoneal macrophages through suppression of the MAPK signalling cascade (Yang et al. 2009)). Mac.13 was defined by its expression of *Ogt* (known to inhibit macrophage inflammatory responses through mTORC1 signalling suppression (Yang et al. 2020)) (**Figure 4.9**). Taken together, this highlights the heterogeneity in the phenotypes of BMDMs differentiated by L929 cell-conditioned media.

4.3.5. Proportions of cell clusters are largely unaffected by *L. donovani* infection or by *Trim24* deletion

Next, we assessed differences in proportions of the UMAP cell clusters between samples, to indicate alterations due to deletion of *Trim24* or due to *L. donovani* infection (**Figure 4.10A**). We saw few differences between the proportions of macrophage cell clusters in WT and KO naive samples. Mac.1 was reduced in KO Naive (19.8% vs 24.7% in WT Naive). The proportion of Mac.2 was slightly higher in KO Naive (19.6% vs 17.6% in WT Naive), similarly in Mac.3 (17.2% vs 15.2%) (**Figure 4.10B**).
We saw minor alterations in proportions of cell clusters in WT_Inf BMDMs compared to WT_Naive BMDMs, mainly in the reduction in proportions of Mac.2 (15.3% Inf vs 17.6% naive) and Mac.3 (12.9% Inf vs 15.2% naive), and the increase in Mac.4 (11.8% vs 8.4%) (**Figure 4.10B**). The other cluster proportions remained largely unchanged in infected WT BMDMs (**Figure 4.10B**). Similar alterations were seen in KO_Inf compared to KO_Naive BMDMs, though in addition cluster Mac.7 showed a reduction in proportion in KO_Inf BMDMs (2.8% Inf vs 5.6% naive) (**Figure 4.10B**).

Comparing KO Inf with WT Inf, an increase in proportion of Mac.3 (21.3% vs 12.9%) was observed (**Figure 4.10B**). Reductions were seen in KO_Inf BMDMs compared to WT_Inf in Mac.1 (17.5% vs 24.7%) and Mac.7 (2.8% vs 5.9%) (**Figure 4.10B**). There was little difference between KO_Inf and WT_Inf proportions in the remaining clusters.

To statistically analyse differences between distributions of cell proportions per clusters, we used a re-randomisation permutation test. We tested against the null hypothesis that the difference in cell proportions for each cluster between conditions is a consequence of sampling a number of random cells for sequencing for each condition. This test pools the cells from two groups together, then randomly sorts them back into the two conditions while maintaining original sample sizes. Proportional differences are then recalculated between conditions for each cluster, and then compared back to the original observed proportions. This simulation is repeated ~10,000 times, and the reported FDR value is the number of

simulations where the simulated proportional difference was as or more extreme than observed divided by the total number of simulations. We found a significant decrease (FDR <0.05, log2FD <-1) in Mac.13 in KO Naive vs WT Naive samples and in WT Inf vs WT Naive samples (**Figure 4.10C**). This was not seen in KO Inf vs KO Naive or KO Inf vs WT Inf (**Figure 4.10C**). However, Mac.13 represents the cluster with the fewest number of cells (7-25 cells), so this significance may not be biologically relevant. Mac.7 was significantly decreased in KO Inf vs KO Naive and in KO Inf vs WT Inf (**Figure 4.10C**). Taken together, these results indicated that *Trim24* and *L. donovani* infection plays minor roles in phenotypic proportions of BMDMs differentiated *in vitro*.

4.3.6. Transcriptional alterations of *Trim24* deficiency in naive BMDMs

Next, we explored differences between KO and WT BMDMs in each cluster to elucidate potential functions of TRIM24 at the steady state. We performed differential gene expression analysis between KO and WT naive samples on a per cluster level. We identified most differentially expressed genes (DEGs) in Mac.1 and Mac.2 (1071 and 986, respectively) (**Figure 4.11A**). 90% of DEGs in Mac.1 were downregulated in KO compared to WT BMDMs (967 DEGs), with the remaining 10% (104 DEGs) upregulated. Similarly, in Mac.2 878 of the DEGs were downregulated and 108 DEGs were upregulated in KO compared to WT BMDMs. The remaining clusters showed progressively lower numbers of DEGs. Only three DEGs were detected in Mac.11, and none in Mac.12 or Mac.13 (**Figure 4.11A**). Clusters were labelled according to decreasing cell number, so the progressively lower DEGs numbers are most likely due to this decrease in cell number.

We then performed Gene Set Enrichment Analysis (GSEA) on all DEGs (FDR<0.05, log2FC >0 or <0, ranked by log2FC) for each cluster using the ClusterProfiler R package and mSigDb HALLMARK gene lists. Significantly differentially expressed gene sets (FDR<0.05) were found only in clusters Mac.1, Mac.2, and Mac.3 (**Figure 4.11B**). Enriched gene sets in Mac.1 and Mac.2 were similar, enriched for genes involved in TNF signalling (*Atf3, Nfkbia, Cxcl2*), IL2 signalling via STAT5, p53 pathway (*Jun, Mdm2, Plk2*), and complement (*C1qa, C1qb, Lgmn*) (**Figure 4.11B&D**). Interestingly, Mac.3 but not Mac.1 or Mac.2 was enriched for type I and II interferon response genes (*Isg15, Ifitm3, Bst2*), consistent with our previous bulk RNAseq data (**Figure 4.11B; Chapter 3**). Downregulated gene sets indicated a subset of naive KO BMDMs to be less glycolytically active than WT BMDMs, with glycolysis a top downregulated gene set in Mac.1 and Mac.2 (*Agl, Mif, Taldo1*) (**Figure 4.11C&E**). Gene sets relating to mTOR signalling (*Xbp1, Trib3, Actr2*), protein secretion (*Adam10, Vamp3, Bnip3*),

and unfolded protein response (*Calr, Slc30a5, Sec31a*) were also significantly decreased in KO BMDMs (**Figure 4.11C&E**).

Taken together, these results confirm our findings from our bulk RNAseq data suggesting a subset of KO BMDMs possess a higher level of interferon signalling genes at the steady state. Furthermore, *Trim24* appears to be a positive regulator of metabolism and mTOR signalling in BMDMs, and may play a role in protein turnover and secretion.

4.3.7. Transcriptional alterations in WT BMDMs induced by *L. donovani* infection

Next, we sought to investigate the effects of *L. donovani* infection on WT BMDMs. Differential gene expression analysis (FDR<0.05, log2FC<0 or >0) revealed the majority of DEGs across all clusters to be downregulated in infected WT BMDMs (WT Inf) compared to naïve control (**Figure 4.12A**). There were 2277 downregulated genes in Mac.1 and 1723 downregulated genes in Mac.2, whereas the numbers of upregulated genes were 285 and 224, respectively in WT Inf compared to naïve BMDMs (**Figure 4.12A**). In Mac.4, Mac.5 and Mac.7 we detected 495, 319, and 119 downregulated genes, respectively (**Figure 4.12A**). Few DEGs were detected in the remaining clusters, likely due to lower cell numbers within these clusters.

GSEA analysis of all DEGs ranked by log2FC revealed significantly up-regulated gene sets in all clusters except Mac.8, Mac.10, Mac.11, Mac.12, and Mac.13 (**Figure 4.12B**). In contrast, downregulated gene sets were only detected in Mac.1, Mac.2, and Mac.9, despite the larger proportion of DEGs being downregulated in most clusters (**Figure 4.12C**). Inflammatory gene sets were upregulated in most clusters with significant gene sets. TNF signalling via NF-kB was upregulated in all clusters with the exception of Mac.7 (**Figure 4.12B & 4.13**). IL6/JAK/STAT3 signalling gene set was upregulated in Mac.1, Mac.2 and Mac.4 (**Figure 4.12B**). Hypoxia-related genes (*Ddit3, Ldha, Hmox1, Dusp1, Atf3, Vegfa*) were upregulated in all clusters shown (**Figure 4.12D**). Interestingly, interferon signalling (**Figure 4.12F**), and mTORC1 signalling (**Figure 4.12E**) were downregulated in WT infected BMDMs compared to naïve in Mac.1 and Mac.2 (**Figure 4.12C**). In terms of cytokine production, we did not see any significant up- or down-regulation of *Il10, Il12a, Nos2, Il1b,* or *Il6* (**Supp. Table 2**). Interestingly, we saw that *Trim24* was downregulated in the Mac.1 WT Infected BMDM cluster compared to WT naive, but not in any other clusters (**Figure 4.14**).

Taken together, these results indicate *L. donovani* infection leads to a hypoxic response accompanied by impairment of mTOR and interferon signalling in WT BMDMs.

4.3.8. Heavily parasitized BMDMs possess an inflammatory phenotype

Next, we asked whether different levels of parasite burden induce further transcriptional changes in BMDMs. We took the *L. donovani*-infected (WT_Inf and KO_Inf) samples, and subset the most highly infected BMDMs by taking cells with positive expression for parasite alpha tubulin, *LdBPK-130330.1* (Ld+). BMDMs with low parasite burden and uninfected bystander BMDMs were then represented as Ld-. We re-integrated these Ld+ BMDMs with Ld- BMDMs from the same sample, and performed dimensionality reduction, differential gene expression, and GSEA (**Figure 4.15A**). Our UMAP representation presented nine cell clusters (**Figure 4.15B**).

Firstly, while we saw Ld+ BMDMs in every cluster (except 8) (**Figure 4.15C**), 74% of all 821 Ld+ cells were found in clusters 0 (45.55%), 3 (8.65%), 4 (13.52%), and 7 (6.33%) (**Table 4.1**). Of these percentages, between 67-92% of Ld+ cells were WT and the remaining 8-33% were KO (**Table 4.2**).

We determined the top five markers expressed by each cluster (by log2FC) (**Figure 4.16**). Clusters with more Ld+ BMDMs expressed genes related to an inflammatory phenotype (*Nos2, Stat1, Ccr1, Ccr5, Il1b*) (**Figure 4.17**). Interestingly, *Arg1* expression was also restricted to these clusters, indicating these cells are undergoing elevated levels of arginine metabolism. In contrast, clusters 1, 2, 5, 6, and 8 expressed more immunoregulatory genes (*Mrc1, Cd163, Il10, C1qa, Cd83, Lpl*) (**Figure 4.17**). Mac.9 represented cells with high expression of *Tnf, Ccl4, Cxcl2, Ptgs2* (**Figure 4.16**), but there were few parasitized BMDMs in this cluster.

Top genes expressed in clusters 0, 3, and 4 also included *Hmox1* (encoding heme oxygenase-1; involved in heme metabolism (Bories et al. 2020)), *Ldha* (encoding lactate dehydrogenase), *Slc2a1* (encoding the GLUT1 glucose transporter), and *Aldoa* (encoding Aldolase A), all of which are essential for glycolysis (Freemerman et al. 2019; Qin et al. 2019; Talaiezadeh et al. 2015). While expression of oxidative phosphorylation (OxPhos)-related genes was detected in all clusters, the immunoregulatory clusters expressed them at higher levels (*Ndufa13, Atp5j2, Cox6b1, Cox5b*) (**Figure 4.18**). Interestingly, clusters 1 and 2 are characterised by their expression of *Hspa1a* and *Hspa1b*, which encode HSP70 stress proteins and inhibit OxPhos (Wang et al. 2012).

Taken together, these results indicate the most highly infected BMDMs have an inflammatory phenotype and skew their metabolism towards glycolysis, while OxPhos largely drives naive/bystander/low parasite burden BMDMs.

Differential gene expression analysis (Log2FC >0 or <0, padj<0.05) revealed 145 upregulated and 157 downregulated genes in WT Ld+ compared to WT Ld- BMDMs, with *LdBPK-130330.1* and *Lars2* (an amino-acyl tRNA synthetase that is involved in mitochondrial protein synthesis (’t Hart et al. 2005)) as the top upregulated genes (**Figure 4.19A**). GSEA of all significantly expressed genes revealed significantly up- and down-regulated gene sets in Ld+ BMDMs. Among the top five significant gene sets in WT Ld+ BMDMs, three were upregulated (TNF signalling via NF-kB (**Figure 4.19B&C**), Reactive Oxygen Species (ROS) pathway (**Figure 4.20B&D**), and Inflammatory response (**Figure 4.20B&E**)), and two were downregulated (complement pathway (**Figure 4.20B&F**) and unfolded protein response (**Figure 4.20B&G**)). Of the inflammatory genes, *Ccr1* and *Ccr5* were upregulated in WT Ld+ BMDMs, consistent with previous literature (Sato et al. 1999; Dasgupta et al. 2003; Bhattacharyya et al. 2008). Interestingly, we also saw upregulation of *Rela* (encoding an NF-kB subunit), *Il7r* (important for tissue macrophage development (Leung et al. 2019), and *Cd14* (an activation marker for macrophages that functions in TLR4 signalling (Wright et al. 1990; Zanoni et al. 2011), in WT Ld+ BMDMs compared to Ld- (**Figure 4.20E**). In addition, 71 genes encoding large and small ribosomal subunit proteins were downregulated in WT Ld+ BMDMs compared to Ld- (**Figure 4.20A&B**), which formed a tight interaction network when submitted to STRINGdb (**Figure 4.20C**).

Finally, we calculated Pearson correlation coefficients of WT Ld+ BMDMs to identify genes highly correlated and anti-correlated with *L. donovani* infection (*LdBPK-130330.1* expression). 17 of the top 20 genes anti-correlating with *LdBPK-130330.1* expression were ribosomal subunit genes (*Rps* and *Rpl* genes) (**Figure 4.21A**). The other three genes were *Eef1g, Eef2* (both involved in protein translation), and *Gnai2* (**Figure 4.21A**).
Lars2 was the most highly correlated gene with *LdBPK-130330.1* (r = 0.52). Among the other most highly correlated genes, there was a mixture of inflammatory (*Klf6, Cxcr4, Cd14, B2m*) and immunoregulatory genes (*Vegfa, Cebpb, Ms4a4a, Id2, Abca1, Trib1*) (**Figure 4.21B**). The hypoxia-induced gene *Hildpa* also positively correlated with *LdBPK-130330.1* (**Figure 4.21B**).

Taken together, these results indicate transcriptional changes in *L. donovani*-infected WT BMDMs is dependent on the level of parasite burden. Higher parasite burden led to inhibition of cytoplasmic translation, and a transition from OxPhos towards glycolysis was observed.

However, experimental confirmation of this through measurement of glycolytic rate vs OxPhos rate through e.g. use of an Agilent Seahorse platform would be required.

4.3.9. TRIM24 alters metabolic and interferon-related transcriptional profile in *L. donovani*-infected BMDMs

Finally, we sought to extrapolate the effects of *Trim24* deletion on *L. donovani*-infected macrophages. In order to gain a more general overview of how *Trim24* deletion affects the BMDM transcriptomic profile after *L. donovani* infection, we performed pseudobulk GSEA analysis of KO infected (KOI) vs WT infected (WTI) BMDMs, using averaged expression data from each whole sample within our scRNA-seq dataset. OxPhos was the top enriched gene set in KOI BMDMs, and the only gene set to be up-regulated (**Figure 4.22**). The other top nine significantly deregulated gene sets were involved in metabolism (Hypoxia, Heme metabolism, glycolysis, mTORC1 signalling), and growth and cell cycle progression (Mitotic spindle, Hedgehog signalling, Androgen response) (**Figure 4.22 & Supp. Table 2**). Interestingly, interferon response gene sets did not show up as top deregulated gene sets in KOI BMDMs, despite upregulation of several ISGs **(Figure 4.22 & Supp. Table 3**). Many of these gene sets are important for cancer progression, and our data has now extended this phenotype to primary murine macrophages.

Differential gene expression analysis (FDR<0.05, log2FC<0 or >0) of individual clusters revealed fewer DEGs compared to WT Infected vs WT Naive. Again, we saw most DEGs in Mac.1 (294 down- and 199 up-regulated), followed by Mac.2 (208 down- and 180 up-regulated), Mac.3 (242 down- and 158 up-regulated), and Mac.4 (116 down- and 142 up-regulated) (**Figure 4.23A**). In the remaining clusters, we saw 369 up- and down-regulated genes. We found no DEGs in Mac.12 or Mac.13, and only two up-regulated genes in Mac.11 (*Rps10, Sh3bgrl3*) (**Figure 4.23A**).

GSEA analysis of DEGs of each cluster revealed up-regulated gene sets including OxPhos in Mac.1, Mac.3 and Mac.8, and type I and II interferon response gene sets in Mac.3 (**Figure 4.23B**). Mac.3 most prominently showed upregulation of OxPhos genes in KO BMDMs (including *Cox8a, Cox5b, Cox6b1, Atp5d, Atph, Atp5e, Ndufb7*), though this can also clearly be seen in Mac.6, Mac.7, and Mac.8 (**Figure 4.23D**). The other clusters showed a sparser upregulation of OxPhos genes, however critical OxPhos genes such as *Cox8a* and *Atp5d* were consistently upregulated in all clusters (**Figure 4.23D**). Though the gene sets for type I and II interferon signalling were specifically upregulated in Mac.3, genes within these gene sets were also upregulated in other clusters (e.g. *Isg15, Ifitm3, Bst2*) (**Figure 4.23E**).

Down-regulated gene sets were found in Mac.1, Mac.3 and Mac.5. Interestingly, the interferon gamma response gene set was down-regulated specifically in Mac.5, with the downregulation of *Herc6, Stat1, Nampt, Rnf213, Samd9l,* and *Cmpk2* (**Figure 4.23C&E**).

Taken together, this data reveals a potential role for TRIM24 as a negative regulator of OxPhos during *L. donovani* infection, which may contribute to a permissive phenotype to facilitate parasite survival. Furthermore, TRIM24 deletion appears to potentiate the interferon response in BMDMs during *L. donovani* infection. However, a dampening of interferon signalling was seen in a specific subset of BMDMs, indicating that TRIM24 may be acting through several mechanisms.

4.4. Discussion

In this chapter, we have i) highlighted the transcriptional heterogeneity of BMDMs differentiated with L929 cell-conditioned media ii) explored the effects of *in vitro L. donovani* amastigote infection on BMDM gene expression at a single cell level, and iii) outlined a potential role for TRIM24 as a regulator of glucose metabolism reprogramming during *L. donovani* infection in BMDMs.

Our transcriptional analysis revealed a high degree of heterogeneity in L929-differentiated BMDMs. We observed some similar BMDM phenotypes to those described by McCarty et al. in their analysis of male B6 BMDMs, namely proliferating cells defined by expression of G2M and S phase genes, and cells with high MHC-II expression (McCarty et al. 2023). However, our other cell clusters appeared to be phenotypically different to those in McCarty et al.'s study. While they describe BMDM clusters defined by *Fabp4*, *S100a4*, and *S100a6* expression, we did not see these markers as cluster-defining in our dataset (McCarty et al. 2023). Our dataset proved to be more heterogeneous, with clusters defined by hypoxia gene signatures, cytokine and chemokine gene signatures, and interferon stimulated gene signatures indicative of the presence of IFNs in the system. This could be attributed to our L929 cell-conditioned media differentiation strategy. An early study showed that L929-differentiated BMDMs have a heightened IFN-stimulated signature in response to TLR signalling, which was abrogated through replacement of L929 cell-conditioned media with non-conditioned media (Fleit & Rabinovitch 1981). This was confirmed recently by Heap et al., who showed through gene ontology analysis of proteomic data from L929-differentiated vs rM-CSF-differentiated BMDMs that response to interferons was enhanced in L929-differentiated BMDMs (Heap et al. 2021).

There is conflicting evidence for the differences in phenotypes of rM-CSF- and L929-differentiated BMDMs. One study showed L929-differentiated BMDMs had impaired TNF and IL-12 release, despite retaining transcriptional response for these genes post-LPS stimulation compared with rM-CSF-differentiated BMDMs (de Brito Monteiro et al. 2020). L929-differentiated BMDMs were also more metabolically active than rM-CSF-differentiated BMDMs (de Brito Monteiro et al. 2020). Conversely, a separate study displayed an opposing phenotype, showing increased release of TNF, IL6 and IFNβ from L929-differentiated C57BL/6 BMDMs after 6 hrs LPS stimulation (Heap et al. 2021). This proteomic study detected other immunomodulatory factors present in L929 cell-conditioned media that could affect BMDM phenotype, including MIF, CCL7, CCL2, CXCL1, CCL9, TGFβ, and GREM1

(Heap et al. 2021), all of which have either inflammatory or immunoregulatory effects on BMDM differentiation and activation (Heap et al. 2021; Xie et al. 2021; Yaddanapudi et al. 2013; Mthunzi et al. 2022; Sierra-Filardi et al. 2014; Orecchioni et al. 2019; Wang et al. 2014). Furthermore, small amounts of GM-CSF have been identified in L929 media (Englen et al. 1995). GM-CSF is known to activate human BMDMs towards a more inflammatory phenotype through upregulation of TNF, IL-1β, IL-12p40, and suppression of IL-10 (Jaguin et al. 2013). Mouse macrophages differentiated with GM-CSF exhibit the opposite effect, showing lower levels of some cytokines (CXCL10, IFN-β, CCL2, CCL5) compared to M-CSF-differentiated BMDMs, and higher mRNA abundance and release of others (TNF, IL-12p40, CCL17, IL-23) (Fleetwood et al. 2009; Fleetwood et al. 2007).

It is clear that differentiation by rM-CSF or L929 cell conditioned media result in separately heterogeneous BMDM populations, and this should be considered when selecting BMDM differentiation protocols. It would be interesting to perform an integrated analysis of this rM-CSF-differentiated BMDM dataset with our L929-differentiated BMDM dataset presented here to explore transcriptional differences at a single cell level further (McCarty et al. 2023).

Secondly, we have identified effects of *Trim24* deletion on the basal transcriptional profiles of B6 BMDMs. Our data suggest that TRIM24 is involved in cellular glucose metabolism in BMDMs; we saw a general decrease in genes relating to glycolysis in naive KO BMDMs compared to WT, as well as mTOR signalling. mTOR is a serine threonine kinase with important roles in regulating cell growth and proliferation (through activation of S6 kinase 1 (S6K1) and eukaryotic translation initiation factor 4E (eIF4E) (Fingar et al. 2004)). It also inhibits autophagy through reversible phosphorylation and inhibition of death-associated protein 1 (DAP1) (Koren et al. 2010), and can inhibit apoptosis through Akt-mediated phosphorylation of its substrates (e.g. BAD, BIM, Caspase 3, and Foxo1/3) (Jacinto et al. 2006; Zhang et al. 2012). mTOR forms two different complexes; mTORC1 (consisting of mTOR, Raptor, and mLST8 as core proteins) and mTORC2 (consisting of mTOR, Rictor, and mLST8) (Saxton & Sabatini 2017). mTORC1 has frequently been associated with promoting glycolysis in cancer cells by increasing the glucose transporter GLUT1 expression (Buller et al. 2008). Raptor-deficient (and therefore mTORC1-deficient) alveolar macrophages have impaired glucose uptake compared to WT and reduced the number of alveolar macrophages in adult B6 mice (Deng et al. 2017). In a recent study, polysome-profiling revealed that infection with *L. donovani* led to early activation of PI3K/AKT/mTOR signalling by identification of elevated ribosomal protein kinase 1 (S6K1; downstream of mTOR signalling) phosphorylation (Chaparro et al. 2020). Inhibition of mTOR signalling through rapamycin treatment increased survival of *L. donovani* parasites in macrophages.

Conversely, blocking of Eukaryotic Initiation Factor 4a (EIF4a) by silvestrol treatment led to impaired parasite survival as measured by Kinetoplastid Membrane Protein 11 (*Kmp11*) gene mRNA abundance (Chaparro et al. 2020).

TRIM24 has previously been linked with mTOR signalling. Mayer et al. showed rapamycin treatment to decrease transcriptional activity of RNA Polymerase I (Pol 1) through post-translational inactivation of TRIM24 (Mayer et al. 2004). Addition of exogenous recombinant TRIM24 reversed this effect in rapamycin-treated NIH3T3 cells (Mayer et al. 2004). More recently, Shah et al. showed a positive correlation between TRIM24 expression in mammary tumours and PI3K/AKT/mTOR signalling genes (Shah et al. 2021). Furthermore, glycolysis was also significantly enhanced in TRIM24-overexpressing tumours (Shah et al. 2021). Thus, our data is consistent with this literature and extends the role of TRIM24 as a positive regulator of mTOR signalling and glycolysis to macrophages.

Thirdly, we have explored the transcriptional profiling of *Leishmania*-infected macrophages *in vitro*. While this has been investigated at a bulk level as discussed previously (Chaparro et al. 2022; Chaparro et al. 2020), here we performed this analysis at the single cell level for the first time. Using this approach, we were able to identify BMDMs expressing the *Leishmania* gene *LdBPK-130330.1* and elucidate transcriptional alterations associated with highly infected cells. We found that BMDMs with high parasite burdens (Ld+) expressed both inflammatory and immunoregulatory factors (e.g. *Nos2* and *Arg1*) but were more skewed towards an inflammatory phenotype. Inflammatory macrophages have been shown to be more proficient in phagocytosis in bacterial infections (*E. coli* (Huang et al. 2017), *Porphyromonas gingivalis* (Lam et al. 2016)). Of note, Lee et al. recently investigated uptake of two strains of *L. major* in M1 (IFNγ+LPS)- vs M2 (IL-4+IL-10)-polarised BMDMs (Lee et al. 2018). They saw a higher percentage of infected cells in M1-polarised BMDMs compared to M2, and clearance of parasites occurred within three days. Additionally, they found that CD206 expression on M2 BMDMs correlated with the uptake of a non-healing *L. major* strain compared to a healing strain. This effect was abolished in *Mrc1*$^{-/-}$ BMDMs (Lee et al. 2018). Furthermore, Ribeiro et al. observed higher phagocytic capacity (and higher nitric oxide expression) in human monocytes exposed to *L. infantum* compared to *L. braziliensis* (Ribeiro et al. 2020). This indicates that visceralising species of *Leishmania* induce more inflammatory macrophage phenotypes with a higher phagocytic capacity compared to *Leishmania* species causing cutaneous leishmaniasis.

WT Ld+ BMDMs were more present in clusters expressing glycolysis-related genes, indicating a metabolic shift away from OxPhos and towards glycolysis in infected cells. It is

known that metabolic changes in host cells are linked to parasite survival in *Leishmania* infection. Activation and stress responses in macrophages cause dramatic metabolic shifts towards glycolysis to meet energy demands *in vitro* and *in vivo* (Newsholme et al. 1986; Michl et al. 1976; Hamilton et al. 1986). Further, LPS/IFNγ-stimulated macrophages possess a much higher glucose consumption rate than IL-4-stimulated macrophages, and has increased mRNA abundance of *Hif1a* (a transcription factor critical for oxygen sensing and the mediation of hypoxic responses (Ratcliffe et al. 1998)) and *Slc2a1* (GLUT1 gene; glucose transporter (Pragallapati & Manyam 2019)) (Rodríguez-Prados et al. 2010). Glycolysis only generates 2 ATP for each glucose molecule as opposed to 36 ATP generated during OxPhos. However, glycolysis can be induced much faster than OxPhos, and so in cells with high energy demand such as activated macrophages, aerobic glycolysis becomes the preferable option (Pfeiffer et al. 2001).

Analysis of B6 peritoneal macrophages infected with *L. major* promastigotes revealed enrichment of glycolysis pathway transcripts at 4 hours post-infection (hpi), which was retained at 24 hpi but not at 48 or 72 hpi (Dillon et al. 2015). Glycolysis is also enhanced in human neutrophils 6 hpi with *L. donovani* (Ohms et al. 2021). Treatment of human neutrophils *in vitro* with a glycolysis inhibitor, 2-deoxyglucose (2-DG) reduced ROS production, and treatment of B6 mice with 2-DG before infection increased liver and spleen parasite burden at 7 days post-infection (Ohms et al. 2021).

L. infantum modulates metabolic pathways in macrophages in a time sensitive manner. Extracellular acidification rate (ECAR) and glycolytic capacity was increased 6 hpi while OxPhos indicators, oxygen consumption rate (OCR), and spare respiratory capacity (SRC) were decreased (Moreira et al. 2015). By 18 hpi, glucose metabolism had shifted back towards an OxPhos-dominated phenotype, with glycolysis decreasing (Moreira et al. 2015). Therefore, initial stages of infection induces glycolysis in line with an initial inflammatory response, and parasite modulation of metabolic pathways restores OxPhos activity to facilitate immunoregulatory macrophage mechanisms. Interestingly, translation of this to *L. donovani* infection seems to be unclear. On one hand, *L. donovani* infection led to induction of OxPhos, but did not appear to affect glycolysis 6 hpi in human monocyte-derived macrophages (Ty et al. 2019). Conversely, Chaparro et al. saw downregulation of genes related to mitochondrial respiratory chain (*Cox18, Ndufa8*), indicating impairment of OxPhos in 6 hpi B6 BMDMs (Chaparro et al. 2020).

A recent immunometabolic profiling study of *L. amazonensis*-infected B6 BMDMs (LIMs) showed a complex transcriptional signature characterised by expression of both inflammatory and regulatory genes, and a shift toward OxPhos that resembled M2 macrophages (Zhang et al. 2022). Interestingly, while they saw increases in glycolytic gene expression in LIMs compared to naive, they did not see an increase in ECAR. This was

postulated to be a result of the parasites blocking inflammatory pathways in the BMDM (which are primed for an M1-type response) in favour of parasite permissive conditions (Zhang et al. 2022).
Our data presented here are in line with that of Chaparro et al., and suggest phenotypical differences between human and mouse macrophages.
We saw a general dampening of interferon response genes (ISGs) in BMDMs infected with *L. donovani* amastigotes for 12 hours, including *Irf7, Ifitm3,* and *Stat2*. This is consistent with data from Chaparro et al., who showed a downregulation of *Irf7, Ifitm3*, and other ISGs in BMDMs infected with *L. donovani* amastigotes, but not with promastigotes, in which they saw more upregulation of immune pathway-related gene sets (Chaparro et al. 2022).

We also looked for genes that positively or negatively correlated with parasite burden (*LdBPK-130330.1* expression). While few genes were highly correlated with parasite burden ($r > 0.2$), we did see a mixture of inflammatory and immunoregulatory genes that positively correlated with *LdBPK-130330.1* expression including *Lars2, B2m, Cebpb, Vegfa,* and *Klf6*.
Lars2 has been implicated in metabolic disorders such as lactic acidosis, hydrops, and sideroblastic anaemia (Riley et al. 2016) and Perrault syndrome (Carminho-Rodrigues et al. 2020). Recently, knockdown of LARS2 led to decreased cell proliferation, increased apoptosis, and accumulation of ROS in human granulosa cells of premature ovarian insufficiency patients (Feng et al. 2022).
Klf6 expression contributes to an inflammatory macrophage phenotype as evidenced by murine *Klf6* knockout BMDMs having lower mRNA abundances of *Tnf, Il1a,* and *Il1b,* in response to LPS and higher mRNA abundances of *Arg1, Mrc1, Retnla,* and *Chi3l3* in response to IL-4 (Date et al. 2014).
Vegfa has previously been shown to be induced following *L major* infection, in a mechanism that is dependent on HIF1α expression in macrophages (Weinkopff et al. 2019). HIF1α is upregulated in response to hypoxic conditions, which prevail during *Leishmania* infections (Bowlin et al. 2021; Hammami et al. 2017). Interestingly, while we saw increases in *Vegfa* in infected WT BMDMs, we did not see any difference in *Hif1a* expression. Of note, we did see a significant decrease in expression of *Hif1an* (encoding an inhibitor of HIF1α). Therefore, *Vegfa* gene regulation could be mediated indirectly by limited inhibition of HIF1α.
Cebpb is a key transcription factor in supporting Ly6C- monocyte pools through upregulation of *Csf1r* (Tamura et al. 2017). *Cebpb* has also been implicated in the polarisation of J774, RAW 264.7 and bone marrow-derived macrophages into an M2 regulatory phenotype through direct association of CREB and subsequent induction of *Msr1, Il10, Il13ra,* and *Arg1* (Ruffell et al. 2009; Lamkin et al. 2019). Therefore, expression of both inflammatory and immunoregulatory genes positively correlate with parasite burden.

Lastly, our data suggests that TRIM24 positively regulates BMDM glucose metabolism by glycolysis during *in vitro L. donovani* amastigote infection. We saw significant enrichment of OxPhos-related genes in *L. donovani* infected KO BMDMs, coupled with a reduction of glycolysis-related genes, and a reduction in mTOR signalling. TRIM24 as a regulator of glucose metabolism has been explored previously in the context of cancer. In a study investigating roles of TRIM24 in cellular metabolism in breast cancer, the authors used lentivirus to overexpress TRIM24 in immortalised human mammary epithelial cells (iHMECs) (Pathiraja et al. 2015). Gene expression profiling using a panel of 420 breast cancer-associated genes led to identification of upregulated genes within gene sets relating to the Citric Acid (TCA) cycle, MAPK signalling, mTOR signalling, and glycolysis (Pathiraja et al. 2015). Surprisingly, measurement of ECAR and OCR revealed TRIM24 to be a positive regulator of both glycolysis and OxPhos (Pathiraja et al. 2015). This has also been seen in human TRIM24 knockout neuroblastoma SH-SY5Y cells, which had impaired OCR and ECAR compared to WT controls (Duan et al. 2021). This is partially consistent with our data, with glycolysis genes being downregulated in KO BMDMs. However, OxPhos genes were enriched in infected KO BMDMs in our data, not consistent with Duan et al. (Duan et al. 2021). More work is therefore required to discern the exact molecular mechanisms for TRIM24's control of glucose metabolism in macrophages during *L. donovani* infection.

A limitation of this analysis strategy is that the detection of parasitized BMDMs in our transcriptomics data (**Figure 4.5B**) did not match up with the distribution of BMDM parasite burden from the Giemsa staining (**Figure 4.2**). This is most likely due to lack of sensitivity during the sequencing process to sufficiently detect parasite genes, though intracellular parasites being less transcriptionally active could also be a possibility. The sensitivity of this method could be improved by performing "dual scRNA-seq", in which the sequencing data is aligned to the whole mouse and whole *L. donovani* genomes simultaneously. This would allow for the combining of all *L. donovani* genes into a single pseudogene to be used to identify parasitized BMDMs and would be most likely to detect BMDMs with lower parasite burdens than what we show here. This approach was performed by Karagiannis et al., which enabled the identification of parasitized HSCs in the bone marrow of BALB/c mice 60 days post-infection (Karagiannis et al. 2022). This approach may improve the discrepancy between our *in vitro* parasite count data vs our *in silico* detection of parasitized BMDMs.

In summary, we postulate that *Trim24* deletion impairs the ability for BMDMs to drive glucose metabolism through glycolysis and shifts the metabolic balance more towards OxPhos, through inhibition of mTOR signalling. Downregulation of *Trim24* in infected

BMDMs therefore inhibits glycolytic mechanisms and accompanying inflammatory effector mechanisms to facilitate parasite survival. Establishment of a dominant OxPhos phenotype in infected BMDMs occurs between 6 and 18 hpi, therefore the time point we used (12 hpi) may be too early to observe an effect on parasite burden in KO BMDMs. *Trim24* deletion may therefore have more of an effect in chronic *L. donovani* infection. In the next chapters, we dive deeper into the immunological effects of *Trim24* deletion *in vivo* through characterization of *Trim24* KO mice at the steady state, and during *L. donovani* infection.

4.5. Figures

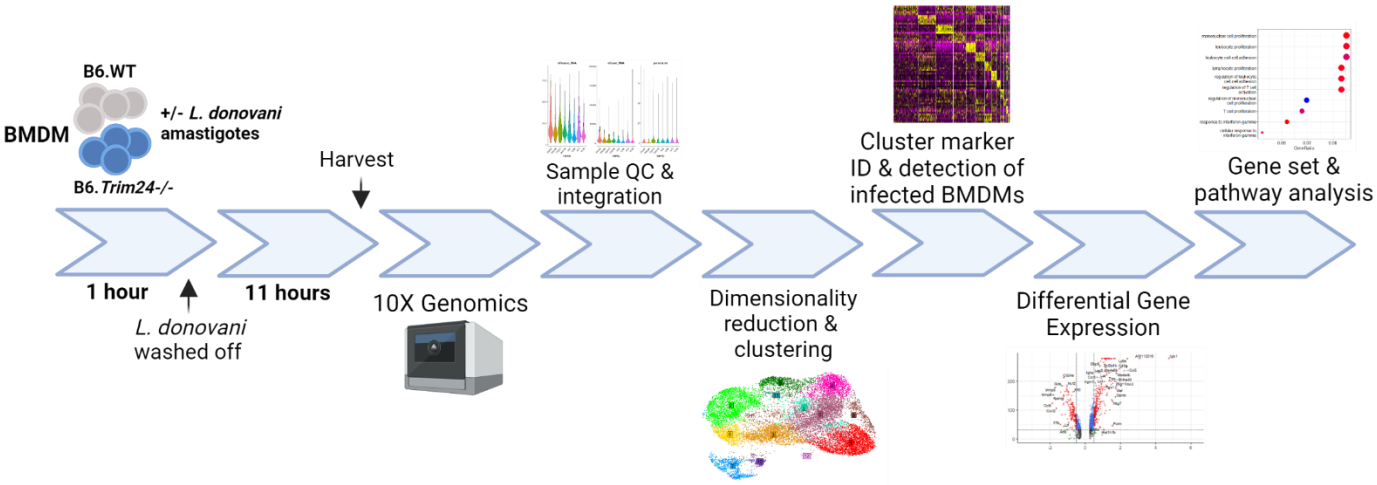

Figure 4.1. Experimental plan for single-cell RNA-sequencing of naïve and *L. donovani*-infected WT and KO BMDMs. BMDMs were freshly differentiated from B6.WT and B6.KO mice as described previously. BMDMs were infected with freshly isolated *L. donovani* amastigotes (MOI 5:1) for 1 hour. After 1 hour, parasites were washed off, and cells were incubated for a further 11 hours for a total of 12 hours infection. After 12 hours, cells were harvested and single-cell RNA-seq was performed using 10X Genomics system. Data underwent QC and filtering steps, and was integrated and analysed using the Seurat R pipeline.

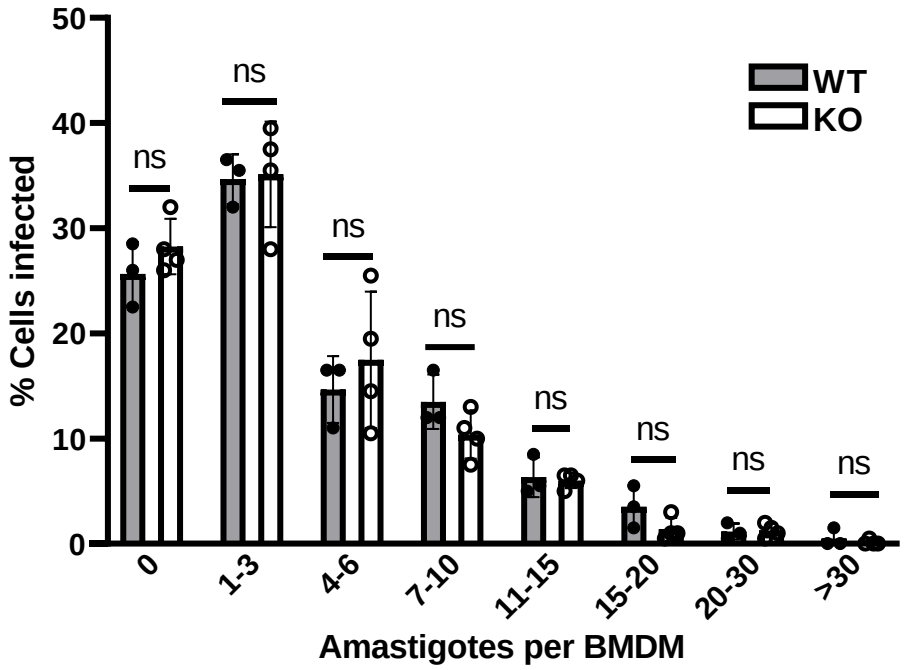

Figure 4.2. Distribution of *L. donovani* amastigotes in WT and KO BMDMs used for scRNA-seq. After 12 hours infection, cells were harvested and stained with Giemsa stain. The number of amastigotes per BMDM was counted by microscopy, and distribution of parasites was plotted. Data is mean ± SD; ns = not significant, multiple t-tests.

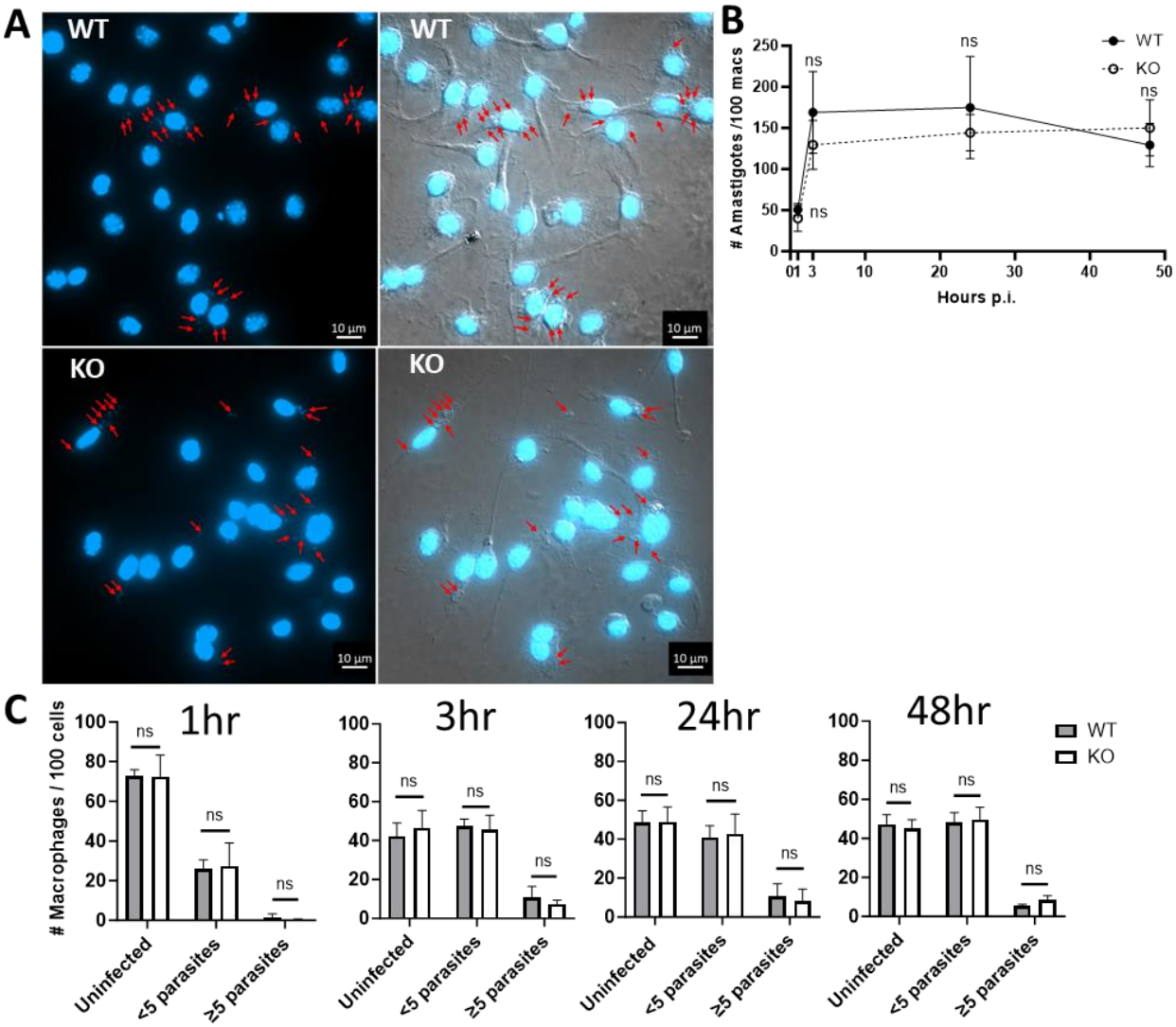

Figure 4.3. TRIM24 does not affect uptake of *L. donovani* amastigotes by BMDMs *in vitro.* WT and KO BMDMs were seeded on four 10-well chamber slides (50,000 cells per well). *L. donovani* amastigotes were added at an MOI of 10:1 for either 1 or 3hrs. After 1hr, one slide was fixed and BMDMs were stained with DAPI. After 3hrs, one slide was fixed and stained with DAPI, and the parasites were washed off the other two slides. The other two slides were left for a further 21 and 45hrs to make a total of 24 and 48hrs, respectively. BMDMs were then fixed and stained for DAPI. DAPI and DIC images were taken on an inverted fluorescence microscope at 100x magnification. **(A)** Microscope images of infected WT and KO BMDMs. DAPI only (**left**) reveals staining of *L. donovani* amastigotes. Merged DAPI and DIC images (**right**) show parasite localisation within BMDMs. Red arrows indicated parasite nuclei. **(B)** Number of intracellular parasites per 100 macrophages. **(C)** Distribution of infection burden of macrophages. Data is mean ± SD; n=3-6 mice per group (two independent experiments); ns = not significant, multiple t-tests.

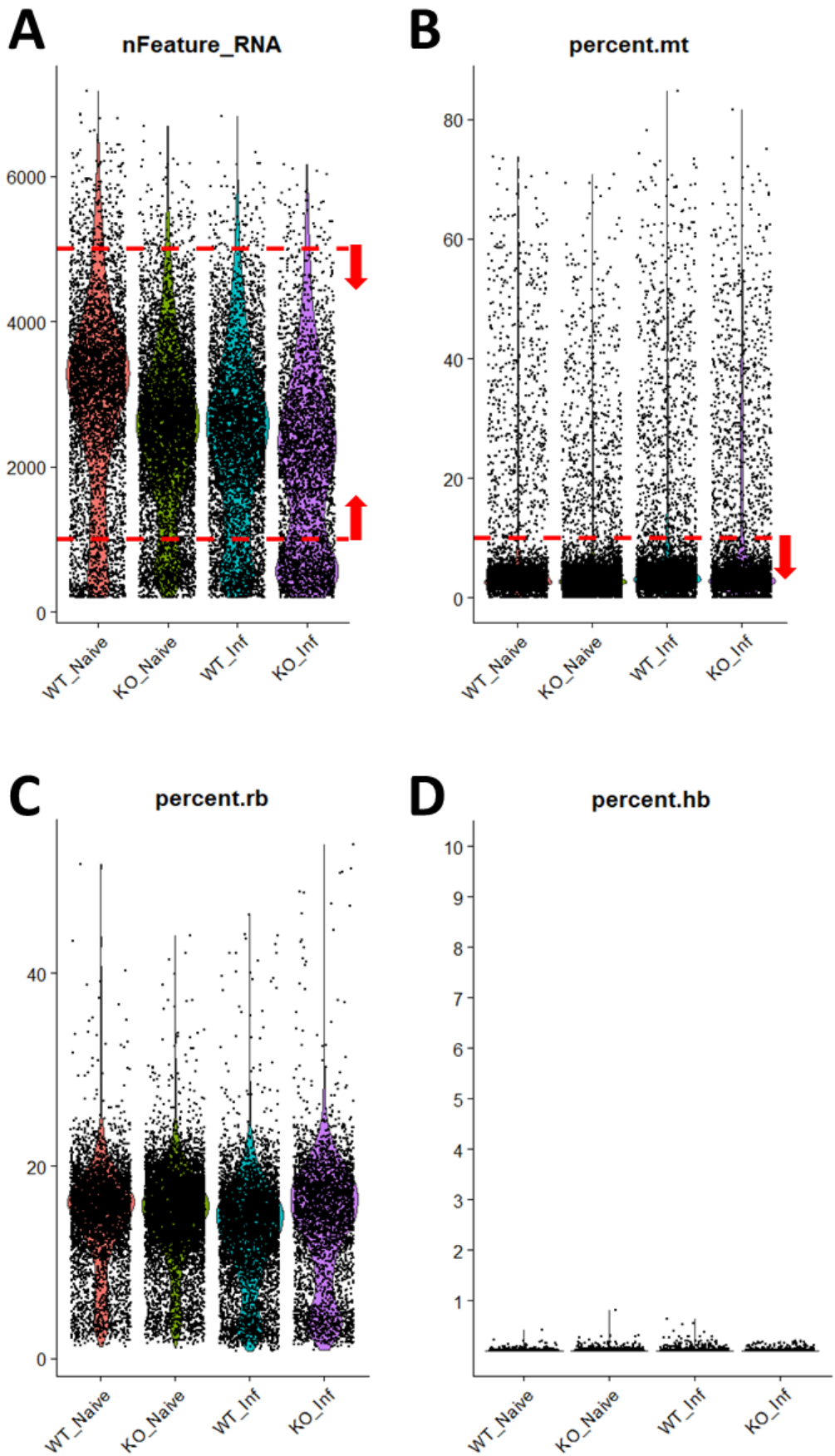

Figure 4.4. QC metrics visualisation & filtering of scRNA-seq datasets. The *L. donovani*-derived alpha-tubulin gene (LdBPK-130330.1) was appended to the mus musculus genome (mm10), and samples were aligned to the edited genome using CellRanger (10X Genomics). Sample datasets were each subjected to quality control and filtering steps independently before sample integration. **(A)** Cells with number of unique genes (nFeatures_RNA) >5000 and <1000 were filtered out. **(B)** Cells with percentage of mitochondrial reads >10% were filtered out. Ribosomal gene percentage **(C)** and haemoglobin gene percentage **(D)** were visualised but not filtered to preserve biological signal.

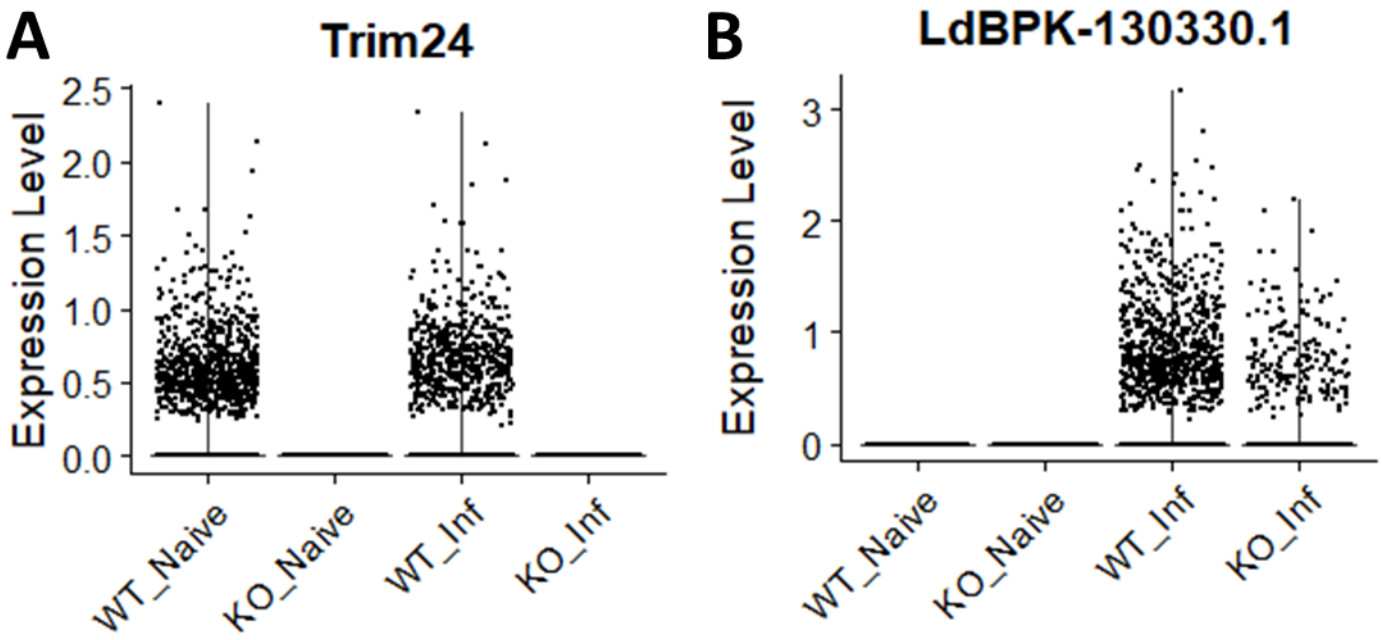

Figure 4.5. Confirmation that *Trim24* expression was absent in KO samples, and *L. donovani* alpha-tubulin (LdBPK-130330.1) transcripts were detected only in infected samples. RNA counts for each sample within the integrated Seurat object were normalised, and violin plots for expression of *Trim24* **(A)** and *LdBPK-130330.1* **(B)** were plotted.

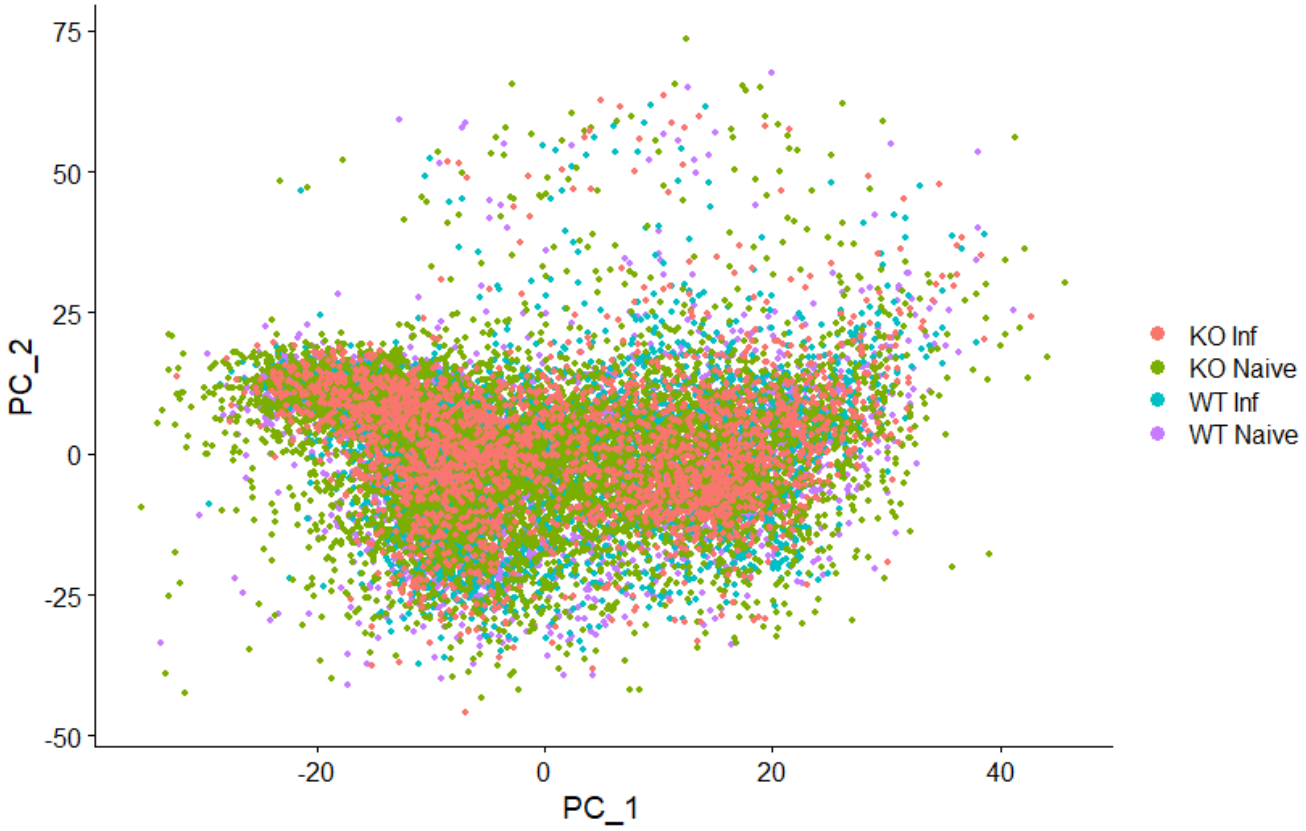

Figure 4.6. Representative PCA plot of scRNA-seq samples. scRNA-seq samples were scaled and normalised using the SCTransform function within the Seurat package. Samples were then integrated together to control for batch effects and allow downstream analysis between experimental conditions. Linear dimensionality reduction was performed through Principal Component Analysis (PCA) and plotted based on the first two principal components (PC_1 and PC_2).

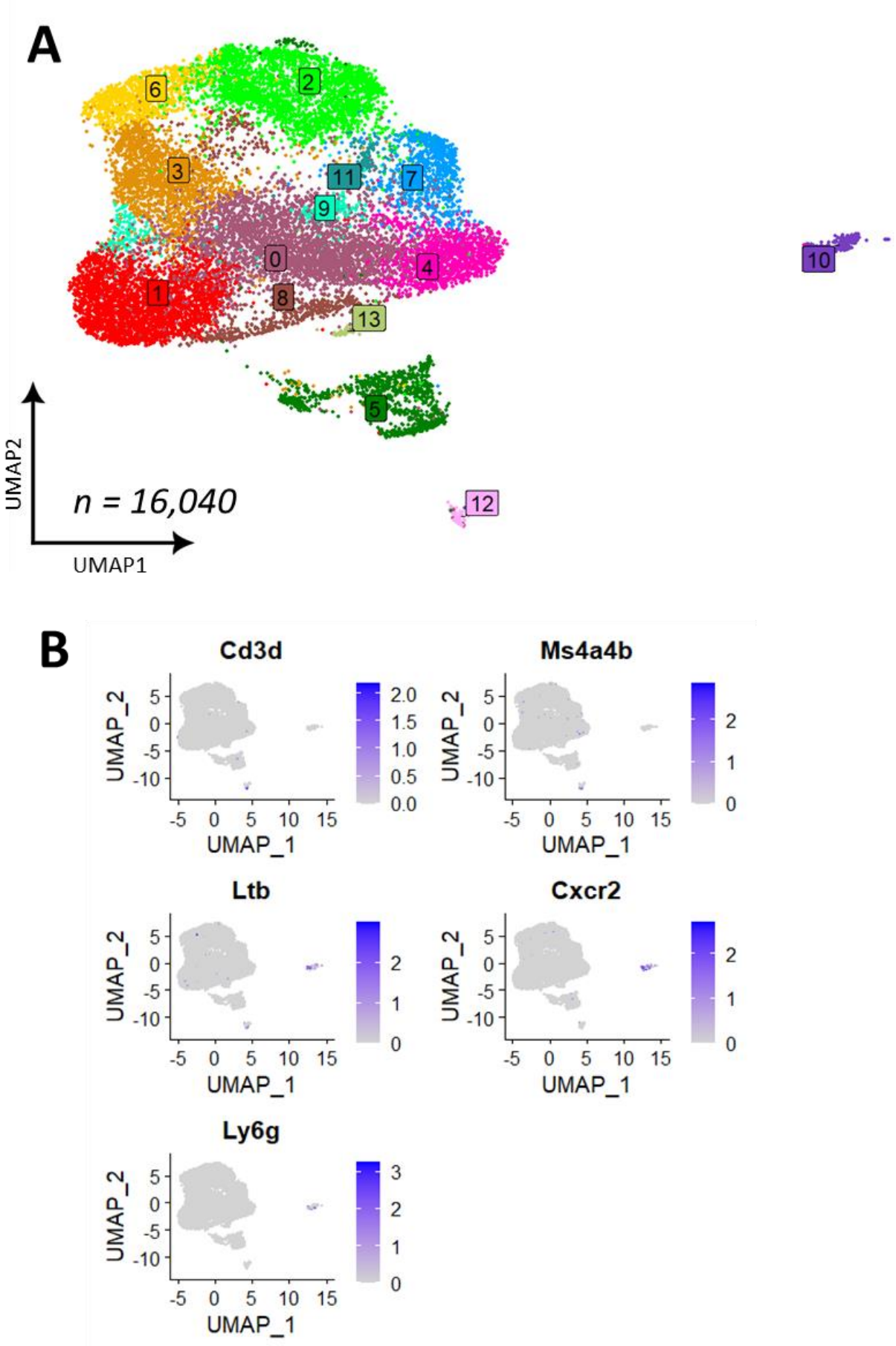

Figure 4.7. Removal of contaminating cells after UMAP projection. (A) Non-linear UMAP projection of integrated samples was performed using Seurat's RunUMAP function. Cells were clustered using the FindClusters and FindNeighbors functions, and plotted on two-dimensional UMAP projection. **(B)** Most highly expressed genes in contaminating clusters 10 (neutrophils; *Cxcr2* and *Ly6g*) and 12 (T cells; *Cd3d, Ms4a4b, Ltb*) were identified using the FindMarkers function, and plotted using the FeaturePlot functions.

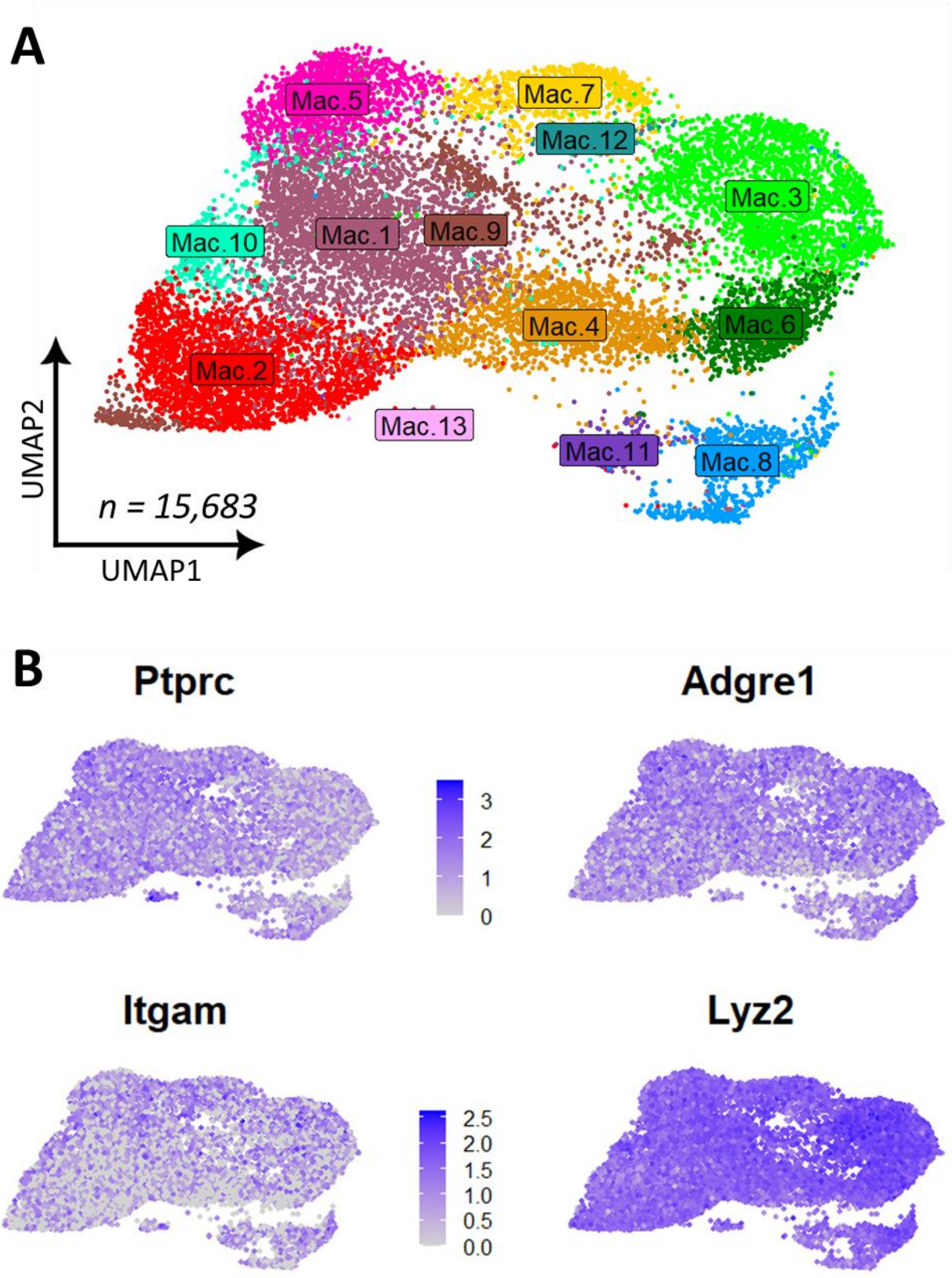

Figure 4.8. Final UMAP projection and detection of leukocyte and macrophage marker genes. (A) After removal of contaminating cells, integrated samples were re-clustered and a final UMAP was generated. **(B)** Expression of *Ptprc* (CD45), *Adgre1* (F4/80), *Itgam* (CD11b), and *Lyz2* (Lysozyme 2) is indicated on UMAP projection. Expression levels are shown on a log2 scale from low (gray) to high (blue).

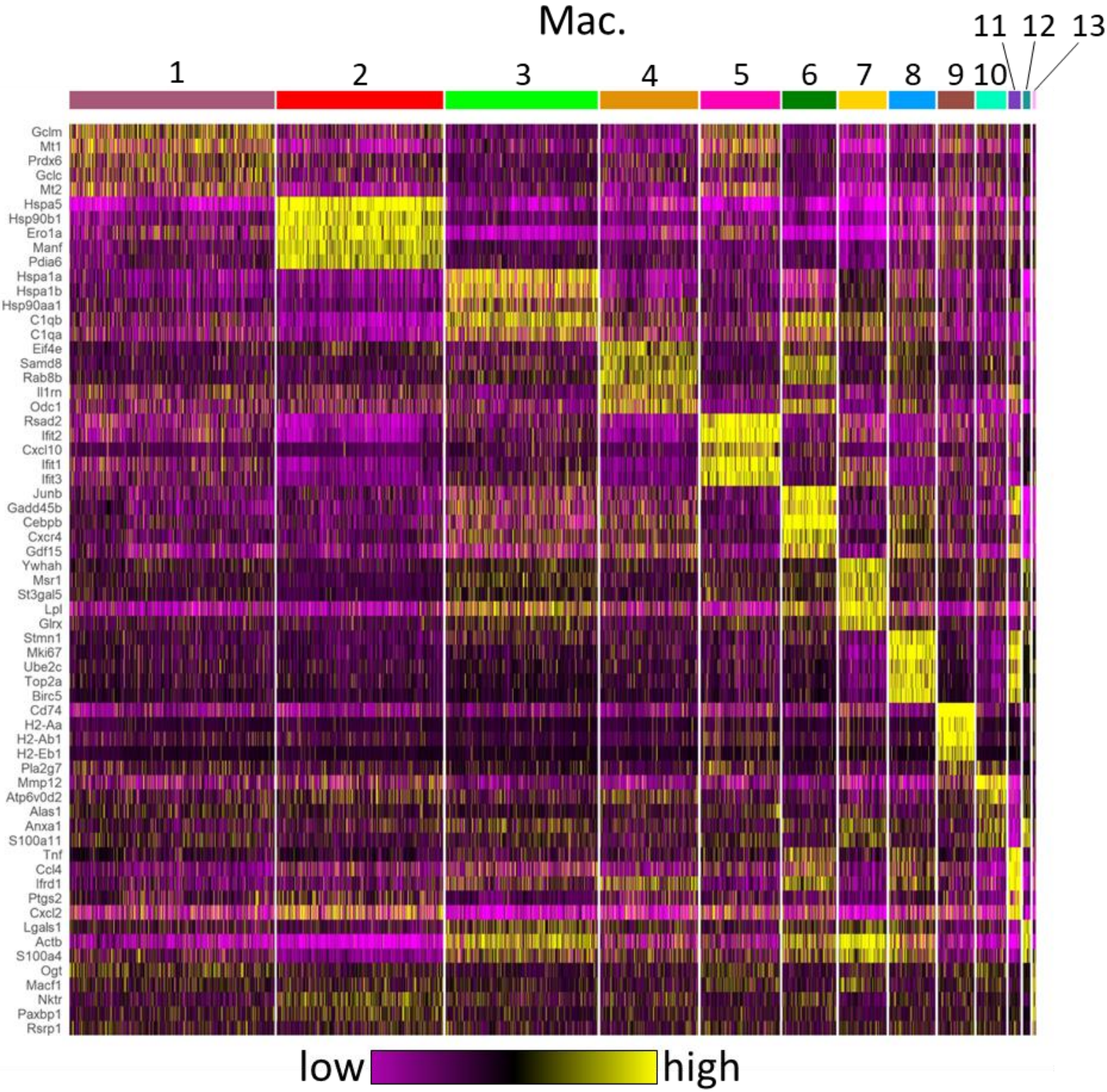

Figure 4.9. Heatmap of top five expressed genes per cluster. The Seurat FindMarkers function was used to identify top expressed genes in each cluster compared to all other clusters. Thresholds were set to filter out genes expressed in <25% cells in each cluster, and only significantly expressed genes (FDR<0.05) were detected. Top five genes per cluster were used for heatmap generation.

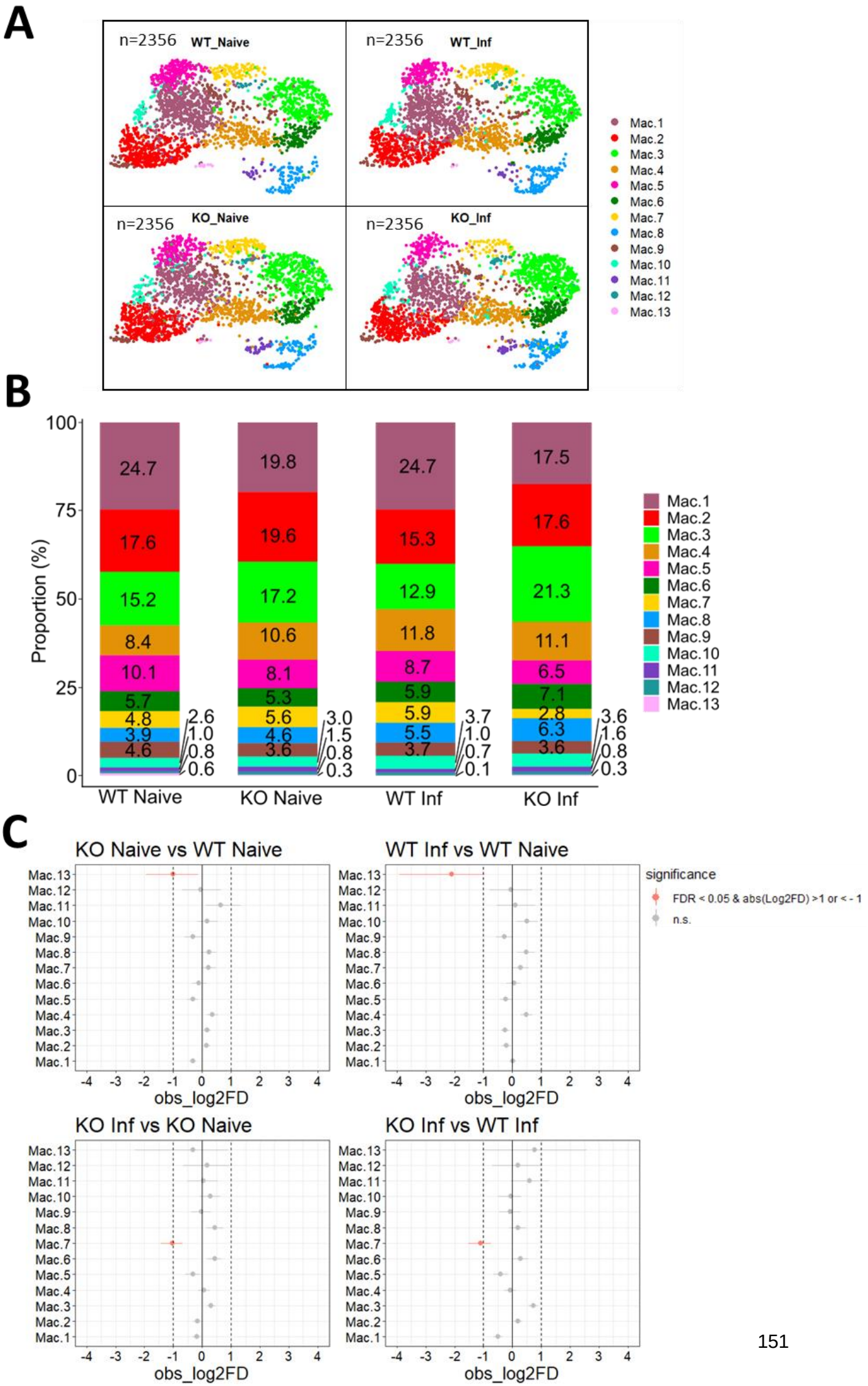
A
n=2356 WT_Naive
n=2356 WT_Inf
n=2356 KO_Naive
n=2356 KO_Inf
Mac.1
Mac.2
Mac.3
Mac.4
Mac.5
Mac.6
Mac.7
Mac.8
Mac.9
Mac.10
Mac.11
Mac.12
Mac.13
B
Proportion (%)
100
75
50
25
0
WT Naive
KO Naive
WT Inf
KO Inf
24.7 17.6 15.2 8.4 10.1 5.7 4.8 3.9 4.6 2.6 1.0 0.8 0.6
19.8 19.6 17.2 10.6 8.1 5.3 5.6 4.6 3.6 3.0 1.5 0.8 0.3
24.7 15.3 12.9 11.8 8.7 5.9 5.9 5.5 3.7 3.7 1.0 0.7 0.1
17.5 17.6 21.3 11.1 6.5 7.1 2.8 6.3 3.6 3.6 1.6 0.8 0.3
C
KO Naive vs WT Naive
WT Inf vs WT Naive
KO Inf vs KO Naive
KO Inf vs WT Inf
obs_log2FD
significance
FDR < 0.05 & abs(Log2FD) >1 or < - 1
n.s.

Figure 4.10. Proportions of cell clusters are not affected by *L. donovani* infection or *Trim24* deletion. (A) Samples were downsampled to identical cell numbers (n=2356) and UMAP was split by sample for visualisation purposes. **(B)** Percentage proportion of clusters within each sample. **(C)** Permutation test was performed on pairs of samples as indicated. Values were considered significant if FDR<0.05 and Log2 Fold Difference (Log2FD) <-1 or >1. Dotted line indicates Log2FD threshold value.

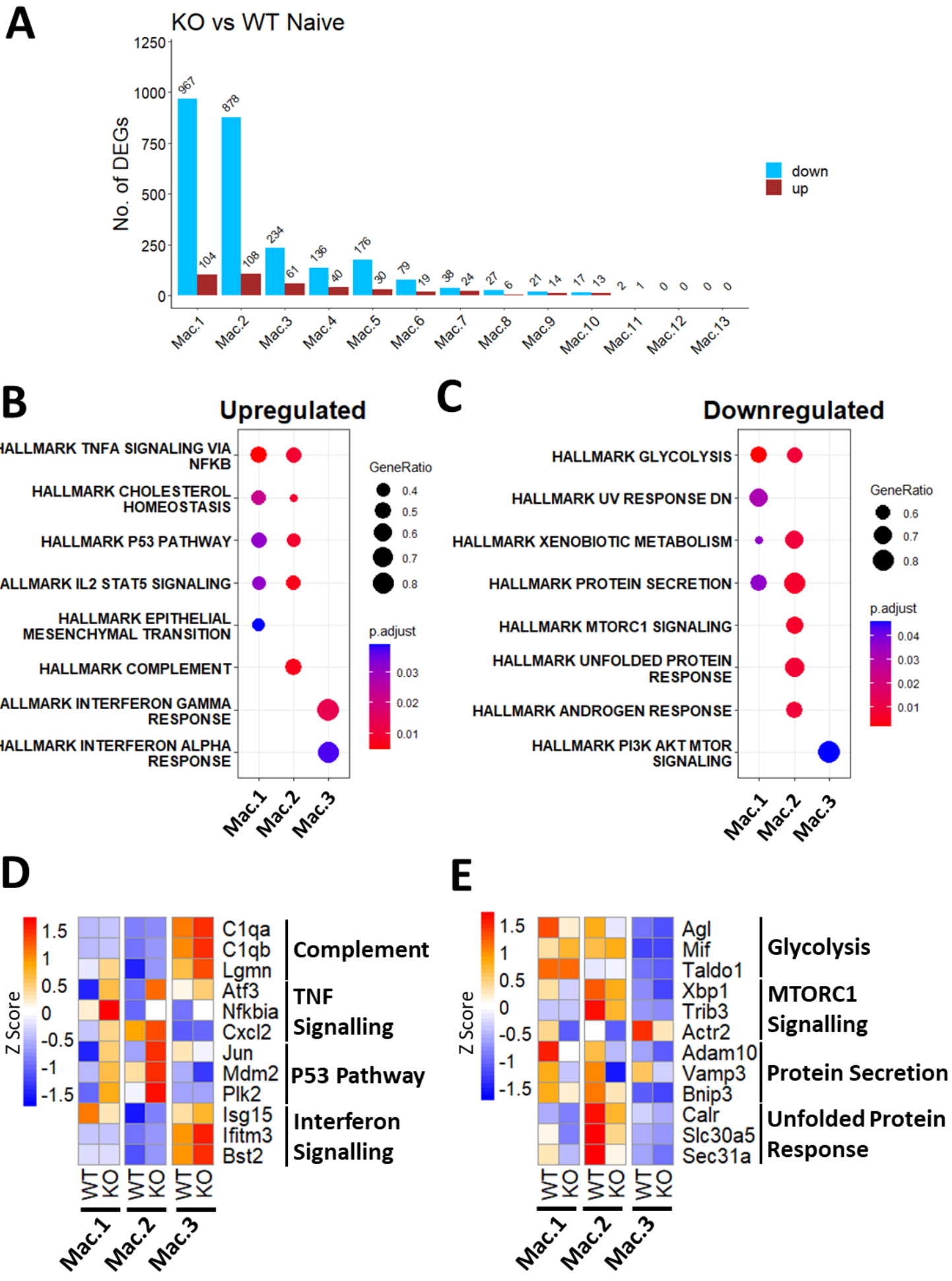
A
KO vs WT Naive
No. of DEGs
1250
1000
750
500
250
0
967
104
878
108
234
61
136
40
176
30
79
19
38
24
27
6
21
14
17
13
2
1
0
0
0
0
Mac.1
Mac.2
Mac.3
Mac.4
Mac.5
Mac.6
Mac.7
Mac.8
Mac.9
Mac.10
Mac.11
Mac.12
Mac.13
down
up
B
Upregulated
HALLMARK TNFA SIGNALING VIA NFKB
HALLMARK CHOLESTEROL HOMEOSTASIS
HALLMARK P53 PATHWAY
HALLMARK IL2 STAT5 SIGNALING
HALLMARK EPITHELIAL MESENCHYMAL TRANSITION
HALLMARK COMPLEMENT
HALLMARK INTERFERON GAMMA RESPONSE
HALLMARK INTERFERON ALPHA RESPONSE
GeneRatio
0.4
0.5
0.6
0.7
0.8
p.adjust
0.03
0.02
0.01
Mac.1
Mac.2
Mac.3
C
Downregulated
HALLMARK GLYCOLYSIS
HALLMARK UV RESPONSE DN
HALLMARK XENOBIOTIC METABOLISM
HALLMARK PROTEIN SECRETION
HALLMARK MTORC1 SIGNALING
HALLMARK UNFOLDED PROTEIN RESPONSE
HALLMARK ANDROGEN RESPONSE
HALLMARK PI3K AKT MTOR SIGNALING
GeneRatio
0.6
0.7
0.8
p.adjust
0.04
0.03
0.02
0.01
Mac.1
Mac.2
Mac.3
D
Z Score
1.5
1
0.5
0
-0.5
-1
-1.5
C1qa
C1qb
Lgmn
Atf3
Nfkbia
Cxcl2
Jun
Mdm2
Plk2
Isg15
Ifitm3
Bst2
Complement
TNF Signalling
P53 Pathway
Interferon Signalling
WT
KO
Mac.1
Mac.2
Mac.3
E
Z Score
1.5
1
0.5
0
-0.5
-1
-1.5
Agl
Mif
Taldo1
Xbp1
Trib3
Actr2
Adam10
Vamp3
Bnip3
Calr
Slc30a5
Sec31a
Glycolysis
MTORC1 Signalling
Protein Secretion
Unfolded Protein Response
WT
KO
Mac.1
Mac.2
Mac.3

Figure 4.11. Effects of *Trim24* deletion on naïve BMDM transcriptional phenotypes. (A) Number of DEGs detected per cluster between KO Naïve and WT Naïve samples. **(B)** Top significantly (p.adjust<0.05) enriched gene sets in KO Naïve BMDMs in Mac.1, Mac.2 and Mac.3. No significantly enriched gene sets were detected in other clusters. **(C)** Top significantly downregulated gene sets in KO Naïve BMDMs in Mac.1, Mac.2 and Mac.3. No significantly downregulated gene sets were detected in other clusters. **(D)** DEGs contributing to indicated upregulated gene sets. **(E)** DEGs contributing to indicated downregulated gene sets. All DEGs were FDR<0.05, log2FC >0 or <0.

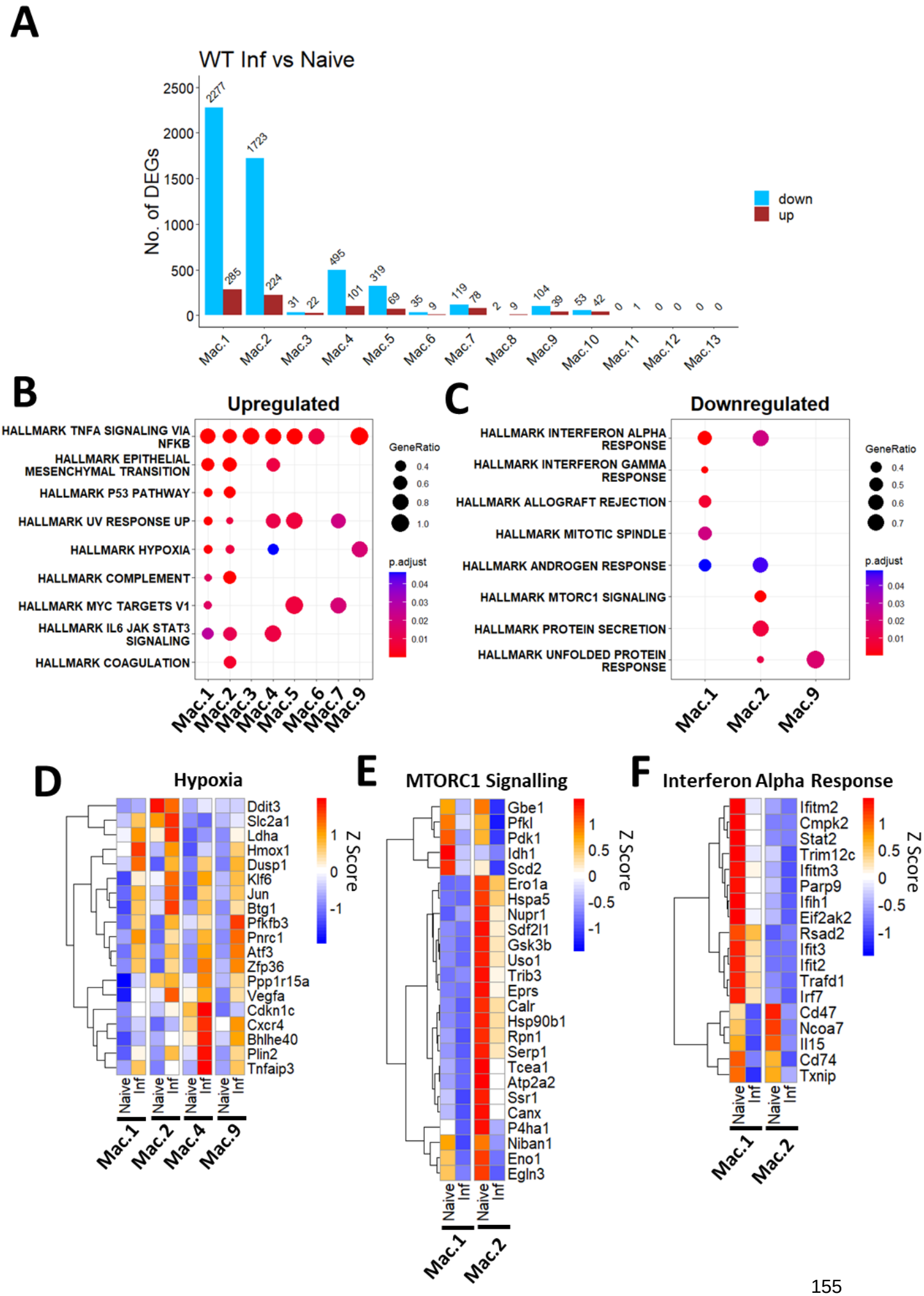
A
WT Inf vs Naive
No. of DEGs
down
up
Mac.1
Mac.2
Mac.3
Mac.4
Mac.5
Mac.6
Mac.7
Mac.8
Mac.9
Mac.10
Mac.11
Mac.12
Mac.13
B
Upregulated
HALLMARK TNFA SIGNALING VIA NFKB
HALLMARK EPITHELIAL MESENCHYMAL TRANSITION
HALLMARK P53 PATHWAY
HALLMARK UV RESPONSE UP
HALLMARK HYPOXIA
HALLMARK COMPLEMENT
HALLMARK MYC TARGETS V1
HALLMARK IL6 JAK STAT3 SIGNALING
HALLMARK COAGULATION
GeneRatio
p.adjust
C
Downregulated
HALLMARK INTERFERON ALPHA RESPONSE
HALLMARK INTERFERON GAMMA RESPONSE
HALLMARK ALLOGRAFT REJECTION
HALLMARK MITOTIC SPINDLE
HALLMARK ANDROGEN RESPONSE
HALLMARK MTORC1 SIGNALING
HALLMARK PROTEIN SECRETION
HALLMARK UNFOLDED PROTEIN RESPONSE
D
Hypoxia
Ddit3
Slc2a1
Ldha
Hmox1
Dusp1
Klf6
Jun
Btg1
Pfkfb3
Pnrc1
Atf3
Zfp36
Ppp1r15a
Vegfa
Cdkn1c
Cxcr4
Bhlhe40
Plin2
Tnfaip3
Naive
Inf
Z Score
E
MTORC1 Signalling
Gbe1
Pfkl
Pdk1
Idh1
Scd2
Ero1a
Hspa5
Nupr1
Sdf2l1
Gsk3b
Uso1
Trib3
Eprs
Calr
Hsp90b1
Rpn1
Serp1
Tcea1
Atp2a2
Ssr1
Canx
P4ha1
Niban1
Eno1
Egln3
F
Interferon Alpha Response
Ifitm2
Cmpk2
Stat2
Trim12c
Ifitm3
Parp9
Ifih1
Eif2ak2
Rsad2
Ifit3
Ifit2
Trafd1
Irf7
Cd47
Ncoa7
Il15
Cd74
Txnip

Figure 4.12. Transcriptional alterations induced by *L. donovani* infection in WT BMDMs. DGE analysis was performed, and numbers of up- and down-regulated genes per cluster were plotted (FDR<0.05, log2FC <0 or >0) **(A)**. GSEA using MSigDB HALLMARK gene sets was performed on significantly up- and down-regulated genes in each cluster, ranked by log2FC values. Top significantly enriched (FDR<0.05 NES>0) **(B)**, and top significantly down-regulated (FDR<0.05, NES>0) **(C)** were plotted. Significantly up- or down-regulated gene sets were only found for clusters shown. Heatmaps were produced to show averaged expression of DEGs (FDR<0.05, log2FC <0 or >0) in each cluster for significantly altered gene sets Hypoxia **(D)**, MTORC1 Signalling **(E)**, and Interferon Alpha Response **(F).**

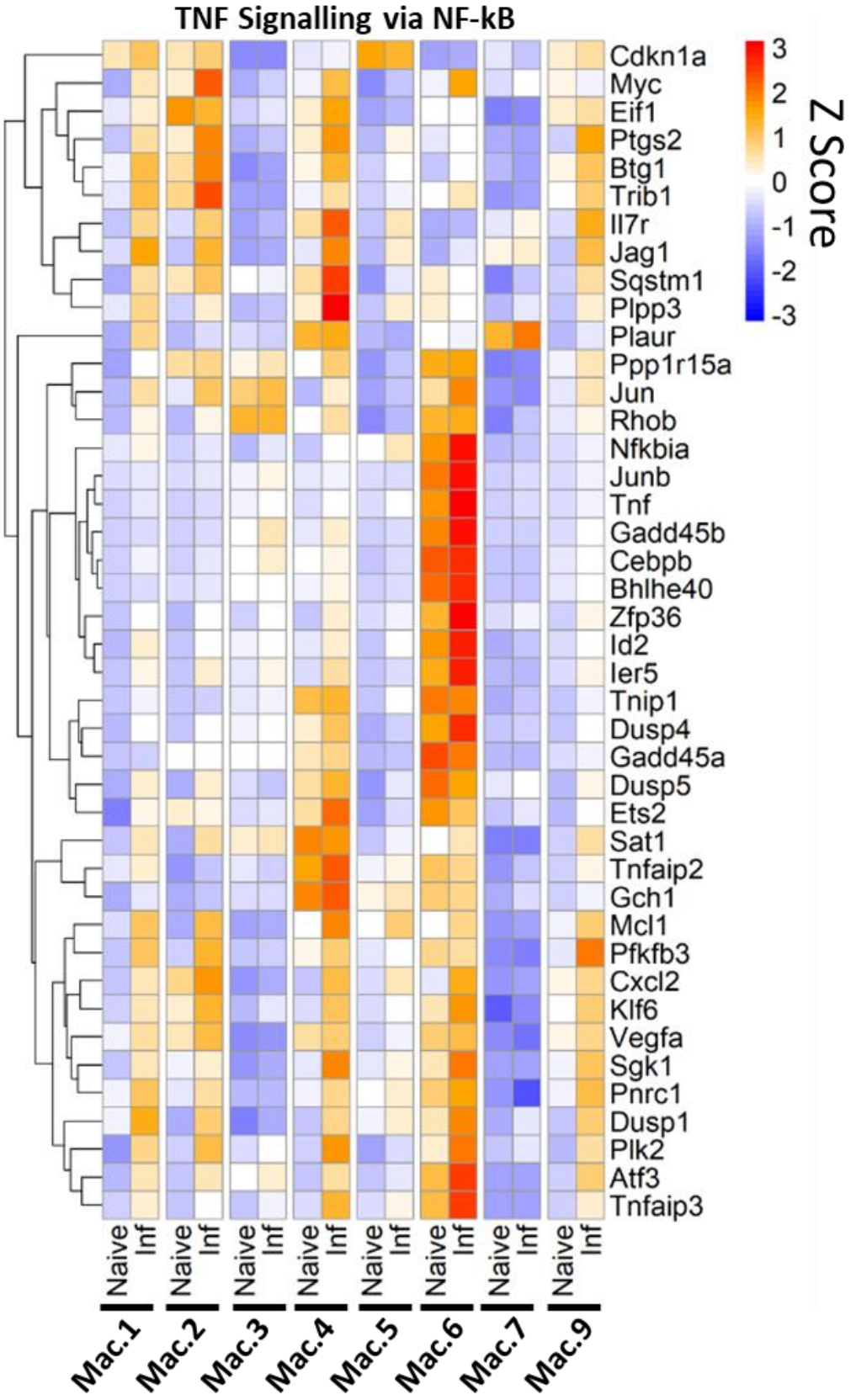

Figure 4.13. Transcripts contributing to TNF Signalling gene set were upregulated in *L. donovani* infected WT BMDMs. Expression levels of each gene were averaged across cell clusters before heatmap generation and represented as Z Score.

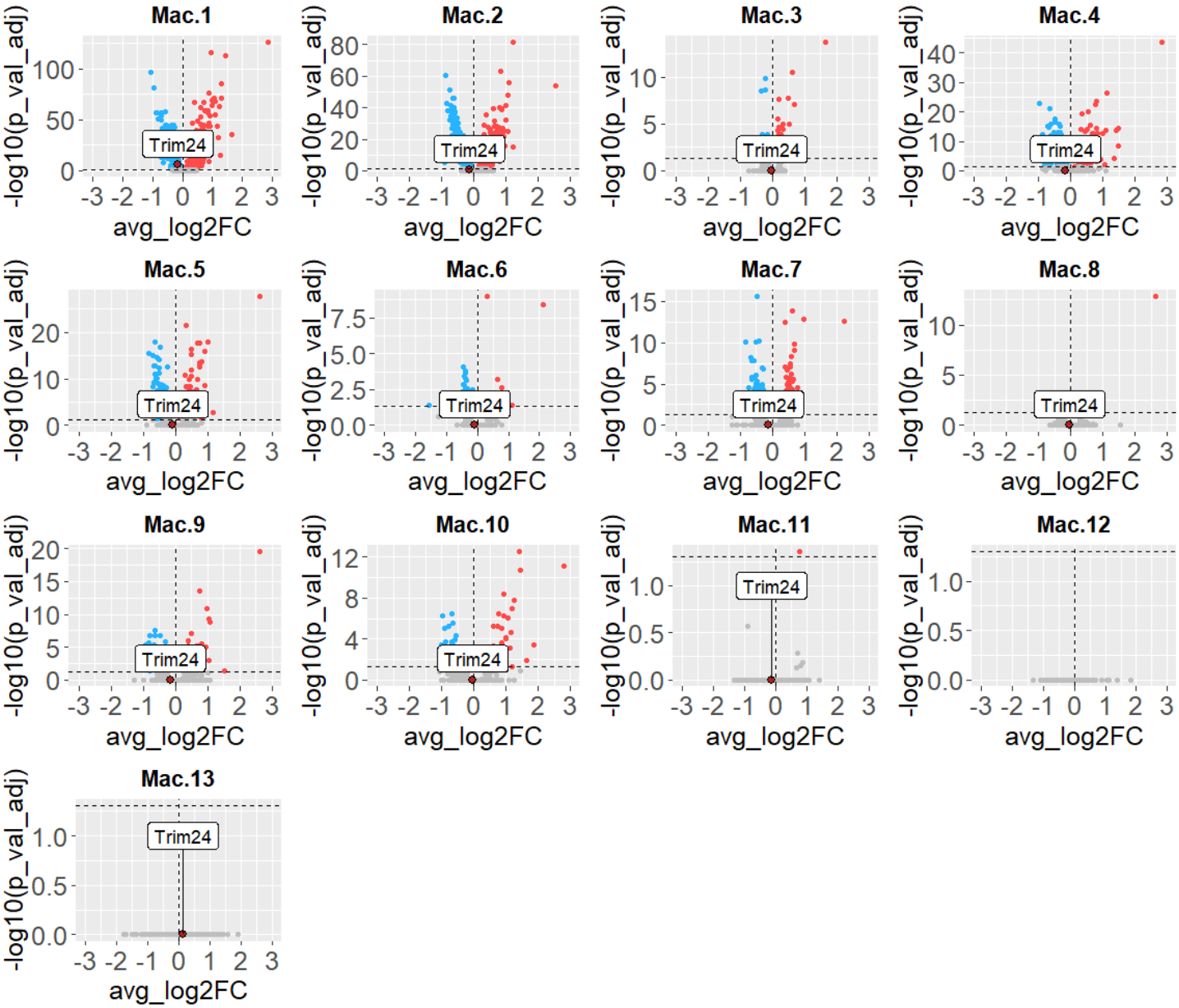

Figure 4.14. Downregulation of *Trim24* in Mac.1 during *L. donovani* infection. DGE analysis was performed on each BMDM cluster between WT infected vs WT Naïve samples (FDR<0.05, log2FC >0 or <0). Volcano plots of all nine clusters is shown (clusters 11-13 gave few DEGs due to low cell number). *Trim24* reads were not found in Mac.12.

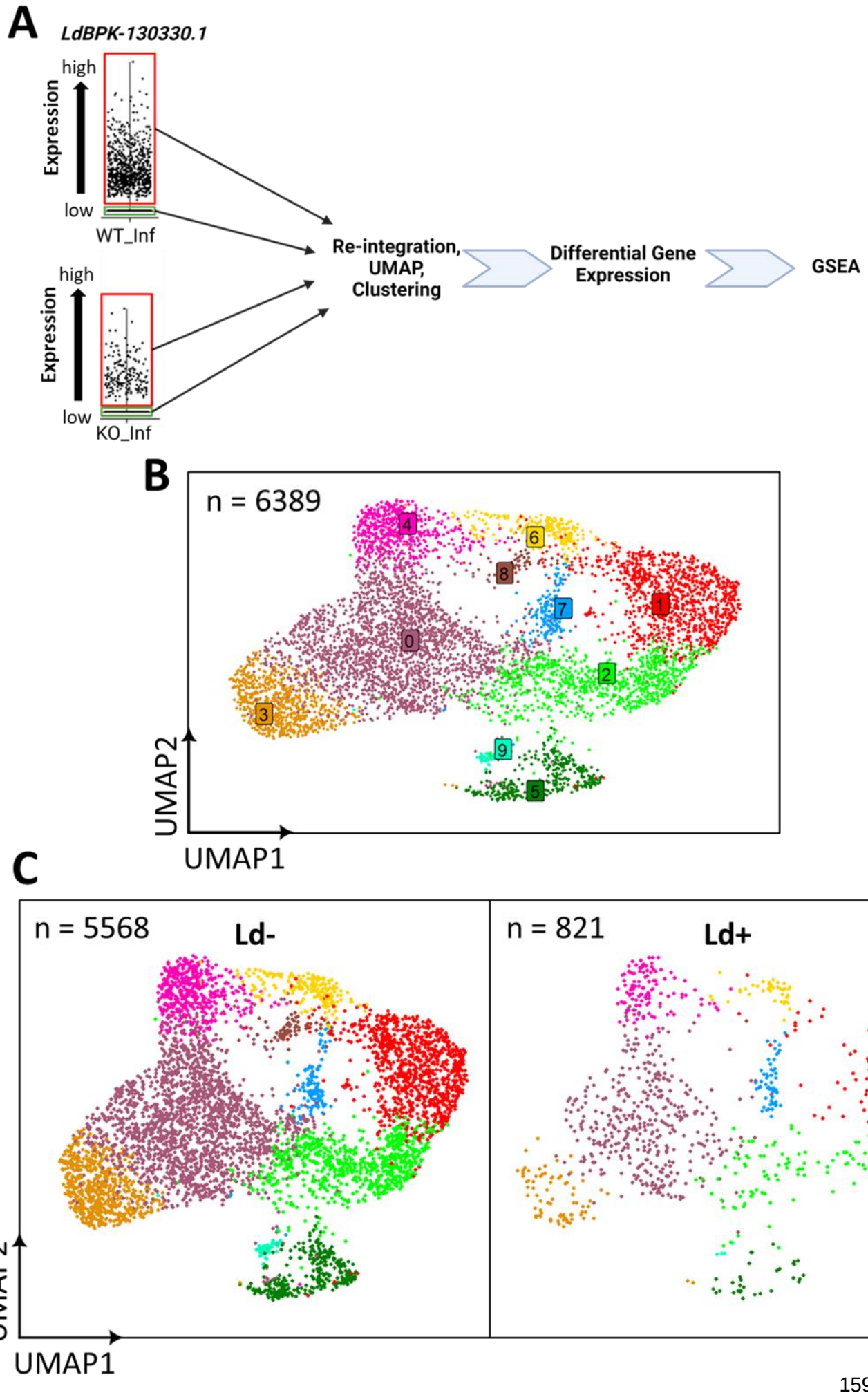
A
LdBPK-130330.1
high
Expression
low
WT_Inf
high
Expression
low
KO_Inf
Re-integration, UMAP, Clustering
Differential Gene Expression
GSEA
B
n = 6389
0
1
2
3
4
5
6
7
8
9
UMAP2
UMAP1
C
n = 5568
Ld-
n = 821
Ld+
UMAP2
UMAP1

Figure 4.15. Re-integration and clustering infected sample populations. (A) Experimental design. WT Inf and KO Inf samples were subset into *LdBPK-130330.1*+ (Ld+) and *LdBPK-130330.1*- (Ld-) populations, integrated, and analysed following the same protocol as previously described. **(B)** Final UMAP projection of integrated Seurat object. **(C)** Distribution of Ld+ BMDMs on final UMAP.

Frequency of Ld+ BMDMs detected per cluster			
Cluster	Ld+	Total Ld+	Ld+ Prop (%)
0	374	821	**45.55**
1	58	821	**7.06**
2	92	821	**11.21**
3	71	821	**8.65**
4	111	821	**13.52**
5	25	821	**3.05**
6	35	821	**4.26**
7	52	821	**6.33**
8	0	821	**0.00**
9	3	821	**0.37**

Table 4.1. Distribution of Ld+ cells per cluster as a proportion of total Ld+ cells (821).

Frequency of Infected BMDMs detected per cluster					
Cluster	Total Ld+	WT Ld+	KO Ld+	WT Ld+ %	KO Ld+ %
0	374	305	69	**81.55**	**18.45**
1	58	43	15	**74.14**	**25.86**
2	92	68	24	**73.91**	**26.09**
3	71	50	21	**70.42**	**29.58**
4	111	94	17	**84.68**	**15.32**
5	25	23	2	**92.00**	**8.00**
6	35	31	4	**88.57**	**11.43**
7	52	43	9	**82.69**	**17.31**
8	0	0	0	**0**	**0**
9	3	2	1	**66.67**	**33.33**

Table 4.2. Distribution of Ld+ cells per cluster per genotype as a proportion of total Ld+ cells per cluster.

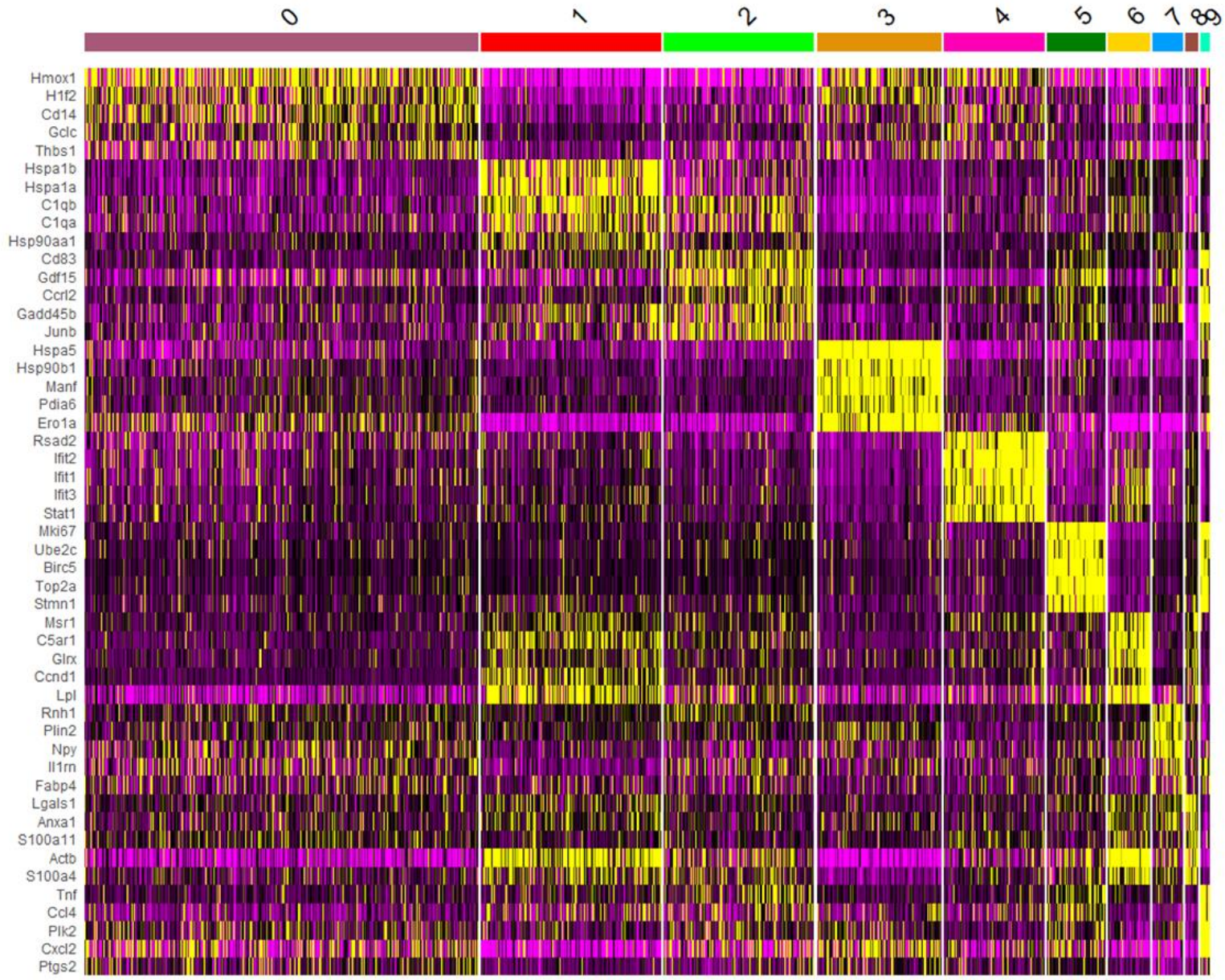

Figure 4.16. Top 5 expressed genes per cluster for Ld+ and Ld- WT and KO BMDMs. The Seurat FindMarkers function was used to identify top expressed genes in each cluster compared to all other clusters. Thresholds were set to filter out genes expressed in <25% cells in each cluster, and only significantly expressed genes (FDR<0.05) were detected. Top five genes per cluster were used for heatmap generation.

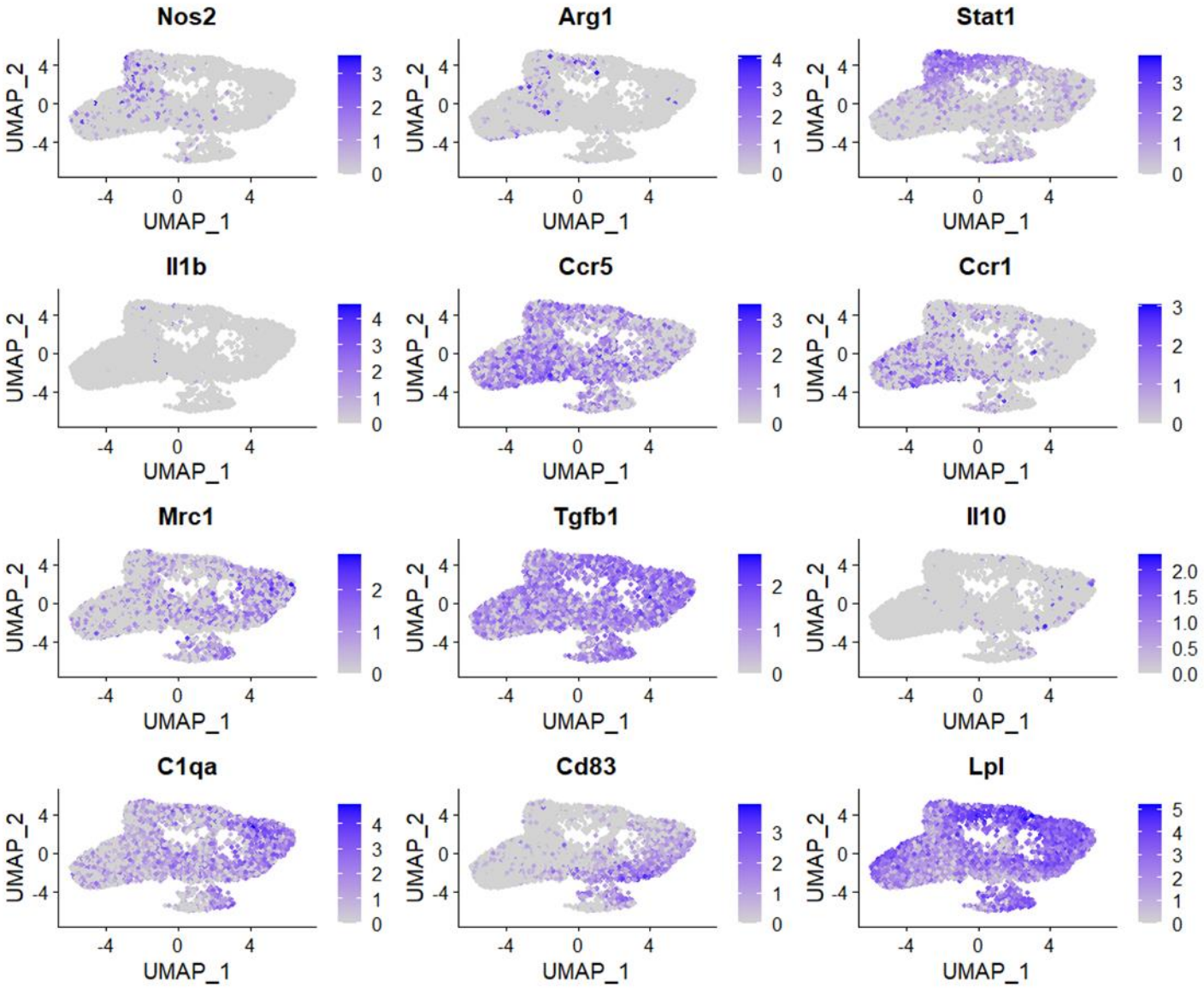

Figure 4.17. Clusters with Ld+ BMDMs have an inflammatory phenotype. Feature plots of whole UMAP indicate expression levels of inflammatory genes (*Nos2, Stat1, Il1b, Ccr5, Ccr1*) and immunoregulatory genes (*Arg1, Mrc1, Tgfb1, Il10, C1qa, Cd83, Lpl*). Expression levels are shown on a log2 scale from low (gray) to high (blue).

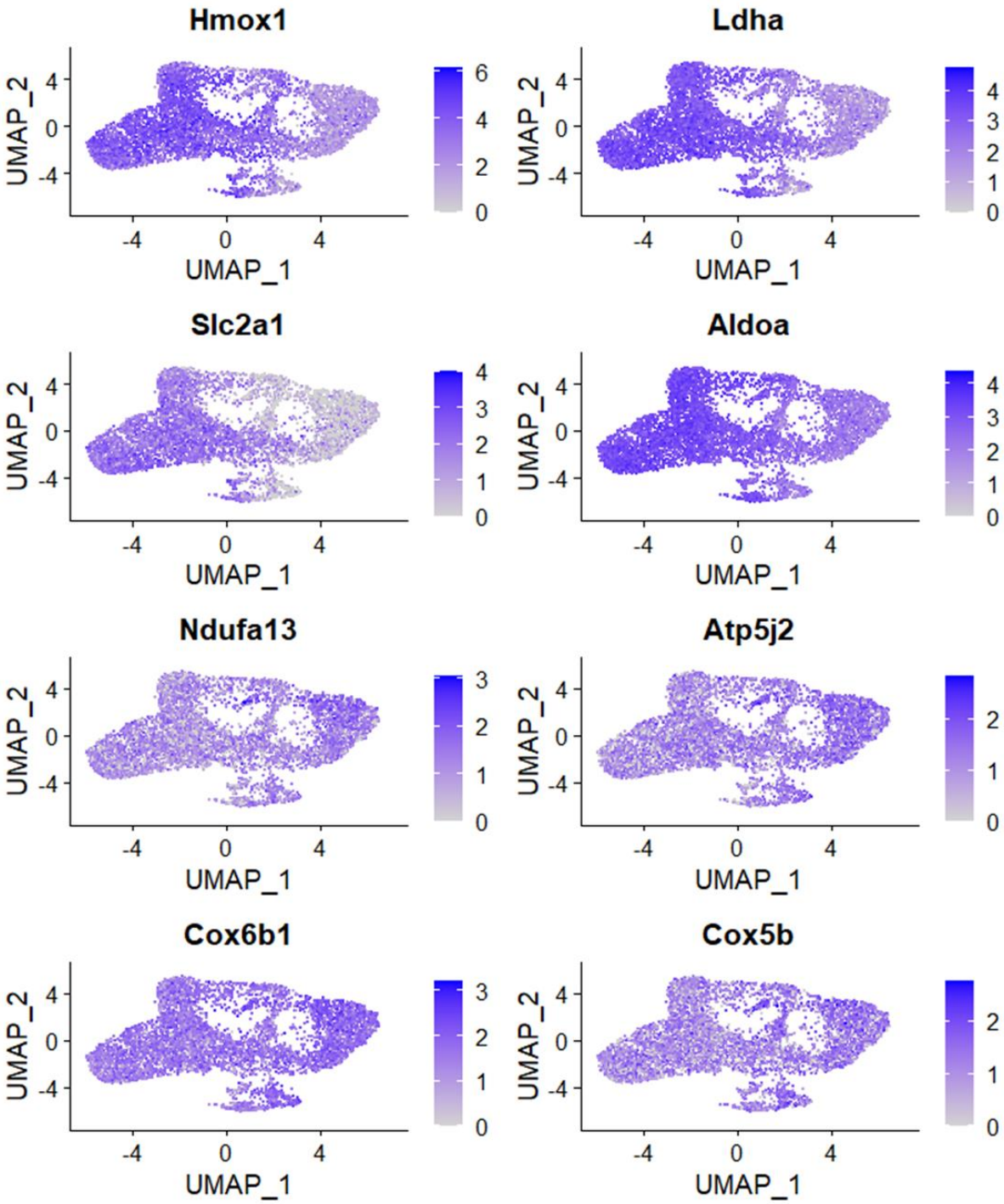

Figure 4.18. Clusters with Ld+ BMDMs are more skewed towards glycolysis than oxidative phosphorylation. Glycolytic genes (*Hmox1, Ldha, Slc2a1, Aldoa*) and oxidative phosphorylation genes (*Ndufa13, Atp5j2, Cox6b1, Cox5b*) are shown on individual feature plots of the whole UMAP. Expression levels are shown on a log2 scale from low (gray) to high (blue).

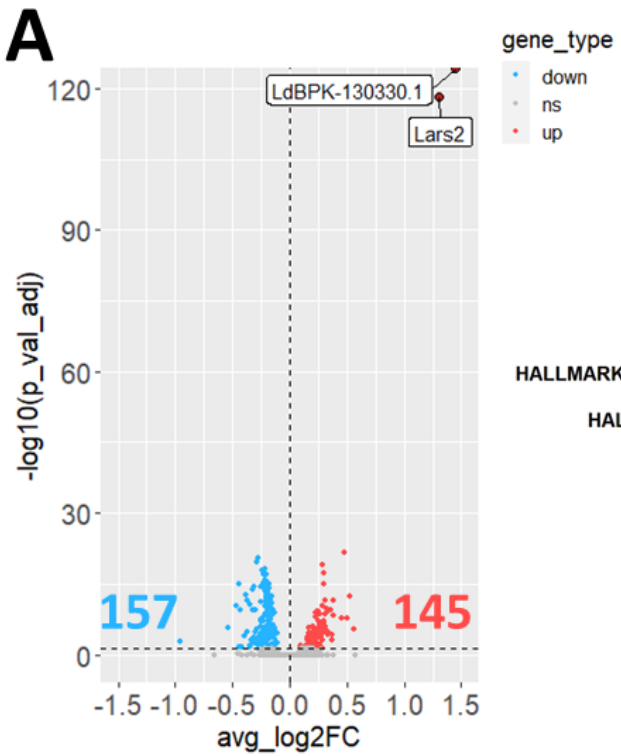
A
gene_type
down
ns
up
LdBPK-130330.1
Lars2
157
145
-log10(p_val_adj)
avg_log2FC

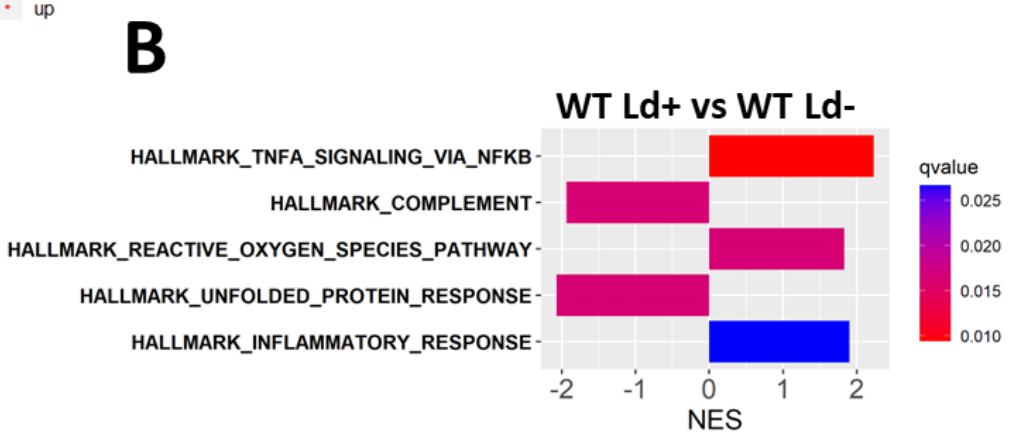
B
WT Ld+ vs WT Ld-
HALLMARK_TNFA_SIGNALING_VIA_NFKB
HALLMARK_COMPLEMENT
HALLMARK_REACTIVE_OXYGEN_SPECIES_PATHWAY
HALLMARK_UNFOLDED_PROTEIN_RESPONSE
HALLMARK_INFLAMMATORY_RESPONSE
NES
qvalue
0.025
0.020
0.015
0.010

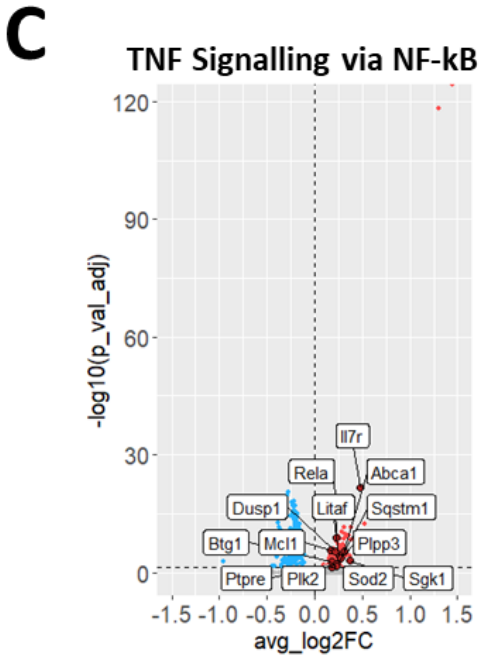
C
TNF Signalling via NF-kB
Il7r
Rela
Abca1
Dusp1
Litaf
Sqstm1
Btg1
Mcl1
Plpp3
Ptpre
Plk2
Sod2
Sgk1
-log10(p_val_adj)
avg_log2FC

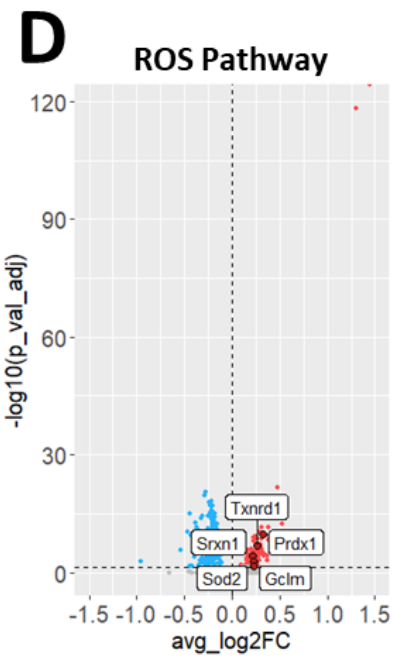
D
ROS Pathway
Txnrd1
Srxn1
Prdx1
Sod2
Gclm
-log10(p_val_adj)
avg_log2FC

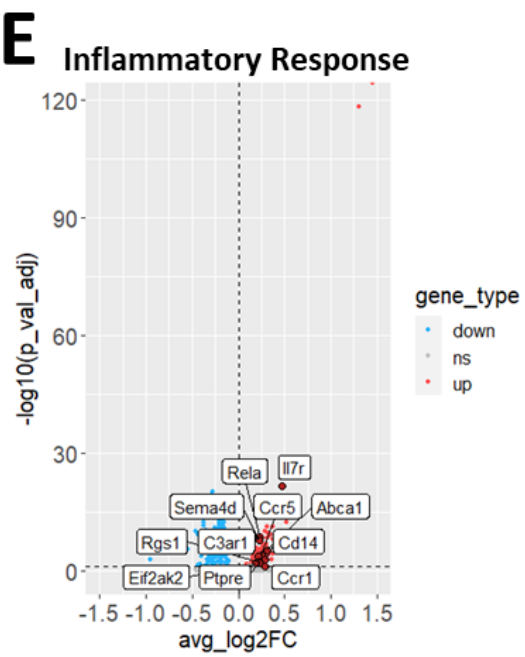
E
Inflammatory Response
Rela
Il7r
Sema4d
Ccr5
Abca1
Rgs1
C3ar1
Cd14
Eif2ak2
Ptpre
Ccr1
gene_type
down
ns
up
-log10(p_val_adj)
avg_log2FC

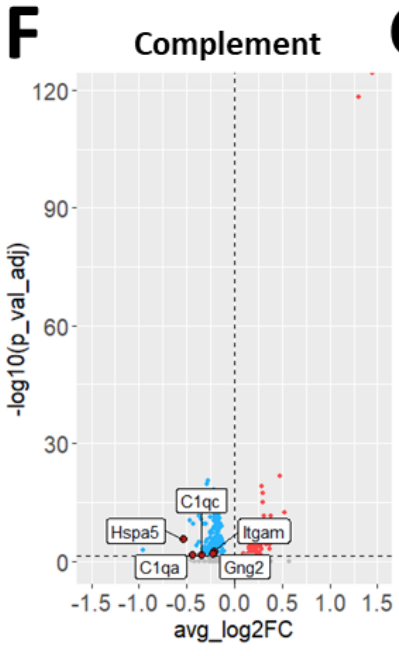
F
Complement
C1qc
Hspa5
Itgam
C1qa
Gng2
-log10(p_val_adj)
avg_log2FC

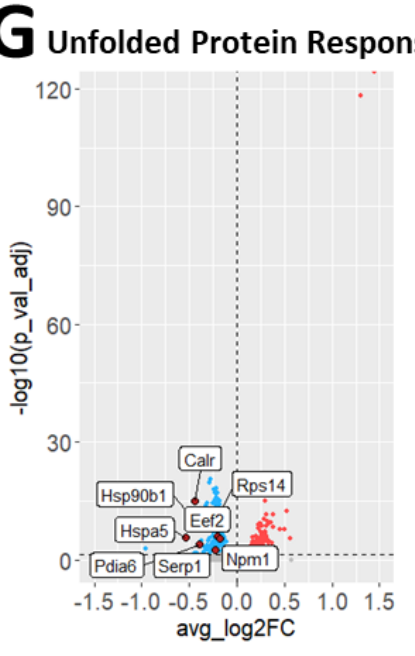
G
Unfolded Protein Response
Calr
Rps14
Hsp90b1
Eef2
Hspa5
Pdia6
Serp1
Npm1
-log10(p_val_adj)
avg_log2FC

Figure 4.19. Up- and down-regulated gene sets in Ld+ vs Ld- WT BMDMs. (A) DGE analysis was performed to identify DEGs between Ld+ and Ld- WT BMDMs (FDR<0.05, log2FC >0 or <0). **(B)** GSEA was performed, and the top five significant gene sets are shown. All genes were then shown on volcano plots, with significantly up-regulated (red; FDR<0.05, log2FC >0) and down-regulated (blue; FDR<0.05, log2FC<0) genes highlighted. Significantly up- or down-regulated genes for TNF signalling **(C)**, ROS pathway **(D)**, Inflammatory response **(E)**, Complement **(F)**, and Unfolded Protein Response **(G)** are labelled on each plot. NES = Normalised Enrichment Score, ns = not significant, up = higher expression in Ld+ than Ld-, down = lower expression in Ld+ than Ld-.

A

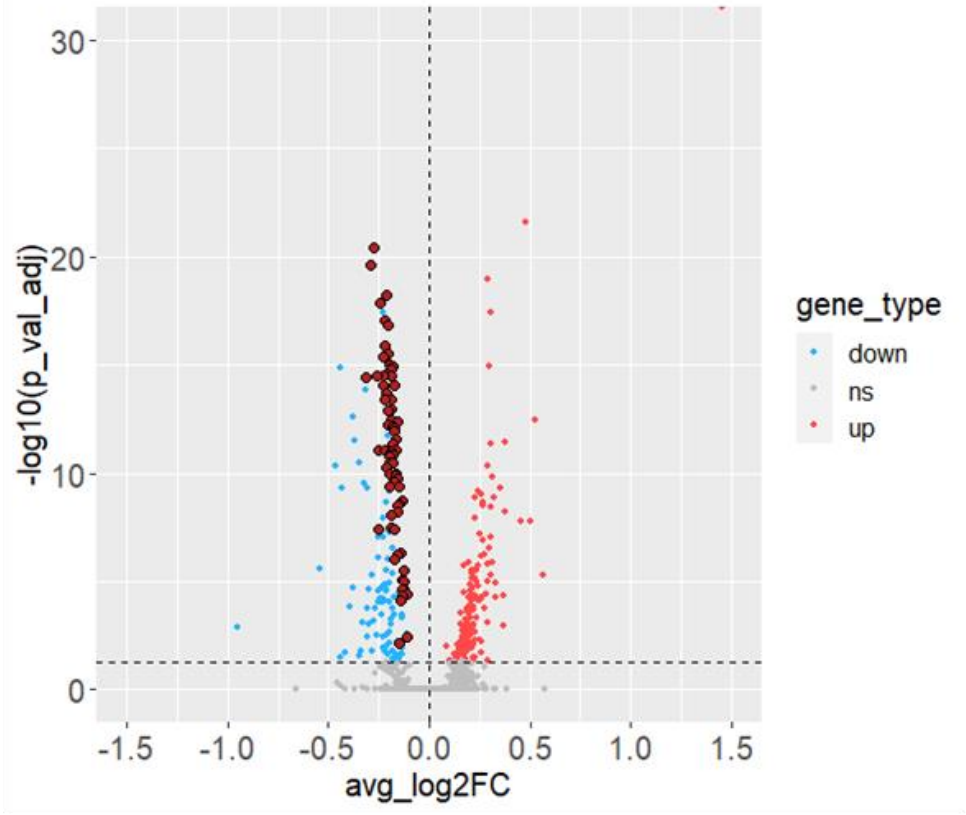

B

Rps4x	Rpl37a	Rps16
Rpl10a	Rpl23	Rps2
Rps24	Rpl11	Rpl19
Rps5	Rps14	Rpl41
Rpl32	Rps20	Rpl27
Rpl17	Rpl27a	Rps12
Rps11	Rpl18	Rps26
Rpl13	Rpl35a	Rpl29
Rpl10	Rpl30	Rps8
Rpl34	Rps10	Rpl22l1
Rps23	Rps18	Rps21
Rpl26	Rps19	Rps17
Rplp0	Rps9	Rpl36a
Rps27a	Rpl22	Rps25
Rps7	Rpl36	Rpl7
Rpsa	Rpl12	Rpl38
Rpl3	Rpl35	Rpl9
Rps29	Rpl39	Rps15
Rps3	Rpl14	Rplp2
Rpl7a	Rpl21	Rps15a
Rpl18a	Rpl37	Rpl8
Rpl15	Rpl28	Rps28
Rpl6	Rplp1	Rps27
Rps13	Rps3a1	

C

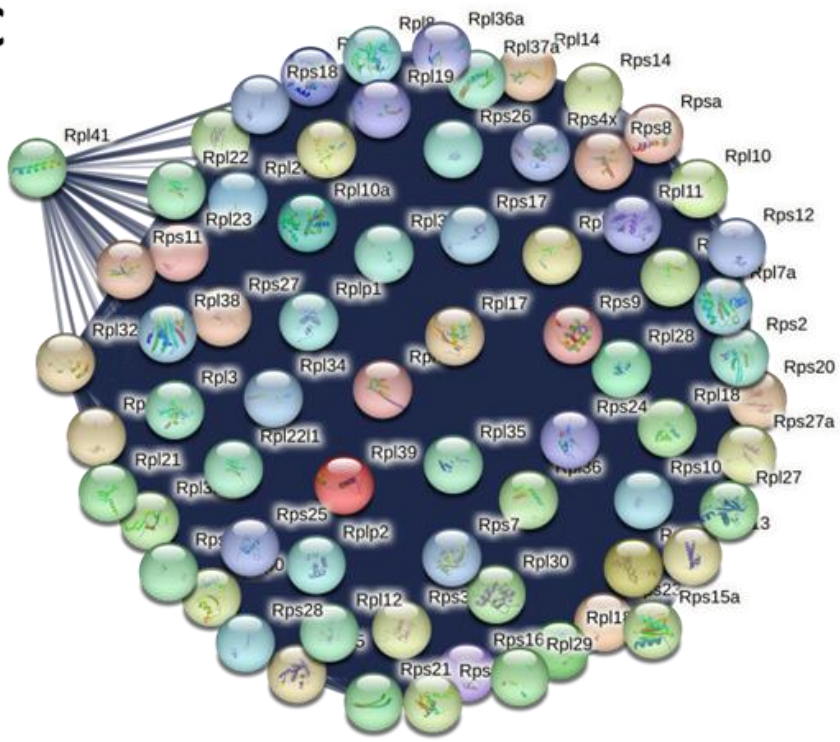

GO-term	description	false discovery rate
GO:0000028	Ribosomal small subunit assembly	5.20e-18
GO:0002181	Cytoplasmic translation	1.93e-48

Figure 4.20. Downregulation of ribosomal subunit genes in WT Ld+ BMDMs. (A) Volcano plot indicating downregulation of ribosomal genes (shown in dark red) in WT Ld+ BMDMs vs WT Ld-. **(B)** List of significantly downregulated ribosomal genes as shown in **A**. **(C)** Ribosomal genes were submitted to STRINGdb for analysis, and an association network was generated with accompanying gene ontology enrichment terms.

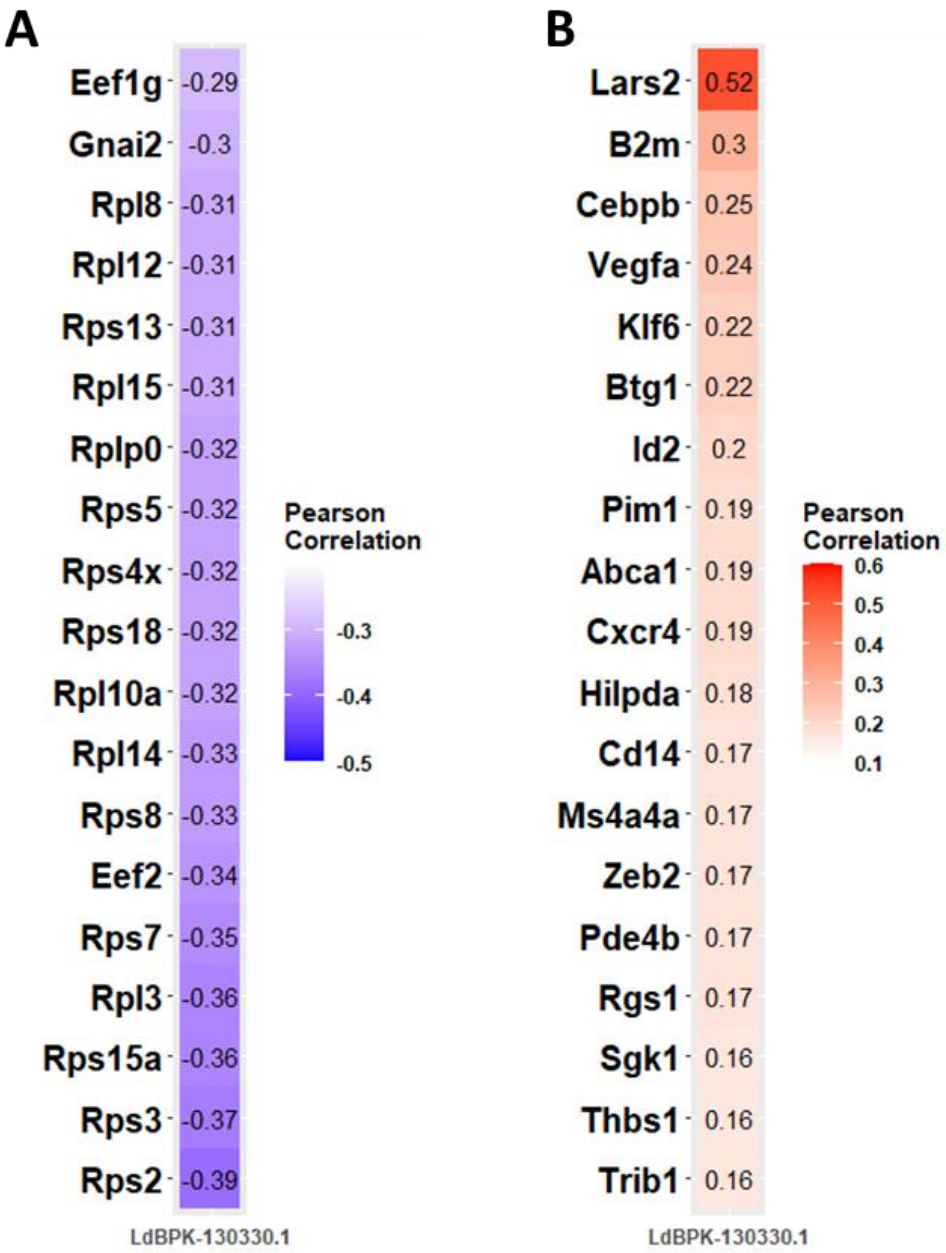

Figure 4.21. Top 20 genes positively and negatively correlating with *LdBPK-130330.1* expression. WT Ld+ BMDMs were subset from the dataset, and Pearson correlation coefficients were calculated for each gene. Gene correlations were then ranked and plotted on heatmaps to show the top 20 negatively **(A)** and positively **(B)** correlating genes. Pearson correlation coefficients are shown for each gene.

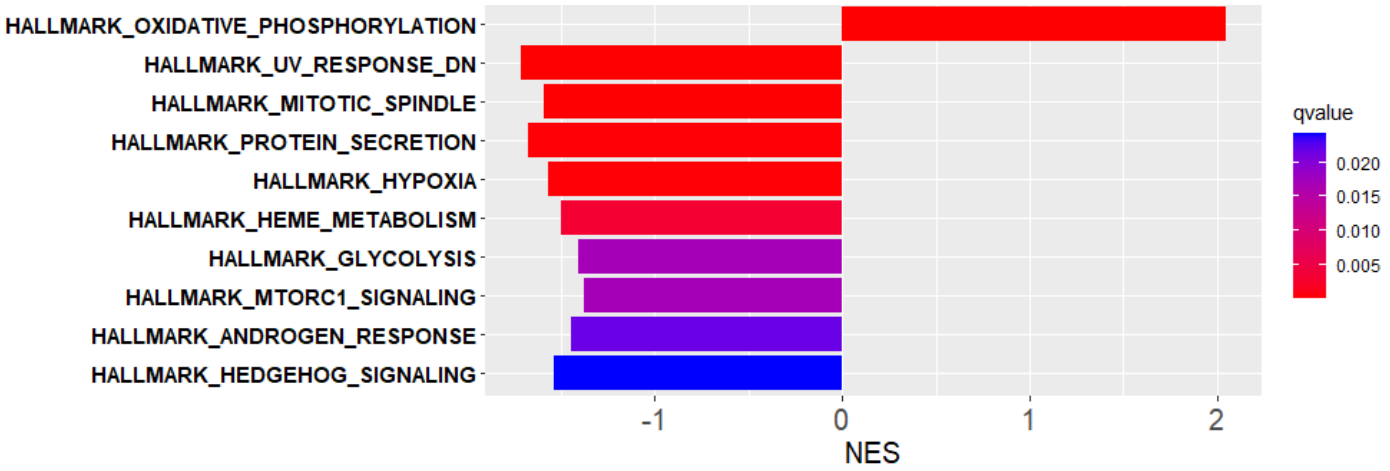

Figure 4.22. Pseudobulk GSEA analysis of KO Infected vs WT Infected samples. Gene expression data for all cells in each sample was averaged, and DGE analysis was performed. Significantly deregulated genes (FDR<0.05, log2FC<0 or >0) were submitted to GSEA analysis. The top ten significantly deregulated gene sets are shown. NES = Normalised Enrichment Score.

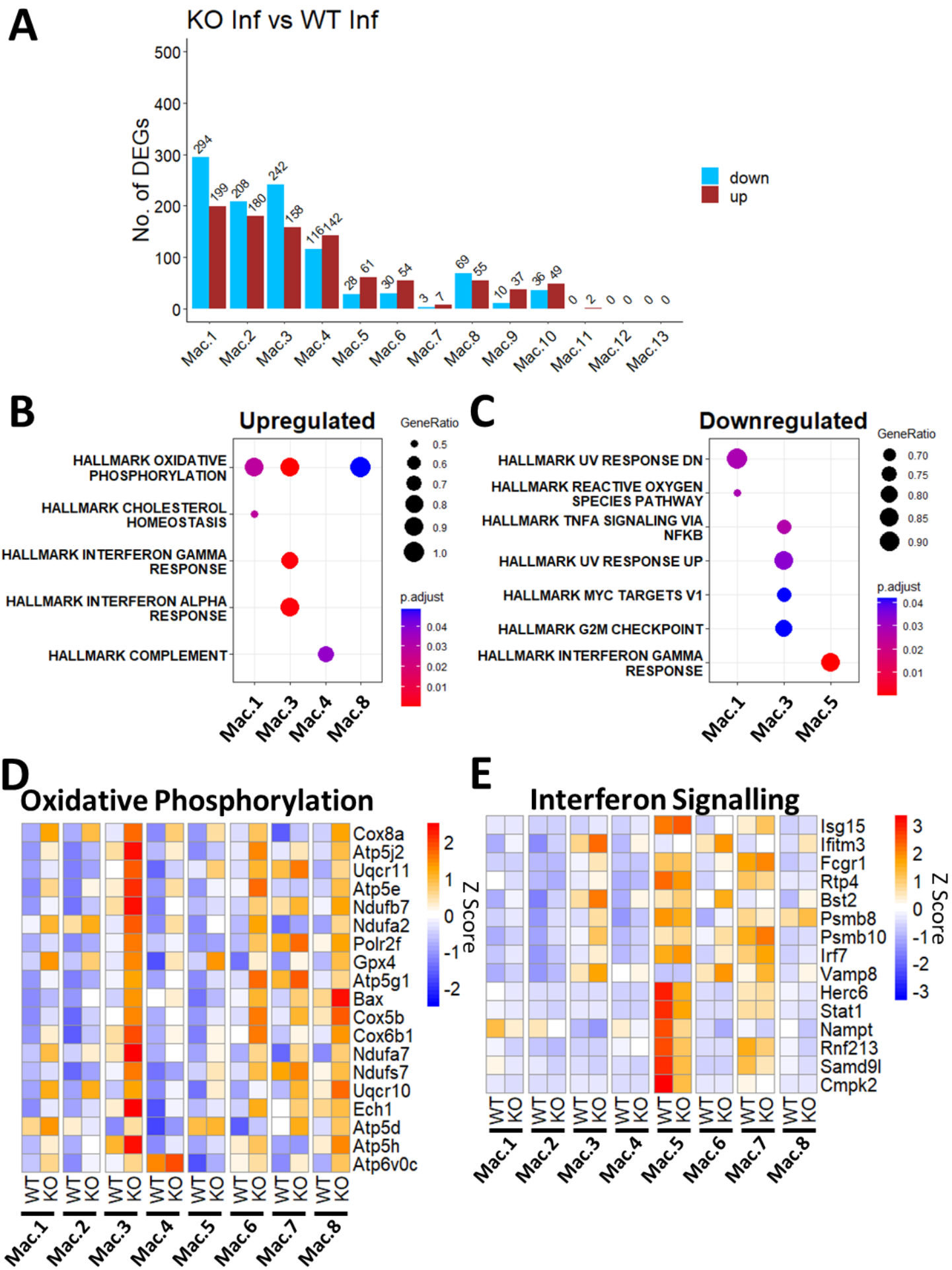
A
KO Inf vs WT Inf
No. of DEGs
down
up
Mac.1
Mac.2
Mac.3
Mac.4
Mac.5
Mac.6
Mac.7
Mac.8
Mac.9
Mac.10
Mac.11
Mac.12
Mac.13
B
Upregulated
GeneRatio
p.adjust
HALLMARK OXIDATIVE PHOSPHORYLATION
HALLMARK CHOLESTEROL HOMEOSTASIS
HALLMARK INTERFERON GAMMA RESPONSE
HALLMARK INTERFERON ALPHA RESPONSE
HALLMARK COMPLEMENT
C
Downregulated
HALLMARK UV RESPONSE DN
HALLMARK REACTIVE OXYGEN SPECIES PATHWAY
HALLMARK TNFA SIGNALING VIA NFKB
HALLMARK UV RESPONSE UP
HALLMARK MYC TARGETS V1
HALLMARK G2M CHECKPOINT
HALLMARK INTERFERON GAMMA RESPONSE
D
Oxidative Phosphorylation
Cox8a
Atp5j2
Uqcr11
Atp5e
Ndufb7
Ndufa2
Polr2f
Gpx4
Atp5g1
Bax
Cox5b
Cox6b1
Ndufa7
Ndufs7
Uqcr10
Ech1
Atp5d
Atp5h
Atp6v0c
Z Score
WT
KO
E
Interferon Signalling
Isg15
Ifitm3
Fcgr1
Rtp4
Bst2
Psmb8
Psmb10
Irf7
Vamp8
Herc6
Stat1
Nampt
Rnf213
Samd9l
Cmpk2

Figure 4.23. *Trim24* deletion favours immunoregulatory energy metabolism shift and upregulation of interferon gene signature. (A) Number of up- and down-regulated DEGs detected per cluster between KO Infected (KO Inf) and WT Infected (WT Inf) BMDMs (FDR<0.05, log2FC <0 or >0). GSEA was then performed on DEGs for each cluster, and the top up- **(B)** and down-regulated **(C)** gene sets are shown. Heatmaps for the first eight clusters showing average expression of differentially expressed genes within the gene sets for Oxidative Phosphorylation **(D)** and Interferon (gamma and alpha) Signalling **(E)**.

Chapter 5. Characterisation of *L. donovani* infection in *Trim24*$^{-/-}$ mice

5.1. Introduction

Established mouse models of *Trim24*-deletion have been generated on the C57BL/6 background with slight variations on the type of knockout mouse (Khetchoumian et al. 2007; Jiang et al. 2015). Knockout strategies in these studies used the Cre-*loxP* approach to disrupt the TRIM24 genes. Khetchoumian et al. used a targeting vector that introduced *loxP* sites either side of exon 4, resulting in the deletion of exon 4 after Cre-*loxP* recombination via CMV-Cre deleter mice (Khetchoumian et al. 2007). The subsequent frameshift mutation resulted in a premature stop codon and expression of a mutant TRIM24 protein that lacked the whole C terminus and part of the N terminal RBCC domain. Thus, transcription and translation of the *Trim24* gene still occurred, but resulted in a non-functional TRIM24 protein in all tissues (Khetchoumian et al. 2007).
Jiang et al. generated a TRIM24 knockout (KO) mouse in which the transcriptional start site and exon 1 of the *Trim24* gene were targeted and excised through Cre-*loxP* recombination, leading to complete abrogation of *Trim24* gene transcription and all three of its potential protein-coding isoforms (Jiang et al. 2015). This group also investigated potential compensatory mechanisms resulting from *Trim24* deletion. TRIM28 and TRIM33 (the other two members within the same TRIM sub-family as TRIM24), are structurally similar to TRIM24 by their possession of a C-terminal PHD-Bromodomain (Rajsbaum et al. 2014). Previous data has shown that these three TRIMs form complexes that contribute to hepatocellular carcinoma (HCC) control (Herquel et al. 2011). Complexes with TRIM24 and TRIM33 were the most abundant, but complexes with all three (TRIM24, TRIM33, and TRIM28) were also found (Herquel et al. 2011). Inactivation of any of these three TRIMs led to HCC formation, and TRIM24 inactivation led to loss of TRIM33 further contributing to HCC progression (Herquel et al. 2011). Therefore, deletion of *Trim24* could lead to compensatory mechanisms through altered expression of TRIM28 and/or TRIM33. This was investigated by Jiang et al., who showed that deletion of *Trim24* did not affect the expression levels of the other two TRIM members within the same TRIM sub-family, TRIM28 and TRIM33, deducing that compensatory mechanisms for TRIM24 deletion were unlikely (Jiang et al. 2015).

Characterisation of KO B6 mice has focused on liver pathology, as TRIM24 is aberrantly expressed in HCC (Jiang et al. 2015; Liu et al. 2014; Zhu et al. 2018; Herquel et al. 2011). Total *Trim24* deletion (via exon 1 excision) led to spontaneous development of HCC as early

as 10 weeks of age, showing increased expression of matrix metalloproteinase and collagen genes in the liver at 10 weeks and lipid-filled lesions that exacerbate with age (Jiang et al. 2015). Fibrosis-related inflammatory genes were also upregulated in KO livers in 2-month-old mice (Jiang et al. 2015). Hepatocyte-specific knockout of TRIM24 led to a similar phenotype (Jiang et al. 2015). However, these KO mice have not yet been immunologically characterised on a single leukocyte-type level. Furthermore, other immune organs such as spleen, bone marrow (BM) and lymph nodes, which are important during VL have had limited to no immunological characterisation.

Mixed BM chimeric mice are a useful tool to screen for intrinsic defects in genetically modified cells, as they allow for the investigation of both genetically altered and control cells exposed to the same environment within the same mouse (Ferreira et al. 2019). Furthermore, using WT recipient mice allows for the restriction of chimerism to the haematopoietic system. Haematopoietic cells are among the cells most sensitive to radiation (Kato et al. 2013; Guo et al. 2015), and so a lethal dose of radiation (1100 rads) can destroy the haematopoietic system while leaving non-haematopoietic cells and tissues intact. Thus, reconstitution of a mixture of WT and genetically modified BM cells into an irradiated WT recipient mouse restricts the genetic modification to haematopoietic lineages. An example of this is in a study performed by Codarri et al., in which they engrafted either WT T cells, T cells deficient in *Il12rb1* (unable to respond to IL-12 or IL-23) or *Il12rb2* (unable to respond to IL-12 alone) to investigate roles of these cytokines in the production of GM-CSF by Th1 and Th17 cells during experimental autoimmune encephalomyelitis (EAE) (Codarri et al. 2011). They found IL-12 (and IFNγ) to be potent negative regulators of GM-CSF production by T helper cells while IL-23 stimulated GM-CSF production, exacerbating EAE pathogenesis.

The bone marrow chimera approach has been used to study the role of TRIM24 previously. Perez-Lloret et al. used 50:50 WT:*Trim24-/-* mixed BM chimeras to show no intrinsic defects in steady state T cell populations (Perez-Lloret et al. 2016). However, this group did not look further into other leukocyte populations that may be affected by absence of TRIM24, and also did not investigate tissues other than spleen (Perez-Lloret et al. 2016). This study did demonstrate a role for TRIM24 in the regulation of IL-1R expression on Th2 cells during *Heligmosomoides polygyrus* infection, showing decreased IL-1R expression on *Trim24*$^{-/-}$ Th2 cells, leading to impaired release of IL-5, IL-13, and IL-10 from *Trim24*$^{-/-}$ Th2 cells in response to infection (Perez-Lloret et al. 2016).

As discussed in **Chapter 1**, TRIM24 (along with IL-10R) has previously been identified as an IPA-predicted upstream negative regulator of genes with enhanced mRNA abundance during *Leishmania* infection. Briefly, transcriptional analysis of splenic tissue in *L. donovani-*

infected BALB/c mice led to the identification of TRIM24 as an potential upstream negative regulator based on the enhanced mRNA abundance of 41 inflammatory genes, including *Stat1, Irf1, Irf7,* and *Cxcl10* (Ashwin et al. 2018). TRIM24 was also predicted to be inhibited in blood endothelial and lymphatic endothelial cells in ear samples from 4-week *L. major*-infected B6 mice, based on 12 and 13 target genes, respectively (Venugopal et al. 2022). Interestingly, TRIM24 was not predicted to be inhibited in macrophages in this study (Venugopal et al. 2022). Transcriptional profiling of *L. donovani*-infected BM-derived macrophages *in vitro* also predicted TRIM24 to be inhibited in macrophages infected with *L. donovani* promastigotes, but not amastigotes (Chaparro et al. 2022), indicating the importance of considering the life stage of *Leishmania* parasites in these experiments. While TRIM24 has been identified as a predicted regulator in these various *in vivo* and *in vitro Leishmania* infection studies, thus far none of these studies have investigated the roles TRIM24 may play during *Leishmania* infection.

5.2. Chapter Aims

- To immunologically characterise KO immune organs important for *L. donovani* infection (spleen, inguinal lymph nodes, BM).

- To utilise the mixed BM chimera system to:
    - Determine relative fitness of KO vs WT leukocyte populations during reconstitution in peripheral blood.
    - Investigate defects of KO leukocytes in liver, spleen, inguinal lymph nodes, and BM in mixed BM chimeras at the steady state and during *L. donovani* infection.

- To determine effects of global TRIM24 deletion on outcome of *L. donovani* infection with respect to parasite burden and cytokine profiles of T cells, monocytes, macrophages, and neutrophils.

5.3. Results

5.3.1. TRIM24 is dispensable for leukocyte development *in vivo*

To immunophenotype KO mice, we harvested spleen, liver, inguinal lymph nodes, and BM, and performed multi-parameter flow cytometry to assess leukocyte numbers in KO and WT mice at the steady state. Cell IDs and marker definitions are listed in **Table 5.1** and the gating strategy is shown in **Figure 5.1**; our antibody panel allowed for the detection of $CD4^+$ ($TCR\beta^+$ $CD4^+$), $CD8^+$ ($TCR\beta^+$ $CD8^+$) and γδ T cells ($TCR\beta^-$ $TCR\gamma\delta^+$), B cells ($B220^+$ $CD19^+$), NK cells ($NK1.1^+$), and myeloid cell populations including dendritic cells (DCs; $CD11c^+$ $MHC^{lo/int/hi}$; $CD11c^+$ $MHCII^-$ cells could also be NK cells (Maroof et al. 2008)), neutrophils ($CD11b^+$ $Ly6C^+$ $Ly6G^+$), monocytes ($CD11b^+$ $Ly6C^{hi/int}$, $Ly6G^-$), and macrophages ($CD11b^+$ $Ly6C^{hi}$ $F4/80^+$). Immunoregulatory 'M2' macrophages were also identified by detection of the mannose receptor CD206 (Xu et al. 2020).

The spleen contained the highest total number of immune cells compared with the other tissues with the exception of BM. In both WT and KO, the majority of the leukocyte population consisted of $CD4^+$ and $CD8^+$ T cells, and B cells (which represented the largest compartment within the spleen) (**Figure 5.2A**). In both WT and KO mice respectively, we detected small numbers of γδ T cells and NK cells (~$1x10^5$), and small but varying numbers of myeloid cell populations, notably DC populations (2-$4x10^5$), neutrophils (~$3x10^5$ each), and macrophages (~$1x10^5$) (**Figure 5.2A**).
In the liver, again the most abundant leukocytes were the B cells (~$2x10^5$), which were closely followed by $CD4^+$ T cells ($1x10^5$) and $CD8^+$ T cells (4-$7x10^4$) (**Figure 5.2B**). We observed ~$2x10^4$ double negative T cells ($CD4^-$ $CD8^-$), and ~$1x10^4$ γδ T cells (**Figure 5.2B**). In the myeloid cell populations, we saw a similar number of MHCII- DCs as $CD8^+$ T cells (4-$6x10^5$), and 1-$4x10^4$ of each of the remaining detected myeloid cell populations (**Figure 5.2B**).
The inguinal lymph nodes consisted almost entirely of T cells ($CD4^+$ and $CD8^+$) and B cells (consistent with previous data), with ~$2x10^5$ of each population present. Of the other populations, we detected ~$1x10^4$ $CD4^-$ $CD8^-$ T cells and γδ T cells, and no NK cells were detected. Of the myeloid cell populations, we detected mostly DC subsets. Few macrophages were detected, and almost no monocytes were detected (**Figure 5.2C**).
In the BM, the majority of cells detected were myeloid-derived, with neutrophils being the most abundant cell type (~$2x10^7$ out of a total of $6.48x10^7$ cells). Macrophages and

monocytes were also detected in abundance (2-3x10^6), and conventional dendritic cells (cDC) and plasmacytoid dendritic cells (pDC) were also detected (**Figure 5.2D**).

Interestingly, we did not identify any differences in proportions or absolute numbers of leukocytes in liver, spleen, BM or inguinal lymph nodes in KO compared to WT mice. To note, there was a population of uncharacterised cells identified in all tissues tested in both WT and KO mice that were negative for all makers in our flow cytometry panel. As we did not include CD45 in our flow cytometry panel as a pan-leukocyte marker, these cells could be stromal cells or other non-immune cells present in each tissue. Taken together, these results indicate that TRIM24 is dispensable for immune cell development at the steady state.

5.3.2. Experimental design of mixed BM chimera generation

Having observed no differences in leukocyte counts in KO immune organs compared to WT, we sought to determine if KO leukocytes possess any intrinsic defects in their reconstitution fitness compared to WT cells at the steady state, and intrinsic defects that may impact progression of *L. donovani* infection (e.g. alterations in cytokine production). To answer this question, we generated 50:50 mixed BM chimeras to track relative fitness of KO leukocyte types compared to WT during immune cell reconstitution over 8-10 weeks (**Figure 5.3**). A 50:50 mixture (confirmed by flow cytometry; **Figure 5.4**) of BM cells from CD45.1^+ B6.WT and CD45.2^+ B6.KO donor mice was injected into lethally irradiated CD45.1^+ B6.WT recipient mice. The WT:KO ratio of the injection BM cell mixture was confirmed by detection of CD45.1 and CD45.2 by flow cytometry (**Figure 5.3**). Recipient mice were left for 4 weeks to allow HSC engraftment and initiation of leukocyte reconstitution. Following this, peripheral blood was taken via tail bleed every two weeks from four weeks post-reconstitution (p.r.) and analysed by flow cytometry to assess rate of leukocyte reconstitution. At 8-10 weeks p.r., mixed BM chimeric mice were infected with 3x10^7 *L. donovani* amastigotes. At 14 (d14) and 28 (d28) days post-infection, chimeric mice were sacrificed and liver, spleen, BM (two femurs and two tibias per mouse), and inguinal lymph nodes were harvested for flow cytometric analysis (**Figure 5.3**).

5.3.3. Skew towards KO cells in peripheral blood during reconstitution

Firstly, at 4, 6, 8, and 10 weeks p.r., blood was taken and flow cytometry was used to identify relative proportions of WT (CD45.1^+ CD45.2^-) and KO (CD45.1^- CD45.2^+) leukocytes. We

identified no difference in the proportion of KO and WT leukocytes in peripheral blood at 4 weeks p.r. (both populations represented 50% of all $CD45^+$ cells) (**Figure 5.5**). Between 4 and 8 weeks p.r., we observed a steady increase in the proportion of KO cells (48.8% → 57% → 66.5%) and simultaneous decline in proportion of WT cells (50.4% → 42.2% → 35.2%) (**Figure 5.5**). Between 8 and 10 weeks the skew towards KO cells increased further but at a reduced rate compared to 4-8 weeks p.r. (64.2% → 66.3%) (**Figure 5.5**). This data indicates an intrinsic competitive advantage of KO cells compared to WT cells during reconstitution.

5.3.4. Relative fitness of lymphocyte populations within observed KO skew in peripheral blood

Next, we investigated leukocyte subtypes that make up the observed skew to check if TRIM24 deletion resulted in a cell type-specific intrinsic advantage compared to WT cells. Thus, we performed multi-parameter flow cytometry on peripheral blood at 4, 6, 8, and 10 weeks p.r. to identify leukocyte subtypes within the $CD45.1^+$ WT and $CD45.2^+$ KO populations. The gating strategy is shown in **Figure 5.6**, and cell marker identities are shown in **Table 5.2**.

Within WT $CD45^+$ cells the proportion of $CD4^+$ and $CD8^+$ T cells remained consistent at ~9% between 4 and 10 weeks p.r., showing no significant difference between any of the timepoints (**Figure 5.7A&B**). The proportions of KO $CD4^+$ and $CD8^+$ T cells were significantly lower than that of WT T cells at 4 weeks p.r. (2% KO $CD4^+$ T vs 9% WT $CD4^+$ T, and 2% KO $CD8^+$ T vs 7% WT $CD8^+$ T) (**Figure 5.7A&B**) and, in contrast to WT, the KO $CD4^+$ T cells showed a gradual increase in proportion from 4-10 weeks p.r. (4wks = 2.9% → 6wks = 6.6% → 8wks = 9.2% → 10wks = 14.3%) (**Figure 5.7A**). A similar effect was also observed in KO $CD8^+$ T cells, though the proportional increase was slightly delayed, only showing statistically significant increases between 8 and 10 weeks p.r. (**Figure 5.7B**). By week 8, the proportions of $CD4^+$ T and $CD8^+$ T cells were not different between WT and KO populations ($CD4^+$ T: KO 14.3% vs WT 10.1%; $CD8^+$ T: KO 8.9% vs WT 8.1%) (**Figure 5.7A&B**).

At 4 weeks, B cell proportions were comparable between WT and KO populations (11.5%) (**Figure 5.7C**). However, by 6 weeks there was a clear competitive advantage of KO B cells over WT (16.3% vs 9.9%). We observed a gradual decrease of B cell proportions in the WT population from 4-10 weeks p.r. (12.5% → 9.9% → 7.7% → 5.1%) along with the

simultaneous gradual increase in the KO B cell proportions between 4 and 8 weeks p.r. (11.5% → 16.4% → 20.5%) (**Figure 5.7C**). The proportion of KO B cells appeared to peak at 8 weeks p.r. (20.5%), and there was a decrease from 8-10 weeks p.r. (20.5% to 17.5%), though this was not significant (**Figure 5.7C**).

The proportion of WT NK cells remained constant at 0.9% from 4-10 weeks p.r. (**Figure 5.7D**). The KO NK cell proportion remained consistent from 4-8 weeks p.r., remaining at ~2.5% from 4-8 weeks p.r. and increasing to 4.1% by 10 weeks (**Figure 5.7D**). There was a significantly higher proportion of KO NK cells than WT at every time point p.r., indicating a potential intrinsic competitive advantage of KO NK cells compared to WT NK cells (**Figure 5.7D**).

5.3.5. Relative fitness of myeloid populations within observed KO skew in peripheral blood

Our flow cytometry panel allowed us to identify several different myeloid cell types. We were not able to detect any $CD11c^+$ $MHCII^+$ dendritic cells. However, we identified several myeloid cell types using a combination of CD11b, Ly6G, Ly6C, and F4/80 (**Table 5.2**). Neutrophils ($CD11b^+$ $Ly6C^{int}$ $Ly6G^+$) made up 25.3% of myeloid cells in the peripheral blood at 4 weeks p.r. (**Figure 5.8A**). Neutrophil proportions declined over time between 4 and 8 weeks p.r. in both the WT and the KO populations (WT: 8.7% → 5.1% → 3.2%; KO: 16.6% → 13.1% → 8.4%), and remained stable between 8-10 weeks p.r. (WT 3.4%, KO 11%) (**Figure 5.8A**). Across all time points, the proportion of KO neutrophils was significantly higher than that of WT (4 wks = 17% vs 8%; 6 wks = 14% vs 5%; 8 wks = 8% vs 3%; 10 wks = 10% vs 3%) (**Figure 5.8A**), indicating a competitive advantage for KO over WT neutrophils.

Monocytes were also detectable through their expression of Ly6C and F4/80. A $Ly6C^{hi}$ population of $CD11b^+$ cells was observed (**Figure 5.6**), which is a characteristic of inflammatory monocytes (Kratofil et al. 2017). These cells were also $F4/80^{hi}$, a marker for macrophages, though it is also expressed on monocytes (**Figure 5.6**). Therefore, we designated these cell inflammatory monocytes/macrophages. These also started at a higher proportion for KO at 4 weeks p.r. (1.5% WT and 3% KO) and declined over time to reach the lowest proportion at 10 weeks p.r. (<0.5% WT and 1.9% KO). This gradual decline was not significant between the fortnightly time points, but was significant when comparing week 4 to week 10 p.r. in both WT and KO populations (**Figure 5.8D**). While the general decline was seen in both genotype pools for this cell type, the proportion of KO cells was significantly higher than WT at all time points p.r. (**Figure 5.8D**).

We also saw a population of intermediate monocytes (which also have inflammatory characteristics), expressing Ly6C to a lesser degree than in inflammatory monocytes (Yang et al. 2014), and not expressing F4/80 (**Figure 5.6**). The proportion of WT intermediate monocytes remained consistent at ~1% throughout the reconstitution period (**Figure 5.8C**). In the KO pool, the proportion increased between weeks 4 and 6 p.r. (2.3% to 3.3%), but by week 10 p.r. this had returned to the level of week 4 p.r. (2.2%) (**Figure 5.8C**). There was a significantly higher proportion of KO intermediate monocytes compared to WT across all time points p.r. (4 wks = 2.3% vs 0.9%; 6 wks = 3.3% vs 0.9%; 8 wks = 2.9% vs 0.6%; 10 wks = 2.2% vs 0.2%) (**Figure 5.8C**).

A population of $CD11b^{+}$ $Ly6C^{-}$ $F4/80^{-}$ monocytes was observed (**Figure 5.6**), characteristic of patrolling monocytes which have more of a role in tissue repair (Yang et al. 2014). The proportion of WT patrolling monocytes remained consistent from weeks 4-8 p.r. (3.1%), and decreased from 8-10 p.r. (3.1% → 1.4%) (**Figure 5.8B**). The proportion of KO patrolling monocytes also remained mostly consistent, though there was an increase in proportion between weeks 6-8 p.r. (2.7% → 4.1%), which then decreased again to 2.7% at week 10 p.r. (**Figure 5.8B**). There was a significantly higher proportion of WT patrolling monocytes than KO at week 4 p.r. (3.3% vs 1.9%), however no significant difference was observed for the remaining time points (**Figure 5.8B**).

We also detected $Ly6C^{+}$ cells that were negative for all other markers in our panel (**Figure 5.6**). These could represent γδT cells, as they are known to express Ly6C (Wiesheu et al. 2020), though we did not include an antibody for TCRγδ in this panel so this would need to be confirmed. There was no difference in proportion of these cells in the WT pool across the reconstitution period (consistent at ~0.15%), whereas their proportion in the KO pool gradually increased (4wks = 0.12% → 6wks = 0.19% → 8wks = 0.22% → 10wks = 0.32%), showing a significantly higher proportion compared to WT by week 10 p.r. (0.3% vs 0.15%) (**Figure 5.8E**).

Finally, we detected an uncharacterised population within each genotype pool that were $CD45^{+}$ but negative for all other markers tested in this panel (**Figure 5.6**). Further analyses are needed to identify these cells beyond their expression of CD45. These uncharacterised cells were not significantly different in their proportions between WT and KO at weeks 4 and 6 p.r. (remaining at ~0.4%) (**Figure 5.8F**). However, from week 6 p.r. we observed an increase of these cells in the KO pool (6wks = 0.54 → 8wks = 0.8% → 10wks = 0.8%),

resulting in significantly more KO than WT cells at weeks 8 and 10 p.r. (0.8% vs 0.2%) (**Figure 5.8F**).

Taken together, the results shown in sections **5.4** and **5.5** show an intrinsic competitive advantage of KO cells compared to WT cells in reconstitution of myeloid cells, NK cells, and B cells. Interestingly, T cell proportions were decreased in the KO population in early stages of reconstitution, but were not significantly different by the end point of this experiment.

5.3.6. Intrinsic advantages of KO leukocytes persist during *L. donovani* infection in a tissue-specific manner

After the observation of a skew towards KO cells in the peripheral blood from 4 weeks p.r., we explored the possibility of tissue-specific differences in the skew towards KO cell populations, and assessed intrinsic competitive advantages of KO leukocytes compared to WT leukocytes in a tissue-specific manner during *L. donovani* infection. Leukocyte populations reconstitute at different rates after engraftment. Auletta and colleagues showed that it takes two months for the splenic immune cell compartment to return to baseline levels (Auletta et al. 2004). Importantly, most immune cell types 'overshoot' their reconstitution in the initial stages of reconstitution, with reconstitution of dendritic cells, macrophages, and polymorphonuclear cells occurring within the first week, followed by B cells and NK cells. Finally, T cells reconstitute last, at 4-8 weeks p.r. (Auletta et al. 2004), consistent with our data on peripheral blood.

We sacrificed mixed BM chimeric mice infected or not with *L. donovani* for 14 or 28 days and measured parasite burden by counting Leishman Donovan Units (LDU). Consistent parasite burden was confirmed from d14- and d28-infected liver and spleen samples (**Figure 5.9B**). Increases in liver and spleen organ weight also increased during infection (**Figure 5.9A**). We sacrificed naive, d14- and d28-infected chimeras and performed flow cytometry on BM, spleen, liver, and inguinal lymph nodes to detect WT ($CD45.1^+$) and KO ($CD45.2^+$) leukocytes.

Firstly, comparing the total WT ($CD45.1^+$) and KO ($CD45.2^+$) cell populations, we observed 65-70% KO in $CD45^+$ cells in the liver, spleen, and inguinal lymph nodes compared to 35-40% WT leukocytes (**Figure 5.10**). This data was consistent with the ratio of KO:WT leukocytes observed in the peripheral blood.
Strikingly, we observed a much more significant skew towards KO leukocytes in the BM, with more than 80% of $CD45^+$ BM cells deficient in TRIM24 (**Figure 5.10**). Upon infection, an

interesting effect was observed in the liver, where the skew in favour of KO cells reduced as the infection progressed, resulting in a 1:1 mixture of WT:KO cells at d28 (**Figure 5.10**). This was also seen in the spleen to a lesser extent, and there were still significantly more KO cells in the spleen at d28 (**Figure 5.10**). In the inguinal lymph nodes and the BM, the ratio of WT:KO cells was maintained at 35:65 and 20:80, respectively (**Figure 5.10**).

Next we sought to identify changes in immune cell composition in the liver, spleen, and BM that occur during *L. donovani* infection, and to elucidate any effects of *Trim24* deletion on cell composition. In all three tissues, we saw increases in the number of $CD4^+$ T cells as the infection progressed in both WT ($CD45.1^+$) and KO ($CD45.2^+$) populations (**Figure 5.11A**). However, we saw comparable numbers of WT and KO $CD4^+$ T cells at each time post-infection measured here (**Figure 5.11A**). $CD8^+$ T cell number increased significantly from Naive to d14, and then further from d14 to d28 in the liver ($4.75x10^5 \rightarrow 1.69x10^6 \rightarrow 3.73x10^6$) (**Figure 5.11B left**). In the spleen, we also saw increases in $CD8^+$ T cell numbers in WT ($2.42x10^6 \rightarrow 4.65x10^6 \rightarrow 7.59x10^6$) and KO ($3.9x10^6 \rightarrow 6.4x10^6 \rightarrow 7.4x10^6$) populations as infection progressed, however this was a smaller increase with statistical significance only seen between WT Naive and WT d28 ($7.59x10^6$ vs $2.42x10^6$). Despite this, we still did not see any differences in the numbers of WT and KO $CD8^+$ T cells at any time point (**Figure 5.11B middle**). In the BM, the numbers of $CD8^+$ T cells remained fairly consistent throughout the infection, with no change in numbers of WT or KO $CD8^+$ T cells between naive and d14 samples ($4.1x10^5$ vs $3.7x10^5$). We saw a significant increase in WT $CD8^+$ T cell number from d14 to d28 ($7x10^5$ vs $4.1x10^5$), which was not seen in the KO populations, however we saw no significant difference when comparing WT and KO $CD8^+$ T cell numbers at any time point in the BM (**Figure 5.11B right**).

We saw tissue-specific effects on B cell number during infection. In the liver and the spleen we saw no significant elevation of KO B cell numbers in naive chimeras compared to WT (**Figure 5.11C left**). Upon *L. donovani* infection, we saw significant expansion of B cells in the liver (**Figure 5.11C left**) and the spleen (**Figure 5.11C middle**) in WT and KO populations in naive vs d28. We saw no difference in WT and KO B cell numbers at each time point in the liver or the spleen (**Figure 5.11C left & middle**). In the BM, there were almost five times more KO than WT B cells in naive chimeras ($4.7x10^6$ vs $8.3x10^5$) (**Figure 5.11C right**). Upon *L. donovani* infection, we saw a marked reduction in the number of B cells, which halved by d14 (WT: $8.3x10^5 \rightarrow 4.9x10^5$; KO: $4.7x10^6 \rightarrow 3.2x10^6$) and reduced even further by d28 (**Figure 5.11C right**). This was observed in both WT and KO populations (WT: d14 = $4.9x10^5$ → d28 = $3.6x10^5$, KO: d24 = $3.2x10^6$ → d28 = $7.9x10^5$).

While there were significantly more KO B cells in naive and d14 mice compared to WT, by d28 the numbers of WT and KO B cells were comparable (**Figure 5.11C right**).

In the NK cells population, we saw similar numbers of WT NK cells in the liver, spleen, and BM (~$1x10^5$) (**Figure 5.11D**). Interestingly, *L. donovani* infection did not appear to affect the numbers of WT NK cells in any of the tissues measured here, as we saw no change in the WT NK cell number at any time point in any tissue (**Figure 5.11D**). In contrast, we did see effects of *L. donovani* infection in KO NK cells in a tissue-specific manner. In the liver, we saw comparable WT and KO NK cell numbers in naive chimeras, however upon infection the number of KO NK cells increased significantly by d14 ($1.8x10^5 \rightarrow 6.4x10^5$) (**Figure 5.11D left**). This time point appeared to be the peak of the NK cell expansion, as the numbers then reduced from d14 to d28 to a similar number as naive chimeras ($3.1x10^5$) (**Figure 5.11D left**). This effect was also seen in the spleen, with a significant increase in KO NK cell number between naive and d14 chimeras ($4.3x10^5 \rightarrow 8.9x10^5$), which then reduced (albeit not statistically significantly) by d28 to $5.5x10^5$ (**Figure 5.11D middle**). There were more KO than WT NK cells in the spleen in d14 ($8.9x10^5$ vs $1.8x10^5$) and d28 ($5.5x10^5$ vs $1.3x10^5$) chimeras (**Figure 5.11D middle**).

We also saw infiltration and expansion of myeloid cell populations during *L. donovani* infection. Amongst WT $CD45.1^+$ cells, we observed low numbers of cDCs in naïve mice in all tissues studied (**Figure 5.12A**). Upon infection, the number of cDCs did not increase significantly in the liver or spleen (**Figure 5.12A left and middle**). In the BM, the trend observed in spleen and liver was significant at d28 p.i. (**Figure 5.12A right**). *L. donovani* infection significantly increased the numbers of KO cDCs compared to naïve in all three tissues with the increase delayed in BM (**Figure 5.12A**).

We saw low numbers of WT and KO inflammatory macrophages in naive chimeras in the liver and spleen, with no difference between KO and WT populations (**Figure 5.12B left & middle**). In contrast, the BM possessed more inflammatory macrophages in naive chimeras (~$3x10^6$) compared to liver and spleen, and KO inflammatory macrophages were five-fold more abundant than WT ($2.5x10^6$ KO vs $5x10^5$ WT) (**Figure 5.12B right**). *L. donovani* infection induced recruitment and expansion of inflammatory macrophages in the liver and spleen (**Figure 5.12B left & middle**). KO inflammatory macrophage numbers significantly increased in d14 vs naive chimeras and remained at this higher level at d28 (**Figure 5.12B left & middle**). Importantly, there were more KO inflammatory macrophages recruited to the liver and spleen during *L. donovani* infection than WT. *L. donovani* infection did not affect BM inflammatory macrophage numbers, however there were more KO inflammatory

macrophages compared to WT in the BM at all time points (~2.5x10^6 vs ~0.5x10^6) (**Figure 5.12B right**).

We saw different total numbers of neutrophils in the liver (~1.5x10^5 in total), spleen (~1x10^6 in total), and the BM (1.2x10^7 in total) in naive chimeras (**Figure 5.12C**). There were more KO than WT neutrophils in the naive liver (1.28x10^5 vs 3.5x10^4) and spleen (7.6x10^5 vs 2x10^5) (**Figure 5.12C left & middle**). However, these were not statistically significant. In the BM, there were 6.25 times more KO neutrophils than WT (1x10^7 vs 1.6x10^6) (**Figure 5.12C right**).
L. donovani infection induced a significant decrease in KO d28 BM neutrophils compared to naive, and no change in WT neutrophil numbers (**Figure 5.12C right**). In contrast, neutrophils were increased after infection in the liver and the spleen. Hepatic KO neutrophils increased significantly in d28 vs naive and d28 vs d14 (1.28x10^5 vs 3.65x10^5 vs 7.43x10^5). However, numbers of WT hepatic neutrophils did not change (**Figure 5.12C left**). In the spleen, KO neutrophils significantly expanded in the first 14 days p.i., which remained consistent at d28 (**Figure 5.12C middle**). WT neutrophil numbers also remained unchanged in the spleen during infection (**Figure 5.12C middle**).

Finally, we investigated the CD11b$^+$ Ly6C$^+$ monocyte population during *L. donovani* infection. We saw no difference in numbers of WT and KO monocytes in the liver (**Figure 5.12D left**) or the spleen (**Figure 5.12D middle**). In contrast, the BM held almost six times more KO monocytes than WT (3.6x10^6 vs 6.3x10^5) (**Figure 5.12D right**). *L. donovani* infection induced infiltration of monocytes in the liver and the spleen (**Figure 5.12D left & middle**). WT monocytes increased in number in the liver and spleen during infection, but were not statistically significant (**Figure 5.12D left & middle**). KO monocytes increased significantly in d14 vs naïve (~5x10^5 vs 1-2x10^5), and in d28 vs d14 (1x10^6 vs 5x10^5), and there were significantly more KO monocytes at d14 and d28 compared to WT (**Figure 5.12D left & middle**). Similar to inflammatory macrophages, *L. donovani* infection did not affect WT or KO BM monocyte populations (**Figure 5.12D right**).

Taken together, these results indicate a competitive advantage of KO leukocytes over WT leukocytes during *L. donovani* infection. With the exception of T cells, we observed a skew towards KO populations in most other cell types at the steady state in mixed BM chimeras. Interestingly, deletion of *Trim24* had a marked effect on the BM compared to liver and spleen, leading to 80% of cells in the BM being deficient in TRIM24. B cell, NK cell, and myeloid cell populations were responsible for this skew, while T cell populations were unaffected, indicating a potential role for TRIM24 during haematopoiesis in the BM.

In general, we saw a similar response to infection in WT and KO leukocyte recruitment and expansion, however the effect was more pronounced in KO populations, indicating a potential increased sensitivity of KO cells to recruitment or expansion signals.

5.3.7. CXCR4-CXCL12 signalling axis is not affected by deletion of *Trim24*

We next sought to understand why the skew towards KO cells was more prominent in the BM compared to other tissues. As the BM is the site of myelopoiesis, B lymphopoiesis, and NK cell development (importantly not T cell development), we hypothesised that retention and homing of leukocytes might be affected by deletion of *Trim24*. The CXCL12-CXCR4 signalling axis is important for homing to and retention of leukocytes in the BM as well as haematopoietic development, as evidenced by both CXCR4 and CXCL12 knockout mice being embryonic lethal (Ma et al. 1998). CXCR4 signalling on HSCs is also vital in the maintenance of the BM HSC pool (Sugiyama et al. 2006).

Our data showing increases in KO B cells, NK cells, and myeloid cells but importantly not T cell populations, in BM led us to hypothesise that retention of these cells in the BM after reaching maturity was affected by *Trim24* deletion. We first used flow cytometry to investigate the surface levels of CXCR4 on different cell types in the BM and in the spleen (**Figure 5.13A**). The MFI of CXCR4 was unchanged on all cell types investigated in both the BM (**Figure 5.13B; left**) and the spleen (**Figure 5.13B; right**).

Next, we sought to answer whether the sensitivity of KO cells to CXCL12 treatment was higher, resulting in increased retention in the BM. After CXCL12 treatment, CXCR4 is rapidly internalised by endocytosis. After CXCR4 is trafficked into endosomes, it is sorted into either recycling endosomes or lysosomes in a ubiquitination-dependent mechanism (Sierra et al. 2010). CXCR4 sorted into recycling $Rab11^{+}$ endosomes is then recycled back to the cell surface (Malik & Marchese 2010; Kumar et al. 2011), where it can respond to further CXCL12.

To test whether TRIM24 affects CXCR4 expression or recycling, we exposed WT and KO BMDMs to 100nM CXCL12 for 30 minutes, and measured the surface expression of CXCR4 by flow cytometry at the indicated time points after CXCL12 treatment. We also used F4/80 as a macrophage marker (**Figure 5.14A**). As expected, we saw a rapid decrease in the MFI of CXCR4 within the first 5 minutes of treatment, which continued to decrease, reaching its lowest point at 30 mins post-treatment (**Figure 5.14B**), consistent with previous data (Bamidele et al. 2015). After 30 mins post-treatment, CXCL12 was washed off, and the cells were incubated for a further 30 mins to allow for CXCR4 receptor recycling to the cell

surface. However, we saw no change in CXCR4 surface expression 30 mins after washing off CXCL12 (**Figure 5.14B**).
Comparing CXCR4 expression in WT and KO cells, we saw a slightly higher baseline expression of CXCR4 in WT BMDMs (**Figure 5.14B**). We saw rapid decrease in CXCR4 surface expression after CXCL12 treatment, but no difference in the MFI of CXCR4 at any time point post-CXCL12 treatment (**Figure 5.14B**). Taken together, these results indicate that TRIM24 does not play a role in CXCR4 surface protein expression or CXCR4 recycling after CXCL12 stimulation under the conditions tested here. More work will be required to identify the role that TRIM24 plays in the retention of BM leukocytes.

5.3.8. Cytokine production capacity of T cells is unaffected by *Trim24* deletion

There is evidence that TRIM24 regulates Th2 cell activation during the airway allergy response (Perez-Lloret et al. 2016). Therefore, we hypothesised that TRIM24 may play a role in B6 T cell responses to *L. donovani* infection.
We used a T cell-specific flow cytometry panel to investigate alterations in activation and cytokine production in restimulated WT and KO T cells from naive and *L. donovani*-infected mixed BM chimeric mice. We processed spleen, liver, and BM tissues in single cell suspensions, and stimulated the cells for 3 hours using a combination of Phorbol 12-myristate 13-acetate (PMA; directly activates protein kinase C), Ionomycin (activates Ca^{2+} signalling), and Brefeldin A (BFA; blocks cytokine secretion by reversibly disrupting the Golgi). This stimulation cocktail bypasses TCR activation and directly leads to inflammatory cytokine production (Ai et al. 2013). Cytokines accumulate in the cells due to the BFA blocking cytokine release from the cells, thereby allowing measurement of cytokine production following stimulation by intracellular flow cytometry.

Firstly, we investigated the presence of Th1 cells in the liver, spleen, and BM following *L. donovani* infection by detecting IFNγ$^+$ T-bet$^+$ CD4$^+$ T cells by flow cytometry (**Figure 5.15A**). In the naive liver, we observed ~20% of WT and KO CD4$^+$ T cells as IFNγ$^+$ T-bet$^+$ (**Figure 5.15B**), whereas in the naive spleen and the BM we detected less than 5% of WT and KO CD4$^+$ T cells expressing IFNγ and T-bet (**Figure 5.15C&D**). Upon *L. donovani* infection, the proportion of Th1 cells increased significantly in both WT and KO populations in liver, spleen, and BM at d14, and further at d28 (**Figure 5.15B-D**). The liver saw the highest proportion of Th1 cells of the three tissues studied (60% of all CD4$^+$ T cells at d28) (**Figure 5.15B**), compared to spleen (40% of all CD4$^+$ T cells) (**Figure 5.15C**), and BM (13% of all CD4$^+$ T cells) (**Figure 5.15D**). The increases in Th1 cells in all tissues was similar between

WT and KO populations at all time points. Taken together, these results show that *L. donovani* infection increases the proportions of Th1 cells in the liver, spleen, and BM, and TRIM24 does not affect this expansion.

Next, we investigated the capacity of KO $CD4^+$ and $CD8^+$ T cells to produce cytokines following infection compared to WT. Following stimulation cocktail treatment, we measured intracellular IL-4 and IL-10 as regulatory cytokines that contribute to disease progression, and IFNγ and TNF as inflammatory cytokines that contribute to infection resolution. In the liver, spleen, and BM, we observed an increase in the capacity for $CD4^+$ T cells to release IFNγ (**Figure 5.16A-D**) and TNF (**Figure 5.16E-H**) as the infection progressed. In the liver, we observed a slight decrease in the capacity for KO $CD4^+$ T cells to produce IFNγ in naïve mice (**Figure 5.16B**), however the proportion of $IFN\gamma^+$ $CD4^+$ T cells was comparable between WT and KO populations at both d14 and d28 after infection (**Figure 5.16B**). In the spleen and the BM, IFNγ-producing $CD4^+$ T cells were comparable between WT and KO populations at d0, d14, and d28, indicating that TRIM24 is dispensable for IFNγ production from $CD4^+$ T cells.

TNF expression was also investigated in $CD4^+$ T cells isolated from naïve or *L. donovani* infected mice. In the liver, the capacity for WT $CD4^+$ T cells to produce TNF remained consistent from d0 to d28 (there is a small increase at d28 compared to d0, however this was not statistically significant) (**Figure 5.16F**). In contrast, the KO population of $CD4^+$ T cells showed a significant increase in their capacity to produce TNF as the infection progressed, similar to IFNγ (**Figure 5.16F**). However, there was no significant difference between WT and KO $CD4^+$ T cells to produce TNF at any of the time points measured here (**Figure 5.16F**). We observed a similar effect in the spleen, with increases in capacity of WT $CD4^+$ T cells to produce TNF, and more significant increases in the KO population (**Figure 5.16G**). No significant difference was seen between WT and KO $CD4^+$ T cells in their ability to produce TNF at any of the time points (**Figure 5.16G**). $CD4^+$ T cells from BM showed a much stronger increase in their ability to produce TNF during infection (**Figure 5.16H**). However, consistent with the data from the liver and spleen, we saw no difference in the ability of KO $CD4^+$ T cells to produce TNF compared to WT (**Figure 5.16H**).

The ability for $CD4^+$ T cells to produce IL-4 was measured at d0 and d28 in WT and KO populations from mixed BM chimeric mice (**Figure 5.17A**). We saw small amounts of IL-4 being produced after restimulation of liver cells *in vitro* at d0 (**Figure 5.17B**). This increased at d28, though this only reached statistical significance in the KO population (**Figure 5.17B**). Despite this, no significant difference was seen between the proportion of $IL\text{-}4^+$ WT and KO

$CD4^+$ T cells in the liver (**Figure 5.17B**). In the spleen and the BM, we saw almost no IL-4-producing $CD4^+$ T cells at d0 (**Figure 5.17C&D**). At d28, we saw significant increases in the proportions of IL-4-producing $CD4^+$ T cells in the spleen and the BM in both WT and KO populations, however there was no difference between WT and KO cells in the ability to produce IL-4 (**Figure 5.17C&D**).

We also measured the ability for WT and KO $CD4^+$ T cells to release IL-10 during *L. donovani* infection in the liver, spleen, and BM (**Figure 5.17E-H**). We saw small numbers of IL-10 producing $CD4^+$ T cells at d0 in both WT and KO populations in all three tissues (**Figure 5.17F-H**). We saw a significant increase in IL-10-producing cells by d14 which occurred in all tissues but was most striking in the BM (**Figure 5.17F-H**). Interestingly, d14 marked the peak of IL-10-producing cell proportions within all three tissues; the proportion decreased slightly but not significantly in the liver and spleen between d14 and d28 (**Figure 5.17F&G**), however in the BM there was a much more striking reduction back down to basal levels at d28 in both WT and KO populations (**Figure 5.17H**). We saw no differences in the ability of KO $CD4^+$ T cells to produce IL-10 at any time point measured here compared to WT.

We also measured the ability for KO $CD8^+$ T cells to produce IFNγ and TNF in the liver, spleen, and BM. In all three tissues, we observed progressive increases in the proportions of $IFN\gamma^+$ WT and KO $CD8^+$ T cells throughout the infection period (**Figure 5.18B-D**). In the liver, the proportion of $IFN\gamma^+$ $CD8^+$ T cells increased significantly from d0 to d14, and this proportion was maintained at d28 (**Figure 5.18B**). However, in the spleen and BM we observed an initial increase in $IFN\gamma^+$ $CD8^+$ T cells from d0 to d14, and also from d14 to d28 (**Figure 5.18C&D**). We did not see any differences in the ability for KO $CD8^+$ T cells to produce IFNγ during infection in any of the tissues, however we did see a small but significant decrease in proportion of $IFN\gamma^+$ KO $CD8^+$ T cells in the spleen at the steady state (d0) (**Figure 5.18C**), indicating an initial deficit in IFNγ production that does not persist through *L. donovani* infection.
TNF production in $CD8^+$ T cells was also measured. In the liver, the proportions of TNF-producing $CD8^+$ T cells remained consistent at all three time points, with no significant differences observed between WT and KO populations (**Figure 5.18F**). Splenic $CD8^+$ T cells showed slightly higher ability to produce TNF during infection, with significant increase observed only between d0 and d28, but no change between WT and KO populations (**Figure 5.18G**). The BM displayed the largest increase in ability to produce TNF in $CD8^+$ T cells during infection, with significant increase seen from d0 to d14 and from d14 to d28 (**Figure 5.18H**). However, no change in the ability for KO $CD8^+$ T cells to produce TNF was

observed at any point compared to WT (**Figure 5.18H**). No IL-10 or IL-4 was detected in $CD8^+$ T cells (data not shown).

Taken together, these results display an enhancement of inflammatory cytokine production (IFNγ and TNF) in $CD4^+$ and $CD8^+$ T cells as a result of *L. donovani* infection which is exacerbated as the infection progresses. We also show an increase in $CD4^+$ T cells producing the regulatory cytokines IL-10 and IL-4 during *L. donovani* infection, with the peak of IL-10 production at d14. These results also indicate that TRIM24 plays little role in the production of these cytokines in T cells during *L. donovani* infection.

5.3.9. *Trim24* deletion does not impair generation of *Leishmania*-specific T cells during *L. donovani* infection

We also used a *Leishmania*-specific MHC II-specific tetramer ($I\text{-}A^b\text{-}PEPCK_{335–351}$ tetramer) to detect *Leishmania*-specific $CD4^+$ T cell responses in WT ($CD45.1^+$) and KO ($CD45.2^+$) cells from chimeric mice (Mou et al. 2015). We included this fluorochrome-conjugated $PEPCK_{335-351}$ tetramer (PEPCK) in a flow cytometry panel to detect *Leishmania*-specific $CD4^+$ T cells in our mixed BM chimeric mice that had been infected with *L. donovani* for 28 days.
After removal of cell debris, dead cells, and $CD45^-$ cells, we identified WT ($CD45.1^+$) and KO ($CD45.2^+$) leukocytes in spleen, liver, and BM cells. We then used a combination of TCRβ, CD4, CD44, and PEPCK to detect *Leishmania*-specific CD4 T cells. We successfully detected $PEPCK^+$ $CD4^+$ $TCR\beta^+$ cells in infected spleen, liver, and BM samples (**Figure 5.19A**). All $PEPCK^+$ $CD4^+$ T cells were also $CD44^+$, consistent with data generated by Mou and colleagues (Mou et al. 2015) (**Figure 5.19A**). Comparing WT and KO $CD4^+$ T cells, we did not see any differences in the proportions of $PEPCK^+$ $CD44^+$ T cells in the BM (**Figure 5.19B**), spleen (**Figure 5.19C**), or liver (**Figure 5.19D**). There also appeared to be little variation in the proportion of the $CD4^+$ T cell subset that becomes antigen experienced between the three tissues investigated here. Taken together, this indicates that TRIM24 is not required for the activation and persistence of activated T cells during *L. donovani* infection 2 and 4 weeks post-infection.

5.3.10. *L. donovani*-induced MHC-II upregulation in monocytes is not affected by *Trim24* deletion

We also investigated the effect of *Trim24* deletion on the expression of MHC-II on $Ly6C^{hi}$ monocyte/macrophages at the steady state and during *L. donovani* infection. MHC-II is

known to be strongly induced on Ly6C^{hi} monocytes during *L. donovani* infection and upon activation (Romano et al. 2021). Romano et al. also showed upregulation of MHC-II in monocytes after infection was in response to IFNγ released from T cells (Romano et al. 2021). Given previous data indicating that TRIM24 is a negative regulator of IFN signalling via the STAT1 pathway (Khetchoumian et al. 2007), we hypothesised that induction of monocyte MHC-II expression would be enhanced in KO mice during *L. donovani* infection. To test this, we sacrificed naive, d14-, and d28-infected mixed BM chimeric mice, and performed flow cytometry to detect MHC-II expression on Ly6C^{hi} monocyte/macrophages (**Figure 5.20E**) from liver, spleen, and BM.

We observed ~20% WT monocytes expressing MHC-II in the liver and the BM at d0 (**Figure 5.20F&H**), and ~40% WT monocytes expressing MHC-II in the spleen at d0 (**Figure 5.20G**). At d14 we observed a significant increase in the number of WT MHC-II^{+} Ly6C^{hi} monocytes in the liver (20% to 80%) (**Figure 5.20F**). We observed similar increases in the spleen (40% at d0 to 80%) (**Figure 5.20G**), and in the BM (20% to 50%) (**Figure 5.20H**). Further increases were observed between d14 and d28, with almost all Ly6C^{hi} monocyte/macrophages showing expression of MHC-II by d28 in the liver and spleen (**Figure 5.20F&G**), and 80% showing expression of MHC-II by d28 in BM (**Figure 5.20H**).

KO populations of Ly6C^{hi} monocyte/macrophages showed similar levels of MHC-II expression to the WT populations in all tissues studied here, with no significant difference between WT and KO MHC-II expression observed at any time point in any of the tissues studied here. Taken together, these results show that TRIM24 does not play a role in Ly6C^{hi} monocyte MHC-II expression at the steady state or during *L. donovani* infection.

5.3.11. Parasite burden after *L. donovani* infection is not affected by deletion of *Trim24*

Our previous data showed that KO macrophages had higher *Nos2* expression and released more NO after TLR4 stimulation *in vitro* (**Chapter 3.2.3.**). As iNOS and NO are essential for *L. donovani* killing (Murray et al. 2006), we hypothesised that KO mice may have an enhanced ability to control parasite burden *in vivo*. To investigate this, WT and KO (non-chimera) mice were infected with an *L. donovani* strain that constitutively expresses the enzyme firefly luciferase (strain *LV9*-RE9H). Upon injection with D-luciferin (the substrate for luciferase), parasite-specific luciferase can enzymatically react with the D-luciferin resulting in bioluminescence which can be detected (total flux) and quantified using an In Vivo Imaging System (IVIS) (Roy et al. 2000). As the parasites are the only source of luciferase in

the mouse, this results in a read out both for total parasite burden and for gross parasite localisation. After infection, mice were imaged once per week for 4-6 weeks to assess parasite burden over time (**Figures 5.21 & 5.22**).

Total flux over the whole body increased from ~10^5 photons/second (p/s) at the basal level (pre-infection) to 10^6 p/s at day 7 (**Figure 5.23A**). Most of the parasites were localised to the liver at day 7, although parasites could also be detected in the hind leg bones, indicating early infection of BM (**Figure 5.22**). Following this, a gradual increase in parasite burden in the whole body region of interest was observed until day 28 p.i. (**Figure 5.22**). Between day 7 and day 28, the parasites are mostly located in the liver and the BM, but are also detectable in the spleen. In these niches, parasites survive and proliferate, leading to increased parasite burden until day 28 (**Figure 5.22**).

While the parasite burden of the whole body appeared to remain constant from day 28 to the end point of day 46 (6 weeks), the simultaneous decline of parasite burden in the liver and increase in parasite burden in the spleen was observed (**Figure 5.22**). At day 35 p.i., there is high splenic signal in the spleen as well as the liver and BM (**Figure 5.22**).

At day 46 p.i., parasite burden was still high in the liver, and the splenic signal was also high (**Figure 5.22**). Parasite burden declined at day 46 (**Figure 5.22**), however due to our restrictions on maximum age of KO mice we were unable to track the infection any further than this point.

No significant difference in parasite burden in the total body region of interest was observed between *Trim24-/-* and WT control mice (**Figure 5.22**). Regions of interest around the liver/spleen and BM revealed no tissue-specific differences in the progression of parasite burden over time via IVIS (**Figure 5.23B&C**). Interestingly, a significant increase in hepatic parasite burden (by LDU) was observed at d29 p.i. but not at d46 in KO mice compared to WT (**Figure 5.24A**). Organ weights of d29 and d46 livers and spleens were comparable between WT and KO mice (**Figure 5.24B**).

Taken together, these results indicate that TRIM24 may play a minor host-beneficial role in controlling hepatic but not splenic parasite burden during the first six weeks of *L. donovani* infection. A longer term infection to investigate roles of TRIM24 in during the chronic phase of infection would be interesting.

5.3.12. Granuloma size and iNOS expression in 29-day infected mice is not affected by *Trim24* deletion

The hepatic response to *L. donovani* infection is granulomatous, resulting in focal points rich in Kupffer cells (liver resident macrophages) expressing iNOS and surrounded by other leukocyte populations (Moore et al. 2013; Murray et al. 2006). Our previous data showed

that TLR4 stimulation induced iNOS to a greater degree in KO macrophages. We therefore examined whether TRIM24 played a role in Kupffer cell iNOS expression.

To investigate this, we harvested livers from WT and KO mice infected with *L. donovani* for 29 days and performed immunofluorescence imaging on whole liver sections using DAPI (nuclear stain) and antibodies against F4/80 (Kupffer cells) and iNOS. In naive WT and KO mouse liver sections, F4/80$^+$ cells were detectable and distributed throughout the tissue, and no iNOS staining was observed (**Figure 5.22A**). After infection there was recruitment of F4/80$^+$ macrophages to the liver in both strains, and F4/80 staining identified granulomas within the liver tissue (**Figure 5.22A**). iNOS staining was visible in both WT and KO infected livers, corresponding to F4/80 staining and granuloma localisation (**Figure 5.22A**). We used StrataQuest software to perform cell segmentation using DAPI and quantified granuloma number and size, and iNOS expression in granulomas.

Firstly, the areas of naive WT and KO liver sections analysed were comparable, and the areas of infected WT and KO liver sections analysed were comparable (**Figure 5.22B**). This is consistent with the total number of cells also being comparable between WT and KO naive and infected samples (**Figure 5.22C**). As expected, in the naive tissue sections no granulomas were detected (**Figure 5.22D**). Granulomas were readily detected in infected livers (**Figure 5.22D**). The number of granulomas detected was not different between WT and KO liver samples, nor was the area of granulomas (**Figure 5.22D&E**). We also measured the staining intensity of iNOS per granuloma as a readout for iNOS abundance and found no difference between WT and KO livers (**Figure 5.22F**). Total number of iNOS$^+$ cells per total section area was unchanged (**Figure 5.22G**), and the number of iNOS$^+$ cells per mm was also unaffected by deletion of *Trim24* (**Figure 5.22H**).
Taken together, this shows that deletion of TRIM24 does not affect the granulomatous response at 29 days p.i. at the level of granuloma number and size, and at the level of iNOS expression per granuloma and per tissue section.

5.3.13. Early interferon response is elevated in KO spleen during *L. donovani* infection

Finally, given previous data indicating a role for TRIM24 in interferon signalling through inhibition of STAT signalling (Tisserand et al. 2011), and our data showing that *Trim24* deletion increases IFNβ release from TLR3/4-stimulated macrophages (**Figure 3.7**), we were interested to explore the effects of *Trim24* deletion on the early interferon response to *L. donovani* infection. Early interferon response to *L. donovani* has been shown previously,

with an induction of an interferon transcriptional signature and *Irf7* expression that peaks at 24 hours after exposure of 14M1.4 cells to *L. donovani* amastigotes *in vitro* (Phillips et al. 2010). A requirement for IRF7 for splenic marginal zone killing of *L. donovani* amastigotes at 5 and 25 hours p.i. in B6 mice was also shown (Phillips et al. 2010).

We infected WT and KO mice with *L. donovani* for 24 hours, and harvested spleen and liver for total RNA extraction and qPCR analysis (**Figure 5.26A**). We then measured the mRNA abundance of the interferon stimulated genes *Ifit1, Usp18, Oas1, Isg15, Irf7*, and *Nos2*. In the liver, we did not see any change in expression of these genes between the WT or KO naive or infected mice. (**Figure 5.26B**). However, in the spleen the signal was more readily detectable. We did not see any change in expression of *Ifit1, Usp18, Nos2, Oas1, Isg15,* or *Irf7* between WT and KO naïve mice (**Figure 5.26C**). In 24hr-infected spleen, we did not see a significant upregulation in any of the tested genes in WT mice (**Figure 5.26C**). In contrast, we saw a more robust interferon response in 24hr-infected KO spleens. *Ifit1, Usp18, Nos2, Oas1, Isg15,* and *Irf7* were all upregulated in infected KO spleens compared to naive, and were significantly higher in infected KO compared to infected WT spleens (**Figure 5.26C**). Taken together, these data indicate a role for TRIM24 as a negative regulator of interferon signalling during the first 24 hours of *L. donovani* infection in the spleen.

5.4. Discussion

Characterisation of KO mice has thus far had a core focus on cancer, in particular HCC and breast cancer (Pathiraja et al. 2015; Jiang et al. 2015; Shah et al. 2021). However, the roles of TRIM24 in *L. donovani* infection have yet to be explored. In this Chapter, we utilised *Trim24*$^{-/-}$ mice in which the transcriptional start site and exon 1 were removed, completely abrogating *Trim24* transcription (Jiang et al. 2015). We have further characterised KO C57BL/6 mice in terms of the immune cellularity of primary and secondary lymphoid organs, and in the context of *L. donovani* infection. We first showed that the numbers of leukocytes in liver, spleen, inguinal lymph nodes, and BM are unaffected by *Trim24* deletion. We observed similar leukocyte numbers in primary and secondary lymphoid organs, indicating that TRIM24 was not required for immune cell development. Shaw recently investigated the impact of *Trim24* deletion on haematopoiesis, showing *Trim24* mRNA to be more abundant in early leukocyte populations (e.g. HSCs) and decreasing as cell maturity progressed (Shaw 2018). Shaw also found no differences in lymphocyte, neutrophil, or monocyte count in *Trim24* KO bone marrow, and no difference in lymphocyte count in KO spleen, consistent with our data presented here (Shaw 2018). Our data therefore extends that of Shaw, providing evidence for the lack of role for TRIM24 in more specific leukocyte subpopulations.

Generation of 50:50 WT:KO mixed BM chimeric mice resulted in a significant skew in favour of KO cells during reconstitution, indicative of an increased fitness of KO cells relative to WT. This observation is not consistent with previously published data but was replicable between experiments. Perez-Lloret et al. used 50:50 WT:*Trim24*$^{-/-}$ mixed BM chimeras in a similar system to ours (although they used irradiated *Rag2*$^{-/-}$ recipient mice) and showed no difference in broad leukocyte subsets 8 weeks post-reconstitution (Perez-Lloret et al. 2016). However, it is not clear which tissue was analysed for this data, and no tissue-specific effects were explored (Perez-Lloret et al. 2016). Furthermore, Shaw showed a reduction in the ability for *Trim24*$^{-/-}$ cells to reconstitute compared to WT cells over 18 weeks in B6 chimeras (Shaw 2018). This study was performed on peripheral blood taken at various time points (including 4, 6, and 8 weeks) post-reconstitution, however only total WT and KO leukocytes were compared, and no data is shown for individual cell types (Shaw 2018). Shaw further showed that *Trim24* deletion did not affect the number of Lin^{-} Sca-1^{+} c-Kit^{+} (LSK) cells in the BM in 12-week and 6-month old B6 mice (Shaw 2018), giving additional evidence for the dispensability of TRIM24 for steady state haematopoiesis. Therefore, *Trim24* deficiency could be affecting non-haematopoietic cells that would not be seen in a mixed BM chimera setting. An adoptive transfer experiment of WT BM cells into KO recipient mice (thereby restricting *Trim24*-deficiency to non-haematopoietic cells) to assess alterations

in parasite burden would be an interesting experiment (though complicated due to the spontaneous development of HCC in KO mice (Tisserand et al. 2011)).

Elevated numbers of most KO myeloid cell types, B cells and NK cells but not T cells led to the hypothesis that KO cells may be retained more in the BM after they reach maturity. The CXCL12-CXCR4 signalling axis is vital for the retention of developing leukocytes in the BM (Noda et al. 2011; Kohara et al. 2007; Sugiyama et al. 2019). This study explored the effects of abrogation of the CXCR4-CXCL12 signalling axis in leukocyte development in the BM, and found severe defects in B lymphopoiesis and myelopoiesis (Ma et al. 1998). An almost complete loss of $B220^+$ $CD43^+$ cells in CXCR4 KO mice treated with and without IL-7 was observed, and a severe impairment of $Gr\text{-}1^+$ $CD11b^+$ cells was also observed (Ma et al. 1998). Importantly, thymic T cell counts remained unaffected by deletion of CXCR4, and the thymus was histologically normal in CXCR4 KO mice (Ma et al. 1998). A more recent study also showed that CXCL12-CXCR4 signalling is essential for the development of NK cells in the BM in adult mice, but not in embryonic stages (Noda et al. 2011). This study also showed impairments of myelopoiesis, consistent with data from Ma et al. (Noda et al. 2011; Ma et al. 1998).
Conditional deletion of CXCR4 (using MxCre mice and inducing CXCR4 deletion after interferon induction by poly(I:C) injection) led to almost complete abrogation of B cells in the BM, and severely reduced numbers of $Gr1^+$ neutrophils and $Ter119^+$ $CD71^+$ erythroid cells (Sugiyama et al. 2006). As well as mature cells, HSCs were also significantly reduced in CXCR4 conditional KO mouse BM (Sugiyama et al. 2006). Thus, we hypothesised that TRIM24 may play a role in CXCR4 signalling, and KO cells would be more sensitive to CXCL12 signalling. Our data showed no difference in the abundance of CXCR4 on the surface of WT and KO leukocytes in the spleen and the BM as measured by flow cytometry. Furthermore, we showed no difference between KO and WT BMDMs in their ability to internalise CXCR4 after CXCL12 treatment. As we only investigated CXCR4 internalisation in BMDMs, TRIM24 could be affecting this process in other cells. Given the roles of TRIM24 (and all other TRIM proteins) in ubiquitination (Ikeda & Inoue 2012), it could also be argued that TRIM24 may contribute to ubiquitination-mediated proteasomal degradation of CXCR4 after internalisation. Therefore, the ubiquitination status of intracellular CXCR4 in WT and KO cells post-CXCL12 stimulation would be interesting to study.

Damage caused by irradiation in chimeras could also be a factor for the chimera-specific advantage of KO cells, and a limitation in this study. A recent study compared total body irradiated (TBI) B6 mice with total marrow irradiated (TMI) B6 mice (where copper compensators over the gut, lungs, and eyes were used to block irradiation in these areas)

(Hui et al. 2017). The authors showed similar irradiation-induced damage in the BM in TMI and TBI mice, but significantly less damage to other organs (including spleen and liver) in TMI compared to TBI mice as measured by IHC (Hui et al. 2017). Furthermore, irradiation of B6 mice led to increased apoptosis of Sca-1$^+$ cells and CD11b$^+$ cells, which correlated with irradiation-induced TNF production (Cachaço et al. 2010). Abrogation of TNF signalling partially protected irradiated BM cells from apoptosis. Long term effects of radiation were also observed, with a significantly lower white blood cell (WBC) count, platelet count, and red blood cell (RBC) count in B6 mice 3 months after irradiation versus non-irradiated B6 mice (Cachaço et al. 2010). Some studies have also reported a bias of CD45.1$^+$ cells over CD45.2$^+$ during leukocyte reconstitution (Jang et al. 2018; Basu et al. 2013), which represents another limitation of the study presented here. While this would not explain the KO skew seen in our data, this limitation should be addressed by repeating the mixed BM chimera experiment, but with CD45.1$^+$ KO cells and CD45.2$^+$ WT cells.

Thus far, TRIM24 has not been explored in the context of *Leishmania* infection. However, through transcriptional profiling and pathway analysis it was predicted to be deregulated during *L. donovani* infection in BALB/c mice *in vivo* (Ashwin et al. 2018)*, in vitro* in promastigote-infected macrophages (Chaparro et al. 2022), and in 4 week *L. major* infected mice (Venugopal et al. 2022). Here, we used 50:50 WT:KO mixed BM chimeras to identify intrinsic functional defects in leukocytes that contribute to *L. donovani* infection progression and resolution.

We observed overall increases in cellularity of spleen and liver as the infection progressed in chimeric mice. This was characterised by increased numbers of CD4$^+$ and CD8$^+$ T cells (Medina-Colorado et al. 2017; Polley et al. 2005), B cells (Mondal et al. 2021), and myeloid cell populations (Cotterell et al. 2000). Extramedullary haematopoiesis, whereby haematopoietic stress causes mobilisation and differentiation of progenitor cells outside of the BM, occurs as a result of *L. donovani* infection, and causes more progenitor cell cycling activity in the spleen than in the BM of BALB/c mice (Cotterell et al. 2000). It is also known that *L. donovani* infection induces myelopoiesis in the BM, which is driven by TNF-dependent expansion of CD4$^+$ T cells and subsequent IFN-γ production leading to loss of quiescence in long term HSC (LT-HSC) populations (Pinto et al. 2017). This induction of myelopoiesis leads to the generation of monocytes expressing Galectin-3 indicating a more regulatory phenotype that could facilitate parasite survival (Abidin et al. 2017). Furthermore, colony forming unit assays have shown increases in the self-renewal capacity of splenic myeloid cells in *L. donovani*-infected hamsters 28 days p.i. (Osorio et al. 2020).

We observed no differences in the infection-induced expansion of CD4$^+$ T, CD8$^+$ T, or B cells in the spleen or liver between WT and KO. KO cells expanded more than WT in these two

organs after infection. By d28, most of the cDCs, neutrophils, monocytes, and macrophages in the spleen and the liver were KO. Whether this is through increased induction of extramedullary haematopoiesis in KO populations or through cellular recruitment because of altered chemokine signalling remains to be investigated. Interestingly, infection of total WT and KO mice did not reveal the same phenotypes seen in the mixed BM chimeras here, and we saw no difference in the numbers of leukocytes in the spleen and liver at d28 post-infection. Thus, the data from the mixed BM chimeras was specific to the mixed BM chimera environment.

There was a progressive increase in Th1 cell (Tbet$^+$ IFNγ$^+$ CD4$^+$) proportion in the spleen, liver and BM as a result of infection, however *Trim24* deficiency did not affect this. Furthermore, no difference in the release of TNF, IFNγ, IL-4 or IL-10 was detected in KO T cells compared to WT. The importance of these cytokines has been discussed in detail in **Chapter 1**. T cell-derived IFNγ and TNF are critical for the induction of anti-*Leishmania* mechanisms (hepatic granuloma formation and iNOS expression in macrophages) (Carneiro et al. 2016), while IL-10 is critical for the establishment of chronic *L. donovani* infection and IL-4 contributes to macrophage "M2-like" polarisation and exacerbation of infection progression (Ghalib et al. 1993; Satoskar et al. 1995). The lack of effect of *Trim24*-deficiency on TNF release is perhaps unsurprising, given our previous *in vitro* data showing that TLR-stimulated KO BMDMs have comparable TNF production to WT (**Figure 3.2A**). However, the lack of difference in IL-4 production is more surprising given previously published data (Perez-Lloret et al. 2016). This study showed that *Trim24*$^{-/-}$ T cells impaired the release of IL-10, IL-13, and IL-5 in restimulated lymph node cells following house dust mite challenge (Perez-Lloret et al. 2016). *Trim24*$^{-/-}$ T cells stimulated with anti-CD3 antibody and IL-1β also had their ability to produce IL-4 and IL-13 completely abolished (Perez-Lloret et al. 2016). Reduced mRNA abundance of *Arg1* and *Relmα* in the small intestine was seen 14 days following *Heligmosomoides polygyrus* infection, indicating a role for TRIM24 in the T cell-mediated response to allergy and helminth infection (Perez-Lloret et al. 2016).

TRIM24 also did not appear to play a role in the generation of *Leishmania* antigen (PEPCK)-specific CD4$^+$ T cells during infection. PEPCK-specific T cells are generated during *L. donovani* infection from Th1 (T-bet$^+$ IFNγ$^{+)}$ and Tr1 (IFNγ$^+$ IL-10$^+$) T cells (Mou et al. 2015; Montes de Oca et al. 2020). Mou et al. used *L. major*-infected BM dendritic cells (BMDCs) to identify specific *Leishmania* peptides in complex with MHC II molecules by using a combination of liquid chromatography-mass spectrometry (LC-MS/MS) and *in silico* approaches (Mou et al. 2015). They identified a peptide, PEPCK$_{335\text{-}351}$, that is highly conserved in all *Leishmania* species, naturally processed by DCs, and predicted to interact

stably with MHC II (specifically I-A^b). Furthermore, $PEPCK_{335-351}$ was shown to induce proliferation and IFNγ production (by flow cytometry and ELISpot) from $CD4^+$ T cells isolated from mice that had been healed from *L. major* infection, but not in naive mice. Mou et al. generated a tetramer of I-A^b-$PEPCK_{335-351}$ (MHC class II-antigen tetramer) that allowed specific detection of antigen-specific $CD4^+$ T cells in C57BL/6 mice during infection with various *Leishmania* species, including *L. donovani, L. major*, and *L. mexicana* (Mou et al. 2015). Importantly, $CD4^+$ T cells that were detected by this tetramer were also $CD44^+$, indicating that they had an activated phenotype (Mou et al. 2015).
Montes de Oca et al. found that abolishment of IL-27 signalling led to increase *Leishmania*-specific Th1 cells and fewer *Leishmania*-specific Tr1 cells, leading to significantly better control of parasite burden (Montes de Oca et al. 2020). While we saw increases in the number of PEPCK-specific T cells at d28 post-infection, we did not see any effect of *Trim24* deletion on this number.

Our data showed no difference in basal expression of MHC-II on KO macrophages or in their ability to upregulate MHC-II during *L. donovani* infection. This was unexpected, as TRIM24 has been identified as a negative regulator of interferon signalling via inhibition of the JAK-STAT pathway (Tisserand et al. 2011). IFNγ has long been known to induce MHC-II expression (Steimle et al. 1994). MHC-II expression on APCs is vital for $CD4^+$ T cell-mediated response to infection. In Th1-dominant infections (e.g. *L. donovani*), Th1 cell-derived IFNγ induces MHC-II expression via IRF-1 activation in APCs, enhancing their antigen presentation capabilities (van den Elsen 2011).

Given our previous data showing iNOS expression to be increased in TLR3/4-stimulated KO BMDMs (**Figure 3.4**), we hypothesised that iNOS might be increased during *L. donovani* infection in KO mice. The hepatic immune response to murine *L. donovani* infection is a dominant Th1 response resulting in the formation of granulomas consisting of infected $iNOS^+$ Kupffer cells (KCs) surrounded by other leukocytes (Murray 2001). Antigen-presenting cells (APCs) release IL-12 following *Leishmania* exposure, which assists in polarising $CD4^+$ T cells to become T-bet^+ Th1 cells (von Stebut et al. 1998; Martínez-López et al. 2015). Th1 cells release abundant IFNγ, TNF and IL-12 causing further Th1 polarisation and stimulating iNOS expression in macrophages (Dayakar et al. 2019). Subsequent release of reactive oxygen species (ROS) such as nitric oxide (NO) is critical in the removal of parasites (Murray et al. 2006). $CD8^+$ T cells also play an important role in the formation of granulomas, as depletion of $CD8^+$ T cells delayed the formation of granulomas during experimental VL (Stern et al. 1988). However, we observed no difference in the number or granulomas at d28 in WT and KO mice, as well as no difference in the number of $iNOS^+$ macrophages ($F4/80^+$)

per granuloma, or the in the amount of iNOS expressed through the whole section of liver analysed. Therefore, hepatic iNOS expression is not affected by *Trim24* deletion *in vivo* during *Leishmania* infection.

A major limitation of this study was the breeding of *Trim24*$^{-/-}$ mice. Due to the emergence of spontaneous HCC in *Trim24*$^{-/-}$ mice that is detectable from ~14 weeks of age (Jiang et al. 2015), we limited the age of our mice to a maximum of 14 weeks for all experiments to limit baseline inflammatory gene expression which could confound our data, and to keep animal suffering to a minimum. As a result, we were unable to breed total KO mice and instead used heterozygous mice for breeding. Offspring were mendelian in their genotypes, however this resulted in 25% KO mice and 25% WT controls per litter. It was therefore difficult to obtain sufficient numbers of age and sex-matched mice for use in planned experiments. Together, our data in this chapter have displayed competitive advantages of KO leukocytes during reconstitution and recruitment that persist through infection. This was most evident in BM. Minimal effects of *Trim24* deletion on cell- and tissue-specific responses to *L. donovani* infection were seen. Despite the lack of functional phenotypic differences found in KO leukocytes, *Trim24* deficiency appeared to impair hepatic control of parasite burden during *L. donovani* infection at d29 but not later, an effect that may be a consequence of increased early type 1 interferon responses. More work will be required to elucidate the exact functions of TRIM24 that bring about this effect.

5.5. Figures

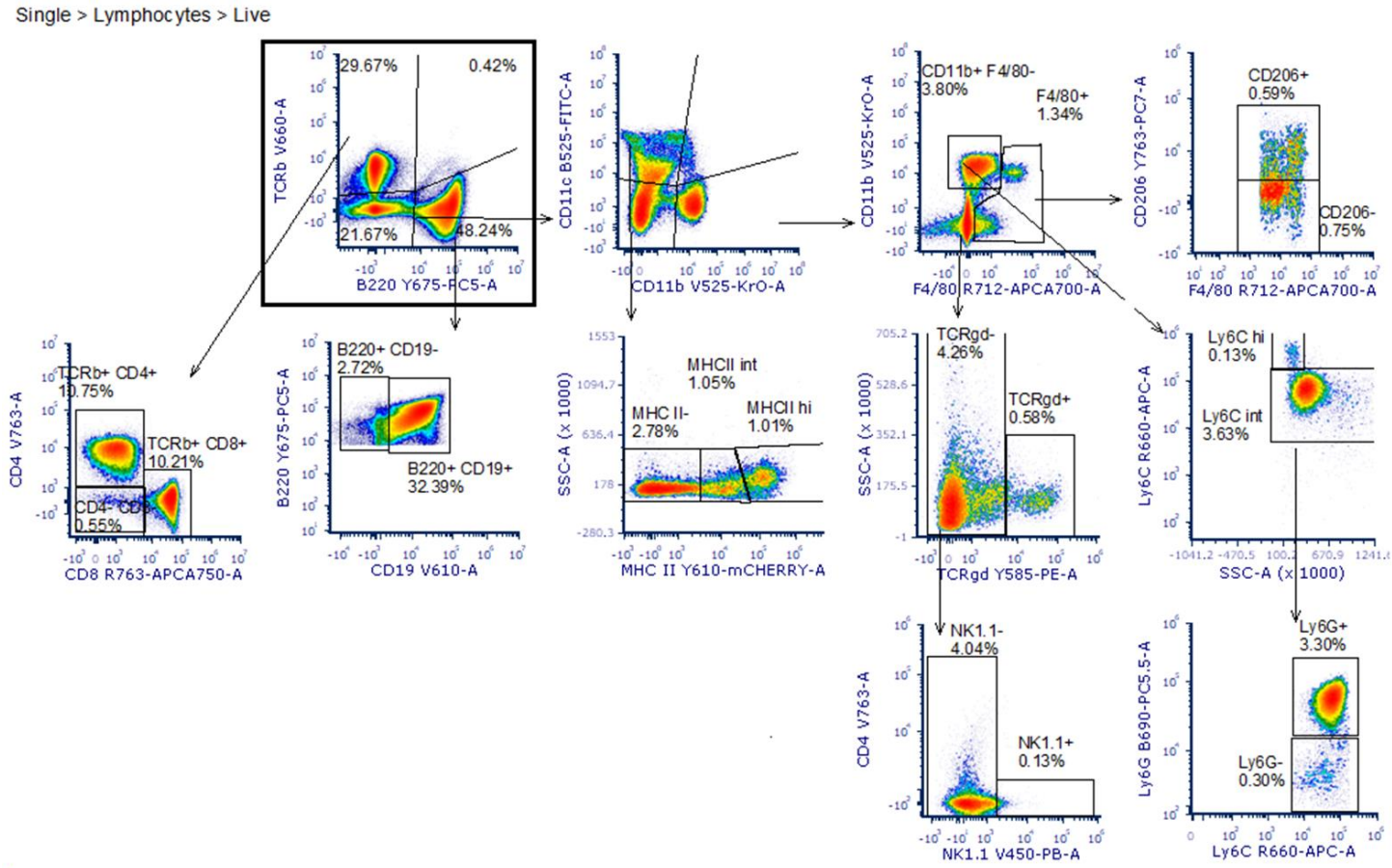

Figure 5.1. Gating strategy for immune cell detection. Representative plots are from a WT spleen sample.

Cell type	Markers
$CD4^+$ T	$TCR\beta^+$ $B220^-$ $CD4^+$ $CD8^-$
$CD8^+$ T	$TCR\beta^+$ $B220^-$ $CD4^-$ $CD8^+$
$CD4^-$ $CD8^-$ T	$TCR\beta^+$ $B220^-$ $CD4^-$ $CD8^-$
B cell	$TCR\beta^-$ $B220^+$ $CD19^+$ $MHCII^+$
γδ T cell	$TCR\beta^-$ $B220^-$ $CD11c^-$ $CD11b^-$ $TCRgd^+$
NK	$TCR\beta^-$ $B220^-$ $CD11c^-$ $CD11b^-$ $TCRgd^-$ $NK1.1^+$
Plasmacytoid Dendritic Cell	$TCR\beta^-$ $B220^+$ $CD19^-$
$CD11c^+$ MHCII-	$TCR\beta^-$ $B220^-$ $CD11c^+$ $MHCII^-$
$MHCII^{int}$ conventional Dendritic Cell	$TCR\beta^-$ $B220^-$ $CD11c^+$ $MHCII^{int}$
$MHCII^{hi}$ conventional Dendritic Cell	$TCR\beta^-$ $B220^-$ $CD11c^+$ $MHCII^{hi}$
$CD11b^+$ $CD11c^+$ DC	$TCR\beta^-$ $B220^-$ $CD11c^+$ $CD11b^+$
Macrophage	$TCR\beta^-$ $B220^-$ $CD11c^-$ $CD11b^{+/-}$ $F4/80^+$ $CD206^-$
M2 Macrophage	$TCR\beta^-$ $B220^-$ $CD11c^-$ $CD11b^{+/-}$ $F4/80^+$ $CD206^+$
Neutrophil	$TCR\beta^-$ $B220^-$ $NK1.1^-$ $CD11c^-$ $CD11b^+$ $Ly6C^{int}$ $Ly6G^+$ $F4/80^-$
Patrolling Monocyte	$TCR\beta^-$ $B220^-$ $NK1.1^-$ $CD11c^-$ $CD11b^+$ $Ly6C^{int}$ $Ly6G^-$ $F4/80^-$
Inflammatory Monocyte	$TCR\beta^-$ $B220^-$ $NK1.1^-$ $CD11c^-$ $CD11b^+$ $Ly6C^{hi}$ $Ly6G^-$ $F4/80^{hi}$
Myeloid-derived cells	$TCR\beta^-$ $B220^-$ $NK1.1^-$ $CD11c^-$ $CD11b^+$ $Ly6C^-$ $Ly6G^-$ $F4/80^-$
Uncharacterised	$TCR\beta^-$ $B220^-$ $NK1.1^-$ $TCRgd^-$ $CD11c^-$ $CD11b^-$ $Ly6C^-$ $Ly6G^-$

Table 5.1. Cell type and marker definitions

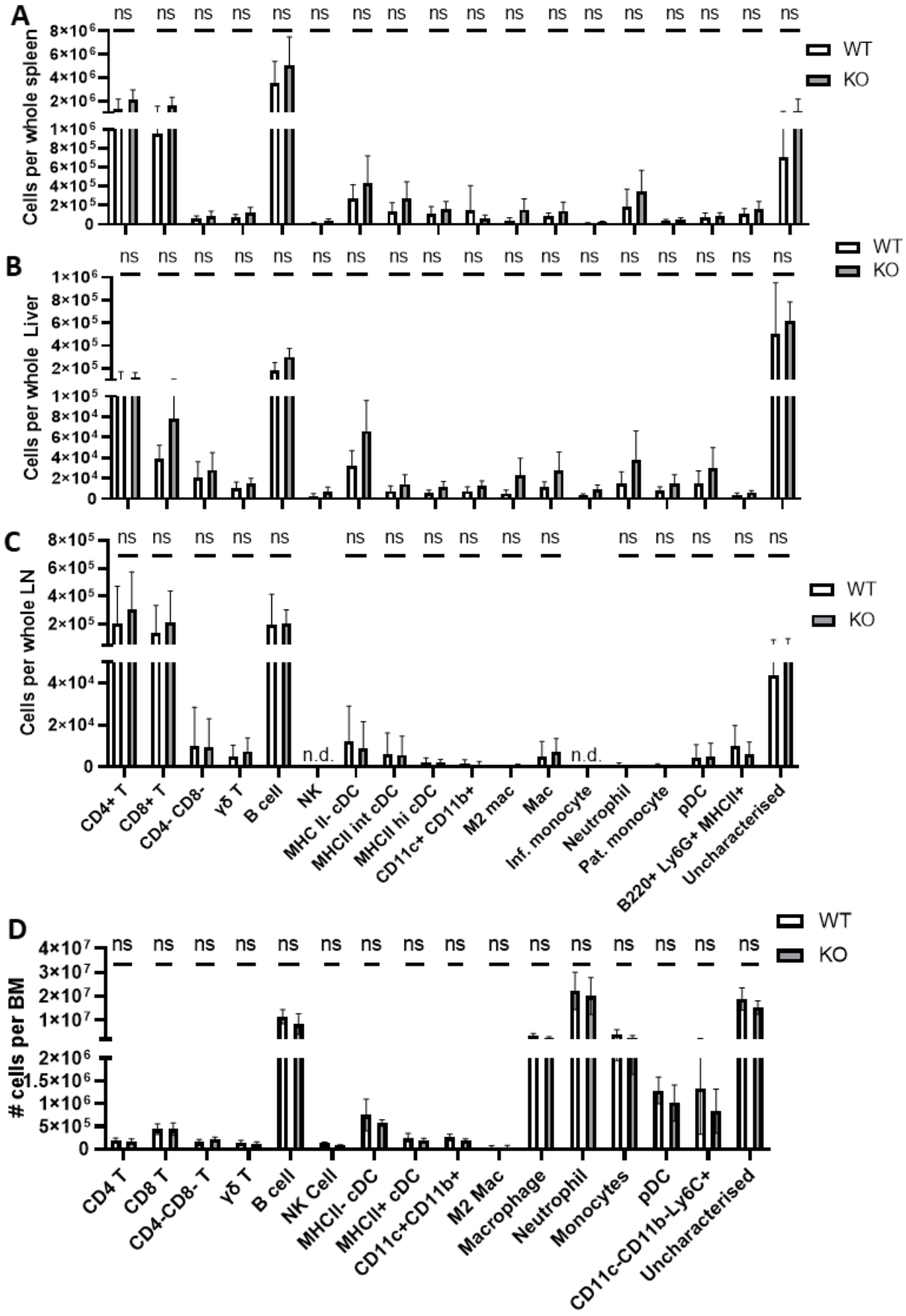
A
Cells per whole spleen
WT
KO
B
Cells per whole Liver
C
Cells per whole LN
n.d.
CD4+ T
CD8+ T
CD4- CD8-
γδ T
B cell
NK
MHC II- cDC
MHCII int cDC
MHCII hi cDC
CD11c+ CD11b+
M2 mac
Mac
Inf. monocyte
Neutrophil
Pat. monocyte
pDC
B220+ Ly6G+ MHCII+
Uncharacterised
D
cells per BM
CD4 T
CD8 T
CD4-CD8- T
γδ T
B cell
NK Cell
MHCII- cDC
MHCII+ cDC
CD11c+CD11b+
M2 Mac
Macrophage
Neutrophil
Monocytes
pDC
CD11c-CD11b-Ly6C+
Uncharacterised

Figure 5.2. Deletion of *Trim24* does not affect immune cell numbers within immune organs. WT and KO C57BL/6 mice were sacrificed, and the spleen **(A)**, liver **(B)**, inguinal lymph nodes **(C)**, and bone marrow **(D)** were processed into single cell suspensions as described in **Chapter 2.7**. Flow cytometry was performed on single cell suspensions using fluorochrome-conjugated antibodies specific for cell surface markers (described in **Table 5.1**). Data was acquired on a CytoFlex LX flow cytometer using the CytExpert software, and analysed using FCS Express 7. Absolute cell counts were calculated by multiplying the proportion of the cell type by the number of cells in the whole organ. Data represents mean ± SD; n=6 WT and 6 KO mice, two independent experiments; ns = not significant, Multiple unpaired t-tests.

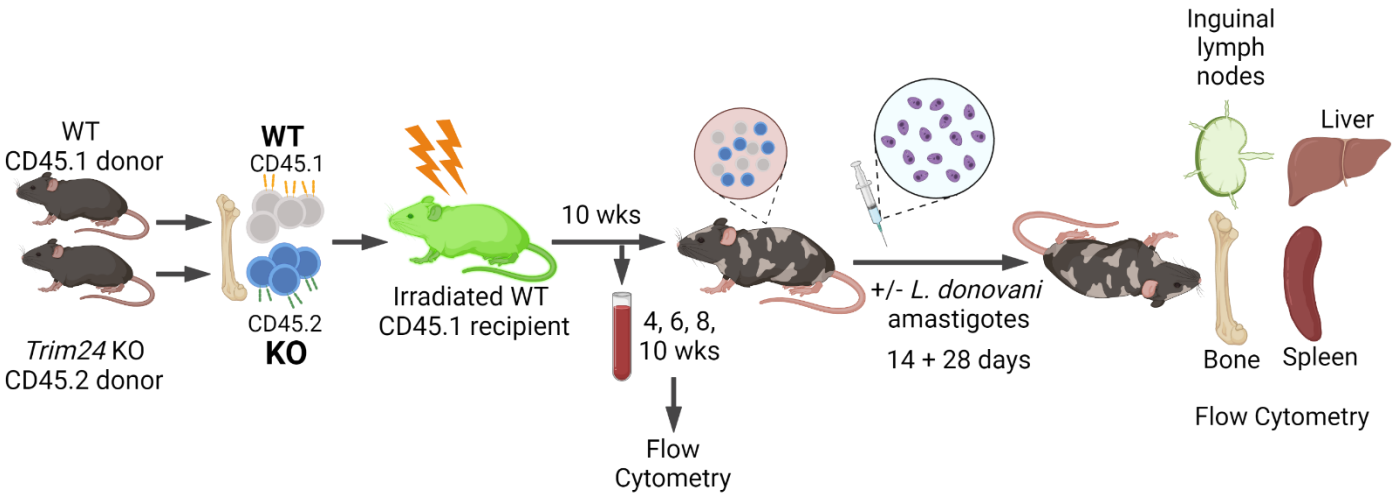

Figure 5.3. Experimental design for generation and infection of 50:50 mixed bone marrow chimeras. BM cells were extracted from WT B6.CD45.1 and KO B6.CD45.2 donor mice. Following RBC lysis, cells were counted and mixed in a 1:1 ratio. 1:1 mixture of WT:KO BM cells were injected into lethally irradiated WT B6.CD45.1 mice via the tail vein. Blood was taken at 4, 6, 8, and 10 weeks for flow cytometric analysis. Chimeras were infected or not with *L. donovani* amastigotes ($3x10^7$ per mouse in 100 µL) at 8-10 weeks post-reconstitution. Chimeras were sacrificed 14 and 28 days post-infection, and spleen, liver, inguinal lymph nodes, and bone marrow were harvested for flow cytometric analysis.

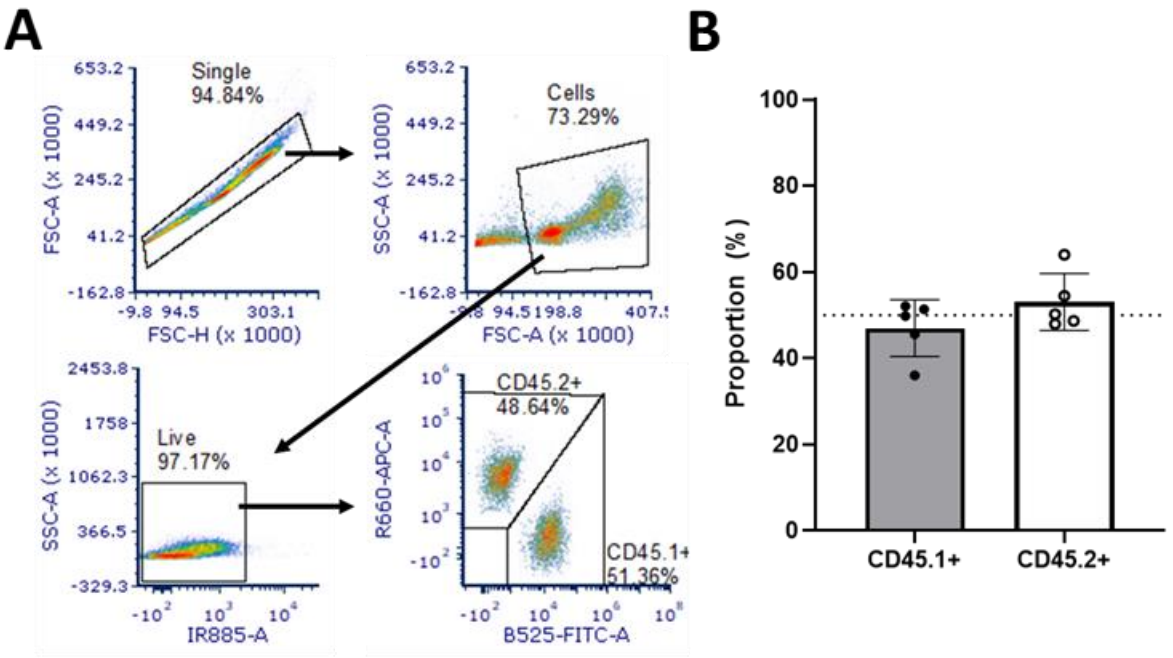

Figure 5.4. Confirmation of 50:50 mixture of BM cells from B6 donor mice. BM cells from donor WT B6.CD45.1 and KO B6.CD45.2 were counted and mixed in a 1:1 ratio. Flow cytometry was performed detecting CD45.1 and CD45.2 to confirm proportion of WT:KO BM cells. **(A)** Gating strategy for identification of CD45.1+ and CD45.2+ cells. **(B)** Bar plot showing proportion of CD45.1+ and CD45.2+ in donor mixture. N=5 technical replicate samples; No significance observed in mixture of donor cells; Student's t-test.

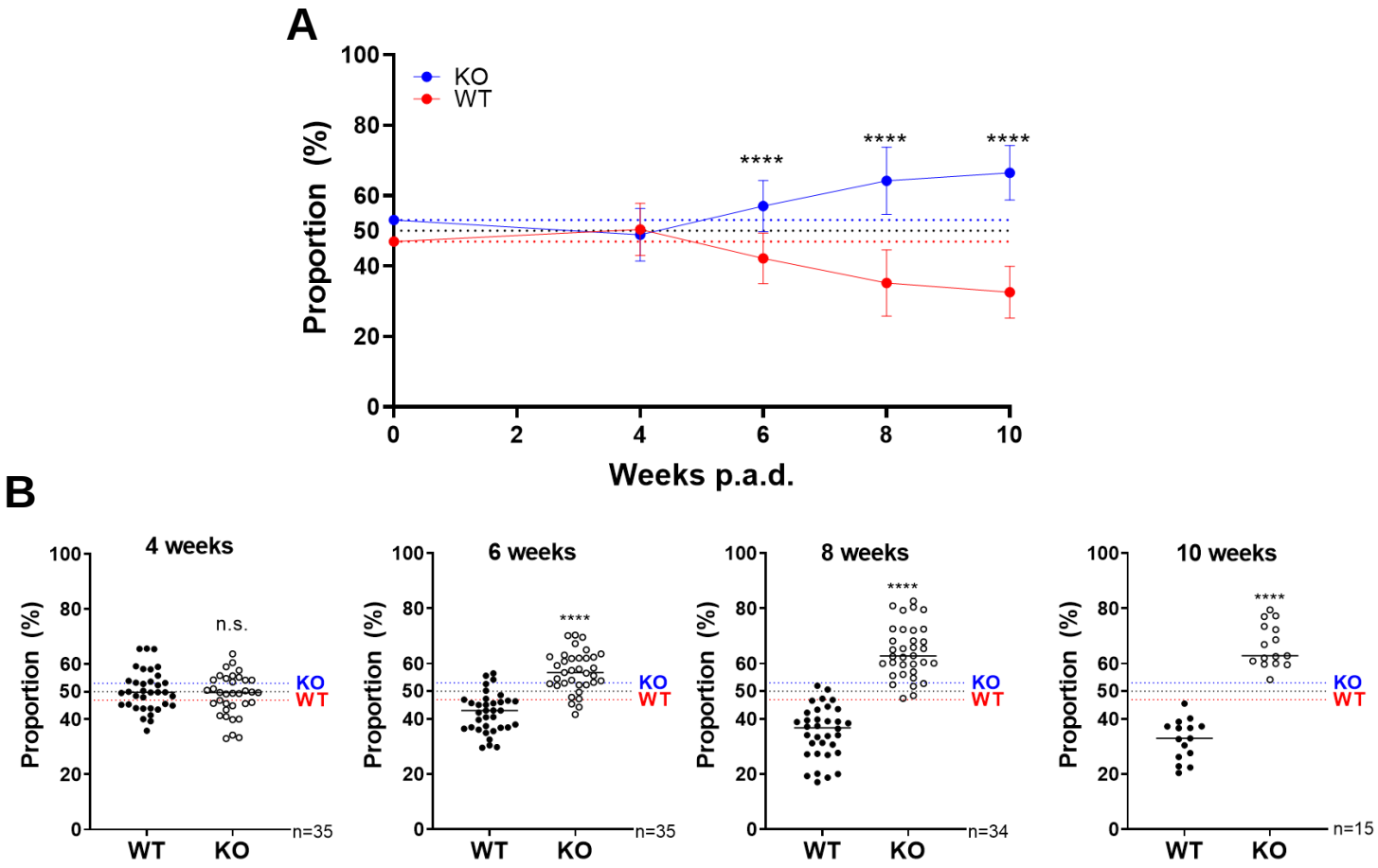

Figure 5.5. KO leukocytes have competitive advantage against WT leukocytes during reconstitution in peripheral blood. After reconstitution of lethally irradiated mice with 1:1 mixture of WT:KO BM cells, blood was taken 4, 6, 8, and 10 weeks post-reconstitution and analysed by flow cytometry to detect CD45.1+ WT leukocytes and CD45.2+ KO leukocytes. **(A)** Proportion of WT (CD45.1+) and KO (CD45.2+) cells at time points post adoptive transfer (p.a.d.) Data are mean ± SD; n = 15-35 chimeric mice (pooled from 2 independent experiments); ****P < 0.0001, Mixed effects analysis with Šidák's multiple comparisons test. **(B)** Proportion of WT and KO cells at each time point post-reconstitution. Dots represent individual mice, and dotted lines show percentage proportion of WT (red) and KO (blue) BM cell mixture injected into recipient mice (black line shows 50%). Data are mean ± SD; n = 15-35 chimeric mice (pooled from 2 independent experiments); ****P < 0.0001, Student's T-test. p.a.d. = post-adoptive transfer.

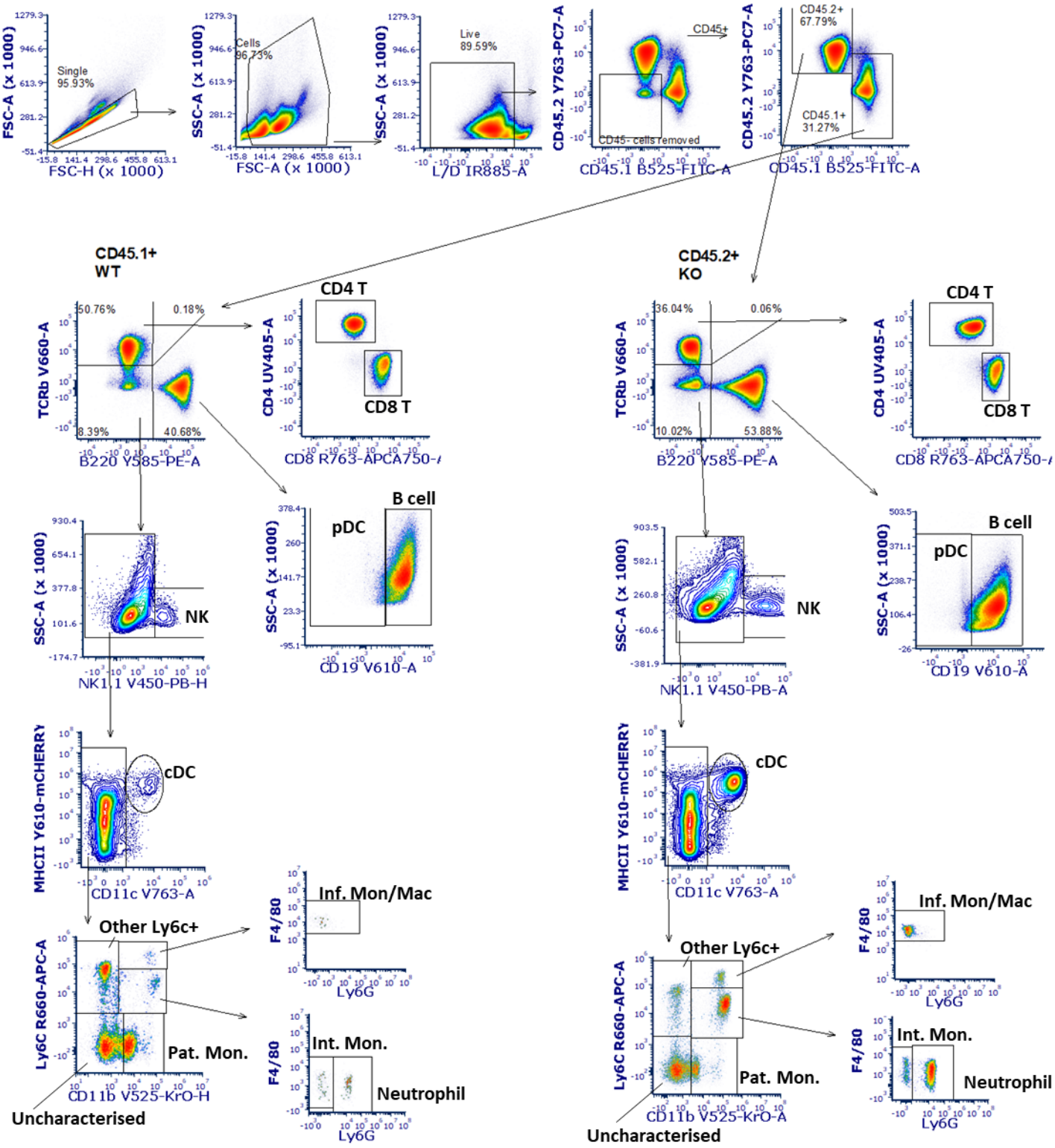

Figure 5.6. Gating strategy for leukocyte detection in peripheral blood of mixed bone marrow chimeric mice.

Cell type	Markers
$CD4^+$ T	$TCR\beta^+$ $B220^-$ $CD4^+$ $CD8a^-$
$CD8^+$ T	$TCR\beta^+$ $B220^-$ $CD4^-$ $CD8a^+$
B cell	$TCR\beta^-$ $B220^+$ $CD19^+$
NK cell	$TCR\beta^-$ $B220^-$ $CD11c^-$ $CD11b^-$ $NK1.1^+$
Conventional Dendritic Cell	$TCR\beta^-$ $B220^-$ $CD11c^+$ $MHCII^+$
Inflammatory Mon/Mac	$TCR\beta^-$ $B220^-$ $NK1.1^-$ $CD11c^-$ $CD11b^+$ $Ly6C^{hi}$ $Ly6G^-$ $F4/80^{hi}$
Neutrophil	$TCR\beta^-$ $B220^-$ $NK1.1^-$ $CD11c^-$ $CD11b^+$ $Ly6C^{int}$ $Ly6G^+$
Intermediate Monocyte	$TCR\beta^-$ $B220^-$ $NK1.1^-$ $CD11c^-$ $CD11b^+$ $Ly6C^{int}$ $Ly6G^-$
Patrolling Monocyte	$TCR\beta^-$ $B220^-$ $NK1.1^-$ $CD11c^-$ $CD11b^+$ $Ly6C^{lo}$
Other Ly6C+	$TCR\beta^-$ $B220^-$ $NK1.1^-$ $CD11c^-$ $CD11b^-$ $Ly6C^{int}$ $F4/80^-$
Uncharacterised	Negative for all markers

Table 5.2. Cell type and marker definitions for leukocytes in peripheral blood of mixed bone marrow chimeric mice. Cells were gated on live single cells, then split into WT ($CD45.1^{+)}$ or KO ($CD45.2^+$). Following this, the same gating strategy was used for WT and KO cell analysis.

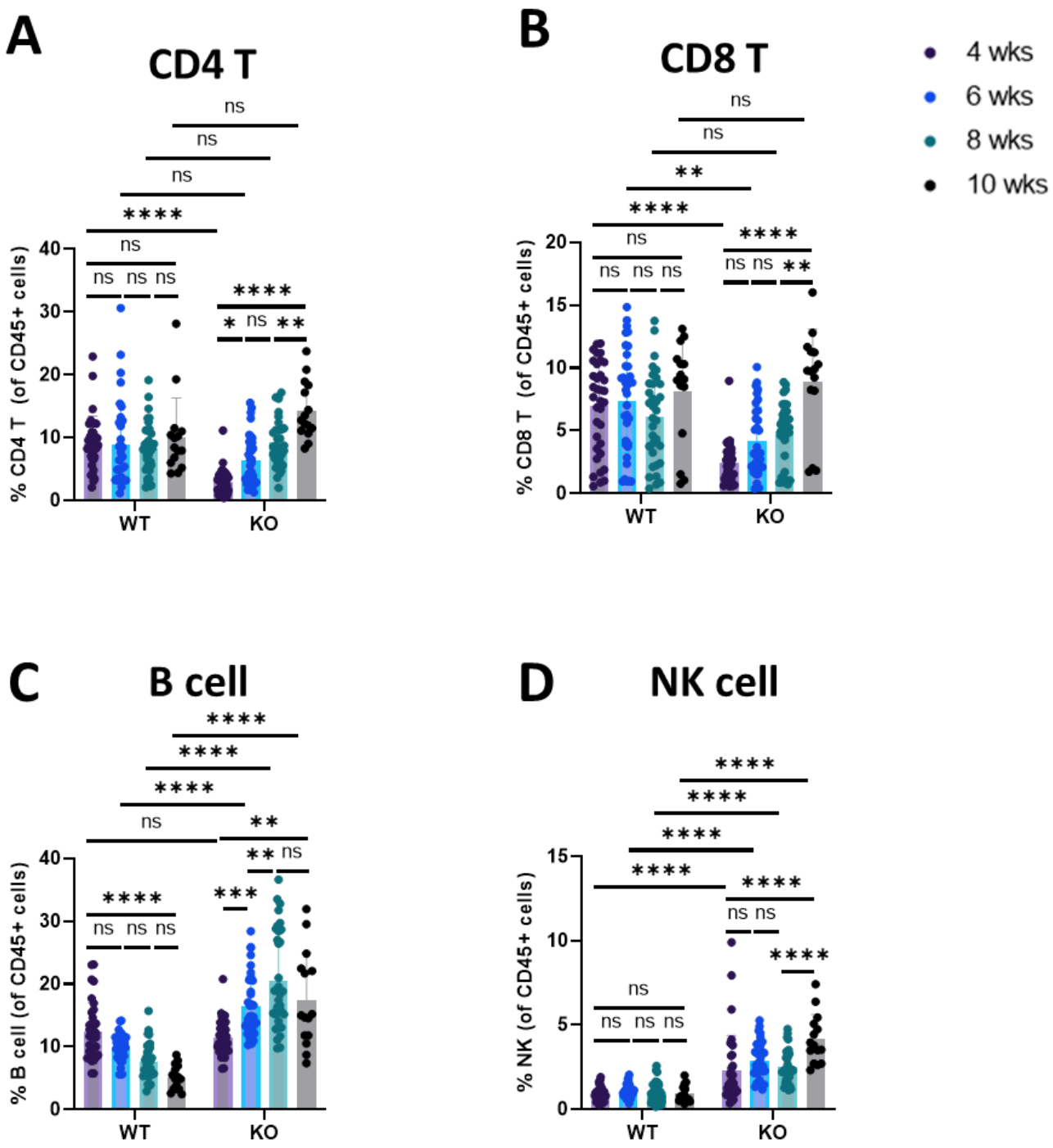

Figure 5.7. Relative fitness of lymphocyte populations in mixed bone marrow chimeras in peripheral blood. Blood was taken from chimeric mice 4, 6, 8, and 10 weeks post-reconstitution via tail bleed. Flow cytometry was used to identify WT ($CD45.1^{+}$) and KO ($CD45.2^{+}$) leukocytes. CD4 T cells **(A)**, CD8 T cells **(B)**, B cells **(C)**, and NK cells **(D)** were identified based on expression of surface markers indicated in **Table 5.2**. Percentages represent proportion of all $CD45^{+}$ cells. Bars show mean ± SD and dots show values of individual mice; n = 15-35 mice (pooled from 2 independent experiments); *P < 0.05, **P < 0.01, ***P < 0.001, ****P < 0.0001, Two-way ANOVA with Tukey's multiple comparisons test. NK = Natural Killer; ns = not significant.

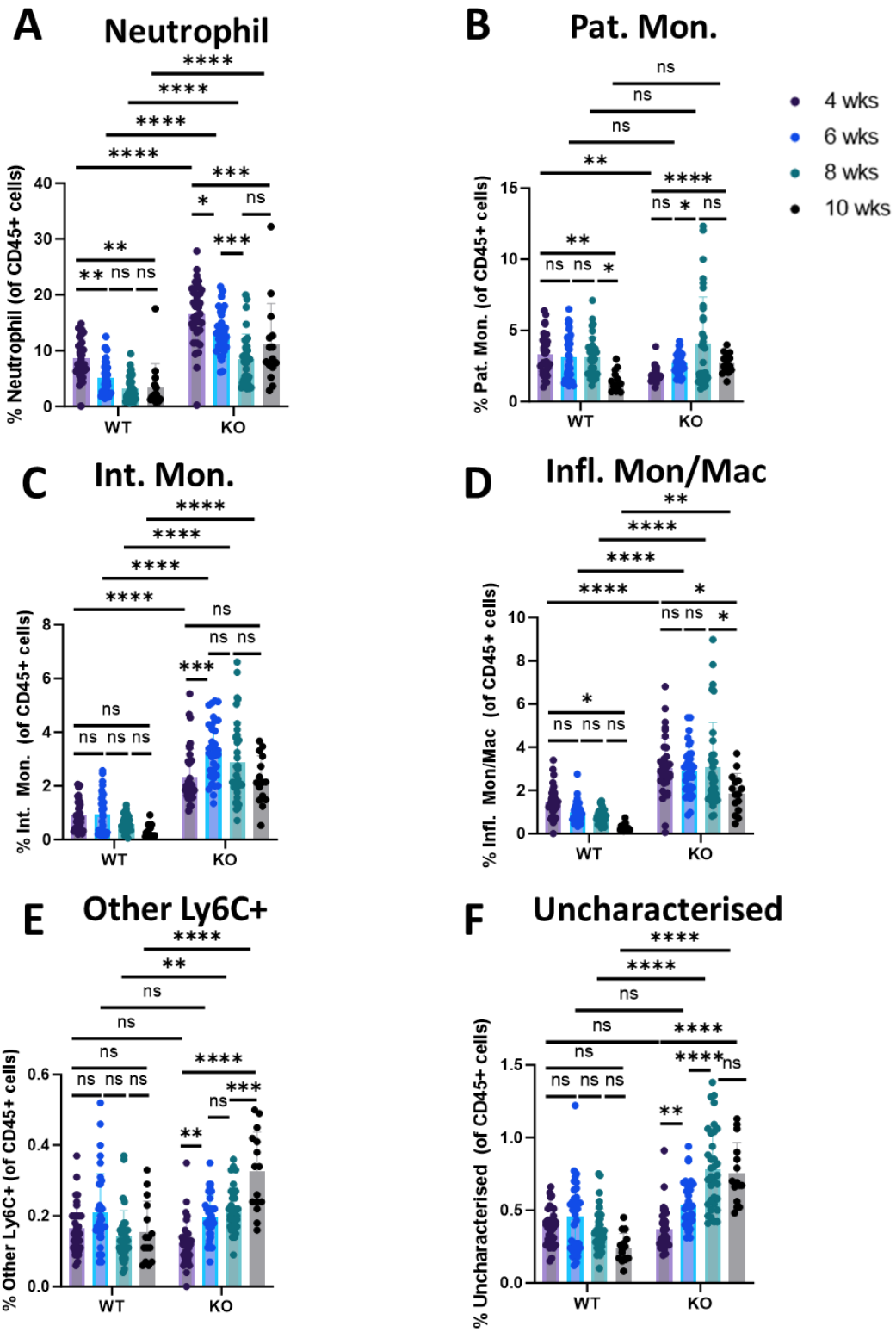

Figure 5.8. Relative fitness of myeloid populations in mixed bone marrow chimeras in peripheral blood. Blood was taken from chimeric mice 4, 6, 8, and 10 weeks post-reconstitution via tail bleed. Flow cytometry was used to identify WT (CD45.1$^+$) and KO (CD45.2$^+$) leukocytes. Neutrophils **(A)**, patrolling monocytes (Pat. Mon.) **(B)**, intermediate monocytes (Int. Mon.) **(C)**, inflammatory monocyte/macrophages (Infl. Mon/Mac) **(D)**, Other Ly6C$^+$ **(E)**, and uncharacterised cells **(F)** were identified based on expression of surface markers indicated in **Table 5.2**. Data is mean ± SD; n = 15-35 mice (pooled from 2 independent experiments); *P < 0.05, **P < 0.01, ***P < 0.001, ****P < 0.0001, Two-way ANOVA with Tukey's multiple comparisons test.

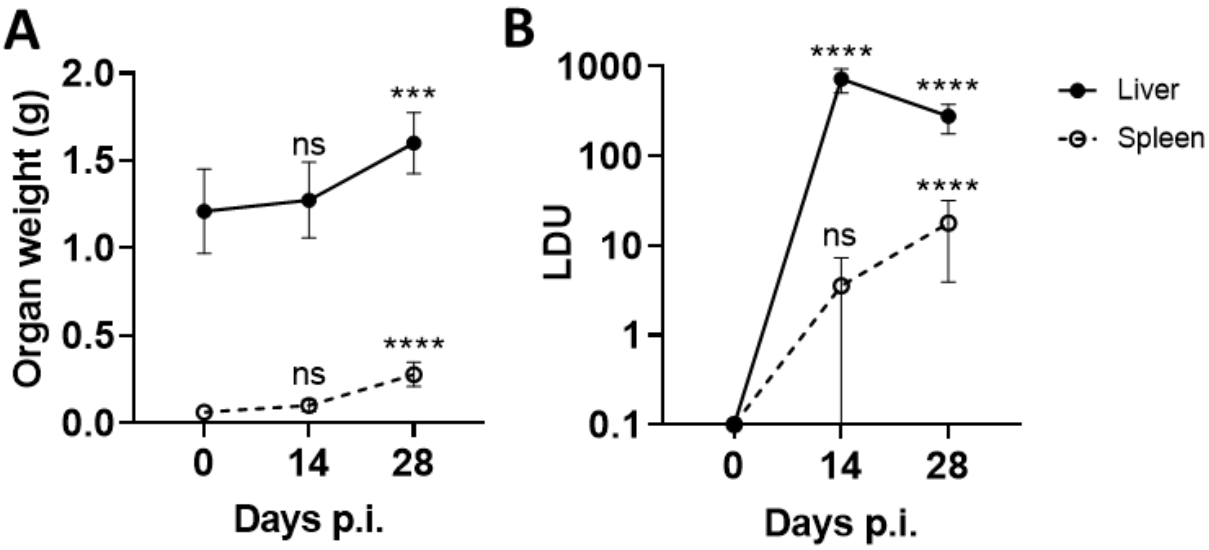

Figure 5.9. Confirmation of establishment of *L. donovani* infection in mixed BM chimeric mice. (A) Whole livers and spleens were excised from sacrificed mixed BM chimeras at each time point and weighed. **(B)** Parasite burden (LDU) in liver and spleen. Sections of liver and spleen were cut, and impression of each tissue were made on Superfrost slides. Impressions were fixed with methanol, and then stained with Giemsa stain. Parasite burden for each tissue was assessed by counting the number of amastigotes per 1000 host nuclei, and multiplying by the organ weight in grams. Data is mean ± SD; n=9-13 chimeras per group; ns = not significant compared to day 0, ***$p < 0.001$, ****$p < 0.0001$, One way ANOVA with Tukey's multiple comparisons test.

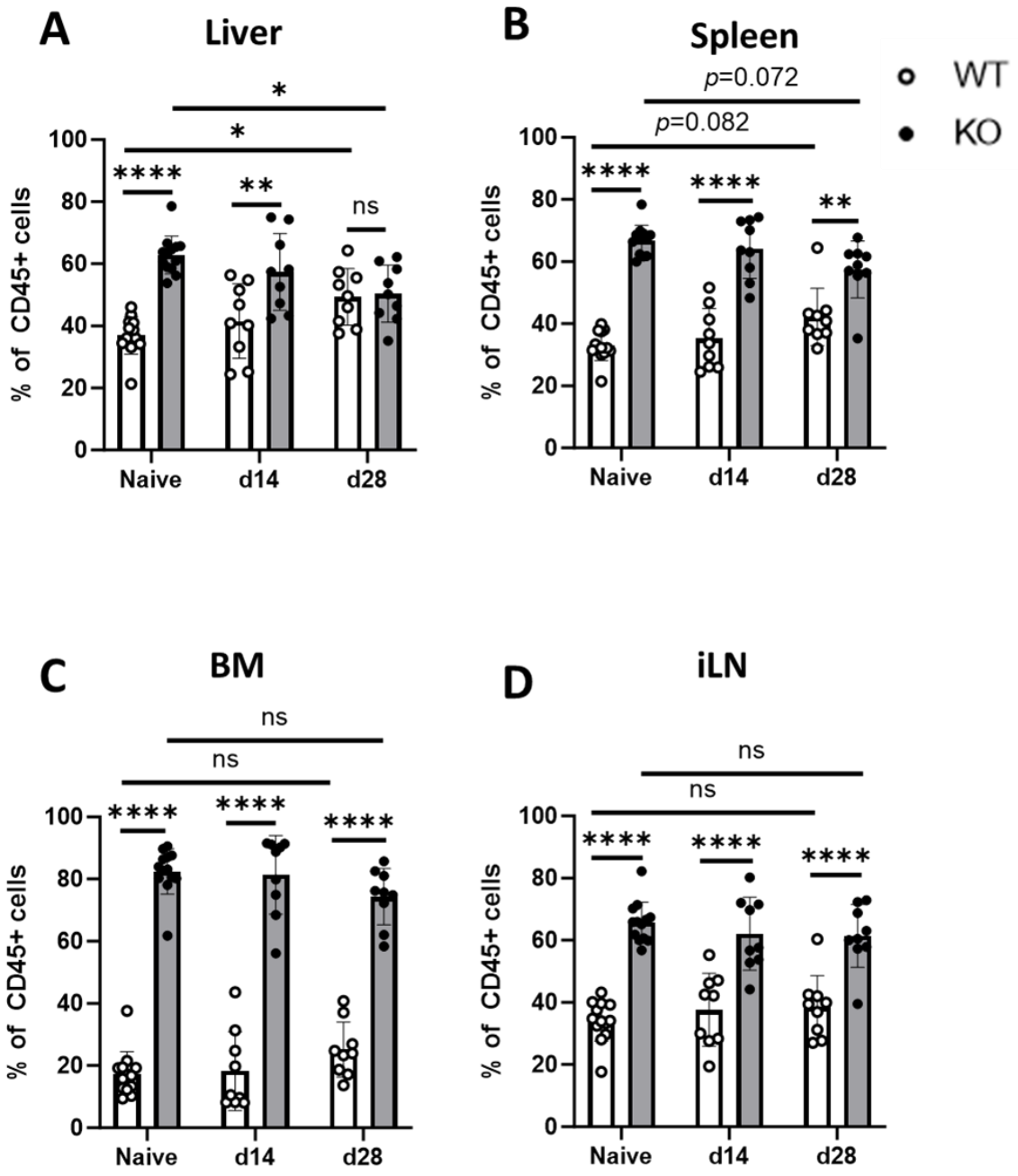

Figure 5.10. Tissue-specific differences in KO leukocyte skew in mixed bone marrow chimeric mice. Liver **(A)**, spleen **(B)**, bone marrow **(C)**, and inguinal lymph nodes **(D)** were taken from naïve, d14- and d28-infected mixed bone marrow chimeric mice and processed into single cell suspensions. Flow cytometry was performed to detect WT ($CD45.1^+$) and KO ($CD45.2^+$) cells within each tissue. $CD45^-$ cells were excluded from the analysis, and proportions of $CD45^+$ (the sum of $CD45.1^+$ and $CD45.2^+$ cells) were analysed. Data represents mean ± SD; n=9-13 chimeras per group (pooled from 2 independent experiments); ns = not significant, $^{**}P < 0.01$, $^{****}P < 0.0001$; Two-way ANOVA with Tukey's multiple comparisons test.

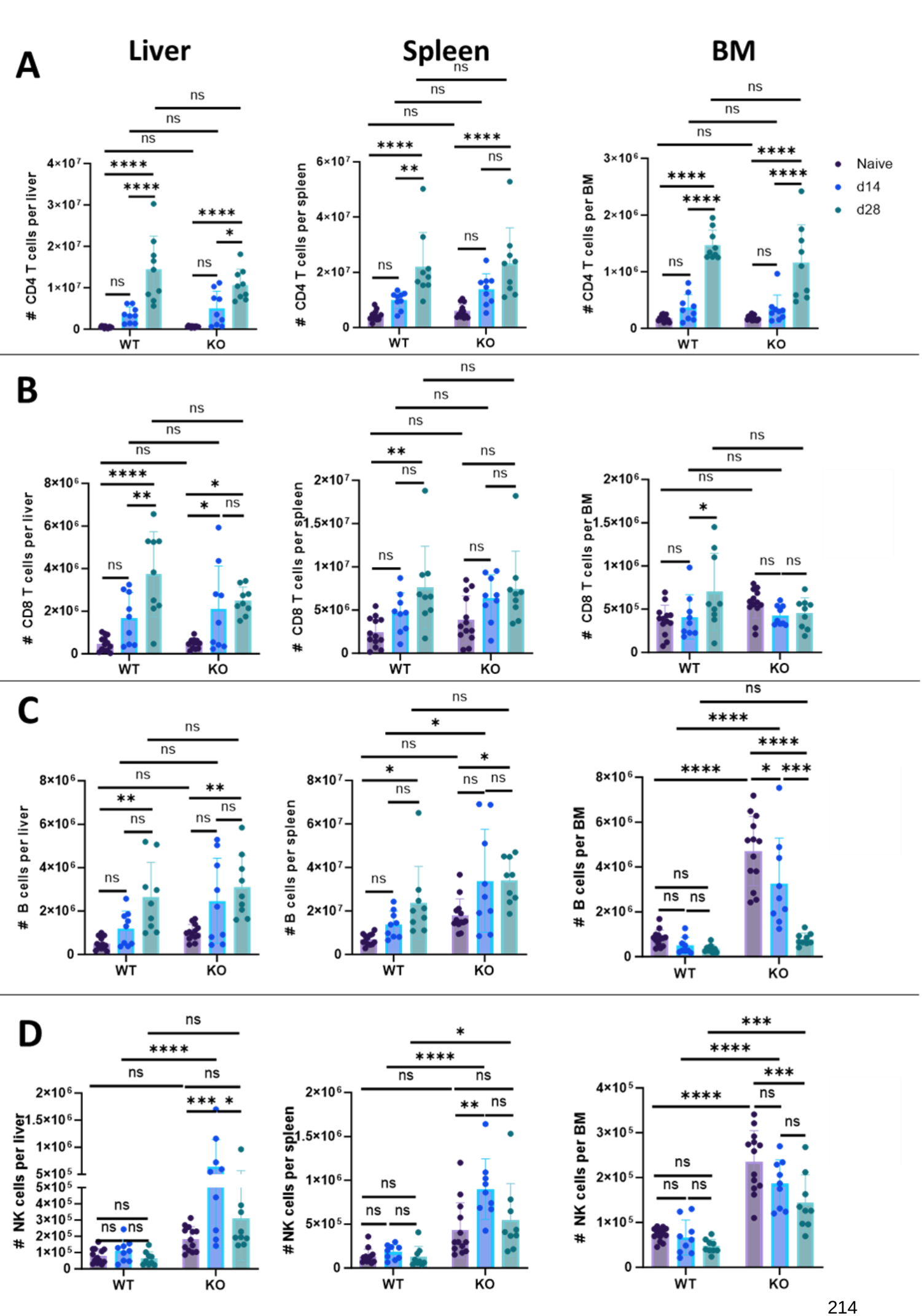
A
Liver
Spleen
BM
CD4 T cells per liver
CD4 T cells per spleen
CD4 T cells per BM
Naive
d14
d28
WT
KO
B
CD8 T cells per liver
CD8 T cells per spleen
CD8 T cells per BM
C
B cells per liver
B cells per spleen
B cells per BM
D
NK cells per liver
NK cells per spleen
NK cells per BM

Figure 5.11. Relative fitness of lymphoid populations in mixed bone marrow chimeras during *L. donovani* infection. Liver, spleen, and BM was taken was from naïve, d14- and d28-infected mixed bone marrow chimeric mice. Flow cytometry was used to identify WT ($CD45.1^{+)}$ and KO ($CD45.2^{+}$) leukocytes. CD4 T cells **(A)**, CD8 T cells **(B)**, B cells **(C)**, and NK cells **(D)** were identified based on expression of surface markers indicated in **Table 5.2**. Data is mean ± SD; n = 9-13 chimeric mice per group (pooled from 2 independent experiments); **P* < 0.05, ***P* < 0.01, ****P* < 0.001, *****P* < 0.0001, Two-way ANOVA with Tukey's multiple comparisons correction. NK = Natural Killer.

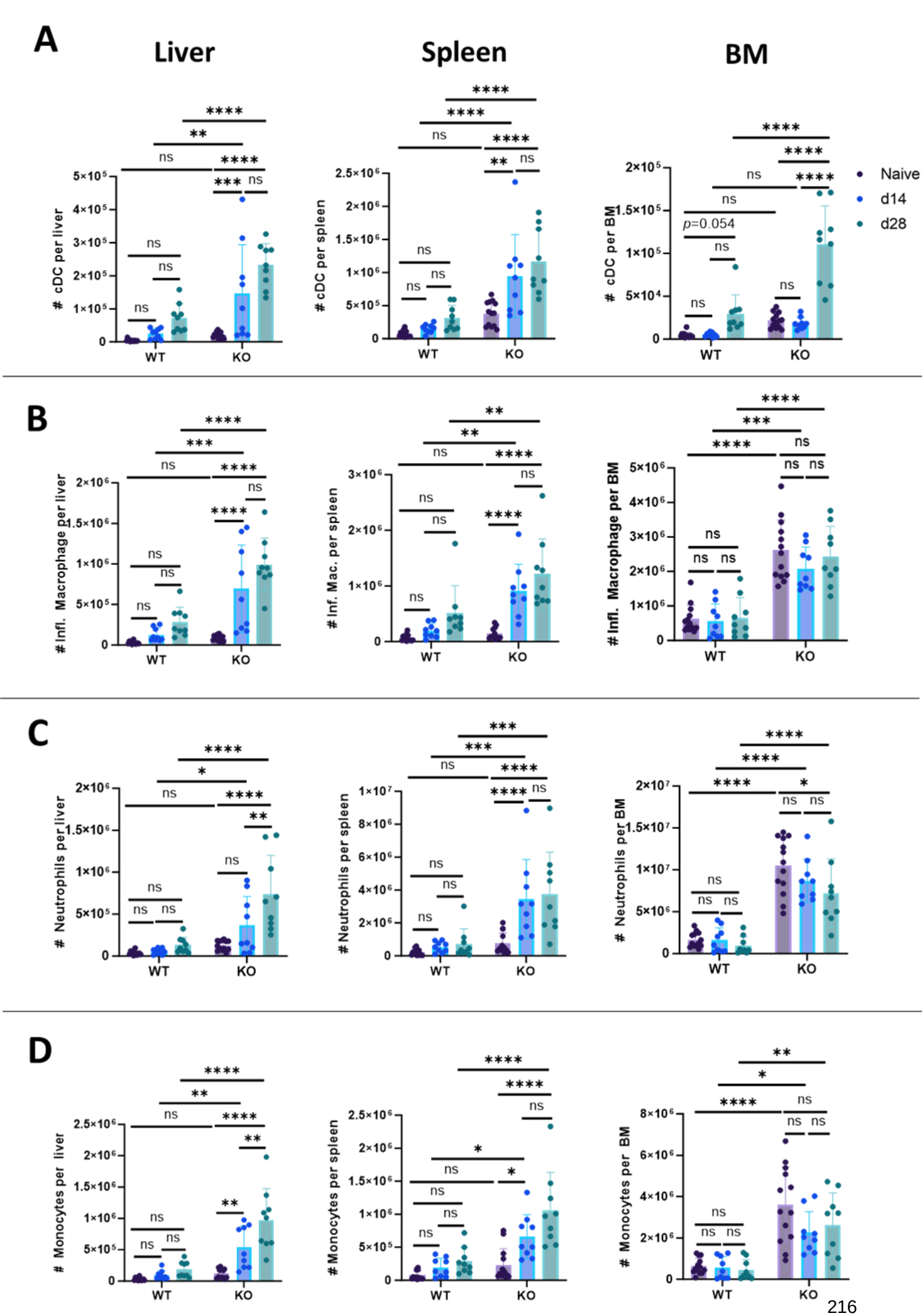
A
Liver
Spleen
BM
cDC per liver
cDC per spleen
cDC per BM
Naive
d14
d28
p=0.054
WT
KO
B
Infl. Macrophage per liver
Inf. Mac. per spleen
Infl. Macrophage per BM
C
Neutrophils per liver
Neutrophils per spleen
Neutrophils per BM
D
Monocytes per liver
Monocytes per spleen
Monocytes per BM

Figure 5.12. Relative fitness of myeloid populations in mixed bone marrow chimeras in immune tissues during *L. donovani* infection. Liver (left), spleen (middle), and BM (right) was taken was from naïve, d14- and d28-infected mixed bone marrow chimeric mice. Flow cytometry was used to identify WT ($CD45.1^+$) and KO ($CD45.2^+$) leukocytes. cDCs ($CD11c^+$ MHC-II^+) **(A)**, inflammatory macrophages ($CD11b^+$ $Ly6C^{hi}$ $F4/80^+$) **(B)**, neutrophils ($CD11b^+$ $Ly6G^+$) **(C)**, and monocytes ($CD11b^+$ $Ly6C^+$) **(D)** were identified based on expression of surface markers indicated in **Table 5.2**. Data is mean ± SD; n = 9-13 chimeric mice per group (pooled from 2 independent experiments); **P* < 0.05, ***P* < 0.01, ****P* < 0.001, *****P* < 0.0001, Two-way ANOVA with Tukey's multiple comparisons correction. cDC = conventional dendritic cell, Infl. Macrophage = Inflammatory macrophage.

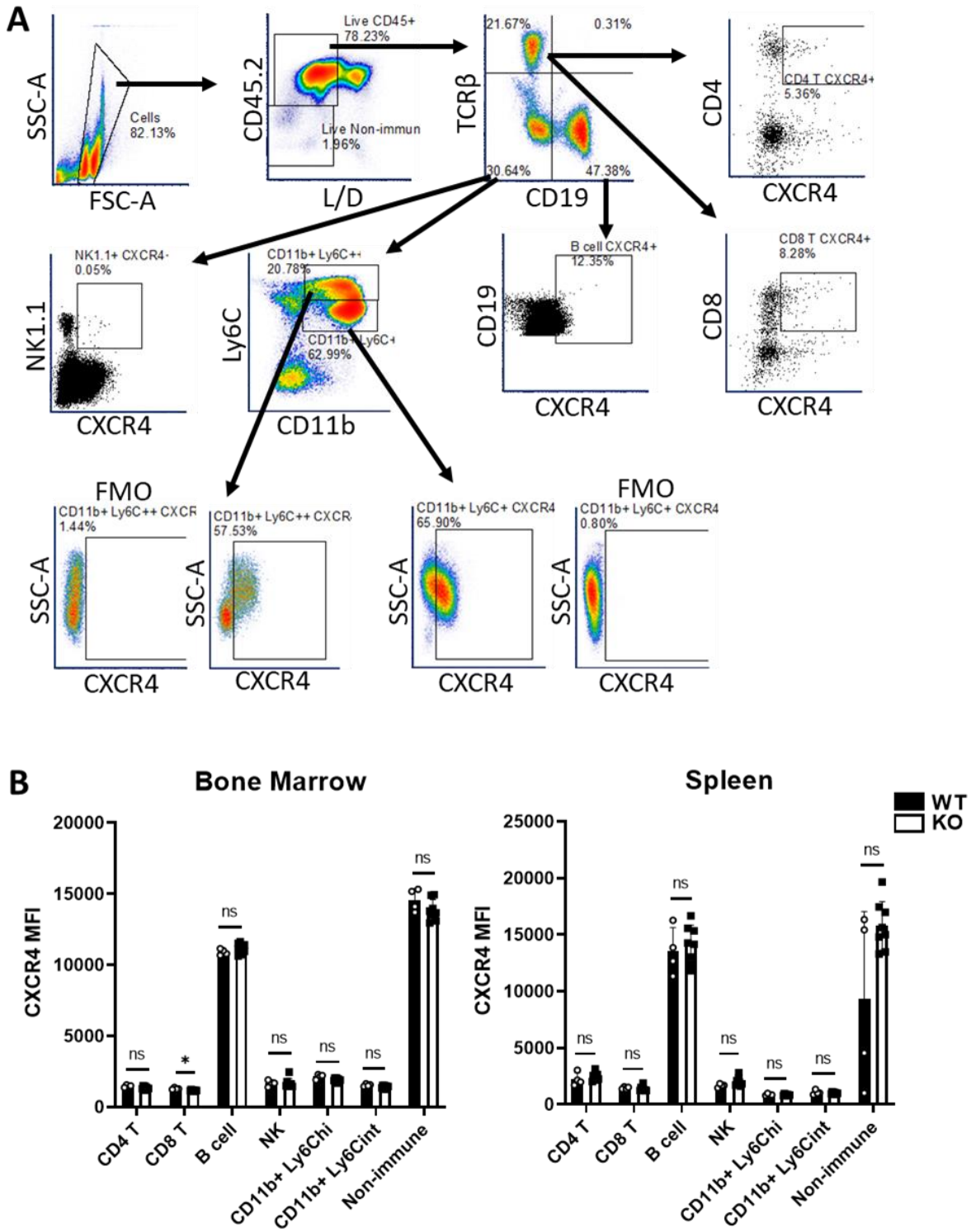

Figure 5.13. CXCR4 abundance on myeloid cell surface membranes is unaltered by deletion of *Trim24*. WT and KO C57BL/6 mice were sacrificed, bone marrow cells were isolated and processed into single cell suspensions as described previously. Flow cytometry was performed to detect immune cell populations using fluorophore-conjugated antibodies detecting CD45.2, TCRβ, CD19, NK1.1, CD11b, Ly6C, Ly6G, and CXCR4. Gating strategy is shown in **(A)**. Data was processed in FCS Express 7 and MFIs are presented in **(B)**. Data represent mean of MFI ± SD, n=4 WT, 8 KO mice. **P*<0.05, multiple t-tests with Holm-Šídák correction.

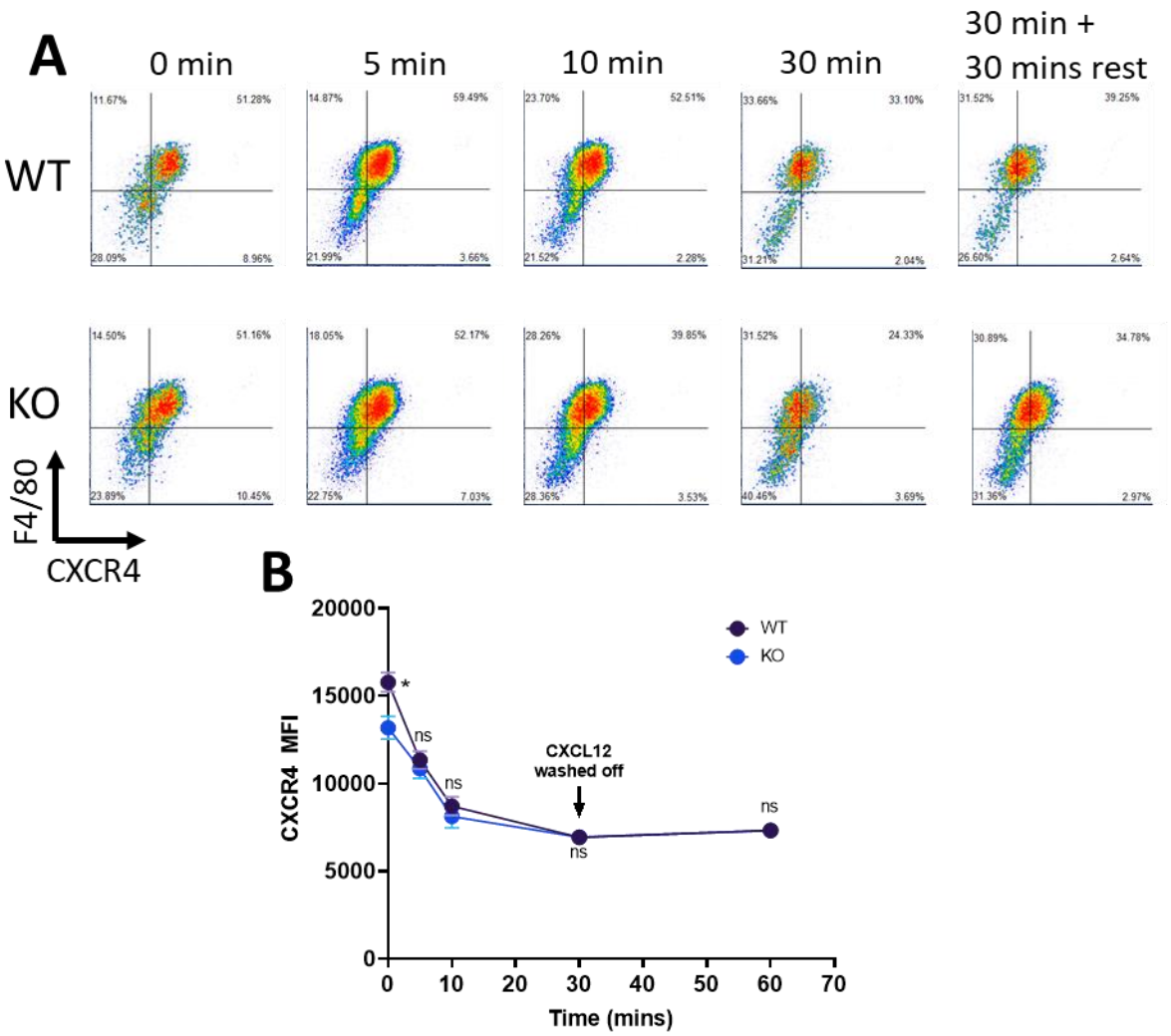

Figure 5.14. **Internalisation of CXCR4 is not affected by deletion of *Trim24* in macrophages.** WT and KO BMDMs were differentiated from isolated WT and KO BM cells for 7 days as described previously. BMDMs were treated with 50nM recombinant CXCL12 for 0, 5, 10, and 30 minutes to induce CXCR4 receptor internalisation. For one group of cells, after 30 mins stimulation, CXCL12 was washed off and the BMDMs were incubated for a further 30 mins. BMDMs were harvested and flow cytometry was performed to detect the macrophage marker F4/80, and CXCR4. Data was analysed in FCS Express 7 (gating shown in **A**). MFI of F4/80$^+$ CXCR4$^+$ cells was quantified at each time point (**B**). Data represents mean of median MFI; BMDMs from n=3 WT and 3 KO mice; **P*<0.05, Two-way ANOVA with Bonferroni correction.

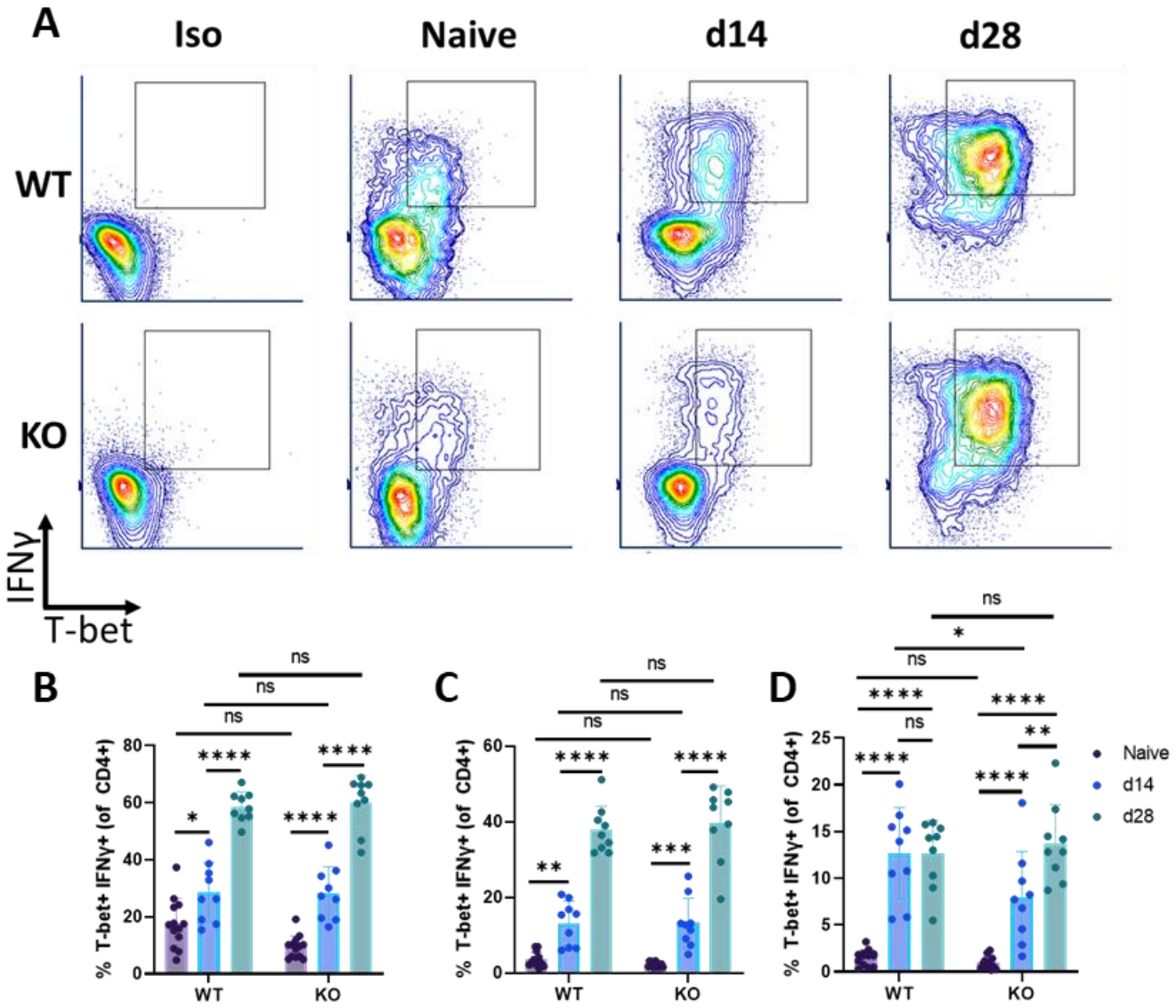

Figure 5.15. *L. donovani*-induced Th1 cell expansion is not affected by deletion of *Trim24*. Naïve, d14- and d28-infected mixed BM chimeric were sacrificed and liver, spleen, and bone marrow cells were stimulated with PMA, Ionomycin, and BFA for 3 hours. Cells were then stained with fluorophore-conjugated antibodies to detect Th1 cells (TCRβ$^+$ CD4$^+$ IFNγ$^+$ T-bet$^+$) and analysed by flow cytometry. Gating strategy is shown in **A**; live cells were gated on TCRβ$^+$ CD4$^{+,}$ and then on IFNγ$^+$ T-bet$^+$ to show Th1 cells. The proportion of Th1 cells within the CD4$^+$ cell population was calculated for the liver **(B)**, spleen **(C)**, and BM **(D)**. Data is mean ± SD; n = 9-13 chimeras per group (pooled data from two independent experiments); ns = not significant, *p < 0.05, **p < 0.01, ***p < 0.001, ****p < 0.0001, Two-way ANOVA with Tukey's multiple comparisons test.

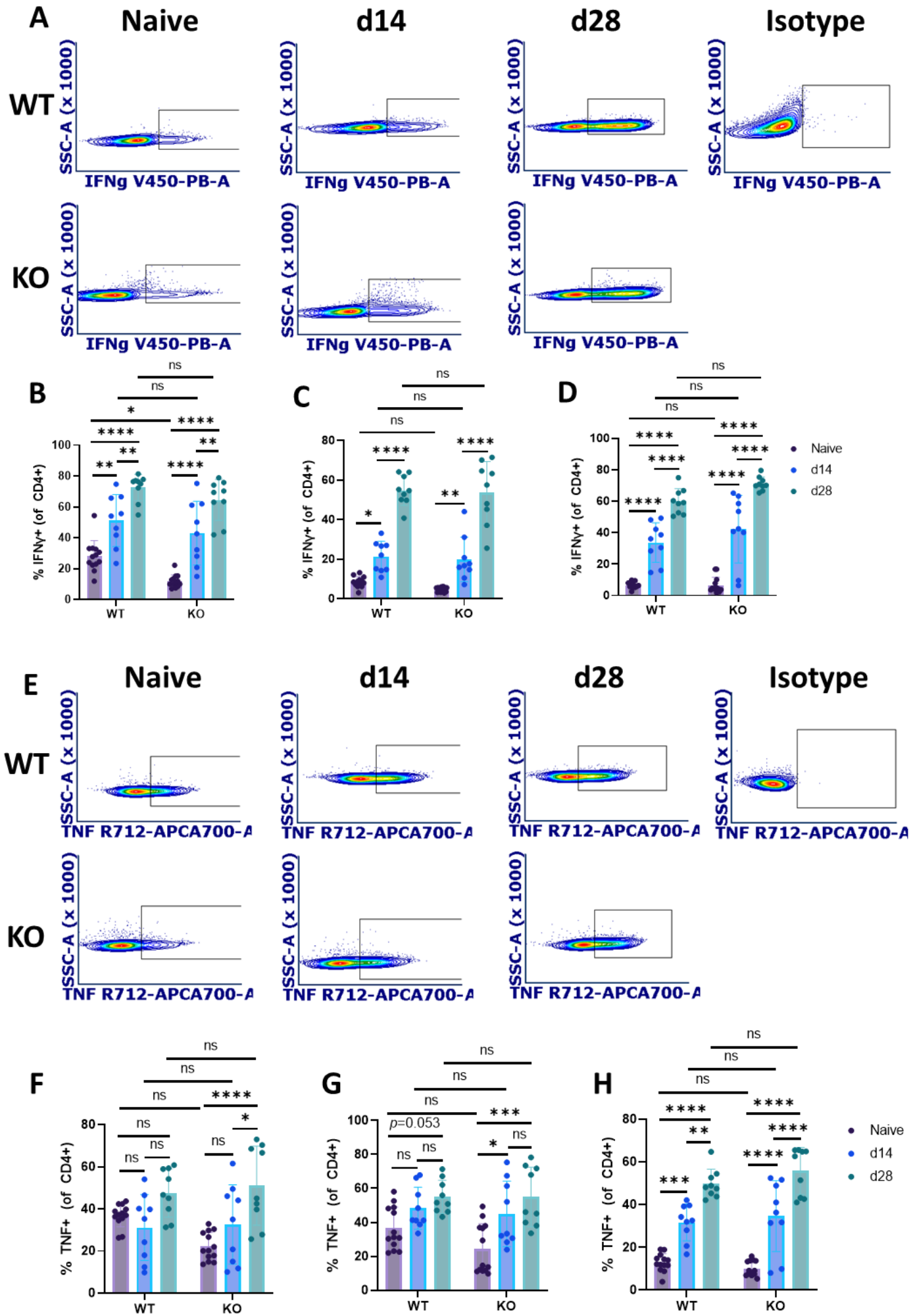
A
Naive
d14
d28
Isotype
WT
KO
SSC-A (x 1000)
IFNg V450-PB-A
B
C
D
% IFNγ+ (of CD4+)
WT
KO
Naive
d14
d28
E
TNF R712-APCA700-A
F
G
H
% TNF+ (of CD4+)
p=0.053
ns

Figure 5.16. Capacity for inflammatory cytokine production in $CD4^+$ T cells is increased during *L. donovani* infection but is unaffected by *Trim24* deletion. Naïve, d14-, and d28 mixed BM chimeras were sacrificed, and liver, spleen, and BM was harvested and processed into single cell suspensions. Cells were stimulated with PMA, Ionomycin, and BFA for 3 hours. Cells were fixed, permeabilised, and stained with fluorophore-conjugated antibodies to detect IFNγ and TNF production in $CD4^+$ T cells (defined as $TCR\beta^+$ $CD4^{+)}$. Gating for IFNγ and TNF is shown in **A** and **E**, respectively. Proportion of $IFN\gamma^+$ and TNF^+ cells was calculated for liver **(B,F)**, spleen **(C,G)**, and BM **(D,H)**. Data is mean ± SD; n = 9-13 mice per group; ns = not significant, *$p < 0.05$, **$p < 0.01$, ****$p < 0.0001$, Two way ANOVA with Tukey's multiple comparisons test.

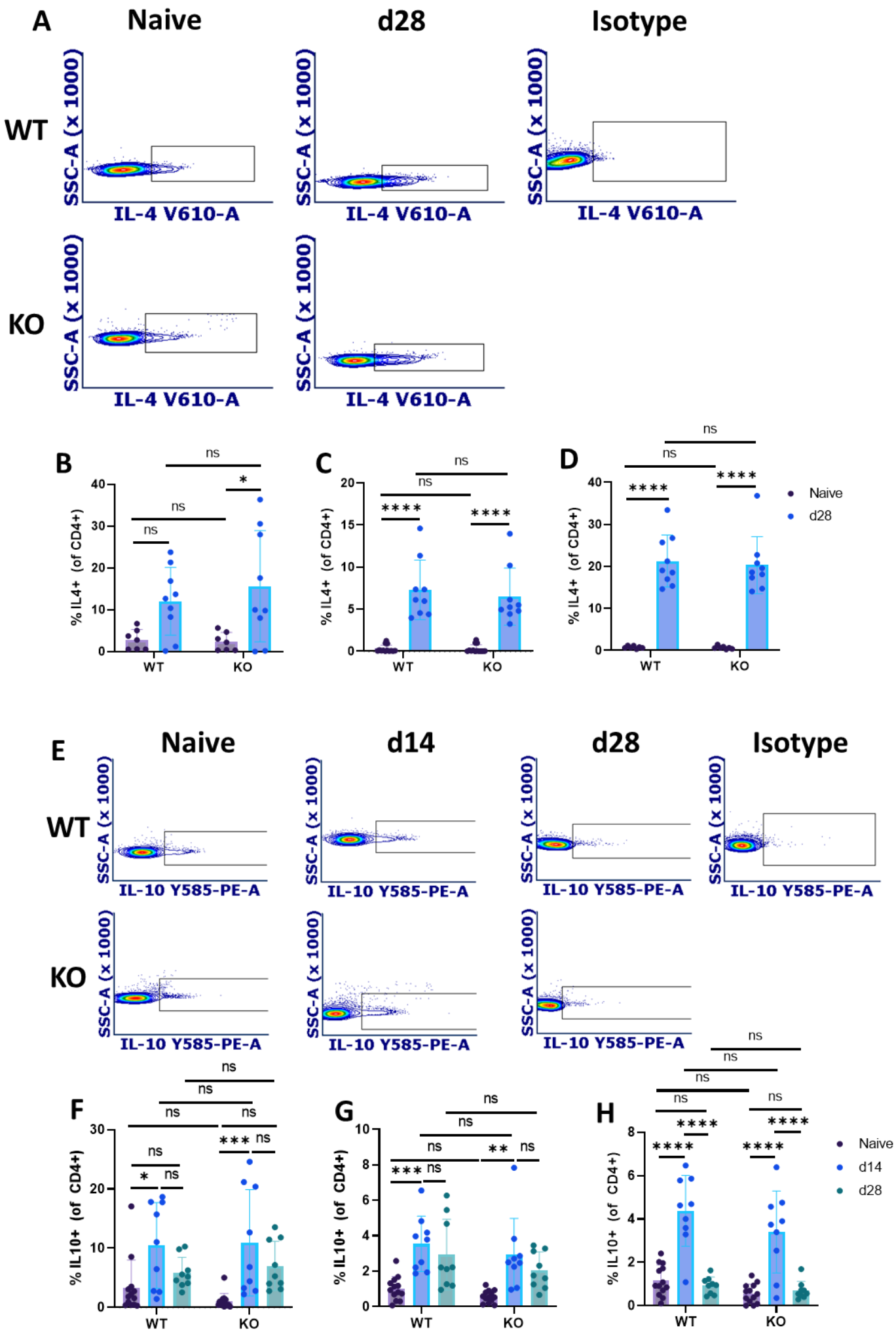
A
Naive
d28
Isotype
WT
KO
SSC-A (x 1000)
IL-4 V610-A
B
C
D
% IL4+ (of CD4+)
ns
*
****
WT
KO
Naive
d28
E
d14
IL-10 Y585-PE-A
F
G
H
% IL10+ (of CD4+)
***
**
Naive
d14
d28

Figure 5.17. Capacity for regulatory cytokine production in CD4$^+$ T cells is increased during *L. donovani* infection but is unaffected by *Trim24* deletion. Naïve, d14-, and d28 mixed BM chimeras were sacrificed, and liver, spleen, and BM was harvested and processed into single cell suspensions. Cells were stimulated with PMA, Ionomycin, and BFA for 3 hours. Cells were fixed, permeabilised, and stained with fluorophore-conjugated antibodies to detect IL-4 and IL-10 production in CD4$^+$ T cells (defined as TCRβ$^+$ CD4$^+$). Gating for IL-10 and IL-4 is shown in **A** and **C**, respectively. Proportion of IL-4$^+$ and IL-10$^+$ cells was calculated for liver **(A,F)**, spleen **(B,G)**, and BM **(C,H)**. Data is mean ± SD; n = 9-13 mice per group; ns = not significant, *$p < 0.05$, **$p < 0.01$, ****$p < 0.0001$, Two way ANOVA with Tukey's multiple comparisons test.

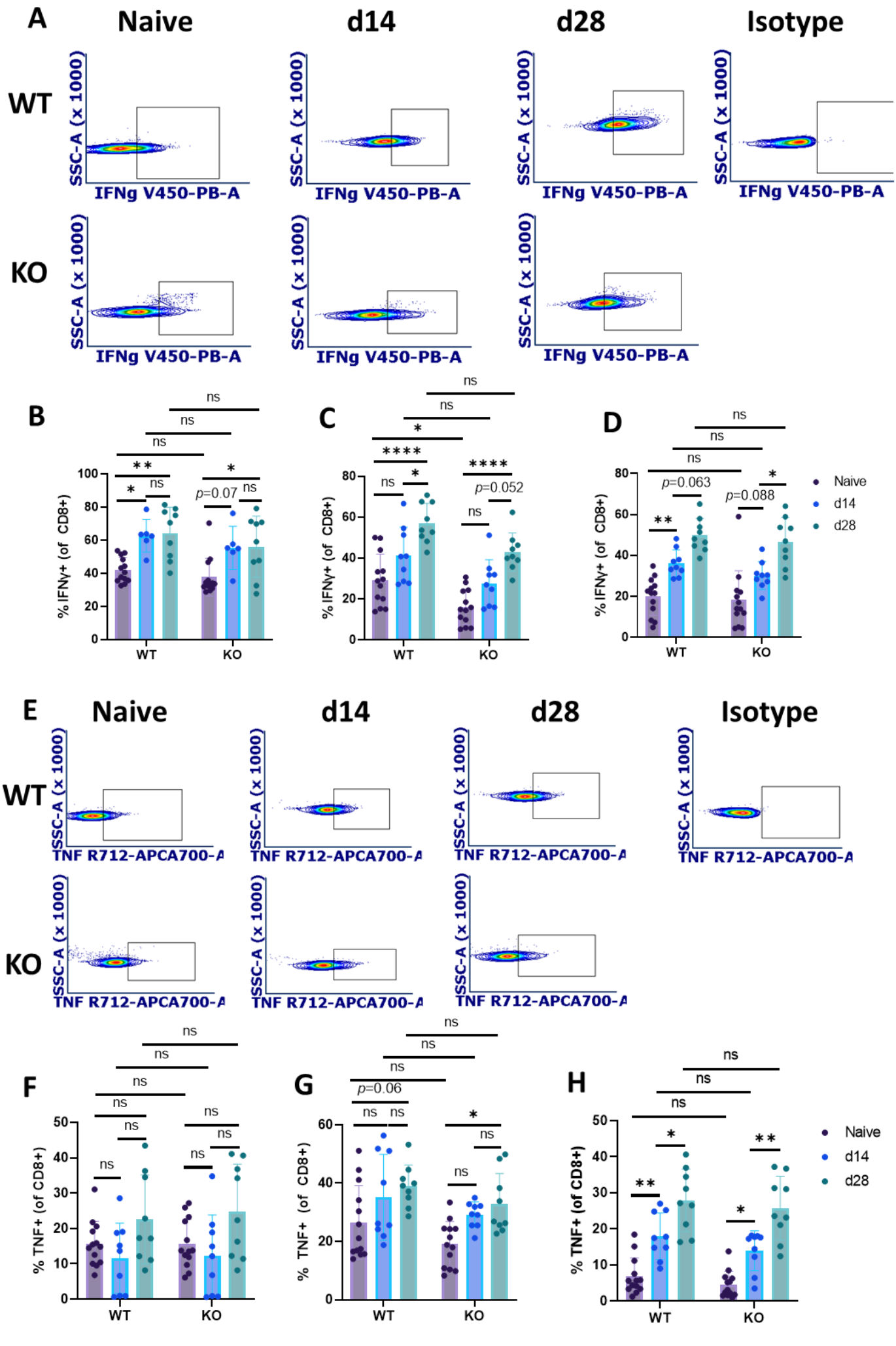
A
Naive
d14
d28
Isotype
WT
KO
SSC-A (x 1000)
IFNg V450-PB-A
B
C
D
% IFNγ+ (of CD8+)
WT
KO
ns
*
**
****
p=0.07
p=0.052
p=0.063
p=0.088
Naive
d14
d28
E
TNF R712-APCA700-A
F
G
H
% TNF+ (of CD8+)
p=0.06

Figure 5.18. Capacity for inflammatory cytokine production in CD8 T cells is increased during *L. donovani* infection but is unaffected by *Trim24* deletion. Naïve, d14-, and d28 mixed BM chimeras were sacrificed, and liver, spleen, and BM was harvested and processed into single cell suspensions. Cells were re-stimulated with PMA, Ionomycin, and BFA for 3 hours. Cells were fixed, permeabilised, and stained with fluorophore-conjugated antibodies to detect IFNγ and TNF production in CD8 T cells (defined as $TCR\beta^+$ $CD8^+$). Gating for IFNγ and TNF is shown in **A** and **E**, respectively. Proportion of $IFN\gamma^+$ and TNF^+ cells was calculated for liver **(B,F)**, spleen **(C,G)**, and BM **(D,H)**. Data is mean ± SD; n = 9-13 mice per group; ns = not significant, **p* < 0.05, ***p* < 0.01, *****p* < 0.0001, Two way ANOVA with Tukey's multiple comparisons test.

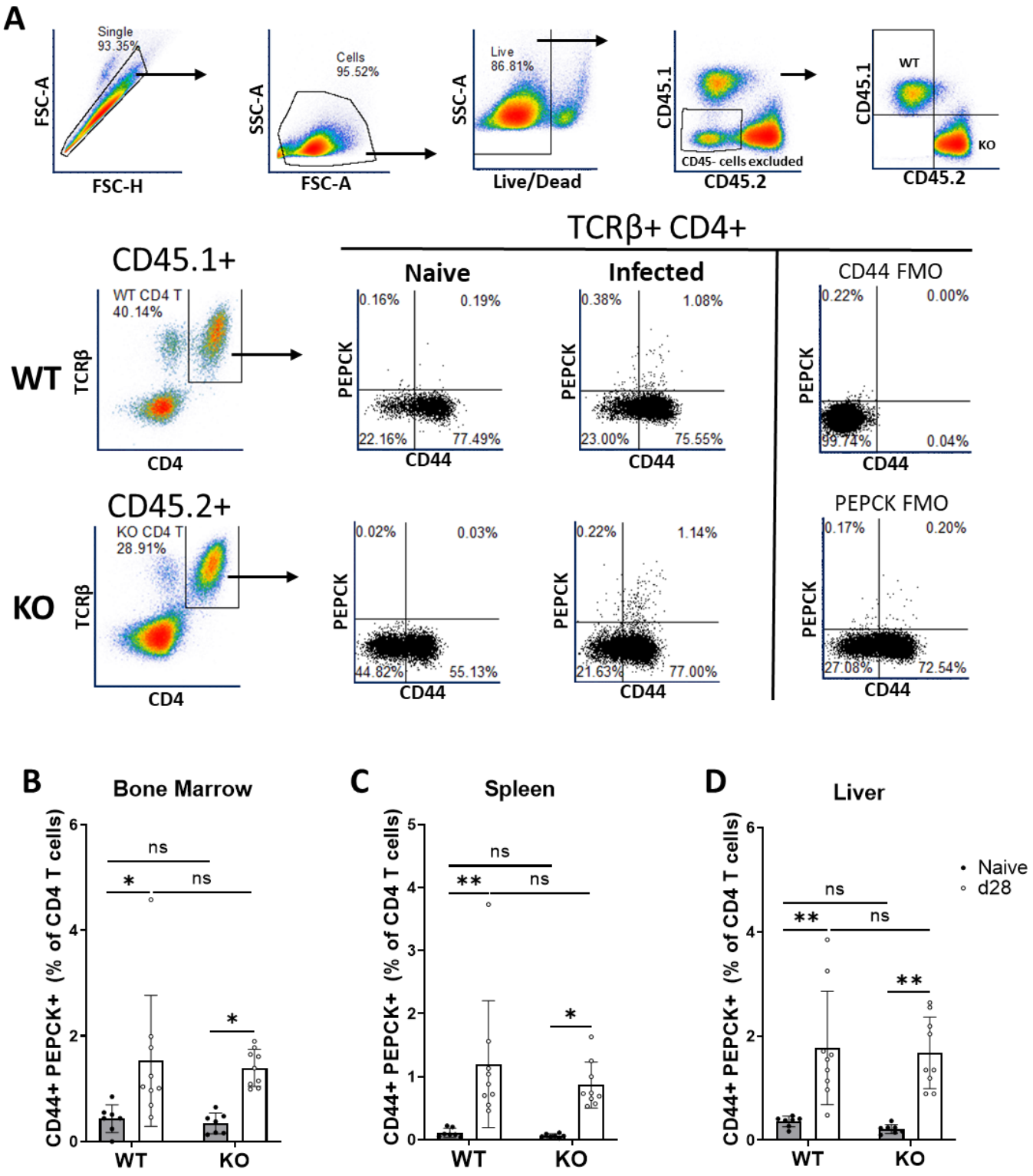

Figure 5.19. *Trim24* deletion does not affect the generation of antigen-specific CD4 T cells during *L. donovani* infection. Single cell suspensions were prepared from BM, spleen and liver of d28-infected mixed BM chimeric mice, and restimulated for 3 hours with BFA, PMA and Ionomycin as described previously. Flow cytometry was then performed to detect *Leishmania*-specific CD4 T cells using a combination of antibodies to detect TCRβ, CD4, CD44 (T cell activation marker), and a fluorochrome-conjugated I-A^b-$PEPCK_{335-351}$ tetramer. **(A)** Gating strategy to detect activated antigen-specific CD4 T cells. The proportion of $CD44^+$ $PEPCK^+$ cell as a proportion of total WT or KO $CD4^+$ T cells was quantified in the BM **(B)**, spleen **(C)**, and liver **(D)**. Data represents mean ± SD; n=7-9 naïve and d28 infected mixed BM chimeras; ***P*<0.01, **P*<0.05, ns=not significant, Two-way ANOVA with Tukey's correction.

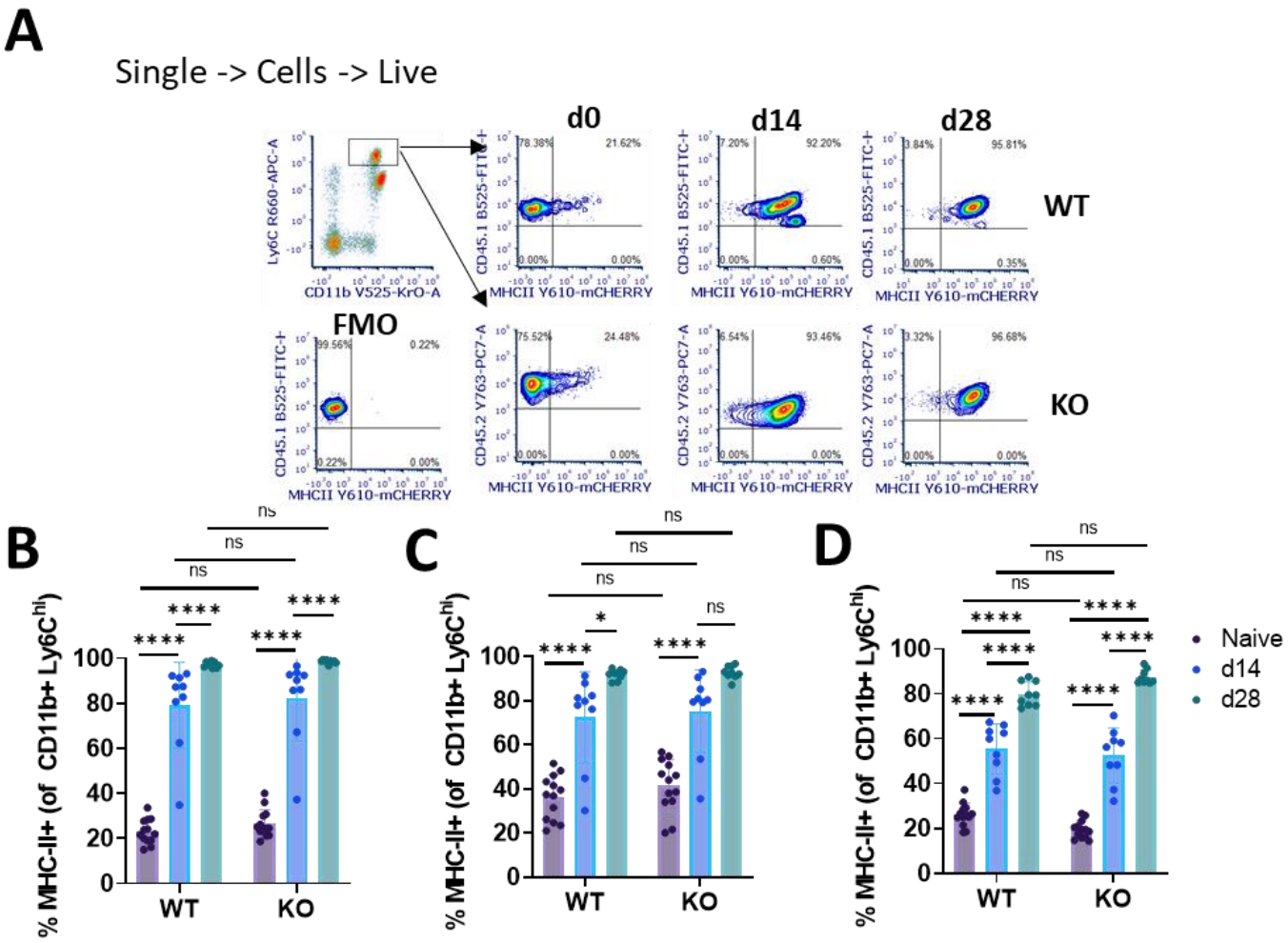

Figure 5.20. *L. donovani*-induced upregulation of MHC-II on Ly6C^{hi} monocytes is not affected by *Trim24* deletion. Naïve, d14- and d28-infected mixed BM chimeric mice were sacrificed, and liver, spleen and BM was excised and processed for flow cytometry. WT (CD45.1^{+}) and KO (CD45.2$^{+)}$ monocytes (CD11b^{+} Ly6C^{hi}) **(A)** were detected using fluorochrome-conjugated antibodies. The proportion of MHCII expressing Ly6C^{hi} monocytes was calculated for each time point in the liver **(B)**, spleen **(C)**, and BM **(D)**. Data is mean ± SD; n=9-13 mixed BM chimeras per group; ns = not significant, *p < 0.05, **p < 0.01, ****p < 0.001; Two-way ANOVA with Tukey's multiple comparisons test.

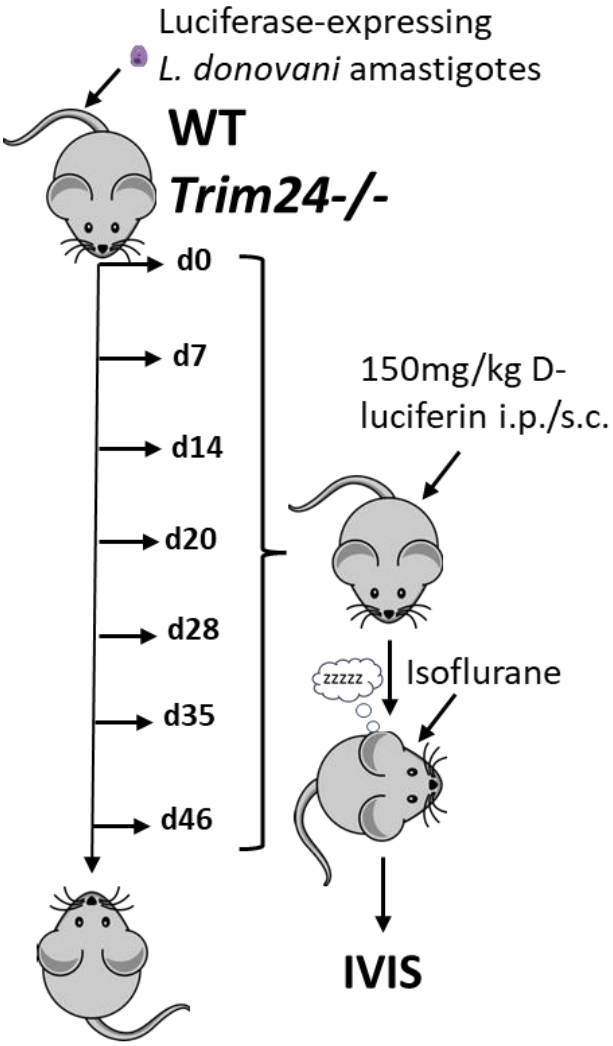

Figure 5.21. Tracking parasite burden via IVIS imaging. WT and KO C57BL/6 mice were injected intravenously with $3x10^7$ luciferase-expressing *L. donovani* amastigotes. Weekly after infection, mice were injected with 150mg/kg D-luciferin, and total flux was measured via IVIS imaging. i.p. = intra-peritoneal, s.c. = subcutaneous.

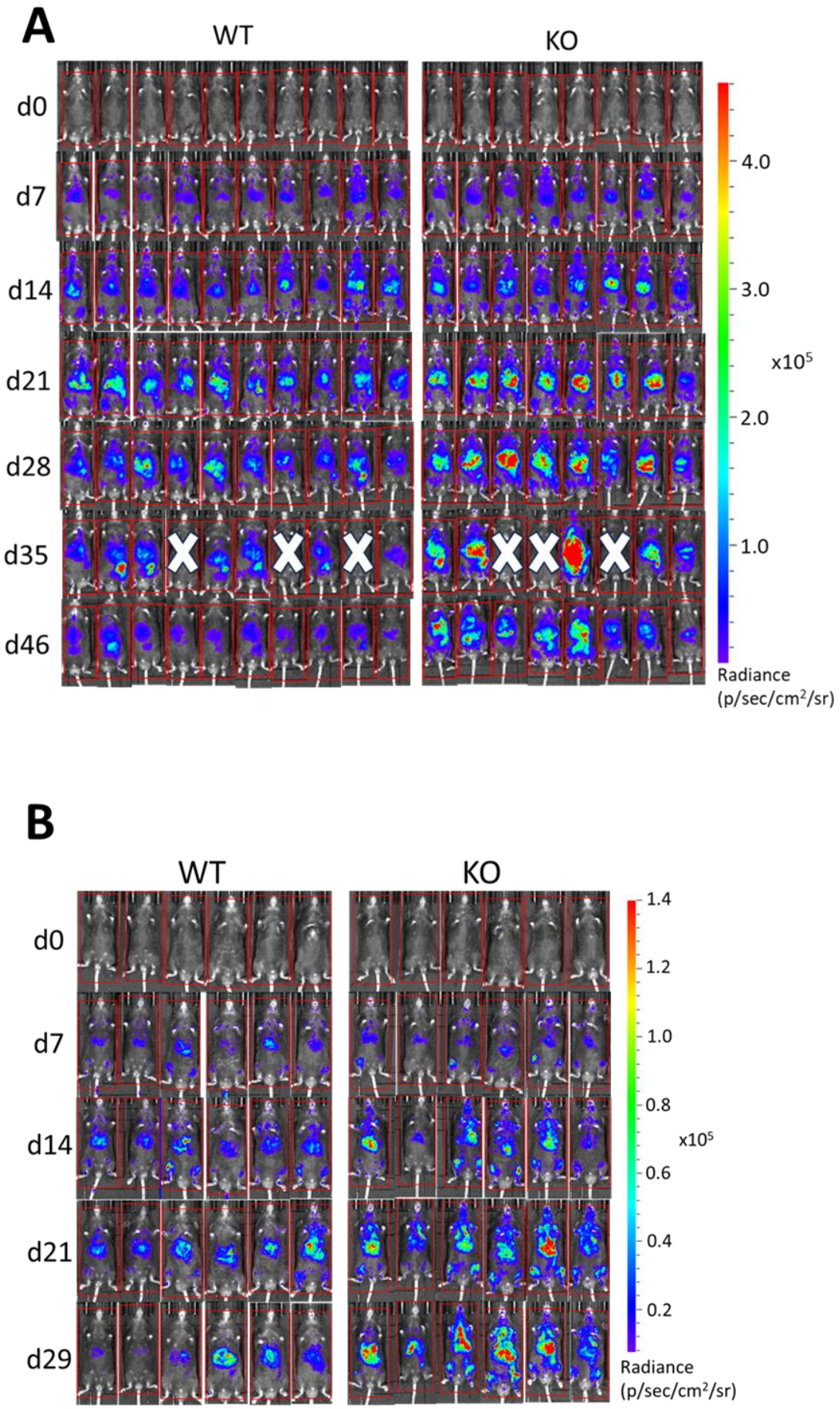

Figure 5.22. IVIS imaging of WT and KO B6 mice during *L. donovani* infection. C57BL/6 WT and KO mice were infected with *LV9*-REH bioluminescent *L. donovani* amastigotes and imaged via IVIS imaging weekly. Data is from two independent experiments with different end points. The first experiment was a 46-day infection (n=10 WT and 10 KO mice) **(A)**, and the second experiment was 29-day infection (n=6 WT and 6 KO mice) **(B)**. Mice with failed D-Luciferin injections at d35 in **(A)** were omitted from analysis and are indicated with a white cross.

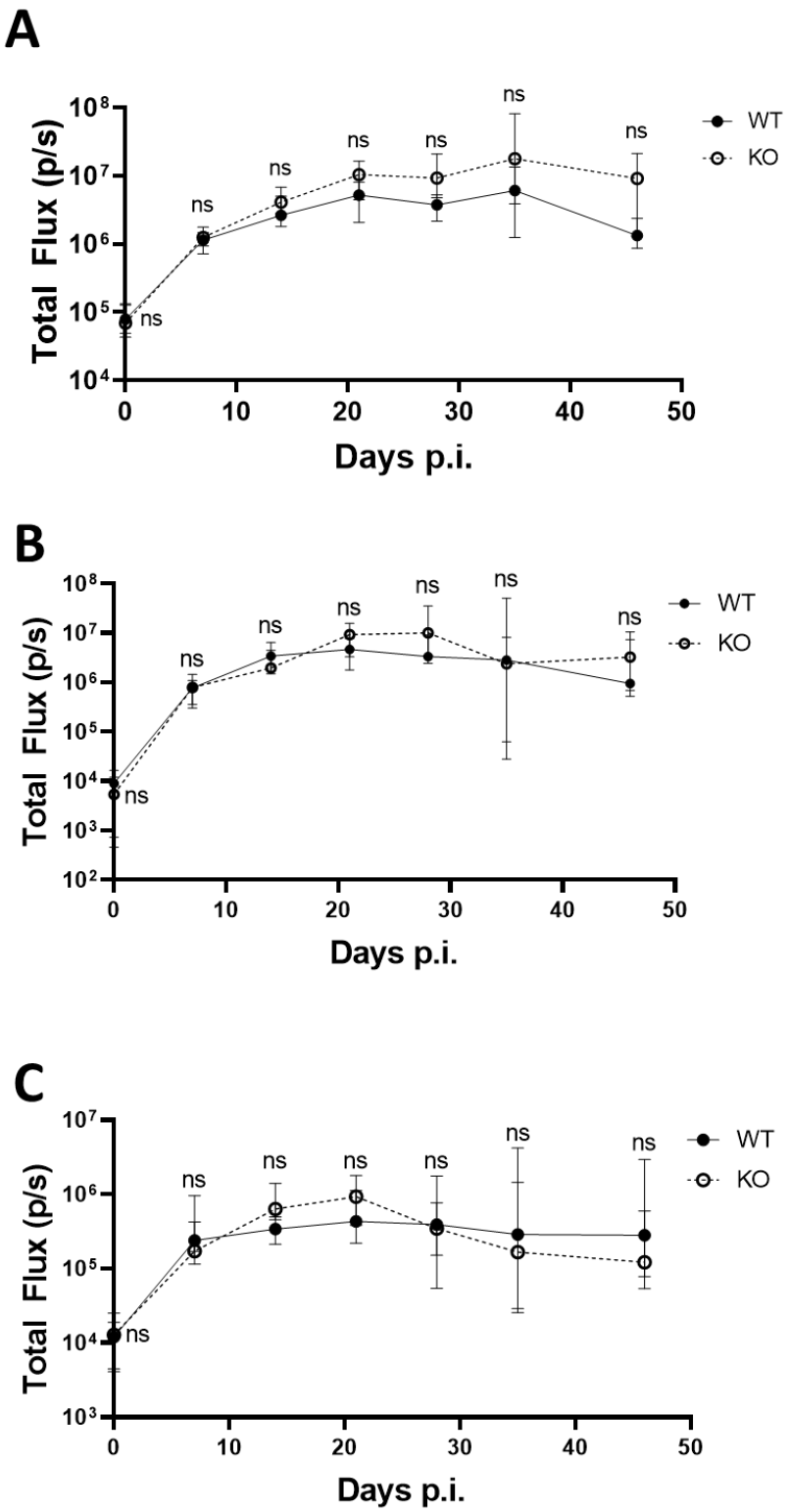

Figure 5.23. Parasite burden of *L. donovani*-infected WT and KO B6 mice measured by IVIS imaging. B6 WT and KO mice were infected with *LV9*-REH bioluminescent *L. donovani* amastigotes and imaged via IVIS imaging weekly. Parasite burden was measured from ROIs from the whole body **(A),** the liver/spleen **(B)**, and the BM **(C)** by measuring Total Flux (photons/second). Data is pooled from two independent experiments with different end points. The first experiment was a 46-day infection (n=10 WT and 10 KO mice), and the second experiment was 29-day infection (n=6 WT and 6 KO mice). Data show median ± 95% confidence interval (CI); ns=not significant, Mixed effects model ANOVA with Tukey's multiple comparisons test.

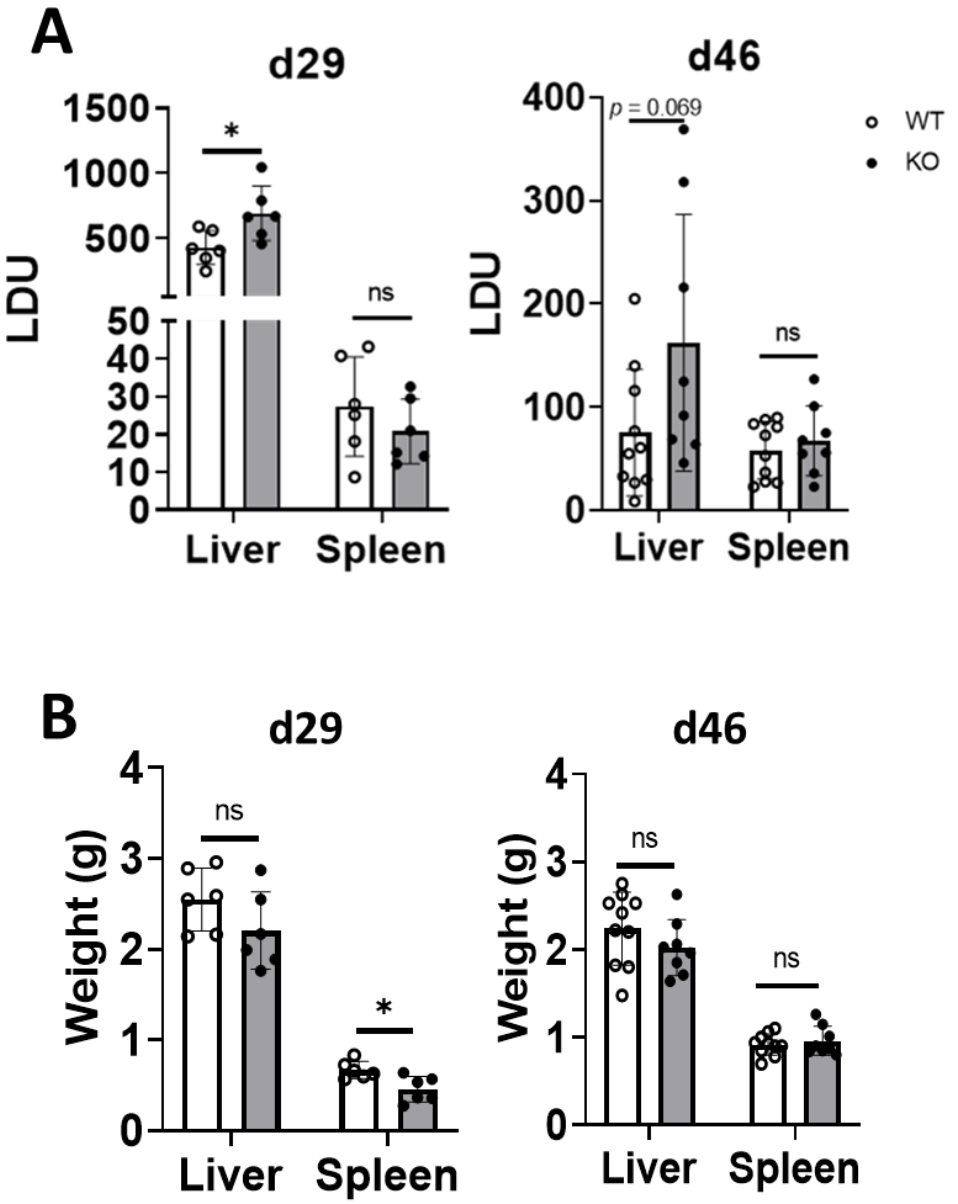

Figure 5.24. Parasite burden of *L. donovani*-infected B6 WT and KO mice by LDU, and organ weights during infection. B6 WT and KO mice were infected with *LV9*-REH bioluminescent *L. donovani* amastigotes for 29 and 46 days. Mice were sacrificed, and impression smears of liver and spleen sections were fixed onto microscope slides and stained with Giemsa. Parasites in liver and spleen were then manually counted by microscopy. LDU = Leishman Donovan units, calculated by multiplying the number of amastigotes per 1000 host cells by the weight of the organ in grams **(A)**. Whole liver and spleen organ weights were also measured **(B)**. Data is from two independent experiments with different end points. The first experiment was a 46-day infection (n=10 WT and 10 KO mice), and the second experiment was 29-day infection (n=6 WT and 6 KO mice); **P*<0.05, ns=not significant, Student's t-test.

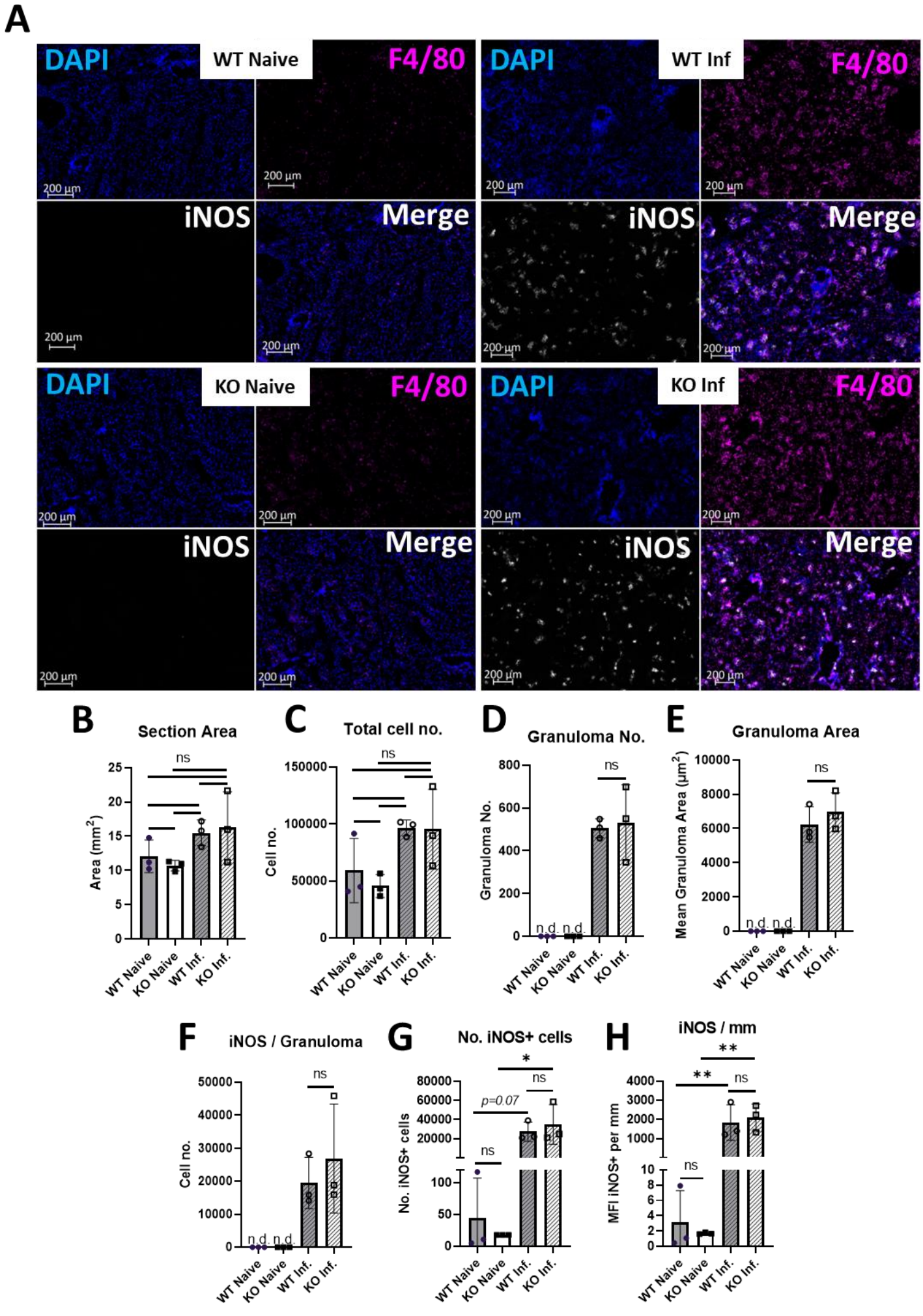
A
DAPI
WT Naive
F4/80
iNOS
Merge
DAPI
WT Inf
F4/80
iNOS
Merge
DAPI
KO Naive
F4/80
iNOS
Merge
DAPI
KO Inf
F4/80
iNOS
Merge
200 µm
B
Section Area
Area (mm²)
C
Total cell no.
Cell no.
D
Granuloma No.
Granuloma No.
E
Granuloma Area
Mean Granuloma Area (µm²)
F
iNOS / Granuloma
Cell no.
G
No. iNOS+ cells
p=0.07
H
iNOS / mm
MFI iNOS+ per mm
ns
n.d.
WT Naive
KO Naive
WT Inf.
KO Inf.

Figure 5.25. *Trim24* deletion does not affect size of granulomas or content of iNOS-expressing cells in the liver during *L. donovani* infection. Frozen liver sections of uninfected and 29-day *L. donovani*-infected WT and KO C57BL/6 mice were stained with fluorophore-conjugated antibodies to detect iNOS expressing macrophages (using the macrophage marker F4/80) **(A)**. Images were collected using the Zeiss AxioScan Z1 slide scanner at 20x resolution. Cell segmentation and quantification was performed using TissueGnostics StrataQuest software. **(B)** Tissue section area. **(C)** Total cell number detected in total section. **(D)** Number of granulomas detected in each tissue section. **(E)** Mean area of granulomas in each tissue section. **(F)** Mean number of $iNOS^+$ cells per granuloma. **(G)** Total number of $iNOS^+$ cells in each tissue section. **(H)** MFI of iNOS per mm in each tissue section. Data represent mean ± SD; n=3 mice analysed per group; One way ANOVA with Tukey correction, **P* < 0.05, ***P* < 0.01. ns = not significant, n.d. = not detected.

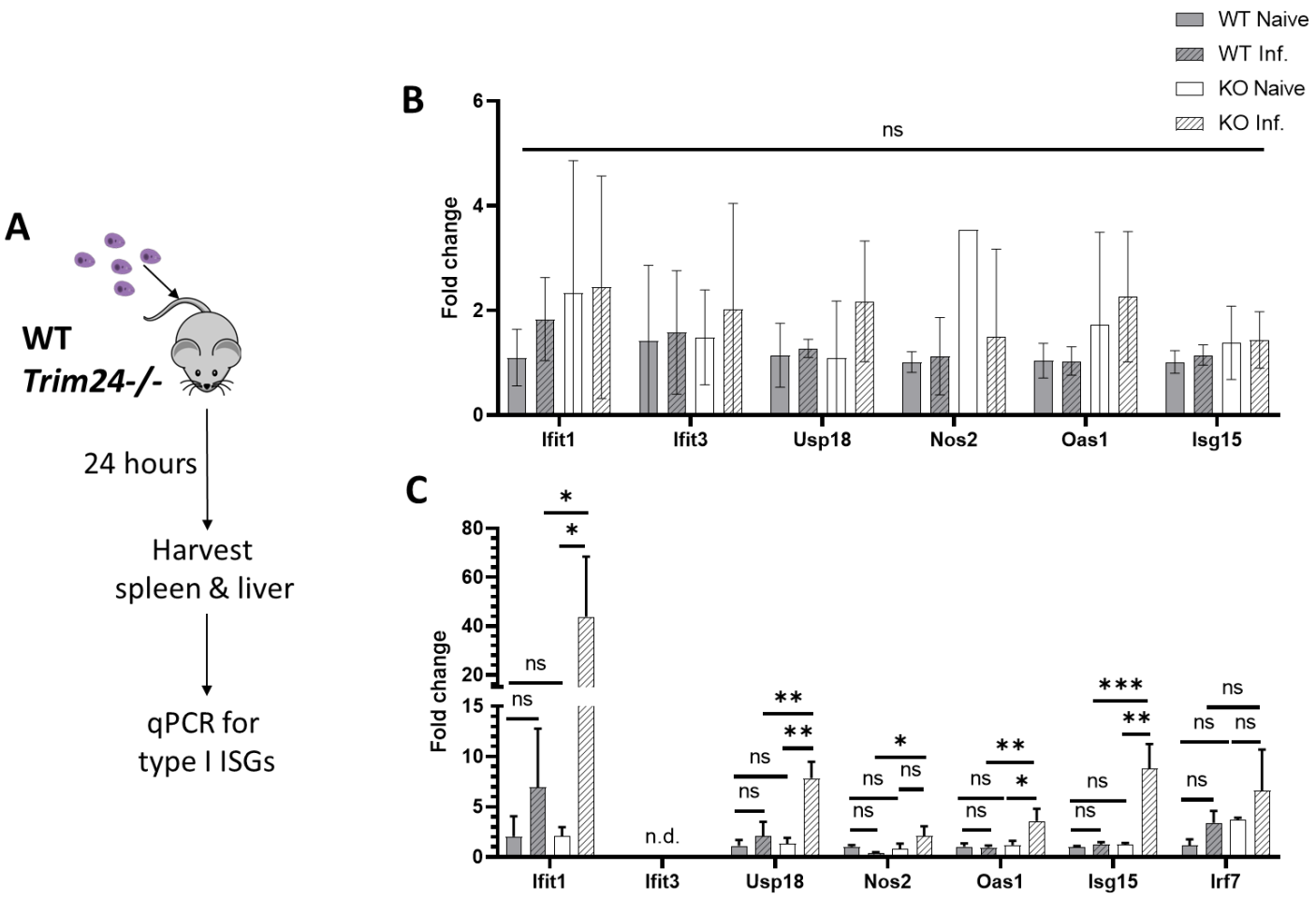

Figure 5.26. Enhanced interferon response in KO spleen 24 hours post-infection. WT and KO B6 mice were infected with *L. donovani* amastigotes for 24 hours. Tissues were harvested, total RNA was extracted and qPCR was performed to determine mRNA abundance of interferon stimulated genes (ISGs) **(A)**. Fold change of each gene was calculated relative to WT naïve samples using the ΔΔCt method for liver **(B)** and spleen **(C)**. Data is mean ± SD; n=3 (2 for KO Naïve); ns = not significant, **P* < 0.05, ***P* < 0.01, ***P* < 0.001, One way ANOVA with Tukey's multiple comparisons test.

Chapter 6. Transcriptional landscape of *L. donovani*-infected WT and KO bone marrow at a single cell level

6.1. Introduction

It has long been established that haematological events are altered by infection with *L. donovani*. Anaemia in VL patients has been consistently described, with levels of anaemia depending on disease severity and averaging at half of normal haemoglobin levels (Wickramasinghe et al. 1987; Varma & Naseem 2010; Cartwright et al. 1948). Anaemia has also been described in the experimental *L. donovani* infection model in Syrian hamsters, where a 2-fold decrease in red blood cell count and haemoglobin levels was recorded 8 weeks after infection (Lafuse et al. 2013). Thrombocytopenia is another haematological alteration that has been widely reported in human (Varma & Naseem 2010) and murine (Preham et al. 2018; Rani et al. 2021) VL. It was recently suggested that thrombocytopenia during VL has many contributing factors, including disruption of megakaryocyte maturation and defective megakaryocyte demarcation membrane system, alterations in levels of hepatic thrombopoietin during infection, and increases in desialylation of platelets during infection (Rani et al. 2021).

Emergency myelopoiesis is another haematological hallmark of *L. donovani* infection in mice. During experimental VL, Long term-HSCs (LT-HSC) were recently shown to move out of quiescence, promote myelopoietic expansion, and eventually become functionally exhausted, losing capacity for self-renewal (Pinto et al. 2017). This was found to be dependent on IFNγ expressed by $CD4^+$ T cells, which in turn was dependent on TNF signalling in the bone marrow (Pinto et al. 2017).
Additionally, Abidin et al. showed that while they did not see a change in the proportion of myeloid progenitor cells during *L. donovani* infection, they saw a striking upregulation of Sca-1 on GMPs (Abidin et al. 2017), associated with an emergency GMP phenotype with increased myeloproliferative potential (Buechler et al. 2013; MacNamara et al. 2011). Furthermore, Abidin et al. showed that increased myelopoiesis and the regulatory-skewed extracellular cytokine environment in the BM favoured infection of new monocytes, thus promoting VL progression (Abidin et al. 2017). In a more recent study, $Ly6C^{hi}$ monocytes were shown to expand in the BM during *L. donovani* infection in B6 mice, a process dependent on IFNγ-producing $CD4^+$ T cells and inhibited by IL-10 (Romano et al. 2021). The resulting monocytes were MHC-II^{hi}, and continued activation of BM monocytes was

dependent on the presence of parasites residing in the BM (Romano et al. 2021). However, relatively little is known of the immune landscape in the BM during *L. donovani* infection.

Single-cell RNA-seq is quickly becoming standard practice in the investigation of cell-specific intrinsic alterations between conditions (e.g. infections). However, to our knowledge only one study has used this approach to study the BM during VL (Karagiannis et al. 2022). Karagiannis et al. used a dual scRNAseq approach to identify rare parasitized cell populations in BALB/c BM and the spleen at 60 days post-infection with *L. donovani* to explore the propensity for parasites to infect non-phagocytic cell types. Distinct parasitized cell clusters were identified in both the spleen and BM. While the main parasitized cell type in the spleen was monocytes, a surprising result was the identification of HSCs as a major parasitized cell type in the BM. This was confirmed in *in vitro* assays in which HSCs isolated from BALB/c mice were successfully infected with Red Fluorescence Protein (RFP)-expressing *L. donovani,* and was attributed to the expression of CD16/32 and CD93 (both known phagocytic receptors (Uribe-Querol & Rosales 2020; Norsworthy et al. 2004)) by HSCs (Karagiannis et al. 2022). This study was focused on the phenotype of parasitized cells in the BM and spleen, and does not explore the effect of infection on the BM immune landscape.

Given the data from the previous chapter showing the competitive advantage of *Trim24*-KO cells compared to WT cells in a mixed BM chimera environment, we performed scRNA-seq on BM extracted from total WT and KO B6 mice (naive and d28 *L. donovani*-infected).

6.2. Chapter Aims

- To use scRNA-seq to:
    - Analyse transcriptional effects of TRIM24 deletion in BM leukocyte cell types at the steady state, and at d28 *L. donovani* infection.

    - Outline a transcriptional landscape of d28 *L. donovani*-infected WT B6 BM.

    - Build upon a previously established model of $CD4^+$ T cell-mediated LT-HSC exhaustion during *L. donovani* infection in WT B6 BM, and determine other driving effects of emergency myelopoiesis.

6.3. Results

6.3.1. Experimental design and workflow

Given our previous data showing a competitive advantage for KO leukocytes in the BM, we sought to investigate effects of *Trim24* deletion in the BM in the steady state and during *L. donovani* infection. We isolated BM from WT and KO mice infected or not with *L. donovani* for 28 days as described in **2.1.3.**, and obtained single cell suspensions of BM samples as described in **2.7.4.** (**Figure 6.1**). Sample sizes were two mice per group, apart from the KO naive group (one mouse). Within each group, BM cells from all mice were pooled. Hepatic and splenic parasite burdens were comparable between WT and KO mice (**Figure 6.2**) Each single cell suspension was diluted to 1000 cells/µL, and 10,000 cells per sample were then processed for library preparation and sequencing. Library preparation was performed by Dr Sally James, and sequencing was performed as described previously (**Methods 2.13**). Based on FastQC summary sequencing data, between 8,134-16,742 cells were sequenced per sample (9,124 in WT Naive; 9,217 in WT Infected; 16,742 in KO Naive; 8,134 in KO Infected), and in total between 19,126-20,228 genes were detected (19,585 in WT Naive; 19,614 in WT Infected; 20,228 in KO Naive; 19,126 in KO Infected) (**Supp. Table 1**).

Quality control (QC) steps similar to those in **Chapter 4** were performed. Cells with mitochondrial gene expression >10%, and cells with too low or too high feature counts (thresholds were set to 500 and 6000, respectively), were filtered out (**Figure 6.3A&B**). Cells with haemoglobin gene percentage >2%, and platelet gene (*Pecam1* and *Pf4*) percentage >0.5% were also filtered out (**Figure 6.3C&D**). As in **Chapter 4**, ribosomal genes were not filtered out but are shown in **Figure 6.3E**. We also confirmed that no *Trim24* reads were detected in KO samples (**Figure 6.3F**).

After QC steps were performed we analysed 32,190 cells (6,889 in WT Naive; 7,065 in WT Infected; 11,526 in KO Naive; 6,710 in KO Infected). We integrated the samples together and perform our downstream analysis workflow (**Figure 6.1**). Briefly, our workflow firstly performed dimensionality reduction followed by low resolution unsupervised clustering to separate distinct cell types. Dimensionality reduction allowed us to transform our data from high-dimensionality to low-dimensionality, and visualise it in a two-dimensional Uniform Manifold Approximation and Projection (UMAP) space. Low-resolution clustering allowed for identification of broad cell types (e.g. T cells, B cells etc.) through the use of consensus markers, in an unsupervised manner. Higher resolution sub-clustering of broad cell types

allowed for more granular identification of cell types within initial broad clusters. Finally, differential gene expression analysis was performed, and the differentially expressed genes (DEGs) were used for gene set enrichment analysis (GSEA) to identify altered pathways in KO mice in the steady state and during infection (**Figure 6.1**).

6.3.2. UMAP representation reveals cell types present in BM

Initial dimensionality reduction and low-resolution clustering (res=0.5) resulted in ten cell types that could be used for further analysis (**Figure 6.4A**); T Lymphocytes (*Trbc2*, *Cd3d*, *Ccl5*, *Cd3g*, *Trbc1*), B Lymphocytes (top genes: *Igkc*, *Ighm*, *Iglc1*, *Cd79a*, *Vpreb3*, *Cd79b*), Neutrophils (*S100a9*, *Ngp*, *Retnlg*, *S100a8*, *Camp*, *Lcn2*), Basophils (*Prss34*, *Mcpt8*, *Cpa3*), Dendritic cells (*Irf8*, *Siglech*, *Cox6a2*), Monocytes (*Ms4a6c*, *Ccr2*, *Ctsc*, *Fn1*), Macrophages (top genes: *Apoe*, *C1qb*, *C1qa*), Haematopoietic Stem and Progenitor Cells (*Cdk6*, *Cd34*, *Sox4, Flt3*), Granulocyte-Monocyte Progenitors (top genes: *Elane*, *Mpo*, *Prtn3*) (**Figure 6.4B.**). Erythroid cells (*Hbb-bs*, *Hba-a1*, *Hbb-bt*, *Hba-a2*, *Car2*) were removed from further analysis due to the RBC lysis step and data QC steps confounding meaningful data from these cells.

6.3.3. Deletion of *Trim24* does not affect proportions of broad cell types at the steady state

We then assessed differences in relative proportions of cell types between WT and KO bone marrow samples at the steady state to confirm our previous data that TRIM24 does not affect the development of leukocytes in the BM *in vivo* (**Figure 5.2D**). Almost 50% of cells in WT and KO BM were neutrophils. This was followed by B cells (25-30%), NK & T cells (~7%), and then other myeloid and progenitor cell clusters that were between 1% and 7% of BM cells at the steady state in both WT and KO mice (**Figure 6.5A&B**). Using a permutation test, we saw no differences in the proportions of any of the cell types in WT and KO bone marrow in the steady state (**Figure 6.5C**), indicating that at the level of broad cell types TRIM24 is dispensable for the development of immune cells in the bone marrow during the steady state.

6.3.4. Alterations in B cell subsets in naive KO BM

While we did not see any differences in the broad cell clusters between naive WT and KO samples, TRIM24 could affect the proportions and functional phenotypes of immune cell subsets.

To investigate the effects of TRIM24 on bone marrow B cells, we sub-clustered the B Lymphocyte cluster at a higher resolution to identify B cells subsets (**Figure 6.6A**). 13 sub-clusters with distinct gene expression profiles were identified using this approach (**Supp. Figure 1A&B**). B cells express developmental stage-specific markers. Immature B cells leave the BM where they mature into MHC-II-expressing mature B cells, subsets of which can mature further into plasma cells (**Figure 6.6B**). Based on marker genes we detected B cell subsets at each stage of development in WT and KO naïve samples (**Figure 6.6C**). Next, we assessed proportional differences between KO and WT B cell subsets. We split the B cell sub-cluster UMAP for visualisation of cluster proportional differences (**Figure 6.6D**). We then determined the proportion of each sub-cluster as a percentage of the whole B cell population within each sample (**Figure 6.6E**).
We used a permutation test (as in **Chapter 4**) to statistically analyse proportional differences between KO and WT B cell subsets (**Figure 6.6F**). Differences were considered significant when log2 fold difference (log2FD) was >0.5 or <-0.5 and FDR <0.05. We saw significant increases in proportions of KO Early pro-B and pro-B clusters (~2-fold increase), and significant decreases in Immature B and pre-B_2 clusters, though these were only ~1.5-fold decreases (**Figure 6.6F**). No significant differences were seen in any of the mature B cell subsets, plasma cells, pre-B_1 or cycling pro-B cells (**Figure 6.6F**).
Taken together, these results indicate that TRIM24 may play a role in the earliest stages of B cell development but does not affect the resulting number of mature B cells or plasma cells in B6 mice.

Next, we performed DGE analysis to identify transcriptional differences in KO B cell clusters compared to WT (FDR<0.05, log2FC >0 or <0). The majority of DEGs detected were downregulated in KO B cells (**Figure 6.7A**), consistent with BMDMs in **Figure 4.12A**. Interestingly, we only identified 5 and 7 DEGs (all downregulated) in early pro-B and pro-B cells, respectively (**Figure 6.7A**). The B cell cluster pre-B_1 showed the most DEGs (111 down, 7 up), and Mature B_2 (53 down, 11 up) and Mature B_3 (44 down, 8 up) showed the next highest DEG numbers (**Figure 6.7A**). We saw fewer DEGs in the remaining cell clusters; cycling pro-B cells (28 down, 14 up), pre-B_2 (13 down, 2 up), immature B cells (22 down, 5 up), mature B_1 (1 down, 0 up), mature B_4 (5 down, 1 up). No DEGs were found in plasma cells (**Figure 6.7A**).

ORA using GO terms of downregulated genes in each cluster revealed gene sets related to cytoplasmic translation and ribosome biogenesis to be significantly down-regulated, common to all clusters (**Figure 6.7B**). Additionally, we saw a decrease in antigen presentation via MHC-II in Mature B_2 and Mature B_3 clusters (**Figure 6.7B**). DEGs responsible for this

gene set enrichment between and common to all B cell clusters were largely *Rps* and *Rpl* genes (**Figure 6.7C**). While we saw too few up-regulated genes in KO B cell clusters to perform ORA, key oxidative phosphorylation-related genes (*mt-Co1, mt-Co2, mt-Co3, mt-Atp6*) were commonly up-regulated.

Taken together, these results reveal the transcriptional diversity of B cells at each stage of development in the BM, and highlight a potential role for *Trim24* in the assembly of ribosomal subunits, and subsequent protein translation in the cytoplasm, despite its dispensability for mature B cell development. Additionally, oxidative phosphorylation appeared to be enhanced in KO B cells. It should be noted that the low cell number in sub-clusters such as plasma cells is a major reason for the lack of detected DEGs. Enrichment for specific subtypes before sequencing would be required to further explore transcriptional differences of specific cell types.

6.3.5. Alterations in T cell subsets in naive KO BM

To investigate differences in naive KO and WT BM T cell populations, we subset the NK & T Lymphocyte cluster (2,871 cells between all four samples) and performed sub-clustering at a higher resolution as for B cell clusters. We identified ten distinct T cell sub-clusters (**Figure 6.8A**). Identification of T cell subsets were determined through interrogation of canonical gene markers. All clusters expressed *Trbc2* and *Cd3d* apart from the NK cell cluster, and $CD4^+$ and $CD8^+$ T cells clustered separately (**Figure 6.8B**). Top expressed genes in the $CD4^+$ cluster were *Cd4, Maf,* and *Furin*. While $CD4^+$ cells expressed *Ifng,* the Th1-like cell cluster expressed it at higher levels, and additionally expressed *Irf4*, previously shown to regulate Th1 cell function (Mahnke et al. 2016). Tregs (*Foxp3, Nrp1*) were also identified within the $CD4^+$ clusters (**Figure 6.8B**). Among the $CD8^+$ clusters, we observed a naive $CD8^+$ cluster (*Cd8a, Cd8b1, Ccr7, Tcf7*), a cytotoxic T cell (CTL) cluster (*Cd8a, Cd8b1, Ccl4, Gzmb*), and a cluster that contained cells expressing *Cd8a* (but interestingly not *Cd8b1*), *Klrk1, Klrc2,* and γδT cell markers such as *Trdc* (**Figure 6.8B**). We identified an NK cell cluster expressing *Ncr1* and *Nkg7* but not *Trbc2* or *Cd3d*, and an iNKT cell cluster expressing *Zeb2* and *Cx3cr1*, which resembled the $KLRG1^+$ population described by Kane et al. (Kane et al. 2022). Finally, we identified a *Trbc2*+ *Cd3d*+ cluster that was defined by strong expression of ISGs (*Ifit1, Rsad2, Ifit3, Usp18*) (**Figure 6.8B**).

We then analysed differences in proportion of KO and WT T cell subsets (**Figure 6.8C-E**). For visualisation and comparison of UMAP representation between the KO and WT naive samples, we downsampled each sample to 425 cells (**Figure 6.8C**). We saw a significant

decrease (FDR<0.05, log2FC<-0.5 or >0.5) in the proportion of Naive_CD8 for KO compared to WT, and significant increases in the IFN_T cluster and the CD8_gdT cluster (**Figure 6.8E**).

DGE analysis of T cell subsets revealed DEGs detected in Naive_CD8 (10 down, 0 up), CD4 (11 down, 3 up), Treg (1 down, 0 up), CD8_gdT (35 down, 4 up), and NK (2 down, 0 up) (FDR<0.05, log2FC<0) (**Figure 6.9A**). All of the downregulated genes detected in naive and $CD4^+$ T cells were present in the 35 downregulated genes in the CD8_gdT cluster. GSEA analysis of the 35 downregulated genes in CD8_gdT cells revealed top enriched gene sets related to cytoplasmic translation and ribosomal subunit biogenesis (**Figure 6.9B**). The majority of these genes were *Rps* and *Rpl* genes, which encode ribosomal subunit proteins. Furthermore, submission of the 35 downregulated genes to STRING-DB revealed a tight interaction network between them (**Figure 6.9C**). Taken together, these results indicate that TRIM24 may play a role in the differentiation of BM $CD8^+$ T cells, and that *Trim24* deficiency is associated with decreased cytoplasmic translation and ribosome biogenesis in T cells.

6.3.6. Alterations in myeloid and progenitor cells in naive KO BM

Finally, to investigate roles of TRIM24 in myeloid cell subtypes, we subsetted the myeloid and progenitor cell populations and performed high-resolution sub-clustering resulting in 19 cell clusters (**Figure 6.10A**). Firstly, we identified basophils (same as in **Figure 6.4A**). We observed a haematopoietic stem and progenitor cell (HSPC) cluster (*Cd34, Npm1, Kit, Flt3, Sox4*), from which two developmental arcs were defined; one of which is the neutrophil development pathway and the other of which is the monocyte and macrophage development pathway (**Figure 6.10A**).

The neutrophil arc allowed for the identification of each distinct stage of neutrophil development arising from the myeloid progenitor population. We identified neutrophil development stages starting from promyelocytes, and continuing to myelocytes, metamyelocytes, band cells, and finally mature neutrophils. These were defined by the expression of azurophilic (primary) (*Ctsg, Elane*), specific (secondary) (*Camp, Ltf*), and gelatinase (tertiary) (*Mmp8*) granule genes that are expressed in a stage-specific manner during neutrophil development (Xie et al. 2020). Mature neutrophils gain expression of *Cxcr2* and *Ly6g*, and in our data the cluster mNeut.4 also possessed high expression of *Il1b* (**Figure 6.10A&B**).

In the monocyte/macrophage arc, we identified a cycling monocyte cluster (*Ccr2, Ms4a4c*) with high expression of cell cycle genes (*Mki67, Stmn1*), and a more classical monocyte cluster (*Ccr2, Ms4a4c, S100a4, F13a1*) (**Figure 6.10A&B**). We also identified a transitional monocyte/macrophage cluster that expressed both monocyte (*Ccr2, Ms4a4c*) and macrophage (*Apoe, C1qa*) genes (**Figure 6.10A&B**). There were two macrophage clusters identified which resembled M1 (*Eno3, Ace, Adgre4*) and M2 (*C1qa, C1qb, Apoe*) macrophages, respectively. Finally, we identified two cDC clusters; cDC1 (*Siglech, Cox6a2, Irf8*) and cDC2 (*Batf3, Olfm1, Ckb*) (**Figure 6.10A&B**).

We then assessed proportional differences between naive KO and WT myeloid subsets as we did for T and B cell subclusters. We downsampled all samples to 4,227 cells per sample, and show the myeloid UMAP split by genotype (**Figure 6.10C**). We then assessed differences in percentage of each subset, and used a permutation test as done previously for statistical analysis (**Figure 6.10D&E**). We observed significant increases (FDR<0.05, log2FC>0.5) in KO compared to WT for Inf_Mon_Mac (2.67% vs 1.87%), mNeut_1 (3.63% vs 2.01%), and mNeut_3 (14.49% vs 9.25%) compared to WT (**Figure 6.10D&E**). We also detected significant decreases (FDR<0.05, log2FC<-0.5) in ncMon (0.95% vs 1.75%), Band_2 (5.52% vs 7.81%), and mNeut_2 (6.69% vs 11.17%) clusters for KO compared to WT (**Figure 6.10D&E**). No significant differences in other subsets were observed (**Figure 6.10D&E**).

DGE analysis of KO vs WT myeloid subsets revealed more DEGs than in T cell and B cell subsets. Of note, whereas the majority of DEGs in T and B cell subsets were downregulated in KO compared to WT, in myeloid subsets there were more upregulated genes (**Figure 6.11A**). In particular, KO GMPs and cMon clusters had the most DEGs (288 up, 107 down and 220 up, 193 down, respectively (**Figure 6.11A**). Earlier KO neutrophil populations had more upregulated genes than downregulated compared to WT, whereas mature neutrophil clusters had more downregulated genes than upregulated (**Figure 6.11A**).

ORA of down-regulated DEGs revealed significantly enriched gene sets related to cytoplasmic translation and ribosome biogenesis, much like in T and B cells (**Figure 6.11A**). Genes within these gene sets were *Rps* and *Rpl* genes, similarly to T and B cells (**Figure 6.11B**). Interestingly, these genes were unchanged in KO neutrophil populations. Instead, KO neutrophil populations had reduced expression of *S100a8* and *S100a9* (involved in neutrophil chemotaxis (Ryckman et al. 2003)), with the difference becoming more pronounced in more mature neutrophil populations compared to WT (**Figure 6.11B**).

Additionally, KO neutrophil populations also downregulated *Dedd2* and *G0s2* (regulators of apoptosis (Roth et al. 2002; Heckmann et al. 2013)) (**Figure 6.11B**).

ORA of up-regulated DEGs revealed significantly enriched gene sets of interferon alpha and gamma signalling in the Mac_DC, mNeut_2, mNeut_3, and Monocyte clusters (**Figure 6.12A**). Upregulation of *Ifitm2* and *Ifitm3* was seen on cMon and Mon_Mac clusters, and upregulation of several chemokine and cytokine receptors was also seen (*Ccr1, Ccr2, Ccr5, Il4ra*) in these clusters (**Figure 6.12B**). Hypoxia-related genes (*Hif1a, Hspa5*) were also upregulated in naive KO monocytes and macrophages compared WT (**Figure 6.12B**). Interestingly, many translation initiation factors were upregulated in KO myeloid cells compared to WT, but mostly in GMPs (**Figure 6.12B**).

Taken together, these results expand the potential role of TRIM24 in cytoplasmic translation and ribosome biogenesis to myeloid and progenitor cells. Furthermore, KO inflammatory monocyte/macrophages had potentiated basal level of interferon response genes at the steady state, consistent with the data in **Chapter 4**.

6.3.7. *L. donovani* infection induces proportional changes in BM cell subsets

In order to uncover the effects of *Trim24* deletion on the BM transcriptional landscape during VL, we must first understand the effects of *L. donovani* infection on the BM of WT mice. To meet this end, we subset the UMAP from **Figure 6.4A** to include only the WT naive (WTN) and WT infected (WTI) samples. The UMAP was then split to show the UMAP of the WT naive and WT infected samples independently (**Figure 6.13A**). The UMAP and proportion barplot shows expansion of NK & T cells (6.8% → 11.5%), macrophages (2.7% → 6.8%), monocytes (6.3% → 14.4%), and GMPs (2.4% → 7.3%) during *L. donovani* infection (**Figure 6.13B&C**) while B cells decreased in BM of infected samples (30% → 5%). Proportions of neutrophils (~47%), DCs (~2%), basophils (1%), and HSPCs (2.7%) were unchanged. As the vast majority of all B cell populations found in naive BM are almost absent during infection, we are unable to perform differential gene expression analysis between naive and infected samples for B cell populations (**Figure 6.14**). Enrichment for BM B cells during *L donovani* infection before sequencing would be required for further investigation.

Previous data predicted TRIM24 to be decreased during *L. donovani* infection but was not itself transcriptionally downregulated in the spleen of infected BALB/c mice (Ashwin et al.

2018). Therefore, we were interested to see if this was also the case in infected BM in B6 mice. Taking the broad UMAP in **Figure 6.4**, we did not see any significant change in expression of *Trim24* in any of the detected cell types during infection (**Figure 6.15**). Interestingly, there appears to be a population of B cells with higher *Trim24* expression in naive BM that is lost during infection (**Figure 6.15**). Further investigation into the roles of TRIM24 in B cell function would be interesting to pursue.

6.3.8. *L. donovani*-induced alterations in BM T cell phenotypes

Almost all of the NK & T cell subclusters changed significantly during *L. donovani* infection. We saw expansion of $CD4^+$ T cells, Th1-like cells, CTLs, and Cycling T cells in infected samples, while NK, Tregs, Naive_CD8, and CD8_gdT clusters decreased (**Figure 6.16A-C**). Infiltration of *Ifng*$^+$ $CD4^+$ T cells and Th1-like cells was observed during infection. The majority of these cells had similarities to Th1 cells, by their expression of the Th1-related genes *Furin* (a proprotein convertase that is essential for maintaining T helper cell polarisation (Pesu et al. 2006; Oksanen et al. 2014)*, Tbx21* (encodes T-bet, a master transcription factor for Th1 cell differentiation (Szabo et al. 2000))*, Ifng, Irf1, Lag3,* and *Tnf* (**Figure 6.17**)*.* There were also some cells in this cluster that expressed Th2-related genes, notably *Gata3*, *Il1rl1, Cxcr4,* and *Ccr4* (**Figure 6.17**)*.* Interestingly, we were not able to detect any of the key Th2-related cytokines *Il4, Il5,* or *Il13.* Thus, the CD4 T cluster contains a mixture of inflammatory and regulatory $CD4^+$ T helper cells. Of note, the Naive_CD8 cluster did not have any expression of polarised T cell markers (*Tbx21, Gata3*) (**Figure 6.17**).

The Th1-like cluster possesses similar transcriptional signatures to the CD4 cell cluster, however this cluster represents distinctly activated effector T cells, expressing higher levels of *Ifng* and *Tnf*. Additionally, Th1-like cells expressed other cytokine genes such as *Il21*, and immune checkpoint genes (*Tnfrsf4, Ctla4, Lag3, Havcr2*) (**Figure 6.17**).

DGE analysis of NK & T cell subsets revealed that $CD4^+$ T cells had the largest number of DEGs (165 down, 152 up) in d28 BM compared to naive. Of the other clusters, CD8_gdT cells had the second highest number of DEGs (73 down, 41 up). CTLs and Naive_CD8 cells had 28 down-, 10 up- and 20 down-, 32 up-regulated genes, respectively (**Figure 6.18A**). Cycling T cells had 13 down- and 19 up-regulated genes compared to WT, and Th1 cells had 11 down-regulated genes and no up-regulated genes (**Figure 6.18A**). No DEGs were found in the remaining clusters. Several key immune response genes were significantly

upregulated in CD4 (*Ifng, Tnf, Csf1, Ccl5, Il21, Ccr5, Stat1, Maf, Ly6a, Cxcr6)* and $CD8^+$ T cells (*Gzmb, Cd8a, Ly6a, Nkg7, Lat*) during infection (**Figure 6.18B&C**).

ORA of significantly down-regulated genes in NK & T cell clusters revealed down-regulation of cytoplasmic translation and response to calcium ions. Additionally, CD4 T, Th1-like, and CD8_gdT cells had significantly down-regulated gene sets for regulation of innate immune response, and response to biotic stimulus (**Figure 6.18D**).
ORA of significantly upregulated genes in d28 vs naïve WT T cell clusters revealed top enriched gene sets in T cell mediated cytotoxicity, cell killing, and lymphocyte-mediated immunity (**Figure 6.18E**). These were enriched in all cell clusters, and the granzyme-mediated programmed cell death signalling pathway was enriched in CTLs and CD8_gdT cells (**Figure 6.18E**).

6.3.9. BM monocytes and macrophages have an inflammatory phenotype during *L. donovani* infection

We also investigated monocyte and macrophage subsets during infection. We took the HSPC, GMP, Cycling Mon, Monocyte, and Macrophage clusters from **Figure 6.4A** and performed sub-clustering as with T cell subsets. We identified ten cell clusters (**Figure 6.19A**), which were named based on manual interrogation of top expressed genes in each cluster compared to all other clusters (**Figure 6.19B**); HPSCs (*Cd34, Adgrg1, Sox4*), DCs (*Siglech, Cd7, Itgax*), pre-Neut (*Retnlg, Ly6g, Mmp9*), common monocyte progenitors (cMoP; *Ms4a3*), pre-Monocytes (*Ly6c2, Ccr2*^{lo}), cycling monocytes (*Ube2c, Nusap1, Cenpf*), classical monocytes (cMon; *Ccr2*^{hi}*, Crip1, Sell*), inflammatory monocytes (*Ccr2*^{hi}*, Ms4a6c, Ly6i, Ly6c2*^{hi}), non-classical monocytes (ncMon; *Nr4a1, Eno3, Ace, Cx3cr1*), M1-like macrophages (M1_Mac; *Fcgr4, Adgre1, Nos2, Saa3, Ccl5*), and regulatory macrophages (Reg_Mac; *Fcgre4, Adgre1, Spic, Mrc1, C1qa*) (**Figure 6.19B**).

Investigation of proportions of monocyte and macrophage clusters revealed an expansion of the two macrophage clusters (Reg_Mac; 5.51% vs 2.69% and M1_Mac; 4.44% vs 1.83%), inflammatory monocytes (iMon; 11.87% vs 4.94%), Cycling Monocytes (18.04% vs 11.82%), pre-Monocytes (pre-Mon; 6.54% vs 2.58%), and pre-Neutrophils (pre-Neut; 7.38% vs 2.36%) for d28 vs naïve samples (**Figure 6.19C-E**). We observed decreases in the proportion of non-classical monocytes (ncMon; 1.64% vs 7.95%) and interestingly in the HSPC cluster (6.5% vs 13.43%) at d28 (**Figure 6.19C-E**). We did not see any significant differences in DCs (5.56% vs 7.73%) or classical monocytes (cMon; 24.35% vs 33.3%) (**Figure 6.19C-E**).

We then performed DGE analysis on each cluster and plotted the number of up- and down-regulated genes for each cluster. Large numbers of DEGs were detected (up-regulated = FDR<0.05 and log2FC>0; down-regulated = FDR<0.05 and log2FC<0) in d28 classical monocytes (350 down, 372 up), cycling monocytes (244 down, 248 up), and in cMoPs (114 down, 229 up) (**Figure 6.20A**). We observed lower DEG numbers in other clusters, ranging from Reg_Mac (32 down, 9 up) to iMon (139 down, 111 up) (**Figure 6.20A**).
To elucidate phenotypic changes in each cluster at d28 compared to naive, we performed ORA on up-regulated and down-regulated genes separately using GO gene set terms. For up-regulated genes, all clusters had enriched gene set GO terms relating to antigen processing and presentation, or MHC class II complex assembly (**Figure 6.20B**). Also, among the top enriched gene set GO terms were relating to response to type I and type II interferons. Cellular response to LPS was also enriched in DCs, pre-Mons, iMons, M1_Macs, and Reg_Macs (**Figure 6.20B**).
For down-regulated genes, among the top enriched gene sets were gene sets relating to cytoplasmic translation and ribosome biogenesis, which was common to all clusters apart from pre-Neuts, ncMons, and Reg_Macs (**Figure 6.20C**). Interestingly, the myeloid cell differentiation GO term was enriched among down-regulated genes, and B cell activation and differentiation was down-regulated in pre-Neuts (**Figure 6.20C**). Cytokine-mediated signalling pathway GO term was also down-regulated among mature monocyte clusters. Cell response to LPS was down-regulated only in Reg_Macs (**Figure 6.20C**).

During *L. donovani* infection, inflammatory macrophages (M1_Mac) upregulated many inflammatory chemokine and cytokine genes (*Nos2, Il1b, Tnf, Il27, Ccl5, Cxcl10, Cxcl9*), cytokine/chemokine receptor genes (*Ccr5, Il12rb1, Il4ra*), transcription factors (*Stat1, Irf1, Cebpb*), antigen presentation genes (*H2-Aa, H2-Ab1, Cd74, Mif*), and many surface protein genes (*Ly6a, Ly6i, Fcgr1, Cd52, Cd274*) (**Figure 6.21**). Inflammatory monocytes (iMon) were similar to M1_Macs, showing similar upregulation of *Ly6a, Ly6i, Stat1, Irf1, Cebpb, Mif, Tnf, Il27, Cxcl10, and Cxcl9*. Down-regulation of *Ccl2* was also observed in iMons and M1_Macs. However, infection-induced expression of *Ccl5* and *Nos2* was specific to M1_Macs. IMons differed from macrophages in their expression of *Ly6c2* (upregulated during infection), and lacked expression of the complement genes *C1qa, C1qb,* and *C1qc* (**Figure 6.21**).
Reg_Macs also upregulated *Stat1, Irf1*, and antigen presentation genes during infection, indicating an activated response to IFNs (**Figure 6.21**). However, Reg_Macs did not upregulate many cytokine genes apart from *Ccl8,* which was previously shown to support the generation of regulatory dendritic cells during *L. donovani* infection (Nguyen Hoang et al.

2010). Interestingly, Reg_Macs down-regulated many regulatory surface protein genes (*Cd55, Cd63, Mrc1*) in response to infection (**Figure 6.21**).
Taken together, these results show expansion of classical and inflammatory monocytes and macrophages in B6 mouse BM during infection and outline transcriptional changes that occur during infection.

6.3.10. Altered cell communication and transcriptional alterations promotes BM myelopoiesis during *L. donovani* infection

Given the literature describing HSPC exhaustion and loss of quiescence during *L. donovani* infection (Pinto et al. 2017), we investigated transcriptomic alterations in our HSPC cluster in infected BM. We detected 114 upregulated and 55 downregulated genes in HSPCs in infected BM (FDR<0.05, log2FC>0 or <0) (**Figure 6.22**). Interestingly, several genes important for the maintenance of quiescence (*Egr1, Klf2, Klf6, Klf4, Ier2*) (Pelletier et al. 2022; Desterke et al. 2021), and genes that make up the AP-1 transcription factor (*Fos, Fosb, Jun, Jund, Junb*) (Passegué et al. 2004; Santaguida et al. 2009) were down-regulated in HSPCs. Furthermore, genes related to myeloid cell differentiation were upregulated in the HSPC cluster (*Ccl5, Csf2rb, Cebpb*) (Ergen et al. 2012; Sato et al. 2020) (**Figure 6.22**). *Ccl5* was also highly expressed by macrophages, $CD4^+$ and $CD8^+$ T cells at d28 compared to naive (**Figures 6.18B & 6.21**)**.** *Cd48*, a marker linked with loss of HSC quiescence and initiation of cell division (Wilson et al. 2008), was also upregulated in the HSPC cluster (**Figure 6.22**)

ORA of up-regulated genes in HSPCs and GMPs revealed top enriched GO terms relating to response to type I and II interferons, and to antigen processing and presentation (**Figure 6.23A**). Top genes associated with these GO terms were robustly upregulated during infection (*H2-Aa, H2-Eb1, Stat1, Gbp2, Igtp*), indicating HSPCs and GMPs are responding to IFNs in the BM niche (**Figure 6.23B**). Moreover, HSPCs had higher expression of *Ifngr2* (but not *Ifngr1*) during infection, further indicating an increased response to IFNγ (**Figure 6.23C**).

To investigate potential interactions between cells that may result in enhanced myelopoiesis during infection, we used the R package CellChat that infers inter-cellular communication networks in scRNA-seq data (Jin et al. 2021). CellChat utilises a curated database of ligand-receptor cell communication networks (CellChatDB; http://www.cellchat.org/) and integrates

this with gene expression data from scRNA-seq data to infer ligand receptor interactions in a given dataset. To note, CellChat uses models of mass action to assign probability values to interactions, and not only considers expression levels of the ligand and receptor genes, but also takes into account multimeric ligands and receptors that are encoded by different genes (e.g. *Ifngr1+Ifngr2*), along with other cofactors that may influence cell communication (soluble agonists/antagonists, co-stimulatory/co-inhibitory receptors) (Jin et al. 2021). Inferred interactions are then statistically analysed with permutation tests (as explained in **Chapter 4**).

We used CellChat to identify differences in "secreted signalling" pathways between leukocytes during infection. Focussing on "IFN-II" signalling (which predicts interactions between *Ifng* and *Ifngr1+Ifngr2*), we saw no inferred interaction in WT naive BM, however in WT d28 BM, we detected inferred interaction between T cell-derived *Ifng* and *Ifngr1+Ifngr2* expressed in HSPCs and GMPs, as well as in monocytes, macrophages, and neutrophils (**Figure 6.23D**). As we saw $CD4^+$ T cells are a major source of *Csf1* in infected BM, we also performed CellChat analysis on the *Csf1-Csf1r* interaction. In WT naive samples we saw basophils as the only source of *Csf1*, which was signalling to GMPs, monocytes and macrophages. In d28 BM, we also saw basophils as a source of *Csf1*, and additionally we saw NK & T cells as another source of *Csf1* (**Figure 6.23E**). GMPs, monocytes, macrophages, and additionally HSPCs were all targets of basophil and T cell-derived *Csf1* in d28 BM (**Figure 6.23E**). Taken together, these results indicate that HSPCs respond to T cell-derived *Ifng* and *Csf1* in d28 but not in naive BM.

Taken together, these results build upon a previously established model of $CD4^+$ T cell-mediated HSC exhaustion and induction myelopoiesis in the BM during *L. donovani* infection.

6.3.11. *Trim24* deficiency does not affect *L. donovani*-induced alterations in BM leukocyte proportions

Finally, we investigated effects of *Trim24* deletion on the transcriptional landscape of *L. donovani*-infected BM. Changes in cell type proportions following *L. donovani* infection were similar in KO samples and WT samples. Expansion of T cells, monocytes, macrophages, and GMPs was observed in the KO Infected (KOI) sample compared to KO Naïve (KON), along with almost complete expulsion of B cells subsets (**Figure 6.24A**). We saw no differences in proportions of almost all cell types between KOI and WT Infected (WTI) samples, with the exception of DCs, which were significantly fewer in the KOI samples (<-1

log2FC) (**Figure 6.24B**). The similarities of the WTI and KOI samples are reflected in their respective UMAPs (**Figure 6.24C**).

6.3.12. *Trim24* deletion induces metabolic changes in myeloid and progenitor cells during *L. donovani* infection

Next, we investigated transcriptional profiles of KO leukocytes during *L. donovani* infection compared to WT. Performing DGE analysis on subclusters of monocytes, macrophages, and T cells revealed very few DEGs (not shown). Therefore, in order to increase signal we performed DGE analysis and ORA on the broader cell types displayed in **Figure 6.4A**.

As we saw in **Chapter 4**, we observed upregulation of OxPhos-related genes in KO HSPCs, GMPs, monocytes, and macrophages compared to WT (*Cox8a, Atp5k, Atp5g1, Ndufa5,* among others) (**Figure 6.25B**). This was most apparent in early leukocytes (HSPCs and GMPs) but was most clearly seen in GMPs (**Figure 6.25A&B**). We also detected significant upregulation of the MYC targets gene set in all four cell types shown (**Figure 6.25A&D**). Interestingly, many of these genes encoded ribosomal subunits or translation initiation factors (*Rps5, Rpl6, Eif3d, Eif2s2*, among others) (**Figure 6.25C**), the same set of genes as were downregulated in most KO leukocytes at the steady state. The RNA binding proteins LARP1 and PABPC1 have been shown to be involved in mRNA stability and degradation (Aoki et al. 2013; Qi et al. 2022), and interestingly these were both downregulated in almost all KO cell types shown here (**Figure 6.25C**).

Interestingly, the top enriched gene set within downregulated genes in KO GMPs and monocytes compared to WT was related to IFNγ response (**Figure 6.26A**). We observed downregulation of *Ifitm2, Ifitm3, Irf5, Ifi30*, and antigen presentation-related genes (*H2-Aa, B2m, H2-D1*) (**Figure 6.26B**). Notably, *Nfkb1* was also downregulated in KO HSPCs and monocytes, and to a lesser extent NK & T cells compared to WT (**Figure 6.26B**).
At the same time, we detected a downregulation of mTOR signalling gene sets in KO GMPs, monocytes, and neutrophils compared to WT (**Figure 6.26A**). Of note, we observed a decrease in the expression of *Cxcr4* in KO HSPCs, GMPs, monocytes, and neutrophils compared to WT, contrasting our data in **Chapter 5** showing no effect of TRIM24 deletion in surface CXCR4 receptor expression and recycling (**Figures 5.13 & 5.14**).

6.3.13. *Trim24* deletion leads to elevated macrophage activation phenotype during *L. donovani* infection

Finally, we investigated differences between KO and WT macrophages during *L. donovani* infection. We took the macrophage cluster from **Figure 6.3** and performed DGE analysis (FDR<0.05, log2FC <0 or >0) to reveal 29 down-regulated and 60 up-regulated genes in KO compared to WT infected macrophages (**Figure 6.27**).

We detected no significant change in the expression of important cytokines from KO macrophages compared to WT (*Il12a, Ccl5, Nos2, Cxcl9, Tnf, Il6, Il27, Ccl8*) (**Figure 6.27**). While ORA of either up- or down-regulated genes in KOI vs WTI macrophages revealed no significantly enriched gene sets (not shown), we saw upregulation of genes in KO macrophages indicating an enhanced activated phenotype. *Atp1b3* was the most highly upregulated gene in KO macrophages compared to WT (**Figure 6.27**; also seen in naive macrophages in **Figure 3.12**). *Cxcl2, Fcgr2b, Slamf7, Itgb2, and Isg15* were also all upregulated in KO macrophages compared to WT (**Figure 6.27**). The three top downregulated genes in KO macrophages during *L. donovani* infection were *Pfn1* (encoding Profilin 1, an actin-binding protein (Alkam et al. 2017)), *B2m* (a component of the MHC class I molecule (Li et al. 2016)), and *Arf5* (a novel positive regulator of mTOR signalling (Makhoul et al. 2023)). Taken together, this data reveals potential multi-factorial roles of TRIM24 in macrophage activation, which plays roles in inflammatory and immunoregulatory processes.

6.4. Discussion

Alterations of haematological events are commonly observed in infections in various forms (e.g. anaemia, thrombocytopenia, pancytopenia) (Varma & Naseem 2010). These complications are found in *L. donovani* infection, and marked increases in myelopoiesis are also observed. Emergency myelopoiesis occurs during *L. donovani* infection in the spleen and the BM (Abidin et al. 2017; Pinto et al. 2017). However, there is still much unknown about the immune landscape of *L. donovani*-infected BM. We have previously shown in **Chapter 5** that KO BM leukocytes possess a competitive advantage compared to WT cells in competitive reconstitution using a mixed bone marrow chimeric model. This was particularly marked in the BM, where 80% of $CD45^+$ cells were deficient in TRIM24. However, we found little differences in leukocyte proportions between total WT and KO mice, and furthermore we did not see differences in expansion of Th1 cells during *L. donovani* infection or in the capacity for $CD4^+$ or $CD8^+$ T cells to produce TNF, IFNγ, IL-10, or IL-4. However, there are still many unanswered questions about the roles of TRIM24 during *L. donovani* infection, particularly with regard to monocyte and macrophage populations. Therefore, in this chapter we have used scRNA-seq to i) investigate transcriptional changes in KO BM leukocytes at the steady state; ii) clarify the immune landscape of *L. donovani* infected BM in B6 mice and show a changed environment that promotes myelopoietic output and loss of quiescence in HSPCs; iii) elucidate roles of TRIM24 in leukocytes during *L. donovani* infection.

Firstly, we have shown an almost global downregulation of ribosomal and cytoplasmic translation-related genes in KO leukocytes in naive BM. In particular, *Rps* and *Rpl* genes (that encode ribosomal subunit proteins) were downregulated in almost all cell types. Ribosomal subunit genes are classed as 5'TOP mRNAs due to the presence of a 5'terminal oligopyrimidine tract (5'TOP) of variable length (5-25 bp) after an m^7G cap (Yoshihama et al. 2002; Cockman et al. 2020). 5'TOP motifs are highly conserved in mRNAs that encode proteins essential for protein synthesis (it is found in all ribosomal proteins and elongation/initiation factors) (Iadevaia et al. 2008). MTORC1 activity plays a vital role in regulating translation of 5'TOP mRNAs. Mechanistically, mTORC1 phosphorylates translation initiation factor 4E binding proteins (4E-BP) to prevent its binding to eukaryotic initiation factor 4E (eIF4E). This allows eIF4E to bind to the m^7G cap of the mRNA transcript, enabling recruitment of eIF4A, eIF4B, and eIF4G to form the eIF4F ternary complex (Cockman et al. 2020). Subsequent recruitment of the pre-initiation complex (PIC) allows for mRNA translation to occur. Inhibition of mTORC1 signalling via rapamycin treatment significantly reduces translation of 5'TOP-containing transcripts (Philippe et al. 2018).

Importantly, we observed decreases in KO 5'TOP mRNA transcripts, the effect of which would occur upstream of translation initiation. Therefore, the effect of *Trim24* deletion appears to be affecting expression or stability of 5'TOP mRNA transcripts. LARP1 is an RNA binding protein that plays an important role in the stabilisation of 5'TOP mRNA transcripts. LARP1 specifically binds to the 5'TOP motif of mRNAs via its La-module, a process dependent on mTOR signalling (Jia et al. 2021; Mattijssen et al. 2021), and acts as a post-transcriptional stabiliser for 5'TOP mRNAs (Aoki et al. 2013). Aoki et al. demonstrated that LARP1 depletion in HEK293 cells significantly reduced the mRNA abundance of 5'TOP mRNAs (Aoki et al. 2013), as observed in our data. Non-phosphorylated LARP1 interacts with 5'TOP mRNAs and inhibits their translation. Upstream mTORC1 activity phosphorylates LARP1, dissociating it from 5'UTRs and allowing 5'TOP mRNA translation (Hong et al. 2017). Therefore, downregulated mTORC1 signalling in KO leukocytes could lead to impaired LARP1 phosphorylation, increasing stability at the cost of reduced translation. Interestingly, while *Rps* and *Rpl* genes were down-regulated in KO myeloid cells, other 5'TOP mRNAs (*Eif2s2, Eif3a, Eif4a1, Eif5, Eif3d*) were upregulated. Gentilella et al. indicated that the 40S ribosomal subunit was important in stabilising 5'TOP mRNAs, and LARP1 and free 40S subunits form complexes with 5'TOP mRNAs to stabilise them (Gentilella et al. 2017). Disruption of either LARP1 or the 40S subunit led to destabilised 5'TOP mRNAs, and impaired ribosome biogenesis checkpoint (IRBC), resulting in stabilised p53 and subsequent cell cycle arrest (Gentilella et al. 2017). Therefore, multiple mechanisms may contribute to stabilisation or expression of ribosomal subunit genes and eukaryotic initiation factor genes. Given the roles of TRIM24 in p53 degradation (Allton et al. 2009), its functions could be extended to this system.

Secondly, we have postulated mechanisms by which the promotion of myelopoiesis occurs during *L. donovani* infection in the BM. Emergency haematopoiesis is a hallmark of VL that occurs in both the BM and in the spleen (extramedullary haematopoiesis), which is in part driven by loss of HSC quiescence (Pinto et al. 2017; Abidin et al. 2017). However, mechanisms behind this are still poorly understood. Here, we perform a transcriptional analysis of *L. donovani*-infected B6 mouse BM at d28 at a single cell level, and uncover a Th1 response-driven environment that favours myelopoiesis.
We saw expansion of *Ifng*$^{+}$ CD4^{+} T cell subsets which possessed a Th1-like phenotype, monocytes, macrophages, and GMPs, indicating enhanced myelopoiesis in the BM during infection. T cell subsets adopted an inflammatory phenotype, with CD4^{+} T cells upregulating many ISGs, *Ifng, Stat1, Il21, Ccr5*, and CTLs upregulating *Nkg7, Gzmb,* and *Cd8a.* Interestingly however, we did not see any expression of *Il10*, which is an important cytokine for VL progression, evidenced by IL-10-deficient BALB/c and B6 mice being highly resistant

to *L. donovani* infection in liver and spleen parasite burdens (Murphy et al. 2001). More recently, Romano et al. showed that IL-10 deficiency also significantly reduced parasite burden in B6 mouse BM following *L. donovani* infection (Romano et al. 2021). However, they also found minimal IL-10 expression from $CD4^+$ T cells in the bone marrow during *L. donovani* infection at d28 (Romano et al. 2021), despite these cells being a major source of IL-10 in the spleen (Stäger et al. 2006; Owens et al. 2012). This is consistent with our data in **Chapter 5**, which showed an elevation in capacity for $CD4^+$ T cells to produce IL-10 at d14 but a reduction back to basal levels by d28. Indeed, it appeared that no cell type detected in our data produced high levels of IL-10, indicating that the source of IL-10 originated outside of the BM or by non-immune cell types that were not present in our dataset. Additionally, effects of IL-10 signalling between d0 and d14 could have lasting effects to make the BM environment more permissive to *L. donovani* parasite survival.
Loss of B cells was observed from the BM following *L. donovani* infection, consistent with previous data (Pinto et al. 2017). B cell expansion occurs in the spleen during *L. donovani* infection (Mondal et al. 2021), so infection-induced mobilisation of B cells from the BM would explain the lack of BM B cells.

We also characterised monocyte and macrophage subsets during *L. donovani* infection. Phenotypes of inflammatory monocytes and inflammatory macrophages were similar. We found upregulation of *Nos2* in inflammatory monocytes and macrophages, along with many other inflammatory genes relating to antigen presentation, interferon response, and other proinflammatory cytokines/chemokines (*H2-Aa, H2-Ab1, Stat1, Irf1, Cxcl10, Cxcl9, Il1b*). Upregulation of these genes was more pronounced in inflammatory macrophages, and expression of some genes (e.g. *Ccl5* & *Saa3*) was restricted to these cells. Regulatory macrophages downregulated *Mrc1* (encoding CD206/mannose receptor), likely due to exposure to high levels of T cell-derived IFNγ (Harris et al. 1992). *Il27* was also upregulated in monocyte and macrophage subsets during *L. donovani* infection. Previous data has shown that blocking IL-27 signalling in B6 mice significantly reduces hepatic parasite burden (Rosas et al. 2006), an effect that was abrogated through additional blocking of IFNγ signalling (Murray 2020). Therefore, IL-27 signalling is host detrimental during experimental VL. Together, the phenotypes of monocytes and macrophages were complex during *L. donovani* infection. A dominant inflammatory phenotype was seen, however expression of regulatory genes was also found, which could be indicative of parasite-monocyte/macrophage interactions facilitating parasite survival.

Ccl5 was upregulated in BM T cells as well as in inflammatory macrophages. Knockout of CCL5 in B6 mice led to fewer myeloid-biased progenitor cells (CMPs, GMPs, MEPs) coupled

with an increase in total lymphocyte number (Ergen et al. 2012). Furthermore, transplantation of CD45.2$^+$ CCL5-overexpressing progenitor cells into CD45.1$^+$ mice led to a decrease in T cell numbers and T cells-related transcription factors (*Gata3, Ikaros*) along with enhanced mRNA abundance of myeloid-skewing transcription factors (*Gata1, Gata2, Sfpi1*) (Ergen et al. 2012). CCL5 expression has also been associated with lower number and impaired functions of myeloid-derived suppressor cells (MDSCs), leading to impaired tumour progression in 4T1 tumour-bearing BALB/c mice (Zhang et al. 2013). Therefore, the upregulation of *Ccl5* we show during *L. donovani* infection could play an important role in increased myelopoiesis reported here and in other studies.
Similarly, while expression of *Csf1* in basophils was observed in both naive and infected mice, CD4$^+$ T cell-derived *Csf1* expression was only seen in infected samples. Increased expression of myelopoietic growth factors (M-CSF, GM-CSF, and G-CSF) has been shown previously in BALB/c mice 42 days post-*L. donovani* infection in the spleen and the BM (Cotterell et al. 2000). This was accompanied by mobilisation of haematopoietic progenitors into the peripheral blood, and significantly more myeloid colony forming units compared to naive control mice (Cotterell et al. 2000). Therefore, our data here extends this model and provides a potential source for increased *Csf1* in the BM during infection in B6 mice. An interesting experiment to test this hypothesis would be the co-culture of naive HSCs with BM T cells isolated from *L. donovani*-infected mice in the presence or absence of an anti-CCL5 or anti-M-CSF antibody, and measuring differences in macrophage colony forming units (CFU-M).

It is known that quiescent HSCs prefer the hypoxic environment of the BM and preferentially use anaerobic glycolysis for glucose metabolism to satisfy the lower ATP requirements of quiescence (Simsek et al. 2010). Loss of quiescence leads to downregulation of the hypoxic response and metabolic shift towards OxPhos to maintain elevated ATP requirements of differentiating HSCs (Simsek et al. 2010). Here we show that HSPCs upregulated several OxPhos-related genes (*mt-Co2, Atp5g2, Atp5g3*), indicating a metabolic shift that would support the notion of loss of HSPC quiescence. Importantly, recent studies have identified HSCs as a major phagocytic cell type in the BM during *L. donovani* infection that harbour parasites as the infection progresses (Karagiannis et al. 2022; Dirkx et al. 2022). *L. donovani*-infected human macrophages selectively enhance OxPhos to produce a parasite-permissive environment (Ty et al. 2019). Thus, HSPCs in our dataset could be harbouring parasites that modulate their metabolic profile to facilitate parasite survival. A dual scRNA-seq approach as was performed by Karagiannis et al. could provide insight into this question (Karagiannis et al. 2022). Together, this study highlighted multi-factorial mechanisms of

inter-cell communication for how alteration of the BM environment supports myelopoiesis during *L. donovani* infection.

Finally, we have shown differences in KO mice in the response to *L. donovani* infection in the BM. Infection induced similar proportional cell changes to WT mice (expansion of T cells, monocytes, macrophages, GMPs). This is in accordance with our and others' previous data indicating TRIM24's dispensability for haematopoiesis (Shaw 2018), and appears to extend this to emergency haematopoiesis. Chemokine-mediated recruitment of leukocytes is important during infection. Therefore, this data further indicates that TRIM24 plays little role in leukocyte recruitment.
Our previous data showed increased iNOS expression in KO macrophages stimulated with LPS compared to WT (**Figure 3.4**). We also displayed conflicting data showing no change in iNOS expression in KO hepatic granulomas at d29 post-infection with *L. donovani* compared to WT (**Figure 5.25**). Therefore, we were interested to see if *Nos2* expression is affected by *Trim24* deletion in our BM dataset. While we show increased *Nos2* expression in inflammatory monocytes and macrophages, this upregulation was comparable between KO and WT mice. Therefore, this is consistent with our hepatic granuloma data, and gives further credence to the dispensability for TRIM24 in *Nos2* expression during *L. donovani* infection.

As discussed above, a shift in glucose metabolism towards OxPhos facilitates a permissive phenotype to parasite survival and disease progression. Here, we have shown that TRIM24 acts as a global negative regulator of OxPhos, seemingly regardless of leukocyte type. We saw increases in OxPhos-related genes during infection in HSPCs, and this effect appears to be exacerbated upon *Trim24* deletion. OxPhos gene set was upregulated in HSPCs, GMPs, monocytes, and neutrophils in KO infected samples compared to WT. Furthermore, we saw a decrease in genes relating to mTOR signalling. TRIM24 has previously been linked to glucose metabolism in isogenic human mammary epithelial cells (iHMECs). Pathiraja et al. showed that overexpression of TRIM24 in iHMECs effectively induced cell cycle progression in iHMECs; significantly more $TRIM24^{+}$ iHMECs were detected in G2M and S phase compared to control cells, and significantly fewer in G1 phase (Pathiraja et al. 2015). Furthermore, TRIM24 overexpression led to a robust induction of glycolysis and TCA cycle genes, showed significant upregulation of mTOR signalling, and increased overall glucose uptake in iHMECs (Pathiraja et al. 2015). This is consistent with our data showing *Trim24* deletion to impair mTOR-related gene expression and skewing glucose metabolism towards OxPhos. Taken together, this extends our data from **Chapter 2** to other myeloid

cells, showing TRIM24 to be a negative regulator of glucose metabolism in response to *L. donovani* infection.

In addition to promoting OxPhos in myeloid and progenitor cells during infection, we also explored the transcriptional phenotype of KO macrophages during *L. donovani* infection. We have previously shown KO naive macrophages to possess a higher basal expression of ISGs *in vitro* (**Figure 3.13** and **Figure 4.12**). Here, we have built on this finding *in vivo* during infection, displaying a KO macrophage phenotype that expressed higher levels of *Isg15* and *Slamf7* (both regulated by IFNγ) compared to WT. SLAMF7 has recently been shown to be associated with a 'super activated' state of synovial macrophage activation in rheumatoid arthritis (Simmons et al. 2022). Stimulation of synovial macrophages with IFNγ potently upregulated SLAMF7 expression. Macrophages released more inflammatory factors (e.g. TNF, IL-1β, IL-6, IL-12B, CXCL1) when treated with an activating SLAMF7 antibody after 24 hours IFNγ potentiation compared to IFNγ treatment alone (Simmons et al. 2022). Furthermore, SLAMF7^{hi} macrophages upregulated OxPhos compared to SLAMF7^{lo} macrophages (Simmons et al. 2022), consistent with our data. Interestingly, there is also evidence for SLAMF7 protecting B6 mice from lethal sepsis by limiting *Tnf, Il6,* and *Il1b* expression (Wu et al. 2023). Therefore, the function of SLAMF7 appears to be context-specific, and has thus far not been explored in the context of *L. donovani* infection. Enhanced *Slamf7* expression in KO could therefore potentiate the inflammatory macrophage phenotype during *L. donovani* infection, or play a more immunoregulatory role.

Together, the data in this Chapter has revealed a transcriptional landscape of experimental *L. donovani*-infected BM in the context of the host immune response in B6 mice. We have revealed a macrophage and CD4$^+$ T cell-driven environment that promotes myelopoiesis through *Ifng, Csf1* and *Ccl5* signalling, coupled with metabolic changes promoting a loss of quiescence HSPC phenotype. Furthermore, we have revealed TRIM24 as a potential regulator of 5'TOP mRNA stability to influence abundance of these mRNAs at the steady state. Furthermore, we have identified TRIM24 as a positive regulator of mTOR signalling and negative regulator of OxPhos during *L. donovani* in the BM, thus potentiating the metabolic shifts observed during infection.

6.5. Figures

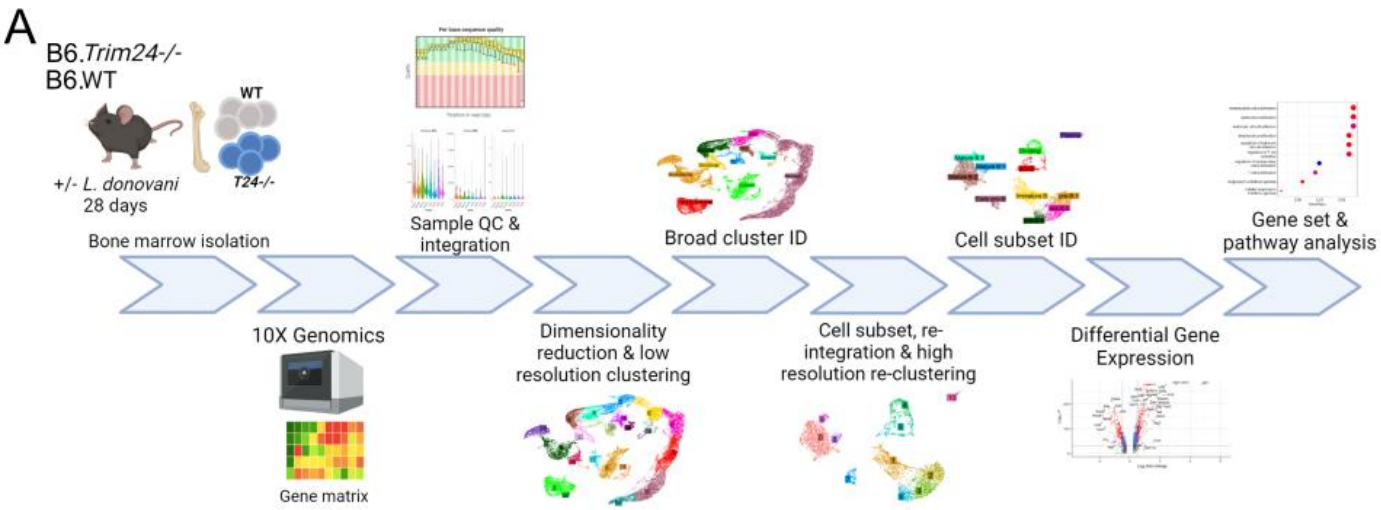

Figure 6.1. Experimental design. WT and KO mice (n=2 mice for groups WTN, WTI, KOI, 1 mouse for group KON) were infected or not with $3x10^7$ *L. donovani* amastigotes via intravenous injection into the lateral tail vein for 28 days. Single cell suspensions were pooled from mice within each group and prepared as described in the Methods section. Cells were then sequenced as described in the Methods section. After sequencing data was aligned to the mouse genome, samples underwent quality control (QC) and filtering steps and subsequently sample were all integrated using the R-based Seurat pipeline. Dimensionality reduction (PCA & UMAP) was performed, and low-resolution clustering revealed broad cell clusters. Broad cell cluster were then subset, re-integrated and re-clustered at a higher resolution to reveal finer cell subtypes. Finally, differential gene expression (DGE) analysis and gene set enrichment analysis (GSEA) was then performed.

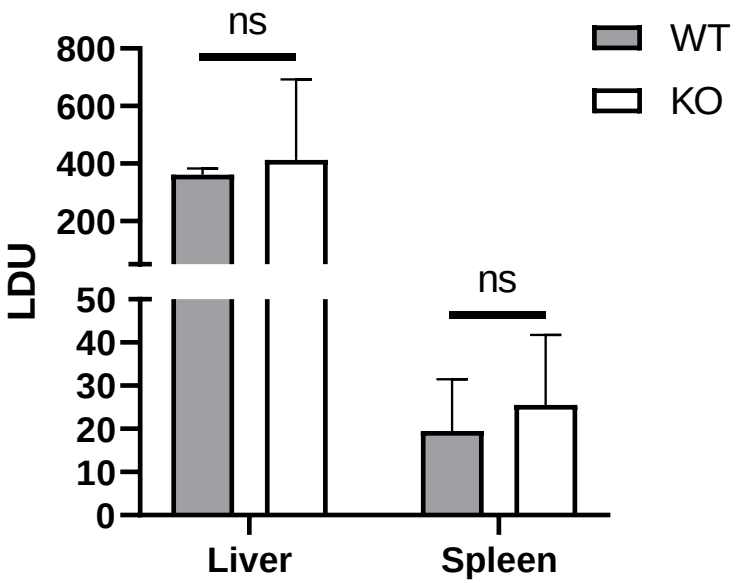

Figure 6.2. Hepatic and splenic parasite burdens are comparable between WT and KO mice. d28-infected WT and KO B6 mice were sacrificed (n=2 WT and 2 KO mice), and impression smears of liver and spleen sections were fixed onto microscope slides and stained with Giemsa. Parasites in liver and spleen were manually counted by microscopy. LDU = Leishman Donovan Units, calculated by multiplying the number of amastigotes per 1000 host cells by the weight of the organ in grams. ns = not significant, student's t-test.

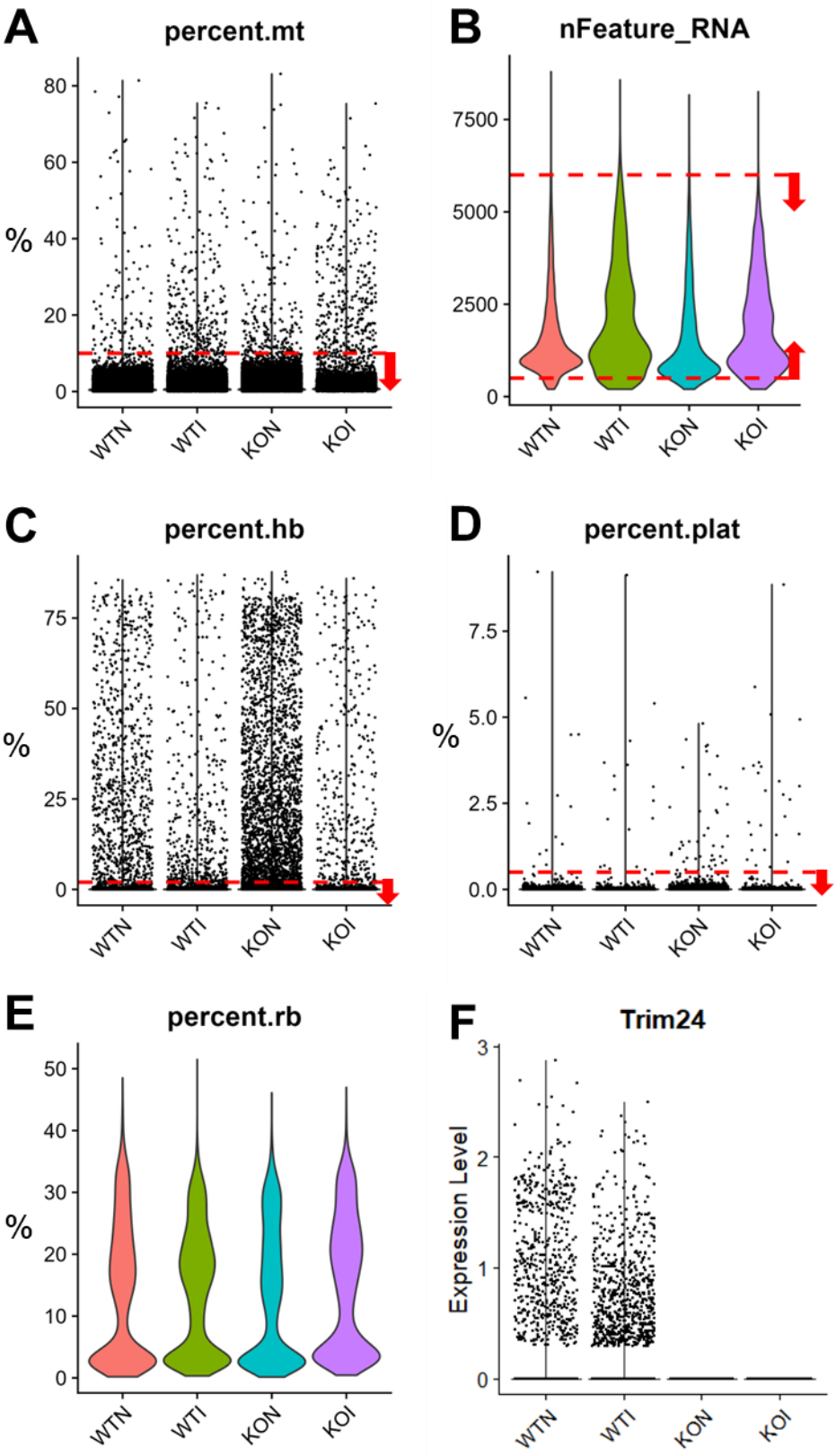

Figure 6.3. QC metrics visualisation & filtering of scRNA-seq datasets. After alignment of scRNA-seq samples to the mouse genome was performed, samples underwent QC and filtering steps, as performed in **Chapter 4**. **(A)** Cells with >10% mitochondrial gene percentage (percent.mt) were filtered out. **(B)** Cells with nFeature_RNA count of <500 & >6000 were filtered out. **(C)** Cells with haemoglobin gene percentage (percent.hb) >2% were filtered out. **(D)** Cells with platelet gene percentage (percent.plat) >0.5% were filtered out. **(E)** Ribosomal gene percentage is shown but cells were not filtered based on ribosomal gene count. **(F)** Normalised counts for *Trim24* detected in each sample.

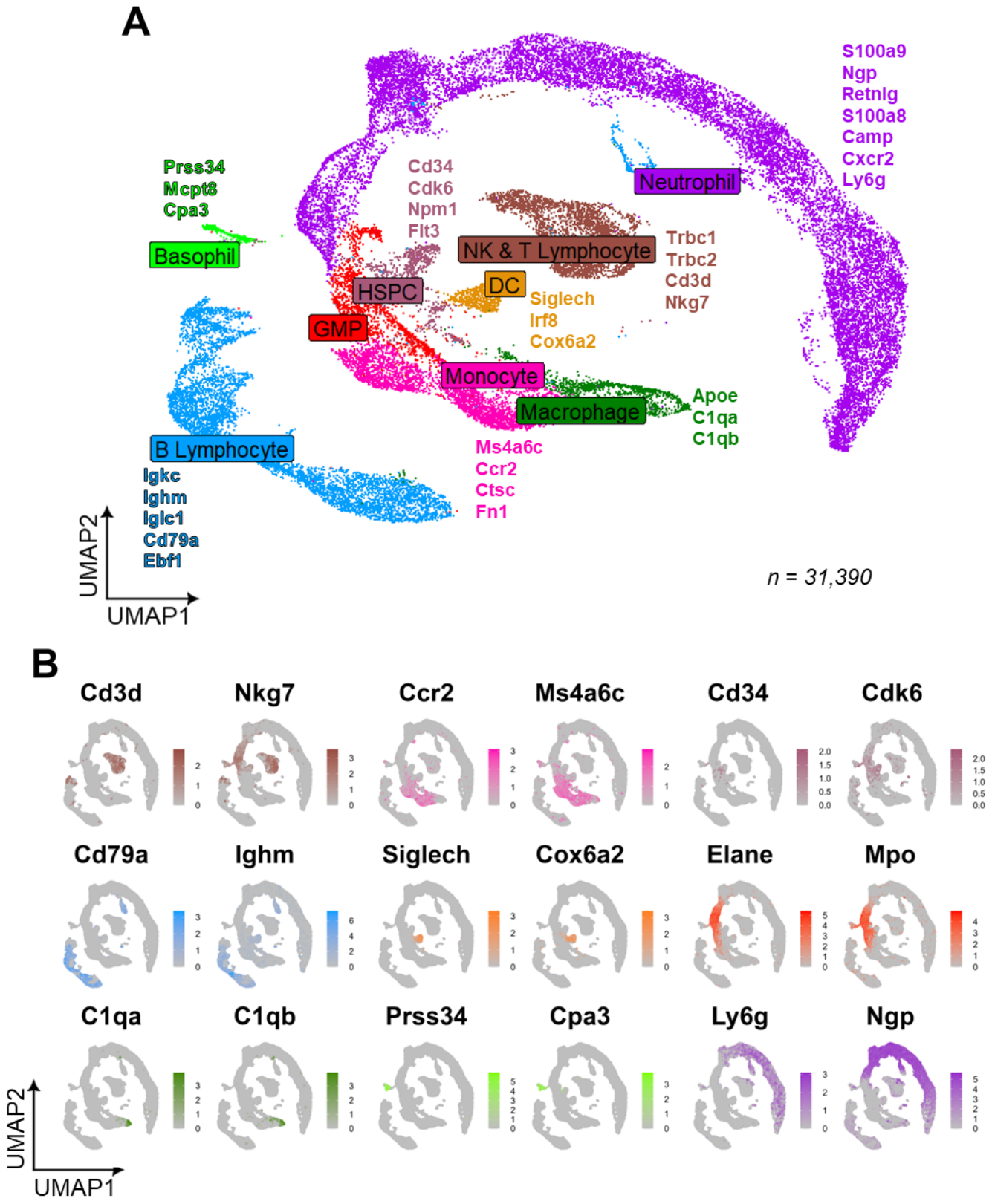

Figure 6.4. UMAP representation of integrated scRNA-seq samples reveals leukocytes detected in BM. UMAP dimensionality reduction was performed on the integrated Seurat, and clustering was performed using a resolution of 0.5. Top expressed genes per cluster were found using the FindAllMarkers function in Seurat, and broad cell types were identified using consensus marker expression. **(A)** UMAP representation of integrated Seurat object, with top consensus marker genes expressed in each broad cluster indicated. **(B)** Feature plots of two marker genes for each broad cluster.

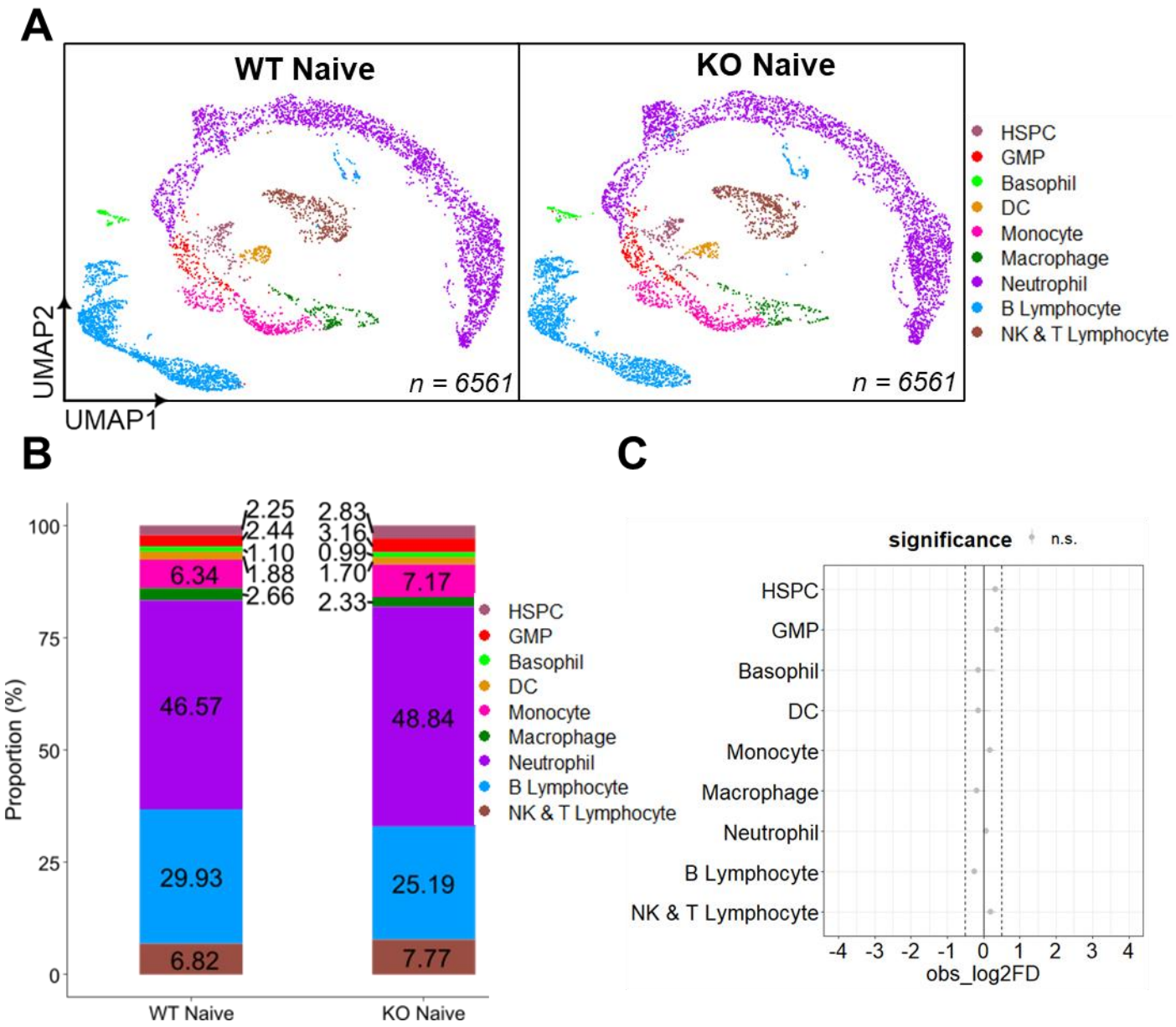

Figure 6.5. *Trim24* deletion does not affect BM leukocyte proportions at the steady state. (A) Integrated Seurat objects were down-sampled to 6,561 cells per sample, and then split by sample for visualisation. **(B)** Stacked bar plot of leukocyte proportions in WT and KO Naïve samples. **(C)** Permutation test plot for differential proportions of KO vs WT Naïve samples. Threshold for log2 fold difference (obs_log2FD) was set to ±0.5, and FDR threshold was 0.05. Both thresholds were required to be considered significant.

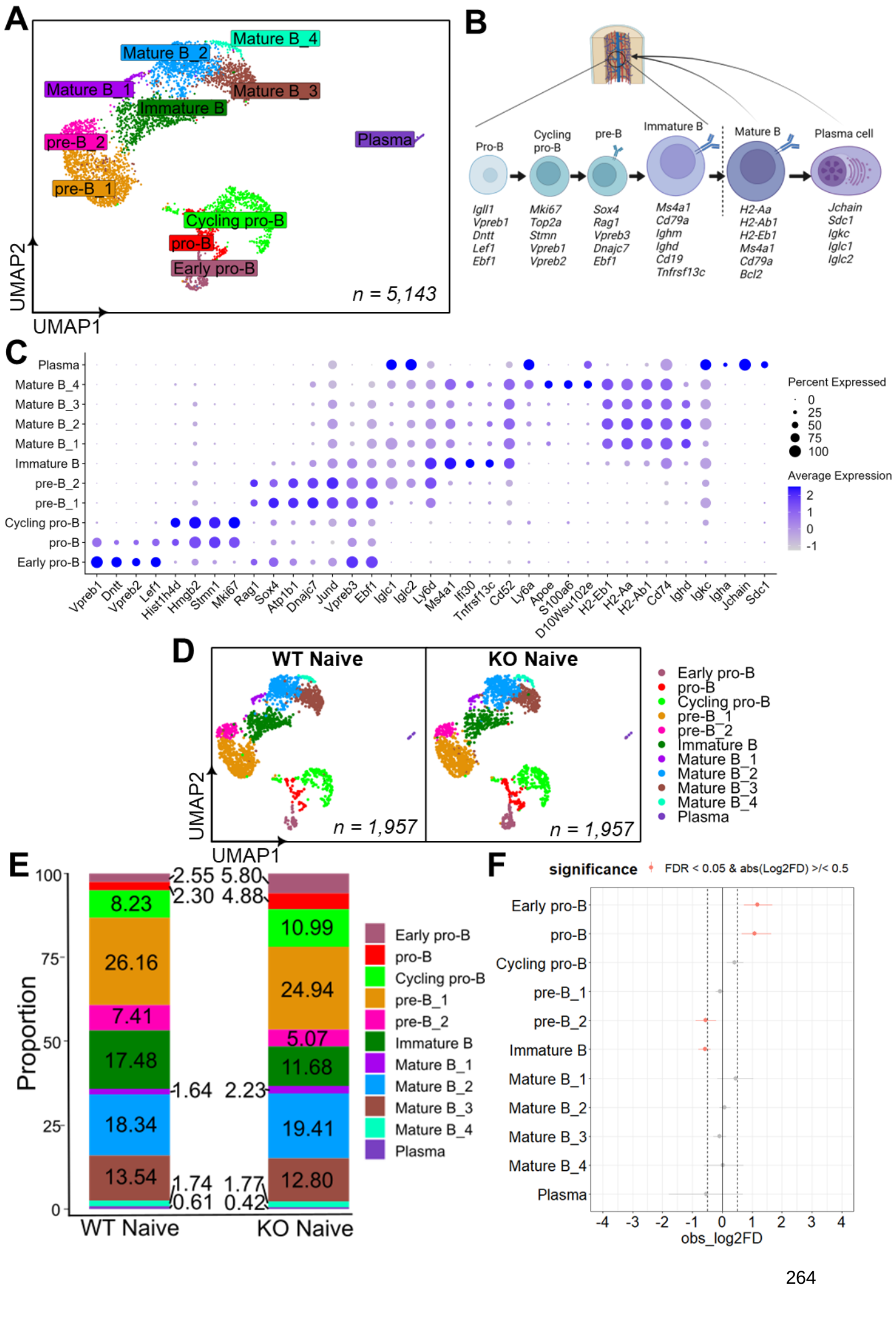
A
Mature B_4
Mature B_2
Mature B_1
Mature B_3
Immature B
pre-B_2
Plasma
pre-B_1
Cycling pro-B
pro-B
Early pro-B
n = 5,143
UMAP2
UMAP1
B
Pro-B
Cycling pro-B
pre-B
Immature B
Mature B
Plasma cell
Igll1 Vpreb1 Dntt Lef1 Ebf1
Mki67 Top2a Stmn Vpreb1 Vpreb2
Sox4 Rag1 Vpreb3 Dnajc7 Ebf1
Ms4a1 Cd79a Ighm Ighd Cd19 Tnfrsf13c
H2-Aa H2-Ab1 H2-Eb1 Ms4a1 Cd79a Bcl2
Jchain Sdc1 Igkc Iglc1 Iglc2
C
Plasma
Mature B_4
Mature B_3
Mature B_2
Mature B_1
Immature B
pre-B_2
pre-B_1
Cycling pro-B
pro-B
Early pro-B
Vpreb1 Dntt Vpreb2 Lef1 Hist1h4d Hmgb2 Stmn1 Mki67 Rag1 Sox4 Atp1b1 Dnajc7 Jund Vpreb3 Ebf1 Iglc1 Iglc2 Ly6d Ms4a1 Ifi30 Tnfrsf13c Cd52 Ly6a Apoe S100a6 D10Wsu102e H2-Eb1 H2-Aa H2-Ab1 Cd74 Ighd Igkc Igha Jchain Sdc1
Percent Expressed
0
25
50
75
100
Average Expression
2
1
0
-1
D
WT Naive
KO Naive
n = 1,957
n = 1,957
UMAP2
UMAP1
Early pro-B
pro-B
Cycling pro-B
pre-B_1
pre-B_2
Immature B
Mature B_1
Mature B_2
Mature B_3
Mature B_4
Plasma
E
Proportion
100
75
50
25
0
2.55 5.80
2.30 4.88
8.23
26.16
7.41
17.48
1.64 2.23
18.34
13.54
1.74 1.77
0.61 0.42
10.99
24.94
5.07
11.68
19.41
12.80
WT Naive
KO Naive
Early pro-B
pro-B
Cycling pro-B
pre-B_1
pre-B_2
Immature B
Mature B_1
Mature B_2
Mature B_3
Mature B_4
Plasma
F
significance
FDR < 0.05 & abs(Log2FD) >/< 0.5
Early pro-B
pro-B
Cycling pro-B
pre-B_1
pre-B_2
Immature B
Mature B_1
Mature B_2
Mature B_3
Mature B_4
Plasma
-4 -3 -2 -1 0 1 2 3 4
obs_log2FD

Figure 6.6. *Trim24* deletion does not affect proportions of B cell subsets at the steady state. (A) B lymphocytes from **Fig. 6.3.** were re-integrated and sub-clustered as described in Methods. Clusters were labelled after interrogation of top expressed genes per cluster. **(B)** Schematic of genes expression at different stages of B cell development in the BM. **(C)** Top 5 genes (by log2FC) expressed per UMAP cluster compared to every other cluster. **(D)** Samples were downsampled to the same cell number, and the UMAP was split by sample to show WT vs KO B cell subsets. **(E)** Percentage proportions of B cell subsets in WT and KO naïve BM. **(F)** Permutation test was performed to statistically compare KO vs WT proportions of B cell subsets. Differences were considered significant where FDR<0.05 and absolute (abs)_log2FD (log2 fold change) was >0.5 or <-0.5.

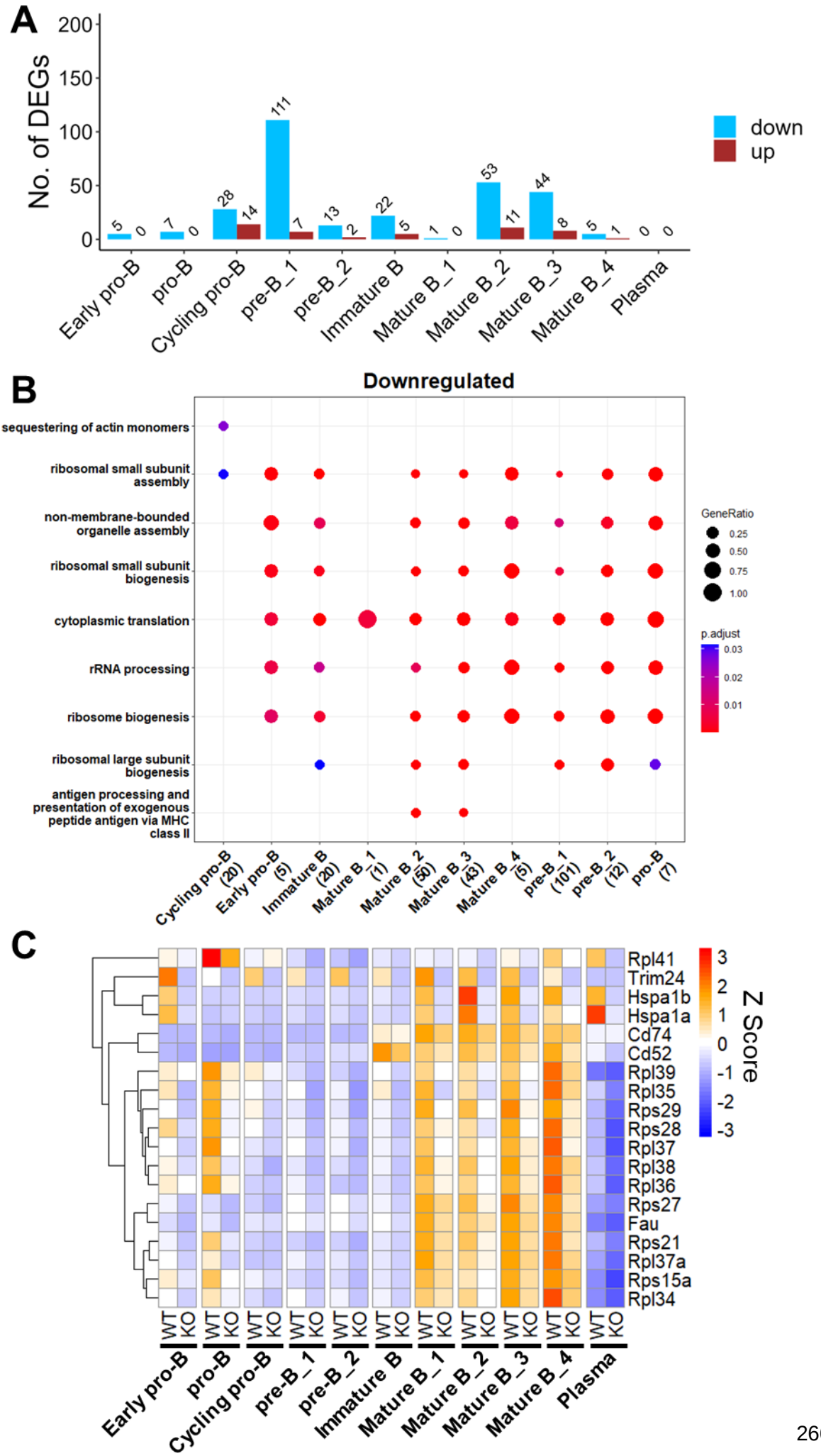
A
No. of DEGs
200
150
100
50
0
down
up
5
0
7
0
28
14
111
7
13
2
22
5
1
0
53
11
44
8
5
1
0
0
Early pro-B
pro-B
Cycling pro-B
pre-B_1
pre-B_2
Immature B
Mature B_1
Mature B_2
Mature B_3
Mature B_4
Plasma
B
Downregulated
sequestering of actin monomers
ribosomal small subunit assembly
non-membrane-bounded organelle assembly
ribosomal small subunit biogenesis
cytoplasmic translation
rRNA processing
ribosome biogenesis
ribosomal large subunit biogenesis
antigen processing and presentation of exogenous peptide antigen via MHC class II
Cycling pro-B (20)
Early pro-B (5)
Immature B (20)
Mature B_1 (1)
Mature B_2 (50)
Mature B_3 (43)
Mature B_4 (5)
pre-B_1 (101)
pre-B_2 (12)
pro-B (7)
GeneRatio
0.25
0.50
0.75
1.00
p.adjust
0.03
0.02
0.01
C
Rpl41
Trim24
Hspa1b
Hspa1a
Cd74
Cd52
Rpl39
Rpl35
Rps29
Rps28
Rpl37
Rpl38
Rpl36
Rps27
Fau
Rps21
Rpl37a
Rps15a
Rpl34
Z Score
3
2
1
0
-1
-2
-3
WT
KO
Early pro-B
pro-B
Cycling pro-B
pre-B_1
pre-B_2
Immature B
Mature B_1
Mature B_2
Mature B_3
Mature B_4
Plasma

Figure 6.7. *Trim24* deficiency downregulates translation and ribosome biogenesis-related genes in steady state B cells. (A) Number of up- and down-regulated genes in naïve KO B cell subsets compared to WT. **(B)** Over-representation analysis (ORA) of downregulated genes in each cluster was performed using the compareCluster function of the ClusterProfiler R package. Top significant Gene Ontology (GO) terms per cluster (P<0.05) are shown. Bracketed numbers indicate number of genes included within GO terms shown in plot. **(C)** Heatmap showing commonly down-regulated genes between B cell subsets.

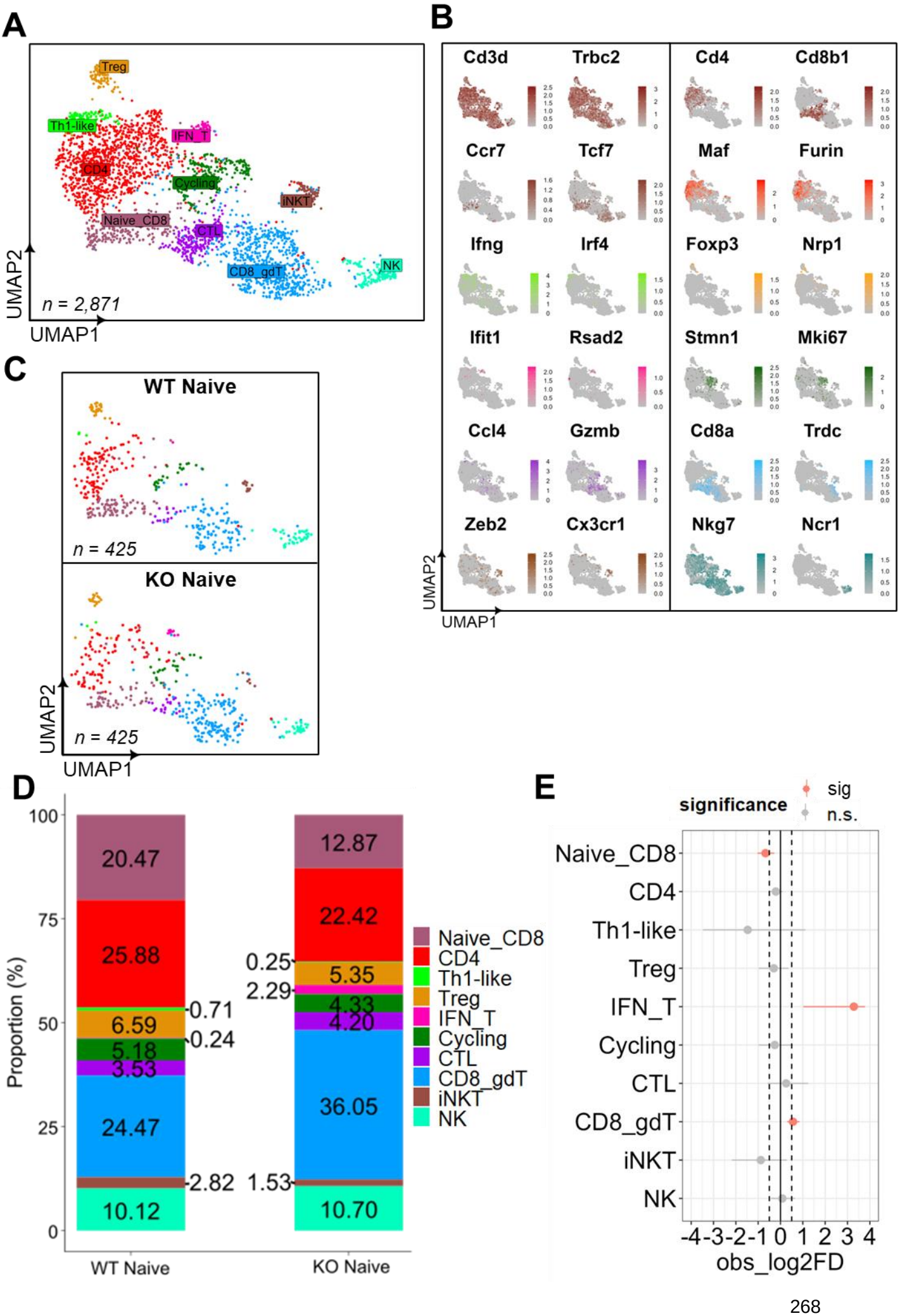
A
Treg
Th1-like
IFN_T
CD4
Cycling
iNKT
Naive_CD8
CTL
CD8_gdT
NK
n = 2,871
UMAP2
UMAP1
B
Cd3d
Trbc2
Cd4
Cd8b1
Ccr7
Tcf7
Maf
Furin
Ifng
Irf4
Foxp3
Nrp1
Ifit1
Rsad2
Stmn1
Mki67
Ccl4
Gzmb
Cd8a
Trdc
Zeb2
Cx3cr1
Nkg7
Ncr1
UMAP2
UMAP1
C
WT Naive
n = 425
KO Naive
n = 425
UMAP2
UMAP1
D
Proportion (%)
100
75
50
25
0
20.47
25.88
6.59
5.18
3.53
24.47
10.12
12.87
22.42
5.35
4.33
4.20
36.05
10.70
0.71
0.24
2.82
0.25
2.29
1.53
WT Naive
KO Naive
Naive_CD8
CD4
Th1-like
Treg
IFN_T
Cycling
CTL
CD8_gdT
iNKT
NK
E
significance
sig
n.s.
Naive_CD8
CD4
Th1-like
Treg
IFN_T
Cycling
CTL
CD8_gdT
iNKT
NK
-4 -3 -2 -1 0 1 2 3 4
obs_log2FD

Figure 6.8. Effects of *Trim24* deletion on proportions of NK & T cell subsets at the steady state. **(A)** NK & T lymphocytes from **Fig. 6.3.** were re-integrated and sub-clustered as described in Methods. Clusters were labelled after detection of top expressed genes per cluster. **(B)** Feature plots of genes expressed by each cluster. **(C)** Samples were downsampled to the same cell number, and the UMAP was split by sample to show WT vs KO cell subsets. **(D)** Percentage proportions of cell subsets in WT and KO naïve BM. **(E)** Permutation test was performed to statistically compare KO vs WT proportions of cell subsets. Differences were considered significant where $p<0.05$ and obs_log2FD (log2 fold change) was >0.5 or <-0.5.

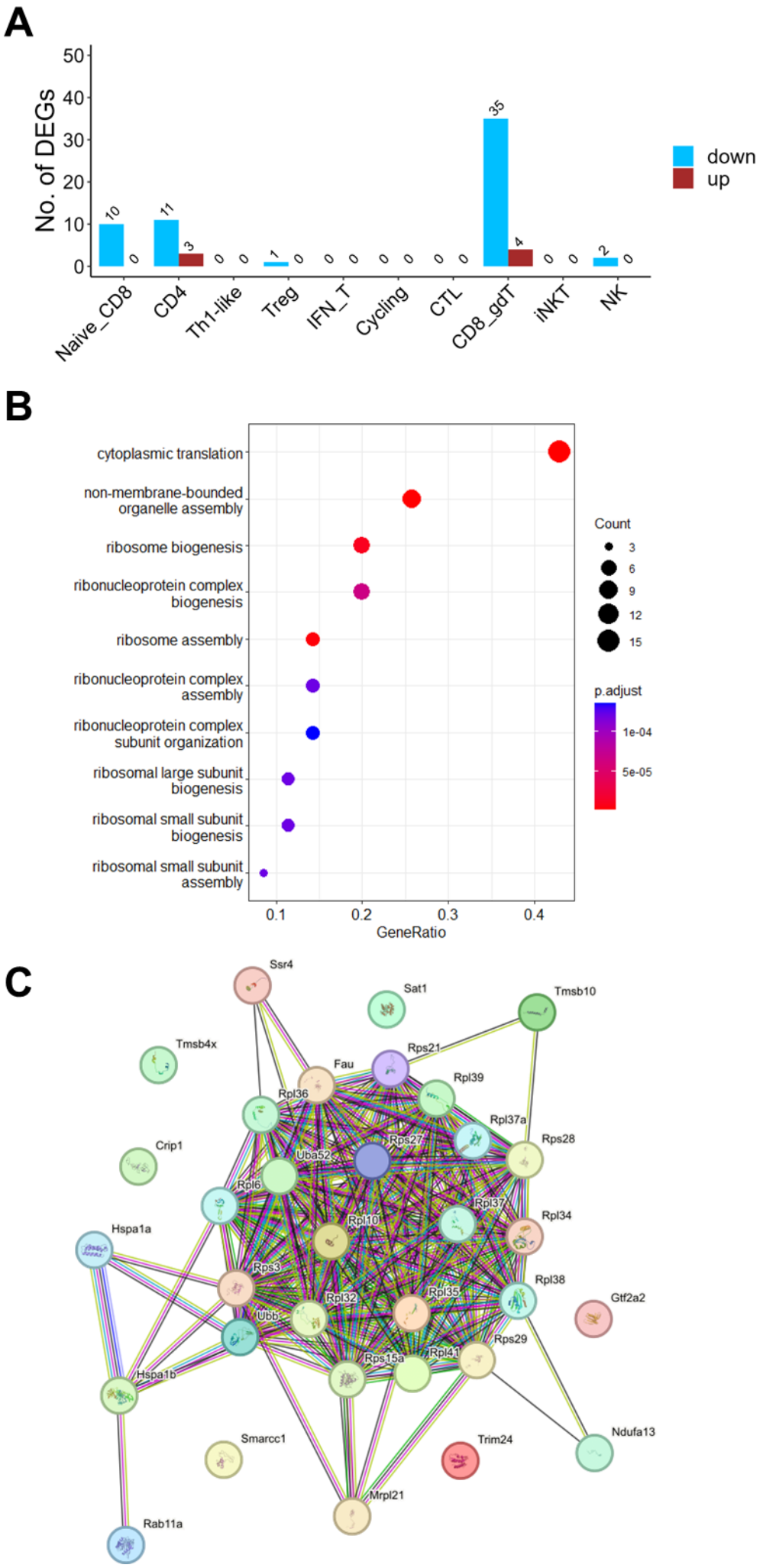
A
No. of DEGs
50
40
30
20
10
0
down
up
10
0
11
3
0
0
1
0
0
0
0
0
0
0
35
4
0
0
2
0
Naive_CD8
CD4
Th1-like
Treg
IFN_T
Cycling
CTL
CD8_gdT
iNKT
NK
B
cytoplasmic translation
non-membrane-bounded organelle assembly
ribosome biogenesis
ribonucleoprotein complex biogenesis
ribosome assembly
ribonucleoprotein complex assembly
ribonucleoprotein complex subunit organization
ribosomal large subunit biogenesis
ribosomal small subunit biogenesis
ribosomal small subunit assembly
0.1
0.2
0.3
0.4
GeneRatio
Count
3
6
9
12
15
p.adjust
1e-04
5e-05
C
Ssr4
Sat1
Tmsb10
Tmsb4x
Rps21
Fau
Rpl39
Rpl36
Rpl37a
Rps28
Crip1
Rps27
Uba52
Rpl6
Rpl37
Rpl34
Rpl10
Hspa1a
Rps3
Rpl38
Rpl35
Gtf2a2
Rpl32
Ubb
Rps29
Rpl41
Rps15a
Hspa1b
Ndufa13
Smarcc1
Trim24
Mrpl21
Rab11a

Figure 6.9. *Trim24* deficiency downregulates translation and ribosome biogenesis-related genes in steady state NK & T cells. (A) Number of up- and down-regulated genes (*P*<0.05, log2FC <0) in naïve KO NK & T cell subsets compared to WT. **(B)** Over-representation analysis (ORA) of the 35 downregulated genes in the CD8_gdT was performed. Top ten significant GO terms per cluster (*P*<0.05) are shown. Bracketed numbers indicate number of genes included within GO terms shown in plot. **(C)** STRING network of down-regulated in the CD8_gdT cluster. Genes shown are all common with down-regulated genes in other clusters.

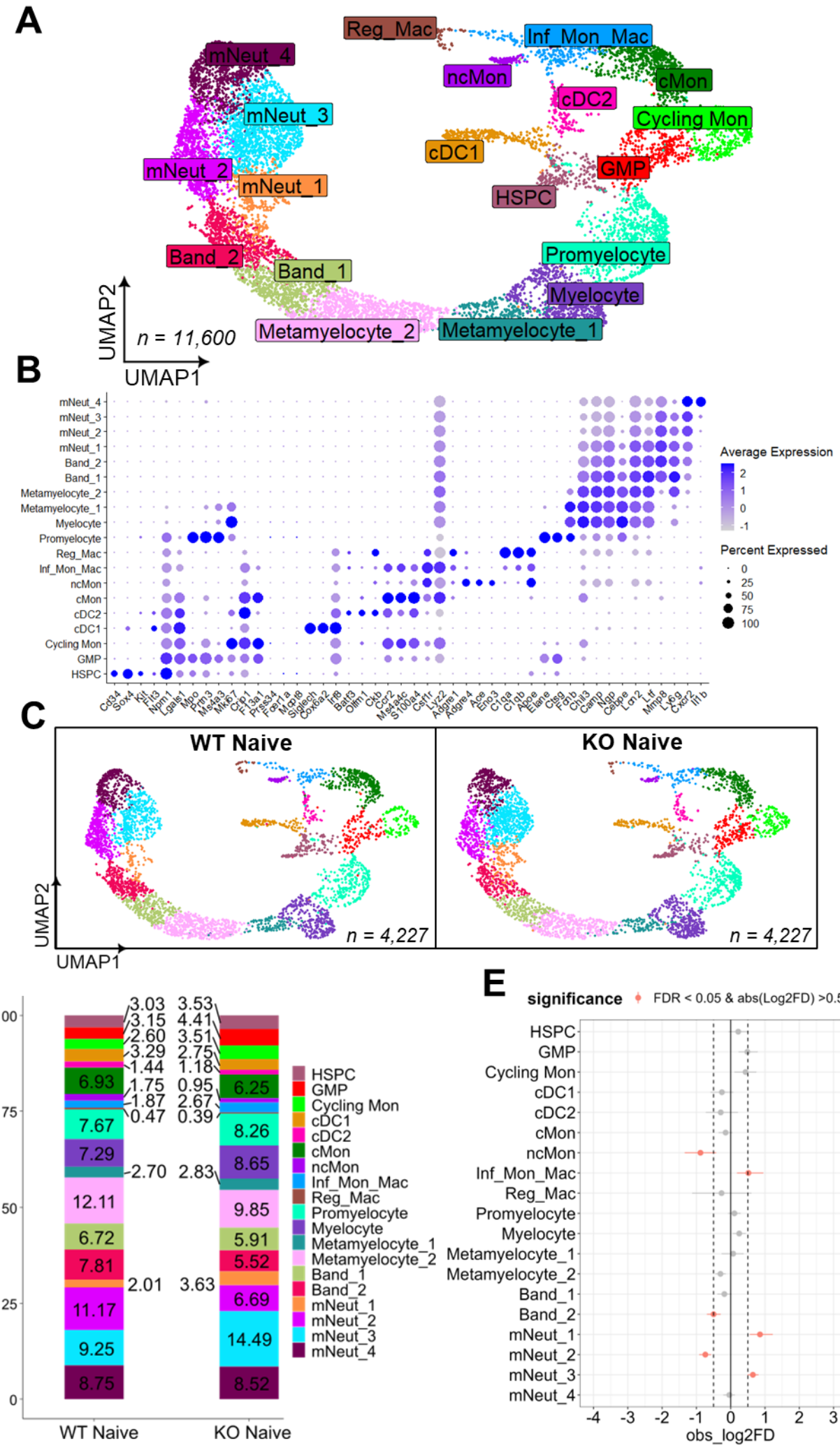
A
Reg_Mac
Inf_Mon_Mac
mNeut_4
ncMon
cMon
cDC2
mNeut_3
Cycling Mon
cDC1
mNeut_2
GMP
mNeut_1
HSPC
Band_2
Promyelocyte
Band_1
Myelocyte
Metamyelocyte_2
Metamyelocyte_1
UMAP2
n = 11,600
UMAP1
B
Average Expression
Percent Expressed
C
WT Naive
KO Naive
n = 4,227
n = 4,227
UMAP2
UMAP1
D
Proportion (%)
WT Naive
KO Naive
E
significance
FDR < 0.05 & abs(Log2FD) >0.5/<- 0.5
obs_log2FD

Figure 6.10. Effects of *Trim24* deletion on proportions of myeloid & progenitor cell subsets at the steady state. (A) Myeloid & progenitor cells from **Fig. 6.3.** were re-integrated and sub-clustered as described in Methods. Clusters were labelled after detection of top expressed genes per cluster. **(B)** Top 5 genes expressed by each cluster. **(C)** Samples were downsampled to the same cell number, and the UMAP was split by sample to show WT vs KO cell subsets. **(D)** Percentage proportions of cell subsets in WT and KO naïve BM. **(E)** Permutation test was performed to statistically compare KO vs WT proportions of cell subsets. Differences were considered significant where $p<0.05$ and obs_log2FD (log2 fold change) was >0.5 or <-0.5.

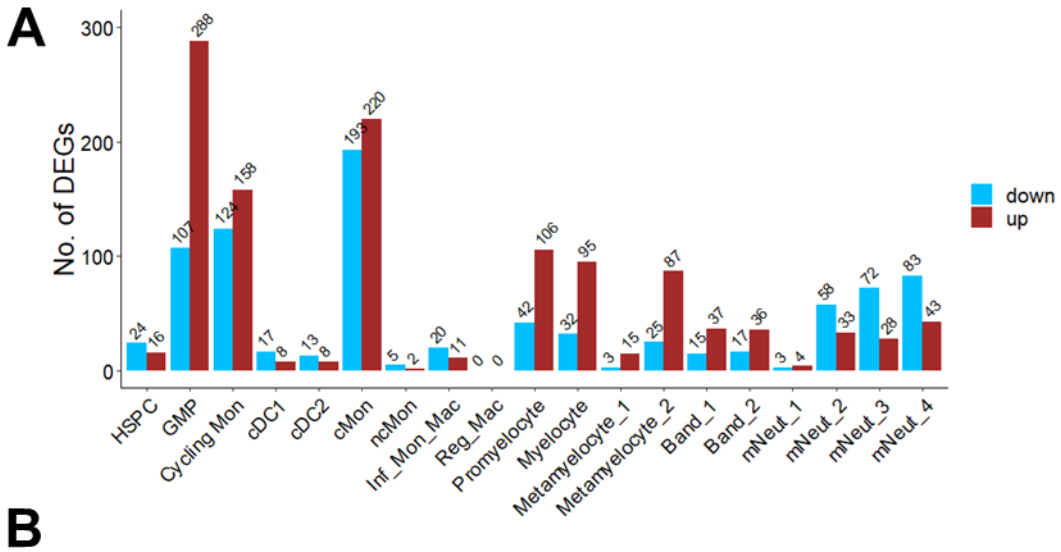
A
No. of DEGs
down
up
HSPC
GMP
Cycling Mon
cDC1
cDC2
cMon
ncMon
Inf_Mon_Mac
Reg_Mac
Promyelocyte
Myelocyte
Metamyelocyte_1
Metamyelocyte_2
Band_1
Band_2
mNeut_1
mNeut_2
mNeut_3
mNeut_4

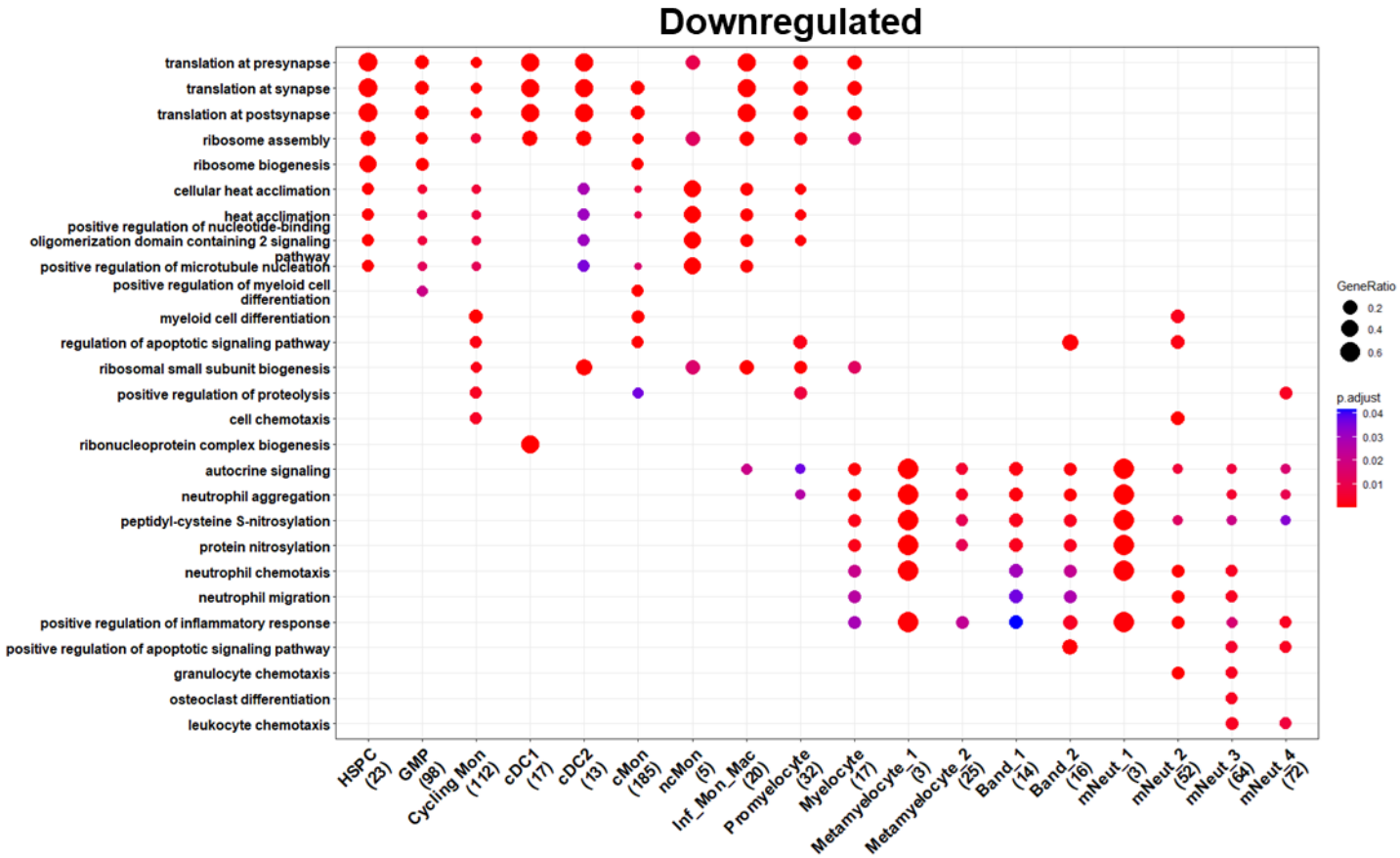
B
Downregulated
translation at presynapse
translation at synapse
translation at postsynapse
ribosome assembly
ribosome biogenesis
cellular heat acclimation
heat acclimation
positive regulation of nucleotide-binding oligomerization domain containing 2 signaling pathway
positive regulation of microtubule nucleation
positive regulation of myeloid cell differentiation
myeloid cell differentiation
regulation of apoptotic signaling pathway
ribosomal small subunit biogenesis
positive regulation of proteolysis
cell chemotaxis
ribonucleoprotein complex biogenesis
autocrine signaling
neutrophil aggregation
peptidyl-cysteine S-nitrosylation
protein nitrosylation
neutrophil chemotaxis
neutrophil migration
positive regulation of inflammatory response
positive regulation of apoptotic signaling pathway
granulocyte chemotaxis
osteoclast differentiation
leukocyte chemotaxis
GeneRatio
p.adjust

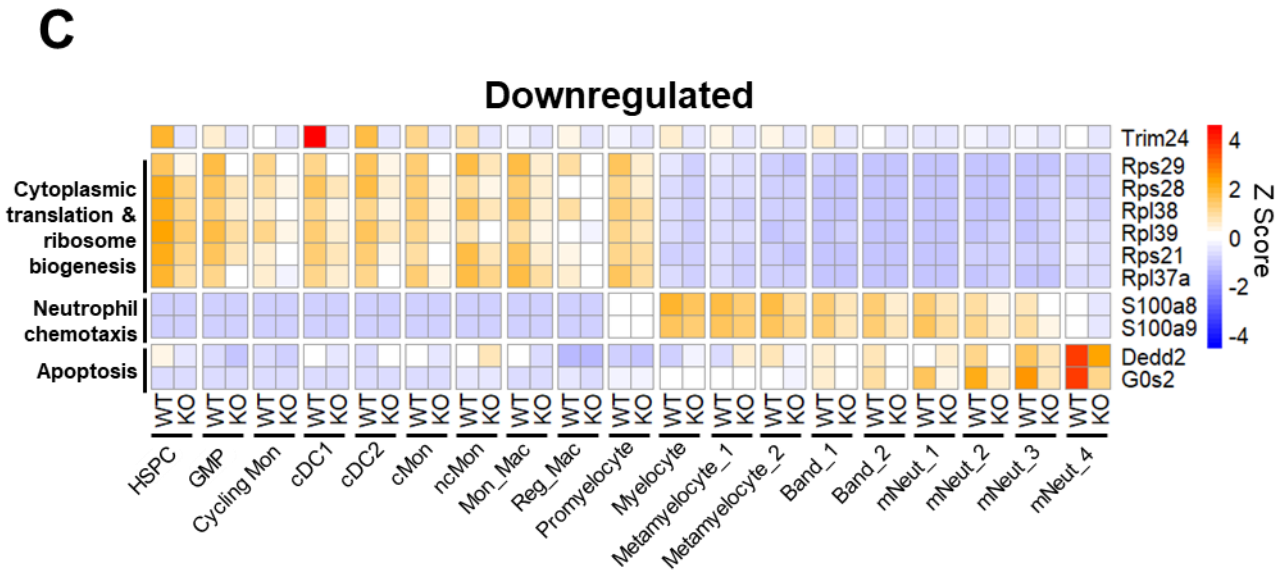
C
Downregulated
Cytoplasmic translation & ribosome biogenesis
Neutrophil chemotaxis
Apoptosis
Trim24
Rps29
Rps28
Rpl38
Rpl39
Rps21
Rpl37a
S100a8
S100a9
Dedd2
G0s2
Z Score
WT
KO

Figure 6.11. *Trim24* deficiency downregulates translation and ribosome biogenesis-related genes in steady state myeloid & progenitor cells. (A) Number of up- and down-regulated genes (*P*<0.05, log2FC <0) in naïve KO myeloid & progenitor cell subsets compared to WT. **(B)** Over-representation analysis (ORA) of down-regulated genes per cluster was performed. Top significant GO terms per cluster (*P*<0.05) are shown. Bracketed numbers indicate number of genes included within GO terms shown in plot. **(C)** Heatmap showing commonly down-regulated genes in KO cells compared to WT between clusters included in significantly enriched GO gene sets.

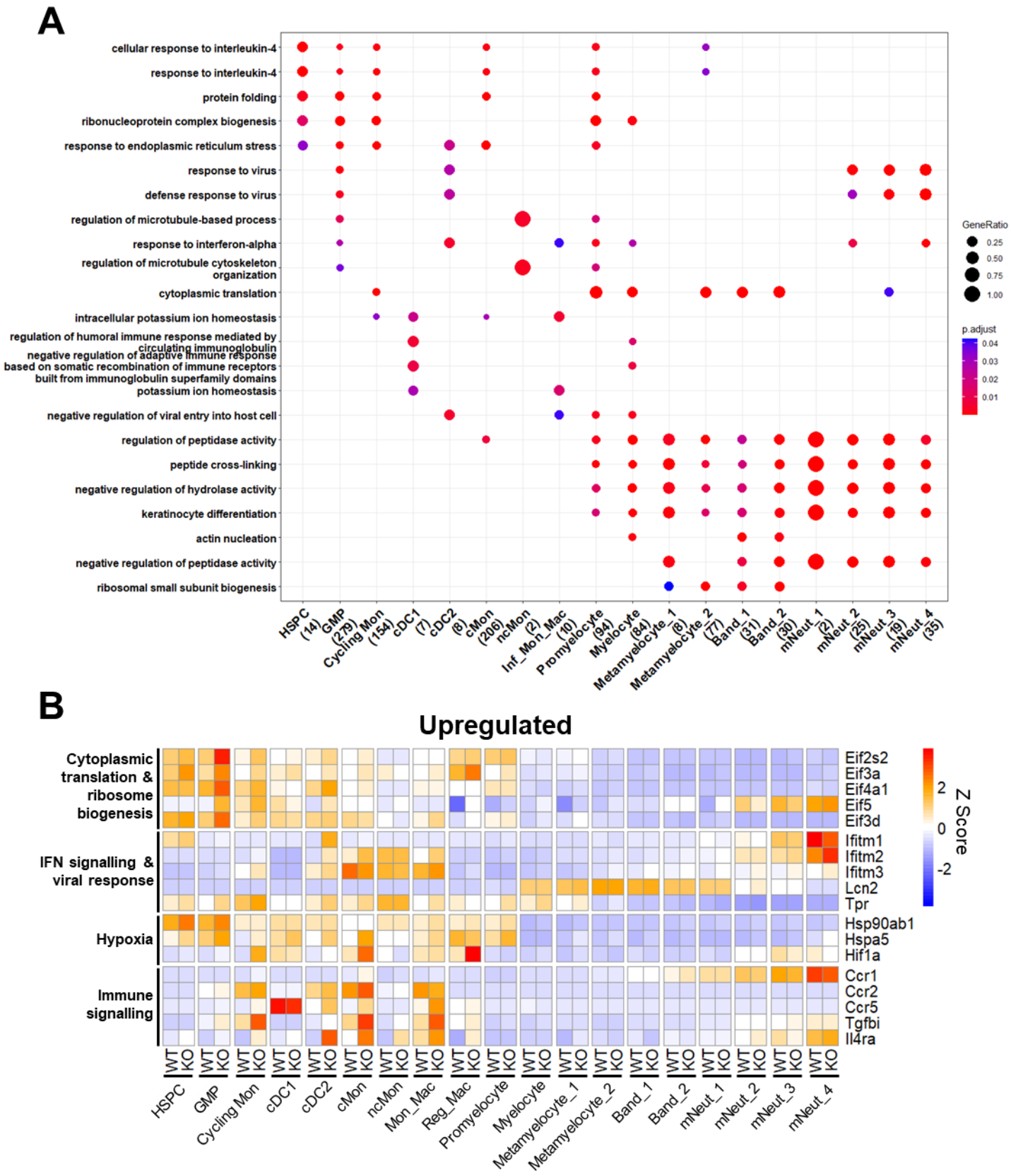

Figure 6.12. *Trim24* deficiency upregulates IFN-related and immune signalling genes in myeloid & progenitor cells. (A) Over-representation analysis (ORA) of up-regulated genes (from **Fig. 6.8A**) per cluster was performed. Top significant GO terms per cluster (P<0.05) are shown. Bracketed numbers indicate number of genes included within GO terms shown in plot. **(B)** Heatmap showing up-regulated genes in KO myeloid/progenitor cells included in significantly enriched GO gene sets.

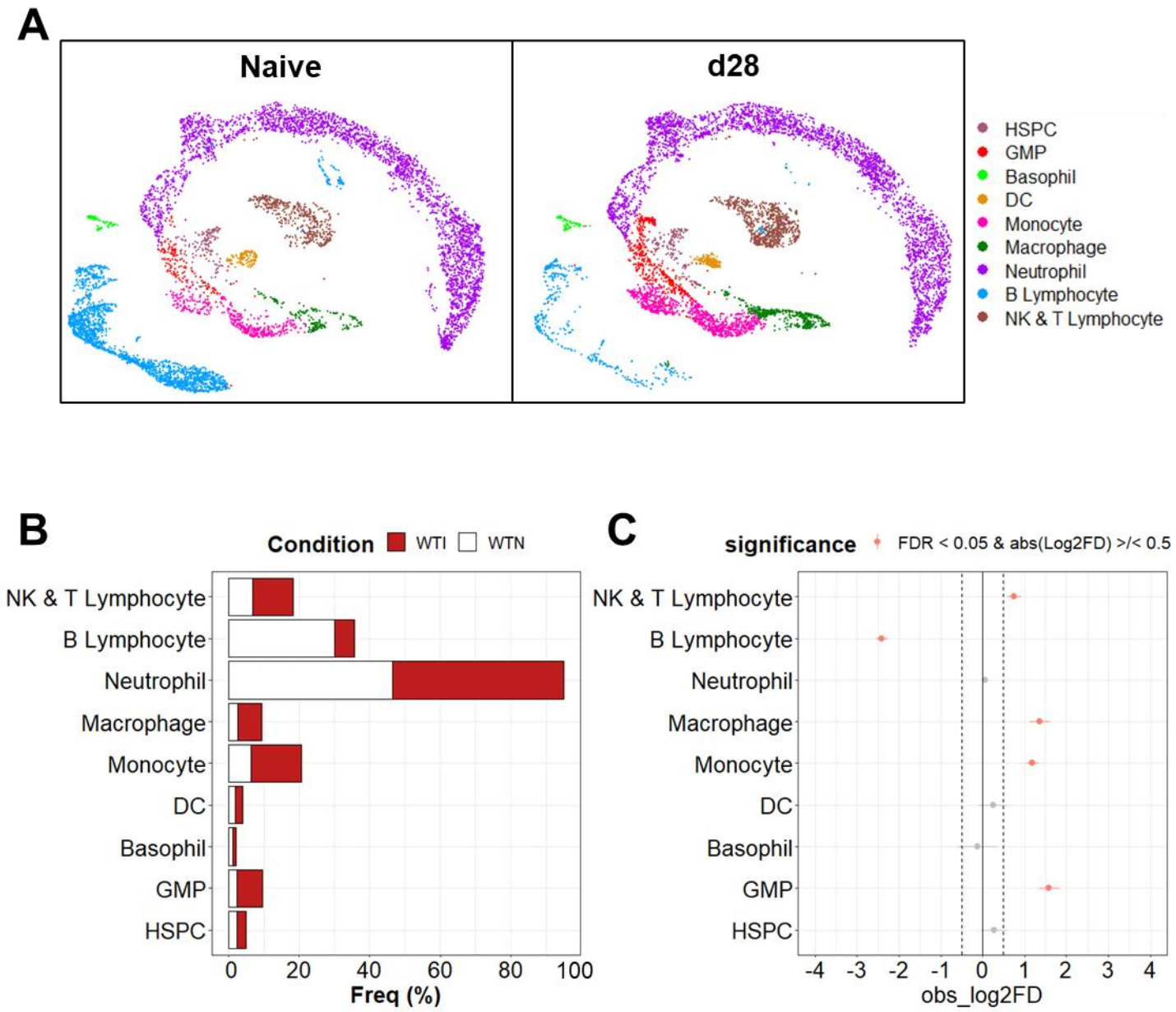

Figure 6.13. *L. donovani* infection induces proportional leukocyte changes in BM. (A) Broad UMAP from **Fig. 6.4A.** was split by sample, and WT Naïve and d28 samples are shown. **(B)** Percentage proportions of broad cell types in WT naïve and d28 BM. WTI = WT d28; WTN = WT naive. **(C)** Permutation test was used to statistically analyse proportional differences between WT d28 and WT naïve BM leukocytes. Differences were considered significant where FDR<0.05 and obs_log2FD (log2 fold change) <-0.5 or >0.5.

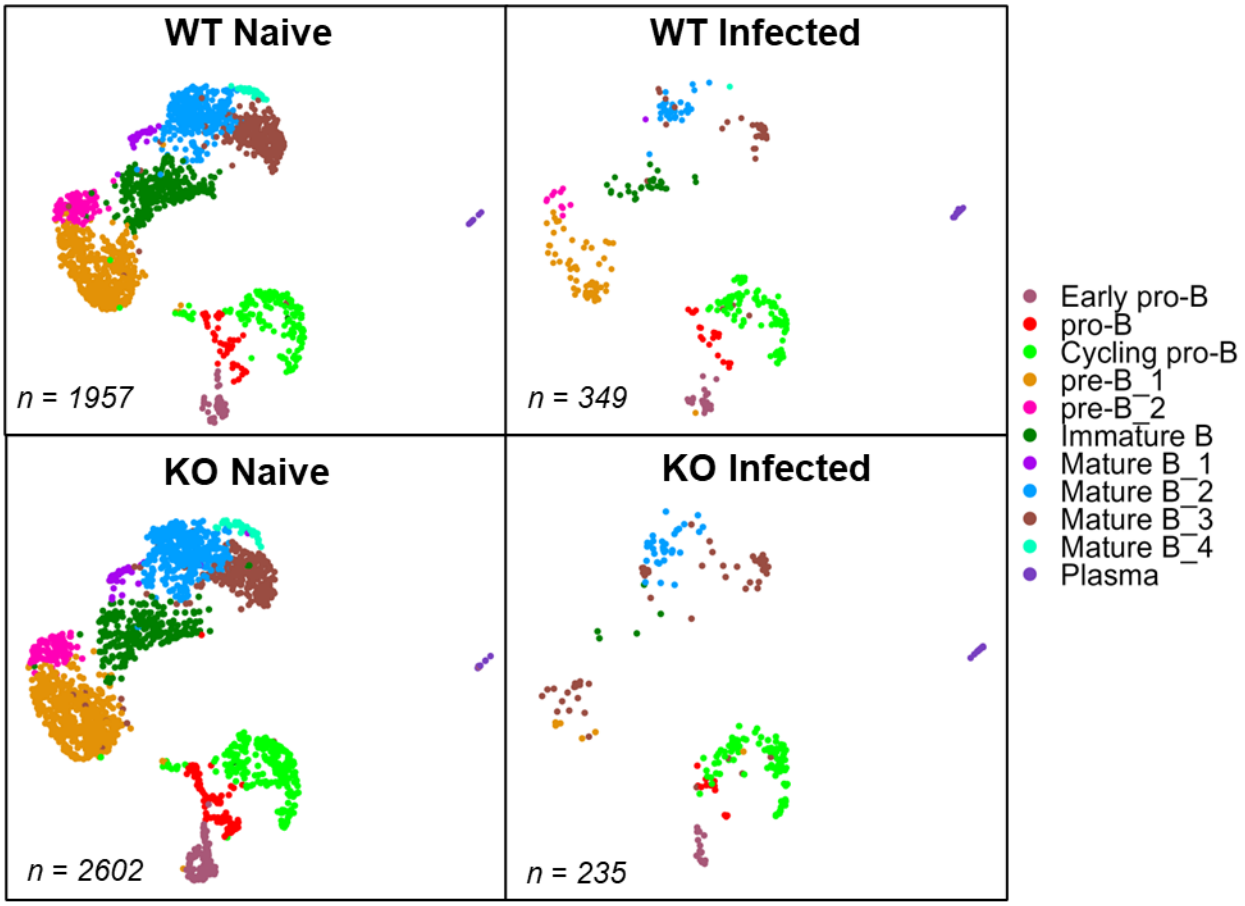

Figure 6.14. *L. donovani* infection results in loss of B cells in the BM in WT and KO mice. UMAP projection of B cell UMAP from **Fig. 6.5,** split by sample.

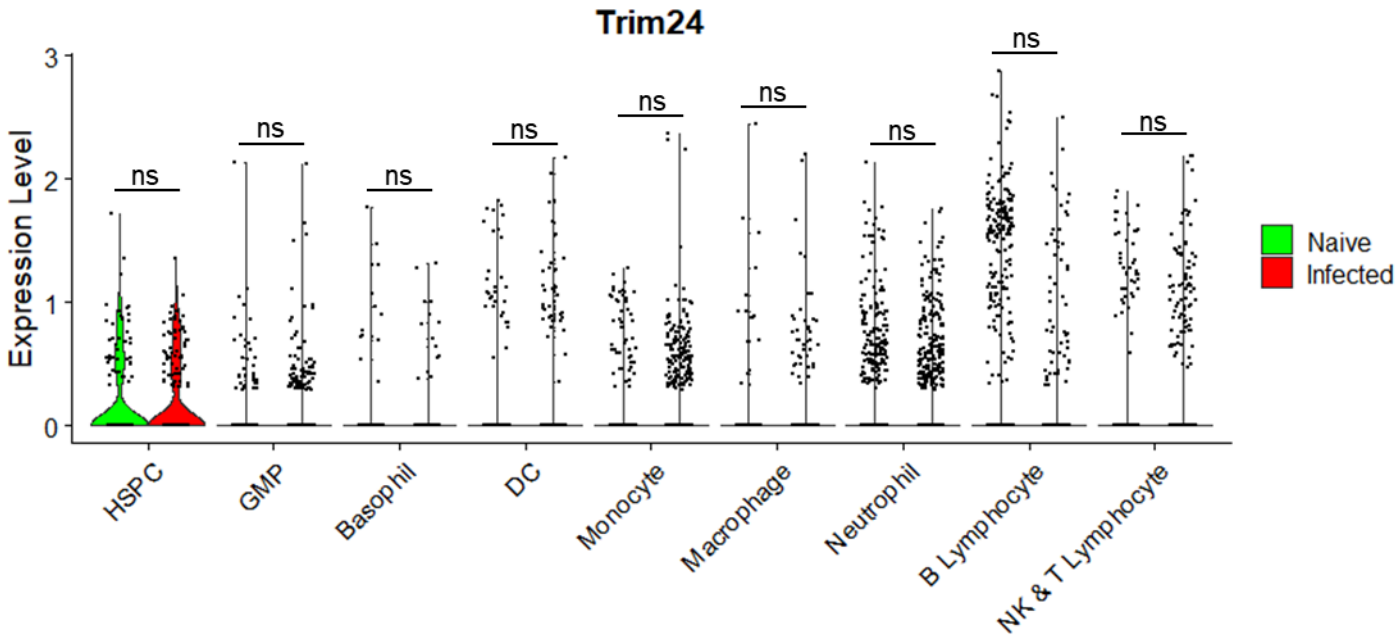

Figure 6.15. *Trim24* is not differentially expressed in broad WT BM cell types during *L. donovani* infection. DGE analysis was performed between WT d28 and naïve cell types to identify significantly up- and down-regulated genes (FDR<0.05, log2FC>0 or <0). Expression levels of *Trim24* in each cell type are displayed.

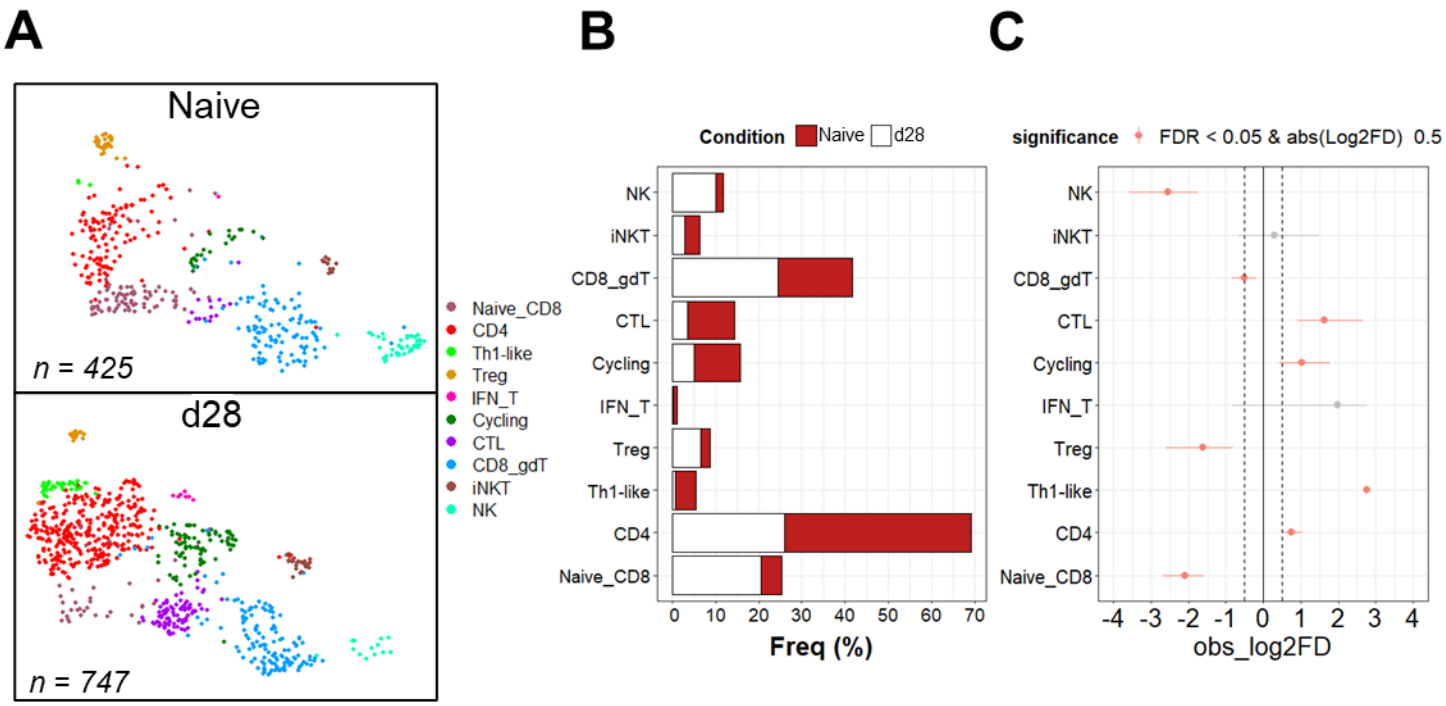

Figure 6.16. *L. donovani* infection causes expansion and reduction of BM NK & T cell subsets. **(A)** UMAP projections of WT naïve and d28 BM NK & T cell subsets. **(B)** Percentage proportions of NK & T cell subsets in WT naïve and d28 BM samples. **(C)** Permutation test was performed on WT d28 vs naïve NK & T cell clusters. Differences were considered significant where FDR<0.05 and obs_log2FD (log2 fold change) <-0.5 or >0.5.

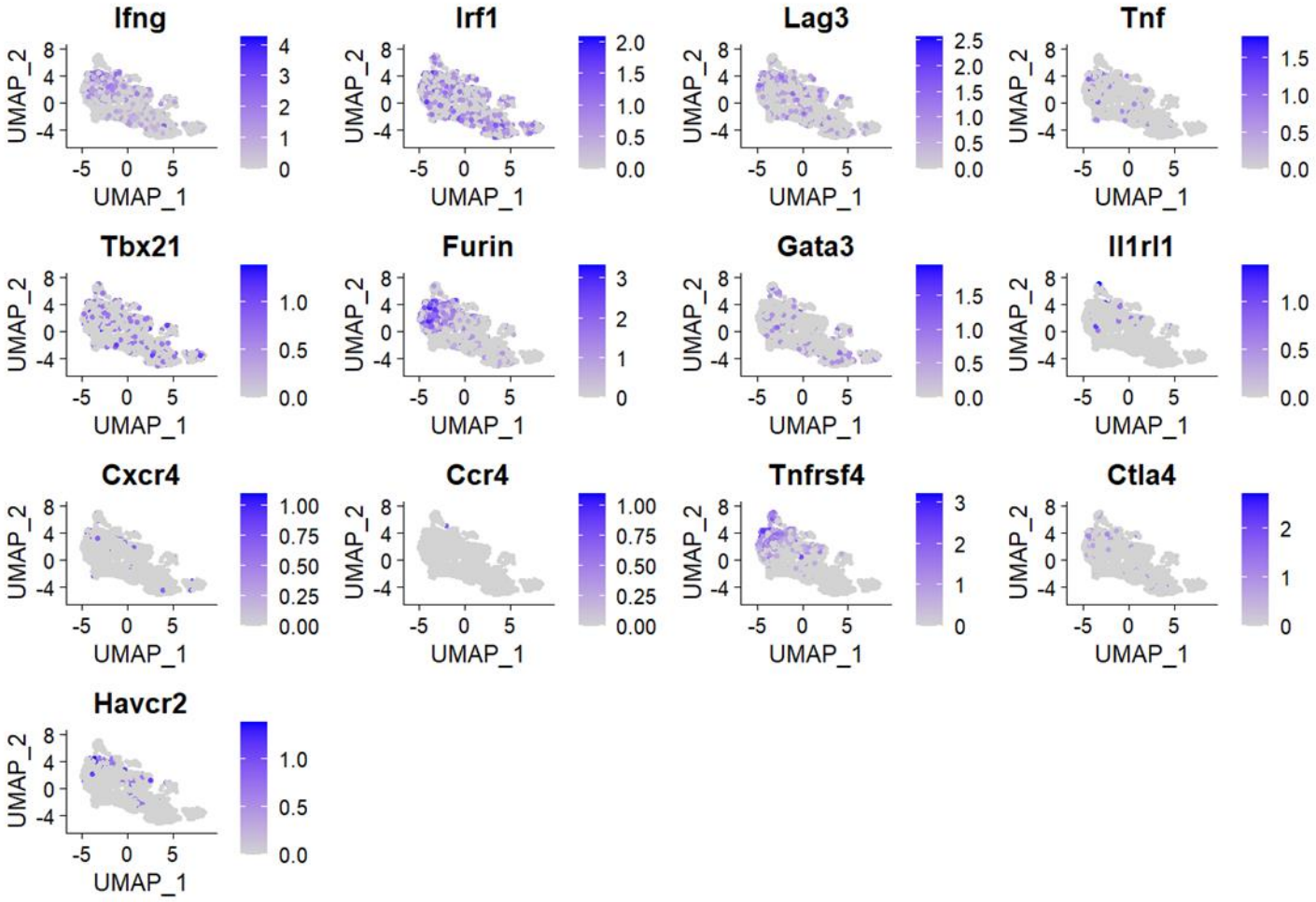

Figure 6.17. Expression of Th1- and Th2-related genes in T cell clusters. Expression levels are represented as Seurat feature plots. High expression = blue, low expression = grey.

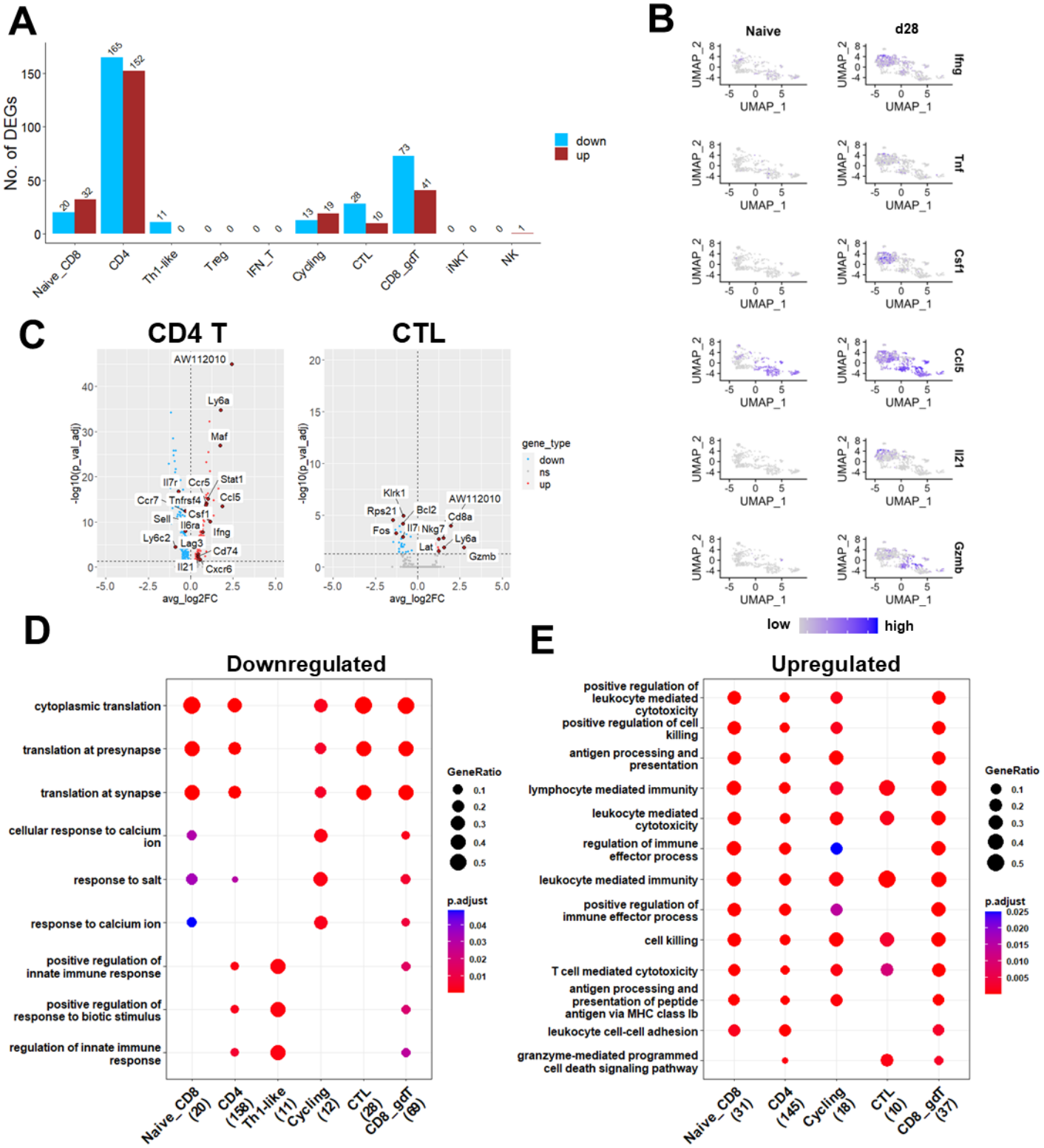

Figure 6.18. *L. donovani* infection induces transcriptional alterations in BM T cells. (A) Number of up- and down-regulated genes (FDR<0.05, log2FC<0 or >0) in each NK & T cell cluster in WT d28 vs naïve samples. **(B)** Volcano plots displaying key up- and down-regulated genes in d28 CD4 T cells and CTLs compared to naïve. **(C)** Feature plots displaying expression of key factors in WT naïve and d28 NK & T cells. **(D)** ORA of down-regulated genes in d28 NK & T cell clusters compared to naïve using GO gene set terms. **(E)** ORA of up-regulated genes in d28 NK & T cell clusters compared to naïve using GO gene set terms.

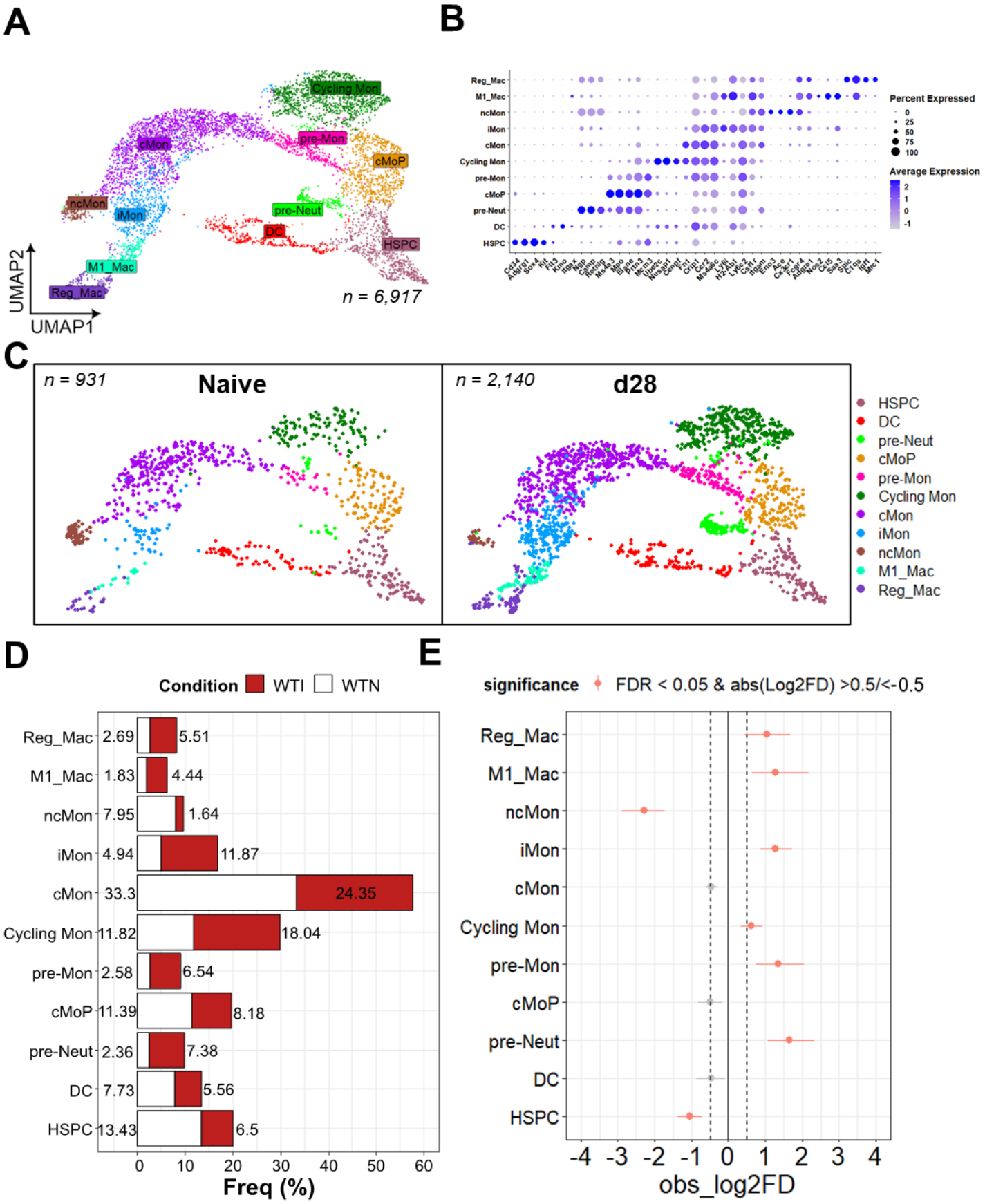

Figure 6.19. Increased myelopoiesis in *L. donovani*-infected BM. (A) Progenitor, monocyte and macrophage cells were sub-clustered and UMAP projection is shown. **(B)** Dot plot of top expressed gene per cluster. **(C)** UMAP from **A** was split by sample, and WT naïve and WT d28 UMAPs are shown. **(D)** Percentage proportions of broad cell types in WT naïve and d28 BM. WTI = WT d28; WTN = WT naive. **(E)** Permutation test was used to statistically analyse proportional differences between WT d28 and WT naïve BM leukocytes. Differences were considered significant where FDR<0.05 and obs_log2FD (log2 fold change) <-0.5 or >0.5.

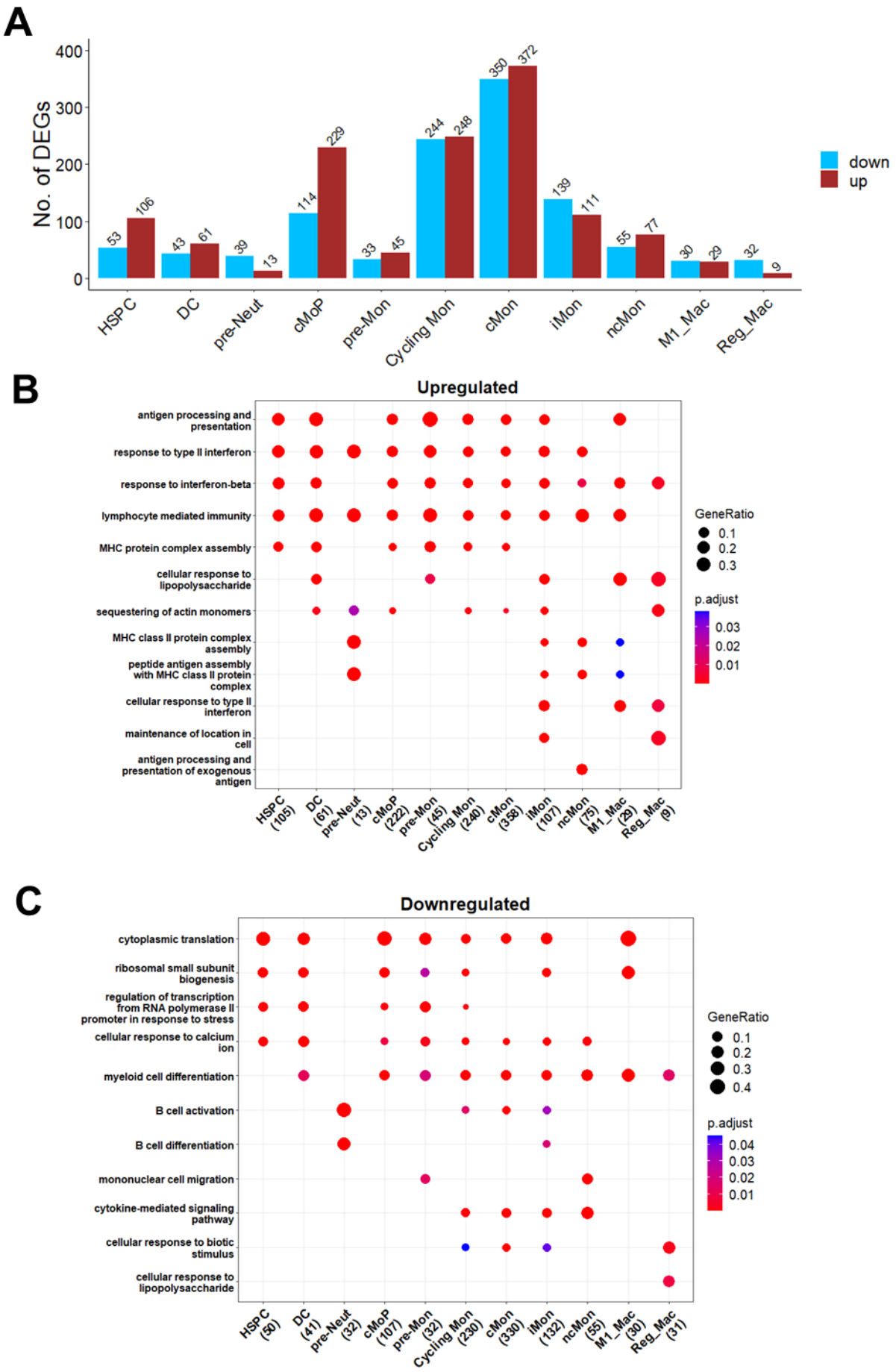

Figure 6.20. ORA of DEGs in monocyte and macrophage subsets. (A) DGE analysis was performed on WT d28 monocyte and macrophage subsets compared to naïve, and number of up-regulated (FDR<0.05, log2FC>0) and down-regulated (FDR<0.05, log2FC>0) is plotted. **(B)** ORA of up-regulated genes in monocyte and macrophage clusters was performed using GO gene set terms. Significantly enriched gene sets are shown (p.adjust<0.05). **(C)** Same for **B** but with down-regulated genes.

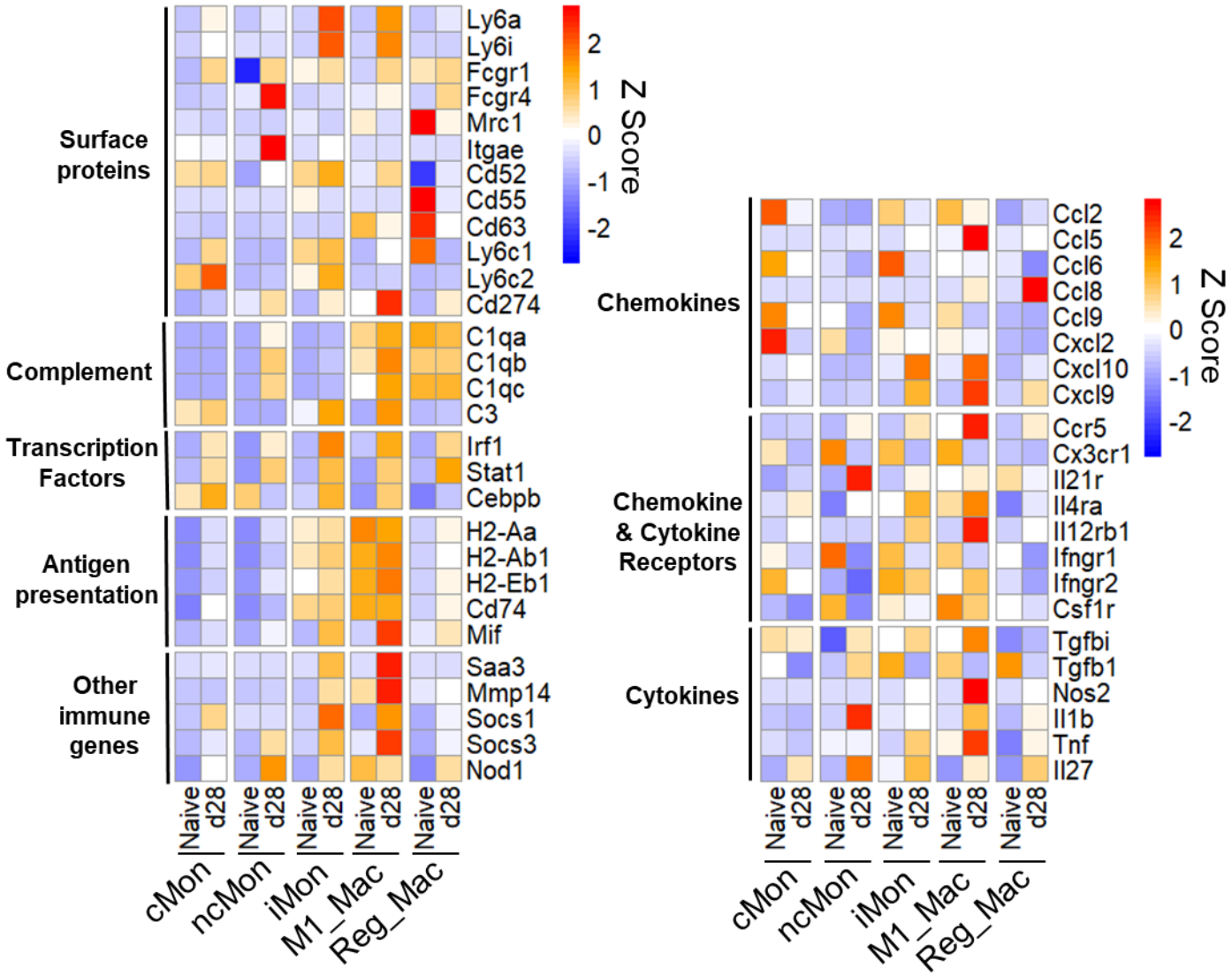

Figure 6.21. Monocyte and macrophage phenotypes during *L. donovani* infection. Average expression levels of immune-related genes in monocyte and macrophage subsets in d28 BM compared to naive.

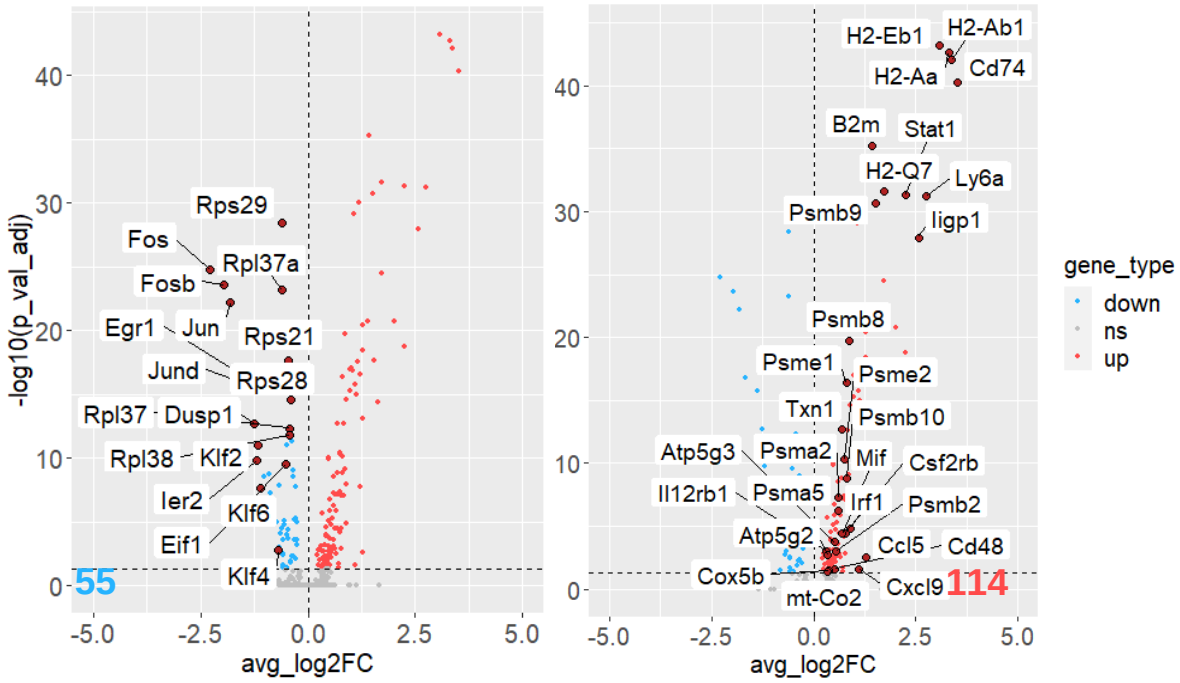

Figure 6.22. Transcriptional alterations in WT HSPCs during *L. donovani* infection promotes myelopoiesis. Volcano plots displaying key down-regulated (FDR<0.05, log2FC<0) (left) and up-regulated (FDR<0.05, log2FC>0) (right) genes in WT d28 vs naïve HSPCs.

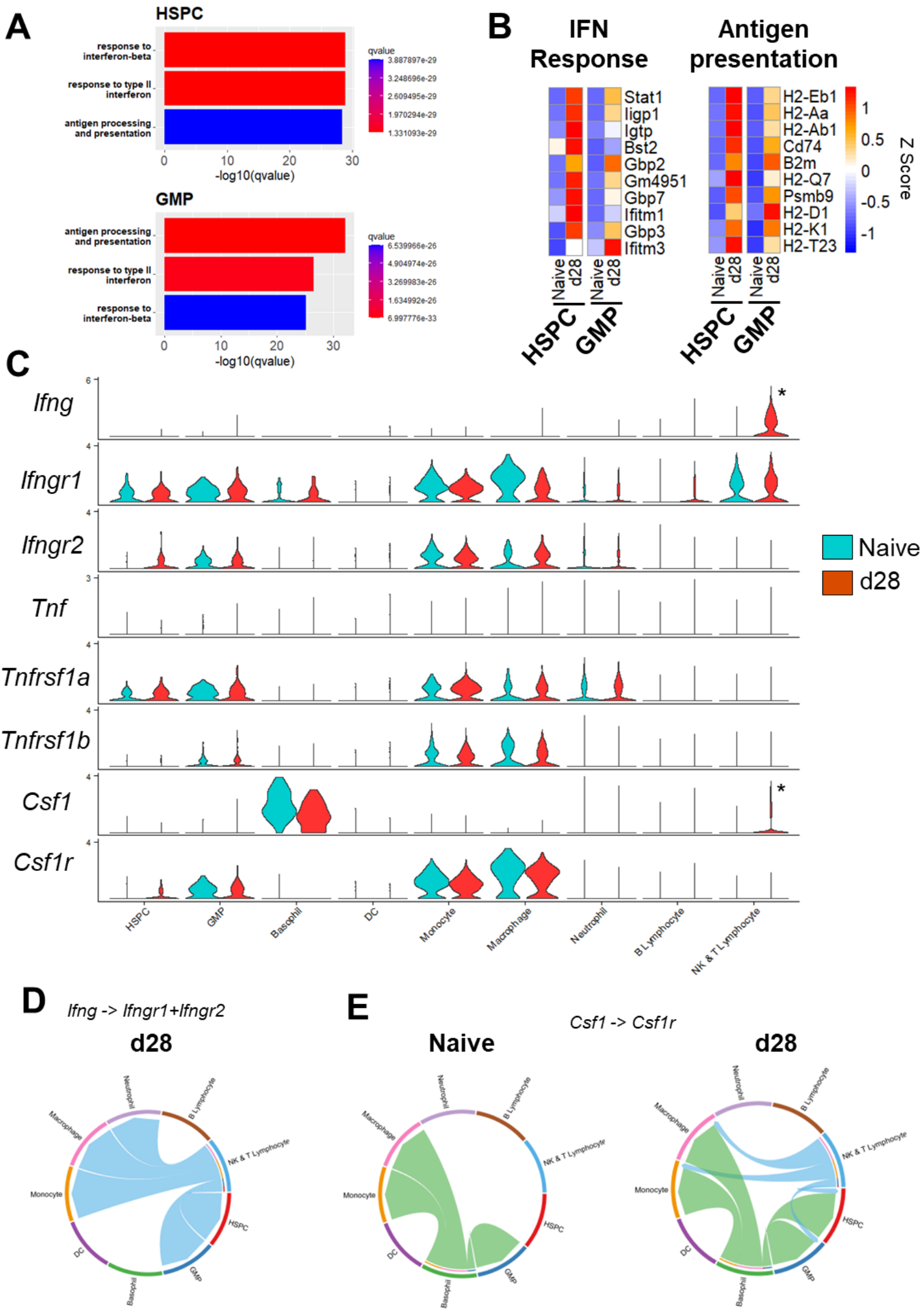
A
HSPC
response to interferon-beta
response to type II interferon
antigen processing and presentation
qvalue
3.887897e-29
3.248696e-29
2.609495e-29
1.970294e-29
1.331093e-29
0
10
20
30
-log10(qvalue)
GMP
antigen processing and presentation
response to type II interferon
response to interferon-beta
qvalue
6.539966e-26
4.904974e-26
3.269983e-26
1.634992e-26
6.997776e-33
0
10
20
30
-log10(qvalue)
B
IFN Response
Antigen presentation
Stat1
Iigp1
Igtp
Bst2
Gbp2
Gm4951
Gbp7
Ifitm1
Gbp3
Ifitm3
H2-Eb1
H2-Aa
H2-Ab1
Cd74
B2m
H2-Q7
Psmb9
H2-D1
H2-K1
H2-T23
Z Score
1
0.5
0
-0.5
-1
Naive
d28
HSPC
GMP
C
Ifng
Ifngr1
Ifngr2
Tnf
Tnfrsf1a
Tnfrsf1b
Csf1
Csf1r
Naive
d28
HSPC
GMP
Basophil
DC
Monocyte
Macrophage
Neutrophil
B Lymphocyte
NK & T Lymphocyte
D
Ifng -> Ifngr1+Ifngr2
d28
E
Csf1 -> Csf1r
Naive
d28

Figure 6.23. Progenitor cells respond to T cell derived *Ifng* and *Csf1* during *L. donovani* infection. **(A)** ORA of up-regulated genes in HSPCs and GMPs in WT d28 vs naïve WT mice was performed. Top three GO enriched GO terms are shown. **(B)** Heatmaps showing upregulation of IFN response genes (left) and antigen presentation-related genes (right) in HSPCs and GMPs during *L. donovani* infection. **(C)** Violin plots displaying expression of *Ifng, Tnf,* and *Csf1* related genes in naïve and d28 cell subsets. Data is derived from UMAPs in **Fig. 6.10.** **P*<0.05. **(D)** CellChat chord plot displaying inferred *Ifng-Ifngr1+Ifngr2* interactions between cell types in d28 WT BM. No interaction was inferred in naïve BM. **(E)** CellChat chord plots displaying inferred *Csf1-Csf1r* interactions between cell types in naïve and d28 WT BM.

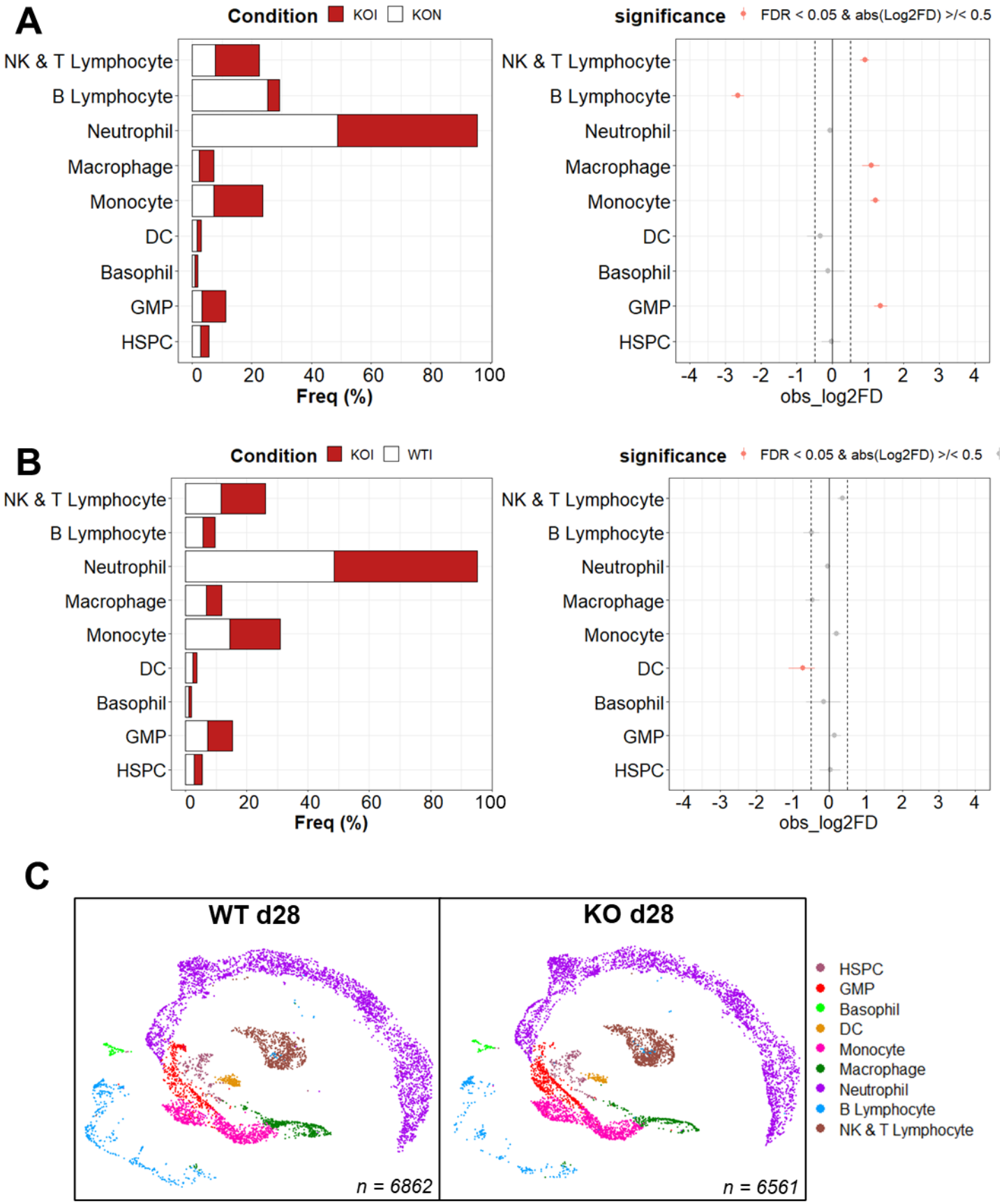

Figure 6.24. *L. donovani* infection of *Trim24* KO mice leads to similar proportional changes to WT mice. (A) Percentage proportions of KO d28 and KO naïve cell types (left) and accompanying permutation test plot (right). **(B)** Percentage proportions of KO d28 vs WT d28 BM cell types (left) and accompanying permutation test plot (right). For permutation plots, differences were considered significant when FDR<0.05 and obs_log2FD (log2 fold change) <-0.5 or >0.5. **(C)** UMAPs of WT d28 and KO d28 BM cell types.

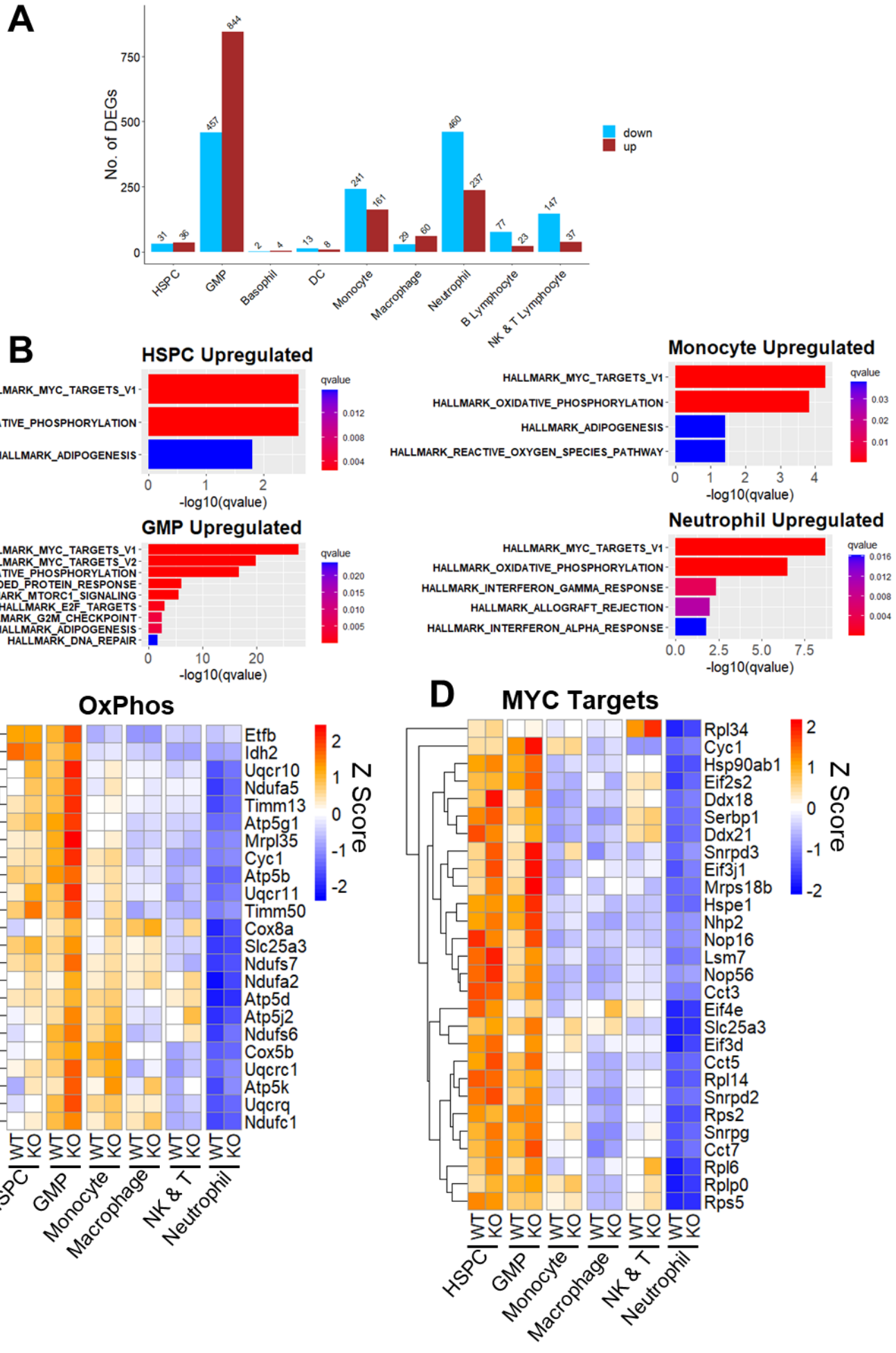
A
No. of DEGs
750
500
250
0
down
up
31
36
457
844
2
4
13
8
241
161
29
60
460
237
77
23
147
37
HSPC
GMP
Basophil
DC
Monocyte
Macrophage
Neutrophil
B Lymphocyte
NK & T Lymphocyte
B
HSPC Upregulated
HALLMARK_MYC_TARGETS_V1
HALLMARK_OXIDATIVE_PHOSPHORYLATION
HALLMARK_ADIPOGENESIS
qvalue
0.012
0.008
0.004
-log10(qvalue)
Monocyte Upregulated
HALLMARK_MYC_TARGETS_V1
HALLMARK_OXIDATIVE_PHOSPHORYLATION
HALLMARK_ADIPOGENESIS
HALLMARK_REACTIVE_OXYGEN_SPECIES_PATHWAY
qvalue
0.03
0.02
0.01
-log10(qvalue)
GMP Upregulated
HALLMARK_MYC_TARGETS_V1
HALLMARK_MYC_TARGETS_V2
HALLMARK_OXIDATIVE_PHOSPHORYLATION
HALLMARK_UNFOLDED_PROTEIN_RESPONSE
HALLMARK_MTORC1_SIGNALING
HALLMARK_E2F_TARGETS
HALLMARK_G2M_CHECKPOINT
HALLMARK_ADIPOGENESIS
HALLMARK_DNA_REPAIR
qvalue
0.020
0.015
0.010
0.005
-log10(qvalue)
Neutrophil Upregulated
HALLMARK_MYC_TARGETS_V1
HALLMARK_OXIDATIVE_PHOSPHORYLATION
HALLMARK_INTERFERON_GAMMA_RESPONSE
HALLMARK_ALLOGRAFT_REJECTION
HALLMARK_INTERFERON_ALPHA_RESPONSE
qvalue
0.016
0.012
0.008
0.004
-log10(qvalue)
C
OxPhos
Etfb
Idh2
Uqcr10
Ndufa5
Timm13
Atp5g1
Mrpl35
Cyc1
Atp5b
Uqcr11
Timm50
Cox8a
Slc25a3
Ndufs7
Ndufa2
Atp5d
Atp5j2
Ndufs6
Cox5b
Uqcrc1
Atp5k
Uqcrq
Ndufc1
Z Score
WT
KO
HSPC
GMP
Monocyte
Macrophage
NK & T
Neutrophil
D
MYC Targets
Rpl34
Cyc1
Hsp90ab1
Eif2s2
Ddx18
Serbp1
Ddx21
Snrpd3
Eif3j1
Mrps18b
Hspe1
Nhp2
Nop16
Lsm7
Nop56
Cct3
Eif4e
Slc25a3
Eif3d
Cct5
Rpl14
Snrpd2
Rps2
Snrpg
Cct7
Rpl6
Rplp0
Rps5
Z Score
WT
KO
HSPC
GMP
Monocyte
Macrophage
NK & T
Neutrophil

Figure 6.25. ORA of upregulated genes in KO vs WT leukocytes reveals metabolic skew towards OxPhos in early KO leukocytes during *L. donovani* infection. DGE analysis and ORA was performed on upregulated genes in KOI vs WTI cell subsets (FDR<0.05, log2FC>0). **(A)** Number of DEGs per cluster. **(B)** ORA of top enriched gene sets in upregulated DEGs in HSPCs, GMPs, monocytes, and neutrophils. **(C)** Heatmap showing average expression of Oxidative Phosphorylation-related genes. All genes shown were upregulated in the GMP cluster (FDR<0.05 log2FC>0). **(D)** Heatmap showing average expression of MYC target genes.

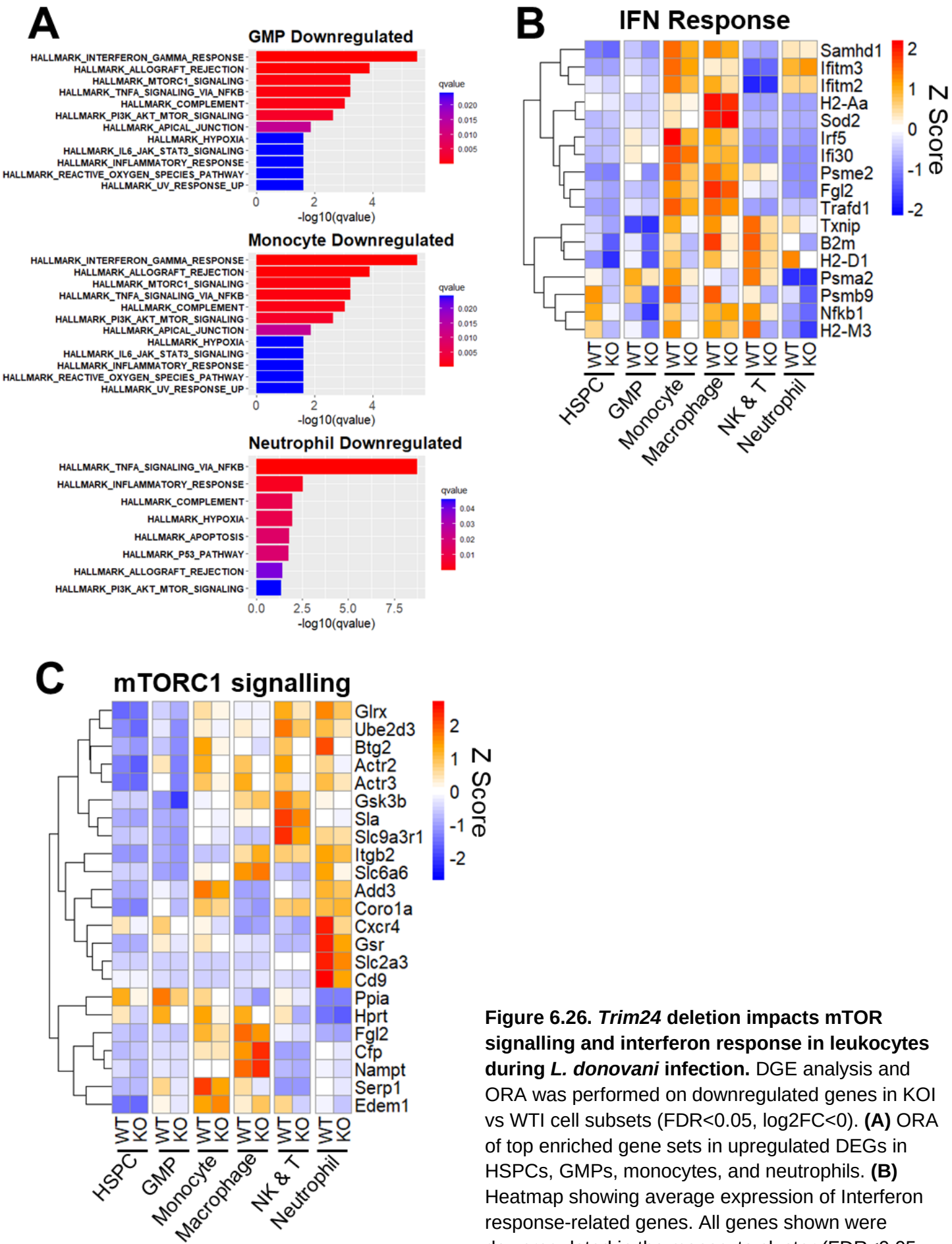

Figure 6.26. *Trim24* deletion impacts mTOR signalling and interferon response in leukocytes during *L. donovani* infection. DGE analysis and ORA was performed on downregulated genes in KOI vs WTI cell subsets (FDR<0.05, log2FC<0). **(A)** ORA of top enriched gene sets in upregulated DEGs in HSPCs, GMPs, monocytes, and neutrophils. **(B)** Heatmap showing average expression of Interferon response-related genes. All genes shown were downregulated in the monocyte cluster (FDR<0.05 log2FC<0). **(C)** Heatmap showing average expression of genes within the mTORC1 signalling gene set.

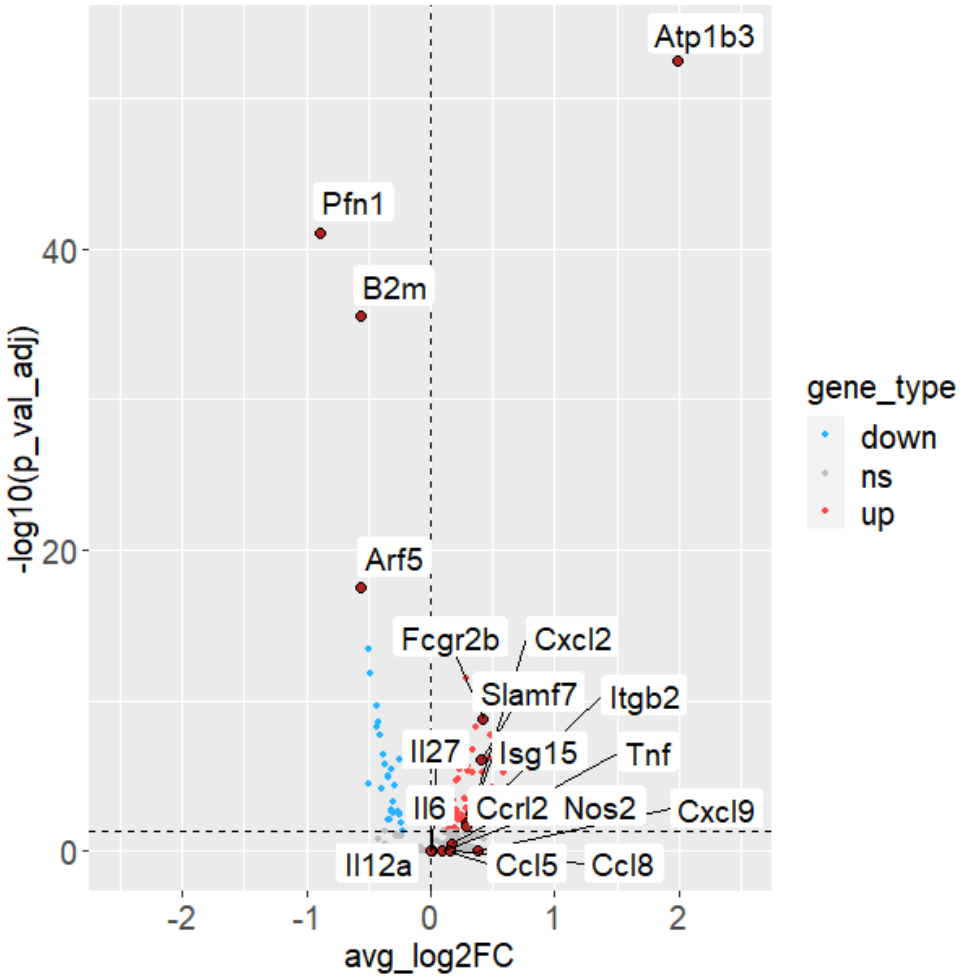

Figure 6.27. Differentially expressed genes in KO vs WT infected macrophages. DGE analysis was performed on the macrophage cluster from **Figure 6.3** between KO and WT infected samples. A log2FC threshold of 0 and an FDR threshold of 0 were used. Ns = not significant

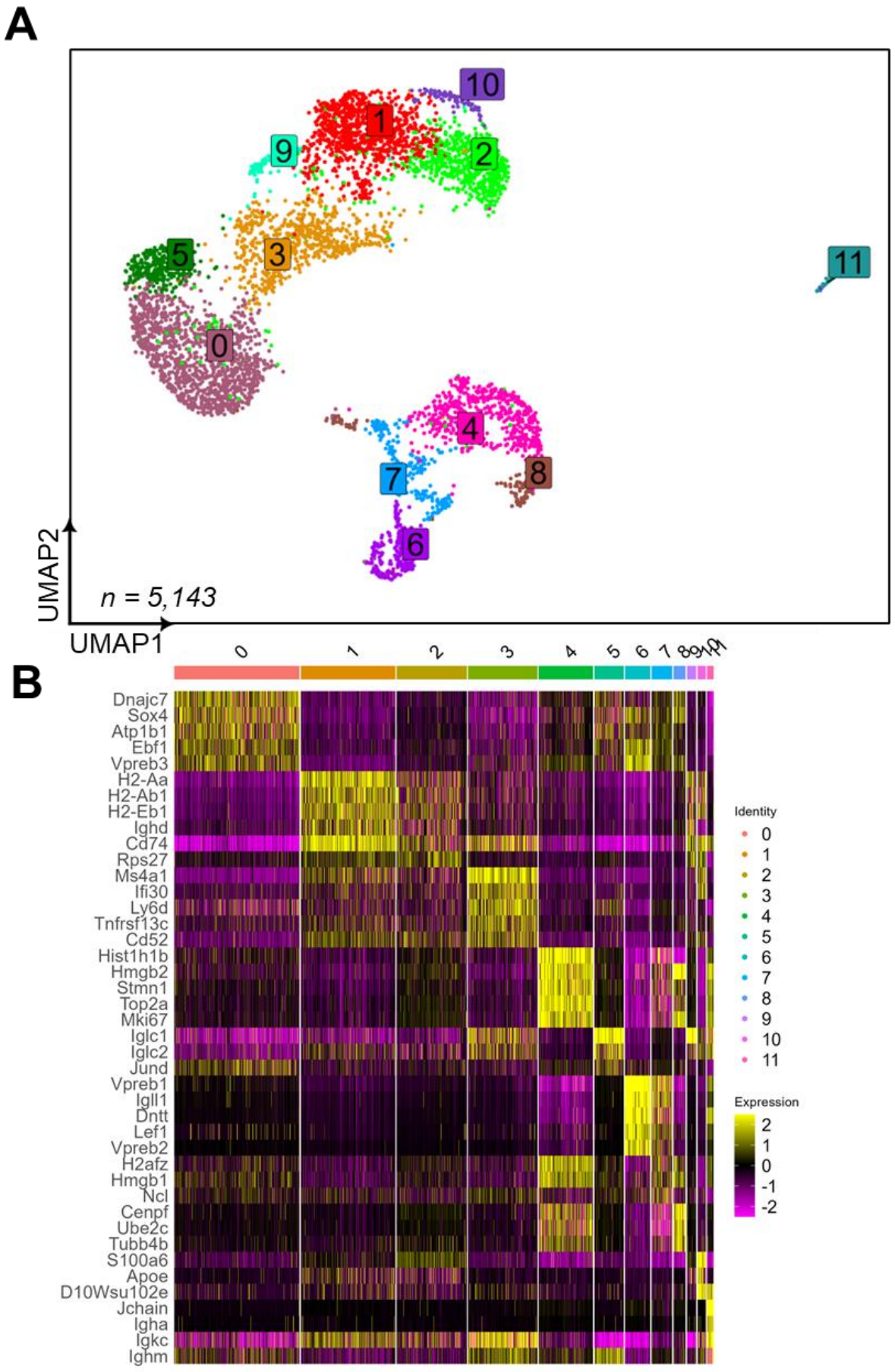

Supplementary Figure 6.1. B cell sub-cluster determination and top gene marker expression per cluster. **(A)** The B lymphocyte cluster was isolated from the UMAP in **Fig. 6.3.,** and sample were re-integrated, and dimensionality reduction, UMAP projection, and sub-clustering was performed at a resolution of 0.6. **(B)** Top expressed genes by log2FC for each cluster compared to all other clusters were determined, and top 5 genes per cluster are shown in a heatmap.

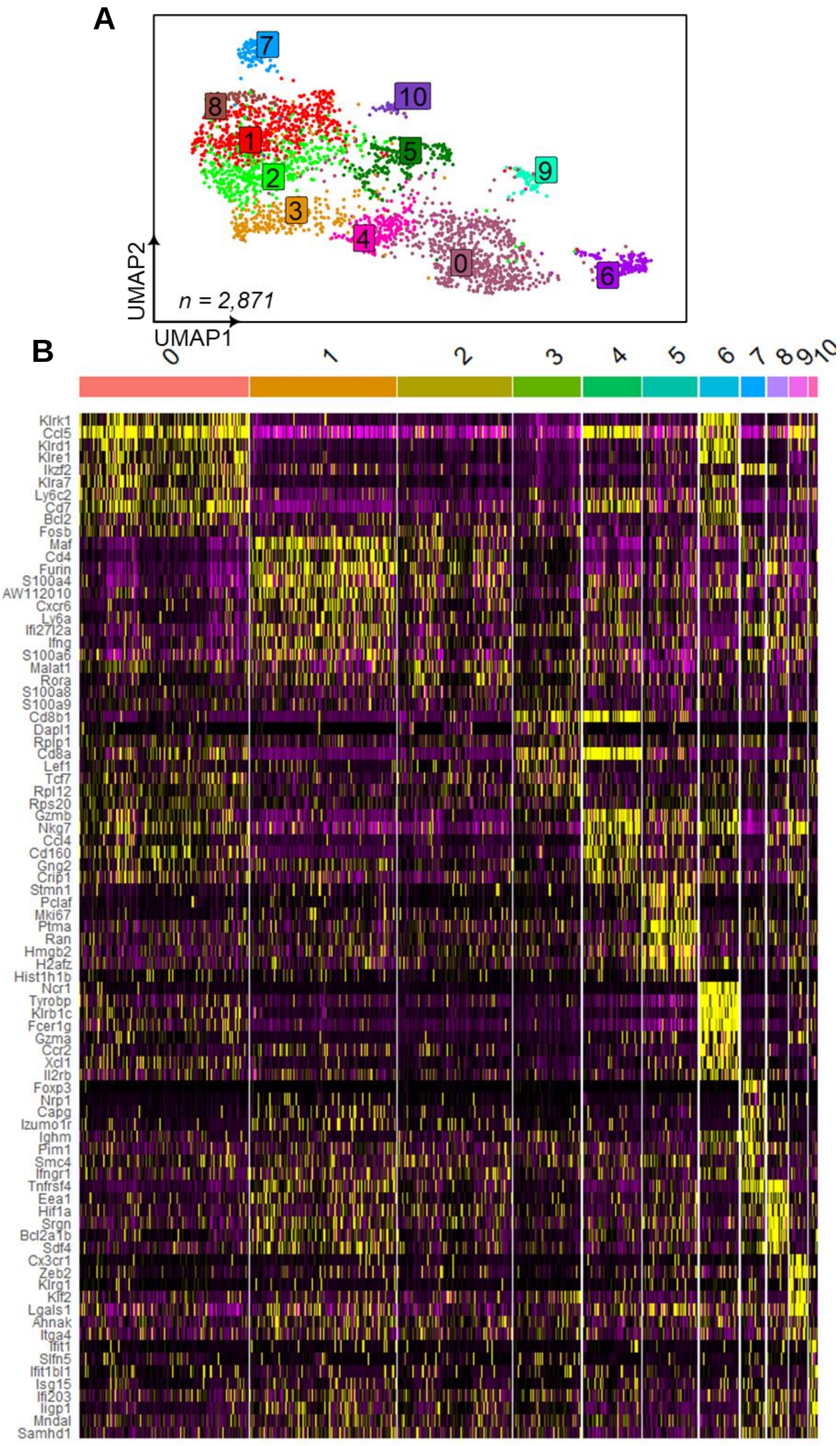
A
7
8
10
1
5
2
9
3
4
0
6
UMAP2
n = 2,871
UMAP1
B
0 1 2 3 4 5 6 7 8 9 10
Klrk1
Ccl5
Klrd1
Klre1
Ikzf2
Klra7
Ly6c2
Cd7
Bcl2
Fosb
Maf
Cd4
Furin
S100a4
AW112010
Cxcr6
Ly6a
Ifi27l2a
Ifng
S100a6
Malat1
Rora
S100a8
S100a9
Cd8b1
Dapl1
Rplp1
Cd8a
Lef1
Tcf7
Rpl12
Rps20
Gzmb
Nkg7
Ccl4
Cd160
Gng2
Crip1
Stmn1
Pclaf
Mki67
Ptma
Ran
Hmgb2
H2afz
Hist1h1b
Ncr1
Tyrobp
Klrb1c
Fcer1g
Gzma
Ccr2
Xcl1
Il2rb
Foxp3
Nrp1
Capg
Izumo1r
Ighm
Pim1
Smc4
Ifngr1
Tnfrsf4
Eea1
Hif1a
Srgn
Bcl2a1b
Sdf4
Cx3cr1
Zeb2
Klrg1
Klf2
Lgals1
Ahnak
Itga4
Ifit1
Slfn5
Ifit1bl1
Isg15
Ifi203
Iigp1
Mndal
Samhd1

Supplementary Figure 6.2. NK & T cell sub-cluster determination and top gene marker expression per cluster. **(A)** The NK & T lymphocyte cluster was isolated from the UMAP in **Fig. 6.3.,** and sample were re-integrated, and dimensionality reduction, UMAP projection, and sub-clustering was performed at a resolution of 0.6. **(B)** Top expressed genes by log2FC for each cluster compared to all other clusters were determined, and top 5 genes per cluster are shown in a heatmap (low expression = black, high expression = yellow).

Chapter 7. General Discussion

Until recently, the immune functions of TRIM24 have remained elusive. Several transcriptomic studies have identified TRIM24 as a predicted upstream negative regulator of a Th1-driven response in *L. donovani* infection both in an experimental murine model of visceral leishmaniasis (Ashwin et al. 2018), and in *in vitro* macrophage studies using amastigote and promastigote forms of *L. major* parasites (Chaparro et al. 2022; Venugopal et al. 2022). However, to date the roles of TRIM24 during VL have not been formally explored. In this study, we sought to elucidate the roles of TRIM24 during experimental VL using a combination of *in vitro* work investigating roles of TRIM24 in macrophage biology, and *in vivo* work using a *Trim24* knockout mouse model and a well established model of experimental VL caused by *L. donovani*. To our knowledge, this is the first instance in which TRIM24 has been formally studied in this infection setting. Additionally, to our knowledge this is the first study to use single cell RNA-seq to uncover the transcriptional landscape of the murine BM during *L. donovani* infection.

Given the importance of macrophage activation in the clearance of parasites during *L. donovani* infection, we first investigated roles of TRIM24 in macrophage activation phenotypes after TLR stimulation. It is known that deletion of *Trim24* in IL-4-stimulated BMDMs leads to an enhanced regulatory phenotype compared to WT via increased transcriptional activity of STAT6 and upregulation of *Arg1*, *Irf4, Mrc1,* and *Ym1* (Yu et al. 2019). LPS stimulation of *Trim24* KO macrophages revealed no change in release of IL-6, or mRNA abundance of *Tnf* or *Il1b* (Yu et al. 2019). In this study, we confirmed no change in release or mRNA abundance of TNF or IL-6 after LPS stimulation over a period of 24 hours. However, we extend this data to find that deletion of *Trim24* increases the expression of iNOS and subsequently the release of nitric oxide (NO) from BMDMs *in vitro* after LPS (and poly I:C) stimulation. Furthermore, we also observed an increase in the release of IFNβ post-TLR3/4 stimulation from KO BMDMs compared to WT. As IFNβ signalling has been shown to be important in the induction of iNOS expression and NO release (Jacobs & Ignarro 2001; Mattner et al. 2000; Bachmann et al. 2017; Vadiveloo et al. 2000), we hypothesise that this increase in iNOS expression by KO macrophages could be explained by the concurrent increased IFNβ release. This will need formal testing through the blocking of IFNβ signalling in KO macrophages after LPS stimulation. Importantly, a new study has demonstrated a mechanism for TRIM24 indirectly negatively regulating release of IL-10 via p300/CBP-mediated production of IFNβ (Hui et al. 2023). It is therefore possible that this mechanism could extend to iNOS expression, and this should be tested. An alternate mechanism by which TRIM24 could be increasing IFNβ release is through mediation of the TRIF-dependent

pathway, which signals through IRF3 and IRF7 to induce a strong type 1 interferon response. Our identification of *Irf7* upregulation in steady state KO BMDMs compared to WT could therefore suggest a mechanism by which TRIM24 acts as a negative regulator or IRF7 expression, thereby limiting IFNβ production. This would need formal testing through inhibition of IRF7 activity in KO and WT BMDMs to assess IFNβ release. Another interesting hypothesis is the post-translational modification of IRF7 via TRIM24 to regulate its activity. Ubiquitination has been reported to be important for both degradation of IRF7 (Yu et al. 2005) and activation of IRF7 (Ning et al. 2008). Therefore, TRIM24 could be regulating IRF7 activation via its E3 ligase RING domain. Expression of a RING-deficient mutant TRIM24 in macrophages followed by assessment of IRF7 ubiquitination status after TLR4 stimulation would therefore be an interesting experiment.

Interestingly, our *in vivo* characterisation of KO mice in the context of *L. donovani* infection revealed no difference in the induction iNOS from macrophages in hepatic granulomas or in BM macrophages and monocytes at d28/d29. Furthermore, in contrast with our prediction that *Trim24* deletion would enhance anti-parasite mechanisms through upregulation of pro-inflammatory mediators, we saw the opposite effect of *Trim24* deletion on hepatic (but not splenic) parasite burden at d29, and no change in hepatic or splenic parasite burden in KO mice at d7, d14, d21, d35, or d46. The increased parasite burden at d29 in the liver appeared to be independent of iNOS expression.

Our transcriptomics data suggests that deletion of *Trim24* exacerbates that metabolic shift towards oxidative phosphorylation observed in *L. donovani*-infected macrophages that is characteristic of an immunoregulatory “M2” macrophage phenotype (Jha et al. 2015). In contrast, inflammatory macrophage phenotypes are associated with increased glycolytic enzyme activity and reduced oxidative phosphorylation (Rodríguez-Prados et al. 2010; Krawczyk et al. 2010).

Our data also indicates that TRIM24 exerts its effects through regulation of the mTOR signalling pathway. mTOR signalling is an important but somewhat complex regulator of glucose metabolism in macrophages, shown to be a regulator of both M1 and M2 macrophage polarisation (Collins et al. 2021; Byles et al. 2013). Deletion of *Tsc1* (which causes constitutive activation of mTOR (Huang & Manning 2009)), has been shown to significantly impair induction of an immunoregulatory phenotype in B6 BMDMs stimulated with IL-4 through increased inhibition of Akt phosphorylation (Byles et al. 2013). Meanwhile, genetic deletion of mTOR or Raptor in a B6 mouse model of sepsis led to increased serum levels of TNF and IL-6 compared to WT controls (Collins et al. 2021). Therefore, this hypothesis that TRIM24 is an indirect regulator of glucose metabolism via mTOR signalling in macrophages would need to be formally tested.

To our knowledge, this study also represents the first report outlining the transcriptional landscape of the BM in d28 *L. donovani*-infected B6 mice. Our data is consistent with previously published literature in our observation of effector T cell and myeloid cell expansion, and increased myelopoiesis (Abidin et al. 2017; Pinto et al. 2017). Critically, we have uncovered several transcriptional phenotypes that are known to contribute to myelopoiesis. Haematopoietic stem and progenitor cells were directly responding to T cell-derived IFNγ. IFNγ signalling is known to drive HSCs into cell cycle (MacNamara et al. 2011; Baldridge et al. 2010), however more recent literature suggests that while T cell-derived IFNγ is critical for loss of LT-HSC quiescence, this effect is independent of intrinsic IFNγ signalling (Pinto et al. 2017). We have also shown that effector $CD4^+$ T cells become a major source of M-CSF in the BM during *L. donovani* infection, a critical growth factor for monocyte and macrophage differentiation (Stanley et al. 1978; Dai et al. 2002), that may play an important role in emergency myelopoiesis. Other sources of M-CSF in the BM such as stromal cells must be taken into account as well (Emoto et al. 2022), as these were not detectable in our dataset. Furthermore, we saw increases in *Ccl5* expression in macrophages, $CD4^+$ and $CD8^+$ T cells, and in HSPCs. CCL5 signalling through CCR5 preferentially enhances myelopoiesis in B6 and BALB/c mice (Ergen et al. 2012; Zilio et al. 2022; Shi et al. 2022).

Finally, *L. donovani* induced expression of mitochondrial genes in HSPCs that are indicative of enhanced OxPhos. This was also detected in *in vitro*-infected BMDMs, exacerbated by loss of TRIM24. Skewing towards OxPhos is an important cellular change that is characteristic of actively dividing HSCs (Simsek et al. 2010; Takubo et al. 2013; Suda et al. 2011). Given previous literature implicating HSCs as a parasite niche in the BM and the parasite-mediated induction of OxPhos (Karagiannis et al. 2022; Dirkx et al. 2022; Ty et al. 2019), it is reasonable to hypothesise that this also contributes to the loss of quiescence and induction of emergency myelopoiesis during *L. donovani* infection. Together, the transcriptional landscape of *L. donovani* infected BM represents an environment that favours the development of myeloid cells and is permissive to parasite survival.

One of the major limitations of this study was in the generation of TRIM24 KO mice. Due to the spontaneous development of HCC previously shown in KO mice that begins to present from ~14 weeks of age, we limited the age of KO mice used in our experiments to 14 weeks. Therefore, our ability to breed homozygous KO mice together for the generation of total KO mice was impacted. Instead, we bred heterozygous *Trim24*$^{dlE1/+}$ mice together to generate total KO mice. Following Mendelian genetics, this resulted in ~25% KO mice per litter (though this did have the advantage of producing WT littermate control mice). Thus, it was

incredibly challenging to produce sufficient age- and sex-matched mice for our planned studies. As we mainly observed differences in myeloid cell populations during *L. donovani* infection, generating a myeloid-specific *Trim24* knockout mouse model by crossing *LysM*-Cre mice with *Trim24* floxed mice would be a useful tool. These mice have been generated recently by Yu et al. to study TRIM24 in tumour-associated macrophage activation, who found no effect of myeloid-specific *Trim24* deletion on the number of leukocytes in BM, spleen, peripheral lymph nodes, and thymus (Yu et al. 2019). We hypothesise that myeloid-specific deletion of *Trim24* will protect mice from spontaneous HCC formation seen in total KO mice (Jiang et al. 2015), and will therefore allow for investigation of myeloid-specific *Trim24* deletion during the chronic phase of *L. donovani* infection.

Together, the data in this thesis extends much of the known roles of TRIM24 and attempts to validate these roles during *L. donovani* infection, a neglected tropical disease in need of novel therapeutic strategies. Though much of the data yielded negative results, our transcriptomic analyses of *L. donovani*-infected WT BMDMs and *L. donovani*-infected B6 mouse BM revealed potential roles for TRIM24 in the regulation of the cellular metabolic state during infection that may result in a more permissive environment for *Leishmania* parasites. Furthermore, we hope our analysis of the transcriptomic landscape of WT *L. donovani*-infected BM in B6 mice will assist in future studies in better understanding VL disease progression and lead to the development of novel therapies.

References

Abadías-Granado, I. et al., 2021. Cutaneous and Mucocutaneous Leishmaniasis. *Actas Dermo-Sifiliograficas*. Available at: http://dx.doi.org/10.1016/j.adengl.2021.05.011.

Abebe, T. et al., 2013. Arginase activity - a marker of disease status in patients with visceral leishmaniasis in ethiopia. *PLoS Neglected Tropical Diseases*, 7(3), p.e2134.

Abidin, B.M. et al., 2017. Infection-adapted emergency hematopoiesis promotes visceral leishmaniasis. *PLoS Pathogens*, 13(8), p.e1006422.

Abraham, N.G. & Drummond, G., 2006. CD163-Mediated hemoglobin-heme uptake activates macrophage HO-1, providing an antiinflammatory function. *Circulation Research*, 99(9), pp.911–914.

Ahlmann-Eltze, C. & Huber, W., 2021. glmGamPoi: fitting Gamma-Poisson generalized linear models on single cell count data. *Bioinformatics* , 36(24), pp.5701–5702.

Ai, W. et al., 2013. Optimal method to stimulate cytokine production and its use in immunotoxicity assessment. *International Journal of Environmental Research and Public Health*, 10(9), pp.3834–3842.

Akaberi, D. et al., 2020. Mitigation of the replication of SARS-CoV-2 by nitric oxide in vitro. *Redox Biology*, 37, p.101734.

Akhoundi, M. et al., 2016. A Historical Overview of the Classification, Evolution, and Dispersion of Leishmania Parasites and Sandflies. *PLoS Neglected Tropical Diseases*, 10(3), p.e0004349.

Alam, M.S. et al., 2002. Role of nitric oxide in host defense in murine salmonellosis as a function of its antibacterial and antiapoptotic activities. *Infection and Immunity*, 70(6), pp.3130–3142.

Ali, H. et al., 2019. Cellular TRIM33 restrains HIV-1 infection by targeting viral integrase for proteasomal degradation. *Nature Communications*, 10(1), p.926.

Alkam, D. et al., 2017. Profilin1 biology and its mutation, actin(g) in disease. *Cellular and Molecular Life Sciences: CMLS*, 74(6), pp.967–981.

Alliot, F., Godin, I. & Pessac, B., 1999. Microglia derive from progenitors, originating from the yolk sac, and which proliferate in the brain. *Brain research. Developmental Brain Research*, 117(2), pp.145–152.

Allton, K. et al., 2009. Trim24 targets endogenous p53 for degradation. *Proceedings of the National Academy of Sciences of the United States of America*, 106(28), pp.11612–11616.

Anderson, C.F., Gerber, J.S. & Mosser, D.M., 2002. Modulating macrophage function with IgG immune complexes. *Journal Of Endotoxin Research*, 8(6), pp.477–481.

Anderson, K. et al., 2022. STAT1 is regulated by TRIM24 and promotes immunosuppression in head and neck squamous carcinoma cells, but enhances T cell antitumour immunity in the tumour microenvironment. *British Journal of Cancer*, 127(4), pp.624–636.

An, N. et al., 2013. Pim1 serine/threonine kinase regulates the number and functions of murine hematopoietic stem cells. *Stem Cells*, 31(6), pp.1202–1212.

Ansari, N.A. et al., 2011. IL-27 and IL-21 are associated with T cell IL-10 responses in human visceral leishmaniasis. *Journal of Immunology* , 186(7), pp.3977–3985.

Aoki, K. et al., 2013. LARP1 specifically recognizes the 3' terminus of poly(A) mRNA. *FEBS Letters*, 587(14), pp.2173–2178.

Arinobu, Y. et al., 2007. Reciprocal activation of GATA-1 and PU.1 marks initial specification of hematopoietic stem cells into myeloerythroid and myelolymphoid lineages. *Cell Stem Cell*, 1(4), pp.416–427.

Asai, A. et al., 2012. CCL1 released from M2b macrophages is essentially required for the maintenance of their properties. *Journal of Leukocyte Biology*, 92(4), pp.859–867.

Ashwin, H. et al., 2018. Tissue and host species-specific transcriptional changes in models of experimental visceral leishmaniasis. *Wellcome Open Research*, 3, p.135.

Aslan, H. et al., 2013. A new model of progressive visceral leishmaniasis in hamsters by natural transmission via bites of vector sand flies. *The Journal of Infectious Diseases*, 207(8), pp.1328–1338.

Auletta, J.J. et al., 2004. Distinct phases in recovery of reconstituted innate cellular-mediated immunity after murine syngeneic bone marrow transplantation. *Biology of blood and marrow transplantation: journal of the American Society for Blood and Marrow Transplantation*, 10(12), pp.834–847.

Bachmann, M. et al., 2017. Type I Interferon Supports Inducible Nitric Oxide Synthase in Murine Hepatoma Cells and Hepatocytes and during Experimental Acetaminophen-Induced Liver Damage. *Frontiers in Immunology*, 8, p.890.

Bain, C.C. et al., 2014. Constant replenishment from circulating monocytes maintains the macrophage pool in the intestine of adult mice. *Nature Immunology*, 15(10), pp.929–937.

Balaraman, S. et al., 2004. Leishmania donovani induces interferon regulatory factor in murine macrophages: a host defense response. *Biochemical and Biophysical Research communications*, 317(2), pp.639–647.

Baldridge, M.T. et al., 2010. Quiescent haematopoietic stem cells are activated by IFN-gamma in response to chronic infection. *Nature*, 465(7299), pp.793–797.

Bamidele, A.O. et al., 2015. IQGAP1 promotes CXCR4 chemokine receptor function and trafficking via EEA-1+ endosomes. *The Journal of Cell Biology*, 210(2), pp.257–272.

Bankoti, R. & Stäger, S., 2012. Differential Regulation of the Immune Response in the Spleen and Liver of Mice Infected with Leishmania donovani. *Journal of Tropical Medicine*, 2012, p.639304.

Bao, Y. et al., 2017. Brd4 modulates the innate immune response through Mnk2-eIF4E pathway-dependent translational control of IκBα. *Proceedings of the National Academy of Sciences of the United States of America*, 114(20), pp.E3993–E4001.

Barnes, B.J. et al., 2020. Novel role(s) for Irf5 in controlling myelopoiesis and erythropoiesis. *Journal of Immunology* , 204(1_Supplement), pp.63.1–63.1.

Basu, S., Ray, A. & Dittel, B.N., 2013. Differential representation of B cell subsets in mixed bone marrow chimera mice due to expression of allelic variants of CD45 (CD45.1/CD45.2). *Journal of Immunological Methods*, 396(1-2), pp.163–167.

Bates, P.A., 2007. Transmission of Leishmania metacyclic promastigotes by phlebotomine sand flies. *International Journal for Parasitology*, 37(10), pp.1097–1106.

Beattie, L. et al., 2010. Dynamic imaging of experimental Leishmania donovani-induced hepatic granulomas detects Kupffer cell-restricted antigen presentation to antigen-specific CD8 T cells. *PLoS Pathogens*, 6(3), p.e1000805.

Beattie, L. et al., 2011. Interferon regulatory factor 7 contributes to the control of Leishmania donovani in the mouse liver. *Infection and Immunity*, 79(3), pp.1057–1066.

Beg, A.A. et al., 1992. I kappa B interacts with the nuclear localization sequences of the subunits of NF-kappa B: a mechanism for cytoplasmic retention. *Genes & Development*, 6(10), pp.1899–1913.

Behre, G. et al., 1999. c-Jun is a JNK-independent coactivator of the PU.1 transcription factor. *The Journal of Biological Chemistry*, 274(8), pp.4939–4946.

Bertrand, J.Y. et al., 2005. Three pathways to mature macrophages in the early mouse yolk sac. *Blood*, 106(9), pp.3004–3011.

Bhattacharyya, S. et al., 2008. A novel approach to regulate experimental visceral leishmaniasis in murine macrophages using CCR5 siRNA. *Scandinavian Journal of Immunology*, 67(4), pp.345–353.

Bichiou, H. et al., 2021. Transcription Factors Interplay Orchestrates the Immune-Metabolic Response of Leishmania Infected Macrophages. *Frontiers in Cellular and Infection Microbiology*, 11, p.660415.

Blackwell, J.M. et al., 1985. Macrophage complement and lectin-like receptors bind Leishmania in the absence of serum. *The Journal of Experimental Medicine*, 162(1), pp.324–331.

Bogdan, C., 2020. Macrophages as host, effector and immunoregulatory cells in leishmaniasis: Impact of tissue micro-environment and metabolism. *Cytokine: X*, 2(4), p.100041.

Boltz-Nitulescu, G. et al., 1987. Differentiation of rat bone marrow cells into macrophages under the influence of mouse L929 cell supernatant. *Journal of Leukocyte Biology*, 41(1), pp.83–91.

Borges da Silva, H. et al., 2015. Splenic Macrophage Subsets and Their Function during Blood-Borne Infections. *Frontiers in Immunology*, 6, p.480.

Bories, G.F.P. et al., 2020. Macrophage metabolic adaptation to heme detoxification involves CO-dependent activation of the pentose phosphate pathway. *Blood*, 136(13), pp.1535–1548.

Bowlin, A. et al., 2021. Hypoxia-Inducible Factor Signaling in Macrophages Promotes Lymphangiogenesis in Leishmania major Infection. *Infection and Immunity*, 89(8), p.e0012421.

Branchini, B.R. et al., 2010. Red-emitting luciferases for bioluminescence reporter and imaging applications. *Analytical Biochemistry*, 396(2), pp.290–297.

de Brito Monteiro, L. et al., 2020. M-CSF- and L929-derived macrophages present distinct metabolic profiles with similar inflammatory outcomes. *Immunobiology*, 225(3), p.151935.

Brittingham, A. et al., 1999. Interaction of Leishmania gp63 with cellular receptors for fibronectin. *Infection and Immunity*, 67(9), pp.4477–4484.

Buates, S. & Matlashewski, G., 2001. General suppression of macrophage gene expression during Leishmania donovani infection. *Journal of Immunology* , 166(5), pp.3416–3422.

Buechler, M.B. et al., 2013. Cutting edge: Type I IFN drives emergency myelopoiesis and peripheral myeloid expansion during chronic TLR7 signaling. *Journal of Immunology* , 190(3), pp.886–891.

Buller, C.L. et al., 2008. A GSK-3/TSC2/mTOR pathway regulates glucose uptake and GLUT1 glucose transporter expression. *American Journal of Physiology. Cell Physiology*, 295(3), pp.C836–43.

Buscher, K. et al., 2017. Natural variation of macrophage activation as disease-relevant phenotype predictive of inflammation and cancer survival. *Nature Communications*, 8, p.16041.

Butler, A. et al., 2018. Integrating single-cell transcriptomic data across different conditions, technologies, and species. *Nature Biotechnology*, 36(5), pp.411–420.

Byles, V. et al., 2013. The TSC-mTOR pathway regulates macrophage polarization. *Nature Communications*, 4, p.2834.

Cabeza-Cabrerizo, M. et al., 2021. Dendritic Cells Revisited. *Annual Review of Immunology*, 39(1), pp.131–166.

Cachaço, A.S. et al., 2010. TNF-alpha regulates the effects of irradiation in the mouse bone marrow microenvironment. *PloS One*, 5(2), p.e8980.

Cai, W. et al., 2019. STAT6/Arg1 promotes microglia/macrophage efferocytosis and inflammation resolution in stroke mice. *JCI Insight*, 4(20). Available at: http://dx.doi.org/10.1172/jci.insight.131355.

Cammas, F. et al., 2000. Mice lacking the transcriptional corepressor TIF1beta are defective in early postimplantation development. *Development* , 127(13), pp.2955–2963.

Campbell, E.M. et al., 2016. TRIM5α-Mediated Ubiquitin Chain Conjugation Is Required for Inhibition of HIV-1 Reverse Transcription and Capsid Destabilization. *Journal of Virology*, 90(4), pp.1849–1857.

Cao, Z. et al., 1996. TRAF6 is a signal transducer for interleukin-1. *Nature*, 383(6599), pp.443–446.

Carminho-Rodrigues, M.T. et al., 2020. LARS2-Perrault syndrome: a new case report and literature review. *BMC Medical Genetics*, 21(1), p.109.

Carneiro, P.P. et al., 2016. The Role of Nitric Oxide and Reactive Oxygen Species in the Killing of Leishmania braziliensis by Monocytes from Patients with Cutaneous Leishmaniasis. *PloS One*, 11(2), p.e0148084.

Carotta, S. et al., 2010. The transcription factor PU.1 controls dendritic cell development and Flt3 cytokine receptor expression in a dose-dependent manner. *Immunity*, 32(5), pp.628–641.

Carthagena, L. et al., 2009. Human TRIM gene expression in response to interferons. *PloS One*, 4(3), p.e4894.

Cartwright, G.E., Chung, H.-L. & Chang, A., 1948. STUDIES ON THE PANCYTOPENIA OF K ALA-AZAR. *Blood*, 3(3), pp.249–275.

Celada, A. et al., 1996. The transcription factor PU.1 is involved in macrophage proliferation. *The Journal of Experimental Medicine*, 184(1), pp.61–69.

Chakravarty, J. & Sundar, S., 2019. Current and emerging medications for the treatment of leishmaniasis. *Expert Opinion on Pharmacotherapy*, 20(10), pp.1251–1265.

Chang, Y.-C. et al., 2014. Role of macrophage sialoadhesin in host defense against the sialylated pathogen group B Streptococcus. *Journal of Molecular Medicine* , 92(9), pp.951–959.

Chaparro, V. et al., 2022. Transcriptional profiling of macrophages reveals distinct parasite stage-driven signatures during early infection by Leishmania donovani. *Scientific Reports*, 12(1), p.6369.

Chaparro, V. et al., 2020. Translational profiling of macrophages infected with Leishmania donovani identifies mTOR- and eIF4A-sensitive immune-related transcripts. *PLoS Pathogens*, 16(6), p.e1008291.

Chappuis, F. et al., 2007. Visceral leishmaniasis: what are the needs for diagnosis, treatment and control? *Nature Reviews. Microbiology*, 5(11), pp.873–882.

Chaussabel, D. et al., 2003. Unique gene expression profiles of human macrophages and dendritic cells to phylogenetically distinct parasites. *Blood*, 102(2), pp.672–681.

Cheekatla, S.S., Aggarwal, A. & Naik, S., 2012. mTOR signaling pathway regulates the IL-12/IL-10 axis in Leishmania donovani infection. *Medical Microbiology and Immunology*, 201(1), pp.37–46.

Chen, J. et al., 2019. TRIM66 reads unmodified H3R2K4 and H3K56ac to respond to DNA damage in embryonic stem cells. *Nature Communications*, 10(1), pp.1–17.

Choudhury, N.R. et al., 2017. RNA-binding activity of TRIM25 is mediated by its PRY/SPRY domain and is required for ubiquitination. *BMC Biology*, 15(1), p.105.

Chrétien, M.-L. et al., 2016. Trim33/Tif1γ is involved in late stages of granulomonopoiesis in mice. *Experimental Hematology*, 44(8), pp.727–739.e6.

Claborn, D.M., 2010. The biology and control of leishmaniasis vectors. *Journal of Global Infectious Diseases*, 2(2), pp.127–134.

Cockman, E., Anderson, P. & Ivanov, P., 2020. TOP mRNPs: Molecular Mechanisms and Principles of Regulation. *Biomolecules*, 10(7). Available at: http://dx.doi.org/10.3390/biom10070969.

Codarri, L. et al., 2011. RORγt drives production of the cytokine GM-CSF in helper T cells, which is essential for the effector phase of autoimmune neuroinflammation. *Nature Immunology*, 12(6), pp.560–567.

Collins, S.L. et al., 2021. mTORC1 Signaling Regulates Proinflammatory Macrophage Function and Metabolism. *Journal of Immunology* , 207(3), pp.913–922.

Coskun, S. et al., 2014. Development of the fetal bone marrow niche and regulation of HSC quiescence and homing ability by emerging osteolineage cells. Cell Rep. 2014; 9 (2) …. *Epub 2014/10/15. doi: 10.1016/j*.

Cotterell, S.E., Engwerda, C.R. & Kaye, P.M., 2000a. Enhanced hematopoietic activity accompanies parasite expansion in the spleen and bone marrow of mice infected with Leishmania donovani. *Infection and Immunity*, 68(4), pp.1840–1848.

Cotterell, S.E., Engwerda, C.R. & Kaye, P.M., 1999. Leishmania donovani infection initiates T cell-independent chemokine responses, which are subsequently amplified in a T cell-dependent manner. *European Journal of Immunology*, 29(1), pp.203–214.

Cotterell, S.E., Engwerda, C.R. & Kaye, P.M., 2000b. Leishmania donovani infection of bone marrow stromal macrophages selectively enhances myelopoiesis, by a mechanism involving GM-CSF and TNF-alpha. *Blood*, 95(5), pp.1642–1651.

Courtine, E. et al., 2012. Combined loss of cRel/p50 subunits of NF-κB leads to impaired innate host response in sepsis. *Innate Immunity*, 18(5), pp.753–763.

Cramer, T. et al., 2003. HIF-1alpha is essential for myeloid cell-mediated inflammation. *Cell*, 112(5), pp.645–657.

Cucak, H., Grunnet, L.G. & Rosendahl, A., 2014. Accumulation of M1-like macrophages in type 2 diabetic islets is followed by a systemic shift in macrophage polarization. *Journal of Leukocyte Biology*, 95(1), pp.149–160.

Curotto de Lafaille, M.A. & Wirth, D.F., 1992. Creation of Null/+ mutants of the alpha-tubulin gene in Leishmania enriettii by gene cluster deletion. *The Journal of Biological Chemistry*, 267(33), pp.23839–23846.

Czimmerer, Z. et al., 2018. The Transcription Factor STAT6 Mediates Direct Repression of Inflammatory Enhancers and Limits Activation of Alternatively Polarized Macrophages. *Immunity*, 48(1), pp.75–90.e6.

Dai, X.-M. et al., 2002. Targeted disruption of the mouse colony-stimulating factor 1 receptor gene results in osteopetrosis, mononuclear phagocyte deficiency, increased primitive progenitor cell frequencies, and reproductive defects. *Blood*, 99(1), pp.111–120.

Dasgupta, B. et al., 2003. Infection of human mononuclear phagocytes and macrophage-like THP1 cells with Leishmania donovani results in modulation of expression of a subset of chemokines and a chemokine receptor. *Scandinavian Journal of Immunology*, 57(4), pp.366–374.

Date, D. et al., 2014. Kruppel-like transcription factor 6 regulates inflammatory macrophage polarization. *The Journal of Biological Chemistry*, 289(15), pp.10318–10329.

Dayakar, A. et al., 2019. Cytokines: Key Determinants of Resistance or Disease Progression in Visceral Leishmaniasis: Opportunities for Novel Diagnostics and Immunotherapy. *Frontiers in Immunology*, 10, p.670.

DeKoter, R.P. & Singh, H., 2000. Regulation of B lymphocyte and macrophage development by graded expression of PU.1. *Science*, 288(5470), pp.1439–1441.

De La Cruz-Herrera, C.F. et al., 2023. Changes in SUMO-modified proteins in Epstein-Barr virus infection identifies reciprocal regulation of TRIM24/28/33 complexes and the lytic switch BZLF1. *PLoS Pathogens*, 19(7), p.e1011477.

Deng, W. et al., 2017. Essential Role of mTORC1 in Self-Renewal of Murine Alveolar Macrophages. *Journal of Immunology* , 198(1), pp.492–504.

Desterke, C., Bennaceur-Griscelli, A. & Turhan, A.G., 2021. EGR1 dysregulation defines an inflammatory and leukemic program in cell trajectory of human-aged hematopoietic stem cells (HSC). *Stem Cell Research & Therapy*, 12(1), p.419.

Dias, B.T. et al., 2019. Neutrophil elastase promotes Leishmania donovani infection via interferon-β. *FASEB journal: official publication of the Federation of American Societies for Experimental Biology*, 33(10), pp.10794–10807.

Dias, B.T. et al., 2022. Toll-Like Receptor- and Protein Kinase R-Induced Type I Interferon Sustains Infection of Leishmania donovani in Macrophages. *Frontiers in Immunology*, 13, p.801182.

Diaz-Griffero, F. et al., 2008. A human TRIM5alpha B30.2/SPRY domain mutant gains the ability to restrict and prematurely uncoat B-tropic murine leukemia virus. *Virology*, 378(2), pp.233–242.

Dillon, L.A.L. et al., 2015. Simultaneous transcriptional profiling of Leishmania major and its murine macrophage host cell reveals insights into host-pathogen interactions. *BMC Genomics*, 16, p.1108.

Dirkx, L. et al., 2022. Long-term hematopoietic stem cells as a parasite niche during treatment failure in visceral leishmaniasis. *Communications Biology*, 5(1), p.626.

Doyle, A.G. et al., 1994. Interleukin-13 alters the activation state of murine macrophages in vitro: comparison with interleukin-4 and interferon-gamma. *European Journal of Immunology*, 24(6), pp.1441–1445.

Duan, L. et al., 2021. Arrayed CRISPR reveals genetic regulators of tau aggregation, autophagy and mitochondria in Alzheimer's disease model. *Scientific Reports*, 11(1), p.2879.

Duan, Z. & Luo, Y., 2021. Targeting macrophages in cancer immunotherapy. *Signal Transduction and Targeted Therapy*, 6(1), p.127.

Duluc, D. et al., 2007. Tumor-associated leukemia inhibitory factor and IL-6 skew monocyte differentiation into tumor-associated macrophage-like cells. *Blood*, 110(13), pp.4319–4330.

Eames, H.L. et al., 2012. KAP1/TRIM28: an inhibitor of IRF5 function in inflammatory macrophages. *Immunobiology*, 217(12), pp.1315–1324.

Edilova, M.I., Akram, A. & Abdul-Sater, A.A., 2021. Innate immunity drives pathogenesis of rheumatoid arthritis. *BiomedicalJjournal*, 44(2), pp.172–182.

Edwards, J.P. et al., 2006. Biochemical and functional characterization of three activated macrophage populations. *Journal of Leukocyte Biology*, 80(6), pp.1298–1307.

El Chartouni, C., Schwarzfischer, L. & Rehli, M., 2010. Interleukin-4 induced interferon regulatory factor (Irf) 4 participates in the regulation of alternative macrophage priming. *Immunobiology*, 215(9-10), pp.821–825.

van den Elsen, P.J., 2011. Expression regulation of major histocompatibility complex class I and class II encoding genes. *Frontiers in Immunology*, 2, p.48.

Emoto, T. et al., 2022. Colony stimulating factor-1 producing endothelial cells and mesenchymal stromal cells maintain monocytes within a perivascular bone marrow niche. *Immunity*, 55(5), pp.862–878.e8.

Englen, M.D. et al., 1995. Granulocyte/macrophage colony-stimulating factor is expressed and secreted in cultures of murine L929 cells. *Journal of Immunological Methods*, 184(2), pp.281–283.

Engwerda, C.R. et al., 2002. A role for tumor necrosis factor-alpha in remodeling the splenic marginal zone during Leishmania donovani infection. *The American Journal of Pathology*, 161(2), pp.429–437.

Ergen, A.V., Boles, N.C. & Goodell, M.A., 2012. Rantes/Ccl5 influences hematopoietic stem cell subtypes and causes myeloid skewing. *Blood*, 119(11), pp.2500–2509.

Fadok, V.A. et al., 1998. Macrophages that have ingested apoptotic cells in vitro inhibit proinflammatory cytokine production through autocrine/paracrine mechanisms involving TGF-beta, PGE2, and PAF. *The Journal of Clinical Investigation*, 101(4), pp.890–898.

Falcão, S.A.C. et al., 2015. Exposure to Leishmania braziliensis triggers neutrophil activation and apoptosis. *PLoS Neglected Tropical Diseases*, 9(3), p.e0003601.

Fang, Z. et al., 2017. Regulation of TRIM24 by miR-511 modulates cell proliferation in gastric cancer. *Journal of Experimental & Clinical Cancer Research: CR*, 36(1), p.17.

Fan, Q.-W. et al., 2013. EGFR phosphorylates tumor-derived EGFRvIII driving STAT3/5 and progression in glioblastoma. *Cancer Cell*, 24(4), pp.438–449.

Farr, L., Ghosh, S. & Moonah, S., 2020. Role of MIF Cytokine/CD74 Receptor Pathway in Protecting Against Injury and Promoting Repair. *Frontiers in Immunology*, 11, p.1273.

Fasching, L. et al., 2015. TRIM28 represses transcription of endogenous retroviruses in neural progenitor cells. *Cell Reports*, 10(1), pp.20–28.

Feng, S. et al., 2022. LARS2 Regulates Apoptosis via ROS-Mediated Mitochondrial Dysfunction and Endoplasmic Reticulum Stress in Ovarian Granulosa Cells. *Oxidative Medicine and Cellular Longevity*, 2022, p.5501346.

Fensterl, V. & Sen, G.C., 2015. Interferon-induced Ifit proteins: their role in viral pathogenesis. *Journal of Virology*, 89(5), pp.2462–2468.

Ferrante, C.J. et al., 2013. The adenosine-dependent angiogenic switch of macrophages to an M2-like phenotype is independent of interleukin-4 receptor alpha (IL-4Rα) signaling. *Inflammation*, 36(4), pp.921–931.

Ferreira, F.M. et al., 2019. Bone marrow chimeras-a vital tool in basic and translational research. *Journal of Molecular Medicine* , 97(7), pp.889–896.

Ferri, F. et al., 2015. TRIM33 switches off Ifnb1 gene transcription during the late phase of macrophage activation. *Nature Communications*, 6(1), p.8900.

Fingar, D.C. et al., 2004. mTOR controls cell cycle progression through its cell growth effectors S6K1 and 4E-BP1/eukaryotic translation initiation factor 4E. *Molecular and Cellular Biology*, 24(1), pp.200–216.

Fitzgerald, K.A. et al., 2003. IKKepsilon and TBK1 are essential components of the IRF3 signaling pathway. *Nature Immunology*, 4(5), pp.491–496.

Fleetwood, A.J. et al., 2009. GM-CSF- and M-CSF-dependent macrophage phenotypes display differential dependence on type I interferon signaling. *Journal of Leukocyte Biology*, 86(2), pp.411–421.

Fleetwood, A.J. et al., 2007. Granulocyte-macrophage colony-stimulating factor (CSF) and macrophage CSF-dependent macrophage phenotypes display differences in cytokine profiles and transcription factor activities: implications for CSF blockade in inflammation. *Journal of Immunology* , 178(8), pp.5245–5252.

Fleit, H.B. & Rabinovitch, M., 1981. Interferon induction in marrow-derived macrophages: regulation by L cell conditioned medium. *Journal of Cellular Physiology*, 108(3), pp.347–352.

Fong, K.-W. et al., 2018. TRIM28 protects TRIM24 from SPOP-mediated degradation and promotes prostate cancer progression. *Nature communications*, 9(1), p.5007.

Formaglio, P. et al., 2021. Nitric oxide controls proliferation of Leishmania major by inhibiting the recruitment of permissive host cells. *Immunity*, 54(12), pp.2724–2739.e10.

Forrester, S. et al., 2022. Tissue specific dual RNA-seq defines host-parasite interplay in murine visceral leishmaniasis caused by Leishmania donovani and Leishmania infantum. *bioRxiv*, p.2022.02.04.479211. Available at: https://www.biorxiv.org/content/10.1101/2022.02.04.479211v1 [Accessed April 5, 2022].

Freemerman, A.J. et al., 2019. Myeloid Slc2a1-Deficient Murine Model Revealed Macrophage Activation and Metabolic Phenotype Are Fueled by GLUT1. *Journal of immunology* , 202(4), pp.1265–1286.

Fujisaka, S. et al., 2011. Telmisartan improves insulin resistance and modulates adipose tissue macrophage polarization in high-fat-fed mice. *Endocrinology*, 152(5), pp.1789–1799.

Fujisawa, T. & Filippakopoulos, P., 2017. Functions of bromodomain-containing proteins and their roles in homeostasis and cancer. *Nature reviews. Molecular Cell Biology*, 18(4), pp.246–262.

van Furth, R. et al., 1972. The mononuclear phagocyte system: a new classification of macrophages, monocytes, and their precursor cells. *Bulletin of the World Health Organization*, 46(6), pp.845–852.

van Furth, R. & Cohn, Z.A., 1968. The origin and kinetics of mononuclear phagocytes. *The Journal of Experimental Medicine*, 128(3), pp.415–435.

Gallo, P., Gonçalves, R. & Mosser, D.M., 2010. The influence of IgG density and macrophage Fc (gamma) receptor cross-linking on phagocytosis and IL-10 production. *Immunology Letters*, 133(2), pp.70–77.

Gallouet, A.-S. et al., 2017. Macrophage production and activation are dependent on TRIM33. *Oncotarget*, 8(3), pp.5111–5122.

Ganser-Pornillos, B.K. et al., 2011. Hexagonal assembly of a restricting TRIM5α protein. *Proceedings of the National Academy of Sciences*, 108(2), pp.534–539.

Gao, F. et al., 2022. HSPA5 Inhibitor Meliorate DSS-Induced Colitis through HSPA1A/CHIP. *Disease Markers*, 2022, p.7115181.

Geissmann, F., Jung, S. & Littman, D.R., 2003. Blood monocytes consist of two principal subsets with distinct migratory properties. *Immunity*, 19(1), pp.71–82.

Geng, Y.J. & Hansson, G.K., 1992. Interferon-gamma inhibits scavenger receptor expression and foam cell formation in human monocyte-derived macrophages. *The Journal of Clinical Investigation*, 89(4), pp.1322–1330.

Gentilella, A. et al., 2017. Autogenous Control of 5′TOP mRNA Stability by 40S Ribosomes. *Molecular Cell*, 67(1), pp.55–70.e4.

van Gent, M., Sparrer, K.M.J. & Gack, M.U., 2018. TRIM Proteins and Their Roles in Antiviral Host Defenses. *Annual Review of Virology*, 5(1), pp.385–405.

Ghaffari, A. et al., 2006. Potential application of gaseous nitric oxide as a topical antimicrobial agent. *Nitric oxide: Biology and Chemistry / Official Journal of the Nitric Oxide Society*, 14(1), pp.21–29.

Ghalib, H.W. et al., 1993. Interleukin 10 production correlates with pathology in human Leishmania donovani infections. *The Journal of Clinical Investigation*, 92(1), pp.324–329.

Ginhoux, F. et al., 2010. Fate mapping analysis reveals that adult microglia derive from primitive macrophages. *Science*, 330(6005), pp.841–845.

Giraldo, M.I. et al., 2020. TRIM Proteins in Host Defense and Viral Pathogenesis. *Current Clinical Microbiology Reports*, 7(4), pp.101–114.

Gomez Perdiguero, E. et al., 2015. Tissue-resident macrophages originate from yolk-sac-derived erythro-myeloid progenitors. *Nature*, 518(7540), pp.547–551.

Gorak, P.M., Engwerda, C.R. & Kaye, P.M., 1998. Dendritic cells, but not macrophages, produce IL-12 immediately following Leishmania donovani infection. *European Journal of Immunology*, 28(2), pp.687–695.

Gordon, S., 2008. Elie Metchnikoff: father of natural immunity. *European Journal of Immunology*, 38(12), pp.3257–3264.

Grabowska, J. et al., 2018. CD169+ Macrophages Capture and Dendritic Cells Instruct: The Interplay of the Gatekeeper and the General of the Immune System. *Frontiers in Immunology*, 9, p.2472.

Gray, M.J. et al., 2005. Induction of arginase I transcription by IL-4 requires a composite DNA response element for STAT6 and C/EBPbeta. *Gene*, 353(1), pp.98–106.

Gregory, D.J. et al., 2008. Comparison of the effects of Leishmania major or Leishmania donovani infection on macrophage gene expression. *Infection and Immunity*, 76(3), pp.1186–1192.

Guilliams, M. et al., 2014. Dendritic cells, monocytes and macrophages: a unified nomenclature based on ontogeny. *Nature Reviews. Immunology*, 14(8), pp.571–578.

Guirado, E., Schlesinger, L.S. & Kaplan, G., 2013. Macrophages in tuberculosis: friend or foe. *Seminars in Immunopathology*, 35(5), pp.563–583.

Guo, C.-Y. et al., 2015. Sensitivity and dose dependency of radiation-induced injury in hematopoietic stem/progenitor cells in mice. *Scientific Reports*, 5, p.8055.

Gurel, M.S., Tekin, B. & Uzun, S., 2020. Cutaneous leishmaniasis: A great imitator. *Clinics in Dermatology*, 38(2), pp.140–151.

Ha, C.T. et al., 2005. Binding of pregnancy-specific glycoprotein 17 to CD9 on macrophages induces secretion of IL-10, IL-6, PGE2, and TGF-beta1. *Journal of Leukocyte Biology*, 77(6), pp.948–957.

Hamilton, J.A., Vairo, G. & Lingelbach, S.R., 1986. CSF-1 stimulates glucose uptake in murine bone marrow-derived macrophages. *Biochemical and Biophysical Research Communications*, 138(1), pp.445–454.

Hammami, A. et al., 2017. HIF-1α is a key regulator in potentiating suppressor activity and limiting the microbicidal capacity of MDSC-like cells during visceral leishmaniasis. *PLoS Pathogens*, 13(9), p.e1006616.

Haque, A. et al., 2017. A practical guide to single-cell RNA-sequencing for biomedical research and clinical applications. *Genome Medicine*, 9(1), p.75.

Harris, N. et al., 1992. Characterization of the murine macrophage mannose receptor: demonstration that the downregulation of receptor expression mediated by interferon-gamma occurs at the level of transcription. *Blood*, 80(9), pp.2363–2373.

’t Hart, L.M. et al., 2005. Evidence that the mitochondrial leucyl tRNA synthetase (LARS2) gene represents a novel type 2 diabetes susceptibility gene. *Diabetes*, 54(6), pp.1892–1895.

Hatakeyama, S., 2017. TRIM Family Proteins: Roles in Autophagy, Immunity, and Carcinogenesis. *Trends in Biochemical Sciences*, 42(4), pp.297–311.

Hay, N. & Sonenberg, N., 2004. Upstream and downstream of mTOR. *Genes & Development*, 18(16), pp.1926–1945.

Heap, R.E. et al., 2021. Proteomics characterisation of the L929 cell supernatant and its role in BMDM differentiation. *Life Science Alliance*, 4(6). Available at: http://dx.doi.org/10.26508/lsa.202000957.

Heckmann, B.L. et al., 2013. The G0/G1 switch gene 2 (G0S2): regulating metabolism and beyond. *Biochimica et Biophysica Acta*, 1831(2), pp.276–281.

He, J. et al., 2021. Sulfiredoxin-1 attenuates injury and inflammation in acute pancreatitis through the ROS/ER stress/Cathepsin B axis. *Cell Death & Disease*, 12(7), p.626.

Held, T.K. et al., 1999. Gamma interferon augments macrophage activation by lipopolysaccharide by two distinct mechanisms, at the signal transduction level and via an autocrine mechanism involving tumor necrosis factor alpha and interleukin-1. *Infection and immunity*, 67(1), pp.206–212.

Hermida, M.D.-R. et al., 2018. Histological Disorganization of Spleen Compartments and Severe Visceral Leishmaniasis. *Frontiers in Cellular and Infection Microbiology*, 8, p.394.

Herquel, B. et al., 2011. Transcription cofactors TRIM24, TRIM28, and TRIM33 associate to form regulatory complexes that suppress murine hepatocellular carcinoma. *Proceedings of the National Academy of Sciences of the United States of America*, 108(20), pp.8212–8217.

Hibbs, J.B., Jr et al., 1988. Nitric oxide: a cytotoxic activated macrophage effector molecule. *Biochemical and Biophysical Research Communications*, 157(1), pp.87–94.

Higgs, R. et al., 2010. Self protection from anti-viral responses--Ro52 promotes degradation of the transcription factor IRF7 downstream of the viral Toll-Like receptors. *PloS One*, 5(7), p.e11776.

Higgs, R. et al., 2008. The E3 ubiquitin ligase Ro52 negatively regulates IFN-beta production post-pathogen recognition by polyubiquitin-mediated degradation of IRF3. *Journal of Immunology* , 181(3), pp.1780–1786.

Hirai, H. et al., 2015. Non-steady-state hematopoiesis regulated by the C/EBPβ transcription factor. *Cancer Science*, 106(7), pp.797–802.

Hoeffel, G. et al., 2012. Adult Langerhans cells derive predominantly from embryonic fetal liver monocytes with a minor contribution of yolk sac-derived macrophages. *The Journal of Experimental Medicine*, 209(6), pp.1167–1181.

Hoeffel, G. et al., 2015. C-Myb(+) erythro-myeloid progenitor-derived fetal monocytes give rise to adult tissue-resident macrophages. *Immunity*, 42(4), pp.665–678.

Honda, K. et al., 2005. IRF-7 is the master regulator of type-I interferon-dependent immune responses. *Nature*, 434(7034), pp.772–777.

Honda, K., Takaoka, A. & Taniguchi, T., 2006. Type I interferon [corrected] gene induction by the interferon regulatory factor family of transcription factors. *Immunity*, 25(3), pp.349–360.

Honda, K. & Taniguchi, T., 2006. IRFs: master regulators of signalling by Toll-like receptors and cytosolic pattern-recognition receptors. *Nature Reviews. Immunology*, 6(9), pp.644–658.

Hong, S. et al., 2017. LARP1 functions as a molecular switch for mTORC1-mediated translation of an essential class of mRNAs. *eLife*, 6. Available at: http://dx.doi.org/10.7554/eLife.25237.

Horvath, R.M. et al., 2023. TRIM24 controls induction of latent HIV-1 by stimulating transcriptional elongation. *Communications Biology*, 6(1), pp.1–14.

Huang, F. et al., 2017. miR-148a-3p Mediates Notch Signaling to Promote the Differentiation and M1 Activation of Macrophages. *Frontiers in Immunology*, 8, p.1327.

Huang, G. et al., 2008. PU.1 is a major downstream target of AML1 (RUNX1) in adult mouse hematopoiesis. *Nature Genetics*, 40(1), pp.51–60.

Huang, J. & Manning, B.D., 2009. A complex interplay between Akt, TSC2 and the two mTOR complexes. *Biochemical Society Transactions*, 37(Pt 1), pp.217–222.

Hui, S. et al., 2017. Early assessment of dosimetric and biological differences of total marrow irradiation versus total body irradiation in rodents. *Radiotherapy and oncology: journal of the European Society for Therapeutic Radiology and Oncology*, 124(3), pp.468–474.

Hui, Z. et al., 2023. Loss of TRIM24 promotes IL-10 expression via CBP/p300-dependent IFNβ1 transcription during macrophage activation. *Inflammation research: Official Journal of the European Histamine Research Society ... [et al.]*, 72(7), pp.1441–1452.

Iadevaia, V. et al., 2008. All translation elongation factors and the e, f, and h subunits of translation initiation factor 3 are encoded by 5'-terminal oligopyrimidine (TOP) mRNAs. *RNA* , 14(9), pp.1730–1736.

Icardi, L., De Bosscher, K. & Tavernier, J., 2012. The HAT/HDAC interplay: multilevel control of STAT signaling. *Cytokine & Growth Factor Reviews*, 23(6), pp.283–291.

Ikeda, K. & Inoue, S., 2012. TRIM proteins as RING finger E3 ubiquitin ligases. *Advances in Experimental Medicine and Biology*, 770, pp.27–37.

Izaguirre, A. et al., 2003. Comparative analysis of IRF and IFN-alpha expression in human plasmacytoid and monocyte-derived dendritic cells. *Journal of Leukocyte Biology*, 74(6), pp.1125–1138.

Jablonski, K.A. et al., 2015. Novel Markers to Delineate Murine M1 and M2 Macrophages. *PloS one*, 10(12), p.e0145342.

Jacinto, E. et al., 2006. SIN1/MIP1 maintains rictor-mTOR complex integrity and regulates Akt phosphorylation and substrate specificity. *Cell*, 127(1), pp.125–137.

Jacobs, A.T. & Ignarro, L.J., 2001. Lipopolysaccharide-induced expression of interferon-beta mediates the timing of inducible nitric-oxide synthase induction in RAW 264.7 macrophages. *The Journal of Biological Chemistry*, 276(51), pp.47950–47957.

Jaguin, M. et al., 2013. Polarization profiles of human M-CSF-generated macrophages and comparison of M1-markers in classically activated macrophages from GM-CSF and M-CSF origin. *Cellular Immunology*, 281(1), pp.51–61.

Jain, A.K. et al., 2014. TRIM24 is a p53-induced E3-ubiquitin ligase that undergoes ATM-mediated phosphorylation and autodegradation during DNA damage. *Molecular and Cellular Biology*, 34(14), pp.2695–2709.

James, L.C. et al., 2007. Structural basis for PRYSPRY-mediated tripartite motif (TRIM) protein function. *Proceedings of the National Academy of Sciences of the United States of America*, 104(15), pp.6200–6205.

Jang, Y. et al., 2018. Cutting Edge: Check Your Mice-A Point Mutation in the Ncr1 Locus Identified in CD45.1 Congenic Mice with Consequences in Mouse Susceptibility to Infection. *Journal of Immunology* , 200(6), pp.1982–1987.

Jha, A.K. et al., 2015. Network integration of parallel metabolic and transcriptional data reveals metabolic modules that regulate macrophage polarization. *Immunity*, 42(3), pp.419–430.

Jia, J.-J. et al., 2021. mTORC1 promotes TOP mRNA translation through site-specific phosphorylation of LARP1. *Nucleic Acids Research*, 49(6), pp.3461–3489.

Jiang, L. et al., 2011. Synthetic spike-in standards for RNA-seq experiments. *Genome Research*, 21(9), pp.1543–1551.

Jiang, S. et al., 2015. TRIM24 suppresses development of spontaneous hepatic lipid accumulation and hepatocellular carcinoma in mice. *Journal of Hepatology*, 62(2), pp.371–379.

Jin, S. et al., 2021. Inference and analysis of cell-cell communication using CellChat. *Nature Communications*, 12(1), p.1088.

Joshi, T. et al., 2009. B7-H1 blockade increases survival of dysfunctional CD8(+) T cells and confers protection against Leishmania donovani infections. *PLoS Pathogens*, 5(5), p.e1000431.

Junghae, M. & Raynes, J.G., 2002. Activation of p38 mitogen-activated protein kinase attenuates Leishmania donovani infection in macrophages. *Infection and Immunity*, 70(9), pp.5026–5035.

Kakuda, D.K. et al., 1999. CAT2-mediated L-arginine transport and nitric oxide production in activated macrophages. *Biochemical Journal*, 340 (Pt 2)(Pt 2), pp.549–553.

Kamijo, R. et al., 1994. Requirement for transcription factor IRF-1 in NO synthase induction in macrophages. *Science*, 263(5153), pp.1612–1615.

Kane, H. et al., 2022. Longitudinal analysis of invariant natural killer T cell activation reveals a cMAF-associated transcriptional state of NKT10 cells. *eLife*, 11. Available at: http://dx.doi.org/10.7554/eLife.76586.

Kanekiyo, M. et al., 2002. Metallothionein modulates lipopolysaccharide-stimulated tumour necrosis factor expression in mouse peritoneal macrophages. *Biochemical Journal*, 361(Pt 2), pp.363–369.

Karagiannis, K. et al., 2022. Dual scRNA-Seq analysis reveals rare and uncommon parasitized cell populations in chronic L. donovani infection. *bioRxiv*, p.2022.07.26.501600. Available at: https://www.biorxiv.org/content/10.1101/2022.07.26.501600v1 [Accessed November 7, 2022].

Kato, K., Omori, A. & Kashiwakura, I., 2013. Radiosensitivity of human haematopoietic stem/progenitor cells. *Journal of Radiological Protection: official Journal of the Society for Radiological Protection*, 33(1), pp.71–80.

Kaur, S. et al., 2008. Effect of dose and route of inoculation on the generation of CD4+ Th1/Th2 type of immune response in murine visceral leishmaniasis. *Parasitology Research*, 103(6), pp.1413–1419.

Kaye, P.M. et al., 2004. The immunopathology of experimental visceral leishmaniasis. *Immunological Reviews*, 201, pp.239–253.

Kaye, P. & Scott, P., 2011. Leishmaniasis: complexity at the host-pathogen interface. *Nature Reviews. Microbiology*, 9(8), pp.604–615.

Khalil, E.A.G. et al., 2014. Safety and efficacy of single dose versus multiple doses of AmBisome for treatment of visceral leishmaniasis in eastern Africa: a randomised trial. *PLoS Neglected Tropical Diseases*, 8(1), p.e2613.

Khetchoumian, K. et al., 2007. Loss of Trim24 (Tif1alpha) gene function confers oncogenic activity to retinoic acid receptor alpha. *Nature Genetics*, 39(12), pp.1500–1506.

Khetchoumian, K. et al., 2004. TIF1delta, a novel HP1-interacting member of the transcriptional intermediary factor 1 (TIF1) family expressed by elongating spermatids. *The Journal of Biological Chemistry*, 279(46), pp.48329–48341.

Khetchoumian, K. et al., 2008. Trim24 (Tif1 alpha): an essential “brake” for retinoic acid-induced transcription to prevent liver cancer. *Cell Cycle* , 7(23), pp.3647–3652.

Kieusseian, A. et al., 2012. Immature hematopoietic stem cells undergo maturation in the fetal liver. *Development* , 139(19), pp.3521–3530.

Kima, P.E. et al., 2000. Internalization of Leishmania mexicana complex amastigotes via the Fc receptor is required to sustain infection in murine cutaneous leishmaniasis. *The Journal of Experimental Medicine*, 191(6), pp.1063–1068.

Kim, J. & Kaartinen, V., 2008. Generation of mice with a conditional allele for Trim33. *Genesis* , 46(6), pp.329–333.

Kodama, H. et al., 1991. Congenital osteoclast deficiency in osteopetrotic (op/op) mice is cured by injections of macrophage colony-stimulating factor. *The Journal of Experimental Medicine*, 173(1), pp.269–272.

Kohara, H. et al., 2007. Development of plasmacytoid dendritic cells in bone marrow stromal cell niches requires CXCL12-CXCR4 chemokine signaling. *Blood*, 110(13), pp.4153–4160.

Kohyama, M. et al., 2009. Role for Spi-C in the development of red pulp macrophages and splenic iron homeostasis. *Nature*, 457(7227), pp.318–321.

Kong, H.J. et al., 2007. Cutting edge: autoantigen Ro52 is an interferon inducible E3 ligase that ubiquitinates IRF-8 and enhances cytokine expression in macrophages. *Journal of Immunology* , 179(1), pp.26–30.

Koppel, E.A. et al., 2004. Identification of the mycobacterial carbohydrate structure that binds the C-type lectins DC-SIGN, L-SIGN and SIGNR1. *Immunobiology*, 209(1-2), pp.117–127.

Koren, I., Reem, E. & Kimchi, A., 2010. DAP1, a novel substrate of mTOR, negatively regulates autophagy. *Current Biology: CB*, 20(12), pp.1093–1098.

Krämer, O.H. et al., 2009. A phosphorylation-acetylation switch regulates STAT1 signaling. *Genes & Development*, 23(2), pp.223–235.

Kratofil, R.M., Kubes, P. & Deniset, J.F., 2017. Monocyte Conversion During Inflammation and Injury. *Arteriosclerosis, Thrombosis, and Vascular Biology*, 37(1), pp.35–42.

Krausgruber, T. et al., 2011. IRF5 promotes inflammatory macrophage polarization and TH1-TH17 responses. *Nature Immunology*, 12(3), pp.231–238.

Krawczyk, C.M. et al., 2010. Toll-like receptor–induced changes in glycolytic metabolism regulate dendritic cell activation. *Blood*, 115(23), pp.4742–4749.

Krishnaraju, K., Hoffman, B. & Liebermann, D.A., 2001. Early growth response gene 1 stimulates development of hematopoietic progenitor cells along the macrophage lineage at the expense of the granulocyte and erythroid lineages. *Blood*, 97(5), pp.1298–1305.

Kumar, A. et al., 2011. Gα13 and Rho mediate endosomal trafficking of CXCR4 into Rab11+ vesicles upon stromal cell-derived factor-1 stimulation. *Journal of Immunology* , 186(2), pp.951–958.

Kumaran Satyanarayanan, S. et al., 2019. IFN-β is a macrophage-derived effector cytokine facilitating the resolution of bacterial inflammation. *Nature Communications*, 10(1), p.3471.

Kumar, G.A. et al., 2019. Leishmania donovani Internalizes into Host Cells via Caveolin-mediated Endocytosis. *Scientific Reports*, 9(1), p.12636.

Kumar, R. et al., 2020. Type I Interferons Suppress Anti-parasitic Immunity and Can Be Targeted to Improve Treatment of Visceral Leishmaniasis. *Cell Reports*, 30(8), pp.2512–2525.e9.

Kupani, M. et al., 2020. IL-10 and TGF-β Induced Arginase Expression Contributes to Deficient Nitric Oxide Response in Human Visceral Leishmaniasis. *Frontiers in Cellular and Infection Microbiology*, 10, p.614165.

Kurotaki, D. et al., 2013. Essential role of the IRF8-KLF4 transcription factor cascade in murine monocyte differentiation. *Blood*, 121(10), pp.1839–1849.

Lafuse, W.P. et al., 2013. Leishmania donovani infection induces anemia in hamsters by differentially altering erythropoiesis in bone marrow and spleen. *PloS One*, 8(3), p.e59509.

Lamkin, D.M. et al., 2019. C/EBPβ regulates the M2 transcriptome in β-adrenergic-stimulated macrophages. *Brain, Behavior, and Immunity*, 80, pp.839–848.

Lam, R.S. et al., 2016. Unprimed, M1 and M2 Macrophages Differentially Interact with Porphyromonas gingivalis. *PloS One*, 11(7), p.e0158629.

Lanoue, A. et al., 2004. SIGN-R1 contributes to protection against lethal pneumococcal infection in mice. *The Journal of Experimental Medicine*, 200(11), pp.1383–1393.

Laskay, T., van Zandbergen, G. & Solbach, W., 2003. Neutrophil granulocytes--Trojan horses for Leishmania major and other intracellular microbes? *Trends in Microbiology*, 11(5), pp.210–214.

Lazzari, E. et al., 2014. TRIpartite motif 21 (TRIM21) differentially regulates the stability of interferon regulatory factor 5 (IRF5) isoforms. *PloS One*, 9(8), p.e103609.

Leão Dias, E. et al., 2008. Canine visceral leishmaniasis (cvl): Seroprevalence, clinical, hematological and biochemical findings of dogs naturally infected in an endemic area of são José DE ribamar municipality, Maranhão state, Brazil. *Ci. Anim. bras.*, pp.740–745.

Le Douarin, B. et al., 1995. The N-terminal part of TIF1, a putative mediator of the ligand-dependent activation function (AF-2) of nuclear receptors, is fused to B-raf in the oncogenic protein T18. *The EMBO Journal*, 14(9), pp.2020–2033.

Lee, S.H. et al., 2018. Mannose receptor high, M2 dermal macrophages mediate nonhealing Leishmania major infection in a Th1 immune environment. *The Journal of Experimental Medicine*, 215(1), pp.357–375.

Lee, S.J. et al., 2002. Mannose receptor-mediated regulation of serum glycoprotein homeostasis. *Science*, 295(5561), pp.1898–1901.

Lei, F. et al., 2020. CSF1R inhibition by a small-molecule inhibitor is not microglia specific; affecting hematopoiesis and the function of macrophages. *Proceedings of the National Academy of Sciences of the United States of America*, 117(38), pp.23336–23338.

Leung, G.A. et al., 2019. The lymphoid-associated interleukin 7 receptor (IL7R) regulates tissue-resident macrophage development. *Development* , 146(14). Available at: http://dx.doi.org/10.1242/dev.176180.

Liang, Q. et al., 2011. Tripartite motif-containing protein 28 is a small ubiquitin-related modifier E3 ligase and negative regulator of IFN regulatory factor 7. *Journal of Immunology* , 187(9), pp.4754–4763.

Liang, T. et al., 2022. STAT1 and CXCL10 involve in M1 macrophage polarization that may affect osteolysis and bone remodeling in extrapulmonary tuberculosis. *Gene*, 809, p.146040.

Li, L., Dong, M. & Wang, X.-G., 2016. The Implication and Significance of Beta 2 Microglobulin: A Conservative Multifunctional Regulator. *Chinese Medical Journal*, 129(4), pp.448–455.

Li, Q. et al., 2011. Tripartite motif 8 (TRIM8) modulates TNFα- and IL-1β-triggered NF-κB activation by targeting TAK1 for K63-linked polyubiquitination. *Proceedings of the National Academy of Sciences of the United States of America*, 108(48), pp.19341–19346.

Lin, C.-F. et al., 2008. IFN-gamma synergizes with LPS to induce nitric oxide biosynthesis through glycogen synthase kinase-3-inhibited IL-10. *Journal of Cellular Biochemistry*, 105(3), pp.746–755.

Lin, J. et al., 2021. The SETDB1-TRIM28 Complex Suppresses Antitumor Immunity. *Cancer Immunology Research*, 9(12), pp.1413–1424.

Lin, S.-C., Lo, Y.-C. & Wu, H., 2010. Helical assembly in the MyD88-IRAK4-IRAK2 complex in TLR/IL-1R signalling. *Nature*, 465(7300), pp.885–890.

Link, V.M. et al., 2018. Analysis of Genetically Diverse Macrophages Reveals Local and Domain-wide Mechanisms that Control Transcription Factor Binding and Function. *Cell*, 173(7), pp.1796–1809.e17.

Liu, L. et al., 2013. TRIM28, a new molecular marker predicting metastasis and survival in early-stage non-small cell lung cancer. *Cancer Epidemiology*, 37(1), pp.71–78.

Liu, S.X. et al., 2020. Trajectory analysis quantifies transcriptional plasticity during macrophage polarization. *Scientific Reports*, 10(1), p.12273.

Liu, T. et al., 2017. NF-κB signaling in inflammation. *Signal Transduction and Targeted Therapy*, 2. Available at: http://dx.doi.org/10.1038/sigtrans.2017.23.

Liu, X. et al., 2014. Overexpression of TRIM24 is associated with the onset and progress of human hepatocellular carcinoma. *PloS One*, 9(1), p.e85462.

Llanes, A., Restrepo, C.M. & Lleonart, R., 2018. ViannaTopes: a database of predicted immunogenic peptides for Leishmania (Viannia) species. *Database: the Journal of Biological Databases and Curation*, 2018. Available at: http://dx.doi.org/10.1093/database/bay111.

Lu, K. et al., 2022. TRIM proteins in hepatocellular carcinoma. *Journal of Biomedical Science*, 29(1), p.69.

Lu, Y.-C., Yeh, W.-C. & Ohashi, P.S., 2008. LPS/TLR4 signal transduction pathway. *Cytokine*, 42(2), pp.145–151.

Lv, D. et al., 2017. TRIM24 is an oncogenic transcriptional co-activator of STAT3 in glioblastoma. *Nature Communications*, 8(1), p.1454.

MacLeod, C.L., Finley, K.D. & Kakuda, D.K., 1994. y+-type cationic amino acid transport: expression and regulation of the mCAT genes. *The Journal of Experimental Biology*, 196(1), pp.109–121.

MacMicking, J.D. et al., 1995. Altered responses to bacterial infection and endotoxic shock in mice lacking inducible nitric oxide synthase. *Cell*, 81(4), pp.641–650.

MacMicking, J.D. et al., 1997. Identification of nitric oxide synthase as a protective locus against tuberculosis. *Proceedings of the National Academy of Sciences of the United States of America*, 94(10), pp.5243–5248.

MacNamara, K.C. et al., 2011. Infection-induced myelopoiesis during intracellular bacterial infection is critically dependent upon IFN-γ signaling. *Journal of Immunology* , 186(2), pp.1032–1043.

Mahnke, J. et al., 2016. Interferon Regulatory Factor 4 controls TH1 cell effector function and metabolism. *Scientific Reports*, 6, p.35521.

Maintz, E.-M. et al., 2014. Introducing single dose liposomal amphotericin B for the treatment of visceral leishmaniasis in rural bangladesh: feasibility and acceptance to patients and health staff. *Journal of Tropical Medicine*, 2014, p.676817.

Makhoul, C. et al., 2023. Arf5-mediated regulation of mTORC1 at the plasma membrane. *Molecular Biology of the Cell*, 34(4), p.ar23.

Malik, R. & Marchese, A., 2010. Arrestin-2 interacts with the endosomal sorting complex required for transport machinery to modulate endosomal sorting of CXCR4. *Molecular Biology of the Cell*, 21(14), pp.2529–2541.

Mallery, D.L. et al., 2010. Antibodies mediate intracellular immunity through tripartite motif-containing 21 (TRIM21). *Proceedings of the National Academy of Sciences of the United States of America*, 107(46), pp.19985–19990.

Mann, S. et al., 2021. A Review of Leishmaniasis: Current Knowledge and Future Directions. *Current Tropical Medicine Reports*, 8(2), pp.121–132.

Mantovani, A. et al., 2004. The chemokine system in diverse forms of macrophage activation and polarization. *Trends in Immunology*, 25(12), pp.677–686.

Ma, Q. et al., 1998. Impaired B-lymphopoiesis, myelopoiesis, and derailed cerebellar neuron migration in CXCR4- and SDF-1-deficient mice. *Proceedings of the National Academy of Sciences of the United States of America*, 95(16), pp.9448–9453.

Marcogliese, P.C. et al., 2018. IRF2BPL Is Associated with Neurological Phenotypes. *American Journal of Human Genetics*, 103(2), pp.245–260.

Marín-Hernández, A. et al., 2009. HIF-1alpha modulates energy metabolism in cancer cells by inducing over-expression of specific glycolytic isoforms. *Mini Reviews in Medicinal Chemistry*, 9(9), pp.1084–1101.

Marín, I., 2012. Origin and diversification of TRIM ubiquitin ligases. *PloS One*, 7(11), p.e50030.

Maroof, A. et al., 2008. Posttranscriptional regulation of Il10 gene expression allows natural killer cells to express immunoregulatory function. *Immunity*, 29(2), pp.295–305.

Martin, E., Nathan, C. & Xie, Q.W., 1994. Role of interferon regulatory factor 1 in induction of nitric oxide synthase. *The Journal of Experimental Medicine*, 180(3), pp.977–984.

Martínez-López, M. et al., 2015. Batf3-dependent CD103+ dendritic cells are major producers of IL-12 that drive local Th1 immunity against Leishmania major infection in mice. *European Journal of Immunology*, 45(1), pp.119–129.

Mass, E. et al., 2016. Specification of tissue-resident macrophages during organogenesis. *Science*, 353(6304). Available at: http://dx.doi.org/10.1126/science.aaf4238.

Mattijssen, S. et al., 2021. The isolated La-module of LARP1 mediates 3' poly(A) protection and mRNA stabilization, dependent on its intrinsic PAM2 binding to PABPC1. *RNA Biology*, 18(2), pp.275–289.

Mattner, J. et al., 2000. Regulation of type 2 nitric oxide synthase by type 1 interferons in macrophages infected with Leishmania major. *European Journal of Immunology*, 30(8), pp.2257–2267.

Ma, X. et al., 2012. Structural basis for the dual recognition of helical cytokines IL-34 and CSF-1 by CSF-1R. *Structure* , 20(4), pp.676–687.

Mayer, C. et al., 2004. mTOR-dependent activation of the transcription factor TIF-IA links rRNA synthesis to nutrient availability. *Genes & Development*, 18(4), pp.423–434.

McAvera, R.M. & Crawford, L.J., 2020. TIF1 Proteins in Genome Stability and Cancer. *Cancers*, 12(8). Available at: http://dx.doi.org/10.3390/cancers12082094.

McCarty, E. et al., 2023. Single cell transcriptomics of bone marrow derived macrophages reveals Ccl5 as a biomarker of direct IFNAR-independent responses to DNA sensing. *Frontiers in Immunology*, 14. Available at: https://www.frontiersin.org/articles/10.3389/fimmu.2023.1199730.

McElrath, M.J., Murray, H.W. & Cohn, Z.A., 1988. The dynamics of granuloma formation in experimental visceral leishmaniasis. *The Journal of Experimental Medicine*, 167(6), pp.1927–1937.

McGrath, K.E. et al., 2003. Circulation is established in a stepwise pattern in the mammalian embryo. *Blood*, 101(5), pp.1669–1676.

McKenzie, G.J. et al., 1999. Simultaneous disruption of interleukin (IL)-4 and IL-13 defines individual roles in T helper cell type 2-mediated responses. *The Journal of Experimental Medicine*, 189(10), pp.1565–1572.

McPeak, M.B. et al., 2017. Frontline Science: Myeloid cell-specific deletion of Cebpb decreases sepsis-induced immunosuppression in mice. *Journal of Leukocyte Biology*, 102(2), pp.191–200.

Mebius, R.E. & Kraal, G., 2005. Structure and function of the spleen. *Nature Reviews. Immunology*, 5(8), pp.606–616.

Medina-Colorado, A.A. et al., 2017. Splenic CD4+ T Cells in Progressive Visceral Leishmaniasis Show a Mixed Effector-Regulatory Phenotype and Impair Macrophage Effector Function through Inhibitory Receptor Expression. *PloS One*, 12(1), p.e0169496.

Meroni, G. & Diez-Roux, G., 2005. TRIM/RBCC, a novel class of “single protein RING finger” E3 ubiquitin ligases. *BioEssays: News and Reviews in Molecular, Cellular and Developmental Biology*, 27(11), pp.1147–1157.

Michl, J., Ohlbaum, D.J. & Silverstein, S.C., 1976. 2-Deoxyglucose selectively inhibits Fc and complement receptor-mediated phagocytosis in mouse peritoneal macrophages. I. Description of the inhibitory effect. *The Journal of Experimental Medicine*, 144(6), pp.1465–1483.

Miki, T. et al., 1991. Development of a highly efficient expression cDNA cloning system: application to oncogene isolation. *Proceedings of the National Academy of Sciences of the United States of America*, 88(12), pp.5167–5171.

Mikkola, H.K.A. et al., 2005. Placenta as a site for hematopoietic stem cell development. *Experimental Hematology*, 33(9), pp.1048–1054.

Mildner, A. et al., 2017. Genomic Characterization of Murine Monocytes Reveals C/EBPβ Transcription Factor Dependence of Ly6C- Cells. *Immunity*, 46(5), pp.849–862.e7.

Minderjahn, J. et al., 2020. Mechanisms governing the pioneering and redistribution capabilities of the non-classical pioneer PU.1. *Nature Communications*, 11(1), pp.1–16.

Mishra, B.B., Gundra, U.M. & Teale, J.M., 2011. STAT6$^{-/-}$ mice exhibit decreased cells with alternatively activated macrophage phenotypes and enhanced disease severity in murine neurocysticercosis. *Journal of Neuroimmunology*, 232(1-2), pp.26–34.

Mondal, D. et al., 2014. Efficacy and safety of single-dose liposomal amphotericin B for visceral leishmaniasis in a rural public hospital in Bangladesh: a feasibility study. *The Lancet. Global health*, 2(1), pp.e51–7.

Mondal, K. et al., 2021. Modulation of Splenic B Cell Subsets during Experimental Leishmania donovani Infection in BALB/c Mice. *Pathogens*, 10(7). Available at: http://dx.doi.org/10.3390/pathogens10070814.

Montes de Oca, M., de Labastida Rivera, F., et al., 2020. IL-27 signalling regulates glycolysis in Th1 cells to limit immunopathology during infection. *PLoS Pathogens*, 16(10), p.e1008994.

Montes de Oca, M., Engwerda, C.R. & Kaye, P.M., 2020. Cytokines and splenic remodelling during Leishmania donovani infection. *Cytokine: X*, 2(4), p.100036.

Moore, J.W.J. et al., 2013. Functional complexity of the Leishmania granuloma and the potential of in silico modeling. *Frontiers in Immunology*, 4, p.35.

Moreira, D. et al., 2015. Leishmania infantum modulates host macrophage mitochondrial metabolism by hijacking the SIRT1-AMPK axis. *PLoS Pathogens*, 11(3), p.e1004684.

Mosser, D.M. & Edelson, P.J., 1984. Activation of the alternative complement pathway by Leishmania promastigotes: parasite lysis and attachment to macrophages. *Journal of Immunology* , 132(3), pp.1501–1505.

Mosser, D.M. & Edwards, J.P., 2008. Exploring the full spectrum of macrophage activation. *Nature Reviews. Immunology*, 8(12), pp.958–969.

Mosser, D.M. & Zhang, X., 2008. Activation of murine macrophages. *Current Protocols in Immunology / edited by John E. Coligan ... [et al.]*, Chapter 14, p.Unit 14.2.

Mou, Z. et al., 2015. Identification of broadly conserved cross-species protective *Leishmania* antigen and its responding $CD4^+$ T cells. *Science Translational Medicine*, 7(310), pp.310ra167–310ra167.

Mthunzi, L. et al., 2022. Gremlin 1 is required for macrophage M2 polarization. *bioRxiv*, p.2022.12.07.519468. Available at: https://www.biorxiv.org/content/10.1101/2022.12.07.519468v1 [Accessed June 16, 2023].

Müller, E. et al., 2017. Toll-Like Receptor Ligands and Interferon-γ Synergize for Induction of Antitumor M1 Macrophages. *Frontiers in immunology*, 8, p.1383.

Murphy, M.L. et al., 1998. Blockade of CTLA-4 enhances host resistance to the intracellular pathogen, Leishmania donovani. *Journal of Immunology* , 161(8), pp.4153–4160.

Murphy, M.L. et al., 2001. IL-10 mediates susceptibility to Leishmania donovani infection. *European Journal of Immunology*, 31(10), pp.2848–2856.

Murray, H.W. et al., 2003. Modulation of T-cell costimulation as immunotherapy or immunochemotherapy in experimental visceral leishmaniasis. *Infection and Immunity*, 71(11), pp.6453–6462.

Murray, H.W., 2020. Targeting IL-27 and/or IL-10 in Experimental Murine Visceral Leishmaniasis. *The American Journal of Tropical Medicine and Hygiene*, 103(5), pp.1938–1941.

Murray, H.W., 2001. Tissue granuloma structure-function in experimental visceral leishmaniasis. *International Journal of Experimental Pathology*, 82(5), pp.249–267.

Murray, H.W. & Nathan, C.F., 1999. Macrophage microbicidal mechanisms in vivo: reactive nitrogen versus oxygen intermediates in the killing of intracellular visceral Leishmania donovani. *The Journal of Experimental Medicine*, 189(4), pp.741–746.

Murray, H.W., Xiang, Z. & Ma, X., 2006. Responses to Leishmania donovani in mice deficient in both phagocyte oxidase and inducible nitric oxide synthase. *The American Journal of Tropical Medicine and Hygiene*, 74(6), pp.1013–1015.

Nagaoka, K. et al., 2005. Association of SIGNR1 with TLR4–MD-2 enhances signal transduction by recognition of LPS in gram-negative bacteria. *International Immunology*, 17(7), pp.827–836.

Naito, M. et al., 1989. Development, differentiation, and maturation of fetal mouse yolk sac macrophages in cultures. *Journal of Leukocyte Biology*, 46(1), pp.1–10.

Nandan, D. et al., 2012. Myeloid cell IL-10 production in response to leishmania involves inactivation of glycogen synthase kinase-3β downstream of phosphatidylinositol-3 kinase. *Journal of Immunology* , 188(1), pp.367–378.

Newsholme, P. et al., 1986. Metabolism of glucose, glutamine, long-chain fatty acids and ketone bodies by murine macrophages. *Biochemical Journal*, 239(1), pp.121–125.

Nguyen Hoang, A.T. et al., 2010. Stromal cell-derived CXCL12 and CCL8 cooperate to support increased development of regulatory dendritic cells following Leishmania infection. *Journal of Immunology* , 185(4), pp.2360–2371.

Nicholson, B. et al., 2001. Sustained nitric oxide production in macrophages requires the arginine transporter CAT2. *The Journal of Biological Chemistry*, 276(19), pp.15881–15885.

Ning, S. et al., 2008. TRAF6 and the three C-terminal lysine sites on IRF7 are required for its ubiquitination-mediated activation by the tumor necrosis factor receptor family member latent membrane protein 1. *Molecular and Cellular Biology*, 28(20), pp.6536–6546.

Noda, M. et al., 2011. CXCL12-CXCR4 chemokine signaling is essential for NK-cell development in adult mice. *Blood*, 117(2), pp.451–458.

Nomura, M. et al., 2016. Fatty acid oxidation in macrophage polarization. *Nature Immunology*, 17(3), pp.216–217.

Norsworthy, P.J. et al., 2004. Murine CD93 (C1qRp) contributes to the removal of apoptotic cells in vivo but is not required for C1q-mediated enhancement of phagocytosis. *Journal of Immunology* , 172(6), pp.3406–3414.

Nylén, S. et al., 2007. Splenic accumulation of IL-10 mRNA in T cells distinct from CD4+CD25+ (Foxp3) regulatory T cells in human visceral leishmaniasis. *The Journal of Experimental Medicine*, 204(4), pp.805–817.

Ohms, M. et al., 2021. Enhanced Glycolysis Is Required for Antileishmanial Functions of Neutrophils Upon Infection With Leishmania donovani. *Frontiers in Immunology*, 12, p.632512.

Oksanen, A. et al., 2014. Proprotein convertase FURIN constrains Th2 differentiation and is critical for host resistance against Toxoplasma gondii. *Journal of Immunology* , 193(11), pp.5470–5479.

Orecchioni, M. et al., 2019. Macrophage Polarization: Different Gene Signatures in M1(LPS+) vs. Classically and M2(LPS-) vs. Alternatively Activated Macrophages. *Frontiers in Immunology*, 10, p.1084.

Osorio, E.Y. et al., 2020. In-situ proliferation contributes to the accumulation of myeloid cells in the spleen during progressive experimental visceral leishmaniasis. *PloS One*, 15(11), p.e0242337.

Owens, B.M.J. et al., 2012. IL-10-producing Th1 cells and disease progression are regulated by distinct CD11c^{+} cell populations during visceral leishmaniasis. *PLoS Pathogens*, 8(7), p.e1002827.

Ozato, K. et al., 2008. TRIM family proteins and their emerging roles in innate immunity. *Nature Reviews. Immunology*, 8(11), pp.849–860.

Pal, B. et al., 2017. Assessment of quality of life in patients with post kalaazar dermal leishmaniasis. *Health and Quality of Life Outcomes*, 15(1), p.148.

Palis, J. et al., 1999. Development of erythroid and myeloid progenitors in the yolk sac and embryo proper of the mouse. *Development* , 126(22), pp.5073–5084.

Palis, J. et al., 2001. Spatial and temporal emergence of high proliferative potential hematopoietic precursors during murine embryogenesis. *Proceedings of the National Academy of Sciences of the United States of America*, 98(8), pp.4528–4533.

Parkash, V. et al., 2021. A clinical study to optimise a sand fly biting protocol for use in a controlled human infection model of cutaneous leishmaniasis (the FLYBITE study). *Wellcome Open Research*, 6, p.168.

Park, B.S. & Lee, J.-O., 2013. Recognition of lipopolysaccharide pattern by TLR4 complexes. *Experimental & Molecular Medicine*, 45(12), pp.e66–e66.

Passegué, E., Wagner, E.F. & Weissman, I.L., 2004. JunB deficiency leads to a myeloproliferative disorder arising from hematopoietic stem cells. *Cell*, 119(3), pp.431–443.

Patel, L.R. et al., 2023. Genome-wide CRISPR-Cas9 screen analyzed by SLIDER identifies network of repressor complexes that regulate TRIM24. *iScience*, 26(7), p.107126.

Pathiraja, T.N. et al., 2015. TRIM24 links glucose metabolism with transformation of human mammary epithelial cells. *Oncogene*, 34(22), pp.2836–2845.

Pelletier, A. et al., 2022. Epigenetic and Transcriptomic Programming of HSC Quiescence Signaling in Large for Gestational Age Neonates. *International Journal of Molecular Sciences*, 23(13). Available at: http://dx.doi.org/10.3390/ijms23137323.

Perez-Lloret, J. et al., 2016. T-cell-intrinsic Tif1α/Trim24 regulates IL-1R expression on TH2 cells and TH2 cell-mediated airway allergy. *Proceedings of the National Academy of Sciences of the United States of America*, 113(5), pp.E568–76.

Pesu, M. et al., 2006. Proprotein convertase furin is preferentially expressed in T helper 1 cells and regulates interferon gamma. *Blood*, 108(3), pp.983–985.

Petit, V. et al., 2019. TRIM33 deficiency in monocytes and macrophages impairs resolution of colonic inflammation. *EBioMedicine*, 44, pp.60–70.

Pfeiffer, T., Schuster, S. & Bonhoeffer, S., 2001. Cooperation and competition in the evolution of ATP-producing pathways. *Science*, 292(5516), pp.504–507.

Philippe, L. et al., 2018. La-related protein 1 (LARP1) repression of TOP mRNA translation is mediated through its cap-binding domain and controlled by an adjacent regulatory region. *Nucleic Acids Research*, 46(3), pp.1457–1469.

Phillips, R. et al., 2010. Innate Killing of Leishmania donovani by Macrophages of the Splenic Marginal Zone Requires IRF-7. *PLoS Pathogens*, 6(3), p.e1000813.

Pimenta, P.F. et al., 1994. Evidence that the vectorial competence of phlebotomine sand flies for different species of Leishmania is controlled by structural polymorphisms in the surface lipophosphoglycan. *Proceedings of the National Academy of Sciences of the United States of America*, 91(19), pp.9155–9159.

Pinto, A.I. et al., 2017. TNF signalling drives expansion of bone marrow CD4+ T cells responsible for HSC exhaustion in experimental visceral leishmaniasis. *PLoS Pathogens*, 13(7), p.e1006465.

Pitale, D.M. et al., 2019. Leishmania donovani Induces Autophagy in Human Blood-Derived Neutrophils. *Journal of Immunology* , 202(4), pp.1163–1175.

Platanitis, E. et al., 2019. A molecular switch from STAT2-IRF9 to ISGF3 underlies interferon-induced gene transcription. *Nature Communications*, 10(1), pp.1–17.

Plüddemann, A., Mukhopadhyay, S. & Gordon, S., 2011. Innate immunity to intracellular pathogens: macrophage receptors and responses to microbial entry. *Immunological Reviews*, 240(1), pp.11–24.

Polley, R. et al., 2006. Adoptive immunotherapy against experimental visceral leishmaniasis with CD8+ T cells requires the presence of cognate antigen. *Infection and Immunity*, 74(1), pp.773–776.

Polley, R. et al., 2005. Chronic Leishmania donovani infection promotes bystander CD8+-T-cell expansion and heterologous immunity. *Infection and Immunity*, 73(12), pp.7996–8001.

Polli, M. et al., 2005. The development of functional B lymphocytes in conditional PU.1 knock-out mice. *Blood*, 106(6), pp.2083–2090.

Porcheray, F. et al., 2005. Macrophage activation switching: an asset for the resolution of inflammation. *Clinical and Experimental Immunology*, 142(3), pp.481–489.

Postat, J. et al., 2018. A Metabolism-Based Quorum Sensing Mechanism Contributes to Termination of Inflammatory Responses. *Immunity*, 49(4), pp.654–665.e5.

Pragallapati, S. & Manyam, R., 2019. Glucose transporter 1 in health and disease. *Journal of oral and maxillofacial pathology: JOMFP*, 23(3), pp.443–449.

Preham, O. et al., 2018. CD4+ T Cells Alter the Stromal Microenvironment and Repress Medullary Erythropoiesis in Murine Visceral Leishmaniasis. *Frontiers in Immunology*, 9, p.2958.

Qing, J. et al., 2020. Mitochondrial metabolism in regulating macrophage polarization: an emerging regulator of metabolic inflammatory diseases. *Acta Biochimica et Biophysica Sinica*, 52(9), pp.917–926.

Qin, W. et al., 2019. S-glycosylation-based cysteine profiling reveals regulation of glycolysis by itaconate. *Nature Chemical Biology*, 15(10), pp.983–991.

Qi, Y., Wang, M. & Jiang, Q., 2022. PABPC1--mRNA stability, protein translation and tumorigenesis. *Frontiers in Oncology*, 12, p.1025291.

Quirino Gustavo F. S. et al., 2016. Interleukin-27 (IL-27) Mediates Susceptibility to Visceral Leishmaniasis by Suppressing the IL-17–Neutrophil Response. *Infection and Immunity*, 84(8), pp.2289–2298.

Rabhi, S. et al., 2016. Lipid Droplet Formation, Their Localization and Dynamics during Leishmania major Macrophage Infection. *PloS One*, 11(2), p.e0148640.

Raes, G. et al., 2005. Arginase-1 and Ym1 are markers for murine, but not human, alternatively activated myeloid cells. *Journal of Immunology* , 174(11), p.6561; author reply 6561–2.

Raes, G. et al., 2002. FIZZ1 and Ym as tools to discriminate between differentially activated macrophages. *Developmental Immunology*, 9(3), pp.151–159.

Rajsbaum, R., García-Sastre, A. & Versteeg, G.A., 2014. TRIMmunity: the roles of the TRIM E3-ubiquitin ligase family in innate antiviral immunity. *Journal of Molecular Biology*, 426(6), pp.1265–1284.

Rajsbaum, R., Stoye, J.P. & O'Garra, A., 2008. Type I interferon-dependent and -independent expression of tripartite motif proteins in immune cells. *European Journal of Immunology*, 38(3), pp.619–630.

Rani, G.F. et al., 2021. Dissecting pathways to thrombocytopenia in a mouse model of visceral leishmaniasis. *Blood Advances*, 5(6), pp.1627–1637.

Ratcliffe, P.J. et al., 1998. Oxygen sensing, hypoxia-inducible factor-1 and the regulation of mammalian gene expression. *The Journal of Experimental Biology*, 201(Pt 8), pp.1153–1162.

Rath, M. et al., 2014. Metabolism via Arginase or Nitric Oxide Synthase: Two Competing Arginine Pathways in Macrophages. *Frontiers in Immunology*, 5, p.532.

Ratna, A. et al., 2021. Myeloid Endoplasmic Reticulum Resident Chaperone GP96 Facilitates Inflammation and Steatosis in Alcohol-Associated Liver Disease. *Hepatology Communications*, 5(7), pp.1165–1182.

Relloso, M. et al., 2002. DC-SIGN (CD209) expression is IL-4 dependent and is negatively regulated by IFN, TGF-beta, and anti-inflammatory agents. *Journal of Immunology* , 168(6), pp.2634–2643.

Requena, J.M. et al., 2000. Immune and clinical parameters associated with Leishmania infantum infection in the golden hamster model. *Veterinary Immunology and Immunopathology*, 76(3-4), pp.269–281.

Reymond, A. et al., 2001. The tripartite motif family identifies cell compartments. *The EMBO Journal*, 20(9), pp.2140–2151.

Ribeiro, C.V. et al., 2020. Leishmania infantum induces high phagocytic capacity and intracellular nitric oxide production by human proinflammatory monocyte. *Memorias do Instituto Oswaldo Cruz*, 115, p.e190408.

Ribeiro-Gomes, F.L. et al., 2012. Efficient capture of infected neutrophils by dendritic cells in the skin inhibits the early anti-leishmania response. *PLoS Pathogens*, 8(2), p.e1002536.

Rice, H.M. et al., 2020. rM-CSF efficiently replaces L929 in generating mouse and rat bone marrow-derived macrophages for in vitro functional studies of immunity to intracellular bacteria. *Journal of Immunological Methods*, 477, p.112693.

van Riel, B. & Rosenbauer, F., 2014. Epigenetic control of hematopoiesis: the PU.1 chromatin connection. *Biological Chemistry*, 395(11), pp.1265–1274.

Riley, L.G. et al., 2016. LARS2 Variants Associated with Hydrops, Lactic Acidosis, Sideroblastic Anemia, and Multisystem Failure. *JIMD Reports*, 28, pp.49–57.

Rodríguez-Prados, J.-C. et al., 2010. Substrate fate in activated macrophages: a comparison between innate, classic, and alternative activation. *Journal of Immunology* , 185(1), pp.605–614.

Romano, A. et al., 2021. Interferon-γ-Producing CD4+ T Cells Drive Monocyte Activation in the Bone Marrow During Experimental Leishmania donovani Infection. *Frontiers in Immunology*, 12, p.700501.

Romano, E. et al., 2018. BNIP3 modulates the interface between B16-F10 melanoma cells and immune cells. *Oncotarget*, 9(25), pp.17631–17644.

Rosas, L.E. et al., 2006. Interleukin-27R (WSX-1/T-cell cytokine receptor) gene-deficient mice display enhanced resistance to leishmania donovani infection but develop severe liver immunopathology. *The American Journal of Pathology*, 168(1), pp.158–169.

Rőszer, T., 2015. Understanding the Mysterious M2 Macrophage through Activation Markers and Effector Mechanisms. *Mediators of Inflammation*, 2015, p.816460.

Roth, W. et al., 2002. Identification and characterization of DEDD2, a death effector domain-containing protein. *The Journal of Biological Chemistry*, 277(9), pp.7501–7508.

Rowe, H.M. et al., 2010. KAP1 controls endogenous retroviruses in embryonic stem cells. *Nature*, 463(7278), pp.237–240.

Roy, G. et al., 2000. Episomal and stable expression of the luciferase reporter gene for quantifying Leishmania spp. infections in macrophages and in animal models. *Molecular and Biochemical Parasitology*, 110(2), pp.195–206.

Roy, S. et al., 2018. An IL-10 dominant polarization of monocytes is a feature of Indian Visceral Leishmaniasis. *Parasite Immunology*, 40(7), p.e12535.

Ruffell, D. et al., 2009. A CREB-C/EBPbeta cascade induces M2 macrophage-specific gene expression and promotes muscle injury repair. *Proceedings of the National Academy of Sciences of the United States of America*, 106(41), pp.17475–17480.

Ryckman, C. et al., 2003. Proinflammatory activities of S100: proteins S100A8, S100A9, and S100A8/A9 induce neutrophil chemotaxis and adhesion. *Journal of Immunology* , 170(6), pp.3233–3242.

Salguero, F.J. et al., 2018. Histopathological and immunohistochemical characterisation of hepatic granulomas in Leishmania donovani -infected BALB/c mice: a time-course study. *Parasites & Vectors*, 11(1), pp.1–9.

Sanchez, J.G. et al., 2014. The tripartite motif coiled-coil is an elongated antiparallel hairpin dimer. *Proceedings of the National Academy of Sciences of the United States of America*, 111(7), pp.2494–2499.

Sanchez, R. & Zhou, M.-M., 2011. The PHD finger: a versatile epigenome reader. *Trends in Biochemical Sciences*, 36(7), pp.364–372.

Santaguida, M. et al., 2009. JunB protects against myeloid malignancies by limiting hematopoietic stem cell proliferation and differentiation without affecting self-renewal. *Cancer Cell*, 15(4), pp.341–352.

Sarkar, A. et al., 2011. Monitoring of intracellular nitric oxide in leishmaniasis: its applicability in patients with visceral leishmaniasis. *Cytometry. Part A: the Journal of the International Society for Analytical Cytology*, 79(1), pp.35–45.

Sato, A. et al., 2020. C/EBPβ isoforms sequentially regulate regenerating mouse hematopoietic stem/progenitor cells. *Blood Advances*, 4(14), pp.3343–3356.

Sato, N. et al., 1999. Defects in the generation of IFN-gamma are overcome to control infection with Leishmania donovani in CC chemokine receptor (CCR) 5-, macrophage inflammatory protein-1 alpha-, or CCR2-deficient mice. *Journal of Immunology* , 163(10), pp.5519–5525.

Satoskar, A., Bluethmann, H. & Alexander, J., 1995. Disruption of the murine interleukin-4 gene inhibits disease progression during Leishmania mexicana infection but does not increase control of Leishmania donovani infection. *Infection and Immunity*, 63(12), pp.4894–4899.

Saxton, R.A. & Sabatini, D.M., 2017. mTOR Signaling in Growth, Metabolism, and Disease. *Cell*, 168(6), pp.960–976.

Scanga, C.A. et al., 2001. The inducible nitric oxide synthase locus confers protection against aerogenic challenge of both clinical and laboratory strains of Mycobacterium tuberculosis in mice. *Infection and Immunity*, 69(12), pp.7711–7717.

Schroder, K. et al., 2004. Interferon-gamma: an overview of signals, mechanisms and functions. *Journal of Leukocyte Biology*, 75(2), pp.163–189.

Schultz, D.C. et al., 2002. SETDB1: a novel KAP-1-associated histone H3, lysine 9-specific methyltransferase that contributes to HP1-mediated silencing of euchromatic genes by KRAB zinc-finger proteins. *Genes & Development*, 16(8), pp.919–932.

Scott, C.L. et al., 2016. Bone marrow-derived monocytes give rise to self-renewing and fully differentiated Kupffer cells. *Nature Communications*, 7, p.10321.

Serbina, N.V. & Pamer, E.G., 2006. Monocyte emigration from bone marrow during bacterial infection requires signals mediated by chemokine receptor CCR2. *Nature Immunology*, 7(3), pp.311–317.

Shadab, M. et al., 2019. RNA-Seq Revealed Expression of Many Novel Genes Associated With Leishmania donovani Persistence and Clearance in the Host Macrophage. *Frontiers in Cellular and Infection Microbiology*, 9, p.17.

Shah, V.V. et al., 2021. Mammary-specific expression of Trim24 establishes a mouse model of human metaplastic breast cancer. *Nature Communications*, 12(1), p.5389.

Shapiro, S.D., Kobayashi, D.K. & Ley, T.J., 1993. Cloning and characterization of a unique elastolytic metalloproteinase produced by human alveolar macrophages. *The Journal of Biological Chemistry*, 268(32), pp.23824–23829.

Shaw, J., 2018. *Trim24 in Normal & Malignant Hematopoiesis*. The Texas Medical Center Library. Available at: https://digitalcommons.library.tmc.edu/utgsbs_dissertations/833/ [Accessed March 16, 2023].

Shi, K. et al., 2022. Bone marrow hematopoiesis drives multiple sclerosis progression. *Cell*, 185(13), pp.2234–2247.e17.

Sierra-Filardi, E. et al., 2014. CCL2 shapes macrophage polarization by GM-CSF and M-CSF: identification of CCL2/CCR2-dependent gene expression profile. *Journal of Immunology* , 192(8), pp.3858–3867.

Sierra, M.I., Wright, M.H. & Nash, P.D., 2010. AMSH Interacts with ESCRT-0 to Regulate the Stability and Trafficking of CXCR4*. *The Journal of Biological Chemistry*, 285(18), pp.13990–14004.

Simmons, D.P. et al., 2022. SLAMF7 engagement superactivates macrophages in acute and chronic inflammation. *Science Immunology*, 7(68), p.eabf2846.

Simsek, T. et al., 2010. The distinct metabolic profile of hematopoietic stem cells reflects their location in a hypoxic niche. *Cell Stem Cell*, 7(3), pp.380–390.

Singh, A.K. et al., 2012. Intracellular pathogen Leishmania donovani activates hypoxia inducible factor-1 by dual mechanism for survival advantage within macrophage. *PloS One*, 7(6), p.e38489.

Singh, P., Mohammad, K.S. & Pelus, L.M., 2020. CXCR4 expression in the bone marrow microenvironment is required for hematopoietic stem and progenitor cell maintenance and early hematopoietic regeneration after myeloablation. *Stem Cells*, 38(7), pp.849–859.

Sironi, M. et al., 2006. Differential regulation of chemokine production by Fcgamma receptor engagement in human monocytes: association of CCL1 with a distinct form of M2 monocyte activation (M2b, Type 2). *Journal of Leukocyte Biology*, 80(2), pp.342–349.

Soler Palacios, B. et al., 2015. Macrophages from the synovium of active rheumatoid arthritis exhibit an activin A-dependent pro-inflammatory profile. *The Journal of Pathology*, 235(3), pp.515–526.

Sreejit, G. et al., 2020. Origins and diversity of macrophages in health and disease. *Clinical & Translational Immunology*, 9(12), p.e1222.

Stäger, S. et al., 2003. Both interleukin-4 (IL-4) and IL-4 receptor alpha signaling contribute to the development of hepatic granulomas with optimal antileishmanial activity. *Infection and Immunity*, 71(8), pp.4804–4807.

Stäger, S. et al., 2006. Distinct roles for IL-6 and IL-12p40 in mediating protection against Leishmania donovani and the expansion of IL-10+ CD4+ T cells. *European Journal of Immunology*, 36(7), pp.1764–1771.

Stäger, S. & Rafati, S., 2012. CD8(+) T cells in leishmania infections: friends or foes? *Frontiers in Immunology*, 3, p.5.

Stanley, A.C. & Engwerda, C.R., 2007. Balancing immunity and pathology in visceral leishmaniasis. *Immunology and Cell Biology*, 85(2), pp.138–147.

Stanley, E.R., Chen, D.M. & Lin, H.S., 1978. Induction of macrophage production and proliferation by a purified colony stimulating factor. *Nature*, 274(5667), pp.168–170.

von Stebut, E. et al., 1998. Uptake of Leishmania major amastigotes results in activation and interleukin 12 release from murine skin-derived dendritic cells: implications for the initiation of anti-Leishmania immunity. *The Journal of Experimental Medicine*, 188(8), pp.1547–1552.

Steimle, V. et al., 1994. Regulation of MHC class II expression by interferon-gamma mediated by the transactivator gene CIITA. *Science*, 265(5168), pp.106–109.

Stein, M. et al., 1992. Interleukin 4 potently enhances murine macrophage mannose receptor activity: a marker of alternative immunologic macrophage activation. *The Journal of Experimental Medicine*, 176(1), pp.287–292.

Stern, J.J. et al., 1988. Role of L3T4+ and LyT-2+ cells in experimental visceral leishmaniasis. *Journal of Immunology* , 140(11), pp.3971–3977.

Stout, R.D. et al., 2005. Macrophages sequentially change their functional phenotype in response to changes in microenvironmental influences. *Journal of Immunology* , 175(1), pp.342–349.

Strong, N. et al., 2013. Inhibitor of differentiation 1 (Id1) and Id3 proteins play different roles in TGFβ effects on cell proliferation and migration in prostate cancer cells. *The Prostate*, 73(6), pp.624–633.

Stuehr, D.J. & Nathan, C.F., 1989. Nitric oxide. A macrophage product responsible for cytostasis and respiratory inhibition in tumor target cells. *The Journal of Experimental Medicine*, 169(5), pp.1543–1555.

Su, C., Li, H. & Gao, W., 2018. TRIM28 is overexpressed in glioma and associated with tumor progression. *OncoTargets and Therapy*, 11, pp.6447–6458.

Suda, T., Takubo, K. & Semenza, G.L., 2011. Metabolic regulation of hematopoietic stem cells in the hypoxic niche. *Cell Stem Cell*, 9(4), pp.298–310.

Sugiyama, T. et al., 2006. Maintenance of the hematopoietic stem cell pool by CXCL12-CXCR4 chemokine signaling in bone marrow stromal cell niches. *Immunity*, 25(6), pp.977–988.

Sugiyama, T., Omatsu, Y. & Nagasawa, T., 2019. Niches for hematopoietic stem cells and immune cell progenitors. *International Immunology*, 31(1), pp.5–11.

Sundar, S. et al., 1997. Circulating T helper 1 (Th1) cell- and Th2 cell-associated cytokines in Indian patients with visceral leishmaniasis. *The American Journal of Tropical Medicine and Hygiene*, 56(5), pp.522–525.

Sun, L. et al., 2015. Ex vivo and in vitro effect of serum amyloid a in the induction of macrophage M2 markers and efferocytosis of apoptotic neutrophils. *Journal of Immunology* , 194(10), pp.4891–4900.

Sun, Y. & Xu, S., 2018. Tumor-Associated CD204-Positive Macrophage Is a Prognostic Marker in Clinical Stage I Lung Adenocarcinoma. *BioMed Research International*, 2018, p.8459193.

Suzuki, M. et al., 2009. Tetraspanin CD9 negatively regulates lipopolysaccharide-induced macrophage activation and lung inflammation. *Journal of Immunology* , 182(10), pp.6485–6493.

Szabo, S.J. et al., 2000. A novel transcription factor, T-bet, directs Th1 lineage commitment. *Cell*, 100(6), pp.655–669.

Tailleux, L. et al., 2005. DC-SIGN induction in alveolar macrophages defines privileged target host cells for mycobacteria in patients with tuberculosis. *PLoS Medicine*, 2(12), p.e381.

Takahashi, K., Yamamura, F. & Naito, M., 1989. Differentiation, maturation, and proliferation of macrophages in the mouse yolk sac: a light-microscopic, enzyme-cytochemical, immunohistochemical, and ultrastructural study. *Journal of Leukocyte Biology*, 45(2), pp.87–96.

Takubo, K. et al., 2013. Regulation of glycolysis by Pdk functions as a metabolic checkpoint for cell cycle quiescence in hematopoietic stem cells. *Cell Stem Cell*, 12(1), pp.49–61.

Talaiezadeh, A. et al., 2015. Kinetic characterization of lactate dehydrogenase in normal and malignant human breast tissues. *Cancer Cell International*, 15, p.19.

Tamura, A. et al., 2017. C/EBPβ is required for survival of Ly6C- monocytes. *Blood*, 130(16), pp.1809–1818.

Tamura, T., Kurotaki, D. & Koizumi, S.-I., 2015. Regulation of myelopoiesis by the transcription factor IRF8. *International Journal of Hematology*, 101(4), pp.342–351.

Tanaka, S. et al., 2018. Trim33 mediates the proinflammatory function of Th17 cells. *The Journal of Experimental Medicine*, 215(7), pp.1853–1868.

Taylor, C.T. & Scholz, C.C., 2022. The effect of HIF on metabolism and immunity. *Nature Reviews. Nephrology*, 18(9), pp.573–587.

Terrazas, C. et al., 2017. Ly6Chi inflammatory monocytes promote susceptibility to Leishmania donovani infection. *Scientific Reports*, 7(1), p.14693.

Thomas, D.D. et al., 2001. The biological lifetime of nitric oxide: implications for the perivascular dynamics of NO and O2. *Proceedings of the National Academy of Sciences of the United States of America*, 98(1), pp.355–360.

Tisserand, J. et al., 2011. Tripartite motif 24 (Trim24/Tif1α) tumor suppressor protein is a novel negative regulator of interferon (IFN)/signal transducers and activators of transcription (STAT) signaling pathway acting through retinoic acid receptor α (Rarα) inhibition. *The Journal of Biological Chemistry*, 286(38), pp.33369–33379.

Toniato, E. et al., 2002. TRIM8/GERP RING finger protein interacts with SOCS-1. *The Journal of Biological Chemistry*, 277(40), pp.37315–37322.

Torres-Guerrero, E. et al., 2017. Leishmaniasis: a review. *F1000Research*, 6, p.750.

Trzebanski, S. et al., 2023. Murine classical monocyte subsets display distinct functions and fates. *bioRxiv*, p.2023.07.29.551083. Available at: https://www.biorxiv.org/content/10.1101/2023.07.29.551083v1 [Accessed October 13, 2023].

Tsai, C.-F. et al., 2021. Regulatory Effects of Quercetin on M1/M2 Macrophage Polarization and Oxidative/Antioxidative Balance. *Nutrients*, 14(1). Available at: http://dx.doi.org/10.3390/nu14010067.

Tsai, W.-W. et al., 2010. TRIM24 links a non-canonical histone signature to breast cancer. *Nature*, 468(7326), pp.927–932.

Tsikas, D., 2007. Analysis of nitrite and nitrate in biological fluids by assays based on the Griess reaction: appraisal of the Griess reaction in the L-arginine/nitric oxide area of research. *Journal of Chromatography. B, Analytical Technologies in the Biomedical and Life Sciences*, 851(1-2), pp.51–70.

Tucci, S. et al., 2017. Triheptanoin: long-term effects in the very long-chain acyl-CoA dehydrogenase-deficient mouse. *Journal of Lipid Research*, 58(1), pp.196–207.

Ty, M.C. et al., 2019. Immuno-metabolic profile of human macrophages after Leishmania and Trypanosoma cruzi infection. *PloS One*, 14(12), p.e0225588.

Uribe-Querol, E. & Rosales, C., 2020. Phagocytosis: Our Current Understanding of a Universal Biological Process. *Frontiers in Immunology*, 11, p.1066.

Vadiveloo, P.K. et al., 2000. Role of type I interferons during macrophage activation by lipopolysaccharide. *Cytokine*, 12(11), pp.1639–1646.

Van Bockstal, L. et al., 2020. Interferon alpha favors macrophage infection by visceral Leishmania species through upregulation of sialoadhesin expression. *Frontiers in Immunology*, 11, p.1113.

Varma, N. & Naseem, S., 2010. Hematologic changes in visceral leishmaniasis/kala azar. *Indian Journal of Hematology & Blood Transfusion: an Official Journal of Indian Society of Hematology and Blood Transfusion*, 26(3), pp.78–82.

Venugopal, G. et al., 2022. In vivo transcriptional analysis of mice infected with Leishmania major unveils cellular heterogeneity and altered transcriptomic profiling at single-cell resolution. *PLoS Neglected Tropical Diseases*, 16(7), p.e0010518.

Wagner, J.M. et al., 2016. Mechanism of B-box 2 domain-mediated higher-order assembly of the retroviral restriction factor TRIM5α. *eLife*, 5, p.e16309.

Wang, C. et al., 2005. MDM2 interaction with nuclear corepressor KAP1 contributes to p53 inactivation. *The EMBO Journal*, 24(18), pp.3279–3290.

Wang, H. et al., 2019. Transcription factors IRF8 and PU.1 are required for follicular B cell development and BCL6-driven germinal center responses. *Proceedings of the National Academy of Sciences*, 116(19), pp.9511–9520.

Wang, L. et al., 2012. Heat shock protein 70 (Hsp70) inhibits oxidative phosphorylation and compensates ATP balance through enhanced glycolytic activity. *Journal of Applied Physiology*, 113(11), pp.1669–1676.

Wang, N., Liang, H. & Zen, K., 2014. Molecular mechanisms that influence the macrophage m1-m2 polarization balance. *Frontiers in Immunology*, 5, p.614.

Wang, Q. et al., 2010. Fra-1 protooncogene regulates IL-6 expression in macrophages and promotes the generation of M2d macrophages. *Cell Research*, 20(6), pp.701–712.

Wang, X.-Q. et al., 2002. Down-regulation of macrophage CD9 expression by interferon-gamma. *Biochemical and Biophysical Research Communications*, 290(3), pp.891–897.

Wang, Y. et al., 2016. KAP1 is overexpressed in hepatocellular carcinoma and its clinical significance. *International Journal of Clinical Oncology*, 21(5), pp.927–933.

Wang, Z. et al., 2016. Complex Regulation Pattern of IRF3 Activation Revealed by a Novel Dimerization Reporter System. *Journal of Immunology* , 196(10), pp.4322–4330.

Wan, X. et al., 2002. A TNF family member LIGHT transduces costimulatory signals into human T cells. *Journal of Immunology* , 169(12), pp.6813–6821.

Watt, S. et al., 2021. Genetic perturbation of PU.1 binding and chromatin looping at neutrophil enhancers associates with autoimmune disease. *Nature Communications*, 12(1), pp.1–12.

Weinkopff, T. et al., 2019. Leishmania Infection Induces Macrophage Vascular Endothelial Growth Factor A Production in an ARNT/HIF-Dependent Manner. *Infection and Immunity*, 87(11). Available at: http://dx.doi.org/10.1128/IAI.00088-19.

Weiss, M. et al., 2013. IRF5 is a specific marker of inflammatory macrophages in vivo. *Mediators of Inflammation*, 2013, p.245804.

Welch, J.S. et al., 2002. TH2 cytokines and allergic challenge induce Ym1 expression in macrophages by a STAT6-dependent mechanism. *The Journal of Biological Chemistry*, 277(45), pp.42821–42829.

Weng, L. et al., 2014. The E3 ubiquitin ligase tripartite motif 33 is essential for cytosolic RNA-induced NLRP3 inflammasome activation. *Journal of Immunology* , 193(7), pp.3676–3682.

WHO, 2019. Leishmaniasis. *World Health Organization*. Available at: https://www.who.int/en/news-room/fact-sheets/detail/leishmaniasis [Accessed December 23, 2019].

Wickramasinghe, S.N., Abdalla, S.H. & Kasili, E.G., 1987. Ultrastructure of bone marrow in patients with visceral leishmaniasis. *Journal of Clinical Pathology*, 40(3), pp.267–275.

Wiesheu, R. et al., 2020. Ly6C defines a subset of memory-like CD27+ γδ T cells with inducible cancer-killing function. *bioRxiv*, p.2020.09.08.287854. Available at: https://www.biorxiv.org/content/10.1101/2020.09.08.287854v1 [Accessed March 9, 2023].

Wiktor-Jedrzejczak, W. et al., 1990. Total absence of colony-stimulating factor 1 in the macrophage-deficient osteopetrotic (op/op) mouse. *Proceedings of the National Academy of Sciences of the United States of America*, 87(12), pp.4828–4832.

Wiktor-Jedrzejczak, W.W. et al., 1982. Hematological characterization of congenital osteopetrosis in op/op mouse. Possible mechanism for abnormal macrophage differentiation. *The Journal of Experimental Medicine*, 156(5), pp.1516–1527.

Wilson, A. et al., 2008. Hematopoietic stem cells reversibly switch from dormancy to self-renewal during homeostasis and repair. *Cell*, 135(6), pp.1118–1129.

Wilson, M.E. & Pearson, R.D., 1988. Roles of CR3 and mannose receptors in the attachment and ingestion of Leishmania donovani by human mononuclear phagocytes. *Infection and Immunity*, 56(2), pp.363–369.

Wright, S.D. et al., 1990. CD14, a receptor for complexes of lipopolysaccharide (LPS) and LPS binding protein. *Science*, 249(4975), pp.1431–1433.

Wu, J. et al., 2020. The E3 ubiquitin ligase MARCH1 regulates antimalaria immunity through interferon signaling and T cell activation. *Proceedings of the National Academy of Sciences of the United States of America*. Available at: http://dx.doi.org/10.1073/pnas.2004332117.

Wu, X. et al., 2006. Proteasome inhibitors uncouple rhesus TRIM5alpha restriction of HIV-1 reverse transcription and infection. *Proceedings of the National Academy of Sciences of the United States of America*, 103(19), pp.7465–7470.

Wu, Y. et al., 2023. SLAMF7 regulates the inflammatory response in macrophages during polymicrobial sepsis. *The Journal of Clinical Investigation*, 133(6). Available at: http://dx.doi.org/10.1172/JCI150224.

Wynn, T.A., Chawla, A. & Pollard, J.W., 2013. Macrophage biology in development, homeostasis and disease. *Nature*, 496(7446), pp.445–455.

Xie, C. et al., 2021. CCL7 contributes to angiotensin II-induced abdominal aortic aneurysm by promoting macrophage infiltration and pro-inflammatory phenotype. *Journal of Cellular and Molecular Medicine*, 25(15), pp.7280–7293.

Xie, X. et al., 2020. Single-cell transcriptome profiling reveals neutrophil heterogeneity in homeostasis and infection. *Nature Immunology*, 21(9), pp.1119–1133.

Xue, D. et al., 2015. Clinical significance and biological roles of TRIM24 in human bladder carcinoma. *Tumour Biology: the Journal of the International Society for Oncodevelopmental Biology and Medicine*, 36(9), pp.6849–6855.

Xue, J. et al., 2014. Transcriptome-based network analysis reveals a spectrum model of human macrophage activation. *Immunity*, 40(2), pp.274–288.

Xu, Z.-J. et al., 2020. The M2 macrophage marker CD206: a novel prognostic indicator for acute myeloid leukemia. *Oncoimmunology*, 9(1), p.1683347.

Yaddanapudi, K. et al., 2013. Control of tumor-associated macrophage alternative activation by macrophage migration inhibitory factor. *Journal of Immunology* , 190(6), pp.2984–2993.

Yamamoto, M. et al., 2003. Role of adaptor TRIF in the MyD88-independent toll-like receptor signaling pathway. *Science*, 301(5633), pp.640–643.

Yang, J. et al., 2014. Monocyte and macrophage differentiation: circulation inflammatory monocyte as biomarker for inflammatory diseases. *Biomarker Research*, 2(1), p.1.

Yang, Y. et al., 2020. OGT suppresses S6K1-mediated macrophage inflammation and metabolic disturbance. *Proceedings of the National Academy of Sciences*, 117(28), pp.16616–16625.

Yang, Y.H. et al., 2009. Annexin-1 regulates macrophage IL-6 and TNF via glucocorticoid-induced leucine zipper. *Journal of Immunology* , 183(2), pp.1435–1445.

Yeamans, C. et al., 2007. C/EBPalpha binds and activates the PU.1 distal enhancer to induce monocyte lineage commitment. *Blood*, 110(9), pp.3136–3142.

Yona, S. et al., 2013. Fate mapping reveals origins and dynamics of monocytes and tissue macrophages under homeostasis. *Immunity*, 38(1), pp.79–91.

Yoshida, H. et al., 1990. The murine mutation osteopetrosis is in the coding region of the macrophage colony stimulating factor gene. *Nature*, 345(6274), pp.442–444.

Yoshihama, M. et al., 2002. The human ribosomal protein genes: sequencing and comparative analysis of 73 genes. *Genome Research*, 12(3), pp.379–390.

Yu, T. et al., 2019. Modulation of M2 macrophage polarization by the crosstalk between Stat6 and Trim24. *Nature Communications*, 10(1), p.4353.

Yu, Y., Wang, S.E. & Hayward, G.S., 2005. The KSHV immediate-early transcription factor RTA encodes ubiquitin E3 ligase activity that targets IRF7 for proteosome-mediated degradation. *Immunity*, 22(1), pp.59–70.

Zajd, C.M. et al., 2020. Bone Marrow-Derived and Elicited Peritoneal Macrophages Are Not Created Equal: The Questions Asked Dictate the Cell Type Used. *Frontiers in Immunology*, 11, p.269.

van Zandbergen, G. et al., 2004. Cutting Edge: Neutrophil Granulocyte Serves as a Vector for Leishmania Entry into Macrophages. *The Journal of Immunology*, 173(11), pp.6521–6525.

Zanoni, I. et al., 2011. CD14 controls the LPS-induced endocytosis of Toll-like receptor 4. *Cell*, 147(4), pp.868–880.

Zhang, D.E. et al., 1994. The macrophage transcription factor PU.1 directs tissue-specific expression of the macrophage colony-stimulating factor receptor. *Molecular and Cellular Biology*, 14(1), pp.373–381.

Zhang, F. et al., 2012. Inhibition of the mTORC2 and chaperone pathways to treat leukemia. *Blood*, 119(25), pp.6080–6088.

Zhang, L. et al., 2017. Bioinformatics methods for identifying differentially expressed genes and signaling pathways in nano-silica stimulated macrophages. *Tumour Biology: the Journal of the International Society for Oncodevelopmental Biology and Medicine*, 39(6), p.1010428317709284.

Zhang, N. et al., 2018. Leishmania parasitophorous vacuole membranes display phosphoinositides that create conditions for continuous Akt activation and a target for miltefosine in Leishmania infections. *Cellular Microbiology*, 20(11), p.e12889.

Zhang, S. et al., 2022. Immunometabolic profiling of in vitro and ex vivo Leishmania-infected macrophages (LIMs) reveals unique polarization and bioenergetic signatures. *bioRxiv*, p.2022.09.08.507100. Available at: https://www.biorxiv.org/content/10.1101/2022.09.08.507100v1.full [Accessed August 10, 2023].

Zhang, W.W. & Matlashewski, G., 1997. Loss of virulence in Leishmania donovani deficient in an amastigote-specific protein, A2. *Proceedings of the National Academy of Sciences of the United States of America*, 94(16), pp.8807–8811.

Zhang, X. et al., 1994. Necessity and sufficiency of beta interferon for nitric oxide production in mouse peritoneal macrophages. *Infection and Immunity*, 62(1), pp.33–40.

Zhang, X., Goncalves, R. & Mosser, D.M., 2008. The isolation and characterization of murine macrophages. *Current Protocols in Immunology / edited by John E. Coligan ... [et al.]*, Chapter 14, p.Unit 14.1.

Zhang, Y. et al., 2013. A novel role of hematopoietic CCL5 in promoting triple-negative mammary tumor progression by regulating generation of myeloid-derived suppressor cells. *Cell research*, 23(3), pp.394–408.

Zheng, C. et al., 2019. Inflammatory Role of TLR-MyD88 Signaling in Multiple Sclerosis. *Frontiers in Molecular Neuroscience*, 12, p.314.

Zhou, A. et al., 2021. Comprehensive Transcriptomic Analysis Identifies Novel Antiviral Factors Against Influenza A Virus Infection. *Frontiers in Immunology*, 12, p.632798.

Zhu, J. & Emerson, S.G., 2002. Hematopoietic cytokines, transcription factors and lineage commitment. *Oncogene*, 21(21), pp.3295–3313.

Zhu, Q. et al., 2020. TRIM24 facilitates antiviral immunity through mediating K63-linked TRAF3 ubiquitination. *The Journal of Experimental Medicine*, 217(7). Available at: http://dx.doi.org/10.1084/jem.20192083.

Zhu, Y. et al., 2018. TRIM24 promotes hepatocellular carcinoma progression via AMPK signaling. *Experimental Cell Research*, 367(2), pp.274–281.

Zijlstra, E.E. et al., 2003. Post-kala-azar dermal leishmaniasis. *The Lancet Infectious Diseases*, 3(2), pp.87–98.

Zilio, S. et al., 2022. CCR1 and CCR5 mediate cancer-induced myelopoiesis and differentiation of myeloid cells in the tumor. *Journal for ImmunoTherapy of Cancer*, 10(1), p.e003131.

Zizzo, G. et al., 2012. Efficient clearance of early apoptotic cells by human macrophages requires M2c polarization and MerTK induction. *Journal of Immunology* , 189(7), pp.3508–3520.

List of Abbreviations

5'TOP mRNA	5'terminal oligopyrimidine tract
APC	Antigen presenting cell
B6	C57BL/6 mouse strain
BFA	Brefeldin A
BM	Bone marrow
BMDM	Bone marrow-derived macrophage
BSA	Bovine serum albumin
CBP	CREB-binding protein
cDC	Conventional dendritic cell
CL	Cutaneous leishmaniasis
CTL	$CD8^+$ Cytotoxic T Lymphocyte
DAPI	4′,6-diamidino-2-phenylindole
DEG	Differentially expressed gene
DGE	Differential gene expression (analysis)
DMEM	Dulbecco's modified eagle medium
EGFR	Epidermal growth factor receptor
ELISA	Enzyme-linked immunosorbent assay
FCS	Foetal calf serum
FDR	False discovery rate
FGFR2	Fibroblast growth factor receptor 2
GM-CSF	Granulocyte-macrophage colony stimulating factor
GMP	Granulocyte-monocyte progenitor
GO	Gene Ontology
GSEA	Gene set enrichment analysis
HCC	Hepatocellular carcinoma
HSPC	Haematopoietic stem and progenitor cells
IFN-I	Type 1 interferon
IFN-II	Type 2 interferon
IFNGR	Interferon gamma receptor
IFNγ	Interferon gamma
iLN	Inguinal lymph node
IRF	Interferon regulatory factor
KC	Kupffer cell

KO	*Trim24* knockout
LdBPK-130330.1	*L. donovani* gene encoding alpha-tubulin
LDU	Leishman Donovan Unit
log2FC	Log_2 fold change
LPS	Lipopolysaccharide
LV9	Ethiopian strain of *Leishmania donovani*
M-CSF	Macrophage colony stimulating factor
mAb	Monoclonal antibody
MCL	Mucocutaneous leishmaniasis
MFI	Mean Fluorescence Intensity
MHC II	Major histocompatibility complex class II
MMM	Marginal zone metallophilic macrophage
MOI	Multiplicity of infection
MPS	Mononuclear phagocyte system
mRNA	Messenger RNA
mTOR	Mechanistic target of rapamycin
mTORC	Mechanistic target of rapamycin complex
MZM	Marginal zone macrophage
NF-kB	Nuclear factor kappa B
NK	Natural killer cell
NO	Nitric oxide
Nos2 / iNOS	Inducible nitric oxide synthase
ns	Not statistically significant
ORA	Over-representation analysis
OxPhos	Oxidative Phosphorylation
p.a.d.	Post-adoptive transfer
p.i.	post-infection
PBMC	Peripheral blood mononuclear cell
PCA	Principal component analysis
pDC	Plasmacytoid dendritic cell
PEPCK	Phosphoenolpyruvate Carboxykinase
PHD	Plant homeodomain
PKDL	Post-kala azar dermal leishmaniasis
PMA	Phorbol-12-myristate-13-acetate

poly I:C	Polyinosinic:polycytidylic acid
QC	Quality control
qPCR	Quantitative polymerase chain reaction
Rara	Retinoic acid receptor alpha
RING	Really interesting new gene domain
RNA	Ribonucleic acid
RP	Red pulp
scRNA-seq	Single cell RNA sequencing
STAT	Signal transducer and activator of transcription
TCR	T cell receptor
Th1 / Th2	T helper cell 1 / 2
TIF	Transcription intermediary factor
TLR	Toll-like receptor
TNF	Tumour necrosis factor
TRIM	Tripartite motif-containing protein
UMAP	Uniform manifold approximation and projection
VL	Visceral leishmaniasis
WP	White pulp
WT	Wild-type